N/0002653--077

Contaminant Transport Parameters for the Groundwater Flow and Contaminant Transport Model of Corrective Action Units 101 and 102: Central and Western Pahute Mesa, Nye County, Nevada

Revision No.: 1

July 2021

Prepared for U.S. Department of Energy under Contract No.DE-NA0002653.

Available for sale to the public from:

U.S. Department of Commerce
National Technical Information Service
5301 Shawnee Road
Alexandria, VA 22312
Telephone: 800.553.6847
Fax: 703.605.6900
E-mail: *orders@ntis.gov*
Online Ordering: *http://www.ntis.gov/help/ordermethods.aspx*

Available electronically at *http://www.osti.gov/bridge*

Available for a processing fee to U.S. Department of Energy and its contractors, in paper, from:

U.S. Department of Energy
Office of Scientific and Technical Information
P.O. Box 62
Oak Ridge, TN 37831-0062
Phone: 865.576.8401
Fax: 865.576.5728
Email: *reports@adonis.osti.gov*

N/0002653--077

CONTAMINANT TRANSPORT PARAMETERS FOR THE GROUNDWATER FLOW AND CONTAMINANT TRANSPORT MODEL OF CORRECTIVE ACTION UNITS 101 AND 102: CENTRAL AND WESTERN PAHUTE MESA, NYE COUNTY, NEVADA

Revision No.: 1
July 2021
Navarro
c/o U.S. DOE
100 N. City Parkway, Suite 1750
Las Vegas, NV 89106

Prepared for U.S. Department of Energy under Contract No.DE-NA0002653..

TABLE OF CONTENTS

TABLE OF CONTENTS (CONTINUED)

TABLE OF CONTENTS (CONTINUED)

TABLE OF CONTENTS (CONTINUED)

TABLE OF CONTENTS (CONTINUED)

TABLE OF CONTENTS (CONTINUED)

LIST OF FIGURES

LIST OF FIGURES (CONTINUED)

LIST OF FIGURES (CONTINUED)

LIST OF TABLES

LIST OF TABLES (CONTINUED)

LIST OF TABLES (CONTINUED)

LIST OF TABLES (CONTINUED)

LIST OF PLATES

LIST OF ACRONYMS AND ABBREVIATIONS

General Acronyms and Abbreviations

1-D	One-dimensional
2-D	Two-dimensional
3-D	Three-dimensional
amsl	Above mean sea level
bgs	Below ground surface
BLM	Bureau of Land Management
BN	Bechtel Nevada
Bq/L	Becquerels per liter
°C	Degrees Celsius
CADD	Corrective action decision document
CAI	Corrective action investigation
CAIP	Corrective action investigation plan
CAP	Corrective action plan
CAS	Corrective action site
CAU	Corrective action unit
CB	Contaminant boundary
CDF	Cumulative distribution function
CFA	Constant fracture aperture
CFR	*Code of Federal Regulations*
cm	Centimeter
CML	Carboxylate-modified latex
COC	Contaminant of concern
CR	Closure report
DCE	Diffusion cell experiment
DWE	Diffusion water experiment
DFN	Discrete fracture network
DZ	Diagenetic Zone
DoD	U.S. Department of Defense
DOE	U.S. Department of Energy
DOE/NV	U.S. Department of Energy Nevada Operations Office
DRI	Desert Research Institute

LIST OF ACRONYMS AND ABBREVIATIONS (CONTINUED)

EM	Environmental Management
EPA	U.S. Environmental Protection Agency
ERP	Environmental Restoration Project
ESF	Exploratory Studies Facility
ET	Evapotranspiration
EV	Exchange volume
FFACO	*Federal Facility Agreement and Consent Order*
FGE	Forced-gradient experiment
FMS	Formation MicroScanner
ft	Foot
ft/day	Feet per day
GIS	Geographic Information Systems
gpm	Gallons per minute
g/cm^3	Grams per cubic centimeter
GPS	Global Positioning System
GW	Groundwater
HDD	Hydrologic Data Document
HFM	Hydrostratigraphic framework model
HGL	HydroGeoLogic, Inc.
HGU	Hydrogeologic unit
HRMP	Hydrologic Resources Management Program
HST	Hydrologic source term
HSU	Hydrostratigraphic unit
ID	Identification
in.	Inch
ISPID	Integrated Sampling Plan Identifier
K	Hydraulic conductivity
K_d	Distribution coefficient
kg/m^3	Kilograms per cubic meter
km	Kilometer
km^2	Square kilometer
kt	Kiloton
LANL	Los Alamos National Laboratory

LIST OF ACRONYMS AND ABBREVIATIONS (CONTINUED)

LLNL	Lawrence Livermore National Laboratory
LNA	Lognormal distribution aperture
LCAP	Length-correlated aperture
M	Molar
m	Meter
M&O	Management and operating
MCL	Maximum contaminant level
m/day	Meters per day
mi^2	Square mile
mL/g	Milliliters per gram
mm	Millimeter
mol/L	Moles per liter
mrem/yr	Millirem per year
m/s	Meters per second
Mt	Megaton
MWAT	Multiple-well aquifer test
MWAT-TT	Multiple-well aquifer test-tracer test
m/yr	Meters per year
N/A	Not applicable
NAD	North American Datum
NC-EWDP	Nye County Early Warning Drilling Program
NDA	Nondestructive assay
NDEP	Nevada Division of Environmental Protection
NEM	Non-Electrostatic Model
NGVD	National Geodetic Vertical Datum
N-I	Navarro-Intera, LLC
NNSA/NFO	U.S. Department of Energy, National Nuclear Security Administration Nevada Field Office
NNSA/NSO	U.S. Department of Energy, National Nuclear Security Administration Nevada Site Office
NNSS	Nevada National Security Site
NR	Not reported
NSTec	National Security Technologies, LLC
NTS	Nevada Test Site
NTTR	Nevada Test and Training Range

LIST OF ACRONYMS AND ABBREVIATIONS (CONTINUED)

NV	Nevada
PDF	Probability density function
PER	Preemptive review
pCi/L	Picocuries per liter
PDF	Probability density function
PDF	Probability distribution function
PM	Pahute Mesa
PM-OV	Pahute Mesa–Oasis Valley
QA	Quality assurance
QAP	Quality Assurance Plan
QC	Quality control
R_c	Cavity radius
RELAP	Reactive Transport LaPlace Inversion code
RME	Radionuclide Migration Experiment
RM/SM	Rainier Mesa/Shoshone Mountain
RN	Radionuclide
RNM	Radionuclide migration
RPd	Rock Properties database
RST	Radiologic source term
SDWA	*Safe Drinking Water Act*
SLd	Stratigraphy-Lithology database
SNJV	Stoller-Navarro Joint Venture
SWNVF	Southwestern Nevada Volcanic Field
SZ	Saturated zone
TD	Total depth
TDD	Transport Data Document
TDRW	Time Domain Random Walk
TTR	Tonopah Test Range
UE	Underground exploratory
UGTA	Underground Test Area
USAF	U.S. Air Force
USGS	U.S. Geological Survey
UTM	Universal Transverse Mercator

LIST OF ACRONYMS AND ABBREVIATIONS (CONTINUED)

UZ	Unsaturated zone
VOIA	Value-of-information analysis
WIPP	Waste Isolation Pilot Plant
WPM-OV	Western Pahute Mesa–Oasis Valley
YF/CM	Yucca Flat/Climax Mine
YM	Yucca Mountain
YMP	Yucca Mountain Project
µg/L	Micrograms per liter

Stratigraphic, Geologic, Hydrostratigraphic, and Hydrogeologic Unit Abbreviations and Symbols

AA	Alluvial aquifer
AL	Almendro Fault
ATCCU	Argillic tuff caldera confining unit
ATCU	Argillic tuff confining unit
ATICU	Ammonia Tanks intrusive confining unit
ATMLFA	Ammonia Tanks mafic lava-flow aquifer
ATWTA	Ammonia Tanks welded-tuff aquifer
BA	Benham aquifer
BAQ	Basal aquifer
BCU	Basal confining unit
BFCU	Bullfrog confining unit
BMICU	Black Mountain intrusive confining unit
BRA	Belted Range aquifer
BWCU	Buttonhook Wash confining unit
BWWTA	Buttonhook Wash welded-tuff aquifer
CA	Carbonate aquifer
CCICU	Claim Canyon intrusive confining unit
CCU	Clastic confining unit
CFCM	Crater Flat composite unit
CFCU	Crater Flat confining unit
CHICU	Calico Hills intrusive confining unit
CHLFA	Calico Hills lava-flow aquifer

LIST OF ACRONYMS AND ABBREVIATIONS (CONTINUED)

CHLFA1	Calico Hills lava-flow aquifer 1
CHLFA2	Calico Hills lava-flow aquifer 2
CHLFA3	Calico Hills lava-flow aquifer 3
CHLFA4	Calico Hills lava-flow aquifer 4
CHLFA5	Calico Hills lava-flow aquifer 5
CHVTA	Calico Hills vitric-tuff aquifer
CHZCM	Calico Hills zeolitized composite unit
CPA	Comb Peak aquifer
CZ	Zabriskie Quartzite
CZw	Wood Canyon Formation
Dg	Guilmette Formation
Ds	Simonson Dolomite
DSs	Sevy Dolomite
DVA	Detached volcanic aquifer
DVCM	Detached volcanic composite unit
DWT	Densely welded tuff
DWZ	Densely welded central zone
FB	Flow breccia
FC-BH	Fluorspar Canyon-Bullfrog Hills detachment fault
FCCM	Fortymile Canyon composite unit
FCCU	Fluorspar Canyon confining unit
FCLLFA	Fortymile Canyon lower lava-flow aquifer
FCLMLFA	Fortymile Canyon lower mafic lava-flow aquifer
FCULFA	Fortymile Canyon upper lava-flow aquifer
FCULFA1	Fortymile Canyon upper lava-flow aquifer 1
FCULFA2	Fortymile Canyon upper lava-flow aquifer 2
FCULFA3	Fortymile Canyon upper lava-flow aquifer 3
FCULFA4	Fortymile Canyon upper lava-flow aquifer 4
FCULFA5	Fortymile Canyon upper lava-flow aquifer 5
FCULFA6	Fortymile Canyon upper lava-flow aquifer 6
FCULFA7	Fortymile Canyon upper lava-flow aquifer 7
FCUMLFA	Fortymile Canyon upper mafic lava-flow aquifer
FCWTA	Fortymile Canyon welded-tuff aquifer

LIST OF ACRONYMS AND ABBREVIATIONS (CONTINUED)

FCWTA1	Fortymile Canyon welded-tuff aquifer 1
GCU	Granitic confining unit
IA	Inlet aquifer
ICU	Intrusive confining unit
IICU	Intracaldera intrusive confining unit
IN	Intrusive
KA	Kearsarge aquifer
Kg	Granitic rocks
Kgg	Gold Meadows stock granite
LA	Lava
LCA	Lower carbonate aquifer
LCA3	Lower carbonate aquifer-thrust plate
LCCU	Lower clastic confining unit
LCCU1	Lower clastic confining unit - thrust plate
LFA	Lava-flow aquifer
LHFL	Lower highly fractured layer
LPCU	Lower Paintbrush confining unit
LTCU	Lower tuff confining unit
LVTA2	Lower vitric-tuff aquifer 2
Mc	Chainman Shale
mCCU	Modified clastic confining unit
mCFCM	Modified Crater Flat composite unit
mCHLFA5	Modified Calico Hills lava-flow aquifer 5
mCHZCM	Modified Calico Hills zeolotic composite unit
mCPA	Modified Comb Peak aquifer
MDc	Late Devonian through Mississippian siliciclastic rocks
MDe	Eleana Formation
MGCU	Mesozoic granite confining unit
MPCU	Middle Paintbrush confining unit
MWT	Moderately welded tuff
NWT	Nonwelded tuff
Oe	Eureka Quartzite
Oes	Ely Springs Dolomite

LIST OF ACRONYMS AND ABBREVIATIONS (CONTINUED)

Op	Pogonip Group
OSBCU	Oak Spring Butte confining unit
PBPCU	Post-Benham Paintbrush confining unit
PBRCM	Pre-Belted Range composite unit
PCM	Paintbrush composite unit
PL	Pumiceous lava
PLFA	Paintbrush lava-flow aquifer
PMNICU	Pahute Mesa Northern Extension intrusive confining unit
PPt	Tippipah Limestone
PVFA	Paintbrush vitric-flow aquifer
PVTA	Paintbrush vitric-tuff aquifer
PWZl	Lower partially welded zone
PWZu	Partially welded upper zone
Qam	Middle alluvium
Qay	Young alluvial deposits
Qb	Quaternary Basalt
Qby	Quaternary Basalts
QF	Quartzofeldspathic
Qs	Quaternary sediments
QTa	Quaternary/Tertiary alluvium
QTc	Quaternary/Tertiary colluvium
QTu	Quaternary/Tertiary undifferentiated surficial deposit
RMICU	Rainier Mesa intrusive confining unit
RMWTA	Rainier Mesa welded-tuff aquifer
RWT	Reworked tuff
RVICU	Redrock Valley intrusive confining unit
SCCC	Silent Canyon Caldera Complex
SCICU	Silent Canyon intrusive confining unit
SCVCU	Subcaldera volcanic confining unit
SFCL	Sparsely fractured center layer
Sl	Laketown Dolomite
SMLFA	Shoshone Mountain lava-flow aquifer
SPA	Scrugham Peak aquifer

LIST OF ACRONYMS AND ABBREVIATIONS (CONTINUED)

SWA	Stockade Wash aquifer
Tac	Calico Hills Formation
Tal	Tuffs of Antelope Springs lower
Tam	Tuffs of Antelope Springs middle
Tau	Tuffs of Antelope Springs
TB	Tuff breccia
Tb	Belted Range Group
Tbd	Dead Horse Flat Formation
Tbdb	Comendite of Basket Valley
Tbdc	Comendite of Chartreuse
Tbdk	Comendite of Kaw Station
Tbdl	Comendite of Lambs Canyon
Tbds	Comendite of Saucer Mesa
Tbg	Grouse Canyon Tuff
Tbgb	Grouse Canyon Tuff, bedded
Tbgp	Grouse Canyon crystal-poor Tuff
Tbgr	Grouse Canyon crystal-rich Tuff
Tbgs	Comendite of Split Ridge
Tbq	Comendite of Quartet Dome
TC	Tuff cone
Tc	Crater Flat Group
TCA	Tiva Canyon aquifer
Tcb	Bullfrog Tuff
Tcblp	Mafic-poor Bullfrog Tuff
Tcblr	Mafic-rich Bullfrog Tuff
Tcbp	Bullfrog Tuff crystal-poor
Tcbr	Bullfrog Tuff crystal-rich
Tcbs	Bullfrog Tuff, Stockade Wash Lobe
Tcbx	Debris-flow breccia related to the Crater Flat Group
Tcby	Bullfrog Tuff, Yucca Mountain Lobe
Tcf	Basalt of Fontina
TCFZ	Thirsty Canyon Fault Zone
Tcg	Latite of Grimy Gulch

LIST OF ACRONYMS AND ABBREVIATIONS (CONTINUED)

Tci	Rhyolite of Inlet
Tcj	Rhyolite of Jorum
TCL	Thirsty Canyon Lineament
Tcp	Prow Pass tuff
Tcpj	Tuff of Jorum
Tcpk	Rhyolite of Kearsarge
Tcps	Rhyolite of Sled
Tcr	Rhyolite of the Crater Flat Group
Tct	Tram Tuff
Tcu	Tuff of Pool
TCU	Tuff confining unit
TCVA	Thirsty Canyon volcanic aquifer
Te	Volcanics of Central Nevada
Tec	Fraction Tuff and related rocks
Tem	Monotony Tuff
Tep	Pahranagat Tuff
Tes	Shingle Pass Tuff
Tf	Volcanics of Fortymile Canyon
Tf/Tfr	Fraction Tuff and related rocks
Tfb	Beatty Wash Formation
Tfbb	Basalt of Chukar Canyon
Tfbw	Rhyolite of Beatty Wash
Tfd	Lava flows of Dome Mountain
Tff	Rhyodacite of Fleur-de-lis-Ranch
Tfl	Tuff of Leadfield Road
Tfn	Trachyte of Donovan Mountain
Tfr	Rhyolite of Rainbow Mountain
Tfs	Rhyolite of Shoshone Mountain
Tft	Intermediate-age basalt
Tfu	Rhyolite of Boundary Butte
Tgc	Caldera moat-filling sediments
Tgm	Late synvolcanic sedimentary rock
Tgnx	Transitional Timber Mountain breccia and sedimentary rocks

LIST OF ACRONYMS AND ABBREVIATIONS (CONTINUED)

Tgp	Rocks of Pavits Spring
Tgw	Rocks of Winapi Wash
Tgy	Basin-fill sediments, undivided
Tgyx	Younger landslide and sedimentary breccia
Th	Calico Hills Formation
THCM	Tannenbaum Hill composite unit
THCU	Tannenbaum Hill confining unit
THLFA	Tannenbaum Hill lava-flow aquifer
Thp	Calico Hills Formation, mafic-poor
Thr	Calico Hills Formation, mafic-rich
Ti	High-silica granodiorite, etc.
Tiy	Younger intrusive rocks
Tk	Volcanics of Kawich Valley
Tka	Rhyolite of Wheelbarrow Peak
Tkl	Latite of Kawich Valley
Tkr	Rhyolite of Belted Peak
Tm	Timber Mountain Group
Tma	Ammonia Tanks Tuff
TMA	Timber Mountain aquifer
Tmab	Ammonia Tanks bedded tuff
Tmap	Ammonia Tanks mafic-poor
Tmat	Rhyolite of Tannenbaum Hill
Tmaw	Rhyolite of Tannenbaum Hill
Tmay	Rhyolite of Tannenbaum Hill
Tmc	Caldera-collapse breccia of Timber Mountain caldera complex
TMCC	Timber Mountain caldera complex
TMCCSM	Timber Mountain caldera complex structural margin
TMCM	Timber Mountain composite unit
TMD	Timber Mountain Dome
TMLVTA	Timber Mountain lower vitric-tuff aquifer
Tmr	Rainier Mesa Tuff
Tmrb	Rainier Mesa bedded tuff
Tmrf	Rhyolite of Fluorspar Canyon

LIST OF ACRONYMS AND ABBREVIATIONS (CONTINUED)

Tmrh	Tuff of Holmes Road
Tmt	Basalt of the Bullfrog Hills
TMUWTA	Timber Mountain upper welded-tuff aquifer
TMVTA	Timber Mountain vitric-tuff aquifer
Tmw	Rhyolite of Windy Wash
TMWTA	Timber Mountain welded-tuff aquifer
Tmx	Timber Mountain landslide breccia
Tn	Tunnel Formation
Tn4JK	Beds 4J-K Tunnel Formation
To	Volcanics of Oak Spring Butte
Ton1	Tunnel bed 1
Ton2	Tunnel bed 2
Tor	Redrock Valley Tuff
Tori	Redrock Valley intrusive
Tot	Tuff of Twin Peaks
Toy	Tuff of Yucca Flat
Tp	Paintbrush Group
Tpb	Rhyolite of Benham
Tpc	Tiva Canyon Tuff
Tpcm	Tiva Canyon Tuff, Pahute Mesa lobe
Tpcp	Crystal-poor Tiva Canyon Tuff
Tpcr	Crystal-rich Tiva Canyon Tuff
Tpcx	Tiva Canyon–landslide breccia
Tpcy	Tuff of Pinyon Pass
Tpcyp	Tuff of Pinyon Pass, crystal-poor
Tpd	Rhyolite of Delirium Canyon
Tpe	Rhyolite of Echo Peak
Tpg	Rhyolite of Black Glass Canyon
Tpk	Rhyolite of Comb Peak
Tpm	Middle Paintbrush Group rhyolites
Tpp	Pah Canyon Tuff
Tpr	Rhyolite of Silent Canyon
Tps	Rhyolite of Scrugham Peak

LIST OF ACRONYMS AND ABBREVIATIONS (CONTINUED)

Tpt	Topopah Spring Tuff
Tptb	Topopah Spring Tuff, bedded
Tptbr	Topopah Spring Tuff bedded crystal-rich
Tptm	Topopah Spring Tuff, Pahute Mesa lobe
Tptp	Topopah Spring Tuff crystal-poor
Tptr	Topopah Spring Tuff crystal-rich
Tptx	Topopah Spring landslide breccia
Tpu	Post-Tiva Canyon rhyolites
Tpv	Rhyolite of Vent Pass
Tpw	Rhyolite of Windy Wash
Tpx	Paintbrush caldera-collapse breccias
Tpy	Yucca Mountain Tuff
Tq	Volcanics of Quartz Mountain
Tqe	Volcanics of Quartz Mountain Lower rhyolite
Tqh	Volcanics of Quartz Mountain Middle rhyolite
Tqm	Dacite of Mount Helen
Tqs	Tuff of Sleeping Butte
Tqt	Tuff of Tolicha Peak
Tr	Tram Ridge Group
Trd	Dikes of Tram Ridge
Trl	Lithic Ridge Tuf
Trr	Rhyolite of Picture Rock
TSA	Topopah Spring aquifer
Tsc	Civet Cat Canyon Member of Stonewall Flat Tuff
Tsp	Spearhead Member of Stonewall Flat Tuff
Tsr	Rhyolite of Stonewall Mountain
Tt	Thirsty Canyon Group
Ttc	Comendite of Ribbon Cliff
Ttg	Gold Flat Tuff
Tth	Trachyte of Hidden Cliff
Ttp	Pahute Mesa and Rocket Wash Tuffs
Tts	Trachytic rocks of Pillar Spring and Yellow Cleft
UCCU	Upper clastic confining unit

LIST OF ACRONYMS AND ABBREVIATIONS (CONTINUED)

UHFL	Upper highly fractured layer
UPCU	Upper Paintbrush confining unit
VCU	Volcaniclastic confining unit
VT	Vitrophyric tuff
VTA	Vitric-tuff aquifer
WTA	Welded-tuff aquifer
WWA	Windy Wash aquifer
YMCFCM	Yucca Mountain Crater Flat composite unit
YVCM	Younger volcanic composite unit
Zj	Johnnie Formation
Zs	Stirling Quartzite
M	Mesozoic
pC	Pre-Cambrian & Paleozoic
Q	Quaternary
T	Tertiary

LIST OF ACRONYMS AND ABBREVIATIONS (CONTINUED)

Elements and Compounds

2,4,5-TFBA	2,4,5-trifluorobenzoic acid
Ac	Actinium
Al	Aluminum
Am	Americium
Ar	Argon
Br	Bromine
C	Carbon
Ca	Calcium
Cd	Cadmium
Cl	Chlorine
Cm	Curium
CO_3	Carbonate
Cs	Cesium
DFBA	Difluorobenzoate
Eu	Europium
^3H	Tritium
HCO_3	Bicarbonate
He	Helium
Ho	Holmium
I	Iodine
K	Potassium
Kr	Krypton
Li	Lithium
Mg	Magnesium
Mn	Manganese
Na	Sodium
Nb	Niobium
Ni	Nickel
NO_3	Nitrate
Np	Neptunium
O	Oxygen

LIST OF ACRONYMS AND ABBREVIATIONS (CONTINUED)

Pa	Protactinium
Pb	Lead
Pd	Palladium
PFBA	Pentafluorobenzoic acid
Pu	Plutonium
Sb	Antimony
Sm	Samarium
Sn	Tin
SO_4	Sulfate
Se	Selenium
Sr	Strontium
Tc	Technetium
TFBA	Trifluorobenzoic acid
Th	Thorium
U	Uranium
Zr	Zirconium
δ^2H	Delta deuterium
$\delta^{18}O$	Delta oxygen-18

1.0 INTRODUCTION

This document presents a summary and framework of available transport data and other information directly relevant to the development of the groundwater transport model for Central and Western Pahute Mesa (PM) corrective action units (CAU). This model is referred to as the "PM CAU transport model" in this document. Central and Western PM are two areas of the Nevada National Security Site (NNSS) that historically were used for underground nuclear testing (Figure 1-1). These nuclear tests resulted in groundwater contamination in the vicinity of the underground test areas. As a result, the U.S. Department of Energy (DOE), Environmental Management (EM) Nevada Program is currently conducting a corrective action investigation (CAI) of the PM underground test areas. This work is a part of the Underground Test Area (UGTA) Activity in accordance with the *Federal Facility Agreement and Consent Order* (FFACO) (1996, as amended).

The CAU groundwater flow and transport model (CAU model) is a major part of the UGTA strategy (FFACO, 1996 as amended). This model provides the contaminant boundary (CB) forecasts required by the FFACO. The transport data necessary for the transport model portion of the CAU model are presented in this report. This document presents the available data to identify ranges of values that will serve as broad constraints on the parameters and ranges for simulation. The specific input values used in the modeling will be documented in the flow and transport model reports. The hydrologic data necessary for the flow model portion of the CAU model are presented in a separate report (Navarro, 2021).

A document addressing the contaminant transport parameters for the groundwater flow and contaminant transport model of PM CAUs was first published in 2003 (Shaw, 2003). A considerable amount of characterization activities including well drilling, well logging, well development, geological characterization, flow testing, multiple-well aquifer testing, sampling, laboratory testing, data analysis, groundwater flow and transport modeling, geochemical modeling, source term characterization, groundwater basin delineation, groundwater discharge studies, and infiltration analysis have taken place since 2003 (listed in Section 1.3), resulting in a large body of published work that has become available since 2004. The current document takes advantage of this work.

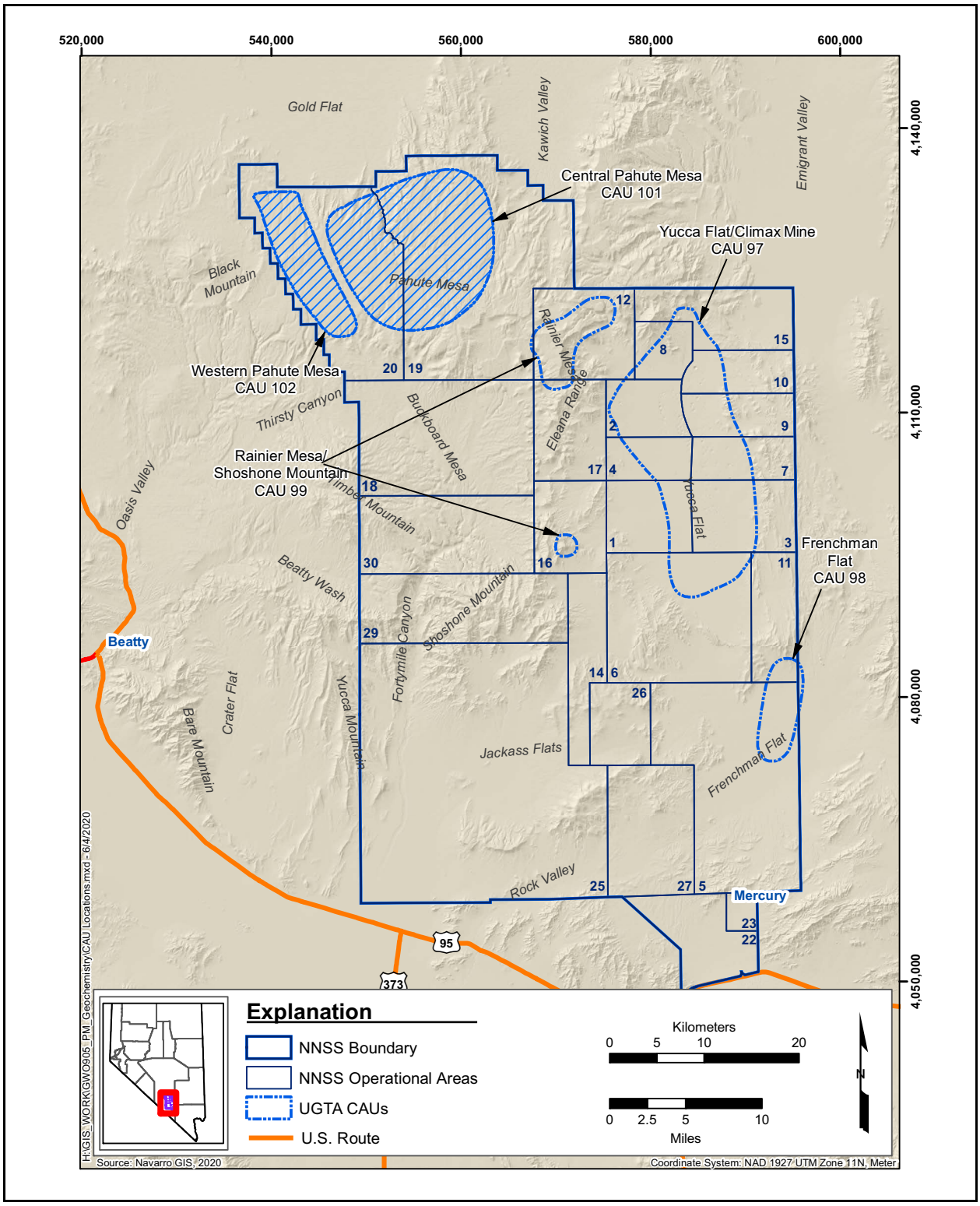

Figure 1-1
Location of the Pahute Mesa CAUs

Where appropriate, data and information documented elsewhere are briefly summarized with reference to the complete documentation.

This section provides a brief summary of the UGTA Activity background and project background, describes the setting of the PM CAUs and nuclear testing at the PM CAUs, followed by a presentation of the purpose and scope of the work described in this document. Brief descriptions of this document's contents are provided at the end of the section.

1.1 UGTA Activity Background

The primary regulatory agreement governing the UGTA Activity is the FFACO (1996, as amended), which was agreed to by the State of Nevada acting by and through the Department of Conservation and Natural Resources, Nevada Division of Environmental Protection (NDEP); U.S. Department of Defense (DoD); and DOE. The FFACO has multiple purposes, including identifying sites of potential historic contamination to ensure that potential impacts of releases into state waters are thoroughly investigated and are subject to corrective actions and closure requirements under the oversight of NDEP. The purposes also include determination of whether releases of contaminants could potentially migrate, and if so, identification of the nature and extent of that migration. The FFACO also stipulates that the corrective action decisions and institutional controls are to be fully protective of human health and the environment. The NNSS and Nevada Test and Training Range (NTTR) are federally controlled lands not accessible to the general public. Potential public exposure to the contaminants of concern (COCs) would be of concern if the COCs were to migrate beyond the boundaries of NNSS and NTTR into the groundwater beneath public or private lands at levels that exceed individual *Safe Drinking Water Act* (SDWA) maximum contaminant levels (MCLs).

The individual locations covered by the agreement are known as corrective action sites (CASs) and are grouped into CAUs. The UGTA CAUs are Frenchman Flat, Central Pahute Mesa, Western Pahute Mesa, Yucca Flat/Climax Mine (YF/CM), and the Rainier Mesa/Shoshone Mountain (RM/SM) CAUs (Figure 1-1). Central Pahute Mesa (CAU 101) and Western Pahute Mesa (CAU 102) are addressed together, and referred to as the PM CAU, due to their adjacent locations and common groundwater regime as well as similarities in testing practices, geology, and hydrology.

The UGTA strategy, defined in Appendix VI of the FFACO (1996, as amended), assumes that active remediation of underground nuclear tests is not feasible with current technology. As a result, the

corrective action for each CAU is based on a combination of characterization and modeling studies, monitoring, and institutional controls. On PM, all deep underground nuclear tests assigned to UGTA are composed of a single detonation each. In this document, when applied to PM, the words "detonation" and "test" are used interchangeably unless otherwise noted.

The UGTA strategy is implemented through the following four-stage approach: (1) corrective action investigation plan (CAIP), (2) corrective action investigation (CAI), (3) corrective action decision document (CADD)/corrective action plan (CAP), and (4) closure report (CR). The project progresses through these stages in a sequential manner as approved by NDEP. There are nine decision points within this strategy that require NDEP concurrence before the project can proceed to the next step. Figure 1-2 illustrates the individual steps and decision points within each strategy stage; major decisions between NDEP and DOE EM Nevada Program (formerly DOE, National Nuclear Security Administration Nevada Field Office [NNSA/NFO]) are highlighted in yellow. Three of the UGTA decision points are at the transition between stages. Nonapproval of decision points by NDEP affects the program progression and can lead to a reassessment of whether the UGTA strategy is achievable.

The technical basis for achieving the UGTA strategy is through an evaluation of the CAU using a combination of (1) data collection; (2) modeling of hydrological setting, radiological source term, and flow and contaminant transport; (3) iterative model evaluations and monitoring; and (4) identification and documentation of land-use policies (institutional controls). This four-component approach is used to accomplish the primary objective of the UGTA strategy, which is to define perimeter boundaries over the next 1,000 years that encompass groundwater that potentially exceeds the radiological standards of the SDWA (*Code of Federal Regulations* [CFR], 2019). The integration and balancing of modeling studies, monitoring, and institutional controls provide the foundation of a risk-informed strategy for regulatory decision-making.

The perimeter boundaries enclose areas potentially exceeding the radiological standards of the SDWA (CFR, 2019). Modeling forecasts of contaminant transport provide the fundamental basis for identifying CBs. A CB is formally defined as a probabilistic model-forecast perimeter and a lower hydrostratigraphic unit (HSU) boundary that delineates the extent of radionuclide (RN)-contaminated groundwater from underground testing over 1,000 years. Simulation modeling of contaminant transport will be used to forecast the location of CBs within 1,000 years and must show the

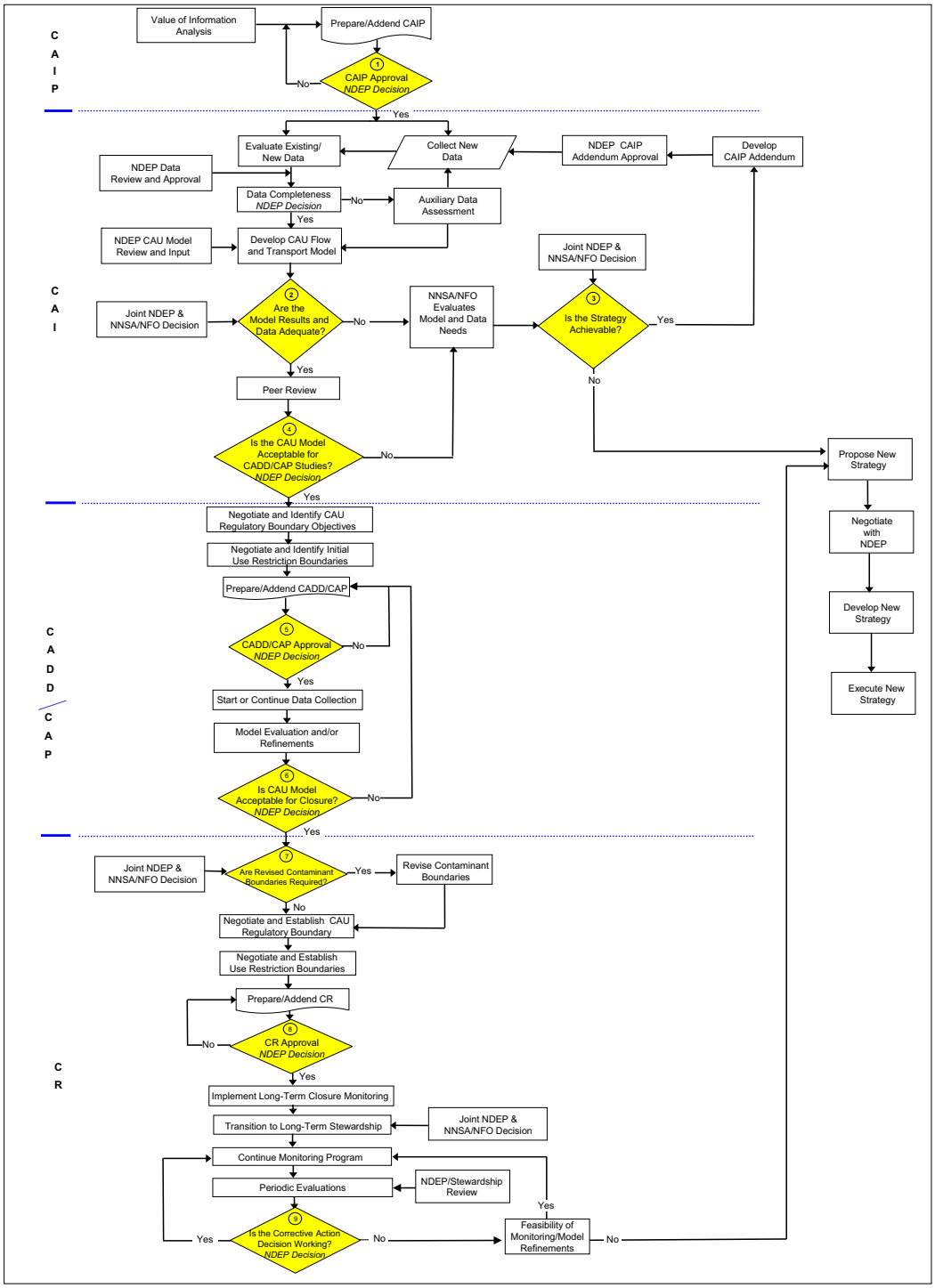

Figure 1-2
FFACO UGTA Strategy Flowchart

95th percentile of the model results boundary (outside of which only 5 percent of the simulations exceed the SDWA standards).

1.1.1 Overview of CAU Modeling Approach

As described above, the technical basis of the UGTA strategy requires the development of a CAU contaminant transport model. This in turn requires the development of a model of the groundwater flow system for the CAU. The groundwater flow system at the NNSS, as well as the sources of contamination, and the processes controlling transport, are complex. Computer models are required as a tool to meet the objectives of the FFACO strategy.

The CAU-scale model consists of two integrated components: the CAU flow model and the CAU transport model. The approach begins with characterization of the subsurface hydrogeology and the flow system. Conceptual models are developed based on the results of characterization and assumptions regarding system processes. These processes are represented mathematically and implemented on computers to represent the system. The CAU flow and CAU transport models will be developed at the CAU scale and will be used to simulate RN concentrations in the groundwater flow system underlying the PM for the 1,000-year time frame. These models will use numerical three-dimensional (3-D) flow and transport simulators that capture the complex geologic structure underlying the PM, including units of variable thickness, faults, and offsets as well as complex transport processes associated with reactive solutes and fractured rock. Details of the CAU flow as well as transport models, along with their results and uncertainty analysis, will be presented in future reports.

Formulation of the CAU transport model requires the development of a conceptual model encompassing physical and chemical transport processes of importance at the PM CAU, presented in Section 3.0. Various parameters required to quantify the processes are also identified in Section 3.0. Data and analysis pertinent for each parameter along with ranges of values or distributions as appropriate are presented in Section 5.0.

A number of supporting models are also required for this work, including a hydrostratigraphic framework model (HFM) (DOE/EMNV, 2020a) which provides a framework for the flow and transport models, a screening model to select the RNs relevant to the transport model (Carle et al., 2020), flow and transport models on a sub-CAU scale (Lu et al., 2021) to assess the system details,

and small-scale discrete fracture network (DFN) models to aid in parameter scaling (Parashar et al., 2019; and Makedonska et al., 2020).

1.1.2 Project Background

At the beginning of the CAIP stage, a value of information analysis (VOIA) was prepared for the PM CAUs in 1998. The CAIP was prepared and revised in an iterative manner from 1998 through 2001. Phase I of the UGTA CAI strategy led to the development of a Phase I Hydrostratigraphic Framework Model (HFM) (BN, 2002), Phase I Transport Data Document (TDD) (Shaw, 2003), Phase I Hydrologic Data Document (HDD) (SNJV, 2004b), Unclassified Source Term Report (SNJV, 2004e), Groundwater Flow Model Report (SNJV, 2006a), and Transport Model Report (SNJV, 2009).
As stated in SNJV (2009), because of the significant uncertainty of the model results, the primary goal of the PM Phase I CAU transport model report was modified through mutual agreement between the DOE and the State of Nevada to assess the primary model components that contribute to this uncertainty. A Phase II CAIP (NNSA/NFO, 2014) was developed, submitted, and signed in 2014. NDEP approved transition from Phase I modeling to Phase II investigation in June 2010. Drilling, completion and testing of new Phase II wells occurred through 2016. Based on the new data and analysis, the update to Phase II CAIP (DOE/EMNV, 2020b) was approved in 2020. Phase II is following the same progression as Phase I: a revised HFM (DOE/EMNV, 2020a) and a revised HDD (Navarro, 2021) to provide the hydrogeologic framework and hydrologic data for developing the Phase II groundwater flow model. Transport parameters and the approaches to apply these parameters for the Phase II PM CAU transport model are presented in this document. This document provides an update to the Phase I TDD, a necessary step toward developing a PM CAU model to aid in defining CBs for the CAU as required by the FFACO (1996, as amended).

1.1.3 Pahute Mesa Background

PM is in the northwestern part of the NNSS. It includes NNSS Areas 19 and 20 (Figure 1-1). PM is an elevated plateau of about 500 square kilometers (km^2) (200 square miles [mi^2]) at an altitude that ranges from 1,676 meters (m) (5,500 feet [ft]) on the western edge to over 2,134 m (7,000 ft) above mean sea level (amsl) throughout the eastern range (Blankennagel and Weir, 1973). Figure 1-3 shows the outline of the Pahute Mesa-Oasis Valley (PM-OV) groundwater (GW) basin within the geographic setting of the NNSS.

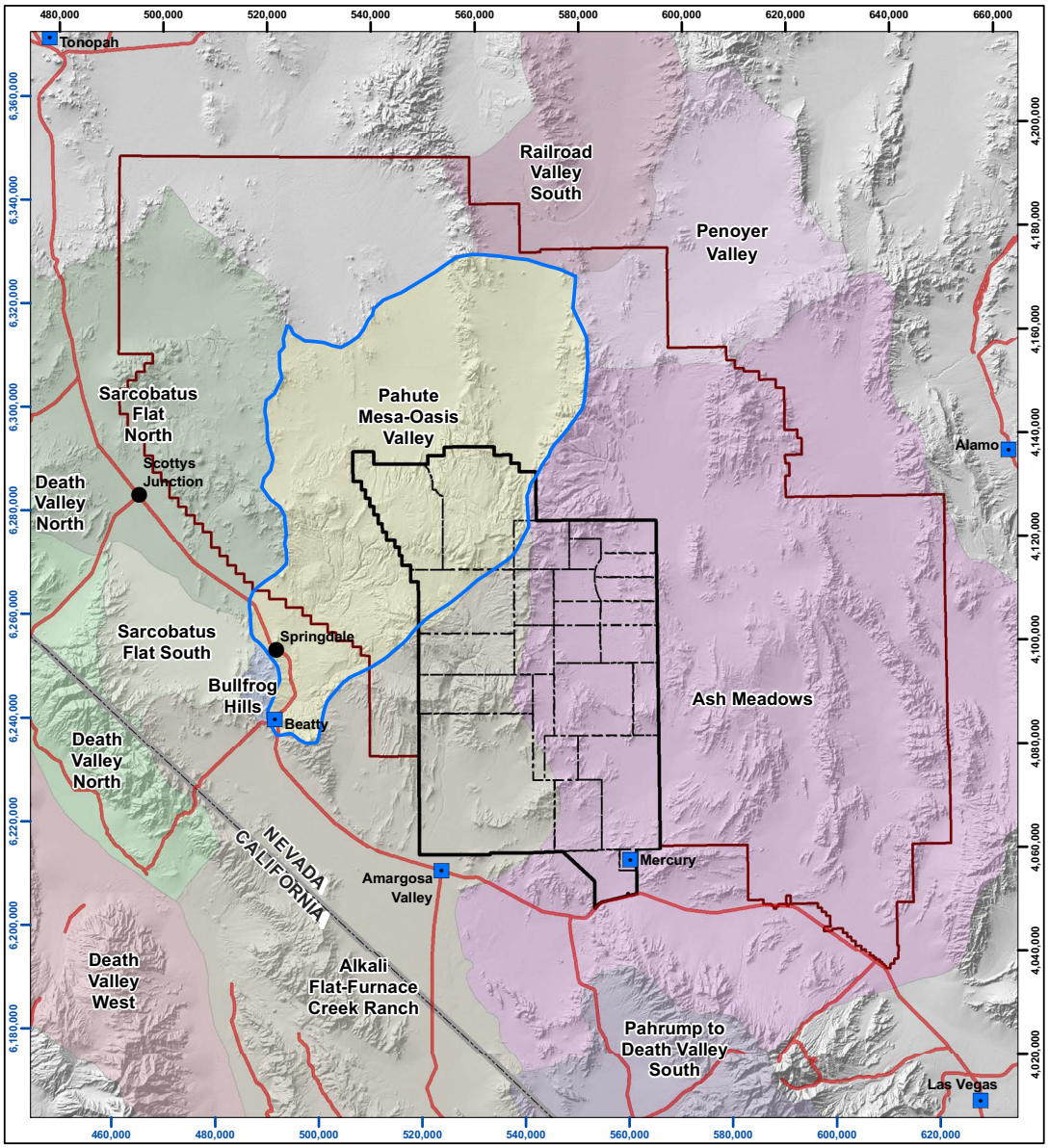

Figure 1-3
Map Showing the Location of the PM-OV Groundwater Basin
Source: Fenelon et al., 2016

The area of interest for the PM CAU includes a region stretching from the northern side of PM south and southwestward to Oasis Valley. Groundwater elevations generally mimic the topography, being highest beneath northern and eastern PM, dropping off gradually to the south and west to Oasis Valley. Groundwater beneath PM generally flows in a southwesterly direction, primarily through fractured lava-flow and welded-tuff aquifers (Jackson et al., 2021), discharging to the surface within the Oasis Valley discharge area in the form of springs. PM geology is dominated by deposition of rock units from volcanic eruptions from nested calderas of the Southwestern Nevada Volcanic Field (SWNVF) (Warren et al., 2000). With the exception of some deeply buried Paleozoic rocks in a few places and some shallow alluvium, all rocks known to underlie PM are volcanic with thickness approaching 5 kilometers (km) (Ferguson et al., 1994).

1.2 Underground Nuclear Testing on Pahute Mesa

PM was used as an underground nuclear testing area of the Nevada Test Site (NTS) (now the NNSS) for 27 years from 1965 to 1992 (NNSA/NFO, 2015). A total of 85 underground nuclear tests were conducted at PM. Three of these tests (SCHOONER, PALANQUIN, and CABRIOLET) were shallow and are not considered as part of the UGTA Activity. (Although these three tests are not assigned to UGTA Activity as defined in the FFACO [1996, as amended], they will be included in the PM CAU transport model for completeness because of known contamination at Well PM-2 that likely came from SCHOONER.) The remaining nuclear tests conducted at PM are those detonated in deep vertical shafts (from 225 m to 1,452 m depth below ground surface [bgs]). A total of 82 such underground nuclear tests were conducted at PM; 33 of these were at or below the water table, and 49 were above the water table. However, of the tests above the water table, only three are potentially more than a 3 cavity radius (R_c) distance above the water table, implying that 79 tests had exchange volumes (EVs) that may be at least partially below the water table. (Cavity dimension based on maximum of unclassified yield range [minimum for HANDLEY] in NNSA/NFO [2015] and Equation 1 in Pawloski [1999]; or measured when yield is specified in Zavarin [2014].) The announced yield or yield ranges for 79 out of 82 tests are between less than 20 kilotons (kt) to 1 megaton (Mt); three tests had announced yields or ranges exceeding 1 Mt, including one test with an announced yield of 1.3 Mt. The 82 tests on PM comprised 60.2 percent of the radiologic inventory from the underground tests on NNSS as of September 30, 2012, based on curies (Finnegan et al., 2016). Media contaminated by the underground nuclear tests on PM are geologic formations within

the unsaturated and saturated zones. Transport via groundwater is the primary potential mechanism of migration for the subsurface contamination away from the PM underground nuclear tests.

1.3 Major Data Collection and Analysis Activities

Major data collection and analysis activities completed for the PM CAU following the publication of PM CAU Phase I Transport model report (SNJV, 2009) are noted below. New data analysis activities are presented throughout the report.

- Installation and testing of 11 wells (as listed in Appendix A).
- Analyses of aquifer tests, yielding estimates of transmissivity, identified the hydraulic connections between wells, and provided calibration data for numerical models (as listed in Appendix A; Garcia et al., 2016).
- Revision of PM HFM based on new data (DOE/EMNV, 2020a).
- Analysis of additional groundwater samples that show where test-derived constituents both are and are not found (Navarro, 2020c).
- Phase II Geochemical and Isotopic Evaluation of Groundwater Flow in the Pahute Mesa–Oasis Valley Flow System (Navarro, 2020a).
- Development of a new yield-weighting method of estimating radiological inventories (Tompson et al., 2019).
- Estimates of porosity derived from analysis of geophysical log data (Navarro, 2019c).
- Additional studies on colloid formation and transport (Zavarin et al., 2015 and 2019; Reimus and Boukhalfa, 2014; and Reimus, 2018).
- Additional studies of fracture analysis (Golder, 2016; Hoaglund, 2017; HGL, 2017).
- Additional matrix diffusion estimates (Telfeyan et al., 2018; Zavarin et al., 2013).
- Additional dispersion studies (Zhou et al., 2005; HGL, 2018a).
- DFN modeling studies (Makedonska et al., 2020; Parashar et al., 2019).
- Updated matrix sorption coefficients (Carle, 2018; Carle et al., 2020).
- Study of regional stress and fracture permeability (Reeves et al., 2017).
- Revision of the delineation of the PM-OV Groundwater Basin (Fenelon et al., 2016).

- Pahute Mesa Conceptual Hydrologic Model Framework (Jackson et al., 2021)
- Standardization of PM single-well aquifer test results (Frus and Halford, 2018).
- Updated Death Valley regional groundwater flow system model and hydrogeologic framework (Belcher and Sweetkind, 2010).
- Groundwater Characterization and Effects of Pumping in the Death Valley Regional Groundwater Flow System (Halford and Jackson, 2020).
- Hydraulic Characterization of Volcanic Rocks in Pahute Mesa Using an Integrated Analysis of 16 Multiple-Well Aquifer Tests (Garcia et al., 2016).
- Assessing Hydraulic Connections Across a Complex Sequence of Volcanic Rocks—Analysis of U-20 WW Multiple-Well Aquifer Test (Garcia et al., 2011).
- Radionuclide Screening Analysis and Transport Parameters for Pahute Mesa (Carle et al., 2020).
- Infiltration studies (Fenelon et al., 2016; Middleton et al., 2019; Hershey et al., 2020).
- Bench scale flow and transport model (Lu et al., 2021).
- Interpretation of mineral diagenesis for assessment of RN transport (Carle, 2020).

1.4 Purpose and Scope

The purpose and scope of the analysis of transport data for the PM CAU are presented in the following subsections.

1.4.1 Purpose

The purpose of the tasks documented in this report is to analyze available information relevant for the simulation of RN transport within the groundwater flow system of PM and vicinity. The information will be used in the development of the PM CAU transport model. This document presents parameters necessary for CAU transport simulation and calibration, and to provide the likely ranges of those parameters. In this way, the document provides ranges from which to select for calibration and to ensure that parameters are constrained by observation.

Specific task objectives were as follows:

- Compile available transport parameter data and supporting information that may be relevant to the PM CAI.
- Assess the level of quality for the data and associated documentation.
- Analyze the data to derive expected values of transport parameters and estimates of the associated uncertainty and variability.

1.4.2 Scope

The scope of this task includes the assessment of data and information relevant to RN transport via groundwater in the PM subsurface. The data and interpretations are derived from a variety of sources including historical documents, new data collected in wells drilled specifically for the purpose of characterization of the PM-OV flow system, and recent published reports. Parameters of interest include half-lives of radioactive isotopes, effective porosity, fracture spacing, fracture aperture, dispersivity, matrix porosity, matrix diffusion coefficients, and matrix sorption coefficients. Descriptions of these parameters are provided in Section 5.0. These parameters address the transport processes of radioactive decay, advection, dispersion, matrix diffusion, and matrix sorption. Additional processes of fracture sorption and colloid facilitated transport, as discussed in Sections 3.2.5 and 3.2.6 are deemed to be of lesser importance for the PM CAU transport model; hence, parameters pertaining to these processes are not presented in Section 5.0. Data analysis includes the following:

1. Data/information compilation
2. Transfer of data from outside the PM-OV flow system
3. Data quality evaluation
4. Data assessment and interpretation activities
5. Discussion of data limitations

Data analysis includes the use of scientific software to assist in developing probability distributions for transport parameters of interest.

The area of investigation was selected to encompass the PM CAU and areas located downgradient that may be impacted. This area includes the PM-OV area and a portion of the Amargosa Desert downgradient of the PM CAU. Figure 1-3 shows the PM-OV groundwater basin. It comprises over 2,700 km^2, encompassing the northwestern portion of the NNSS and adjacent lands to the west

managed by the U.S. Air Force (USAF) and the Bureau of Land Management (BLM). The PM-OV Groundwater Basin includes Timber Mountain, Black Mountain, most of Oasis Valley, and Thirsty Canyon.

Even though the area of interest is limited to the PM-OV basin, information considered relevant to this task may be obtained from other nearby sites. Nearby sites include other underground test areas, the Yucca Mountain Site, and other sites in the NNSS region. The justification for the transfer of data from other sites was documented. The available data have been collected at various scales ranging from core-scale to field-scale experiments and were analyzed at their original scale. The issue of upscaling the data to the scale of the PM CAU transport model is addressed in Section 4.0.

1.5 Document Organization

This document consists of six sections and seven appendices:

- Section 1.0 provides an introduction, FFACO background, project background, purpose, and scope.
- Section 2.0 describes the regional setting and local hydrostratigraphic framework.
- Section 3.0 provides a conceptual model of transport at PM.
- Section 4.0 presents data analysis.
- Section 5.0 presents transport parameter data.
- Section 6.0 provides a list of references used in the document.
- Appendix A contains a listing of references detailing the additional work and analyses completed during Phase II.
- Appendix B contains brief descriptions of the HSUs used to construct the PM-OV model.
- Appendix C contains a justification of the use of nondirect datasets for developing parameter distributions for the PM modeling effort.
- Appendix D contains tables of data supporting the discussion of matrix porosity.
- Appendix E contains brief notes on the literature review for each location with fracture porosity estimates.

- Appendix F contains a description of the dispersivity data compiled for the RM/SM CAU (SNJV, 2008); augmented by data for Yucca Flat C well site.

- Appendix G contains a description of the diffusion data compiled for the RM/SM CAU (SNJV, 2008), augmented by more recent data from Telfeyan et al. (2018).

- Appendix H contains responses to NDEP comments on the draft version of this document.

2.0 REGIONAL SETTING AND LOCAL HYDROSTRATIGRAPHIC FRAMEWORK

Selected components of the PM-OV HFM (DOE/EMNV 2020a) are summarized in this section to support the contaminant transport data assessment presented in this report. Components described include the regional setting and local hydrostratigraphic framework.

2.1 Regional Setting

The PM-OV groundwater basin, as defined in Fenelon et al. (2016) (Figure 2-1), is part of the Death Valley regional groundwater flow system. A conceptual model of the PM-OV groundwater flow system of the NNSS was developed during the regional evaluation (DOE/NV, 1997). In subsequent investigations, the area of investigation and the PM-OV groundwater basin were modified and enlarged (BN, 2002; Fenelon et al., 2016). Summary descriptions of the NNSS regional hydrogeologic framework and groundwater occurrence and movement are presented in this section.

2.1.1 Regional Hydrogeologic Framework

The hydrogeologic framework used in the PM-OV HFM is based on the conceptual hydrologic system established for the NNSS area by Winograd and Thordarson (1975) and Blankennagel and Weir (1973). This early work was summarized and updated in Laczniak et al. (1996), the UGTA Phase I hydrostratigraphic regional model (IT, 1996c; BN, 2002), and the UGTA Phase II HFM (NSTec, 2014). The PM-OV HFM (DOE/EMNV, 2020a) supersedes the previous draft (NSTec, 2014) and published PM HFM reports. The PM-OV HFM (DOE/EMNV, 2020a) contains the relevant details, summary discussion, and supporting information regarding the history and development of the HFM.

The rocks of the NNSS have been classified using a two-level classification scheme, in which hydrogeologic units (HGUs) are grouped to form HSUs (Prothro, 2009; DOE/EMNV, 2020a). The HGUs are used to categorize rocks according to their ability to transmit groundwater, which is mainly a function of the rocks' primary lithologic properties, degree of fracturing, and secondary mineral alteration. The complex hydrologic properties of the volcanic rocks of the NNSS and vicinity

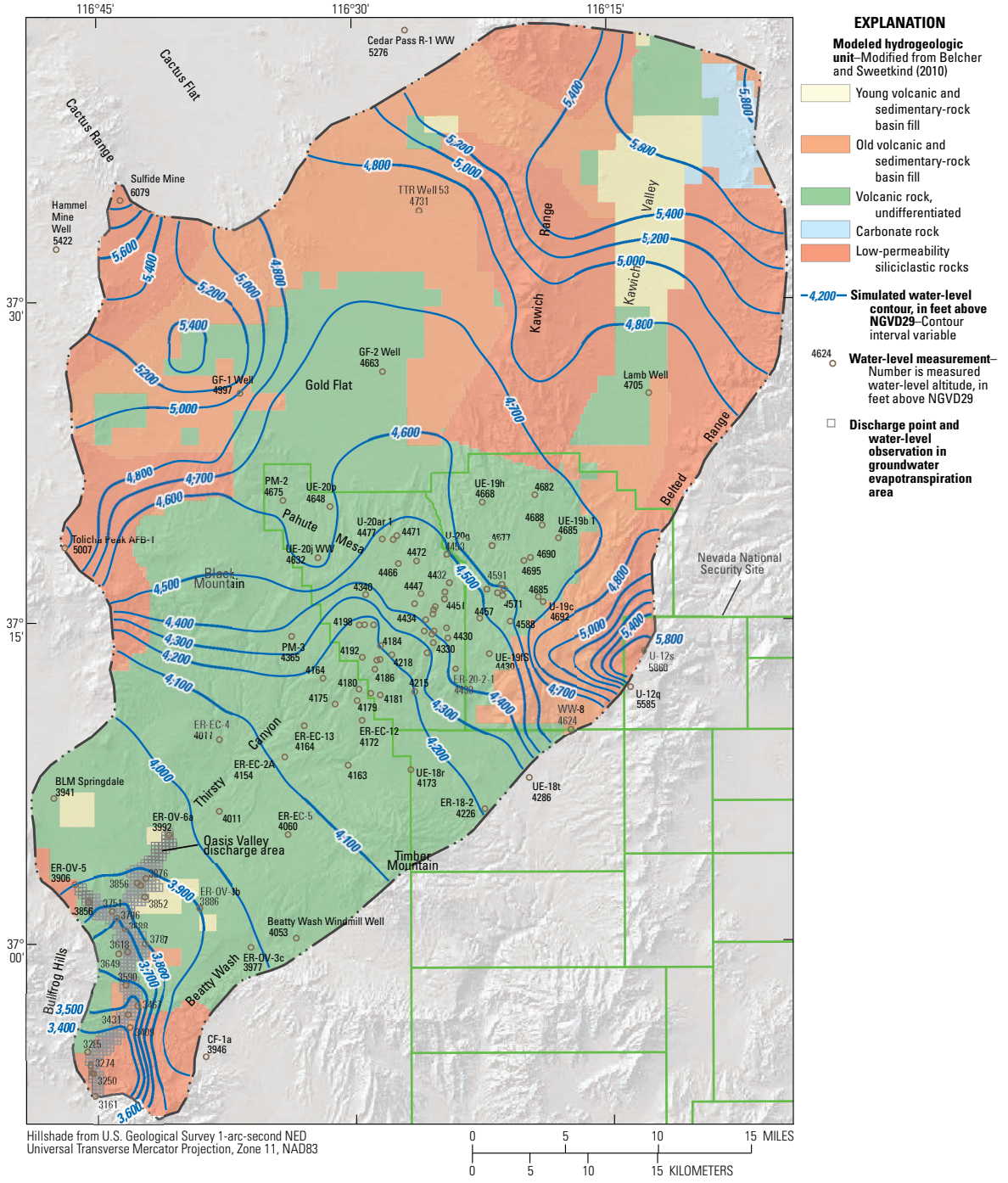

Figure 2-1
Features of the PM-OV HFM Groundwater Flow System Region
Source: Fenelon et al., 2016

are best addressed in terms of HGUs (Blankennagel and Weir, 1973; Winograd and Thordarson, 1975). The concept of HSUs made up of groups of similar HGUs is also very useful in volcanic terrains because stratigraphic units can differ greatly in hydrologic character both laterally and vertically. The HSUs serve as "layers" in the PM-OV area and NNSS CAU-scale HFMs. Further discussion and explanation of HGUs and HSUs are found in Sections 2.1.1.1 and 2.1.1.3.

The PM Phase II HFM was expanded to include the entire PM-OV groundwater basin area, as defined in Fenelon et al. (2016). The additional area to the north, south, east, and west significantly increases the size of the model domain. This new model domain is the basis for the PM-OV HFM and fully incorporates the PM CAU model. This additional area resulted in an increase in the number of structural elements (i.e., faults and caldera margins) and HSUs in the PM-OV HFM. Surface mapping, geophysics, and limited borehole information provide the majority of data in the new areas. The lower data density (e.g., fewer boreholes and lower-resolution geophysics) of the northern extension results in a lower resolution of the modeled HSU distribution in this area. However, given the minimal amount of recharge (Fenelon et al. 2016) and the presence of confining and composite units under the depositional basins in the northern extension (i.e., Gold Flat and Kawich Valley), there is only a minimal impact regarding geologic uncertainty. This uncertainty is acceptable based on the fact that the area is upgradient of the sources and the areas through which transport will occur. Therefore, the need for higher-resolution hydrostratigraphic information is less than in the testing areas and downgradient of them.

The following paragraphs summarize the components that make up the PM-OV HFM, addressing HGUs, stratigraphy, HSUs, and structural features, respectively.

2.1.1.1 Hydrogeologic Units

The rocks of the NNSS and UGTA CAUs have been categorized into one of nine HGUs, which are the alluvial aquifer (AA), four volcanic HGUs, two intrusive HGUs, and two HGUs that represent the pre-Tertiary rocks (Table 2-1). Table 2-2 provides a definition and brief description of significant hydrologic properties of each HGU. Section 4.0 of the PM-OV HFM report (DOE/EMNV, 2020a) provides additional detailed discussion of the HGUs present in the model.

Table 2-1
Summary of Hydrologic Properties for HGUs at the NNSS Used in the PM-OV HFM

HGU [a]			Fracture Density [b, c]	Relative Hydraulic Conductivity [c]
Alluvial aquifer (AA)			Very Low	Moderate to Very High
Vitric-tuff aquifer (VTA)			Low	Low to Moderate
Welded-tuff aquifer (WTA)			Moderate to High	Moderate to Very High
Lava-flow aquifer (LFA)[d]	Pumiceous lava	Vitric	Low	Low to Moderate
		Zeolitic	Low	Very Low
	Stoney lava and vitrophyre		Moderate to High	Moderate to Very High
	Flow breccia		Low to Moderate	Low to Moderate
Tuff confining unit (TCU)			Low	Very Low to Very High
Intra caldera intrusive confining unit (IICU)			Low to Moderate	Very Low
Granitic confining unit (GCU)			Low to Moderate	Very Low
Carbonate aquifer (CA)			Low to High (Variable)	Low to Very High
Clastic confining unit (CCU)			Moderate	Very Low to Low [e]

[a] See Table 2-2 for hydrogeologic nomenclature.
[b] Including primary (cooling joints in tuffs) and secondary (tectonic) fractures.
[c] The values presented are qualitative estimates based on data from published (IT, 1996a; Blankennagel and Weir, 1973; and Winograd and Thordarson, 1975) and unpublished sources (i.e., numerous UGTA, Los Alamos National Laboratory [LANL], and Lawrence Livermore National Laboratory [LLNL] drill-hole characterization reports).
[d] Abstracted from Prothro and Drellack, 1997.
[e] Fractures tend to be sealed by the presence of secondary minerals.

Note: Contaminant transport parameters associated with the HGUs are described in Section 5.0.

Alluvial HGU

The deposits of alluvium (alluvial aquifer) fill the main depositional basins of the NNSS, and generally consist of an unconsolidated to partially consolidated mixture of boulders, gravel, sand, silt, and clay derived from volcanic and Paleozoic sedimentary rocks (Slate et al., 1999). Overall, the alluvium is typically thin and unsaturated over much of the PM-OV HFM. Only in the deeper depositional basins (e.g., Gold Flat, Kawich Valley, and Oasis Valley) is the alluvium thicker and saturated below the water table.

Volcanic HGUs

The volcanic rocks within the study area can be categorized into four HGUs based on primary lithologic properties, degree of fracturing, and secondary mineral alteration. The HGUs are vitric-tuff aquifers (VTAs) (e.g., nonwelded, bedded, and reworked); tuff confining units (TCU) (zeolitic and/or

Table 2-2
HGUs of the PM-OV HFM

HGU	Typical Lithologies	Hydrologic Significance
Alluvial aquifer (AA) [a]	Unconsolidated to partially consolidated gravelly sand, eolian sand, and colluvium; thin, basalt flows of limited extent	Has characteristics of a highly conductive aquifer, but less so where lenses of clay-rich paleocolluvium or playa deposits are present.
Vitric-tuff aquifer (VTA)	Bedded tuff; ash-fall and reworked tuff; vitric	Constitutes a volumetrically minor HGU. Generally does not extend far below the static water level due to tendency to become zeolitized under saturated conditions. Significant interstitial porosity (20 to 40 percent) and matrix permeability. Typically insignificant fracture permeability.
Welded-tuff aquifer (WTA)	Welded ash-flow tuff; vitric to devitrified	Degree of welding greatly affects interstitial porosity (less porosity as degree of welding increases) and permeability (greater fracture permeability as degree of welding increases).
Lava-flow aquifer (LFA)	Rhyolite lava flows; includes flow breccias (commonly at base) and pumiceous zones (commonly at top)	Generally a caldera-filling unit (with exceptions: i.e. ER-20-12). Hydrologically complex; wide range of transmissivities; fracture density and interstitial porosity differ with lithologic variations.
Tuff confining unit (TCU)	Zeolitized bedded tuff with interbedded, but less significant, zeolitized, nonwelded to partially welded ash-flow tuff	May be saturated but measured transmissivities are very low. May cause accumulation of perched and/or semiperched water in overlying units, where fractured or faulted transmissivities maybe much greater.
Intra caldera intrusive confining unit (IICU)	Highly altered, highly injected/intruded country rock and granitic material	Assumed to be impermeable. Conceptually underlies each of the SWNVF calderas and Calico Hills. Developed for this study to designate basement beneath calderas as different from basement outside calderas.
Granite confining unit (GCU)	Granodiorite, quartz monzonite	Relatively impermeable; forms local bulbous stocks, north of Rainier Mesa and Yucca Flat; may contain perched water.
Carbonate aquifer (CA)	Dolomite, limestone	Transmissivity values differ greatly and are directly dependent on fracture frequency.
Clastic confining unit (CCU)	Argillite, siltstone, quartzite	Clay-rich rocks are relatively impermeable; more siliceous rocks are fractured, but with fracture porosity generally sealed due to secondary mineralization.

[a] AA is also an HSU in the PM-OV HFM.

argillic altered volcanic rocks); welded-tuff aquifers (WTAs) (welded vitric to devitrified ash-flows); and lava-flow aquifers (LFAs). These HGUs host the majority of the important flow paths within the PM-OV groundwater basin.

VTAs, consisting principally of nonwelded and bedded tuffs, are usually found above the water table and have only limited volumetric extent in the PM-OV HFM below the water table. VTA HGUs are typically dominated by matrix permeability and porosity and do not normally support extensive fracture systems. In part based on extended exposure to saturated or hydrothermal conditions, relatively high matrix porosity, permeability, and the reactive nature of the vitric (volcanic glass) material itself vitric tuffs (i.e., nonwelded and bedded) are frequently altered to zeolites and clays. The formation of zeolites and clays significantly reduces the permeability of the rock.

TCUs are altered volcanic rocks (i.e., zeolitic, argillic, or quartzofeldspathically altered) that generally act as confining units across the PM. Alteration primarily affects the volcanic glass material. Recent work by Carle (2020) presents a detailed mineralogical analysis of the PM area. As alteration progresses, matrix porosity may remain similar to or be significantly reduced relative to the unaltered rock while the matrix permeability is significantly reduced. The reduction of permeability and porosity occurs due to the growth of minerals in the pore space of the vitric rocks. However, since both zeolites and clays can store water within their respective structures, there is only a minor change in porosity. Zeolitic and argillic rocks do not typically support well-developed fracture systems. Where the TCUs occur at higher elevations (e.g., Pahute Mesa and Rainier Mesa), perched water zones may form on the top of the units (Winograd and Thordarson, 1975; Fenelon et al., 2016; Jackson and Fenelon, 2018). While generally acting as competent confining units, there are instances where TCUs are fractured and transmissivity is much greater (Jackson et al., 2021). Fractured rock is ubiquitous across PM, and open fractures when present in the material may control hydraulic conductivity to a greater extent than the lithology. HGUs have considerable overlap in the ranges of their particular hydraulic conductivities, and the average values for WTA, LFA, and TCU HGUs are similar (Navarro, 2021).

WTAs, such as welded ash-flow tuffs, are widely distributed within the HFM. These HGUs are typically devitrified (i.e., crystallized) but may be vitric and have minimal matrix porosity and permeability. However, they sustain fractures more readily, and have hydrologic properties dominated by fracture permeability and porosity. The fractures can be both thermal (i.e., cooling joints) or tectonic in origin. Overall they have relatively high permeability (Blankennagel and Weir, 1973; Winograd and Thordarson, 1975; Laczniak et al., 1996; IT, 1996c; Prothro and Drellack, 1997). Welded ash-flow tuffs are typically widely distributed within and outside the source caldera.

LFAs may be devitrified (i.e., crystallized) or vitric. However, lava flows tend to have more erratic and localized distributions, typically associated with one or more vents, than the WTAs and are typically found within the source caldera. Flow through LFAs is also dominated by fracture porosity and permeability. An LFA (Calico Hills Lava-Flow Aquifer #5 [CHLFA5]) identified during drilling of Well ER-20-12 is a significant exception to the norm of an LFA being located inside the caldera margins.

Pre-Tertiary HGUs (Paleozoic and Precambrian)

The pre-Tertiary rocks beneath the study area are categorized by one of two HGUs based on primary lithologic properties, degree of fracturing, and secondary mineral alteration. The two HGUs are the carbonate aquifers (CA) and clastic confining units (CCU).

CCUs are made up of siliciclastic rocks (e.g., quartzites, siltstones, and shales) and typically are aquitards or confining units. Siliciclastic rocks may be fractured. However, these fractures are typically filled by secondary mineralization (e.g., calcite, silica). The siliciclastic confining units form the base of the PM-OV HFM (DOE/EMNV, 2020a).

CAs, limestone and dolomite rocks, tend to be aquifers (Winograd and Thordarson, 1975; Laczniak et al., 1996). The carbonate rocks that make up the CA have a wide variation in their hydrologic properties. Matrix permeability and porosity is typically low unless enhanced by fracturing or solution activities (e.g., fault or solution breccia) (Winograd and Thordarson, 1975).

Intrusive HGUs

The intrusive confining unit (ICU) category includes intracaldera intrusive confining units (IICU) and the granitic confining unit (GCU). These rocks are relatively impermeable and are considered to behave as a confining unit. The IICUs conceptually underlie the calderas of the SWNVF, as well as other calderas in the PM-OV HFM. The GCU, which consists of Mesozoic age granitic stocks (i.e., granodiorite and quartz monzonite), is exposed to the north of Rainier Mesa and Yucca Flat areas of the model.

The distribution of these units in the subsurface is unknown. The Climax stock in extreme northern Yucca Flat (Houser et al., 1961; Walker, 1962; Maldonado, 1977) and the Gold Meadows stock in the extreme eastern part of the PM-OV model area (Snyder, 1977) may serve as analogs for the GCU.

2.1.1.2 Stratigraphic Units

An idealized stratigraphic section is shown in Figure 2-2 and has been grouped and subdivided, in part according to work and mapping completed at the NNSS and surrounding area over the past 50 years (e.g., Ekren et al., 1971; Slate et al., 1999; Warren, 2000a; Fridrich et al., 2007). Extensive mapping and multiple drill holes allow the detailed subdivision of these units over a significant portion of the area of interest.

Note that while many of the stratigraphic units are widely distributed, their various properties and characteristics (e.g., welding, thickness, porosity, permeability, alteration) may vary significantly with distance from their source. Section 4.0 of the PM-OV HFM report (DOE/EMNV, 2020a), in addition to the previously referenced reports, provides additional detail regarding stratigraphic units, their extent, and properties.

2.1.1.2.1 Quaternary (Q)

The Quaternary units in the PM-OV HFM are principally alluvium, colluvium, and younger basalt flows. The alluvium consists of fine (clay/silt/sand) to coarse (gravel/cobble) material that is unconsolidated to partially consolidated and frequently exhibits some level of sorting, grading, and bedding.

Alluvial material has undergone some transport and sorting from its source area to the point of deposition. In some of the depositional basins (e.g., Gold Flat and Kawich Valley) fine-grained playa sediments, mostly silts and clays, have been deposited. These sediments inhibit downward infiltration of surface water, limiting recharge to the underlying groundwater system. Colluvium typically consists of relatively coarser and more angular material than alluvial sediments and has not been transported far from the parent source. Alluvium and colluvium are typically unsaturated except where they occur in deeper depositional basins (e.g., Gold Flat, Kawich Valley, and Oasis Valley) (DOE/EMNV, 2020a). Ekren, Slate, and others (Ekren et al., 1971; Slate et al., 1999) have noted that the base of the Tertiary section is marked by the presence of coarse gravels, comprised of Paleozoic material, which may, or may not, contain altered volcanics. This unit appears to be similar to the Paleocolluvium identified in Yucca Flat.

The basalt lava flows, vents, and cones in the model area are primarily Pliocene to Holocene in age and exhibit some level of permeability based on fracturing and other permeable zones (e.g., flow

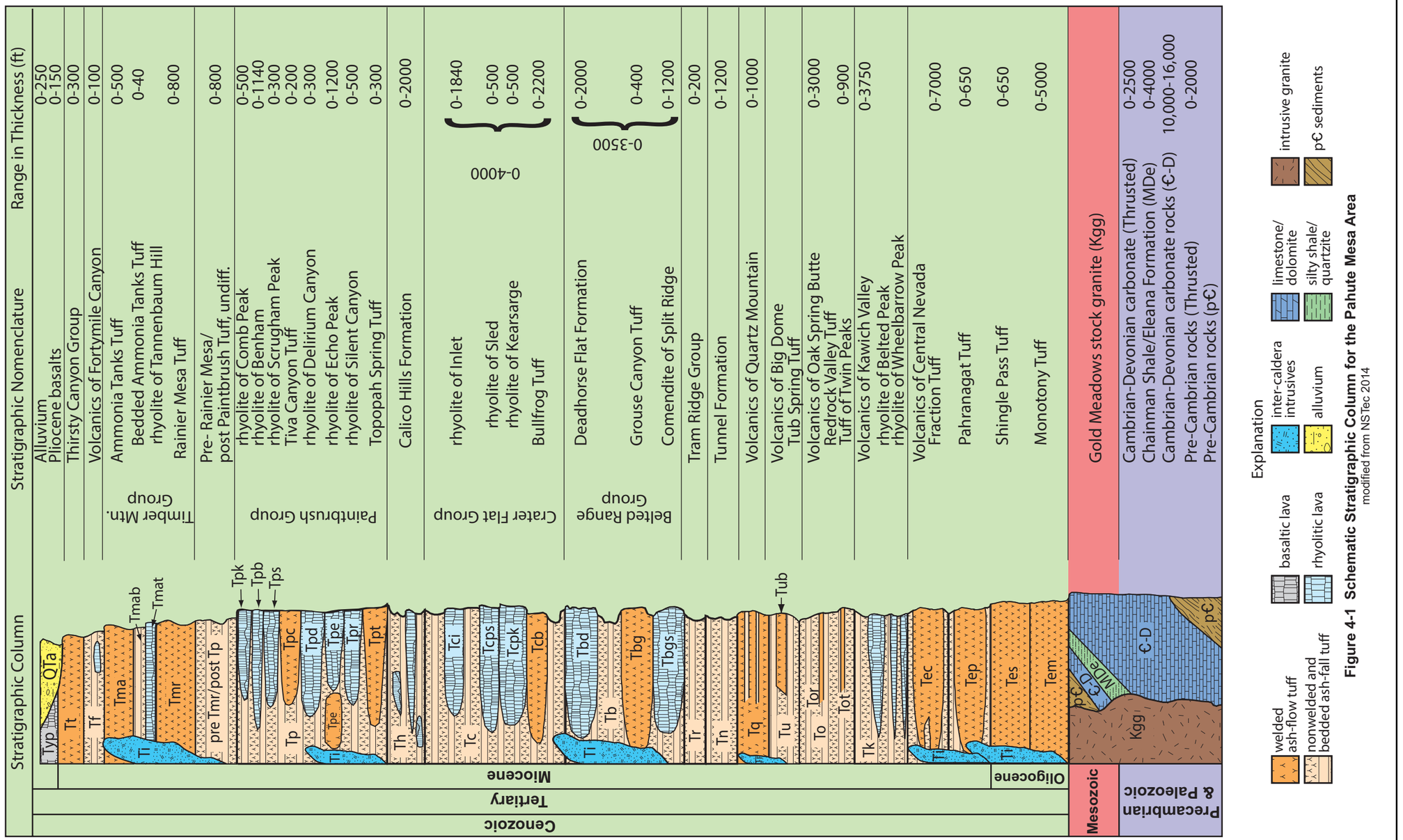

Figure 4-1 Schematic Stratigraphic Column for the Pahute Mesa Area
modified from NSTec 2014

Figure 2-2
Schematic Stratigraphic Column for the PM-OV HFM
Source: Modified from NSTec, 2014

breccias and scorrias). However, most of these flows are above the water table and typically unsaturated in the PM-OV HFM area (Slate et al., 1999).

2.1.1.2.2 Tertiary (T)

Tertiary units in the PM-OV HFM consist principally of igneous units with minor sediments. The volcanic rocks include pyroclastic rocks (i.e., ash-flows, ash-falls), lava flows, and small intrusive bodies.

Pyroclastic rocks are made up of a spectrum of welded to nonwelded ash-flows, nonwelded ash-falls, and bedded (including reworked) material. Porosity and permeability are controlled, in part, by degree of welding, alteration, and fracturing (initial thermo-mechanical and subsequent tectonic). As a general rule, the greater the degree of welding, the greater the fracturing and hence increased secondary permeability and porosity. Conversely, the lesser the degree of welding and crystallization, the greater the potential alteration (zeolitic or argillic) and the lower the fracture frequency and resulting secondary permeability and porosity.

Alteration, both zeolitic and argillic, principally occurs in initially vitric nonwelded, bedded, and reworked tuffs. These rocks have been saturated (i.e., below a paleo or current water table) for some duration. Alternatively, the rocks may have been affected by a hydrothermal system (e.g., Cactus Range, Gabbard Hills).

Zeolitic rocks (e.g., portions of the Paintbrush, Calico Hills, and Crater Flat Formations) typically have moderate to high porosity similar to when they were vitric. However, they have lower permeability. The reduction of permeability occurs due to the growth of zeolite and clay minerals in the pore space of the vitric rocks. However, since both zeolites and clays can store water in their respective structures, there is only a minor change in porosity.

A number of the pyroclastic (stratigraphic) units are of large volume and widely distributed throughout the area of interest (e.g., Topopah Spring, Tiva Canyon, Rainier Mesa, and Ammonia Tanks) (DOE/EMNV, 2020a; Appendix C, Table C-1). These stratigraphic units have been further subdivided based on rock properties (e.g., welding and crystallization) and comprise multiple HSUs. Many of the younger volcanics (e.g., Thirsty Canyon Group) have surface expression and are above or extend downward to just below the water table and are typically unsaturated. These younger

units may have substantial vitric portions. Surface expressions of the nonwelded to reworked portions of these younger units may have been heavily dissected by geologic processes (e.g., erosion and faulting).

Lava flows, which were initially deposited on the surface and have been buried by subsequent lava or pyroclastic flows, have a more erratic and limited distribution compared to pyroclastic flows. They also show a marked zoning to their rock properties such as permeability and porosity. Much of the variability exhibited by lava flows is controlled by the thickness of the different zones within the flow and the subsequent alteration.

In a typical rhyolitic lava flow aquifer (e.g., CHLFA5) the outer zone is composed of pumiceous material that may be zeolitized and relatively impermeable. This is followed by one to three zones of densely welded vitric to crystallized lava that may be heavily fractured. Finally, a lower zone can be present that may also be zeolitized and impermeable (Prothro and Drellack, 1997). See Figure 2-3 for a schematic view of a rhyolitic lava flow. The PM-OV HFM report (DOE/EMNV, 2020a) provides a more detailed discussion of LFAs and their properties.

2.1.1.2.3 Mesozoic (M)

Cretaceous granitic (i.e., granodiorite and quartz monzonite) intrusive units (e.g., Gold Meadows Stock) are GCUs and make up the Mesozoic units present in the PM-OV HFM. These units are relatively impermeable and are treated as confining units. They are poorly exposed on the Rainier Mesa and not exposed on the PM. There are a number of other small intrusives exposed in the northern portion of the PM-OV HFM (DOE/EMNV, 2020a).

2.1.1.2.4 Precambrian & Paleozoic (pC)

Paleozoic units are composed of a mixture of siliciclastic (e.g., quartzite, siltstone, and shales) units and carbonate sediments (e.g., limestone and dolomite). Siliciclastic units, CCUs, are typically confining units and the carbonates, CAs, tend to behave as aquifers. Many of the carbonates exhibit low permeability and porosity unless subsequently enhanced by solution or tectonic activity. The Precambrian units in the area are composed predominantly of silicilastic sediments and metasediments with one known outcrop of crystalline basement material in the Trappman Hills on the western side of the PM-OV HFM.

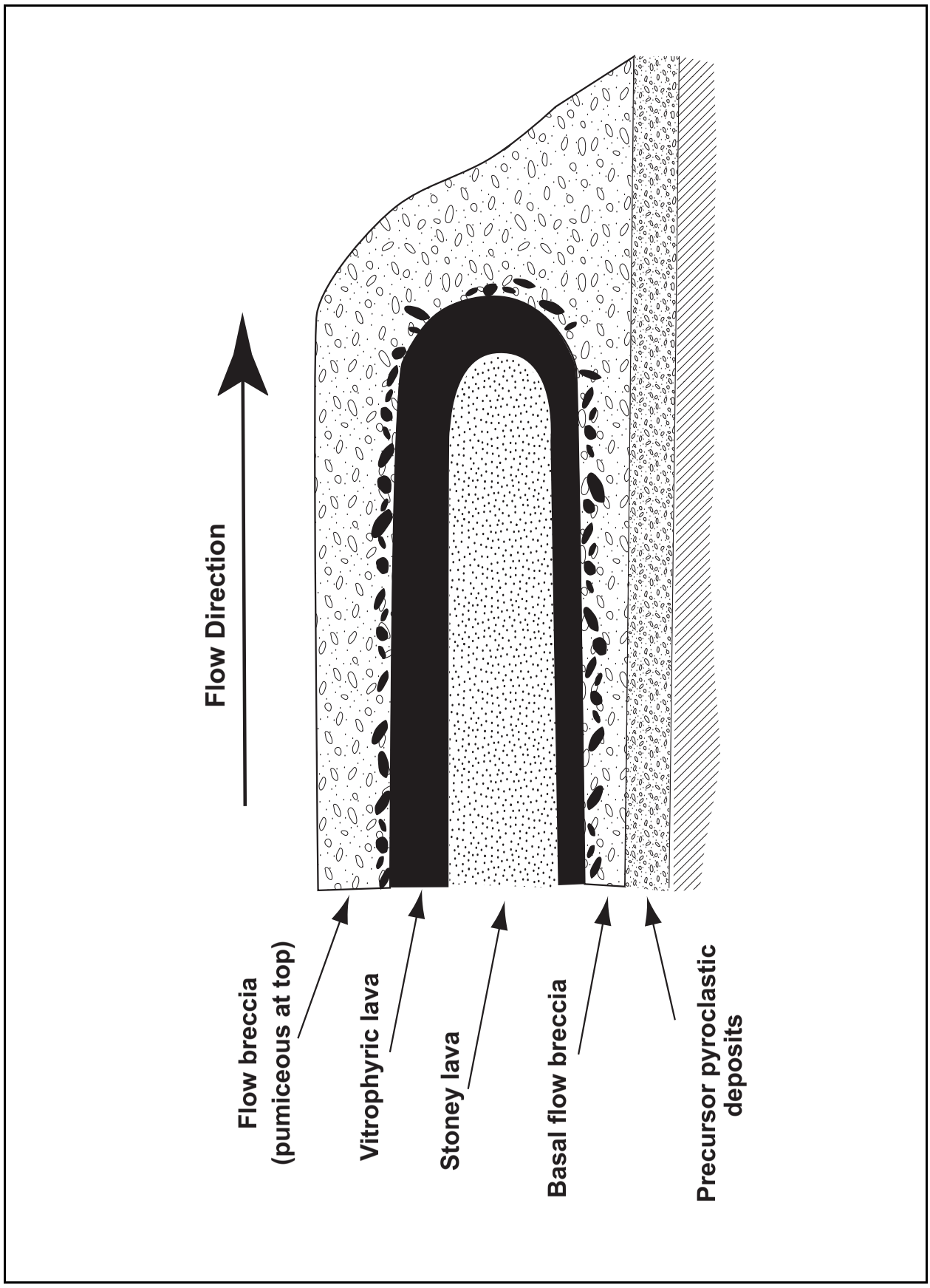

Figure 2-3
Schematic Section through a Rhyolitic Lava Flow
Source: Modified from Cas and Wright, 1987

2.1.1.3 Hydrostratigraphic Units

HSUs are groupings of contiguous stratigraphic units that have a particular hydrogeologic character, such as being either an aquifer (unit through which water moves readily) or a confining unit (a unit that generally is impermeable to water movement). HSUs may incorporate multiple HGUs but are named and defined on the basis of the dominant HGU. Definitions from the PM-OV HFM (DOE/EMNV, 2020a) for the 77 HSUs are provided in Table B-1 (see Appendix B), and a correlation chart with all CAUs on the NNSS is provided on Plate 1. HSUs are listed in approximate order from surface to basement.

The HSUs stratigraphic position is based on volcanic stratigraphy, lithologic properties related to depositional environment, postdepositional alteration, and degree of welding. Outside the caldera complexes, structural relationships depicted on hand-drawn cross sections, surface map data, and borehole lithostratigraphic logs were used to assist in determining the distribution of volcanic HSUs. A structural block model (Warren et al., 2000) was also used for additional guidance in this area. The PM-OV HFM report (DOE/EMNV, 2020a) provides the rationale and detailed information regarding model parameters and stratigraphy.

Additionally, the dominant lithology of some units may change or pinch out laterally (e.g., LFA close to the source vents, WTA farther away, and finally nonwelded TCU or VTA at distal edges). Another simplification addresses the caldera roots. In the PM-OV HFM area, the plutonic or hypabyssal igneous rocks that likely occur at depth below the calderas are modeled as intrusive confining units (ICU) which are similar in their hydrologic properties to the CCU.

2.1.1.4 Structural Features of the PM-OV HFM

Geologic structural features are an important part of the hydrologic framework of the groundwater flow system of the PM-OV area. They define the geometric configuration of the flow domain, including the distribution, thickness, and orientation of rock units. The depositional patterns of many of the geologic units occurring in the area may have been strongly influenced by synvolcanic structures, including caldera faults and some normal faults. Figure 2-4 provides an overview of some of the significant structures incorporated into the PM-OV HFM and their spatial relationship to discharge areas. Geologic structures on the NNSS, NTTR, and surrounding areas were identified on

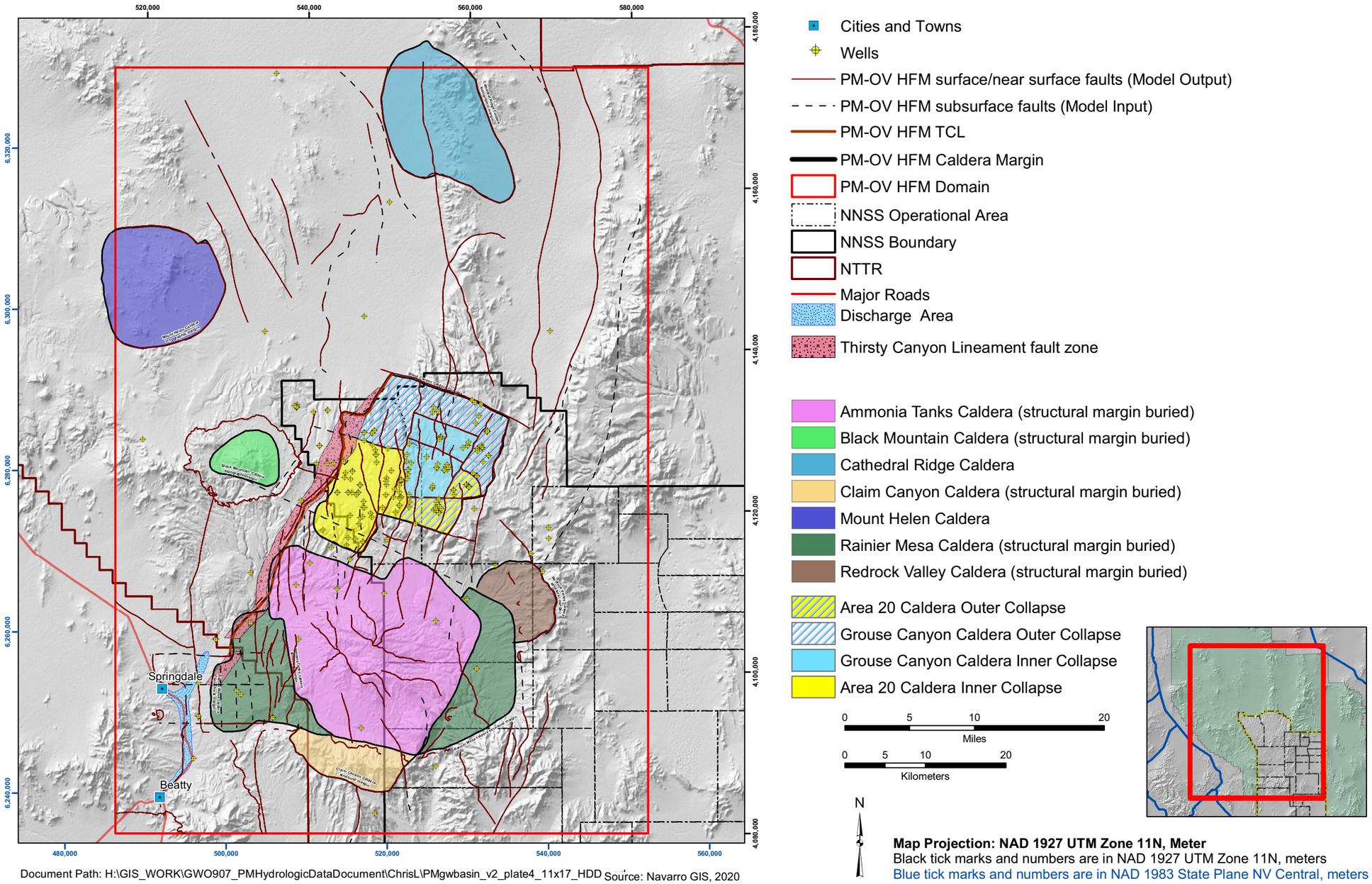

Figure 2-4
Structural Features of the PM-OV HFM

the basis of surface mapping, drilling activities, and geophysical data collection. Section 3.0 of the PM-OV HFM (DOE/EMNV, 2020a) provides more detailed discussion, references, and information.

The PM-OV HFM includes a total of 105 structural elements, which are either faults or calderas. Faulting (e.g., caldera-related and Basin & Range), for example, may result in juxtaposition of units with different hydrologic properties or may influence depositional thickness. Structures themselves may influence flow patterns by acting as conduits for flow or barriers to flow (Prothro et al., 2009; DOE/EMNV, 2020a). For example, data collected during the drilling of Well ER-20-12 in 2015 indicates that the Ribbon Cliff Structural Zone has greater offset than previously suspected and may have enhanced the hydraulic connectivity to HSUs south of the zone (NNSA/NFO, 2015). Faults included in the PM-OV HFM were those with the greatest offset, throughgoing structures, or that seem to form significant structural boundaries.

The Thirsty Canyon Lineament (TCL) (Mankinen et al., 1999; Grauch et al., 1999) and related Thirsty Canyon Fault Zone (TCFZ) (Hildenbrand et al. 1999; Mankinen et al., 2003) are important features of the PM-OV HFM (Navarro, 2018; DOE/EMNV, 2020a). Development of the TCL and the TCFZ concepts and subsequent incorporation into the PM-OV HFM are discussed in detail in Wurtz and Day (2018). The TCL is a north–northeast-trending, geophysically inferred feature that has been identified on regional gravity and aeromagnetic maps (Mankinen et al., 1999 and 2003).

The lineament extends from just west of Well ER-EC-8, northeastward beneath western PM east of the Black Mountain caldera to the southern edge of Gold Flat. Hildenbrand et al. (1999) suggested that the TCL represents a fault zone, rather than a single structure and that the fault zone is an older structure that may have influenced subsequent caldera activity. Geophysical and geologic profiles across the lineament by Mankinen et al. (1999 and 2003) indicate that the lineament is characterized by a zone of en echelon faults 2 to 3 km (1.2 to 1.9 mi) wide. Figure 2-5 provides a map of the gravity inversion data, interpreted cross sections (profiles) focused on the area of the interpreted TCFZ, locations of cross sections (profiles), and stratigraphic information regarding units in the TCFZ.

Nine calderas have been included in the PM-OV HFM. These calderas reflect a variety of geometries and collapse processes. Caldera-collapse processes include the “piston,” down-sag, trap-door, and piecemeal collapse. Some of the calderas seem to have collapsed along pre-existing linear faults, resulting in polygonal boundaries (Kane et al., 1981; Ferguson et al., 1994).

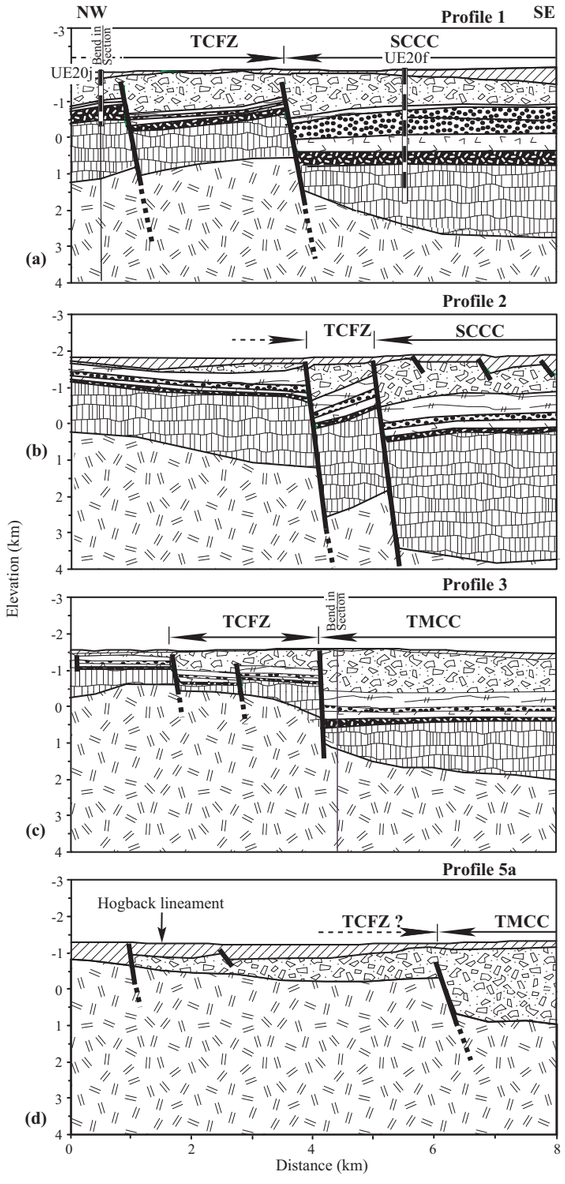

Geologic interpretation of subsurface structure along profiles crossing the Thirsty Canyon lineament. Vertical exaggeration is 0.6.
(**Modified from Mankinen et al, 2003**)

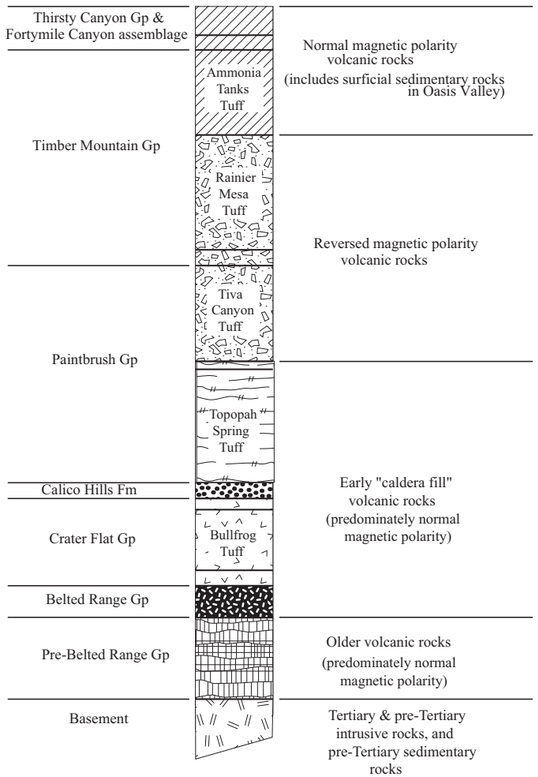

Generalized volcanic stratigraphy of the study area. Unit patterns are the same as shown in our geologic interpretations of the geophysical models. Horizontal lines in the column denote unit boundaries within the larger volcanic groups. Only the names of the major stratigraphic subdivisions are shown on the column. Unit thicknesses schematically depict the erupted magma volumes as estimated by Sawyer and others (1994). (**Modified from Mankinen et al, 2003**)

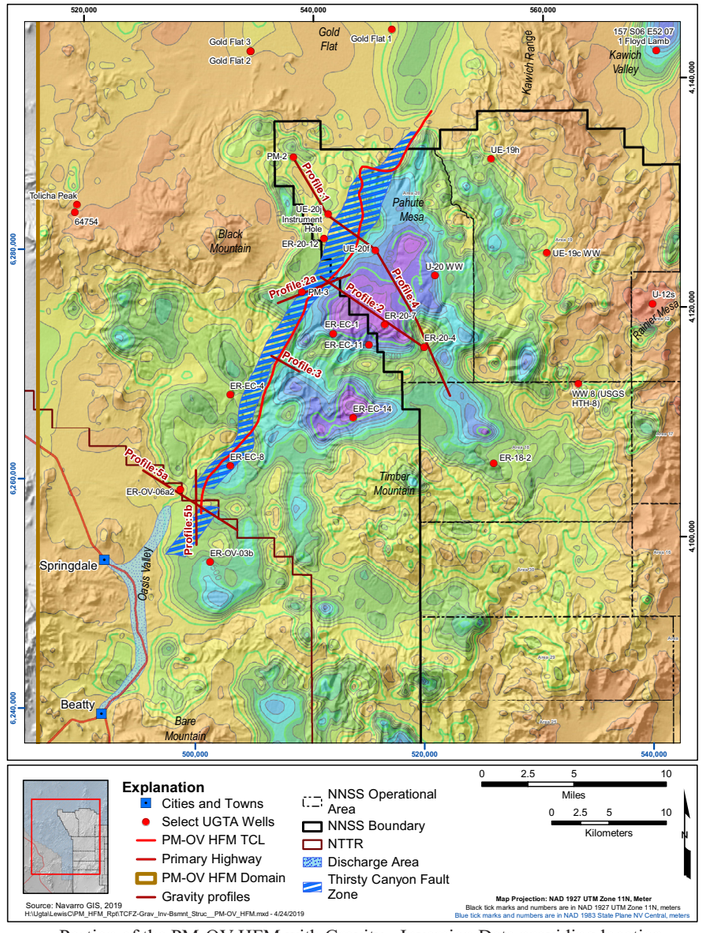

Portion of the PM-OV HFM with Gravity - Inversion Data providing location of the Thirsty Canyon Lineament as used in the PM-OV HFM
Figure also shows PM-OV Discharge Area and inferred Thirsty Canyon Fault Zone

(Gravity - Inversion Data **Modified from USGS MF-2381-E**)
(Thirsty Canyon Fault Zone **Modified from Mankinen et al, 2003**)

Mankinen, E.A., T.G. Hildenbrand, C.J. Fridrich, E.H. McKee, and C.J. Schenkel. 2003. Geophysical Setting of the Pahute Mesa - Oasis Valley Region Southern Nevada, Report 50. Reno, NV: Nevada Bureau of Mines and Geology, University of Nevada Mackay School of Mines.

Blakely, R.J., and D.A. Ponce. 2001. Map Showing Depth to Pre-Cenozoic Basement in the Death Valley Ground-water Model Area, Nevada and California. Miscellaneous Field Studies Map MF-2381-E. Scale 1:250,000. Denver, CO: U.S. Geological Survey.

Figure 2-5
Geophysical and Geologic Information Related to the Thirsty Canyon Lineament and Fault Zone of the PM-OV HFM

2.1.2 Groundwater Occurrence and Movement

Figure 2-1 is a map depicting the region of the PM-OV groundwater flow system including water level contours, generalized geology, and selected wells. As seen from the water level contours shown in Figure 1-3, groundwater in the PM-OV groundwater basin generally flows to the south–southwest. Hydraulic property data for rocks relevant to the PM-OV HFM have been reassessed and are presented in the HDD (Navarro, 2021). A comprehensive hydrologic conceptual model of groundwater flow in the PM-OV groundwater basin is given in Jackson et al. (2021).

2.1.2.1 Groundwater Occurrence

Within the NNSS and surrounding area, groundwater occurs in alluvial, volcanic, and carbonate materials. Saturated alluvial materials are present in Oasis Valley, Kawich Valley, and Gold Flat. Saturated Tertiary volcanics are present throughout the PM-OV basin. The distribution and thickness of alluvial and volcanic aquifers are highly variable throughout the PM-OV HFM and many HSUs are interpreted to be discontinuous. In most instances, AAs are confined to a valleys bounded by mountain ranges and are localized discontinuous aquifers in the PM-OV basin.

Within the PM-OV flow system, the shallowest depth to groundwater is zero in the Oasis Valley discharge area, where regional springs discharge to the land surface compared to more than 610 m (2,000 ft) beneath PM on the northern portions of the NNSS (IT, 1996b; DOE/NV, 1997). Details of water-level information are provided in Appendix C, Table C-1 of the HDD (Navarro, 2021). Perched groundwater is found locally throughout the NNSS and occurs within and on top of the TCUs and, to some extent, overlying units. In the highlands, springs emerge from perched groundwater lenses. Spring discharge rates are low and this water is used mostly by wildlife.

2.1.2.2 Groundwater Movement

Within the PM-OV groundwater flow system, groundwater movement is controlled by hydrologic properties of the rocks which are influenced by geologic conditions.The general direction of groundwater flow in the PM-OV groundwater basin is from north to south and east to southwest. The direction of groundwater flow is locally influenced in areas where structural and geologic conditions have controlled the distribution and thickness of aquifer and confining units. In some areas of the PM-OV flow system, groundwater encounters structural and geologic conditions, such as structural highs composed of confining units such as the lower clastic confining unit (LCCU),

that promote an upward flow component. The upward flow component brings water to discharge at the surface at regional springs (e.g., springs in the Beatty-Oasis Valley area).

Groundwater recharge results from precipitation in the higher elevations, primarily PM, Rainier Mesa, and Timber Mountain. Additional groundwater recharge may take place in the Kawich Range and the Belted Range (Hevesi et al., 2003; Middleton et al., 2019). Most of recharge occurs from spring snowmelt following winters of above-normal precipitation (Jackson and Fenelon, 2018). Infiltration occurs along stream channels, and minor infiltration potentially occurs in playas. Recharge rates and distributions have been estimated for the model area and are described in the HDD (Navarro, 2021).

Within the PM-OV groundwater basin groundwater discharges to the surface in the form of springs, seeps and evapotranspiration (ET) in Oasis Valley. Artificial discharge occurs as groundwater pumpage from water supply wells (public and domestic), agricultural and stock wells, and industrial wells. Public, domestic, and industrial water supply wells for the NNSS produce water from the carbonate, volcanic, and alluvial aquifers. South of the NNSS, private and public water supply wells are completed in the AA. Discharge from the PM-OV area is discussed in the HDD (Navarro, 2021).
HSU Model Development

The approach followed to develop the PM-OV HFM is summarized in this section. The model area is shown in Figure 1-3.

The PM-OV HFM was constructed using EarthVision, Version 10 (Dynamic Graphics, 2019), a 3-D geologic model building and visualization software package. Input data included the PM Phase II HFM, new drill-hole data from Well ER-20-12, digital elevation model data, outcrop, geologic, and fault data from surface geologic mapping for the northern extension of the model, and relevant geophysical and interpretive data for the TCL and TCFZ (Wurtz and Day, 2018; DOE/EMNV, 2020a).

Where necessary, the data were supplemented with control points generated from geophysical data, cross sections, and structure-contour maps. A control point is a manually generated data point used to facilitate the automated contouring of data. During development, the model underwent an iterative process of model builds, internal geologic reviews, and quality assurance (QA)/quality control (QC) checks.

Historically, an initial HSU model was constructed based on the conceptual model of the NNSS hydrologic system described by Winograd and Thordarson (1975). Additional modifications and refinements were made by personnel from the U.S. Geological Survey (USGS) and various DOE contractors resulting in the PM-OV HFM. For details regarding model development and refinement, see the PM Extended HFM Data Document (Navarro, 2019d) and the PM-OV HFM (DOE/EMNV, 2020a).

2.2 PM-OV HFM Summary

An HFM has been built for the PM-OV groundwater flow system. Figure 2-6 provides a 3-D view of the PM-OV HFM. Details regarding the HFM and model development may be found in the PM-OV HFM report (DOE/EMNV, 2020a) and the PM Extended HFM Data Document (Navarro, 2019d) respectively. Figure 2-7 provides a north–northeast to south–southwest HSU cross section along the general flow direction and a west–east HSU cross section perpendicular to the general groundwater flow direction. Both of these cross sections are from the PM-OV HFM (DOE/EMNV, 2020a), where additional cross sections and detailed information regarding this CAU-scale model can be found.

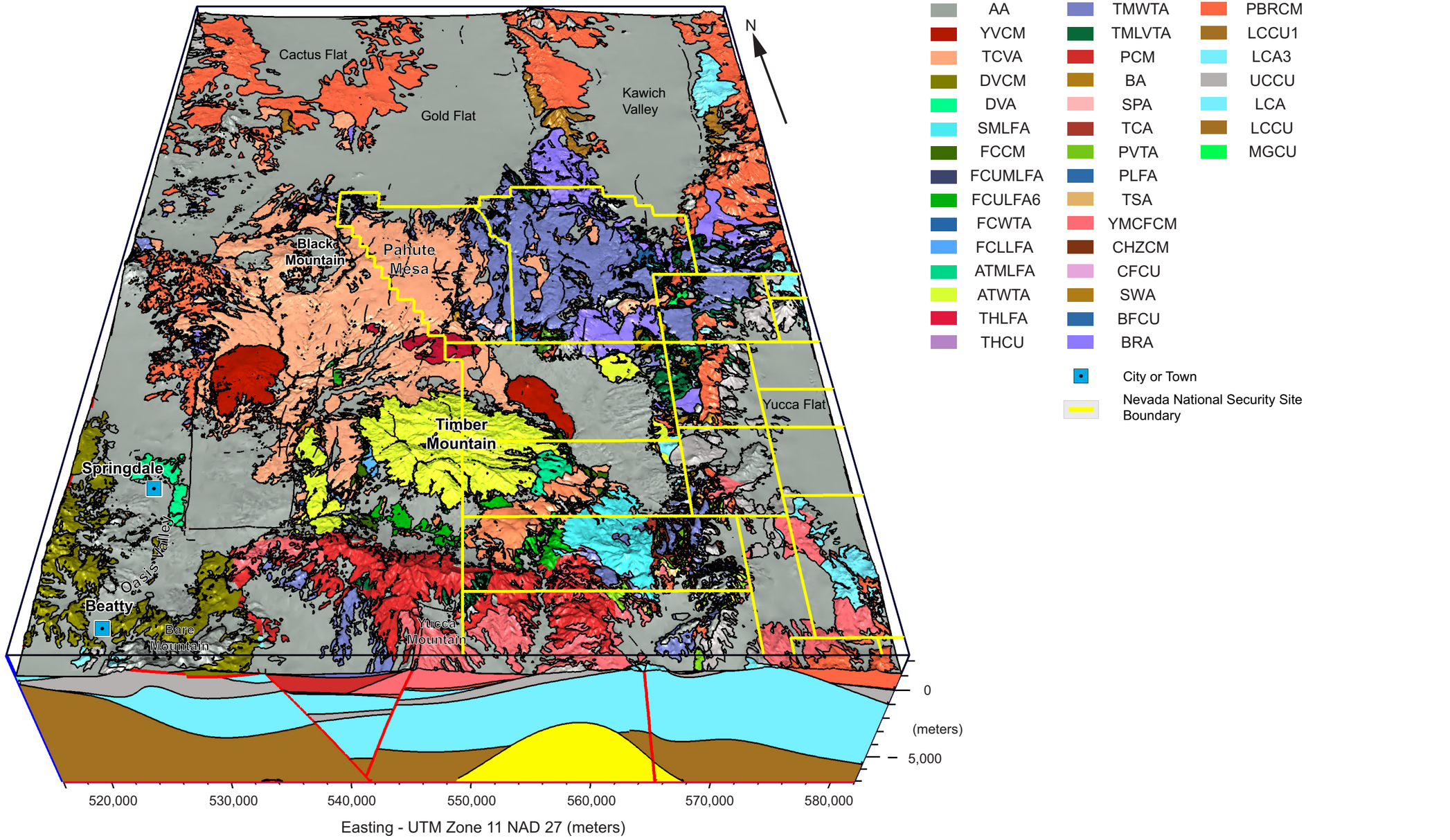

Figure 2-6
3-D View of the Hydrostratigraphic Model of the PM-OV Area

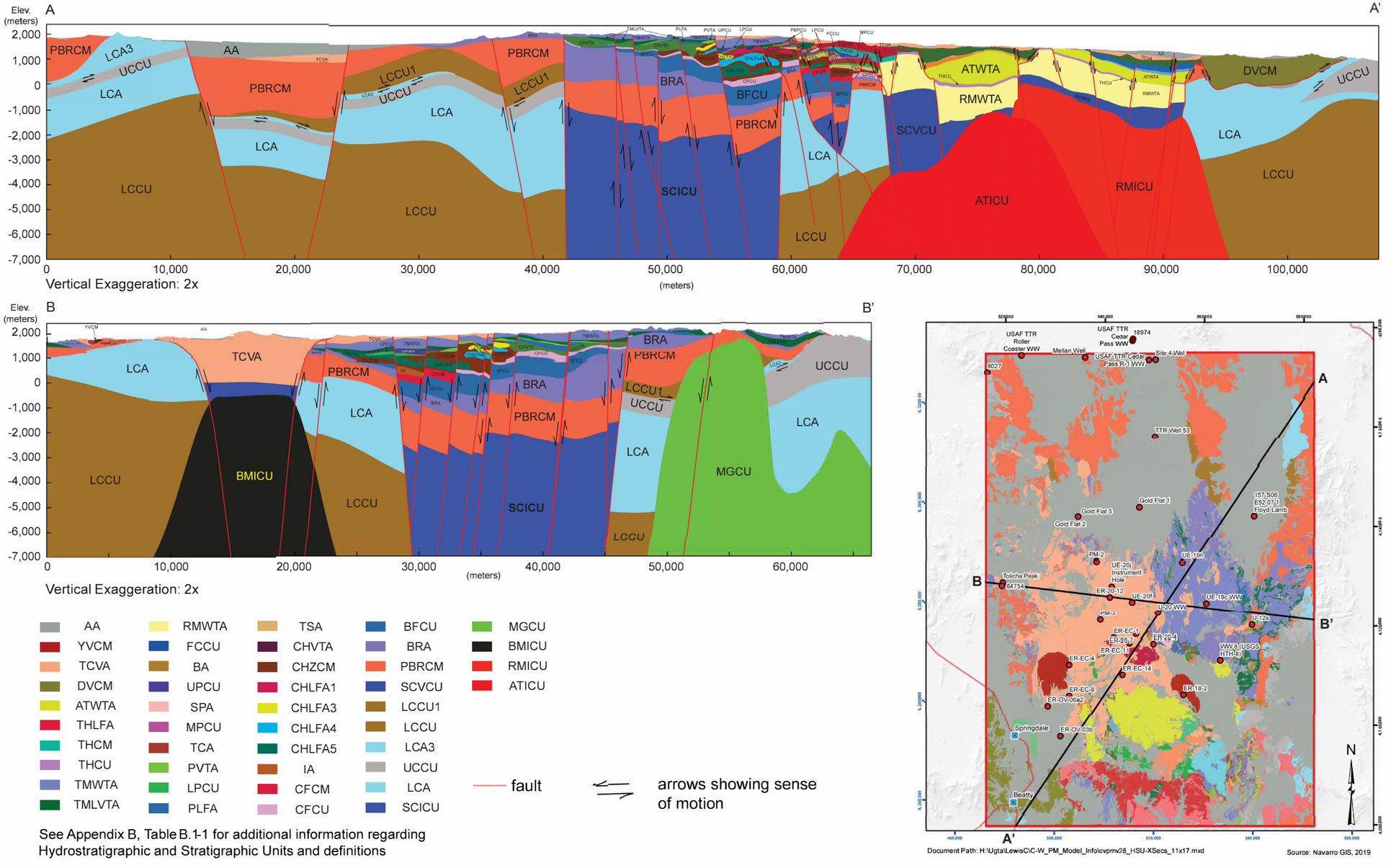

Figure 2-7
North–Northeast to South–Southwest and West–East Cross Sections through the PM-OV HFM

3.0 CONCEPTUAL MODEL OF TRANSPORT AT PAHUTE MESA

Development of a conceptual model is an important step before developing a simulation model (e.g., in the context of groundwater flow modeling, see ASTM D5447-17). This conceptual model encompasses physical and chemical groundwater transport processes of importance at the PM CAU in the PM-OV groundwater basin, as noted in Section 1.1.3, and forms the framework upon which the computational PM CAU transport model is built. Conceptually, the potential transport of RNs at PM resulting from nuclear testing at PM can be divided into two distinct regimes: (1) origin and release of RNs to the flow system discussed in Section 3.1, and (2) migration of RNs away from the source locations to the potential receptors discussed in Section 3.2.

3.1 Origin and Release of RNs

A total of 82 underground nuclear tests involving 82 nuclear detonations were conducted at the PM CAUs from 1965 to 1992 by detonating nuclear devices emplaced in drilled vertical holes. Sixty-four tests were detonated at Central Pahute Mesa (CAU 101), and 18 were detonated at Western Pahute Mesa (CAU 102). The locations of these underground nuclear tests are shown in Figure 3-1. Additionally three near-surface tests, also shown in Figure 3-1, were conducted within this area as part of the Plowshare program: SCHOONER (CAU 374), PALANQUIN (CAU 373), and CABRIOLET (CAU 372). All three of these CAUs were closed under the Soils activity with the recommendation that no further corrective action was needed (DOE/NV, 2011a and b). Although these three CAUs are not assigned to the UGTA Activity as defined in the FFACO (1996, as amended), they will be included in the PM CAU model as potential RN sources for completeness because of known groundwater contamination at Well PM-2 (see Figure 2-5, lower right inset, for the location of Well PM-2). (These contaminants are thought to have originated from SCHOONER).

Underground nuclear tests deposit radioactive elements in the subsurface in the vicinity of the test locations. A comprehensive unclassified inventory providing an estimate of radioactivity remaining underground from nuclear testing, the radiologic source term (RST), for the NNSS is found in the *Nevada National Security Site Underground Radionuclide Inventory, 1951–1992* (Finnegan et al.,

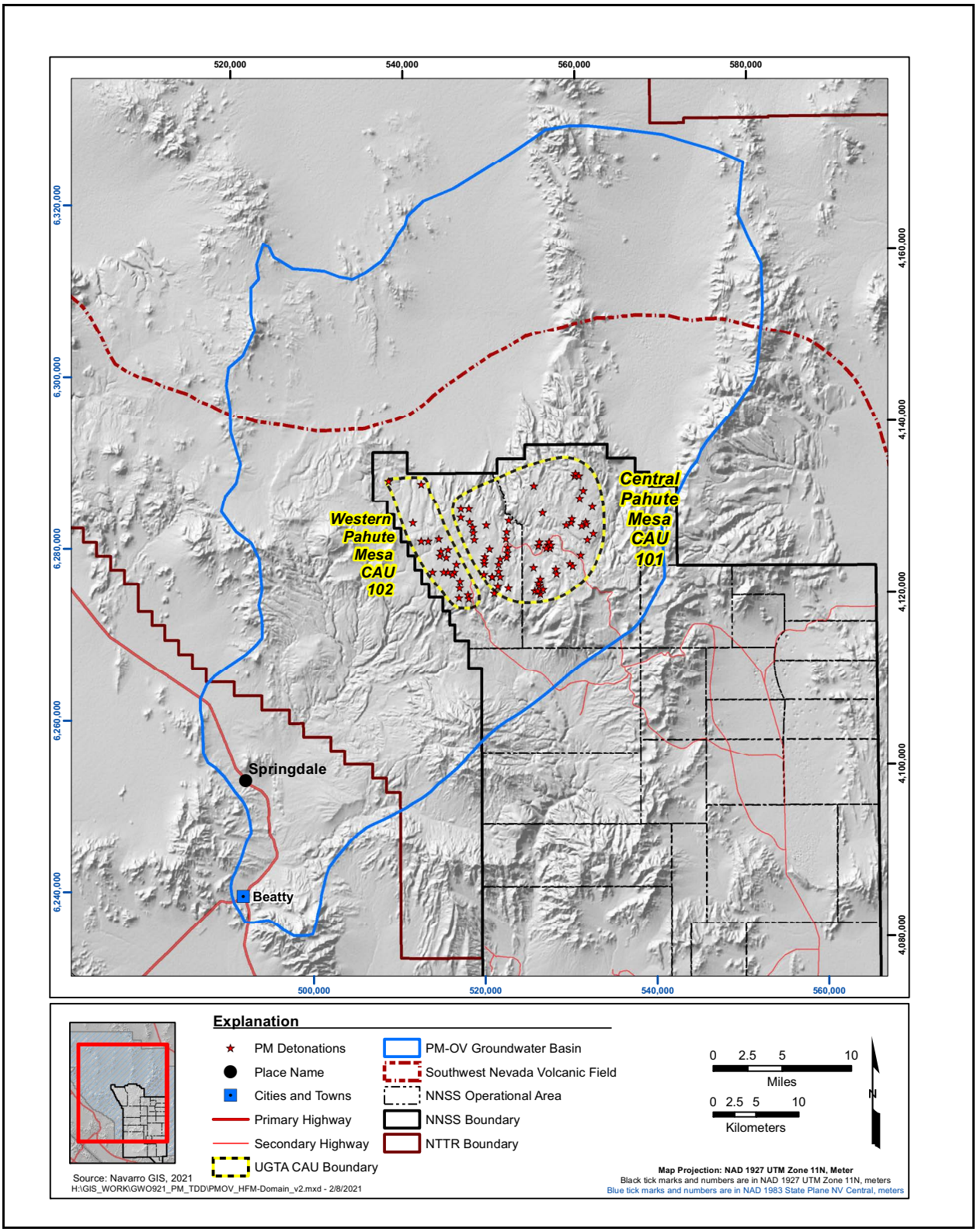

Figure 3-1
Map Showing the PM-OV Groundwater Basin and PM Test Locations

2016). Finnegan et al. (2016) present aggregated inventories for five sub-areas corresponding to the principal geographic test centers at the NNSS that roughly correspond to UGTA CAUs. For the PM CAUs, the radiologic inventory is aggregated and reported separately for NNSS Area 19 and Area 20. They do not present inventories for individual tests.

The RST is defined to be the total amount of residual radioactivity remaining underground after an underground nuclear test, regardless of its physical form and spatial distribution. Following detonation, portions of the RST are partitioned into gaseous, water-based, rubble-based, and melt-glass physical forms, as a function of their elemental properties and phenomenological effects associated with the detonation.

The RST is not available for transport with groundwater in its entirety due to its relative insolubility (Finnegan et al., 2016). The hydrologic source term (HST) is defined as that portion of the RST that is released over time into groundwater occupying saturated rock or into subsurface gases and water moisture occupying partially saturated rock. Release is governed by complex mechanisms and processes that transfer radioactive compounds from the RST into groundwater or to moisture in the unsaturated zone (UZ) as a result of (1) the immediate impacts of the detonation, (2) residual transient effects taking place after a detonation, and (3) ambient, longer-term processes occurring well after a detonation.

There are uncertainties associated with the initial RST, impact of detonations on the near-field, and RN release mechanisms leading to HST. Conservative estimates lead to overestimation of the types and quantities of RNs available for transport through groundwater. Hence, available observations of RNs near and downgradient from the sources are used to constrain the HST for the PM CAU transport model.

3.1.1 Unclassified RN Inventory

The Finnegan et al. (2016) inventory includes four categories: (1) residual fissile and tracer materials, (2) actinides, (3) tritium (^{3}H), and (4) products of neutron activation of device parts and the surrounding geologic medium. Criteria for inclusion of RNs in the inventory are discussed in the Finnegan et al. (2016) report. The Finnegan et al. (2016) RN inventory, decay-corrected to September 30, 2012, for PM is provided in Table 3-1. The inventory includes 43 radiological contaminants that have half-lives greater than 10 years (with the exception of europium [^{154}Eu], which has a half-life of

Table 3-1
RN Inventory for Pahute Mesa (decay corrected to September 30, 2012)
(Page 1 of 2)

RN	Category	Half-Life (Years)	Curies	
			Pahute Mesa Area 19	Pahute Mesa Area 20
^{3}H	Tritium	12.32	5.76E+06	1.91E+07
^{14}C	Activation	5,715	2.19E+02	4.68E+02
^{26}Al	Activation	7.1E+05	8.97E-04	8.373-03
^{36}Cl	Activation	3.01E+05	9.11E+01	1.57E+02
^{39}Ar	Activation	269	6.08E+02	1.18E+03
^{40}K	Natural	1.27E+09	1.59E+02	3.17E+02
^{41}Ca	Activation	1.03E+05	5.05E+02	1.27E+03
^{59}Ni	Activation	7.6E+04	1.60E+01	2.98E+01
^{63}Ni	Activation	101	1.50E+03	2.72E+03
^{85}Kr	Fission	10.76	1.37E+04	1.57E+04
^{90}Sr	Fission	28.78	3.58E+05	4.22E+05
^{93}Zr	Fission	1.5E+06	1.89E+01	2.37E+01
^{93m}Nb	Activation	16.1	1.25E+03	2.15E+03
^{94}Nb	Fission	2.0E+04	7.93E+01	9.85E+01
^{99}Tc	Fission	2.13E+05	1.34E+02	1.78E+02
^{107}Pd	Fission	6.5E+06	5.96E-01	1.00E+00
^{113m}Cd	Fission	14.1	1.87E+02	2.79E+02
^{121m}Sn	Fission	44	1.38E+03	2.07E+03
^{126}Sn	Fission	2.3E+05	8.08E+00	1.19E+01
^{129}I	Fission	1.57E+07	4.15E-01	5.60E-01
^{135}Cs	Fission	2.3E+06	1.39E+01	1.84E+01
^{137}Cs	Fission	30.07	4.39E+05	5.65E+05
^{151}Sm	Fission	90	1.98E+04	3.06E+04
^{150}Eu	Activation	36	5.31E+01	7.27E+02
^{152}Eu	Activation	13.54	4.13E+03	1.07E+04
^{154}Eu	Activation	8.593	1.41E+03	2.64E+03
^{166m}Ho	Fission	1.2E+03	3.05E+01	2.86E+01
^{232}Th	Actinide (device+natural)	1.40E+10	1.15E+01	2.32E+01
^{232}U	Actinide (device)	69.8	7.16E+01	1.42E+02
^{233}U	Actinide (device)	1.592E+05	6.51E+01	1.18E+02

Table 3-1
RN Inventory for Pahute Mesa (decay corrected to September 30, 2012)
(Page 2 of 2)

RN	Category	Half-Life (Years)	Curies	
			Pahute Mesa Area 19	Pahute Mesa Area 20
^{234}U	Actinide (device+natural)	2.46E+05	7.70E+01	7.03E+01
^{235}U	Actinide (device+natural)	7.04E+08	1.29E+00	1.34E+00
^{236}U	Actinide (device)	2.342E+07	2.21E+00	2.65E+00
^{238}U	Actinide (device+natural)	4.47E+09	6.83E+00	1.25E+01
^{237}Np	Actinide (device)	2.14E+06	1.21E+01	2.50E+01
^{238}Pu	Actinide (device)	87.7	2.44E+03	4.07E+03
^{239}Pu	Actinide (device)	2.410E+04	7.68E+03	1.26E+04
^{240}Pu	Actinide (device)	6.56E+03	2.04E+03	4.40E+03
^{241}Pu	Actinide (device)	14.4	1.12E+04	2.65E+04
^{242}Pu	Actinide (device)	3.75E+05	1.37E+00	2.28E+00
^{241}Am	Actinide (device)	432.7	1.85E+03	4.86E+03
^{243}Am	Actinide (device)	7.37E+03	1.20E-02	1.77E-01
^{244}Cm	Actinide (device)	18.1	5.53E+02	1.02E+03
		Total	6.63E+06	2.02E+07

Source: Finnegan et al., 2016

Note: Data are decay-corrected to September 30, 2012.

8.593 years). The reported inventory for ^{40}K represents its natural abundance in the host rock. The reported inventories for thorium-232 (^{232}Th), uranium-234 (^{234}U), uranium-235 (^{235}U), and uranium-238 (^{238}U) represent contributions from the host rock and from the test device. An RST for an individual test in a CAU may be estimated from the aggregate RST reported for that CAU using a yield-weighted procedure outlined in Tompson et al. (2019). Due to radioactive decay, the relative proportion of RN classes (i.e., ^{3}H, fission products, actinides, and activation products) present in the subsurface RST changes over time. Figure 3-2 shows this change over a span of 1,000 years. The figure shows that ^{3}H, which represents the highest amount of radioactivity in Table 3-1 in year 2012, drops below the activity of the fission products in about 70 to 100 years, and decays to negligible amounts in approximately 300 years. The fission products dominate the total around 100 years and roughly equal the percentage of remaining actinides in about 120 years. After that

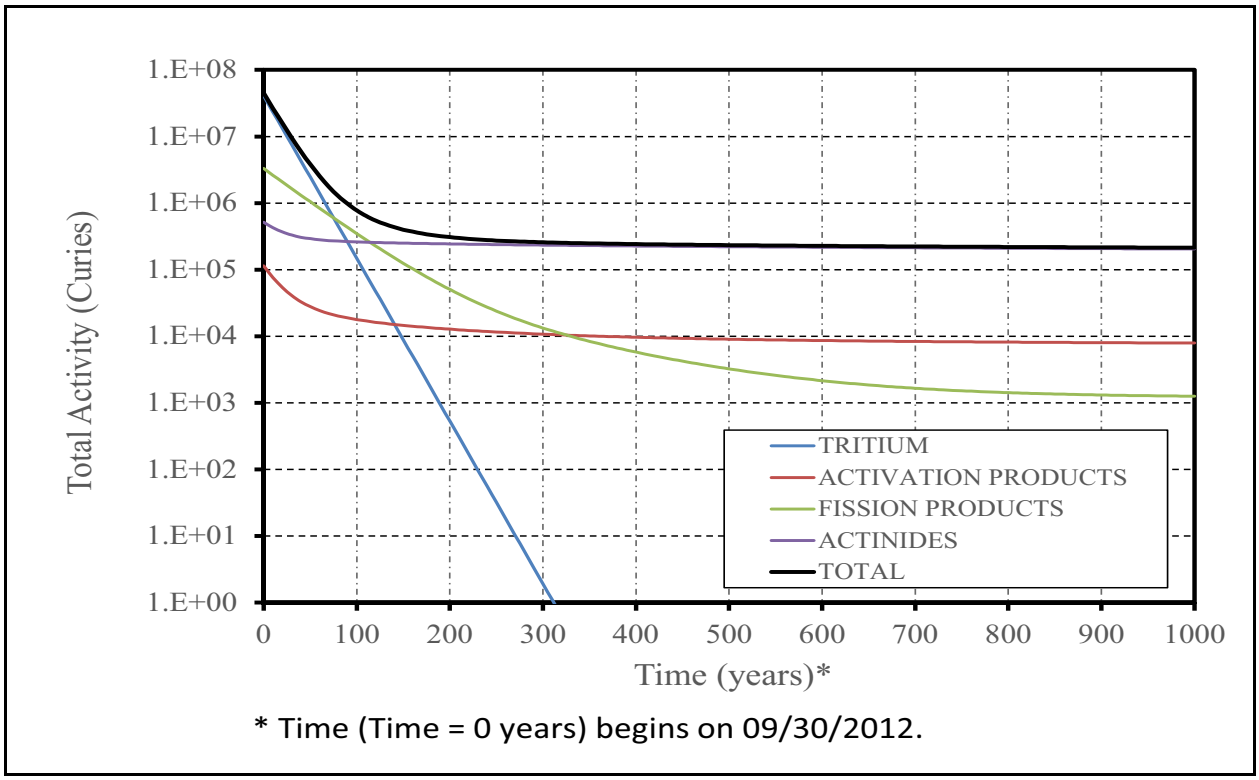

Figure 3-2
Total Activity of Each RN Class Decayed over 1,000 Years
Source: Finnegan et al., 2016

point, the actinides dominate the RNs remaining in the RST. Note that in order to assess the influence of any RN on the CB, factors such as mobility, MCLs, and ability to transport via groundwater have to be taken into account in addition to the availability in the RST.

3.1.2 Impact of Detonations on the Near-field Environment

An underground nuclear explosion releases an immense amount of thermal and mechanical energy (U.S. Congress/OTA, 1989). With the exception of the three near-surface tests, SCHOONER, PALANQUIN, and CABRIOLET, all the tests at PM were emplaced deep, with working-point depths ranging from 225.55m (~740 ft) to 1452.372 m (~4,765 ft). For these deep tests, an open cavity is generated, filled with steam, vaporized rock, and vaporized RST RNs. Within tenths of a second after the explosion, shock waves created by the explosion travel outward, crushing and fracturing the rock (U.S. Congress/OTA, 1989). A shock wave propagates outward, first inelastically and later elastically, reaching the ground surface and then rebounding.The inelastic portion of the shock deposits energy into the rock, melting portions of it and crushing, fracturing, and heating the solid rock beyond the cavity wall. The high-pressure steam and gas expand the cavity further through

physical displacement and compression of its rock wall. Through this process, the cavity grows to a maximum radius, R_c, with damaged areas created beyond the wall to distances of 2 to $3R_c$. Elastic unloading causes the material to rebound radially and try to return to its original position. A compressive tangential hoop stress is formed when the stress field in the rebounded rock is greater than the cavity pressure. This compressive or "residual hoop stress" closes radial fractures that were opened during cavity expansion. The internal pressures and temperatures decline; vaporized rock condenses and coalesces into a melt-glass phase that forms at the bottom of the cavity zone; and the overburden rock above the cavity collapses into the cavity, filling the void and creating a rubble chimney above the cavity. This collapsed zone may or may not extend to the surface, depending upon the competence of overlying rocks (U.S. Congress/OTA, 1989; Pawloski, 1999; Tompson et al., 2011). Residual RNs are distributed in the glass, condensed water, the rubble, or remain as gases. Vaporized RNs circulate in the expanding cavity and condense as a function of their vapor pressures and decreasing P and T conditions in the cavity. Refractory species drop out first, into the accumulating melt. Volatile species will also find their way into the fractured rock porosity around the cavity perimeter (where water has boiled off) and condense there. More volatile species move farther than less volatile species. Vapor movements may be larger in UZ areas. The general process of cavity formation and overburden collapse is depicted in Figure 3-3 (Pawloski, 1999).

For three near-surface tests included in the PM transport CAU model, it can be expected that the near-field processes will differ for these tests compared to the deeper tests described in the previous paragraph, in that the cavity and gas bubble created by the detonation is likely to breach the ground surface, leading to a crater formation and allowing ejection of some portion of the RNs that may get vented or redeposited on the crater and surrounding ground surface (Russell, 2019). In the PM CAU transport model, as a conservative approach, the entire inventory allocation of ^{3}H for the near-surface tests will be placed at the water table surface for developing transport forecasts.

The extent of the disturbed and altered geologic material depends on the explosive yield of the nuclear device as well as the nature of the geologic material surrounding the device. Conceptualization of the pre- and post-test geologic conditions in rocks at PM is based on information available during hole construction, emplacement, post-test data collection (Pawloski, 1999), and numerical simulation for two focused studies at the TYBO-BENHAM (Wolfsberg et al., 2002) and CHESHIRE (Pawloski et al., 2001) sites in Area 20. Additional pertinent

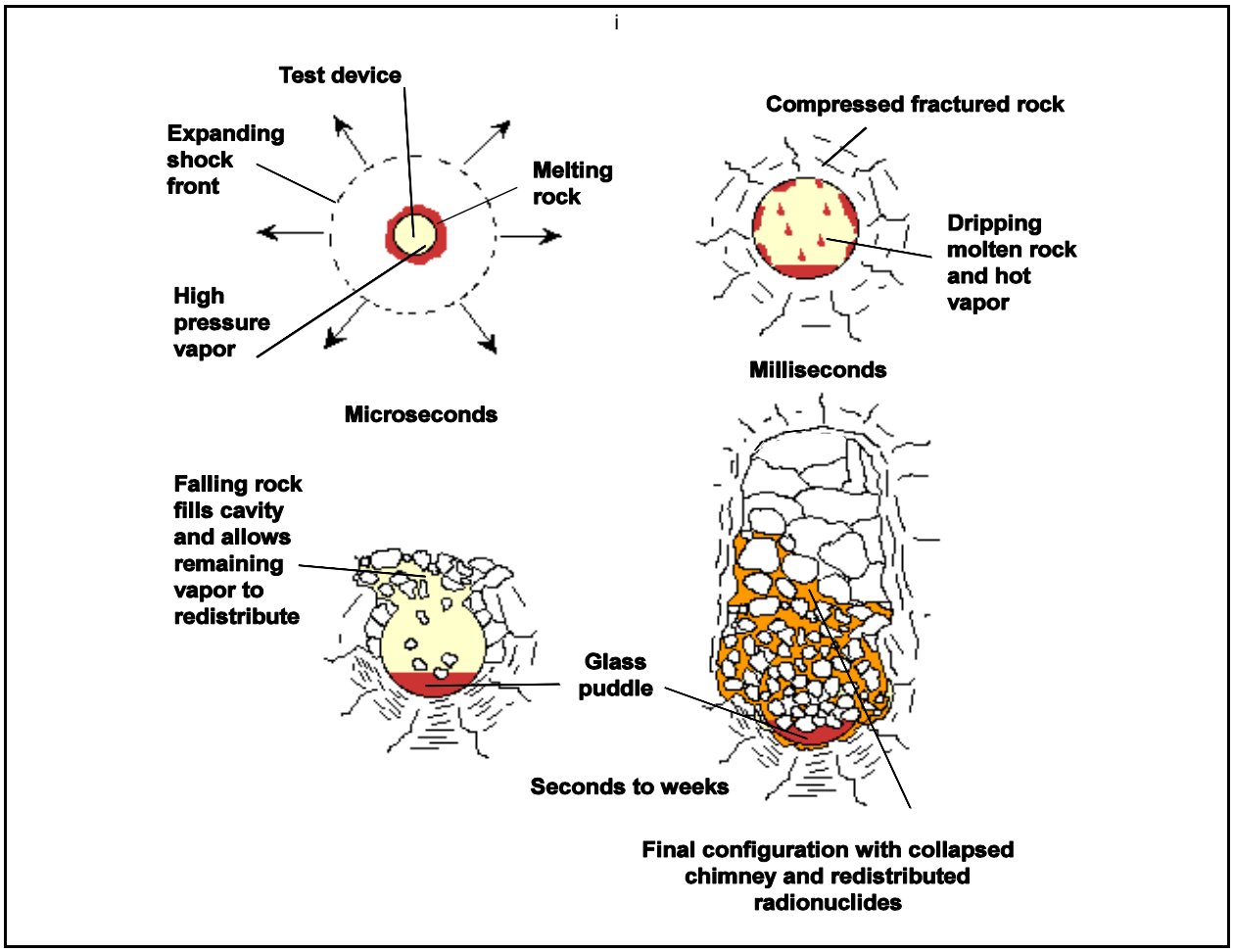

Figure 3-3
Nuclear Test Cavity Formation Collapse
Source: Pawloski et al., 2008

literature that describes underground nuclear testing phenomenology includes Germain and Kahn (1968), Butkovich and Lewis (1973), Butkovich (1976), and the U.S. Congress/OTA (1989).

3.1.3 Distribution of RNs in the Near-field

RST RNs from the nuclear explosion are deposited non-uniformly in different sections of the blast-affected volume based on the chemical traits of the individual RNs produced during the blast (Finnegan et al., 2016). The high melting point, low vapor pressure, refractory species (plutonium [Pu], europium [Eu], americium [Am], neptunium [Np]) predominantly precipitate with the molten rock and become locked into the glass matrix.These species will become available for release only upon dissolution of the glass. Glass dissolution is a function of temperature and the dependence of glass dissolution rates on temperature is exponential (Zavarin et al., 2019).

Therefore, RN release from melt glass is expected to be greatest soon after the detonation and decrease exponentially as the glass cools. Tompson et al. (2011) state that less than a few percent of the melt glass is expected to dissolve over the 1,000-year regulatory timeframe, although glass dissolution can still play a significant role in transport of actinides and other refractory minerals because of their high levels in the melt glass (Tompson et al., 2011) and colloid formation contributing to enhanced mobilization (Zavarin et al., 2019).

Detonations performed within high-permeability rock will allow flow of groundwater to cool the cavity and melt glass more quickly than detonations performed in low-permeability rock, which must cool primarily by heat conduction (Pawloski et al, 2001). However, the low-permeability rock and sorbing minerals will greatly moderate RN movement away from the cavity. Either prolonged elevated temperatures promote significant melt glass dissolution in a low permeability setting with limited transport, or shortened elevated temperatures inhibit melt-glass dissolution in a higher permeability setting with more transport. An example of this is shown by Carle et al. (2003) for the CHESHIRE and ALMENDRO sites. Carle et al. (2003) simulated the hydrothermal conditions at the CHESHIRE site and predicted resaturation of the test cavity with groundwater 20 days after the detonation. The nuclear melt-glass temperature was predicted to be 160 ºC, dropping to 90 ºC 700 days later. In contrast, the unusually low permeability of the surrounding rock at the ALMENDRO site resulted in predicted resaturation occurring after 7 years with nuclear melt-glass temperatures predicted to be 215 ºC, remaining at 160 ºC 23 years after detonation (Zavarin et al., 2019).

Prior to their condensation, the species with low melting points and higher vapor pressures (^{3}H, iodine-129 [^{129}I], chlorine-36 [^{36}Cl]) circulate into the rubble or surrounding fractured rock. These species can travel in either a vapor or liquid phase. These are expected to be flushed from the cavity as water returns to the cavity after the cavity cools sufficiently to allow liquid water to be present. For tests conducted in the UZ, some fraction of the volatile species can be distributed in the UZ. Noncondensible volatile species, particularly krypton-90 (^{90}Kr), xenon-137 (^{137}Xe), and $^{14}CO_2$ are transported as gases through the rubble and are concentrated higher in the cavity and in the chimney relative to the refractory RNs (Finnegan et al., 2016).

Additional processes known to occur during the cavity formation and collapse that affect RN availability and release include hydrodynamic fracturing, prompt injection, groundwater mounding,

and movement on pre-existing fractures (Pawloski, 1999). Hydrodynamic fracturing is a process by which high-pressure gas and steam are forced into existing or newly created fractures in the rocks. Hydrodynamic fracturing is the most likely mechanism to breach residual stress and permit RNs to promptly travel away from the cavity. The injected gas causes the fractures to expand out to a distance of 2 or $3R_c$ from the explosion point under normal conditions (Pawloski, 1999), thereby increasing the permeability of the rocks and allowing faster migration of contaminants. Reduction of cavity pressure after the initial explosion can cause the fractures to close over time. In some cases where weak rocks exist locally in the vicinity of the working point, prompt injection of RNs directly into the surrounding rock can move contaminants out from the cavity area. While this mechanism can be expected to be more prominent for the volatile species, particularly those in the gas phase, there is some evidence that refractory species may also be transported by prompt injection (Nimz and Thompson, 1992). There are three conclusive cases of prompt injection of RNs in Yucca Flat (Nimz and Thompson, 1992). Pawloski (1999) stated that while systematic investigation of prompt injection has not been conducted for PM, none has been noted at PM. Drilling data from some near-field wells (e.g., ER-20-6#1 near BULLION) suggest that prompt injection, possibly associated with hydrofracturing or with occurrences of high permeability layers, did occur up to distances slightly exceeding $3R_c$, although the ^{235}U concentrations in excess of natural levels at ER-20-6#1 were in trace amounts (Rose et al., 2000). (Cavity dimension based on maximum of unclassified yield range [minimum for HANDLEY] in NNSA/NFO [2015] and Equation 1 in Pawloski [1999]; or measured when yield is specified in Zavarin [2014].) It is expected that an EV with a radius of $3R_c$ is sufficiently large to encompass the majority of these effects.These effects were addressed for RM/SM (Tompson et al., 2011; DOE/EMNV, 2019c) and YF/CM (Navarro, 2019a) by selecting EV radii that ranged from 1 to 3 times R_c for specific RNs. The same approach will be followed for PM. Transient effects of groundwater mounding have been noted in some wells on Pahute Mesa (Jackson and Fenelon, 2018). These effects are noted to be transients that die down faster if the hydraulic conductivity is large enough. Refilling of water into the detonation cavity can occur if water is available in the pore space, and this will be accounted for in the aqueous source term concentration used as input to the PM CAU transport model.

3.1.4 RN Release into the Groundwater Flow System

As described in Section 3.1.2, an underground nuclear detonation results in the formation of a cavity surrounded by a disturbed zone (Pawloski et al., 2001)—a zone of rubblized and fractured rock

including a portion of the chimney. The EV describes the region surrounding the detonation location where RNs are deposited within the fractured and porous rock mass, as opposed to incorporated in the melt glass. RNs in the EV are subject to geochemical processes including surface complexation, ion exchange, and precipitation. RNs in the melt-glass zone can be subject to the same geochemical processes but glass dissolution must first take place. Melt-glass alteration leads to the formation of clay and zeolite secondary minerals that may exist in the form of colloids (Zavarin et al., 2019). The portion of the EV that lies below the water table is conceptualized to be water saturated and in hydraulic communication with the surrounding geologic formations. Heterogeneity in the source rocks can have a significant effect on release potential from a cavity or rubblized zone (Pawloski et al., 2001).

Portions of the chimney below the water table are also conceptualized as being saturated with groundwater and in hydraulic communication with the surrounding geologic formations (Pawloski et al., 2001). Transport of RNs due to thermal convection of water in the chimney is possible for some tests when sufficient residual heat is available in the cavity and the chimney is in the saturated zone (SZ). If the contaminants in the water move up the chimney and intercept a high-permeability layer, this layer could serve as a preferential, high-flux pathway downgradient. This phenomenon was reported by Wolfsberg et al. (2002) at the TYBO-BENHAM sites, by Pawloski et al. (2001) at the CHESHIRE site, and by Carle et al. (2003) at the CHESHIRE, GREELEY, and ALMENDRO sites. Detectable levels of Pu were measured in Wells ER-20-5-1, ER-20-5-3, and ER-20-7 near the TYBO test, but the isotopic signature matched that of BENHAM, a test 1,300 m upgradient (Zavarin, 2012; Kersting et al., 1999). The inference is that the Pu was moved up the chimney at BENHAM by thermal convection, where it was released into a higher-permeability unit that is intercepted by the well near TYBO. Another conclusion from the Pu observations is that detectable levels of adsorbing RNs (cobalt-60 [^{60}Co], cesium-137 [^{137}Cs], and $^{152/154/155}$Eu) may be transported along with the Pu on colloidal-size particles moving through the fractured portions of the groundwater aquifers (Kersting et al., 1999). However, while detectable, Pu concentrations in downgradient wells have not been observed above SDWA standards and are unlikely to do so in the future (Zavarin et al., 2019).

The PM CAU transport model will conservatively treat both the cavity and the saturated portion of the chimney as potential sources.

3.1.5 Defining Contaminant Levels

RN levels that constitute groundwater contamination are based on the SDWA radiological MCLs (CFR, 2020). MCLs are regulatory standards established by the U.S. Environmental Protection Agency (EPA) for chemical and radioactive constituents in drinking water. The MCLs for RN categories are presented in Table 3-2.

Table 3-2
Maximum Contaminant Levels

RN Category	MCL
Beta and photon emitters (combined)	4 mrem/yr
Gross alpha particles [a]	15 pCi/L
Radium-226/228 ($^{226/228}$Ra) (combined)	5 pCi/L
Uranium (U)	30 µg/L

Source: CFR, 2020

[a] Gross alpha MCL includes ^{226}Ra but excludes radon and uranium.

The combined dose from all beta and photon RNs present in a water source must be less than 4 millirem per year (mrem/yr). Each single RN has a unique concentration of radioactivity (i.e., dose-compliant concentration), which, when in isolation, equates to a 4-mrem/yr dose (EPA, 2002). The beta- and photon-emitting radionuclides included in the RST (Finnegan et al., 2016) are presented in Table 3-3. Note that the concentration equivalents leading to a 4-mrem/yr dose for some RNs included in the inventory have not been established by the EPA.

Similarly, the MCL for all alpha-emitting RNs, with the exception of U and radon (Rn), collectively (i.e., summed together) is 15 picocuries per liter (pCi/L). ^{232}Th, Neptunium-237 (^{237}Np), plutonium-238 (^{238}Pu), ^{239}Pu, ^{240}Pu, ^{242}Pu, ^{241}Am, ^{243}Am, and curium (^{244}Cm) are the alpha-emitting radionuclides included in the NNSS radionuclide inventory (Finnegan et al., 2016). The MCL for these radionuclides, combined, is therefore 15 pCi/L. Because U is not included in the gross alpha MCL, an adjusted gross alpha measurement (gross alpha minus U activity) is used for regulatory purposes.

The MCL for U is based on its total mass rather than the radioactivity. The combined mass of U isotopes must not exceed 30 micrograms/liter (µg/L) (EPA, 2002). The 30-µg/L MCL is based on the relative abundance of U isotopes observed in nature and typically corresponds to an activity of

Table 3-3
Beta- and Photon-Emitter MCLs

Radionuclide	MCL (pCi/L)	Radionuclide	MCL (pCi/L)
Tritium (^{3}H)	20,000	Technetium-99 (^{99}Tc)	900
Carbon-14 (^{14}C)	2,000	Palladium-107 (^{107}Pd)	--
Aluminum-26 (^{26}Al)	--	Cadmium-113m (^{113m}Cd)	--
Chlorine-36 (^{36}Cl)	700	Tin-121m (^{121m}Sn)	--
Argon-39 (^{39}Ar)	--	Tin-126 (^{126}Sn)	--
Potassium-40 (^{40}K)	--	Iodine-129 (^{129}I)	1
Calcium-41 (^{41}Ca)	--	Cesium-135 (^{135}Cs)	900
Nickel-59 (^{59}Ni)	300	Cesium-137 (^{137}Cs)	200
Nickel-63 (^{63}Ni)	50	Europium-150 (^{150}Eu)	--
Krypton-85 (^{85}Kr)	--	Samarium-151 (^{151}Sm)	1,000
Strontium-90 (^{90}Sr)	8	Europium-152 (^{152}Eu)	200
Niobium-93m (^{93m}Nb)	1,000	Europium-154 (^{154}Eu)	60
Zirconium-93 (^{93}Zr)	2,000	Holmium-166 (^{166}Ho)	90
Niobium-94 (^{94}Nb)	--	Plutonium-241(^{241}Pu)	300

Source: EPA, 2002

-- = Not available

27 pCi/L (EPA, 2001). The relative abundance of U isotopes reported in the RST (Table 3-1) is not consistent with that observed in nature, and 30 µg/L of total U in test-impacted groundwater will likely result in activities much greater than 27 pCi/L. In addition to a greater relative abundance of isotopes with higher specific activities (^{234}U and ^{235}U), three U isotopes in the RST (^{232}U, ^{233}U, and ^{236}U) do not exist in nature (Finnegan et al., 2016). In the case of greater U activities per mass, EPA (2001) recommends that drinking water systems mitigate U levels to 30 pCi/L or less.

The MCL for ^{226}Ra and ^{228}Ra combined is 5 pCi/L. Although ^{226}Ra and ^{228}Ra are radioactive decay products in the ^{238}U and ^{232}Th decay series respectively, they were not included in the RST (Finnegan et al., 2016). The contribution of ^{226}Ra and ^{228}Ra from underground nuclear testing was considered negligible when compared to background from the decay of natural U and Th (Kersting et al., 2003).

3.1.6 Hydrologic Source Term

As discussed in Section 3.1, the HST is defined as the portion of RST that is released over time into groundwater occupying saturated rock or into subsurface gases and moisture occupying partially saturated rock. The PM CAU transport model will focus on a subset of RNs in the HST that are

relevant or potentially relevant to addressing contaminant level thresholds for EPA drinking water standards.

A screening analysis has been performed (Carle et al., 2020) to examine which of the 43 RNs listed in Finnegan et al. (2016) should be included in the contaminant transport modeling. The screening model was designed to estimate plausible aqueous concentrations of RNs in the EV for underground tests. It took into account inventory available, partitioning, EV radius ranges, porosity, and sorption properties with uncertainties, to forecast ranges of concentrations. Where available, measured RN concentrations in groundwater samples collected from the near-field environment (e.g., post-shot wells) were compared with the screening model forecasts to build confidence in the results. When screening model forecasts support a 100-year persistence of a concentration above the MCL within the EV, the RN was judged to be a viable candidate for transport modeling. The screening model is not applicable to the near-surface tests. The screening model also identified potentially relevant RNs based on a 0.1 MCL threshold.

The RNs ^{3}H, ^{90}Sr, ^{129}I, ^{137}Cs, and $^{239/240}$Pu have been reported above the MCL in water samples from the near-field environment (i.e., post-shot wells) and were also determined by the screening model to exceed their MCL in the EV. These RNs are identified as relevant to HST and therefore are marked as being important for inclusion in the PM CAU transport model. In addition, Carle et al. (2020) conservatively evaluated ^{233}U, ^{234}U, and ^{238}U based on the 15 pCi MCL for gross alpha particle activity and ^{232}U based on a lower effective MCL of 3.6 pCi/L (equivalent to the 4 mrem/year dose-compliant concentration). This approach conservatively accounted for the larger activity-to-mass ratio of U associated with the RST when compared to that observed in nature, which was used for establishing the 30 µg/L MCL (see Section 3.1.5). They concluded that these U isotopes were relevant to the HST, and therefore important for inclusion in the PM CAU transport model. These U isotopes either exceeded the gross alpha MCL in samples (^{234}U), exceeded the gross alpha MCL when combined with other isotopes (^{238}U), and/or were found to exceed the MCL based either on gross alpha or dose-compliant concentration in the screening models (^{232}U, ^{233}U, and ^{234}U). The RNs that were determined potentially relevant to the HST (for which either groundwater sampling or the screening model indicate 100-year persistence above 0.1 MCL) include ^{14}C, ^{36}Cl, ^{99}Tc, ^{237}Np, and ^{238}Pu. These RNs are marked for potential inclusion in the PM CAU transport model. Remaining RNs from the 43 reported by Finnegan et al. (2016) have neither been observed in the field at greater than 0.1 MCL nor are they predicted to migrate at levels above 0.1 MCL in the screening models, and are

recommended for exclusion from the PM CAU transport model. The screening analysis also recommends additional attention to the daughter products of the ^{238}U and ^{232}Th decay chains (e.g., ^{226}Ra and ^{228}Ra) that were not included in the inventory (Carle et al., 2021).

3.1.7 RN Observations

Measurements of RN concentrations in groundwater samples are useful for evaluating the PM CAU transport model predictions. As discussed in Section 3.1.6, data from the near-field environment are valuable in screening analysis to constrain the RNs that may need to be included in the transport model. RN data from near-field and far-field wells will be used to calibrate the transport model and/or provide further confidence in the simulations. Evidence of RN migration away from test locations will be compared with simulated results of the PM CAU transport model. Additionally, time series of RN concentrations from cavity samples may be used to compare with simulated concentration declines at the same locations. RN observations for samples collected from near-field and far-field wells are summarized below. A subsequent report will include a comprehensive evaluation of groundwater sampling and sampling results for the PM CAU.

3.1.7.1 RNs Observations in Groundwater from Test Cavities

Many of the detonations within the PM CAU had post-shot drill backs into the cavities to extract melt glass and other constituents to diagnose test performance. Groundwater samples were collected for RN analysis from nine drill-back locations accessing groundwater within the detonation cavity/chimney environment. These locations, shown in Figure 3-4, are identified with "PS" in their name. Four of these locations (U-19ad PS 1A at CHANCELLOR, U-19q PS 1D at CAMEMBERT, U-19v PS 1D at ALMENDRO, and U-20n PS 1D at CHESHIRE) have been sampled multiple times and analyzed for a suite of RNs. The other drill-back locations were sampled a single time primarily for ^{3}H; gamma-emitting RNs were also included for a few locations. The reported ^{3}H activity in these samples collected between 2003 and 2019 ranged from 9.2E+05 pCi/L (U-20i PS 1D at BOXCAR) to 8.5E+07 pCi/L (U-19v PS 1D at ALMENDRO) (Navarro, 2020c). While the ^{3}H activities were several orders of magnitude above the 20,000-pCi/L SDWA MCL, most other measured RNs were well below their MCL in samples collected from these locations with the following exceptions (Navarro, 2020c):

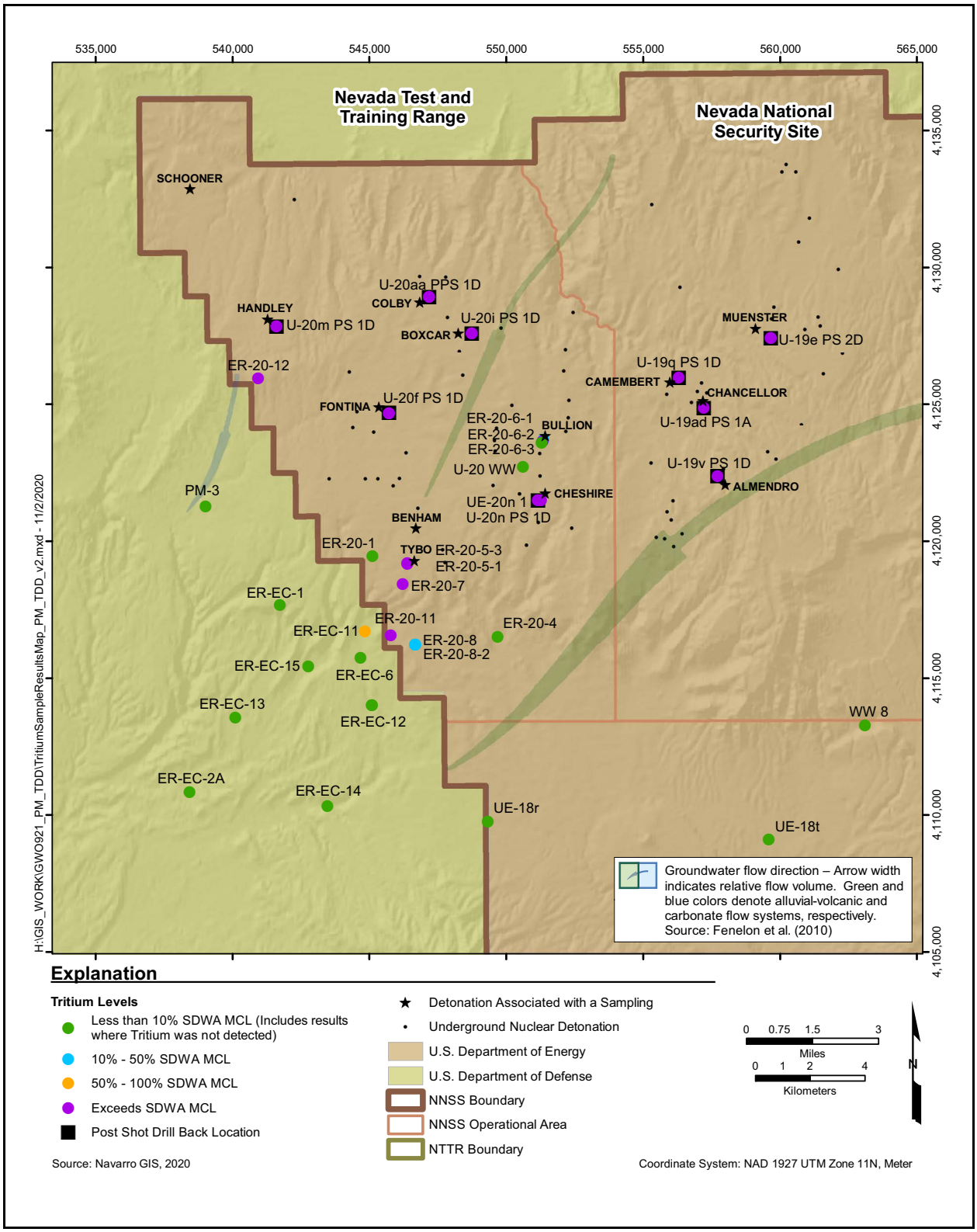

Figure 3-4
Tritium Relative to SDWA MCL in PM and Downgradient Groundwaters

- U-19ad PS 1A accesses the CHANCELLOR cavity. Although ^{3}H exceeded its MCL by up to 3 orders of magnitude (2004 to 2008), the only other RNs exceeding their MCLs are ^{90}Sr, ^{129}I, ^{137}Cs, and $^{239/240}Pu$. Gross alpha activities also exceed the MCL.

- U-19v PS 1D accesses the ALMENDRO cavity. Although ^{3}H exceeded its MCL by up to 4 orders of magnitude (1993 to 2009), the only other RN exceeding its MCL is ^{129}I.

- U-20n PS 1D accesses the CHESHIRE cavity or near the cavity depending on the date sampled. Although ^{3}H exceeded its MCL by up to 4 orders of magnitude (1983 to 2005), the only other RNs exceeding their MCLs are ^{90}Sr and ^{137}Cs.

- U-20f PS 1D is associated with the FONTINA test. The gross alpha, gross beta, and ^{3}H MCLs were exceeded. Samples were bailed and were limited to gross alpha, gross beta, ^{3}H, and gamma emitters (including ^{137}Cs). Drilling mud was present in the well, which likely impacted the samples.

Observations at the other UGTA CAUs also indicate that ^{3}H is present in groundwater above the 20,000-pCi/L MCL when sampling the near-field environment of an underground detonation but, with few exceptions, no other RNs are reported above their MCL (DOE/EMNV, 2019a). It is important to note that the full suite of RNs relevant to the HST was not analyzed at these near-field sampling locations and not all detection limits were below the MCL. In addition, care was taken not to recirculate contaminated drilling mud to the surface to prevent inadvertent exposure to RNs. Drilling mud lost to the cavity or chimney during this process would likely impact RNs susceptible to sorption to clay minerals (e.g., Cs, Sr, Eu, Np, Am, and Pu), leading to reduced aqueous activities for these RNs. On the other hand, samples containing drilling mud would likely result in elevated concentrations of these RNs.

3.1.7.2 RN Observations in Groundwater Downgradient of Test Cavities

RNs have been observed in water samples from wells located downgradient of three underground nuclear detonations on PM: BENHAM, HANDLEY, and CHESHIRE (Figure 3-4). RNs observed downgradient of BENHAM also may result from other sources, including the TYBO detonation. Tritium has been detected above the MCL at ER-20-12 (2.2 km downgradient from HANDLEY), ER-20-5-1 and ER-20-5-3 (1.3 km downgradient from BENHAM and 0.28 km from TYBO), ER-20-7 (2.1 km downgradient from BENHAM), ER-20-11 (4.0 km downgradient from BENHAM), and UE-20n 1 (0.3 km downgradient from CHESHIRE). These detonations are among the largest (upper quartile) in PM based on the maximum of the announced yield range, or the minimum of the announced yield range for HANDLEY (i.e., >1 Mt) (NNSA/NFO, 2015). The flow velocity of the

20,000 pCi/L front is around 62 meters per year (m/yr) at HANDLEY and around 84 m/yr at BENHAM (Rehfeldt and Wilborn, 2020).

Four other RNs (^{14}C, ^{137}Cs, ^{129}I, and ^{238}U) are observed at concentrations exceeding 10 percent of the MCL at locations near the sources (ER-20-5-1, ER-20-7, and/or UE-20n 1) where the ^{3}H activities range from 1.4E+07 to 5.6E+07 pCi/L (Figure 3-4). The ^{137}Cs activity was reported above 0.1 MCL (40 pCi/L) in a sample collected from ER-20-6-1 in 1996; the ^{3}H activity for this sample was reported as 1.7E+06 pCi/L. Since that time, the ^{3}H in this well has reduced to 340 to 390 pCi/L (Figure 3-4); unfortunately this sample was not analyzed for ^{137}Cs. ^{238}U also exceeds 0.1 MCL in ER-20-5-3, ER-20-6-2, and ER-20-8. The U in these samples appears to be of natural origin (i.e., dissolution of uranium-bearing minerals present in volcanic rocks) based on $^{235}U/^{238}U$ ratios (Zavarin, 2005; Paces et al., 2002). ^{90}Sr exceeding 10 percent of its MCL was also reported in groundwater samples from ER-20-5-3, ER-20-6-1, ER-20-6-3, and ER-20-7. These ^{90}Sr results are considered unreliable because of a known spectral interference when high ^{3}H is present and the lack of detectable ^{90}Sr in subsequent samples at ER-20-5-3 and ER-20-7 when using an alternative method that removes the interference (Navarro, 2020c). Only single samples from ER-20-6-1 and ER-20-6-3 collected in 1996 are available. Detectable levels of $^{239/240}Pu$, associated with colloids, have been reported for several downgradient wells (ER-20-5-1, ER-20-5-3, ER-20-7, ER-20-8, ER-20-8-2, ER-20-12, and ER-EC-11) at concentrations (0.002 to 0.76 pCi/L) well below the 15-pCi/L gross alpha MCL (Navarro, 2020c).

Gross alpha values above 15 pCi/L have also been reported in downgradient wells ER-20-5-1, ER-20-5-3, ER-20-6-2, and ER-20-7. The elevated gross alpha values include alpha emission from naturally occurring RNs and are therefore not attributed solely to underground nuclear testing.

Additional downgradient wells (e.g., U-20 WW and ER-20-4) are within the PM CAU (Figure 3-4). Although some RNs of natural origin (e.g., ^{14}C, ^{36}Cl, ^{238}U) have been observed, no test-related RNs (e.g., ^{3}H) have been detected at these locations. These results represent equally valuable information regarding RN migration on PM.

3.1.7.3 Implications of RN Observations for Transport Modeling

Transport modeling will rely on RN observations, screening analysis, and transport parameter data to help reduce predictive uncertainty. Based on the Carle et al. (2020) screening analysis, only 10 RNs

(^{3}H, ^{90}Sr, ^{129}I, ^{137}Cs, ^{232}U, ^{233}U, ^{234}U, ^{238}U, and $^{239/240}$Pu) potentially exceed their MCL or substantially contribute to gross alpha MCL in the groundwater within the PM nuclear test cavities (i.e., contaminant source). Five other RNs (^{14}C, ^{36}Cl, ^{99}Tc, ^{237}Np, and ^{238}Pu) were determined to exceed 10 percent of their MCL at the source.

Currently, ^{3}H accounts for about 90 percent of the NNSS RN inventory (based on curies) for underground nuclear tests (Finnegan et al., 2016). As shown in Figure 3-2, ^{3}H will remain the largest portion of the RN inventory (greater than 50 percent) for approximately the next 67 years. Fission products (including ^{90}Sr, ^{129}I, ^{137}Cs) then become the largest proportion of the inventory but fall below actinides shortly after 100 years (Figure 3-2). The two fission products, ^{90}Sr and ^{137}Cs, make up approximately 96 percent of the total fission products but have relatively short half-lives of about 30 years (Table 3-1). Actinides (including U, Np, and Pu) make up the majority of the inventory over the rest of the 1,000-year compliance period.

While actinides persist in the environment over the 1,000-year compliance period as a result of their long half-lives (Table 3-1), they are mostly trapped within the melt glass in the nuclear test cavities and only a small fraction is accessible to groundwater. In addition, sorption to the aquifer material also inhibits migration of actinides and the fission products, including ^{90}Sr and ^{137}Cs. This lack of mobility of most RNs exceeding their MCL in the near-field environment is consistent with the lack of MCL exceedances generally observed in downgradient sampling locations.

Available transport parameter data (details presented in Section 5.0) are at spatial and temporal scales much smaller than those required for the PM CAU transport model. However, RN measurements at wells reflect transport parameters over large spatial and temporal scales similar to those at which HSU-scale transport properties are defined. This is because RNs enter the groundwater in the source regions and are transported over time via groundwater to distal locations. Concentrations expected to occur at distal locations represent the integrated effects of transport processes along the entire length of the transport pathway. It is assumed in this work that the RN concentrations measured in the groundwaters sampled from wells represent the local values of concentrations. Hence, the RN data from wells located several kilometers from the point of release incorporate processes active over that distance for the past three to five decades. For modeling purposes, the sample results are interpreted to represent the integrated effect of processes over timescales of decades and spatial scales of kilometers. Parameter values obtained by calibration to the well data represent integrated values over

timescales of decades and spatial scales of kilometers that are pertinent to RN transport behavior relevant to the CB forecasts.

3.2 Migration of RNs

RNs from underground nuclear tests at PM can be transported with groundwater flowing through water saturated geologic formations toward areas of natural or anthropogenic discharge. Origin of groundwater at PM is primarily from precipitation recharge occurring at the mesa, with smaller amounts entering from the northern portion of the basin (Halford and Jackson, 2020). The overall groundwater flow direction beneath the PM testing areas is southwesterly towards the Oasis Valley near Beatty, Nevada (Navarro, 2020b).

Evaluation of RN transport at PM requires the knowledge of flow velocities within the domain, which will be obtained from the PM CAU flow model. All tests conducted at PM were within the PM-OV groundwater basin. The flow model domain is chosen so that lateral boundaries coincide with the no-flow boundaries of the PM-OV groundwater basin except for the discharge area in the southwest portion of the model (Navarro, 2020b). Important HSUs and structural features, discussed in Section 2.0, are explicitly represented in the PM CAU flow model. The flow model will be calibrated by optimizing hydraulic conductivities and storativities to hydrologic data, including steady-state pressure heads measured at monitoring wells, cross-hole responses to pumping at wells, head gradients, transmissivity measurements, infiltration estimates, and discharge estimates. Flow model calibrations will also be informed by flow paths and transport velocities estimated from RN measurements (Rehfeldt and Wilborn, 2020) and geochemical data (Navarro, 2020a and 2020c). Transport of RNs through the geologic formations at PM is affected by multiple physical and chemical processes that depend both on the hydrogeologic system and its properties, and the specific properties of the RNs. The migration processes relevant for evaluating RN transport at PM, summarized in this section, include radioactive decay of the species, advection in porous and fractured media, dispersion, diffusion of RNs from fracture water into matrix water, sorption onto immobile minerals, and colloid-facilitated transport. These processes are included in the PM CAU transport model with the exception of colloid-facilitated transport, which is discussed in Section 3.2.6. Detailed discussions of the data and distributions of parameters required as inputs to the PM CAU transport model are presented in Section 5.0. Transport parameters in general can show variability depending on HSU, HGU, scale, depth, diagenetic zone (DZ), and water chemistry. These

variabilities are specific to each parameter, and are discussed in subsections of Section 5.0 for each transport parameter of importance to the PM CAU transport model.

3.2.1 Radioactive Decay

Radioactive decay is the process by which a nucleus of an unstable element or isotope (radioisotope) loses energy by radiation and converts to another element or isotope. The rate at which a radioisotope decays is given by the equation:

$$\frac{dN}{dt} = -\lambda \bullet N \qquad (3\text{-}1)$$

where

N = number of nuclei of the radioisotope at a given time t
dN = number of nuclei that decay in a small time increment dt
λ = decay constant, related to the half-life ($T_{1/2}$) as: $\lambda = \ln(2)/T_{1/2}$

Decay constants (or half-lives) of RNs are fixed properties of the specific isotopes (determined by the mass number and atomic number of the isotopic nucleus) and are not dependent on the environmental factors such as the geological media, fluid composition, pressures, or temperatures. Hence, the half-lives listed in Table 3-1 are taken from Finnegan et al. (2016) as fixed values.

Kersting et al. (2003) examined potential decay chains associated with RNs included in the NNSS RST that are not produced naturally (i.e., ^{232}Th and ^{238}U decay chains were not included). The most important chain was identified as ^{241}Pu -> ^{241}Am -> ^{237}Np (Kersting et al., 2003). As part of Phase I modeling, field-scale streamtube simulations from the TYBO detonation were conducted to, among other things, address assumptions regarding radioactive decay daughter products (see Appendix C of SNJV, 2009). Atoms of Np present near the front of a plume arise either by transport of Np in the aqueous phase, or via the decay of Pu or Am that arrive there via colloid-assisted transport. Sorption coefficient for Np in the SZ at PM (see Section 5.9) is much lower than that of Pu and Am, leading to lower affinity for colloid-assisted transport and higher mobility for the aqueous phase. Combined with the longer half-life of Np, this led to the result (see Appendix C of SNJV, 2009) that Np arising from decay of Pu or Am atoms transported via colloid-assisted transport makes only a small contribution to the total activity. Therefore, decay chains and their daughter products are not included in the radioactive decay process, as simulated in the PM CAU transport model. However, Carle et al. (2020) recommend additional attention to the daughter products of the ^{238}U and ^{232}Th decay chains

(e.g., ^{226}Ra and ^{238}Ra) that are not included the inventory. This recommendation is currently being evaluated and will be addressed in future documents.

3.2.2 Advective Transport of Dissolved RNs

Dissolved, aqueous RNs are able to advect with the groundwater moving through porous and fractured media in the flow system (colloid-facilitated transport is addressed in Section 3.2.6). Typical pore sizes (fractions of microns) and fracture apertures (micron or larger) are much greater than the sizes of the aqueous RNs (nanometers), and solutes are expected to occur at low concentrations (e.g., 1,500 pCi/L, or ~2E-03 gm/L based on natural relative abundance for U [Carle et al. 2020]). Their effect on the fluid density and fluid viscosity (Ozbek et al., 1997) is expected to be small. Hence, it is assumed that their effect on the motion of the pore fluid is negligible. The conceptual model assumes that the RNs dissolved in the pore fluid have negligible effect on fluid density and are carried along by the pore fluid moving at its local velocity. The advective flow paths correspond with the groundwater flow paths and the fluid velocity determines the rate of movement of aqueous RNs along flow paths (sorption is addressed in Section 5.9). For saturated flow, the fluid velocity, v, is related to the Darcy flux, q, of the groundwater via flowing porosity, ϕ_{eff}, by:

$$v = \frac{q}{\phi_{eff}} \qquad (3\text{-}2)$$

The Darcy flux, q, required by this equation is obtained from the flow model. The PM CAU flow model is expected to be a numerical model that represents the flow system on a discretized mesh yielding values of hydraulic heads and fluxes averaged over the computational blocks, which are expected to range from tens to hundreds of meters in size. Generally, the flux can vary with position, and it can vary with time if time-dependent scenarios are considered. The flowing porosity, ϕ_{eff}, is a property of the geological medium. ϕ_{eff} is supplied to the PM CAU transport model on the scale of computational blocks, and it can vary with position due to the heterogeneities of the geological media. For modeling purposes, within a geologic unit, the porosity is assumed to be spatially constant but uncertain.

In the single-porosity model of geologic media, the flowing porosity is a large fraction of the entire porosity of the medium, typically assumed to be equal to the matrix porosity; and stagnant portions of the porosity, if any, do not play a significant role in the flow and transport considerations. Units modeled as single-porosity media include VTAs, AAs, and unfractured confining units. TCUs are

also generally modeled as single-porosity media unless otherwise indicated by available transport data. This is because, as noted in Section 2.1.1.1, while generally acting as competent confining units, there are instances where TCUs are fractured and transmissivity is much greater (Jackson et al., 2021).

The transport parameter required by the PM CAU transport model is the effective porosity, ϕ_{eff}, discussed in Section 5.3.

3.2.2.1 Dual-Porosity Conceptualization of Fracture Flow

In fractured media such as welded tuffs, some bedded tuffs, and lava flows at PM that can sustain open fractures, the hydraulic conductivity of the fractures is many orders of magnitude greater than that in the rock matrix surrounding the fractures. Hence, fluid flow occurs preferentially in the fractures, and the flow through the rock matrix can be neglected. Thus, the flowing porosity used for advection is the fracture volume divided by the bulk volume, which is typically much smaller than the matrix porosity. Thus, for the same flux, simulated fluid velocities are much higher in fractured rock than they are for porous media. This representation of a geological media is called an equivalent continuum approach, where the groundwater flow is described with the use of average values of hydraulic conductivities and porosities; the influence of heterogeneities within a member is incorporated into the model via dispersion and matrix diffusion (discussed in Sections 5.7 and 5.8). This treatment represents a considerable simplification of the complex fracture network observed in volcanic rocks. The use of an abstracted dual-porosity model is acceptable because the model is intended to be used in large-scale simulations. However, the material properties for use in the abstracted model are scale-dependent and difficult to estimate. In numerical modeling studies, such uncertainties are commonly addressed through sensitivity analyses using a broad range of parameter values to assess the importance of the uncertain parameters to the final model. Permissible range of values for uncertain parameters is constrained by available field-scale data, such as the RN measurements at multiple wells at PM. An alternative is to evaluate the equivalent parameters necessary for simulation using a DFN approach.

DFN approaches capture the high degree of heterogeneity that fractures impart to a flow system. DFN models typically start with measured/estimated fracture statistics, generate a large number of system realizations, and solve flow and transport equations at scales finer than fracture spacing to evaluate upscaled average material properties. By solving for flow and transport in individual elements of a

fracture network, DFN approaches can (while computationally intensive and impractical for large scales required by the PM CAU model) evaluate upscaled equivalent conductivity tensors, porosities, fracture spacing and aperture, dispersivities, and diffusivities for equivalent continuum approach. For example, Makedonska et al. (2020) estimated ranges for equivalent effective porosities, dispersivities, fracture apertures, and spacing for use in continuum transport models using DFN models for the Topopah Spring aquifer (TSA), lava-flow aquifer (LFA), and Tiva Canyon aquifer (TCA) at PM. Results of DFN modeling are presented in Section 5.6.

For fracture-dominated systems, the matrix is conceptualized as stagnant, and effective porosity is approximately the fracture porosity. The transport parameter required by the PM CAU transport model for advective flow is the effective porosity, ϕ_{eff}, discussed in Section 5.3.

3.2.3 Dispersion

Hydrodynamic dispersion of solutes in groundwater describes the spreading phenomenon at a macroscopic level by the combined action of mechanical dispersion and molecular diffusion (EPA, 1988). Dispersion is caused by velocity variations at scales less than the scale of observation (SNJV, 2004a). At typical scales of observation, dispersion is a mixing process, which causes dilution of the solute within the plume while spreading nonzero concentration over a greater spatial extent (Freeze and Cherry, 1979). Dispersion is represented in the transport equations as a mass flux term expressed in terms of concentration gradient premultiplied by a dispersion coefficient tensor (Bear, 1972). The dispersion tensor includes a modified coefficient of molecular diffusion and terms that are products of the velocity vector and the dispersivity tensor (or dispersivity). A complete dispersivity tensor, which is a fourth-rank tensor, has 81 components of which 36 components are nonzero (Bear, 1972) for anisotropic materials and 21 components are nonzero for isotropic materials. A simplified form in common use is the Burnett and Frind (1987) tensor that uses three components. The transverse anisotropic dispersivity models of Poreh (1965), require four dispersivities. Lichtner et al. (2002) proposed a dispersivity tensor for axisymmetric medium with two longitudinal and two transverse dispersivities. Field data has shown the dispersivities to be dependent on the scale of the problem (Gelhar et al.,1992; Neuman, 1990). It is common practice in groundwater modeling (Freeze and Cherry, 1979) to represent the effects of dispersion with the use of three independent dispersivities: the longitudinal dispersivity along the direction of the bulk fluid velocity, and two

transverse dispersivities orthogonal to the flow direction. This is the approach used in the PM CAU transport model.

As noted in Section 3.2.2 describing advection, the fluid velocity used by the PM CAU transport model is an average over the computational blocks, which can range in size from tens of meters to kilometers. The PM CAU transport model includes zones representing the HSUs and major structural features such as faults identified in the HFM. However, these zones are coarse, and it is recognized that material heterogeneities and features exist that are not included explicitly in the HFM. These heterogeneities can cause divergence and/or convergence of flow paths within the zones assumed to have single material properties. For example, not every fault in the model domain may be represented explicitly. The presence of faults in an otherwise homogeneous zone could affect the tortuous nature of flow in that zone over the scale of hundreds of meters to kilometers. Likewise, lava beds in a zeolitic confining unit can change the local nature of flow paths. At the very small scale, velocities differ along flow paths between the grains or within fractures. None of these processes are accounted for explicitly in the PM CAU transport model. Rather, dispersion terms and coefficients are used in the transport model to represent spreading and molecular diffusion along and transverse to the advective flow paths computed in the flow model.

Simulation modeling of contaminant transport will be used to forecast the location of CBs within 1,000 years and must show the 95th percentile of the model results (boundary outside of which only 5 percent of the simulations exceed the SDWA standards) (FFACO, 1996 as amended). Transport of contaminants at concentrations below the SDWA standards at the leading edges of a plume, as might occur due to longitudinal and transverse dispersion, does not affect the forecasts of CB. Field data have shown the dispersivities to be dependent on the scale of the problem (Gelhar et al., 1992; Neuman, 1990; Zhou et al., 2005; Schulze-Makuch, 2005). Makedonska et al. (2020) present insights obtained in scaling dispersivities up to 250-m scale using detailed DFN simulations based on fracture statistics. Dispersivity values at field scale are typically obtained by calibrating flow and transport models to contaminant measurements. Identification of a single optimal model is not possible in data-limited situations, and multiple conceptual models could acceptably reproduce observed data; however, the dispersivity values estimated by each model may be quite different (SNJV, 2004a). This makes it difficult to definitively determine the appropriate dispersivity at large scales from current data.

As employed in the PM CAU transport model, the parameters required to represent dispersion are longitudinal and transverse dispersivities. They are documented in Section 5.7.

3.2.4 Matrix Diffusion

In fractured rock zones (e.g., WTAs and LFAs), the permeability of fractures is many orders of magnitude greater than that of the rock matrix. Hence, it is assumed that fluid flow occurs only in fractures and that stagnant fluid resides in the saturated rock matrix. This is the dual-porosity model of the rock formation where solutes advect with the fluid flowing in the fractures, and diffuse in and out of the fluid within the rock matrix. Within the matrix, due to low permeability, the velocity for the bulk movement of the groundwater is effectively zero. Subsequently, the advection of the solute while in the matrix is effectively zero. The Brownian motion of the solute molecules becomes dominant, and the effect of advection resumes when the solute diffuses back into the fracture. The result is a delay: Bulk solute movement through the fractures is thus retarded due to matrix diffusion. Numerous theoretical, laboratory, and field studies support the validity of the matrix diffusion conceptual and numerical model, showing that single effective material properties cannot adequately capture the complex transport behavior of a solute that advects in fractures (e.g., Sudicky and Frind, 1981; Maloszewski and Zuber, 1985; Bechtel SAIC, 2004; and Reimus and Callahan, 2007).

For fractured rock zones represented by the dual-porosity approach in the PM CAU transport model, matrix diffusion is idealized by a model of uniform flow and transport within a system of equally spaced parallel plate fractures. Solutes diffuse between fractures and the matrix according to concentration gradients and the surface area-to-volume ratio of the fractures from which they diffuse. Diffusion is limited by the volume of matrix material into which diffusion occurs, which is determined by the spacing between fractures. Over time, the concentrations of solute in the matrix can increase, thus reducing the concentration gradient driving diffusion out of the fractures. For limited-duration source releases, the fractures are flushed of solute first and then the concentration gradient is reversed, causing diffusion back into the fractures from matrix storage. This behavior is often seen in laboratory and field experiments in long concentration tails of breakthrough curves, well after peak arrival times. The effect is to slow the rate of RN advection in fractures and to reduce concentrations in the mobile phase. Near-source locations diffusion into and later out of matrix blocks can lead to prolonged elevated concentrations in the groundwater sweeping past the zones with

high concentrations. This can lead to source concentrations that decrease over time only by radioactive decay.

This conceptual model is a considerable simplification of the actual processes that occur in complex fracture networks. In reality, fractures intersect and are of variable length and aperture. Diffusion out of some fractures can actually lead to interference of diffusion or enhancement of concentrations in other fractures. However, at the CAU scale, an abstraction is appropriate and designed to capture the net effect of fracture-matrix interactions with CAU gridblock-scale parameters. The parameters are uncertain, which is addressed by stochastic sampling of fracture and matrix properties. Some guidance on the likely ranges of equivalent parallel-plate fracture spacing and apertures is available from DFN models (Makedonska et al., 2020; Parashar et al., 2019; Pham et al., 2020).

The transport parameters required for representing matrix diffusion in the PM CAU transport model are matrix porosity (see Section 5.2), effective porosity (see Section 5.3), fracture spacing (see Section 5.5), fracture aperture (see Section 5.6), and matrix diffusion coefficient (or free water diffusion coefficient and matrix tortuosity) (see Section 5.8).

3.2.5 Matrix and Fracture Sorption

Sorption reactions occur between the rock surfaces in contact with the pore fluid and some of the RNs, tending to retard the transport of these RNs. The reactive minerals known to occur in PM rocks include zeolite, smectite, mica, hematite, and calcite (Zavarin et al., 2004; Carle, 2020; Carle et al,. 2020). Sorption reactions are chemical reactions that involve the distribution of chemical constituents between water and solid surfaces. In single-porosity media, the reactions occur as the solute comes into contact with the immobile minerals along the flow paths between the grains. In double-porosity media, the solute can react with rock surfaces bounding the fractures and also diffuse into the rock matrix and react with the pore walls within the matrix.

Sorption reactions between the aqueous RNs and minerals on the rock surfaces can result in reduced mobility for the reactive RNs. Although the RN-rock reactions can be complex, they are represented in the PM CAU transport model by a constant called the sorption coefficient, K_d (Freeze and Cherry, 1979). The use of the K_d approach requires that the reactions must be in equilibrium, instantaneous (kinetics), linear, and reversible. The sorption coefficient K_d is RN-specific, and also depends on the mineralogy and specific surface area of the rock matrix surfaces exposed to the pore water, chemical

composition of the pore water, and temperature. Some RNs such as ^{3}H, ^{36}Cl, and ^{129}I are considered to be nonreactive and do not sorb. Some RNs are moderately adsorbing, such as U and Np; or strongly sorbing such as ^{238}Pu, $^{239/240}Pu$, ^{137}Cs, and ^{90}Sr (Carle, 2018).

The transport parameters required for representing matrix sorption in the PM CAU transport model are RN-specific K_ds for each HSU/HGU, presented in Section 5.9, matrix porosity presented in Section 5.2, and bulk rock density presented in Section 5.4. In fractured media, sorption reactions occur between surfaces of fractures and some of the RNs, tending to retard the transport of these RNs. As a simplification in the PM CAU transport model, sorption reactions on fracture surfaces are neglected. This is a conservative assumption, further justified by the fact that the reactive surface area that would be available for sorption reactions is quite small relative to the reactive surface area that a solute encounters in the rock matrix once it diffuses out of the fracture.

3.2.6 Colloid-Facilitated Transport

Sorption mechanisms can cause certain RNs to bond to small mobile particles (i.e., colloids). "Small" here means submicrometer size, small in comparison to average fracture aperture, but larger than the solute molecules. These particles can move with the groundwater within fractures but they are not able to diffuse into the matrix pores. This reduces the retardation of RNs due to molecular diffusion into stagnant matrix, potentially increasing the mobility of these RNs. For example, data from Well ER-20-5-1 suggest that Pu (as well as Eu, Co, Cs) migrated downgradient via colloid transport (Kersting et al., 1999; Zavarin, 2012). However, those data also suggest that the activity of RNs that do transport downgradient from the cavities via colloids is very small at PM, well below the MCL.

Kersting et al. (1999) identified Pu concentrations ~0.03 Becquerels per liter (Bq/L) (~0.8 pCi/L compared to Pu-MCL of 15 pCi/L) 1.3 km downgradient from the BENHAM test and determined that the migration was facilitated by colloids. Kersting et al. (1999) also suggest that other RNs including isotopes of Eu, Co, and Cs are transported with colloidal material in groundwaters at PM.

For colloid-facilitated transport of RNs to have a significant impact on the CB estimates, the RN must exist in the source region in sufficient quantities, colloids must exist in sufficient quantities in the water, RNs must be able to access and bind to the colloids in sufficient concentrations, and the colloids must transport downgradient with groundwater.

Zavarin et al. (2015) and Zavarin et al. (2019) document long-term (~3-year) laboratory experiments on nuclear melt-glass alteration that were conducted under conditions that "represent the range of hydrothermal conditions in underground nuclear test cavities when nuclear melt glass is in contact with groundwater" (e.g., at temperatures ranging from 25 degrees Celsius [°C] to 200 °C) to identify the mechanisms controlling Pu mobilization. It was found that colloid concentrations in water are temperature-dependent, with higher temperatures producing higher colloid concentrations. Thus, it was concluded that, based on the median colloid concentration reported for NNSS groundwater, "Colloid concentrations (and associated Pu concentrations) measured in our 140 and 200 °C samples are about two orders of magnitude higher than the median colloid concentrations observed at the NNSS." It was also concluded that "the early-time elevated temperatures expected at underground nuclear tests are likely to yield maximum Pu fluxes to groundwater (and maximum Pu concentrations) and that release rates under long-term ambient conditions will be substantially reduced."

Reimus (2018) addressed the question of whether Pu should continue to be considered as an RN that could potentially define the CBs. He concluded that, unless some unlikely combination of circumstances occurs, it is unlikely that Pu concentrations would ever exceed the MCL at off-site locations and that Pu would never surpass ^{3}H in radiological significance unless it is at some distant time in the future when ^{3}H has decayed to a level below the MCL. (Specifically, he said, "It would have to be a relatively high-yield test with Pu concentrations at least as high as measured in the CHANCELLOR cavity, with high initial glass temperatures at the time of water immersion, with an aquifer unit intersecting the chimney near the top of the cavity, and probably relatively close to the NNSS boundary [or with a very low-volume, channel-like pathway to the boundary] so that there is limited opportunity for mixing and dilution of the "plume." Furthermore, colloid filtration and Pu desorption from colloids would have to be very limited in both the cavity/chimney system and in the downgradient aquifer.") But even then, other nonsorbing or weakly sorbing RNs (e.g., ^{129}I, ^{14}C, ^{36}Cl) are likely to surpass Pu.

Given these conclusions, it is assumed that the influence of colloid-facilitated transport on the extent of the forecast CB is minor, in large part because of the lateral extent of contamination associated with more mobile and dose-significant RNs (e.g., ^{3}H, ^{129}I) over the time period of interest.

4.0 DATA ANALYSIS

Data analysis is the process of compiling, assessing, and interpreting available data in preparation for flow and transport modeling. Data come in a wide variety of types, from a wide variety of sources, and represent a wide variety of scales. The process of analyzing the data can be summarized in the following six steps, which are explained below: (1) compilation of existing data in the study area, (2) transfer of applicable data from outside the PM-OV area, (3) assignment of data quality indicators, (4) calculation of the expected values, range of uncertainty, and statistical distribution, (5) assessment of data scale and likely impacts to the CAU model, as applicable, and (6) discussion of data limitations and the possible impacts to the model.

4.1 Data Compilation/Generation

The compilation of existing data is a multistep process of identifying existing data, acquiring the data, and compiling the data into structured databases. As will be discussed later, certain data inputs required for CAU scale models necessitate data processing through numerical models representing semianalytical solutions to the flow equations. Data types of interest and data sources are discussed in the following sections.

4.1.1 Data Types

Major data types of interest to this report are transport parameters and supporting information. Information needed to support CAU contaminant transport modeling include radioactive decay constants, porosity (matrix and effective), fracture spacing, fracture aperture, dispersivity, matrix diffusion parameters, and contaminant-rock sorption parameters.

The following types of supporting information are recorded, as required and when available:

- Site or core information
- Chemical constituent
- Method of data collection or type of test
- Scale of measurement
- Date of data collection

- Stratigraphic unit
- Lithology
- Alteration
- HSU
- Method of data analysis
- Observed parameter value
- Parameter spatial distribution
- Uncertainties
- Any references relating to the data records
- Any noted deficiencies

References to the specific sources of information are provided along with the data in Section 5.0.

4.1.2 Data Sources

A great many sources for the data have been identified. In many cases, existing databases developed as part of the NNSS regional groundwater flow and transport modeling were used as starting points. These data were supplemented with new data collected as part of ongoing UGTA field investigations and existing data not previously identified as well as separate studies conducted by project participants.

Most of the new data evaluated in this report for the PM area come from numerous organizations, including the NNSS management and operating (M&O) team, LLNL, LANL, Desert Research Institute (DRI), USGS, and the DOE Environmental Services Contractor. Historic data are available in many publications. Data compilation is an ongoing iterative process. Typically, much of the data is compiled during the CAI, supplemented with older data relating to the investigation and testing activities at the NNSS.

Site-Specific Data

Site-specific data is data collected within or near the boundaries of the CAU study area, which is defined as the PM-OV groundwater basin area (Figure 1-3). These data are directly applicable to the HSUs in the study area.

Yucca Mountain Data

Yucca Mountain is the proposed geologic storage location for commercial high-level waste in the United States. A great deal of high-quality data has been collected and analyzed during investigations

of the Yucca Mountain Site. The northern portion of the Yucca Mountain Project (YMP) site is within the southern portion of the PM-OV HFM domain. The geology in the YMP region has many similarities with the geology of the PM CAU as well as a number of differences. A process was developed to assess the transferability of YMP data for use in the PM CAU model.

Other Data

In some cases, the data from much more distant sites may be used to estimate parameter values. Data from distant sites will be used only in cases where the data from the study area or the YMP site are nonexistent or very limited. As with the YMP data, the transferability of all data will be assessed prior to use in the PM CAU model.

4.2 Data Transfer Methodology

It has been proposed that using data from other sites to reduce flow and transport parameter uncertainty is an appropriate approach when developing models in a sparse data environment (Freeze et al., 1990), such as that of the Kawich Valley, Gold Flat and Black Mountain areas of PM-OV groundwater model. This type of approach incorporates flow and transport parameter data from investigations of similar environments for parameters to be used in modeling of the study area. Use of data from other sites can be both cost-effective and necessary for a modeling effort in a sparse data environment. Nearby sites considered as potential sources of additional data for the PM CAU are other UGTA CAUs and Yucca Mountain. Rock genesis and evolution factors that influence flow and transport parameters, the general transfer methodology, and the case of YMP data transfer are described in this section.

4.2.1 Rock Genesis and Evolution Factors Influencing Flow and Transport Parameters

Rock genesis and evolution may influence the flow and transport of groundwater in the subsurface environment in a variety of ways. The factors that influence flow and transport parameters include the overall geologic history of the area, lithology, alteration, stress history, and groundwater chemical composition. The overall data transfer process for UGTA data is provided in detail in SNJV (2004d).

4.2.2 General Transfer Methodology

The use of flow and transport data from other study areas to develop parameter distributions for flow and transport modeling of UGTA CAUs can be justified by examining specific similarities that may exist between various investigation areas. It must be shown that there is sufficient similarity between the two areas, considering the various factors mentioned in the previous subsection. A general approach for the transfer of data from one area to another may be accomplished using the following strategy:

- For each parameter of interest, sites need to be identified that may contain data of the same type.
- The degree of similarity between the candidate study area and PM, in terms of geological setting, geographical distance, and rock types must be identified.
- Once the source of the flow and transport parameter data is identified, the factors affecting the specific parameter need to be clarified. For example, if it can be shown that a parameter is influenced by lithology, then transfer of data from another HSU or another site with similar lithology would increase confidence in the use of transfered data.
- Finally, if sufficient data are present in the original study area, a statistical comparison can be made of the data from the other area to see if the two datasets are comparable. If it can be shown that the two datasets have comparable distributions, it would provide further justification for the incorporation of the data into the existing dataset.

4.2.3 YMP Data Transfer

The Yucca Mountain Site Characterization Project implemented one of the largest hydrologic and geologic characterization studies of volcanic rocks ever conducted. The proximity and similar hydrogeologic environment of the Yucca Mountain Site to PM make it particularly attractive as a source of potential data for the UGTA modeling effort. A detailed rationale for the transfer of data from the YMP is provided in Appendix C; however, a brief summary is presented here:

- Both areas are located in the SWNVF.
- Volcanic rocks in both areas are the result of similar depositional processes.
- Both areas contain similar lithologic units and even lithologic units from the same source area.
- Both areas have experienced similar types of alteration, including devitrification and zeolitization of volcanic material.

- Both areas have undergone similar types of regional tectonic stresses, resulting in similar fracture orientations in the two areas.
- Both have similar groundwater chemistry.

As a result of the two areas' similarities, the use of flow and transport parameter data from the Yucca Mountain area can be justified in helping to develop parameter distributions for the PM-OV modeling effort. Note that the data are actually transferred on an HSU-by-HSU basis. In others words, data for a given parameter are transferred only between HSUs that have relevant similar characteristics.

4.3 Data Qualification

The data qualification process varies depending on the type of parameter. Type-specific quality evaluation procedures are described in the corresponding section of this document.

4.4 Analysis Methods Used

Methods of analysis vary depending on the type of hydrologic data considered. See approach subsections of the analysis sections for the specific methods used.

4.5 Data Analysis Limitations

Data limitations need to be identified. These limitations may be related to the level of data documentation, the data collection method, the data analysis method, or other factors that may limit confidence in the values. Within the discussion of each dataset, data limitations will be noted.

5.0 TRANSPORT PARAMETERS

Major data types of relevance include radioactive decay constants, effective porosity, matrix porosity, fracture spacing, fracture aperture, dispersivity, matrix diffusion coefficients, and sorption coefficients. Details for these parameters are the subject of this section. Note that the HSU assignments in the PM CAU transport model are identical to those in the PM CAU flow model.

5.1 Radioactive Decay Constants

The radioactive decay constants are well-defined properties of the specific RNs, independent of the geologic medium and the ambient underground conditions. Decay constants (λ) are related to the half-life ($T_{1/2}$) as $\lambda = \ln(2)/T_{1/2}$. Half-lives are obtained from Finnegan et al. (2016) and are presented in Table 3-1.

5.2 Matrix Porosity

There are several types of porosity. Of particular interest are matrix and effective porosities. For fractured geologic units these two types of porosity are distinct, while for porous geologic units the two overlap. In fact, matrix porosity measurements may be used to approximate the effective porosity of porous geologic units. Thus, following a discussion of the role of matrix porosity in RN transport in groundwater, this section includes descriptions of the evaluation of the matrix porosity data available for the HSUs of the PM-OV area.

5.2.1 Role of Matrix Porosity in Contaminant Transport

The role of matrix porosity depends on whether the host geologic media are porous or fractured. In porous geologic media, water movement occurs through the rock matrix, through the connected pores measured as effective porosity. In fractured rock material, the portion of the rock that is not fractured is considered the matrix. It is generally accepted that water movement is primarily through the fractures in the rock, but not all fractures transmit measurable quantities of water. Therefore, the volume of rock through which the majority of water flows is a small percentage of the total rock volume. The matrix represents the majority of the rock volume. In fractured saturated geologic units,

the volume of water in the matrix porosity may be greater by factors of up to 100 or more than the volume in the fractures. This large reservoir of water in the matrix may be extremely important to the simulation of RN migration. If RNs migrate from the fracture into the matrix via a process called matrix diffusion, the RNs will slow down relative to the water flowing in the fractures. The matrix porosity, coupled with the matrix diffusion coefficient, govern the movement of the RNs into and out of the matrix. Thus, matrix porosity is expected to be an important parameter in the simulation of RN migration in the groundwater system of PM.

5.2.2 Data Compilation

Matrix porosity data are widely available from many of the boreholes in the NNSS and vicinity. The porosity data are described and presented in the following subsections.

5.2.3 Data Types

The Phase I Pahute Mesa TDD (Shaw, 2003) provides estimates of porosity for many of the HSUs in the PM CAU transport model. These initial estimates are based on core and cuttings analysis in the laboratory and interpretations of geophysical logs. Where possible—and this applies to the large majority of the HSUs in the model—these initial estimates have been supplemented with porosity estimates derived from recent (Navarro, 2019c) interpretations of geophysical logs, specifically density logs.

The density log data analysis used to determine matrix porosity in fact yields total porosity. In most fractured rock aquifers, the total porosity is the sum of matrix porosity and effective or fracture porosity. Fracture porosities are typically less than 1 percent, whereas matrix porosity may be 25 percent or more. The total porosity is, therefore, a good estimator of the matrix porosity of fractured rocks in most cases. In the case of porous rocks, matrix porosity is equivalent to total porosity. In the discussion in this report of porosity derived from density log data, the porosity is referred to as matrix porosity whether the rock type is generally fractured or not.

5.2.4 Data Sources

The porosity dataset from the Phase I PM TDD (Shaw, 2003) was supplemented by the analysis of the density logs of a select group of Phase I and II Pahute Mesa wells as documented in Navarro (2019c). The analysis of the density log data provides estimates of porosity for a number of HSUs for which an

estimate is not provided in Shaw (2003). In addition, values of porosity derived from the analysis of cores and cuttings (Wood, 2009) are compared to estimates derived from the analysis of density logs.

The Phase I PM TDD (Shaw, 2003) matrix porosity data were mainly derived from the interpretations of geophysical logs. A small subset of the data was derived from core measurements.The porosity dataset is built on the porosity database compiled during the data analysis phase of the regional groundwater model (IT, 1996d). The database of porosity values was updated to include the most recent geologic information, and any additional data not available in 1996. The new dataset includes additional data from the YMP and the Environmental Restoration Project (ERP). Data types prioritized for documentation and quality evaluation are the porosity values. The level of documentation for each data record was assessed to provide the users with some basis for traceability of the reported values. The levels were assigned to each record to assess the documentation available for each porosity value. The levels assigned do not reflect the accuracy or reliability of the reported data, only the level of documentation.

Table 5-1 lists the HSUs found in the PM CAU transport model and the sources for the estimates of average HSU matrix porosity given in this report. The first column lists the HSUs in the model. Multiple appearances of the same HSU in the model are not included (e.g., CHLFA1, CHLFA2). Not all of the HSUs listed are found in the boring logs of wells within the PM-OV HFM area. The HSUs found in the borings of the PM-OV HFM area are shown in the second column. The third and fourth columns show the sources for the estimates of average matrix porosity given in this report. Forty of the HSUs in the PM CAU transport model have estimates of average matrix porosity derived from the analysis of density log data (Navarro, 2019c). Thirty-one of the HSUs have estimated average matrix porosity values in the Phase I Pahute Mesa TDD (Shaw, 2003).

The HSU assignments in the PM CAU transport model reflect the PM-OV HFM (DOE/EMNV, 2020a). Although nine of the HSUs in the transport model are not found in borings in the PM-OV HFM area, these HSUs are in the PM-OV HFM. The depths of the borings affect the HSUs they are able to intercept. Although an HSU is thought to be present, based on lines of evidence other than the physical borings, the borings themselves may not be deep enough to show them. In addition, the borings are generally not closely spaced and the model area is large, leaving geologic interpretation to define the areas between borings.

Table 5-1
HSUs in PM CAU Transport Model and Sources of Estimates of Average Matrix Porosities
(Page 1 of 3)

HSUs in the PM-OV Basin Flow Model	HSUs Reflected in the PM-OV HFM Area Borings	Average HSU Porosity Estimated from Lithologies	Average HSU Porosity Sourced from Phase I Pahute Mesa TDD
AA	YES	NO	YES
ATCCU	NO	NO	YES
ATICU	NO	NO	YES
ATWTA	YES	YES	NO
BA	YES	YES	YES
BFCU	YES	YES	NO
BRA	YES	YES	YES
BWCU	YES	YES	NO
BWWTA	YES	NO	NO
CFCM	YES	YES	YES
CFCU	YES	YES	NO
CHLFA	YES	YES	NO
CHVTA	YES	YES	YES
CHZCM	YES	YES	YES
CPA	YES	YES	NO
DVA	YES	YES	YES
DVCM	NO	NO	YES
FCCM	YES	YES	YES
FCCU	YES	YES	NO
FCLLFA	YES	YES	NO
FCULFA	YES	YES	NO
FCWTA	YES	YES	NO
IA	YES	YES	YES
KA	YES	YES	YES
LCA	NO	NO	YES
LCCU	YES	NO	YES
LPCU	YES	YES	NO
MGCU	NO	NO	YES
MPCU	YES	YES	NO
PBPCU	YES	YES	NO
PBRCM	YES	YES	YES

Table 5-1
HSUs in PM CAU Transport Model and Sources of Estimates of Average Matrix Porosities
(Page 2 of 3)

HSUs in the PM-OV Basin Flow Model	HSUs Reflected in the PM-OV HFM Area Borings	Average HSU Porosity Estimated from Lithologies	Average HSU Porosity Sourced from Phase I Pahute Mesa TDD
PCM	YES	YES	YES
PLFA	YES	YES	YES
PMNICU	NO	NO	YES
PVTA	YES	YES	YES
RMICU	NO	NO	YES
RMWTA	YES	YES	NO
SCVCU	NO	NO	YES
SPA	YES	YES	NO
TCA	YES	YES	NO
TCVA	YES	YES	YES
THCM	YES	YES	YES
THCU	YES	YES	NO
THLFA	YES	YES	YES
TMLVTA	YES	YES	NO
TMUWTA	YES	YES	NO
TMWTA	YES	YES	NO
TSA	YES	YES	YES
UCCU	NO	NO	YES
UPCU	YES	YES	NO
WWA	YES	YES	YES

Table 5-1
HSUs in PM CAU Transport Model and Sources of Estimates of Average Matrix Porosities
(Page 3 of 3)

HSUs in the PM-OV Basin Flow Model	HSUs Reflected in the PM-OV HFM Area Borings	Average HSU Porosity Estimated from Lithologies	Average HSU Porosity Sourced from Phase I Pahute Mesa TDD
YMCFCM	YES	YES	YES
YVCM	YES	NO	YES

AA = Alluvial aquifer
ATCCU = Ammonia Tanks caldera confining unit
ATICU = Ammonia Tanks intrusive confining unit
ATWTA = Ammonia Tanks welded-tuff aquifer
BA = Benham aquifer
BFCU = Bullfrog confining unit
BRA = Belted Range aquifer
BWCU = Buttonhook Wash confining unit
BWWTA = Buttonhook Wash welded-tuff aquifer
CFCM = Crater Flat composite unit
CFCU = Crater Flat confining unit
CHLFA = Calico Hills lava-flow aquifer
CHVTA = Calico Hills vitric-tuff aquifer
CHZCM = Calico Hills zeolitic composite unit
CPA = Comb Peak aquifer
DVA = Detached volcanic aquifer
DVCM = Detached volcanic composite unit
FCCM = Fortymile Canyon composite unit
FCCU = Fluorspar Canyon confining unit
FCLLFA = Fortymile Canyon lower lava-flow aquifer
FCULFA = Fortymile Canyon upper lava-flow aquifer
FCWTA = Fortymile Canyon welded-tuff aquifer
IA = Inlet aquifer
KA = Kearsarge aquifer
LCA = Lower carbonate aquifer
LCCU = Lower clastic confining unit
LPCU = Lower Paintbrush confining unit
MGCU = Mesozoic granite confining unit
MPCU = Middle Paintbrush confining unit
PBPCU = Post-Benham Paintbrush confining unit
PBRCM = Pre-Belted Range composite unit
PCM = Paintbrush composite unit
PLFA = Paintbrush lava-flow aquifer
PMNICU = Pahute Mesa Northern Extension intrusive confining unit
PVTA = Paintbrush vitric-tuff aquifer
RMICU = Rainier Mesa intrusive confining unit
RMWTA = Rainier Mesa welded-tuff aquifer
SCVCU = Subcaldera volcanic confining unit
SPA = Scrugham Peak aquifer
TCA = Tiva Canyon aquifer
TCVA = Thirsty Canyon volcanic aquifer
THCM = Tannenbaum Hill composite unit
THCU = Tannenbaum Hill confining unit
THLFA = Tannenbaum Hill lava-flow aquifer
TMLVTA = Timber Mountain lower vitric-tuff aquifer
TMUWTA = Timber Mountain upper welded-tuff aquifer
TMWTA = Timber Mountain welded-tuff aquifer
TSA = Topopah Spring aquifer
UCCU = Upper clastic confining unit
UPCU = Upper Paintbrush confining unit
WWA = Windy Wash aquifer
YMCFCM = Yucca Mountain Crater Flat composite unit
YVCM = Younger volcanic composite unit

5.2.5 Data Quality

The data used in this analysis conforms to the project quality assurance plan (QAP). Most of the data were generated under the UGTA QAP. The data used that were not specifically from work done under the project QAP are from programs with equivalent QAP standards as described in Appendix C.

5.2.6 Data Description and Evaluation

The matrix porosity estimates in the Pahute Mesa Phase I TDD (Shaw, 2003) were supplemented, where possible, with recent interpretations of geophysical logs, specifically density logs. In addition, some matrix porosity values derived from core measurements are compared with estimates of average

HSU matrix porosity. Discussion of the core measurement data and the estimates derived from the density logs follow.

Averages of the calculated porosity values, by HSU, for sample locations below the water table were calculated for comparison with the average matrix porosity values by HSU derived from the analysis of density log data (Navarro, 2019c).

5.2.6.1 Estimates of Matrix Porosity Derived from Density Log Data

During the drilling of a new well, a suite of geophysical logs for subsurface investigation is acquired from the open borehole. These logs provide a set of depth-specific physical measurements of rock properties and provide information on borehole conditions. Each type of log provides several datasets.

Estimates of matrix porosity were developed from the geophysical logs of a set of Phase I and II PM wells. This evaluation is documented in the Pahute Mesa Geophysical Log Data Evaluation for Matrix Porosity data document (Navarro, 2019c). The estimates of porosity derived from the density logs are considered to provide the best estimate of matrix porosity and are the data presented in this report.

The Navarro (2019c) analysis evaluated the density log records to develop estimates of matrix porosity. The estimates were sorted by lithology, HGU, and HSU. The lithology estimates in turn were used to develop estimates of average matrix porosity for HSUs that were not found in the borehole logs examined. This was done on the basis of using the values for the lithologies that on average in the PM area compose the HSU in question. A detailed explanation of this analysis is included in Appendix D.

Table 5-2 is a summary table showing the estimated average matrix porosities assigned to each of the HSUs in the PM CAU transport model. The table is broken down by the source used to assign the values of matrix porosity. The first values shown are those derived using weighted averages of the matrix porosities for the lithologies of which they are composed, as described above. The next category is those values for which an average matrix porosity could not be calculated in this way. The porosity values in this group are taken from either Table 5-7 or 6-15 of the Phase I Pahute Mesa TDD (Shaw, 2003). The last category is matrix porosities for which it was not possible to derive an

Table 5-2
Summary of Estimated Average Matrix Porosities
(Page 1 of 3)

HSUs in the PM-OV Basin Flow Model	Estimated Average Matrix Porosity (%)	Estimated Weighted Standard Deviation	Fraction of HSU Represented by Lithologies for Which There Are No Estimated Porosities
Porosity Estimates Based on Lithologies			
ATWTA	17.7	6.0	0.01
BA	20.4	7.7	0.00
BFCU	28.2	10.3	0.00
BRA	19.7	7.3	0.02
BWCU	28.3	11.1	0.18
CFCM	25.5	8.7	0.00
CFCU	28.4	9.6	0.02
CHLFA	20.8	7.4	0.01
CHVTA	28.2	10.1	0.00
CHZCM	29.1	9.2	0.02
CPA	19.9	7.3	0.00
DVA	26.4	9.2	0.00
FCCM	29.8	9.6	0.05
FCCU	29.3	9.9	0.00
FCLLFA	21.9	9.6	0.00
FCULFA	20.5	7.5	0.03
FCWTA	23.8	9.1	0.07
IA	19.3	7.1	0.00
KA	20.6	7.6	0.00
LPCU	29.8	9.0	0.00
MPCU	30.1	8.4	0.00
PBPCU	29.8	8.6	0.00
PBRCM	24.7	8.5	0.01
PCM	17.4	6.7	0.00
PLFA	20.7	7.7	0.00
PVTA	29.5	9.8	0.00
RMWTA	16.3	5.3	0.00
SPA	19.4	6.5	0.00
TCA	17.1	6.3	0.16

Table 5-2
Summary of Estimated Average Matrix Porosities
(Page 2 of 3)

HSUs in the PM-OV Basin Flow Model	Estimated Average Matrix Porosity (%)	Estimated Weighted Standard Deviation	Fraction of HSU Represented by Lithologies for Which There Are No Estimated Porosities
TCVA	23.3	8.1	0.18
THCM	28.4	8.4	0.05
THCU	29.2	10.6	0.00
THLFA	20.8	7.6	0.00
TMLVTA	29.3	9.6	0.08
TMUWTA	18.5	6.9	0.07
TMWTA	18.1	6.6	0.17
TSA	17.3	6.2	0.00
UPCU	29.9	8.7	0.04
WWA	20.2	7.5	0.01
YMCFCM	24.3	9.1	0.00
Porosity Estimates Directly from the Pahute Mesa Phase I TDD (Table 5-7)			
HSU	**Lower Bound**	**Mean**	**Upper Bound**
AA[a]	23.8	32.0	40.2
ATICU[a]	5E-06	5E-05	9E-03
DVCM	6.0	34.1	75.0
LCA	1.0	5.0	9.7
LCA3	1.0	5.0	9.7
LCCU	0.2	3.3	10.0
MGCU	0.2	1.8	10.3
RMICU	0.2	1.8	10.3
SCVCU[a]	0.1	0.4	0.6
UCCU[a]	5E-06	3E-05	5E-04
YVCM	6.0	34.1	75.0

Table 5-2
Summary of Estimated Average Matrix Porosities
(Page 3 of 3)

HSUs in the PM-OV Basin Flow Model	Estimated Average Matrix Porosity (%)	Estimated Weighted Standard Deviation	Fraction of HSU Represented by Lithologies for Which There Are No Estimated Porosities
Porosity Estimates Taken From the Pahute Mesa Phase I TDD Based on Similarity of the HSUs[b]			
HSU	**Lower Bound**	**Mean**	**Upper Bound**
ATCCU	4.0	41.0	70.0
BWWTA	4.4	28.6	68.4
PMNICU	0.2	1.8	10.3

[a] Value for effective porosity (Shaw, 2003 [Table 6-15])
[b] Assignment based on written communication (email) from C. Lewis (Navarro) June 2, 2020

average value based on the lithologies and which are not listed in either Table 5-7 or 6-15 of the Phase I Pahute Mesa TDD. The values here are assigned based on the similarity of the HSU in question to an HSU that is estimated based on lithologies or found in Table 5-7 of the Phase I Pahute Mesa TDD. For those estimates of matrix porosity developed based on the HSU component lithologies, the HSU is reported, as well as the estimated average matrix porosity and associated standard deviation, The fourth column in this section reports the fraction of the HSU represented by lithologies for which density log estimates of average matrix porosity were not available. For the HSUs that did not have sufficient data to estimate values based on the component lithologies, the values were drawn from the PM Phase I TDD. For these HSUs, the HSU is reported, as well as the lower-bound, mean, and upper-bound values.

5.2.6.2 Comparison of Core- and Geophysical Log-Derived Porosity

A large compilation of matrix porosity and related field measurements has been compiled by the USGS (Wood, 2009). This compilation contains data from a variety of locations in and around the NNSS. The data include the analysis of rock core and cuttings reporting the well name, depth of sample bgs, and calculated porosities amongst other fields. In this report, this compilation of data is referred to as the Rock Properties database (RPd).

The RPd data were matched with HSUs and lithologies from the PM-OV HFM (DOE/EMNV, 2020a) based on the well name and sample depth bgs. Once the RPd data were sorted, they were further divided between those samples collected above the water table and those collected below, the water table. The source of the water levels used for this purpose is the USGS Professional Paper No. 1771 (Fenelon et al., 2010). The porosity data from the RPd were compared to the density log-derived estimates for matrix porosity.

As a means of comparing the various methods of estimating porosity, Figure 5-1 shows a plot of porosities estimated using three different approaches. The data were sorted on the basis of the density log porosity value and plotted from smallest to largest value along the x-axis. Further presentation and discussion of the data is given in Appendix D. The first approach is to estimate porosity from density log records recorded in the respective HSU; the second approach is to estimate an average porosity based on the average porosities of the lithologies that make up the HSU; and the third approach is to use core sample measurements to calculate porosity. Figure 5-1 shows agreement among all methods used within standard deviations presented for data, although the agreement begins to deteriorate for those HSUs with average estimated porosities of 20 percent and greater.

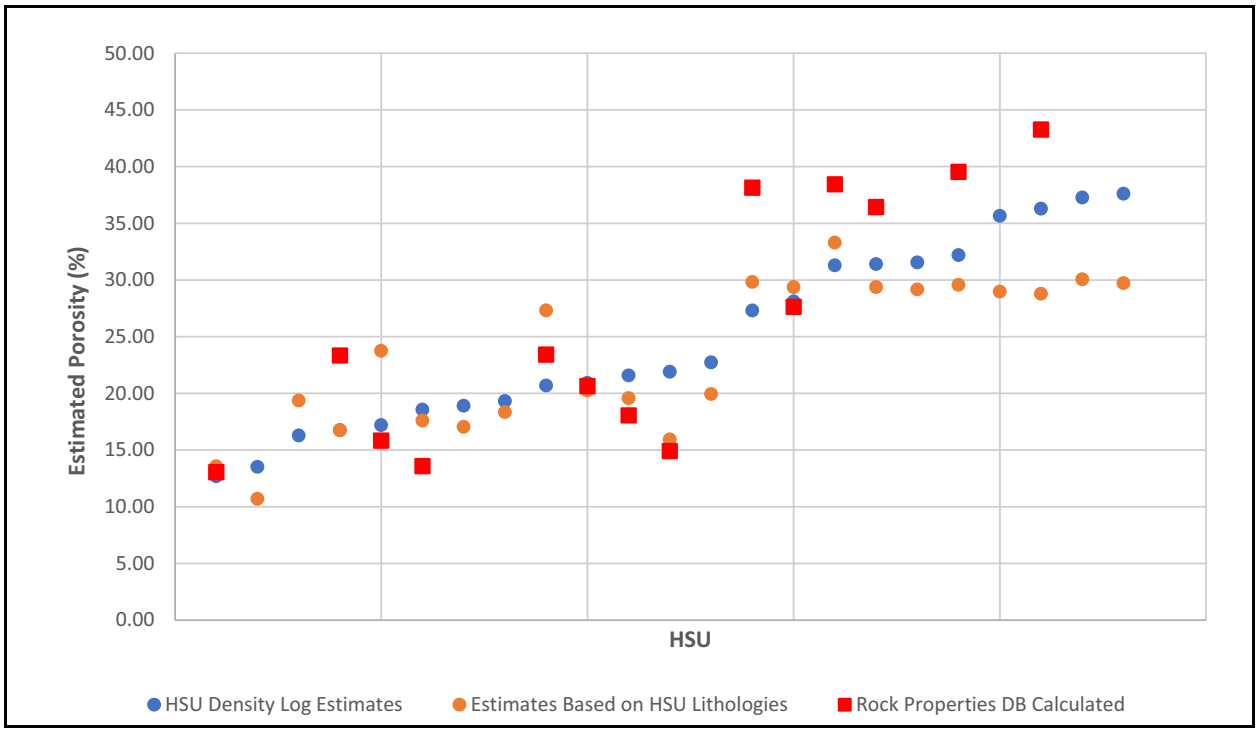

Figure 5-1
Crossplot of Geophysical Log-derived and Core-derived Porosity Values

5.2.6.3 Assessment of Porosity Changes with Depth

The matrix porosities estimated by density log analysis, by HSU, were evaluated for linear trends with increasing depth bgs. Linear trends were fit in Excel to porosity versus depth bgs data plots for each of the 23 HSUs with this data. Table 5-3 shows the results, listed by HSU. Table 5-3 shows that the linear fits to the data were poor and generally not significant. In addition to the slopes and R^2 values associated with the estimated matrix porosity, the length of the interval over which they were measured is shown. Some of the HSUs, like the BRA, have measurements that come from a limited depth interval. As such, they are unlikely to exhibit changes with depth. Others, however, like the CHZCM, have measurements collected over large vertical intervals. Figure 5-2 is a plot of the slopes versus the length of the vertical interval over which the measurements were taken. All of the density log estimates of matrix porosity were taken below the water level. If the estimated matrix porosity values were decreasing with depth, the plot should show increasingly negative slopes with greater depth intervals over which the measurements were collected. However, this is not what is seen. Although there is significant variation in the values taken over a depth interval of less than 500 ft, the average values collected over greater depth do not show a decrease with greater measurement interval.

Table 5-3
Summary of Linear Trends, R^2 Values, and Measurement Intervals by HSU
(Page 1 of 2)

HSU	Slope of Linear Trend	R^2 Value for Trendline Fit to Data	Vertical Interval Over Which Measurements Taken (ft)
BA	-4.38E-07	1.14E-09	1,437.00
BRA	5.91E-02	3.65E-01	393.00
CFCM	-3.17E-03	2.59E-02	1,040.00
CFCU	-3.89E-03	1.11E-01	1,066.25
CHLFA	-1.47E-02	6.00E-01	1,356.50
CHZCM	-1.06E-02	5.74E-01	2,579.75
CPA	5.61E-03	8.31E-02	1,258.00
FCCM	-8.63E-03	3.85E-01	1,896.00
FCCU	-1.14E-02	2.65E-01	1,420.75
FCULFA	-4.88E-03	5.28E-02	871.50
LPCU	-8.86E-04	1.41E-03	1,337.75
MPCU	-6.83E-03	8.82E-03	254.50

Table 5-3
Summary of Linear Trends, R^2 Values, and Measurement Intervals by HSU
(Page 2 of 2)

HSU	Slope of Linear Trend	R^2 Value for Trendline Fit to Data	Vertical Interval Over Which Measurements Taken (ft)
PBPCU	-1.14E-01	1.79E-01	75.75
PBRCM	1.52E-02	2.31E-01	517.00
RMWTA	-9.90E-03	2.87E-01	1,281.25
SPA	-1.82E-02	1.56E-01	395.75
TCA	2.08E-04	1.87E-04	1,531.75
THCM	-1.33E-02	1.13E-01	625.75
THCU	-3.09E-02	1.52E-01	199.75
TMLVTA	7.21E-03	1.54E-02	569.00
TMWTA	-3.07E-02	5.25E-01	192.00
TSA	-1.67E-03	7.79E-03	1,689.50
UPCU	1.27E-03	4.26E-03	1,529.75

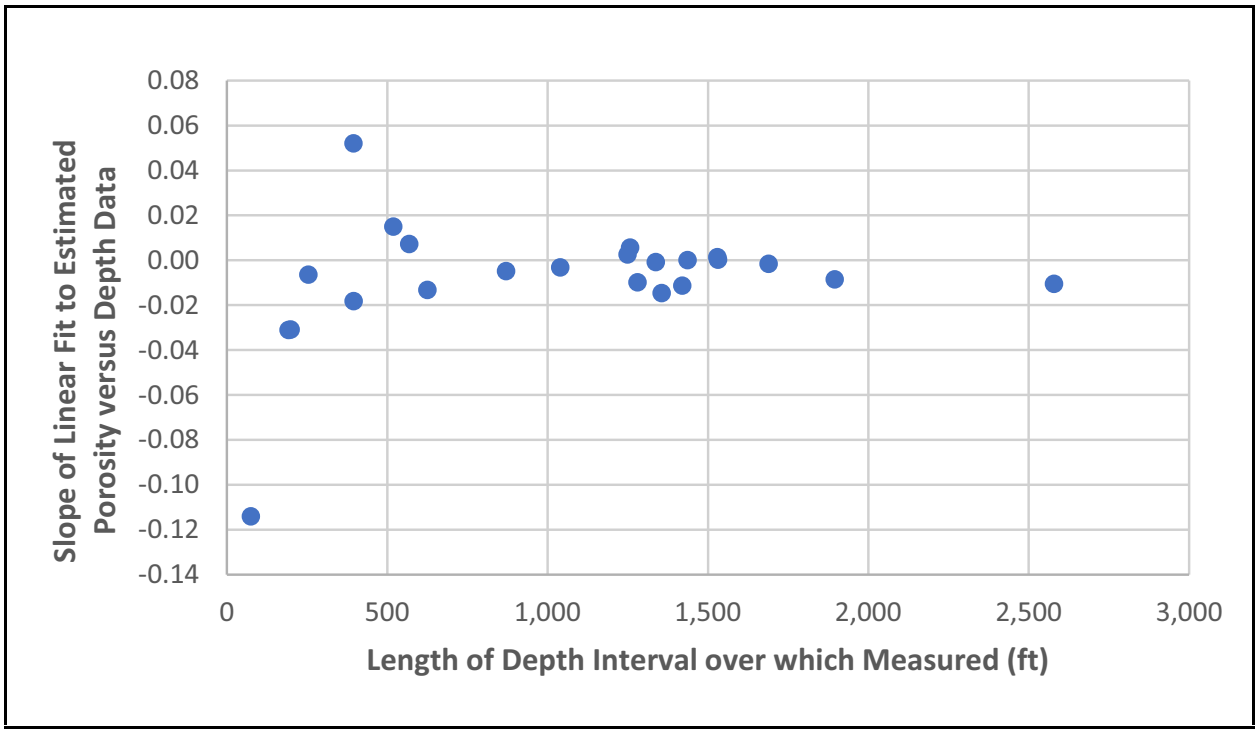

Figure 5-2
Plot of Slopes versus Measurement Intervals

Carle (2020) provides insights that impact the matrix porosity values assigned to units deeper in the model. He discusses the effects of diagenesis on porosity, grain density and other rock properties. He states that majority of the tests at PM were situated in the zeolitic zone and that laboratory measurements may tend to overestimate porosities and grain densities. Based on the Pahute Mesa Hydrologic Conceptual Model, it is expected that shallower, more permeable units will control the transport of RNs from Pahute Mesa.

5.2.7 Data Limitations

Most of the data were derived from geophysical logging of boreholes that penetrated a relatively short distance into the SZ. Some of the data appear to have a trend of decreasing values of porosity with depth; however, the amount of data below the water table is comparatively small for some of the HSUs. The porosities reported from the density log data are derived from measurements taken in situ, but they remain estimates. In addition, the analysis of density log data, although from wells at PM, represents a relatively small sample overall. The density log analyses of lithologies used to estimate average matrix porosities are constrained by the same concern. The percentages of the lithologies that represent each HSU are variable so a single set of percentages for an HSU may not be fully accurate everywhere.

5.2.8 Scaling Considerations

The density log measurements represent conditions very near the boreholes in which the measurements were taken. Overall, the volume of material for which there are measurements is very small in comparison to the total volume of any specific HSU, HGU, or lithology.

Additional complications related to heterogeneity are the result of widely different lithologies in one HSU. Consider, for example, a package of welded tuffs sandwiched between nonwelded tuffs in a single composite unit HSU. Care will be required to use a matrix porosity that best reflects the different lithologies in the HSUs.

5.2.9 Summary of Matrix Porosity by HSU

Table 5-4 is a summary of the matrix porosity ranges assigned to each of the HSUs expected in the PM CAU transport model. The table shows the HSU acronym and full name in the leftmost columns. To the right of that, the table is broken into three sections. The first section reports the data for the

Table 5-4
Summary of Pahute Mesa Estimated Matrix Porosities
(Page 1 of 3)

HSU	HSU Name	Matrix Porosity Estimated by Lithologies (%)	Standard Deviation	Fraction of HSU Represented by Lithologies with No Estimated Porosities	Density Log Data Below the Water Table			Porosity Estimates from the Pahute Mesa Phase I TDD (Shaw, 2003)		
					Minimum	Average	Maximum	Minimum	Average	Maximum
AA	Alluvial Aquifer	--	--	--	--	--	--	23.8	32.0	40.2
ATCCU	Ammonia Tanks Caldera Confining Unit	28.3[a]	11.1	0.18	--	--	--	--	--	--
ATICU	Ammonia Tanks Intrusive Confining Unit	--	--	--	--	--	--	0.2	1.8	10.3
ATWTA	Ammonia Tanks Welded-tuff Aquifer	17.7	6.0	0.01	--	--	--	--	--	--
BA	Benham Aquifer	20.4	7.7	0.00	6.7	20.9	54.6	3.5	20.4	33.6
BFCU	Bullfrog Confining Unit	28.3	10.3	0.00	--	--	--	--	--	--
BRA	Belted Range Aquifer	19.7	7.3	0.02	3.5	21.9	47.2	--	--	--
BWCU	Buttonhook Wash Confining Unit	28.3	11.1	0.18	--	--	--	--	--	--
BWWTA	Buttonhook Wash Welded-tuff Aquifer	--	--	--	--	--	--	4.4	28.6	68.4
CFCM	Crater Flat Composite Unit	25.5	8.7	0.00	5.0	17.2	49.8	2.0	17.5	60.0
CFCU	Crater Flat Confining Unit	28.4	9.6	0.02	14.1	21.9	36.5	--	--	--
CHLFA	Calico Hills Lava-flow Aquifer	20.8	7.4	0.01	3.8	18.9	54.9	--	--	--
CHVTA	Calico Hills Vitric-tuff Aquifer	28.2	10.1	0.00	--	--	--	28.0	40.7	49.0
CHZCM	Calico Hills Zeolitic Composite Unit	29.1	9.2	0.02	6.5	28.1	55.0	0.0	9.2	75.0
CPA	Comb Peak Aquifer	19.9	7.3	0.00	4.2	22.7	54.8			
DVA	Detached Volcanics Aquifer	26.4	9.2	0.00	--	--	--	2.0	17.5	60.0
DVCM	Detached Volcanics Composite Unit	--	--	--	--	--	--	6.0	34.1	75.0
FCCM	Fortymile Canyon Composite Unit	29.8	9.6	0.05	7.9	31.3	52.5	6.0	34.1	75.0
FCCU	Fortymile Canyon Confining Unit	29.3	9.9	0.00	18.8	37.6	54.4	--	--	--
FCLLFA	Fortymile Canyon Lower Lava-flow Aquifer	21.9	9.6	0.00	--	--	--	--	--	--

Table 5-4
Summary of Pahute Mesa Estimated Matrix Porosities
(Page 2 of 3)

HSU	HSU Name	Matrix Porosity Estimated by Lithologies (%)	Standard Deviation	Fraction of HSU Represented by Lithologies with No Estimated Porosities	Density Log Data Below the Water Table			Porosity Estimates from the Pahute Mesa Phase I TDD (Shaw, 2003)		
					Minimum	Average	Maximum	Minimum	Average	Maximum
FCULFA	Fortymile Canyon Upper Lava-flow Aquifer	20.5	7.5	0.03	5.7	19.3	40.0	--	--	--
FCWTA	Fortymile Canyon Welded-tuff Squifer	23.8	9.1	0.07	--	--	--	--	--	--
IA	Inlet Aquifer	19.3	7.1	0.00	--	--	--	2.0	17.5	60.0
KA	Kearsarge Aquifer	20.6	7.6	0.00	--	--	--	2.0	17.5	60.0
LCA	Lower Carbonate Aquifer	--	--	--	--	--	--	1.0	5.0	9.7
LCCU	Lower Clastic Confining Unit	--	--	--	--	--	--	0.2	3.3	10.0
LPCU	Lower Paintbrush Confining Unit	29.8	9.0	0.00	7.6	27.3	54.5	--	--	--
MGCU	Mesozoic Granite Confining Unit	--	--	--	--	--	--	0.2	1.8	10.3
MPCU	Middle Paintbrush Confining Unit	30.1	8.4	0.00	19.2	37.3	51.9	--	--	--
PBPCU	Pre-belted Range Composite Unit	29.8	8.6	0.00	12.7	32.2	43.4	--	--	--
PBRCM	Pre-belted Range Composite Unit	24.7	8.5	0.01	10.2	21.6	42.6	3.2	17.2	29.5
PCM	Paintbrush Composite Unit	17.4	6.7	0.00	--	--	--	2.0	17.5	60.0
PLFA	Paintbrush Lava-flow Aquifer	20.7	7.7	0.00	--	--	--	2.0	23.6	45.1
PMNICU	Pahute Mesa North Intrusive Confining Unit	--	--	--	--	--	--	0.2	1.8	10.3
PVTA	Paintbrush Vitric-tuff Aquifer	29.5	9.8	0.00	--	--	--	10.0	43.5	57.0
RMICU	Rainier Mesa Intrusive Confining Unit	--	--	--	--	--	--	0.2	1.8	10.3
RMWTA	Rainier Mesa Welded-tuff Aquifer	16.3	5.3	0.00	2.2	12.7	44.4	--	--	--
SCVCU	Subcaldera Volcanic Confining Unit	--	--	--	--	--	--	0.1	0.4	0.6
SPA	Scrugham Peak Aquifer	19.4	6.5	0.00	2.8	16.3	36.4	--	--	--
TCA	Tiva Canyon Aquifer	17.1	6.3	0.16	5.2	18.6	49.8	2.0	17.5	60.0

Table 5-4
Summary of Pahute Mesa Estimated Matrix Porosities
(Page 3 of 3)

HSU	HSU Name	Matrix Porosity Estimated by Lithologies (%)	Standard Deviation	Fraction of HSU Represented by Lithologies with No Estimated Porosities	Density Log Data Below the Water Table			Porosity Estimates from the Pahute Mesa Phase I TDD (Shaw, 2003)		
					Minimum	Average	Maximum	Minimum	Average	Maximum
TCVA	Thirsty Canyon Volcanic Aquifer	23.3	8.1	0.18	--	--	--	14.3	46.4	70.9
THCM	Tannenbaum Hill Composite Unit	28.4	8.4	0.05	13.8	31.5	55.3	4.0	41.0	70.0
THCU	Tannenbaum Hill Confining Unit	29.2	10.6	0.00	25.2	35.7	50.1	--	--	--
THLFA	Tannenbaum Hill Lava-flow Aquifer	20.8	7.6	0.00	--	--	--	2.0	17.5	60.0
TMLVTA	Timber Mountain Lower Vitric-tuff Aquifer	29.3	9.6	0.08	5.3	36.3	48.3	--	--	--
TMUWTA	Timber Mountain Upper Welded-tuff Aquifer	18.5	6.9	0.07	--	--	--	--	--	--
TMWTA	Timber Mountain Welded-tuff Aquifer	18.1	6.6	0.17	6.5	13.5	23.1	--	--	--
TSA	Topopah Spring Aquifer	17.3	6.2	0.00	5.1	16.8	42.1	2.0	17.5	60.0
UCCU	Upper Clastic Confining Unit	--	--	--	--	--	--	5.0E-06[b]	3.0E-05[b]	5.0E-04[b]
UPCU	Upper Paintbrush Confining Unit	29.9	8.7	0.04	8.0	31.5	53.9	--	--	--
WWA	Windy Wash Aquifer	20.2	7.5	0.01	--	--	--	2.0	17.5	60.0
YMCFCM	Yucca Mountain Crater Flat Composite Unit	24.3	9.1	0.00	--	--	--	6.0	34.1	75.0
YVCM	Younger Volcanic Composite Unit	--	--	--	--	--	--	6.0	34.1	75.0

[a] Based on similarity of HSU to the BWCU. Personal communication from C. Lewis (Navarro) 06/04/2020.
[b] Effective porosity values from Table 6-15 (Shaw, 2003)

-- = No estimate available

HSUs for which it was possible to estimate matrix porosity based on the component lithologies. In this section, the average matrix porosity and associated standard deviation are shown as well as the fraction of the HSU composed of lithologies for which no density log estimates of porosity were available (Navarro, 2019c). The second section reports the estimates of porosity directly derived from the density logs evaluated. The minimum, average, and maximum values are shown. In the third section, the values of matrix porosity found in the PM Phase I TDD are reported. The minimum, average, and maximum values are shown. For an HSU such as the BA, estimates of matrix porosity are available in all three categories. For others, such as the BFCU, only a single source is available.

5.3 Effective Porosity

This section includes descriptions of the role of effective porosity in RN transport in groundwater, the available effective porosity data, and the analysis of the data and associated results. For porous media, the effective porosity (with some caveats) is represented by the matrix porosity discussed in Section 5.2. The fractured volcanic aquifers are expected to be the primary transport units within the volcanic caldera areas. The fracture porosity of fractured rock units is discussed in this section. The remaining HSUs—vitric tuff aquifers, tuff confining units, intrusive volcanic confining units, and carbonate aquifers—are then discussed.

5.3.1 Role of Effective Porosity in Contaminant Transport

Effective porosity affects the movement of contaminants in groundwater because it is an important factor in determining the magnitudes of groundwater velocity and matrix diffusion. The velocity of groundwater is calculated as the volumetric flow rate per cross-sectional open area. The area open to flow is the interconnected pore space through which water flows and is generally characterized by the effective porosity. Effective porosity can be related to the groundwater velocity via the equation:

$$v = \frac{q}{\phi_{eff}} \qquad (5\text{-}1)$$

where

v = mean groundwater velocity length/time [L/T]
q = groundwater-specific discharge [L/T], which is the volumetric flow rate divided by the cross-sectional area
$Ø_{eff}$ = effective porosity [dimensionless]

In fractured media, as previously noted, two components of the porosity can be identified: a fracture porosity and a matrix porosity. Water primarily flows through the more permeable fracture openings. Thus, the fracture porosity generally controls the velocity of groundwater. In fractured media, fracture porosity is considered the effective porosity for modeling purposes. The range of effective porosity in porous media (typically 15 to 40 percent) can result in a factor of 2 or 3 variation in groundwater velocity; but for fractured systems, the effective porosity variation (<0.01 to 10 percent [Freeze and Cherry, 1979]) can produce several orders of magnitude variation in pore velocity.

In fractured media, permeable fractures are separated by blocks of unfractured rock material that constitute the matrix rock. Contaminants can diffuse into and sorb onto the rock matrix. The diffusion and adsorption processes are governed, in part, by the magnitude and distribution of matrix porosity.

5.3.2 Data Limitations

There are two types of limitations for these data that apply to all values discussed here: those due to sparse data and those due to uncertainties in the methods used to estimate porosity. Data for estimating effective porosity have been collected at few locations, representing only a subset of the HGUs in the PM-OV region. While some data specific to the NNSS are available, uncertainty distributions for effective porosity must rely on the use of data from other sites and expert judgment. Effective porosity cannot be measured directly but must be estimated from fracture data or tracer migration experiments.

5.3.3 Effective Porosity for Porous Media

Effective porosity is always less than or equal to total porosity due to the adhesion of water to solids, unconnected pores, and dead-end pores. The difference between the total and effective porosity increases as the size of the grains in the rock decreases (de Marsily, 1986) and as the amount of cementation increases (Bradley, 1992). Thus, for small-grained, well-cemented sediments, the effective porosity could be significantly lower than the total porosity but for unconsolidated, large-grained sediments, the effective porosity could be about equal to the total porosity. De Marsily (1986), citing Castany (1967), presents a comparison of effective and total porosity as a function of grain size. That comparison shows an effective-to-total porosity ratio ranging from about 0.5 for fine-grained clay (grain size of 0.0003 millimeter [mm]) to 0.9 for fine gravel (grain size of 30 mm). Using a radial diffusion method on core samples, van der Kamp et al. (1996) found a ratio of

effective-to-total porosity of 0.43 to 1 for a low-permeability aquitard. In a controlled experiment using clean, coarse silica sand, van der Kamp et al. (1996) found that the effective porosity was close to the total porosity. Hudak (1994) measured effective and total porosity on unconsolidated sand samples and found that the two closely match. In summary, the effective porosity for systems that behave as a porous media can be estimated as 50 to 100 percent of the total porosity (Section 5.2) depending on the characteristics of the media (e.g., grain size, consolidated or unconsolidated).

5.3.4 Effective Porosity for the Fractured Volcanic Aquifers

This section includes descriptions of the available effective porosity data for the fractured volcanic aquifers, and the associated data analysis and results. The effective porosity of the fractured volcanic aquifers plays a more crucial role than that of the alluvium because the transport of RNs is expected to occur in volcanic aquifers. Fracture porosity data for the WTA and LFA HGUs were evaluated in detail because of their relevance to flow and transport at the PM CAU. Fracture porosity data that were previously developed for the YF/CM CAU TDD (SNJV, 2007) and updated for the YF/CM CAU flow and transport modeling report (N-I, 2013) were examined with respect to site characteristics in an effort to identify relationships between these:

- Fracture porosity values and rock characteristics
- Fracture porosity and structural features

Data from other CAUs and site locations were included in the evaluation because of the sparse site-specific data for PM CAU. The data sources, evaluation methodology, and results are presented below.

5.3.4.1 Data Sources

Fracture porosity estimates have been developed from evaluation of tracer test data, borehole hydraulic conductivity data from analysis of pumping tests and/or borehole flow logging results, DFN numerical modeling and fracture spacing and aperture data from observations of borehole core and analysis of borehole image logs. The tracer test data have been used in three ways to estimate fracture porosity:

1. Calculation of fracture porosity using the assumption of groundwater plug flow and the arrival time of the peak concentration of a conservative tracer. SNJV (2007) provides the analyses for the plug flow equation for a convergent-flow tracer test and for a two-well recirculating-flow

tracer test. The arrival time of the peak concentration is obtained directly from the observed tracer-recovery data from samples taken from the pumping well in the tracer tests.

2. Calculation of fracture porosity using the assumption of plug flow and the mean fluid residence time as determined using the semianalytical method Reactive Transport LaPlace Inversion code (RELAP) (Reimus and Haga, 1999). The mean fluid residence time is obtained by performing a least squared fit of the simulated to observed breakthrough curves by simultaneously fitting mean fluid residence time, mass injected, Peclet number, and mass transfer coefficient (function of matrix porosity, fracture half aperture, and matrix diffusion coefficient).

3. Estimation of aquifer properties through calibration of a numerical model to observed tracer-recovery data and particle tracking.

Borehole hydraulic conductivity and fracture spacing data have been used to estimate fracture porosity using the cubic law relationship for flow between two parallel, smooth plates. The hydraulic conductivity data are estimated through analysis of pumping tests or borehole flow logging results. The fracture spacing data are estimated based on analysis of borehole image logs or observations on core (SNJV, 2007). A detailed discussion of the methodology for estimating fracture porosity from hydraulic conductivity and fracture spacing data is provided in SNJV (2007).

Fracture porosity has also been estimated using fracture spacing and aperture data using the methodology described in Wolfsberg et al. (2002). The sources for the fracture spacing and aperture data are analyses of borehole image logs and/or observations of core.

Transport and volumetric porosity have been estimated using aquifer-specific fracture statistics for length, transmissivity, and orientation for different fracture sets (NSTec, 2014) along with a stochastic DFN approach to generate realizations of possible fracture networks (Makedonska et al., 2020).

5.3.4.2 Data Evaluation

The available literature was reviewed in an effort to collect information related to the stratigraphy, rock characteristics, and structural features associated with the different sites from which data were obtained and used to calculate/estimate fracture porosity values. Table 5-5 summarizes the fracture porosity data for the WTA and LFA HGUs and includes the following:

- The location or study associated with the fracture porosity value

Table 5-5
Summary of Fracture Porosity and Hydraulic Conductivity Estimates, Location, CAU, Stratigraphic Unit, General Site Description, and Data Sources
(Page 1 of 3)

Location	CAU	Unit	Porosity Data Type	Fracture Porosity		K Data Type	Hydraulic Conductivity (ft/d)		General Description	Fracture Porosity Estimation Method	Notes	Sources(s) of Data and Site/Well Information
				Min	Max		Min	Max				
Welded-Tuff Aquifer (WTA)												
C-Holes	YM	Prow Pass (Tcp)	Tracer Test Data	1.80E-03	6.00E-03	Slug/ Pumping Test	2.62	9.84	NW to DW, fault zone at base of wells in lower Bullfrog and upper Tram members, T decreases as distance from faults increases (Geldon et al., 2002)	plug flow method using (1) peak arrival time and (2) mean residence time from RELAP analysis (Bechtel SAIC, 2004)	located on Bow Ridge, a spur of Yucca Mountain; flow occurs in discrete zones, hydraulically connected between flow zones; Geldon et al. (2002) states rocks appear to respond to pumping as a single aquifer, the designation of separate aquifers and confining units may not be appropriate	Bechtel SAIC Co., LLC (2004) Geldon et al. (2002) SNJV (2007)
		lower Bullfrog (Tcb)		3.00E-03	3.00E-03		98.43	196.85				
Exploratory Studies Facility	YM	Topopah Springs tuff (Tpt), middle nonlithophysal zone		2.00E-03	4.00E-03	na - testing conducted in unsaturated zone			nonlithophysal, densely fractured, numerous areas with small brecciated zones	random-walk particle method incorporating Fickian transport	located in Yucca Mountain; testing conducted in unsaturated zone	Freifeld (2001)
USW H-4	YM	Prow Pass (Tcp), Bullfrog (Tcb), Tram		1.10E-04	8.40E-04	Pumping Test	3.08	12.14	welded tuff	calculated from K and borehole fracture spacing	located on Yucca Mountain at the NTS boundary; flow in discrete zones (Erickson and Waddell, 1985)	Erickson and Waddell (1985) Whitfield et al. (1984)
ER-EC-5	WPM-OV	mafic-rich Ammonia Tanks (AT) Tuff	Hydraulic and Borehole Fracture Data	1.80E-04	3.70E-04	Pumping Test / Flow Logging	4.01	318.00	MW, QF, abundant felsic phenocrysts, clinophyroxene present, higher fracture density than underlying mafic-poor AT (DOE/NV, 2004)	calculated from K and borehole fracture spacing (IT, 2002; SNJV, 2007)	well located on upthrown side of slightly offsetting fault located about 1500-2000 ft to the west of the well, well is located in the moat of the Timber Mountain caldera complex; increase in water production noted at two depths in the upper Ammonia Tanks Tuff (DOE/NV, 2004)	DOE/NV (2004) IT (2001) IT (2002a) SNJV (2007)
		mafic-poor Ammonia Tanks (AT) Tuff		1.30E-04	2.20E-04		4.85	111.78	MW to DW, QF, abundant felsic phenocrysts, clinophyroxene present, lower fracture density than mafic-rich AT (DOE/NV, 2004)			
TYBO/BENHAM	PM	Topopah Springs Aquifer (TSA)	Borehole Fracture Data	4.98E-04	4.98E-04	na - fracture porosity data are from multiple boreholes and are not correlated to a specific hydraulic conductivity			shows a typical ash-flow tuff welding profile; NW to PW top and base with MW to DW interior; partially opened fracture observed in MW PW portion; mineral coating and partial filling of fractures with quartz, smectite, feldspar, and mica, extensive fracturing (Wolfsberg et al., 2002)	log average of values calculated from fracture spacing and fracture aperture data assuming single set of fracture (low value) and 3 orthogonal fracture sets (high value) (Wolfsberg et al., 2002)	located on southern edge of Pahute Mesa	Drellack et al. (1997) Wolfsberg et al. (2002)
Discrete Fracture Network Model	PM	Topopah Springs Aquifer (TSA)	Transport (Top - Bottom)	3.32E-04	3.32E-04	--	--	--	--	mean value for 100 realizations	mean values for the model	Makedonska et al. (2020)
			Transport (North - South)	3.03E-04	3.03E-04							
			Transport (East - West)	3.39E-04	3.39E-04							

Table 5-5
Summary of Fracture Porosity and Hydraulic Conductivity Estimates, Location, CAU, Stratigraphic Unit, General Site Description, and Data Sources
(Page 2 of 3)

Location	CAU	Unit	Porosity Data Type	Fracture Porosity		K Data Type	Hydraulic Conductivity (ft/d)		General Description	Fracture Porosity Estimation Method	Notes	Sources(s) of Data and Site/Well Information
				Min	Max		Min	Max				
Discrete Fracture Network Model	PM	Tiva Canyon Aquifer (TCA)	Transport (Top - Bottom)	1.58E-04	1.58E-04	--	--	--	--	mean value for 100 realizations	mean values for the model	Makedonska et al. (2020)
			Transport (North - South)	1.96E-04	1.96E-04							
			Transport (East - West)	2.12E-04	2.12E-04							
Lava Flow Aquifer (LFA)												
BULLION FGE (ER-20-6 wells)												
IT (1998) plug flow	PM	Calico Hills Formation (Th)	Tracer Test Data	4.90E-03	6.80E-03	na - values given below for ER-20-6#1 and ER-20-6#2			mafic poor, DV, rhyolitic lava flow, possible blast induced fracturing (Prothro et al., 1997)	plug flow and peak tracer arrival time	located in Silent Canyon caldera complex, numerous surface fault traces	IT (1998) Prothro et al. (1997) Reimus and Haga (1999) SNJV (2007)
IT (1998) model calibration				1.80E-02	2.30E-02					model calibration		
Reimus & Haga (1999) RELAP & plug flow				3.60E-04	2.10E-02					plug flow and RELAP mean residence time		
ER-20-6#1	PM	Calico Hills Formation (Th)	Hydraulic and Borehole Fracture Data	4.20E-04	4.80E-04	Pumping Test	5.87	8.69	mafic poor, DV, rhyolitic lava flow, possible blast induced fracturing (Prothro et al., 1997)	calculated from K and fracture spacing based on core observations	located in Silent Canyon caldera complex, numerous surface fault traces	IT (1998) Prothro et al. (1997) UGTA Fracture Database (2007) SNJV (2007)
ER-20-6#2	PM	Calico Hills Formation (Th)		1.70E-04	2.00E-04		3.48	5.15	mafic poor, DV, rhyolitic lava flow, possible blast induced fracturing (Prothro et al., 1997)	calculated from K and fracture spacing based on core observations	located in Silent Canyon caldera complex, numerous surface fault traces	
ER-EC-1	WPM-OV	Benham Formation (Tpb) of Paintbrush Group	--	1.00E-04	3.70E-04	Flow Logging	2.30	194.79	rhyolitic lava, DV and silicic	calculated from K and fracture spacing based on core observations	located within the Timber Mountain caldera complex, also considered to be within the Silent Canyon caldera complex	DOE/NV (2000a) IT (2001) IT (2002b) SNJV (2007)
ER-EC-4	WPM-OV	trachyte of Ribbon Cliff (Tct) of Thirsty Canyon Group		1.80E-04	4.80E-04	Flow Logging	12.50	305.45	lava, DV, minor vitric, Z, QF	calculated from K and fracture spacing based on core observations	located just west of geophysically inferred N-NE striking structure (Thirsty Canyon lineament)	DOE/NV (2000b) IT (2001) IT (2002c) SNJV (2007)

Table 5-5
Summary of Fracture Porosity and Hydraulic Conductivity Estimates, Location, CAU, Stratigraphic Unit, General Site Description, and Data Sources
(Page 3 of 3)

Location	CAU	Unit	Porosity Data Type	Fracture Porosity		K Data Type	Hydraulic Conductivity (ft/d)		General Description	Fracture Porosity Estimation Method	Notes	Sources(s) of Data and Site/Well Information
				Min	Max		Min	Max				
TYBO/BENHAM	PM	Lava flow in the Calico Hills Zeolitized Composite Unit (CHZCM)	Borehole Fracture Data	2.09E-03	2.09E-03	na - fracture porosity data are from multiple boreholes and are not correlated to a specific hydraulic conductivity			zeolitized composite unit with an embedded lava flow	log average of values calculated from fracture spacing and fracture aperture data assuming single set of fracture (low value) and 3 orthogonal fracture sets (high value)	located on southern edge of Pahute Mesa	Drellack et al. (1997) Wolfsberg et al. (2002)
Discrete Fracture Network Model	PM	Lava Flow Aquifer (LFA)	Transport (Top - Bottom)	1.25E-04	1.25E-04	--	--	--	--	mean value for 100 realizations	mean values for the model	Makedonska et al. (2020)
			Transport (North - South)	1.10E-04	1.10E-04							
			Transport (East - West)	1.22E-04	1.22E-04							

Source: Modified from Intera, 2014; Table 1

-- = No data available

- The CAU in which the data were collected
- The stratigraphic unit associated with the fracture porosity value
- The type of data used to calculate/estimate the fracture porosity value
  - Tracer test data
  - Hydraulic conductivity and borehole fracture spacing data
  - Borehole fracture spacing and aperture data
- The minimum and maximum fracture porosity values estimated from the data
- The type of data used to estimate hydraulic conductivity
- The minimum and maximum hydraulic conductivity
- A general description of the stratigraphic unit
- The method by which the fracture porosity values were calculated/estimated
- Notes, if any, regarding the location and/or other potentially useful information
- Source(s) of the information

Brief notes on the literature review for each location with a fracture porosity estimate are provided in Appendix E. The locations of the fracture porosity data are shown by HGU in Figure 5-3. On this figure, the symbol shape indicates the HGU and the color of the text label indicates the type of data used to estimate a fracture porosity. Fracture porosity values are available for the WTA HGU in these locations:

- Yucca Mountain (YM) near the boundary of the NNSS site (C-Holes complex, USW H-4, Exploratory Studies Facility [ESF])
- Western Pahute Mesa-Oasis Valley (WPM-OV) area (ER-EC-5)
- PM (TYBO/BENHAM)

Fracture porosity values are available for the LFA HGU in these areas:

- WPM-OV area (ER-EC-1, ER-EC-4)
- PM (TYBO/BENHAM, BULLION, ER-20-6#1)

In addition, transport and volumetric porosities were estimated via DFN modeling.

Note from Table 5-5 that several estimates of fracture porosity in the LFA HGU are available for the vicinity of the BULLION detonation from the BULLION forced-gradient experiment (FGE) and Wells ER-20-6#1 and ER-20-6#2, which were tracer injection/sampling wells during the BULLION FGE.

Figures 5-4 and 5-5 show the fracture porosity data for the WTA and LFA HGUs, respectively. The label on the left side of each figure provides the stratigraphic unit, type of data used to estimate

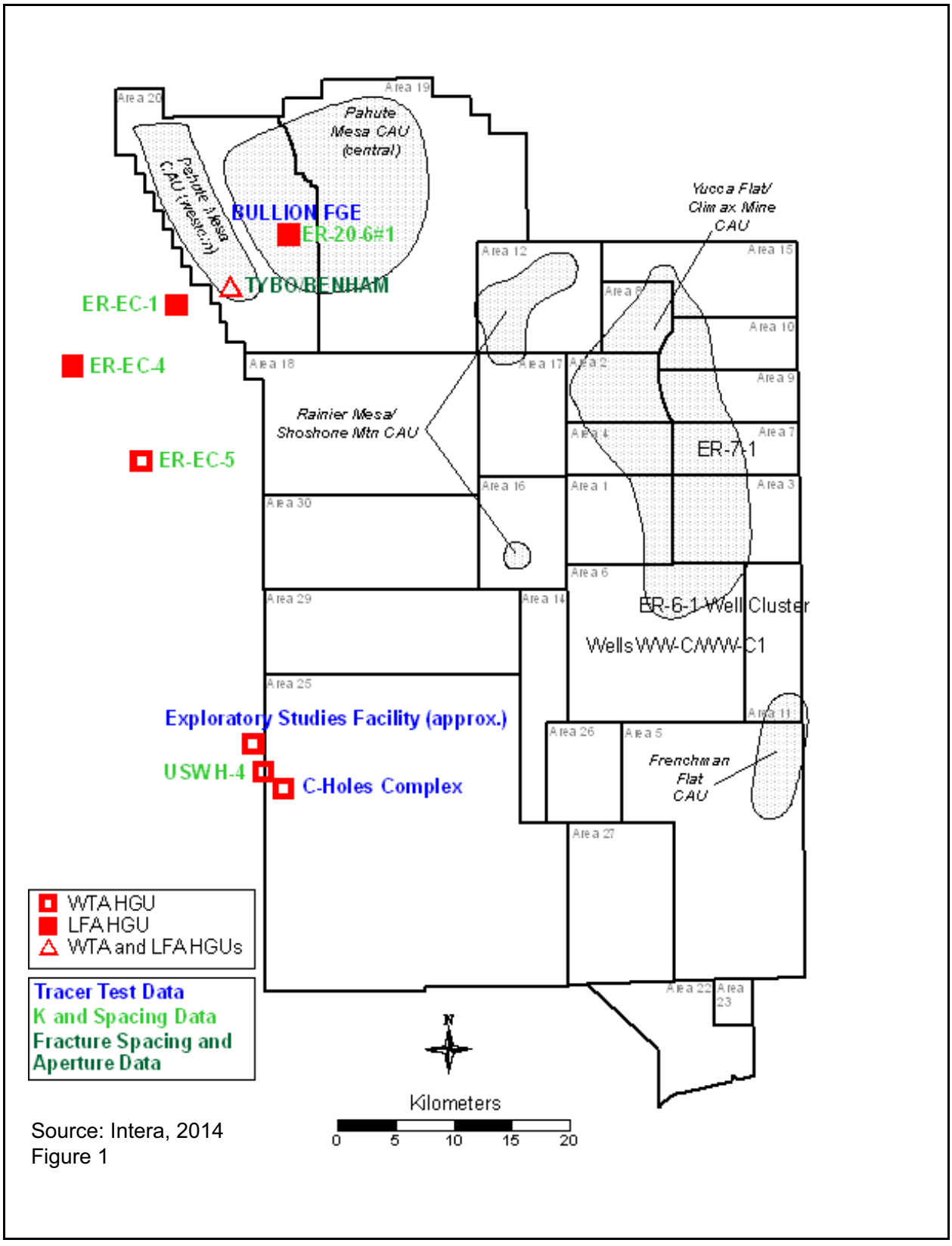

Source: Intera, 2014
Figure 1

Figure 5-3
Map Showing Locations with Estimates of Fracture Porosity by HGU and Data Type

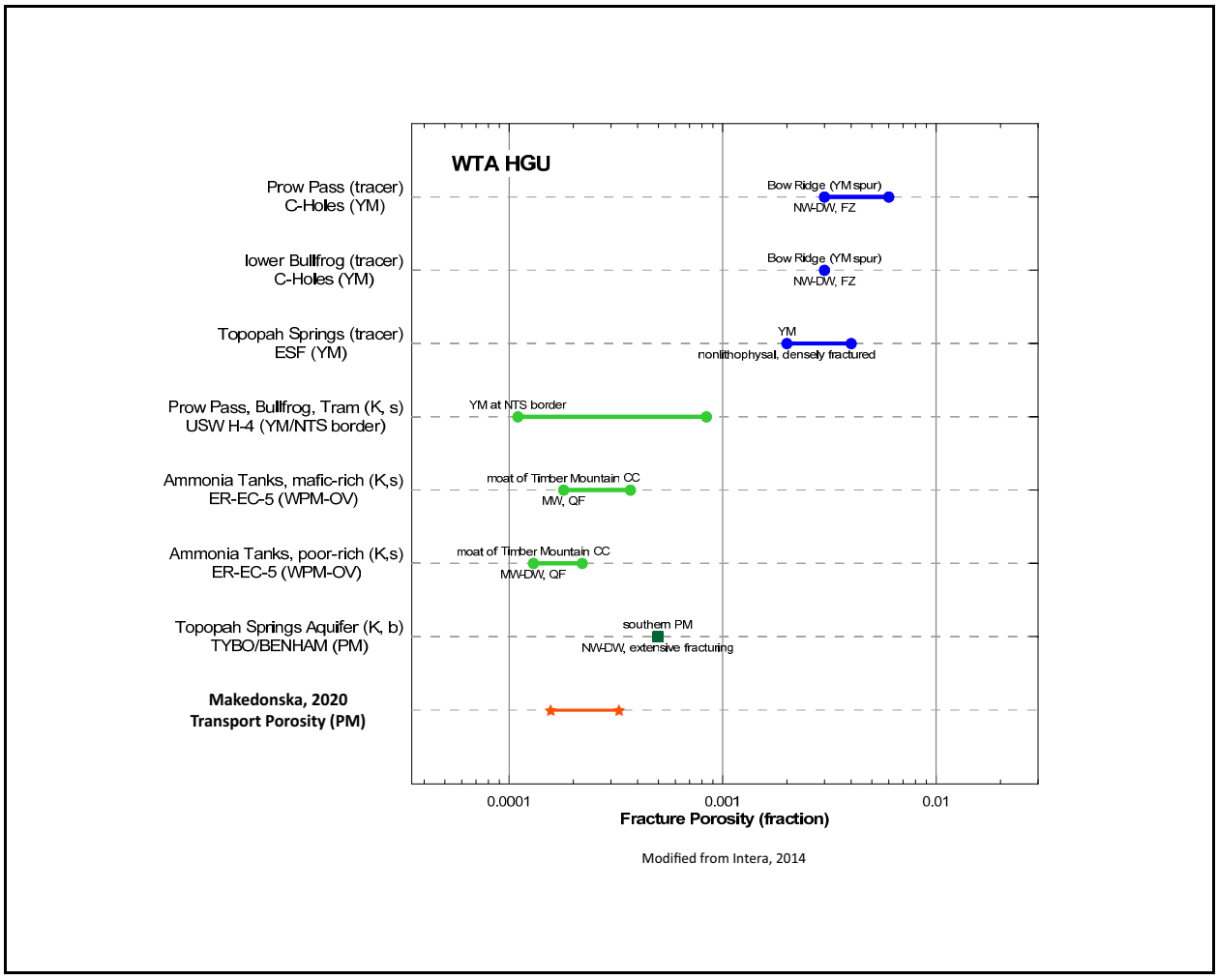

Figure 5-4
Fracture Porosity Estimates for the WTA HGU
Data from tracer tests (blue), hydraulic tests (green), and DFN estimates (red).

fracture porosity, location, and CAU. The fracture porosity values are shown in different colors for the three different types of data used to estimate the fracture porosity. The data on each figure is annotated with the location where the data were collected and a brief description of the characteristics of the stratigraphic unit. An important observation from these figures is that the fracture porosity values estimated from tracer test data are generally about an order of magnitude greater than the fracture porosity values estimated from hydraulic and borehole fracture data. There are three possible explanations for these differences:

1. The difference between the fracture aperture characteristics that control hydraulic responses versus the fracture aperture characteristics that control tracer migration.

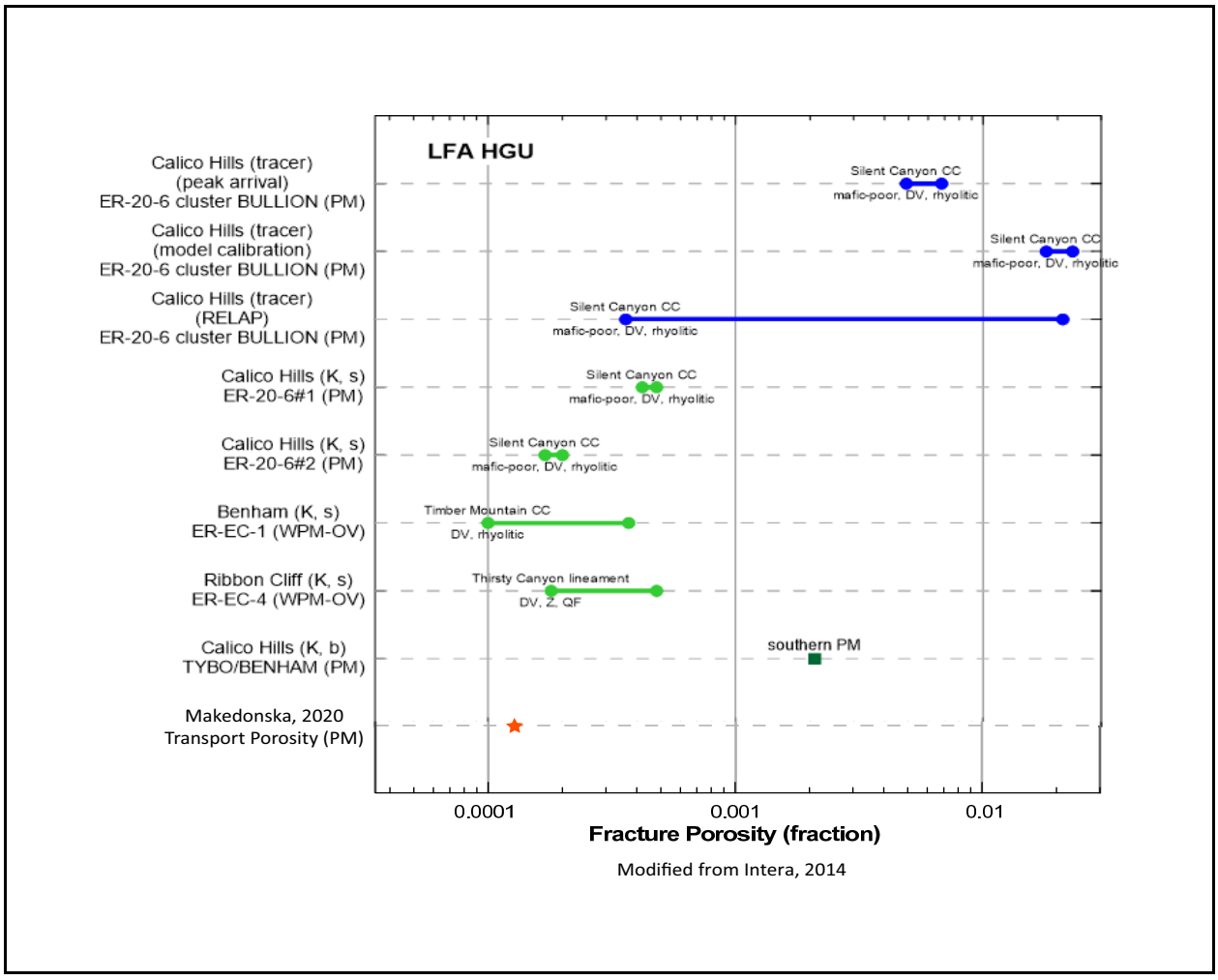

Figure 5-5
Fracture Porosity Estimates for the LFA HGU
Data from tracer tests (blue), hydraulic tests (green), and DFN estimates (red).

2. The fracture characteristics are different at the locations with tracer tests versus the locations with hydraulic and borehole fracture data.

3. The actual paths of the tracers from the injection to sampling points was longer than assumed in the analysis (Parashar et al., 2019).

A discussion examining each of these possibilities follows.

5.3.4.3 Hydraulic versus Transport Effective Aperture and Fracture Porosity

The effective aperture for hydraulic tests, referred to as the hydraulic fracture aperture, will be most impacted by the smaller aperture regions because those are the areas that offer the most resistance to

flow, while migration during tracer tests is controlled by the arithmetic mean of the fracture apertures, referred to as the transport fracture aperture (Tsang, 1992).

Using the parallel plate model, fracture porosity is related to fracture aperture through the relationship:

$$\varphi_f = \frac{b}{s} \qquad (5\text{-}2)$$

where

φ_f = fracture porosity
b = fracture aperture
s = fracture spacing (Wolfsberg et al., 2002)

For the same fracture spacing, the fracture porosity calculated using Equation (5-3) and the hydraulic fracture aperture, referred to as the hydraulic fracture porosity, is smaller than the fracture porosity calculated using the transport fracture aperture, referred to as the transport fracture porosity. Figure 5-6 shows a comparison of hydraulic fracture porosities and transport fracture porosities at three locations in and near the NNSS along with a line representing a transport fracture porosity one order of magnitude larger than a hydraulic fracture porosity. These data support the conclusion that the difference between the fracture porosity values calculated from hydraulic and tracer test data is a function of the difference in the effective fracture aperture strongly influencing the results from each type of test.

5.3.4.4 Variability in Fracture Characteristics by Location

The information obtained from the literature review and summarized in Table 5-5 is sufficient to make a few general observations about the conceptualization of the rocks at the locations of tracer test data used to estimate fracture porosity (i.e., C-holes complex, YM ESF, BULLION). Each of these sites is discussed briefly below. In general, there are insufficient data at locations with fracture porosity calculated only from hydraulic conductivity and fracture spacing to develop a conceptualization of fracturing at those locations.

C-Holes Complex - WTA HGU

Tracer testing at the C-holes complex was conducted in the Prow Pass and underlying lower Bullfrog tuffs, both of which are considered to be WTAs. Geldon et al. (2002) indicate the presence of a fault in the lower portion of the Bullfrog Tuff and the upper portion of the underlying Tram Tuff at the

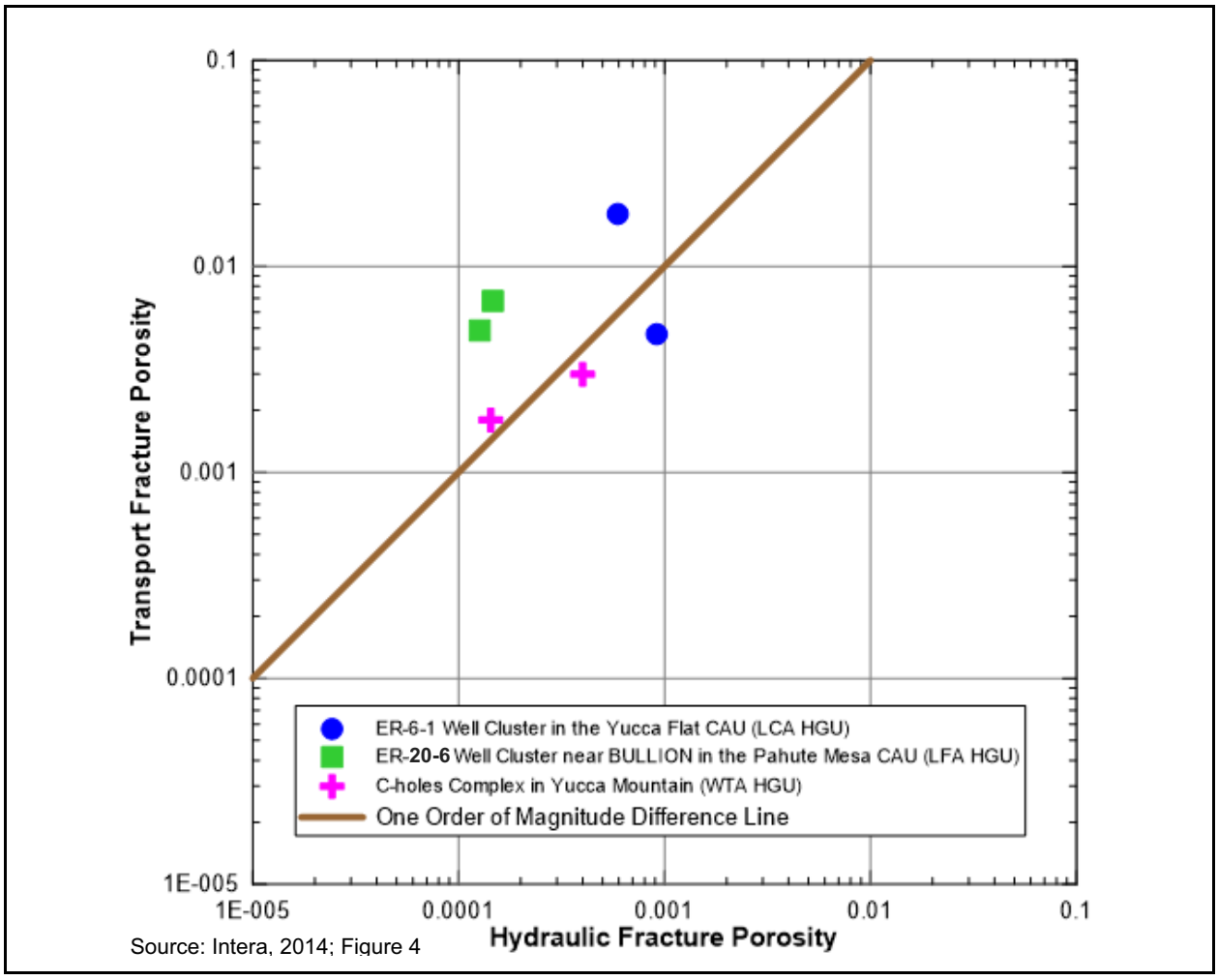

Figure 5-6
Comparison of Hydraulic Fracture Porosity and Transport Fracture Porosity

location of this complex. They also state that the hydraulic data show a decrease in the estimated transmissivity at the boreholes as the distance from the faults increases. If the degree of fracturing (magnitude of spacing and apertures) is related to hydraulic conductivity, the results observed by Geldon et al. (2002) suggest that fracturing of the rocks in the vicinity of the borehole decreases as the distance from the faults increases and implies a correlation between fracturing and faulting.

However, the calculated fracture porosities for the Prow Pass and lower Bullfrog tuffs are similar (Figure 5-4). It is suggested in Intera (2014) that this similarity indicates that the fracture porosity, at least at this location, appears to be independent of the degree of fracturing.

In conclusion, the hydraulic data suggest an increase in fracturing with a decrease in distance to faults and the calculated fracture porosities appear to be independent of distance to faults at the location of the C-holes complex.

Yucca Mountain Exploratory Studies Facility (ESF) – WTA HGU

Freifeld (2001) interpreted gas tracer test data from tests conducted at YM in the ESF. These tests were conducted in welded tuff of the Topopah Springs Tuff above the water table. In describing the rocks tested, he indicated they were densely fractured and included numerous areas with small brecciated zones. The presence of brecciated zones, as well as dense fracturing, suggests the possibility of nearby faulting. They also suggest that the estimated fracture porosity at this location is high due to dense fracturing.

ER-20-6 Wells near BULLION - LFA HGU

Tracer testing was conducted in the Calico Hills Formation (LFA HGU) at the ER-20-6 well complex in the vicinity of the BULLION underground detonation. The closest point in the wells to the BULLION detonation is about $1.5R_c$ from the detonation (R_c calculated based on the maximum of the unclassified yield range [NNSA/NFO, 2015; Carle, 2021]). Prothro et al. (1997) suggest the possibility of blast-induced fracturing at these wells, indicating the possibility that fracturing at the location of these wells may be higher than at other locations in the Calico Hills Formation. Enhanced fracturing induced by the detonation may be a reason for the high fracture porosities estimated from the results of the BULLION FGE.

In summary, the discussion of the C-holes complex, ESF, and ER-20-6 wells indicate the possibility of enhanced fracturing at these locations due to the proximity of a fault at the C-holes complex and detonation-induced fracturing at the ER-20-6 wells. Although information in Freifeld (2001) for the ESF is insufficient to deduce the reason for enhanced fracturing, he does indicate that the site of the tracer test is densely fractured.

5.3.4.4.1 Investigation of Relationship between Fracture Porosity and Hydraulic Conductivity

An investigation was conducted to determine whether a relationship between hydraulic conductivity and fracture porosity is observed at locations with a fracture porosity estimate. The purpose for this investigation was to see if locations with larger hydraulic conductivity are also locations with larger

fracture porosity based on the assumption that hydraulic conductivity is greater where fracturing is greater. In addition to this data, Makedonska et al. (2020) arrived at conclusions regarding transport and total fracture porosity. This information is discussed at the end of this section.

The hydraulic conductivity data for sites with a fracture porosity estimate can be found in Table 5-5. Figures 5-7 and 5-8 summarize the available hydraulic conductivity data for the locations with fracture porosity estimates in the WTA and LFA HGUs, respectively. The following first discusses data for the WTA HGU and then for the LFA HGU.

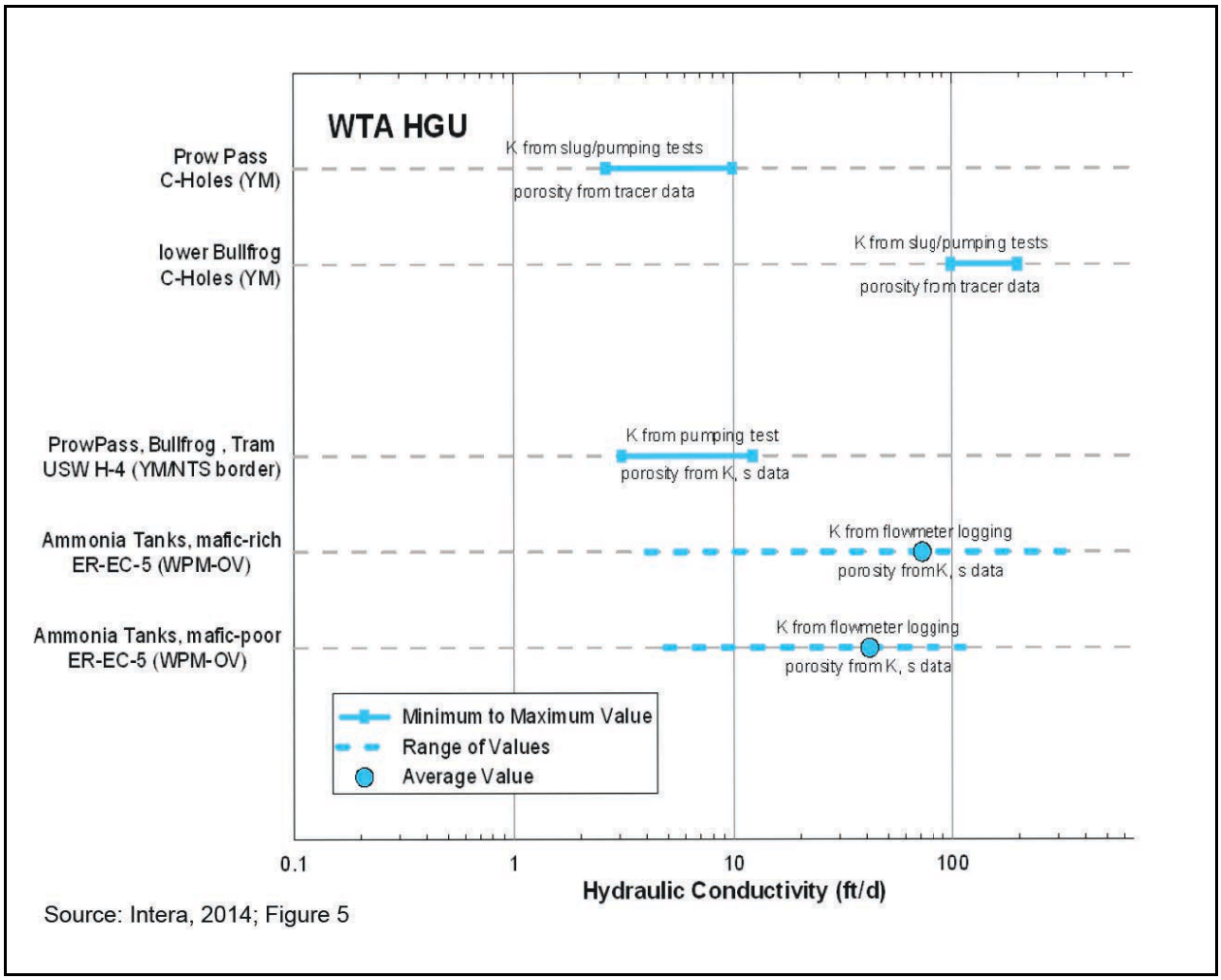

Figure 5-7
Estimated Hydraulic Conductivities in the WTA HGU at Locations with Fracture Porosity Estimates

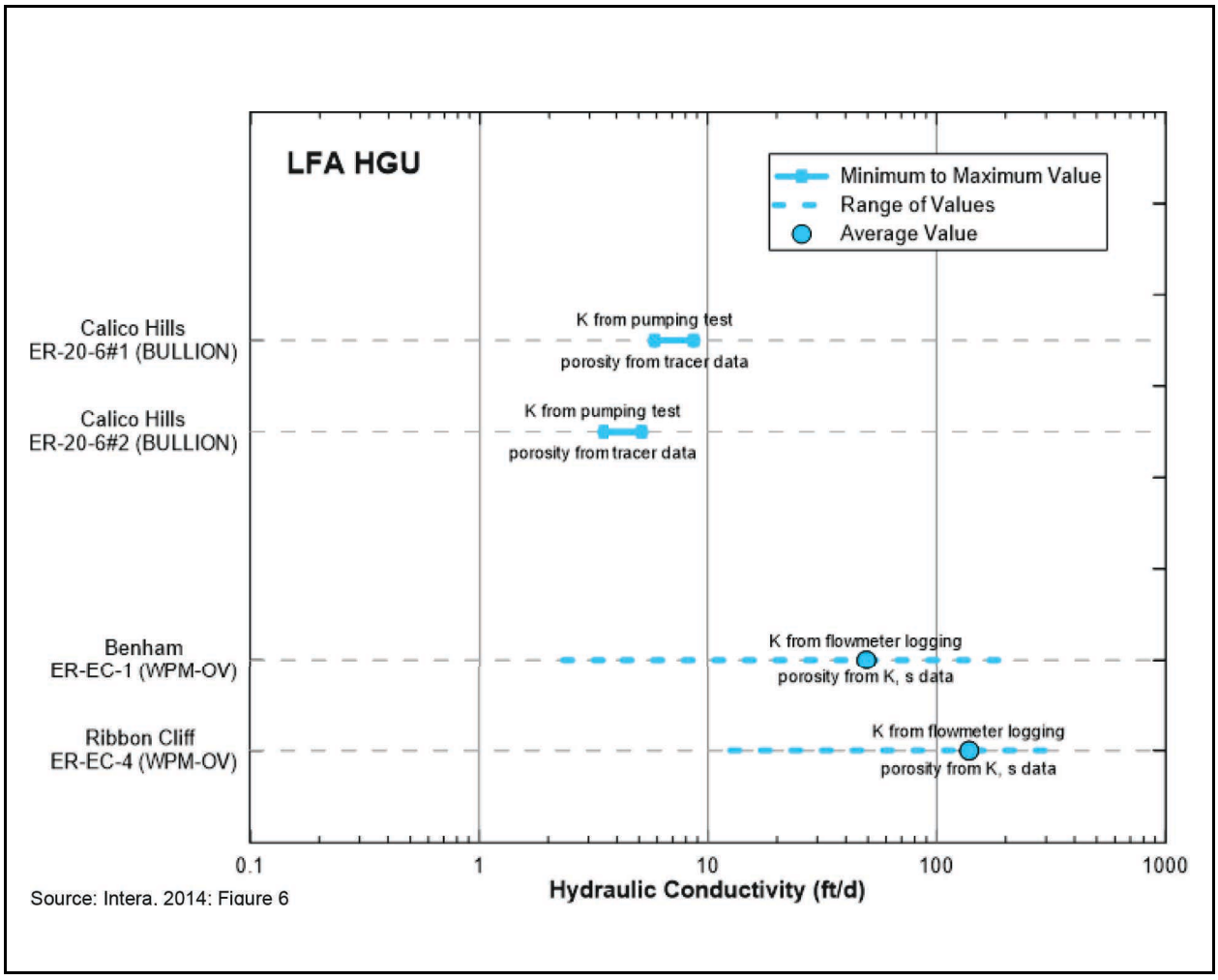

Figure 5-8
Estimated Hydraulic Conductivities in the LFA HGU at Locations with Fracture Porosity Estimates

WTA HGU

As stated above, Geldon et al. (2002) observed a lower hydraulic conductivity in the Prow Pass Tuff than in the Bullfrog Tuff at the C-holes complex. Figure 5-7 shows that the estimated hydraulic conductivity for the Prow Pass Tuff is about one and a half orders of magnitude lower than that for the Bullfrog Tuff. Geldon et al. (2002) attribute this observation to greater fracturing in the Bullfrog Tuff than in the Prow Pass Tuff due to the Bullfrog Tuff being located closer to faults. Based on the tracer test data, the estimated fracture porosity in the Prow Pass and lower Bullfrog tuffs is very similar, indicating no identifiable correlation to proximity to faults. These results suggest that, at the C-holes complex, fracture porosity appears to be independent of proximity to faults.

Figure 5-7 shows the hydraulic conductivity data for boreholes USW H-4 and ER-EC-5, which generally fall within the range of hydraulic conductivities observed at the C-holes complex. However, the fracture porosities calculated based on hydraulic conductivity and fracture spacing data at these two boreholes are about an order of magnitude lower than the fracture porosities estimated for the C-holes complex based on tracer test data. If higher hydraulic conductivities correspond to a higher degree of fracturing, then the fracture porosities determined at USW H-4 and ER-EC-5 should be similar to those determined at the C-holes complex. The comparison of the hydraulic and tracer test-derived fracture porosities supports the conclusion that fracture porosities calculated from hydraulic data are smaller than those obtained from tracer test data.

LFA HGU

The hydraulic conductivity data for locations with fracture porosity data in the LFA HGU show lower hydraulic conductivity values at the ER-20-6 cluster near the BULLION detonation and higher values at ER-EC-1 and ER-EC-4 in the western PM-OV area (Figure 5-8). These results are opposite of those observed for the fracture porosity data, which show higher values at the ER-20-6 cluster based on tracer data and lower values at ER-EC-1 and ER-EC-4 based on hydraulic conductivity and fracture spacing data. These differences again suggest that using hydraulic conductivity and fracture spacing to calculate fracture porosity provides an underestimate.

Findings of Makedonska et al. (2020)

Makedonska et al. (2020) used DFN modeling to evaluate fracture transport characteristics. They found that transport porosity was only 20 to 30 percent of the total fracture porosity due to flow channeling through the longest, most transmissive fractures, which caused much of the fracture porosity to be effectively bypassed. It was assumed that the mechanical aperture was 1 to 3 times the hydraulic aperture so the differences between the transport and total fracture porosity are attributable to network effects.

5.3.4.4.2 Evaluation Results

A review of the fracture porosity data shows that values determined from the analysis of tracer test data are typically about an order of magnitude higher than those calculated from hydraulic conductivity and fracture spacing (Figures 5-4 and 5-5). The reason for this difference is related to the effective fracture aperture during hydraulic and tracer tests. The effective aperture is controlled by the

smaller aperture regions during hydraulic tests because those are the areas that offer the most resistance to flow. The effective aperture is controlled by the arithmetic mean of the fracture apertures for migration during tracer tests (Tsang, 1992).

The fracture porosity data from tracer tests in the WTA HGU provide data for three different stratigraphic units, all of which have a similar fracture porosity (Figure 5-4). Figure 5-9 shows a comparison of estimated fracture porosity values for the WTA and LFA HGUs. This figure shows that the magnitude of the fracture porosity is similar for both HGUs and is a function of the type of data used to calculate the fracture porosity value and appears to be independent of HGU. A review of the fracture porosity data in SNJV (2007) for the WTA, LFA, and LCA HGU show very little difference in the estimated values or ranges for all three HGUs. Note that the majority of these data are from the NNSS site, but some data for the LCA are from the Waste Isolation Pilot Plant (WIPP) site, which is a fractured dolomite. This suggests little effect of HGU on estimated fracture porosity.

5.3.4.5 Summary

A review of the fracture porosity data was conducted by evaluating the effect of the type of data used to calculate the fracture porosity, the stratigraphic unit, and the HGU. In addition, characteristics of the sites at which fracture porosity data are available were assessed. Fracture porosity values calculated from tracer test data are generally about an order of magnitude higher than those calculated from hydraulic conductivity and fracture spacing data. This difference was determined to be due to the different effective fracture apertures controlling hydraulic and tracer responses and not due to differences in characteristics of the sites. This conclusion was based on a comparison of values at three sites at or near the NNSS. The fracture porosity values calculated from the tracer test data at these sites are about an order of magnitude greater than those calculated from the hydraulic data (Figure 5-6). In addition, departures from the assumed flow geometry of the solution can yield longer flow paths, which can be interpreted as higher than actual values of porosity.

An attempt was made to assess the difference in rock characteristics between the locations with fracture porosity data to develop a representative conceptual model of fracturing for each fracture porosity value. This could not be accomplished because the level of investigation at sites with tracer test data is greater than that for sites with hydraulic data only. Therefore, the ability to characterize fracturing at sites with hydraulic data only was limited. In addition, since the two types of data result

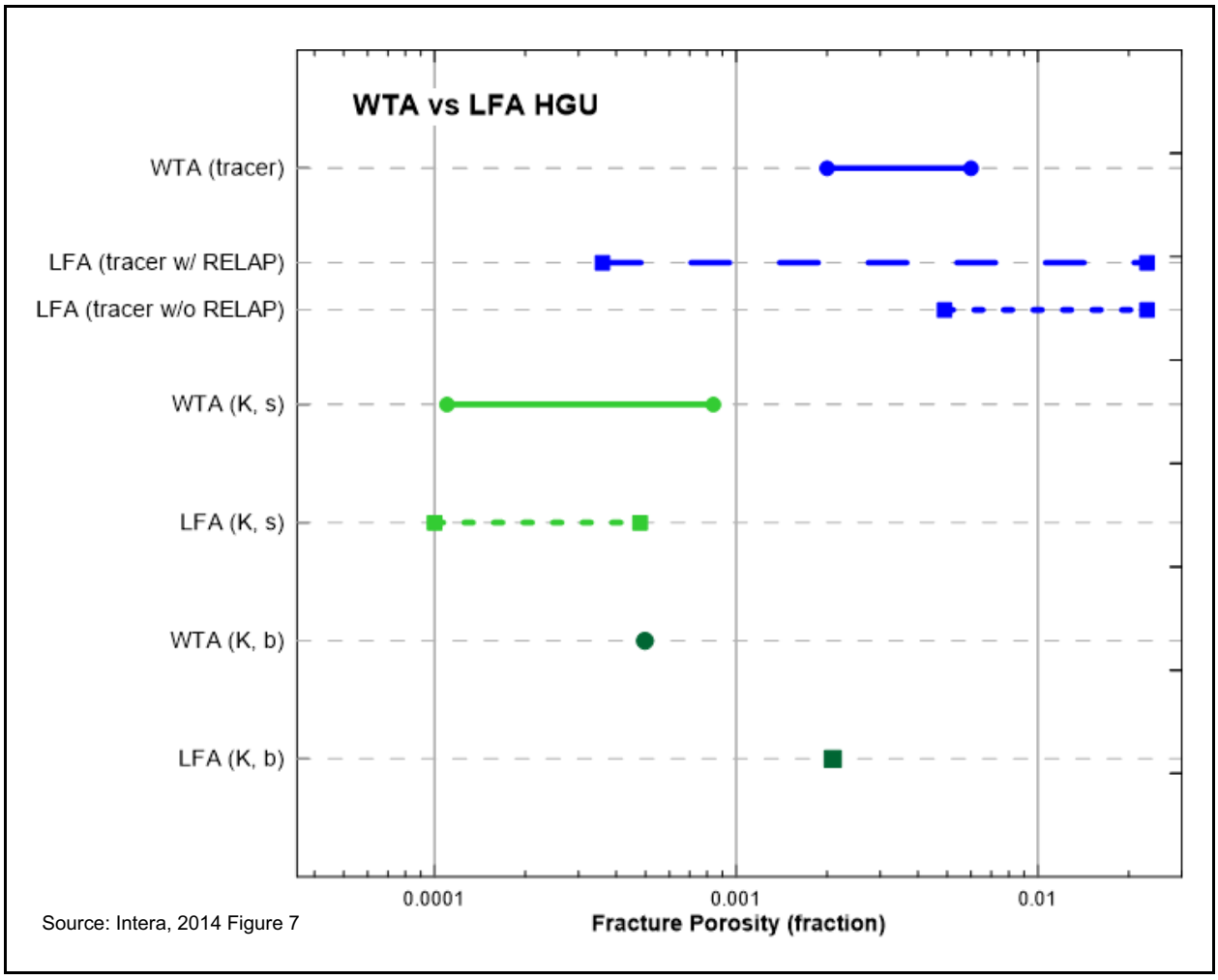

Figure 5-9
Comparison of Fracture Porosity Estimates for the WTA and LFA HGUs

in very different estimates of fracture porosity due to inherent controls on the data itself, conceptual models for the fracture porosity estimates could not be developed.

A comparison of fracture porosity values for different HGUs and stratigraphic units showed little dependence on stratigraphy. For example, fracture porosity values estimated from tracer test data in three different stratigraphic units in the WTA HGU are very similar (Figure 5-4). A comparison of fracture porosity values in the WTA and LFA HGUs shows little difference for values calculated from hydraulic data and slightly higher values in the LFA HGU than the WTA HGU for values calculated from tracer data (Figure 5-9). Including the fracture porosity data for the LCA HGU given in SNJV (2007), a comparison of data between HGUs shows very little difference in the estimated values or

ranges for all three HGUs. In general, fracture porosity values estimated from tracer test data regardless of HGU indicate a range of about 8E-4 to 2E-2.

Large uncertainty is associated with fracture porosity and thus the corresponding effective porosity. The available data will be used for setting bounds on the range of permissible values for this parameter. Matching model forecasts to the measured RN observations at sampling wells will help constrain the range of values for the purpose of forecasting CBs.

5.3.5 Effective Porosity for the TCUs

The TCUs, when viewed as HSUs, are considered to be relatively impermeable and "confining." Although these confining units are treated as porous units for the purposes of effective porosity, there are known instances where they display significant fracturing and transmissivity. Hence, for the sake of completeness, the fracture porosity for the TCU (HGU) has been calculated (Shaw, 2003) for two wells on PM using a parallel plate model.

5.3.5.1 Data Sources

Specific sources for data required to estimate fracture porosity of the TCU are listed in Table 5-6. In the more general case where flow through the VTAs and TCUs is expected to be primarily via porous flow, the porosity data are built on the porosity database compiled during the matrix porosity analysis, as discussed in Section 5.2.

Table 5-6
Fracture Porosity of Tuff Confining Unit

Parameter	Report Reference
Hydrostratigraphic/ Hydrogeologic Classification	DOE/EMNV, 2020a
Fracture Location	IT, 2001
Fracture Orientation	IT, 2001
Hydraulic Conductivity	IT, 2002a and e

Source: Modified from Shaw, 2003 (Table 6-10)

5.3.5.2 Development of Parameter Ranges

Estimates of fracture porosity of the TCU were obtained from calculations based on parallel plate models of fracture networks (Shaw, 2003; Section 6.4.2.2). Values of effective porosity estimated using parallel plate models are shown in Table 5-7. Hydraulic conductivity values required to estimate apertures are listed in the table. Fracture spacing was calculated from fracture frequency data. Although fractured portions of the confining units are not expected to be a dominant component of the units, fracture porosity is present in the TCU HGU in some areas. The breakdown of the HSUs into the lithologies that comprise them is found in Table D-2. It is noted that the values reported in Table 5-7 for TCU are about one or two orders of magnitude lower than those reported in Table 5-5 for the fractured volcanic aquifers.

5.3.6 Intrusive Confining Units and the Clastic Confining Units

Deep volcanic intrusives are believed to underlie the calderas. The ICUs, which are represented by intrusive rocks in the HSU model (DOE/EMNV, 2020a), are assumed to be fractured rocks, but the majority of the fractures are expected to be healed due to mineral precipitation or overburden pressure. There are no data regarding the porosity of these intrusive units on PM. However, Lee and Farmer (1993) summarize a large amount of information on fluid flow in fractured rock. They showed that fracture porosity typically ranges from 5×10^{-6} to 5×10^{-4} for clastic, metavolcanic, and crystalline rocks. At the Stripa site in Sweden, the flow porosity is in the range of 1×10^{-5} to 2×10^{-4} (Neretnieks et al., 1989). In the Climax Stock, a granitic intrusive in northern Yucca Flat, the porosity of core samples averaged 9×10^{-3} (Walker, 1962). An appropriate range of effective porosity for the fractured intrusive confining units is taken to be 5×10^{-6} to 9×10^{-3}.

5.3.7 The Carbonate Aquifer HGU

The following discussion of the CA HGU is taken from DOE/EMNV (2020a). CAs are composed of Paleozoic dolomite and limestone. Transmissivity values vary greatly and are directly dependent on fracture frequency. CAs have very low matrix porosity but can be highly fractured, particularly near faults (Winograd and Thordarson, 1975). These Paleozoic carbonate rocks form the regional aquifer (Laczniak et al., 1996).

Table 5-7
Estimate of Fracture Porosity for the TCU

Well	Interval Name	Top of Interval (m)	Bottom of Interval (m)	Hydraulic Conductivity Minimum (m/s)	Hydraulic Conductivity Maximum (m/s)	Fracture Spacing (m)	Aperture Minimum (m)	Aperture Maximum (m)	Fracture Porosity Minimum	Fracture Porosity Maximum	HGU	HSU
ER-EC-2A	Screen 1	504.7	681.5	1.12E-07	1.85E-07	16.40	1.31E-04	1.55E-04	8.00E-06	9.46E-06	TCU	FCCM
ER-EC-2A	Screen 2-2	1,003.2	1,066.8	7.32E-08	1.19E-07	10.50	9.81E-05	1.15E-04	9.34E-06	1.10E-05	TCU	FCWTA
ER-EC-8	Screen Joint 1	199.3	249.4	5.53E-05	1.31E-04	4.20	6.58E-04	8.78E-04	1.57E-04	2.09E-04	TCU	FCCM
ER-EC-8	Screen Joint 2	231.0	267.8	5.25E-05	1.89E-04	4.20	6.47E-04	9.91E-04	1.54E-04	2.36E-04	TCU	FCCM
ER-EC-8	Screen Joint 3	249.4	286.1	5.43E-06	2.01E-05	4.20	3.04E-04	4.70E-04	7.23E-05	1.12E-04	TCU	FCCM
ER-EC-8	Screen Joint 5	286.1	320.0	7.26E-07	1.78E-05	4.20	1.55E-04	4.51E-04	3.70E-05	1.07E-04	TCU	FCCM

Source: Shaw, 2003 (Table 6-13)

The CA HGU will be conceptualized as a dual-porosity medium in the PM CAU transport model due to its fractured nature. It is assumed that no advective flow or transport occurs in the matrix. The fracture porosity will be used as the effective porosity for the CA HGU.

The LCA is not a significant rock type in the PM-OV CAU-scale flow and transport model. It is present in less than 1 percent of the flow model cells and almost none of those are downgradient of the testing areas. The LCA is below the volcanics and near the model bottom at 0 m elevation. However, a number of data sources were reviewed regarding the fracture porosity to be assigned. The references reviewed are shown in Section 5.3.7.1. An expanded detail of the data review is provided in Appendix E.

5.3.7.1 Data Sources

The data presented to provide recommended values for the effective porosity of the CA HGU are drawn from a number of sources. These include the following:

- Tracer test analyses
- Hydraulic conductivity and fracture aperture analyses
- Fracture spacing and aperture analyses
- Analysis of geophysical logging data
- A literature review
- Previous values used in numerical models for the NNSS

Each of these data sources with references is discussed in Appendix E.

5.3.7.2 Summary and Recommended Distributions for CA

The data sources reviewed discuss fracture porosity data for the CA HGU determined by several methods and used or recommended in previous NNSS modeling studies. The values used in developing the distribution for the effective porosity must be consistent with the conceptual model that will be used for this HGU in the PM CAU transport model. That conceptualization is a double-porosity system with advective flow and transport through fractures only, and matrix participation only through molecular diffusion from and to the fractures. The fracture porosities considered to be consistent with this conceptualization are summarized in Table 5-8 and graphically illustrated in Figure 5-10.

Based on the results of the evaluation of fracture porosities for the CA HGU, a range in effective porosity of 2×10^{-4} to 2×10^{-2} (interpreted values are rounded to one significant figure) is recommended for the CA HGU (Table 5-8 and Figure 5-10). The recommended distribution for sampling this range is skewed log triangular with a peak at 5×10^{-3}. This distribution reflects the fact that fracture porosities determined from tracer tests are considered more representative and less uncertain than those determined from hydraulic conductivities and fracture spacings.

5.4 Bulk Rock Density

Bulk rock density is the mass per unit volume of a rock. It is used to determine the matrix retardation coefficient and is a necessary parameter for the transport calculations. Values for a number of HSUs were provided in the *Yucca Flat/Climax Mine CAU Flow and Transport Model Report* (N-I, 2013). Table 5-9 shows the values given. The table shows the HSUs for which values were estimated, the mean and standard deviations, as well as an estimate of the distribution type.

Density well logs were used to estimate values of matrix porosity, as described in Section 5.2. The density logs provide an estimate of bulk rock density, which is used with estimated grain and fluid densities to estimate the matrix porosity. These values, sorted by HGU and then HSU are shown in Tables 5-10 and 5-11. Tables 5-10 and 5-11 show the HGUs and HSUs for which density log analysis was provided as well as the values of the average and standard deviation and the number of samples included.

5.5 Fracture Spacing

The role of fracture spacing in contaminant transport, compiled fracture spacing data, and the development of fracture spacing distributions to be used in the PM CAU transport model are discussed in this section.

5.5.1 Role of Fracture Spacing

Considering contaminant transport through dual-porosity media, the fracture spacing affects (1) the estimation of mass transfer from the fractures to the matrix by defining the volume of storage for solutes diffusing into the matrix and the surface area across which diffusion occurs, and (2) velocity of the fluid flowing through the fractures via the cubic law for hydraulic conductivity. The fracture

Table 5-8
Summary of Estimated Effective Porosity Ranges for the Carbonate Aquifer and Recommended Ranges

Source	Effective Porosity (fraction)		Location	Method
	Minimum	Maximum		
Tracer Tests				
SNJV, 2007 (based on test data from Winograd and West, 1962)	5.9×10^{-4}	4.3×10^{-3}	WW-C and WW-C1 in Yucca Flat	Plug flow method using peak-concentration arrival time
SNJV, 2007	4.7×10^{-3}	1.7×10^{-2}	ER-6-1 Well Cluster in Yucca Flat	Plug flow method using peak-concentration arrival time
SNJV, 2006c	1.1×10^{-2}	1.8×10^{-2}	ER-6-1 Well Cluster in Yucca Flat	Plug flow method using mean residence time from RELAP analysis
Jones et al., 1992	5.0×10^{-4}	1.5×10^{-3}	Culebra Dolomite at the WIPP site in New Mexico	Model calibration to tracer breakthrough curves
SNJV, 2007	1.0×10^{-3}	3.1×10^{-3}	Culebra Dolomite at the WIPP site in New Mexico	Plug flow method using peak-concentration arrival time
Calculated from Hydraulic Conductivity and Fracture Spacing Data				
SNJV, 2007	2.0×10^{-4}	2.0×10^{-3}	ER-6-1#2 and ER-7-1 in Yucca Flat	K from hydraulic tests
Calculated from Fracture Spacing and Fracture Aperture Data				
SNJV, 2007	1.9×10^{-3}	9.4×10^{-3}	ER-6-1#2 and ER-7-1 in Yucca Flat	Calculated from fracture aperture and spacing
Recommend Range for the PM CAU Transport Model				
SNJV, 2007	2×10^{-4}	2×10^{-2}	Pahute Mesa	Recommended range based on review and analyses

Source: SNJV, 2007 (Table 8-21)

K = Hydraulic conductivity

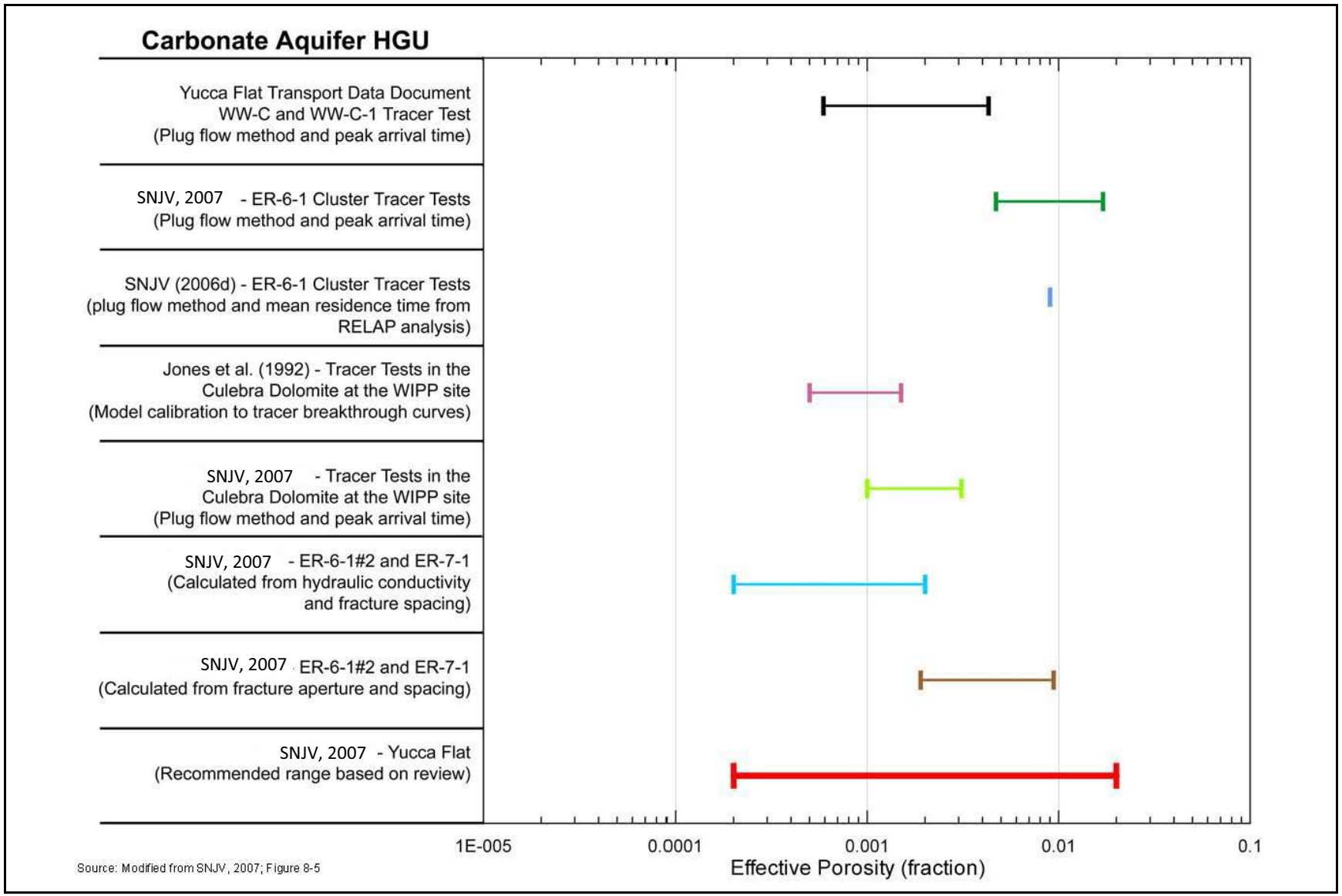

Figure 5-10
Estimated Effective Porosity Ranges for the Carbonate Aquifer HGU

Table 5-9
Estimates of Bulk Rock Density from N-I (2013)

HSU	Mean (kg/m^3)	Standard Deviation	Distribution
LCA	2,454.7	181.4	Normal
ATCU	2,163.5	59.9	Normal
OSBCU	1,839.7	178.0	Normal
LTCU	1,649.5	99.4	Normal
TSA	2,098.1	227.1	Normal
UTCU	1,649.5	99.4	Normal
TM-LVTA	1,429.1	198.2	Normal
TM-WTA	2,098.1	227.1	Normal
TM-UVTA	1,429.1	198.2	Normal
AA1	1,787.0	78.4	Normal
AA2	1,787.0	78.4	Normal
AA3	1,787.0	78.4	Normal

Source: Modified from N-I, 2013

Table 5-10
Bulk Rock Densities by HGU Estimated from Density Log Data

HGU	Average Bulk Density (g/cm^3)	Standard Deviation	Count
LFA	2.24	0.12	21,169
TCU	2.09	0.16	44,856
VTA	1.97	0.12	1,429
WTA	2.31	0.12	30,468

Table 5-11
Bulk Rock Densities by HSU Estimated from Density Log Data
(Page 1 of 2)

HSU	Average Bulk Density (g/cm^3)	Average Bulk Density Standard Deviation	Count
BA	2.23	0.10	5,911
BRA	2.22	0.16	782
CFCM	2.30	0.09	6,867
CFCU	2.22	0.05	2,683

Table 5-11
Bulk Rock Densities by HSU Estimated from Density Log Data
(Page 2 of 2)

HSU	Average Bulk Density (g/cm³)	Average Bulk Density Standard Deviation	Count
CHLFA	2.25	0.15	3,287
CHZCM	2.11	0.20	10,646
CPA	2.17	0.13	3,107
FCCM	2.06	0.15	4,098
FCCU	1.96	0.13	7,904
FCULFA	2.22	0.08	3,404
LPCU	2.13	0.12	8,259
MPCU	1.94	0.08	1,009
PBPCU	2.03	0.08	304
PBRCM	2.24	0.07	1,033
RMWTA	2.38	0.10	9,121
SPA	2.22	0.08	1,577
TCA	2.27	0.09	8,965
THCM	2.08	0.11	2,437
THCU	1.97	0.07	800
TMLVTA	1.96	0.13	1,116
TMWTA	2.35	0.04	385
TSA	2.30	0.12	10,290
UPCU	2.06	0.14	3,937

porosity and fracture aperture are correlated to hydraulic conductivity and fracture spacing using the parallel plate assumption and the cubic law as shown in the following equation:

$$\phi_f = \left(\frac{12 K \mu_w}{\rho_w g B^2} \right)^{\frac{1}{3}} \qquad (5\text{-}3)$$

where

ϕ_f = fracture porosity [L/L]
K = hydraulic conductivity [L/t]
μ_w = viscosity of water [M/(Lt)]
ρ_w = density of water [M/L³]
g = gravitational constant [L/t²]
B = fracture spacing [L]

5.5.2 Data Compilation

Two sources are cited for the development of fracture spacing. The first is fracture spacing derived from fracture frequency. Fracture frequency [also called lineal fracture intensity and identified as P_{10} in HGL (2017)] is defined as the number of fractures divided by a known length. Typically, this length is measured along a borehole. The inverse of P_{10} is a measure of the average fracture spacing along the borehole. The second source is the DFN modeling (Makedonska et al., 2020).

Fracture frequency data have been obtained at the NNSS in two ways: (1) observations from borehole cores, and (2) analysis of borehole image logs. Both methods are subject to inaccuracies because of damage to cores and borehole walls during coring and/or drilling and because of the inability to observe vertical fractures in a vertical borehole. These types of data are available only at a few locations and do not provide comprehensive spatial coverage. Observations in outcrops allow more detailed areal evaluation but are not likely representative of rock fracturing at depth.

Data related to fracture frequency were acquired from the following sources:

- Fracture observations for several Phase I wells (ER-18-2, ER-20-2#1, ER-20-5#1, ER-20-5#3, ER-EC-1, ER-EC-2A, ER-EC-4, ER-EC-5, ER-EC-6, ER-EC-7, ER-EC-8, UE-18r, and UE-20-bh#1) were obtained from analyses of borehole televiewer, formation microimager, or microresistivity electronic scanner logs (Shaw, 2003).

- Fracture observations for some Phase I wells (ER-20-6#1, ER-20-6#2, ER-20-6#3, ER-EC-1, and ER-EC-6) were reinterpreted by Golder (2016) as part of their fracture analysis work (HGL, 2017).

- Fracture observations for Phase II wells (ER-20-4, ER-20-7, ER-20-8, ER-20-11, ER-20-12, ER-EC-11, ER-EC-12, ER-EC-13, ER-EC-14, and ER-EC-15) were obtained from analysis of borehole image logs or well completion reports (Prothro, 2009, 2010a and b, 2011a and b, 2012a and b, 2013a and b; NNSA/NFO, 2016).

Stratigraphy, lithology, HSU, and HGU intervals for each well were obtained from the PM HFM (DOE/EMNV, 2020a) and well completion diagrams.

5.5.3 Data Evaluation

To obtain fracture spacing, calculations were required to obtain values for the following four types of quantities:

- Fracture frequency [L^{-1}]
- Average dip [degrees]
- Corrected frequency [L^{-1}]
- Total corrected frequency [L^{-1}]

To calculate the fracture frequency, fractures in an HGU interval were grouped according to dip angle. Categories were as follows:

- $0° \le dip \le 30°$
- $30° < dip \le 60°$
- $60° < dip \le 90°$

The average fracture frequency, N_r, was then calculated by dividing the number of fractures counted in a category by the interval depth in meters. The average dip in degrees for each of the three categories was calculated.

Fracture frequencies derived from data collected from a vertical borehole that intersects nonhorizontal fractures are biased. The true fracture spacing (distance between two parallel fractures measured perpendicular to the fracture plane) is not the same as the fracture spacing observed in the borehole. To account for this orientation bias, it is necessary to correct the fracture frequency (NRC, 1996) using the following equation:

$$N_c = \frac{N_r}{\cos(f)} \qquad (5\text{-}4)$$

where

N_c = corrected average fracture frequency
N_r = average fracture frequency
f = average dip angle (degrees) for that category measured from the horizontal

The total corrected frequency is then obtained by summing corrected frequencies for each category. Corrected fracture spacing values are calculated as the inverse of total corrected frequency. The corrected fracture spacing is used with the estimated apertures to provide estimates of fracture porosity.

5.5.4 Scaling Considerations

Although fracture frequency data are available at the borehole scale, the spacing of interconnected fractures at the CAU scale is the data of interest for the PM CAU transport model. It is expected that the spacing of interconnected fractures at the CAU scale will be much greater than at the scale of tracer tests (tens of meters) or at the borehole scale. As the amount of data required to estimate fracture spacing at the CAU scale is extremely costly and time-consuming to obtain, estimates of fracture spacing were developed based on the data available (i.e., fracture observations in boreholes). The work by Makedonska et al. (2020) provides one estimate of upscaled fracture spacing.

5.5.5 Data Limitations

Fracture spacing data are limited by four biases that affect estimation of fracture size and frequency through data collection: length bias, orientation bias, truncation bias, and censoring (Berkowitz, 2002). Small fractures will be underrepresented, as there is a lower probability of intersecting smaller fractures (length bias). Fractures parallel to the sampling plane will also be underrepresented (orientation bias). Fractures shorter than a predetermined length are usually not mapped (truncation bias). A censoring bias is introduced because the sample area is finite, and the fracture traces might not be completely visible (Baecher et al., 1977). Unfortunately, censoring bias is most important for longer fractures, which are assumed to be the more conductive fractures.

5.5.6 Development of Parameter Distributions

The compiled corrected average fracture spacing values for WTA, LFA, and TCU are shown in Figures 5-11, 5-12, and 5-13, respectively. A cumulative distribution function (CDF) derived from the data is also shown on each figure. Based on the compiled data, the fracture spacing distributions are chosen to be lognormal, truncated at plus/minus two standard deviations.

The calculated statistical information regarding the fracture spacing is presented in Table 5-12. The fracture spacing data and derived lognormal distributions are shown in Figure 5-14 for WTA, Figure 5-15 for LFA, and Figure 5-16 for TCU. Each of these figures shows the following: lognormal probability density function (PDF) based on the data as a red curve, mean value of the data as a solid vertical black line, the locations of plus/minus 1 standard deviation of the data as dash-dotted vertical black lines, and the locations of plus/minus 2 standard deviations of the data as dotted vertical black lines.

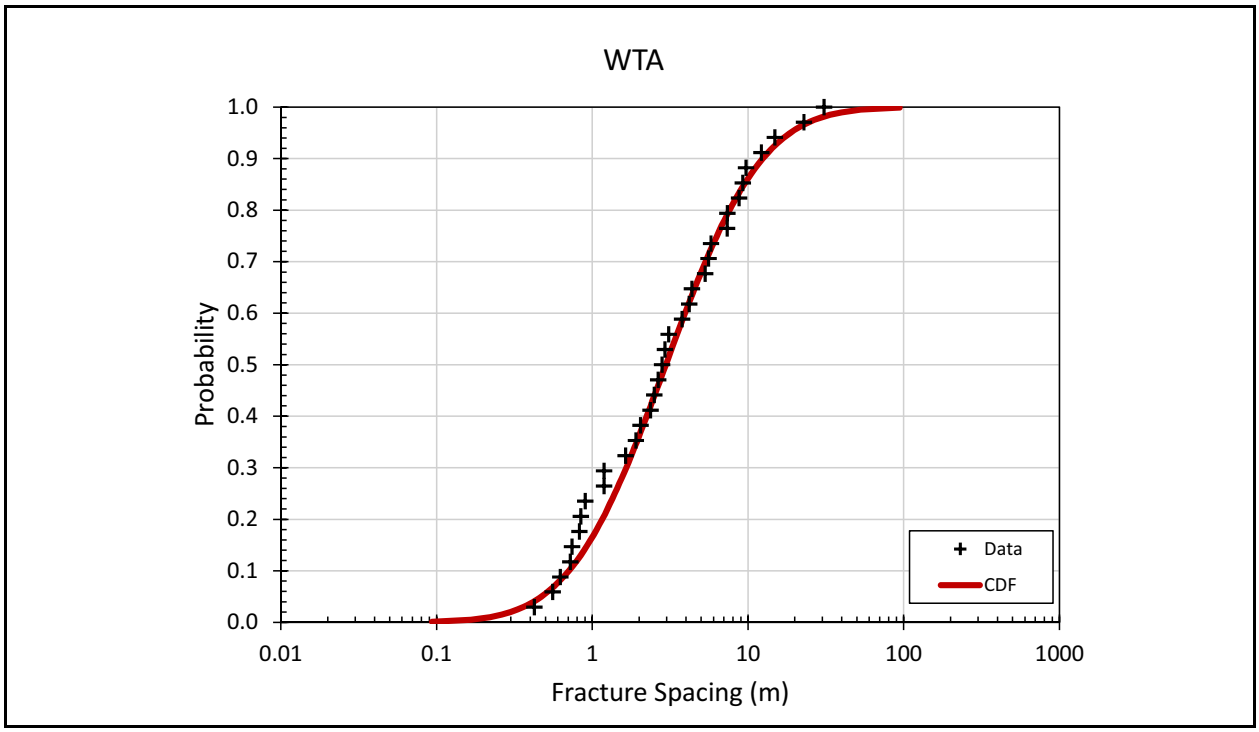

Figure 5-11
WTA Fracture Spacing Data

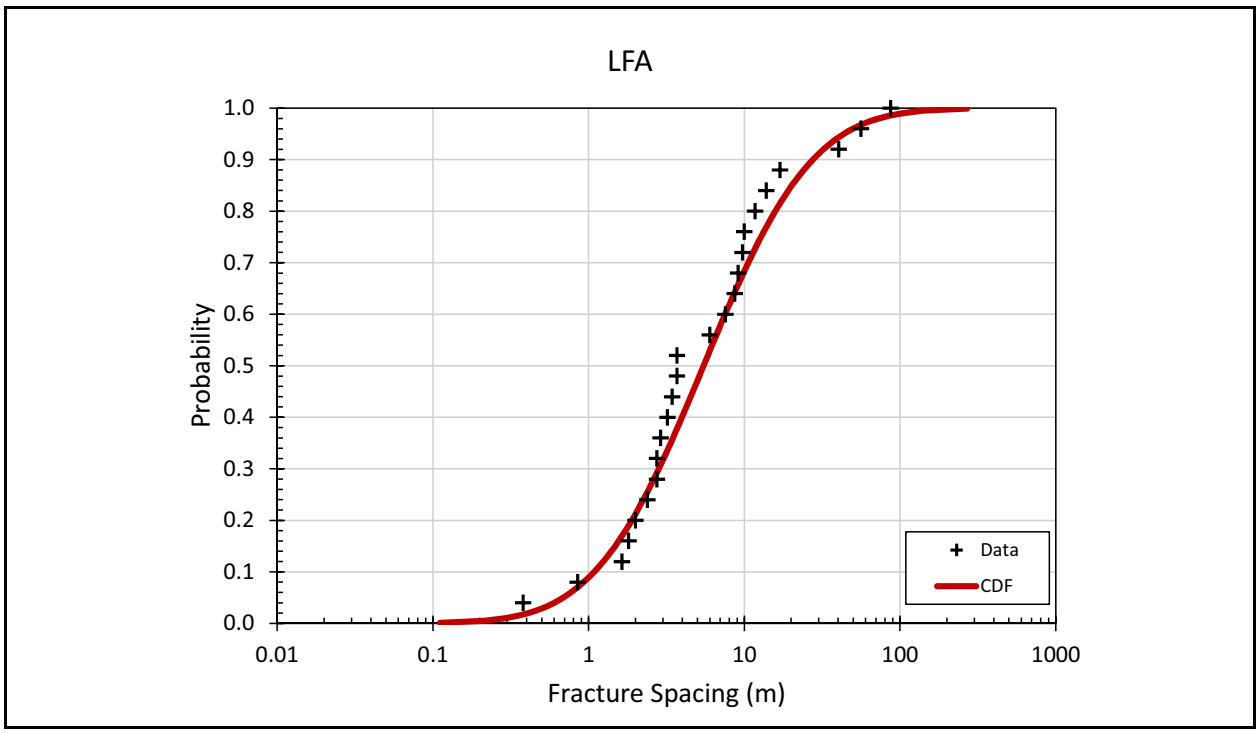

Figure 5-12
LFA Fracture Spacing Data

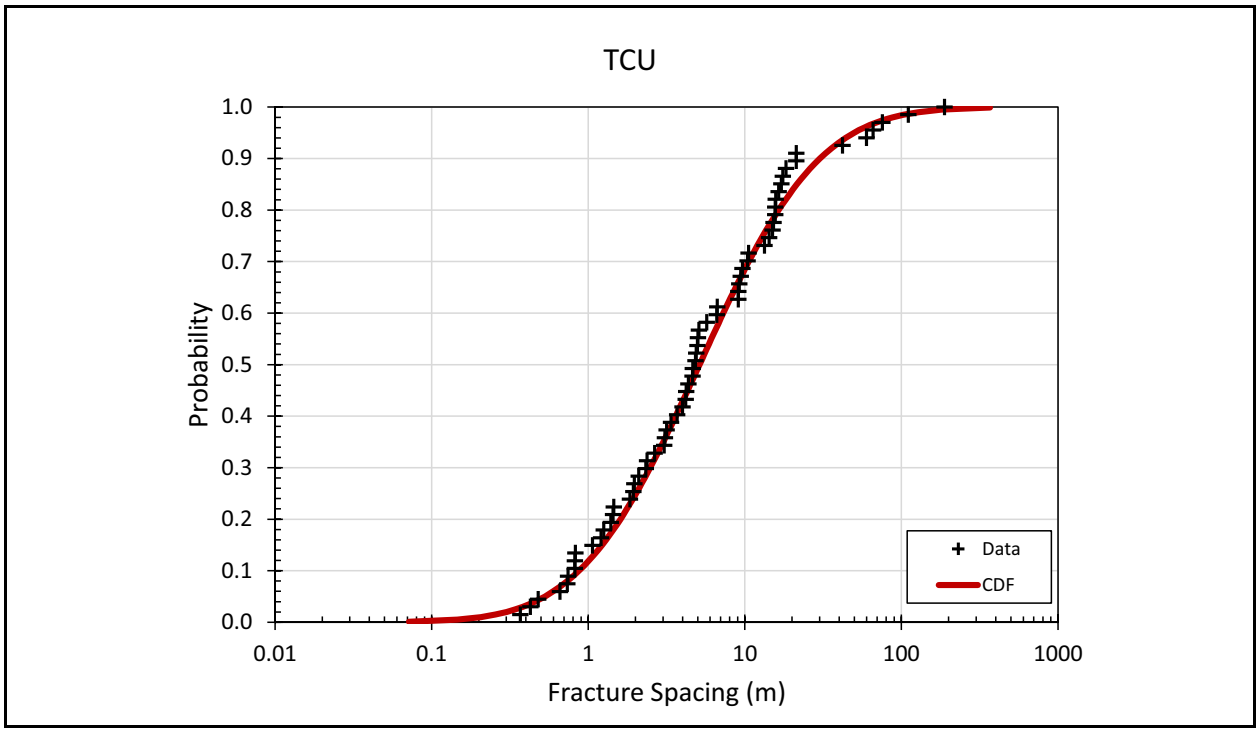

Figure 5-13
TCU Fracture Spacing Data

Table 5-12
Fracture Spacing Statistics

HGU	Fracture Spacing (m)			
	Mean	Standard Deviation	Minimum	Maximum
WTA	5.36	6.60	-7.84	18.56
LFA	12.33	20.07	-27.81	52.48
TCU	14.05	28.78	-43.50	71.60

Note: Minimum and maximum values defined as mean +/- 2 standard deviations

The LCA is conceptualized as consisting of fault zones and the country rock, with the fault zones being more highly fractured than the country rock. Because the fault zones are considered to be more fractured, the fracture porosity will be higher in the fault zones than in the country rock. Across the CAU scale of the model, the actual fracture spacing in the LCA will be heterogeneous in both the lateral and vertical directions. However, obtaining observed data on fracture spacing that capture this heterogeneity would require extensive data collection at spatial scales that are impractical. The LCA is not expected to play a significant role in transporting RNs at PM because, as noted in Section 5.3.7,

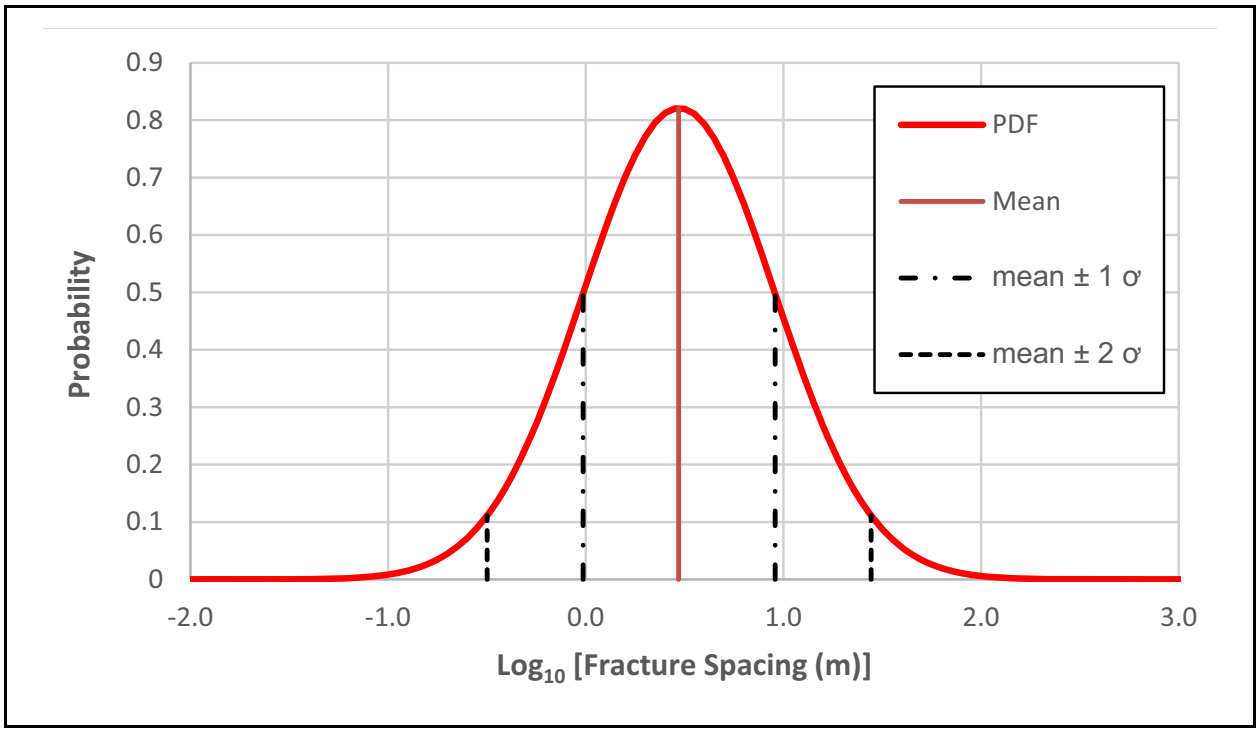

Figure 5-14
WTA Fracture Spacing Distribution

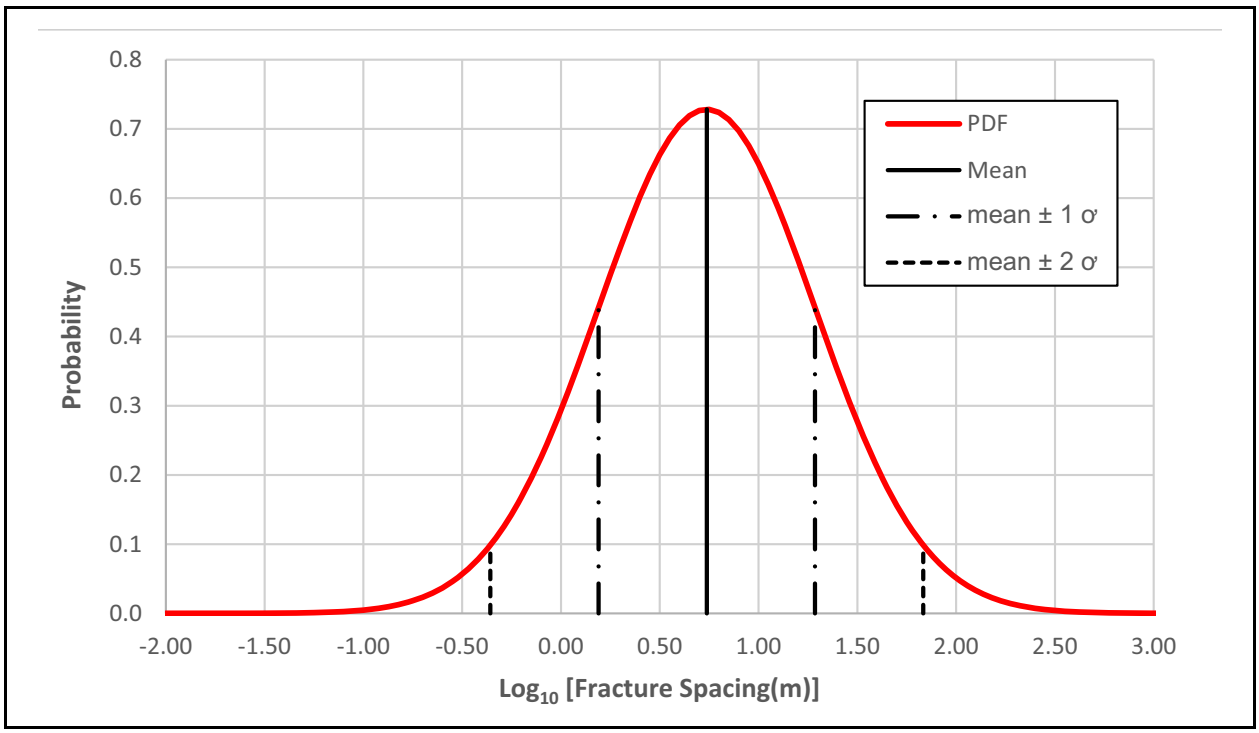

Figure 5-15
LFA Fracture Spacing Distribution

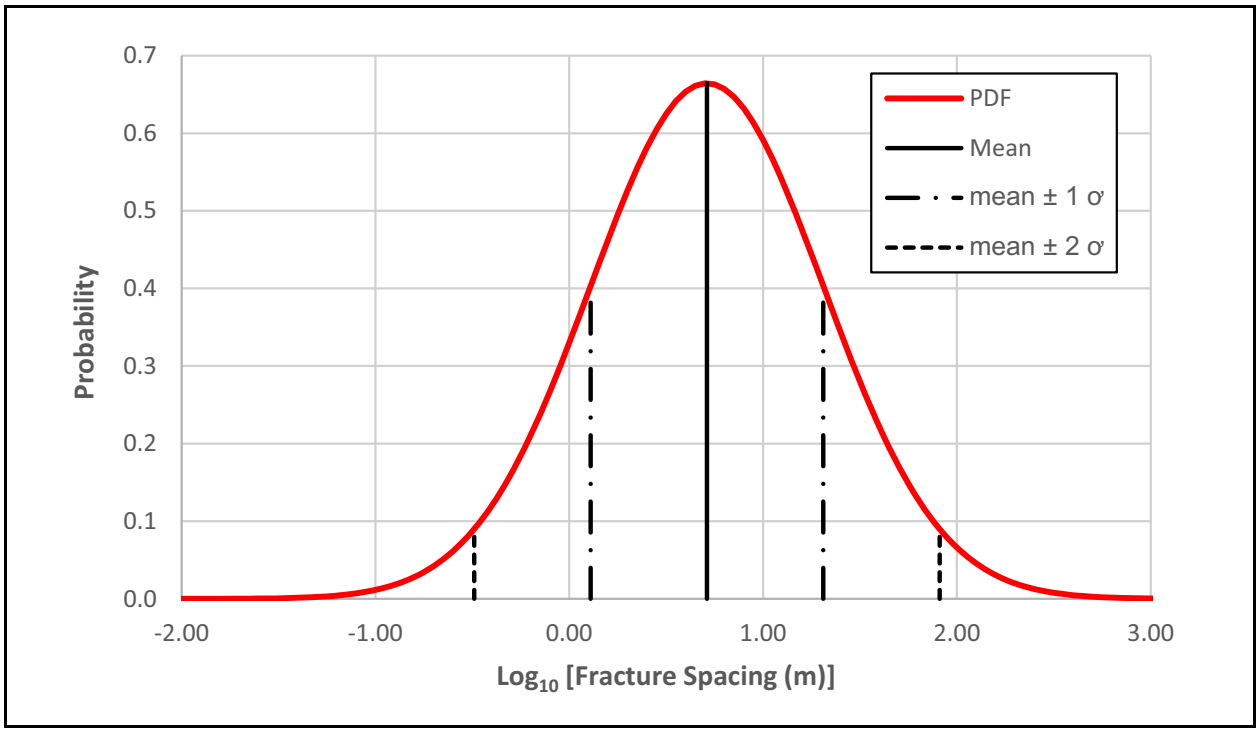

Figure 5-16
TCU Fracture Spacing Distribution

it is not a significant rock type in the PM-OV CAU-scale flow and transport model. It is present in less than 1 percent of the flow model cells, almost none of which are downgradient of the testing areas. The LCA is below the volcanics and near the model bottom at 0 m elevation.

5.5.6.1 Fracture Spacing as Estimated by Makedonska et al. (2020)

Makedonska et al. (2020) developed a DFN model to simulate flow and transport at PM. To quote, "This report describes the results of discrete fracture network (DFN) simulations for the Topopah Spring aquifer (TSA), Lava Flow aquifer, and Tiva Canyon aquifer (TCA), at Pahute Mesa on the Nevada National Security Site (NNSS), formerly the Nevada Test Site. The research focuses on calculating upscaled groundwater flow and contaminant transport parameters using DFNs generated according to fracture characteristics observed in the TSA, LFA and TCA at Pahute Mesa. The highly fractured and heterogeneous nature of these aquifers makes them candidates for stochastic DFN modeling of RN transport on a small scale with subsequent upscaling. One hundred independent DFN realizations are generated for each aquifer, and the upscaled parameters for continuum simulations of subsurface flow and transport in fractured media at Pahute Mesa are calculated. Our goal is to implement a modeling approach that can translate parameters to larger-scale models that account for

local-scale flow and transport processes, such as channelization of flow and transport along a few well-connected, large fractures. Additionally, to simulate advective and advective-diffusive transport through the fracture networks, the Time Domain Random Walk (TDRW) approach is applied to account for matrix diffusion into a finite half-space. Moreover, a novel approach to calculate dynamic (active) fracture surface area to reflect flow channeling is implemented."

The modeling resulted in the summary statistics for fracture spacing, as shown in Table 5-13. The carbonate aquifer was not part of this analysis. Table 5-13 shows that the apertures calculated are dependent on the flow direction. The distinction in the apertures based on flow direction is not strictly incorporated in the comparisons to other methods which follow. A maximum or minimum value selected for the comparisons will be for the maximum or minimum in either the North-South or East-West flow direction.

Table 5-13
Summary Statistics for Equivalent Continuum Parallel Plate Fracture Spacing

	Fracture Spacing (m)		
	Top - Bottom	**North - South**	**East - West**
TSA			
Minimum	2.1	1.54	1.83
Maximum	17.5	7.74	8.34
Average	4.03	2.4	2.6
Standard Deviation	2.36	1.01	1.24
LFA			
Minimum	4.51	4.48	4.87
Maximum	21.2	26.2	16.2
Average	6.25	7.78	6.32
Standard Deviation	2.77	4.43	1.92
TCA			
Minimum	5.01	3.55	2.7
Maximum	38.5	26.3	18.3
Average	14.4	8.73	6.23
Standard Deviation	7.37	3.8	3.08

Source: Makedonska et al., 2020 (Table 5)

Figure 5-17 compares the values of fracture spacing estimated from fracture frequency and those derived through the DFN modeling of Makedonska et al. (2020). The fracture spacing ranges for the TSA, LFA, and TCA from Makedonska et al. (2020) are designated with an "(M)" to clearly separate them from the fracture spacing values estimated from fracture frequencies. Makedonska et al. (2020) provided values for fracture spacing top to bottom, north to south, and east to west. For the values shown in Figure 5-17, the larger values in terms of average value and standard deviation were chosen between either the north-to-south or east-to-west value sets. All ranges shown depict the average value plus/minus 2 standard deviations. Reference to the figure shows that, with the exception of the fracture spacing range estimated for the TSA, all of the value ranges are comparable.

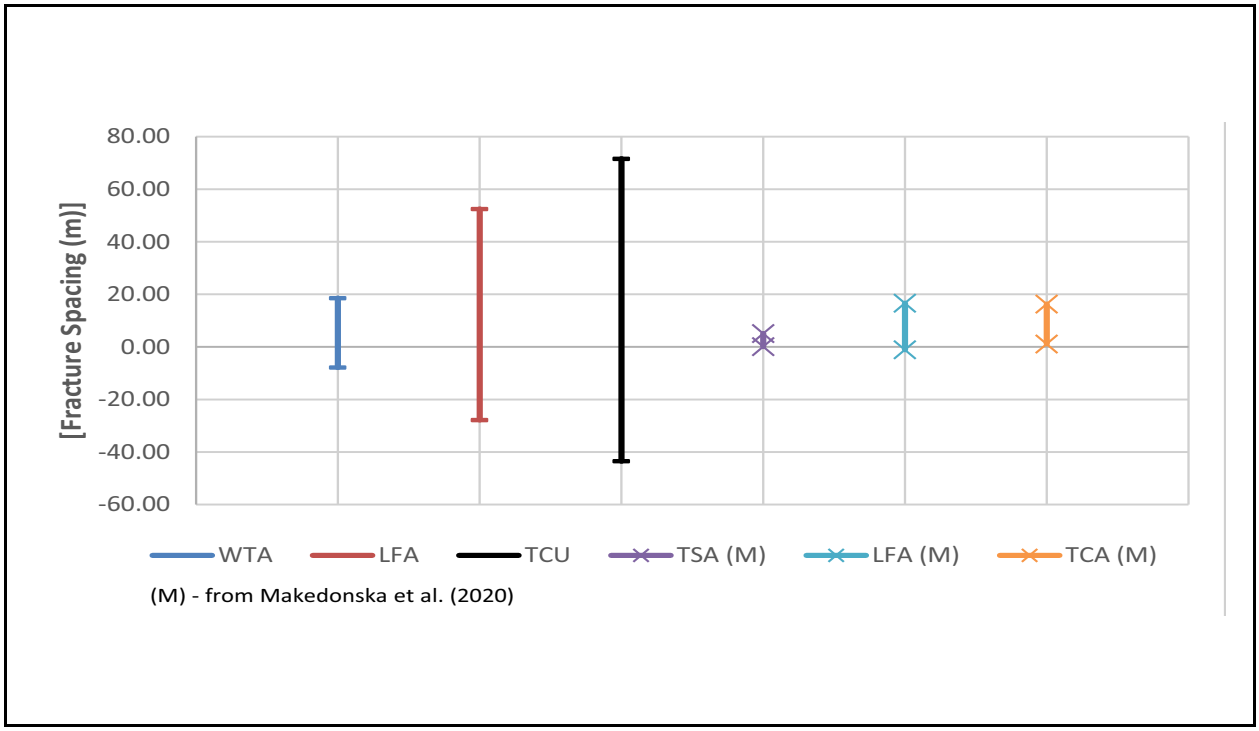

Figure 5-17
Comparison of Fracture Spacing Ranges

5.6 Fracture Aperture

Fracture aperture is a key factor determining the rate of groundwater flow and RN migration through fractured rock. The width of the apertures determines the cross-sectional area available for flow through fractured rock which, in turn, controls the velocity and quantity of groundwater flow. This section presents a new set of aperture widths based on estimated hydraulic conductivities and fracture spacings as well as reviewing values used in past modeling efforts.

5.6.1 Data Evaluation

5.6.1.1 Calculation of Aperture

Although fracture aperture can be observed in borehole core and borehole image logs, Berkowitz (2002) states that mechanical measurements of fracture aperture are of little value in characterizing fractures for flow and transport because they do not capture the influence of the internal geometry of the fracture plane on hydraulic resistance to flow and effective fracture aperture for transport. Therefore, fracture aperture values for the PM CAU transport model were calculated from other fracture parameters (i.e., estimates of hydraulic conductivity and fracture spacing).

The relationship between fracture aperture, hydraulic conductivity and gradient can be derived from the cubic law defining volumetric flow rate between parallel smooth plates in the direction of flow presented in Domenico and Schwartz (1990):

$$Q = \frac{\rho_w g b^2}{12 \mu_w}(bw)\left(\frac{dh}{ds}\right) \qquad (5\text{-}5)$$

where

Q = volumetric flow rate (L^3/t)
ρ_w = density of water (M/L^3) = 998.2 kg/m^3 (20 °C)
g<= gravitational constant (L/t^2) = 9.80665 m/s^2
b = fracture aperture (L)
μ_w = dynamic viscosity of water (M/(Lt) = 1.002×10^{-3} pascal-second (Pa-s) (20 °C) = 1.002×10^{-3} kg/(m·s)
w = fracture width perpendicular to flow direction and aperture (L)
dh/ds = hydraulic gradient (L/L)

Based on Darcy's law, the volumetric flow rate Q, in Equation 5-6, can be written in the following form (Domenico and Schwartz, 1990):

$$Q = KA\left(\frac{dh}{ds}\right) \qquad (5\text{-}6)$$

where

A = (B+b)w ≈ Bw = discharge area perpendicular to the flow direction (L^2)
B = fracture spacing (L)

The fracture aperture can then be calculated from Equations 5-5 and 5-6, giving the following:

$$b = \left(\frac{12K\mu_w B}{\rho_w g}\right)^{1/3} \quad (5\text{-}7)$$

Distributions for fracture aperture (b) were developed for the LFA,WTA, and TCU HGUs based on values of hydraulic conductivity and fracture spacing. Distributions were developed based on HGUs rather than HSUs because there is only one data point for many HSUs. The distributions developed have defined means and standard deviations, as well as minimum and maximum values based on plus or minus two standard deviations.

The hydraulic conductivity values used for the WTA, LFA, and TCU HGUs are from the *Hydrologic Data for the Groundwater Flow and Contaminant Transport Model of Corrective Action Units 101 and 102: Central and Western Pahute Mesa, Nye County, Nevada* report (Navarro, 2021).
Only values derived from pumping tests were used. For the CA HGU, the hydraulic conductivity distribution was taken from the Phase I Flow and Transport Model for CAU 97 report (N-I, 2013). A lognormal distribution with a mean of 0.16 and a standard deviation of 1.34 in units of meters per day (m/day) was used. Table 5-14 shows the values of hydraulic conductivity with standard deviations and minimum and maximum values.

Table 5-14
Log_{10} Values of Hydraulic Conductivity

HGU	Log_{10} *K* (ft/day)			
	Mean	Standard Deviation	Minimum (mean -2σ)	Maximum (mean +2σ)
WTA	9.78E-02	1.57E+00	-3.04E+00	3.24E+00
LFA	6.54E-01	7.73E-01	-8.92E-01	2.20E+00
TCU	-1.38E-02	1.06E+00	-2.13E+00	2.11E+00
CA	0.16+00	1.34+00	-2.52+00	2.84+00

Slug hydraulic tests only test a limited volume of rock in the immediate vicinity of the borehole and the results are greatly affected by the condition and degree of development of the borehole. Slug test values are noted to routinely be lower than the pump test values by one to two orders of magnitude. Given their limitations, they were not used. The fracture spacing data used was as developed in this report with the exception of that for the CA HGU. For the CA HGU, a fixed value of 3 m was used as the fracture spacing per N-I (2013). Table 5-15 shows the values of fracture spacing used with standard deviations and minimum and maximum values. Figures 5-18 through 5-21 show plots of the CDFs of estimated apertures for the WTA, LFA, TCU, and CA HGUs respectively. Table 5-16 lists the estimated mean, minimum, and maximum fracture apertures for each of the HGUs calculated from fracture spacing and hydraulic conductivity. The number of values available for hydraulic conductivity and fracture spacing are also shown in Table 5-16. Because the numbers of values available for hydraulic conductivity were different from that for fracture spacing, the mean, minimum, and maximum fracture aperture values were estimated using the respective mean, minimum, and maximum values of fracture spacing and hydraulic conductivity yielding the three estimates of fracture aperture shown for each HGU.

Table 5-15
Log_{10} Values of Fracture Spacing

HGU	Log_{10} Fracture Spacing (m)			
	Mean	Standard Deviation	Minimum (mean -2σ)	Maximum (mean +2σ)
WTA	0.47	0.49	-0.50	1.44
LFA	0.74	0.55	-0.36	1.83
TCU	0.71	0.60	-0.49	1.91
CA	0.48	N/A	0.48	0.48

N/A = Not applicable

5.6.1.2 Measured Apertures from Drellack et al. (1997)

During 1995 and 1996, core of volcanic rock from borings at Pahute Mesa and Timber Mountain was examined to determine fracture properties, to include aperture. In addition, borehole video logs and scanner records were analyzed. This analysis is recorded in the Drellack et al. (1997) report. To quote the report, “Fracture data from cores collected from eight drill holes in the Pahute Mesa/Timber Mountain area are presented in this report. Fracture analyses were performed on two continuous cores

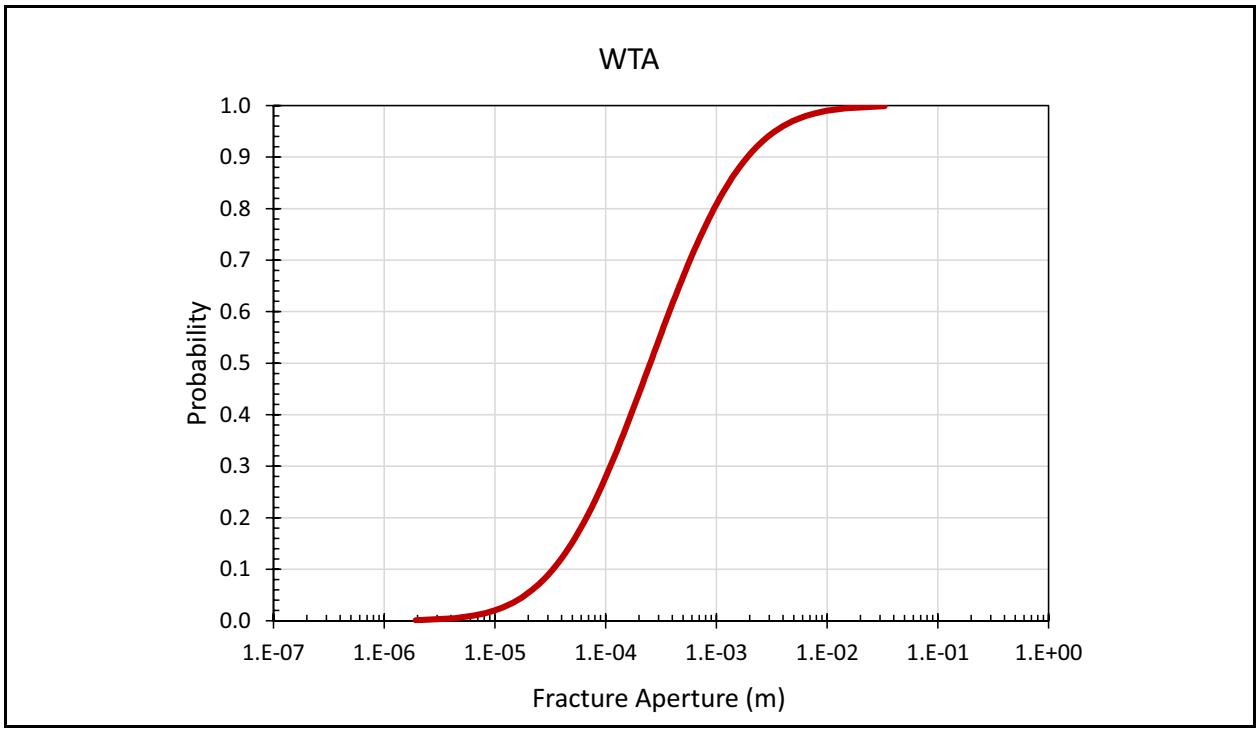

Figure 5-18
CDF of Estimated Fracture Aperture in the WTA HGU

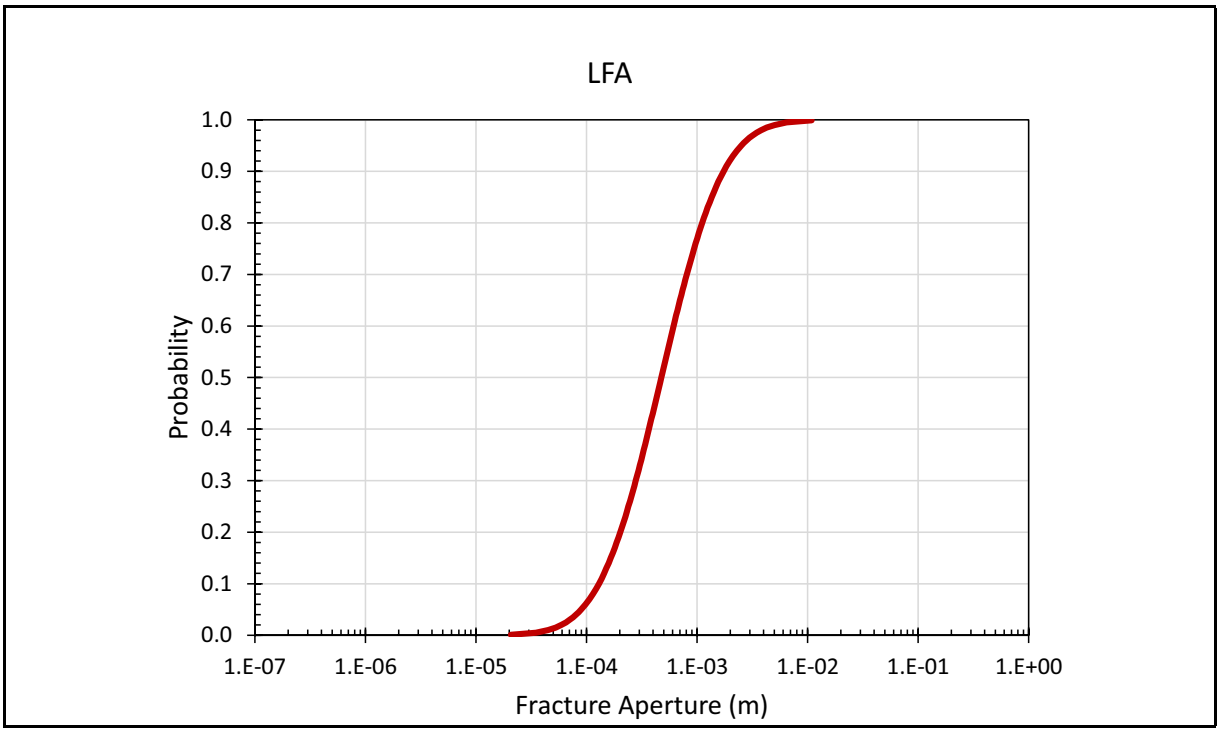

Figure 5-19
CDF of Estimated Fracture Aperture in the LFA HGU

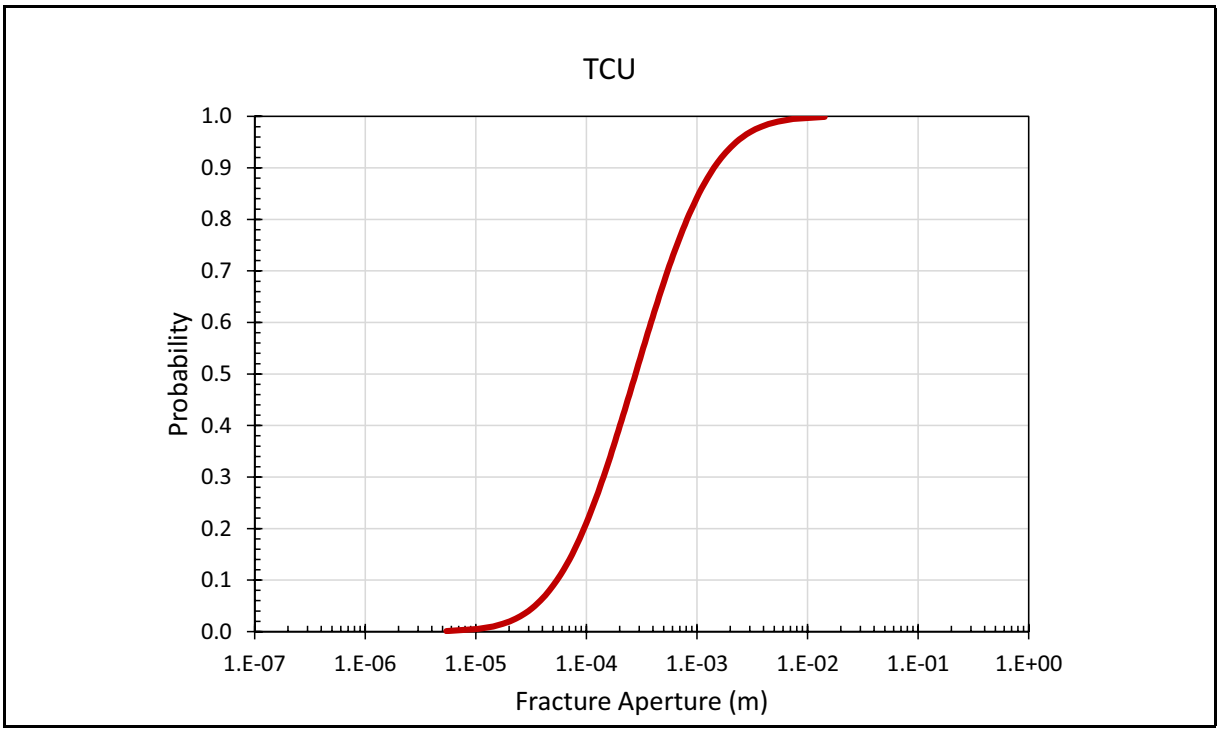

Figure 5-20
CDF of Estimated Fracture Aperture in the TCU HGU

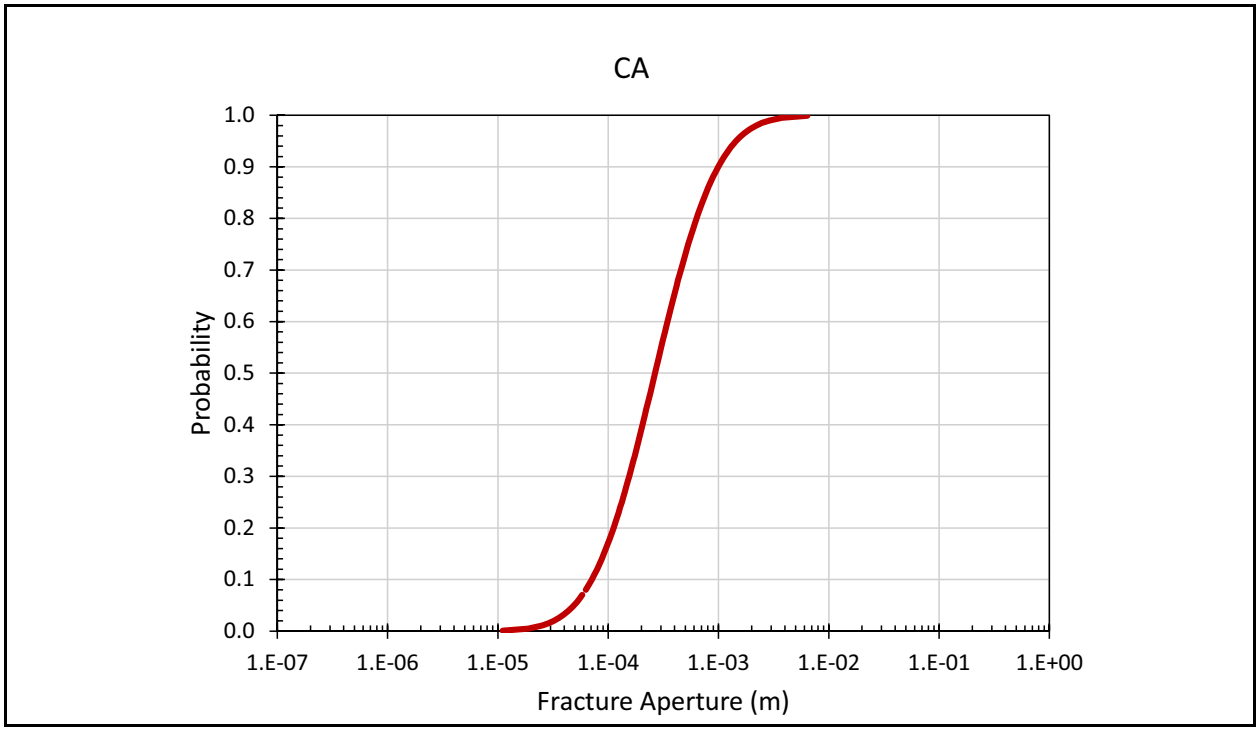

Figure 5-21
CDF of Estimated Fracture Aperture in the CA HGU

Table 5-16
Estimated Fracture Apertures (from Hydraulic Data)

Fracture Aperture Lognormal Distribution Log_{10} b (m)				
HGU	**# of Values Hydraulic Conductivity / Fracture Spacing**	**Mean**	**Minimum**	**Maximum**
WTA	8 / 34	-3.60	-4.97	-2.23
LFA	10 / 25	-3.32	-4.2	-2.44
TCU	3 / 67	-3.56	-4.66	-2.45
CA	77 / 16	-3.58	-4.47	-2.68

from drill holes UE-18t and UE-19x and core segments from six other drill holes (UE-18r, U-20c, UE-20c, UE-20e#l, UE-20f, and UE-20bh#l). Also, fracture analyses using borehole televiewer and Formation MicroScanner (FMS) data were performed on four wells (UE-18r, UE-20bh#l, ER-20-2#1, and ER-20-5#1), two of which (ER-20-2#1 and ER-20-5#1) were not cored."

Table 5-17 summarizes the findings regarding aperture reported by Drellack et al. (1997) obtained from core inspection. The table also shows the length of the core examined by HGU in that study. The minimum and maximum in Table 5-17 are formed from the data taken from Table 4-2 of Drellack et al. (1997), and the averages are taken from the same table. Section 1.3.1 of Drellack et al. (1997) states that "A total of 1,578 meters (m) (5,177 feet) of core was examined from December 1995 to February 1996. … A total of 2,851 natural fractures was examined during the analysis. Because only natural fractures were described, it was necessary to differentiate between natural fractures and breaks induced during coring or handling." The estimated "percent open" of the fractures examined is included in the same table and ranges from 1 to 99 percent, depending on the boring and HGU examined.

5.6.1.3 Fracture Apertures Estimated for the Rainer Mesa Flow and Transport Modeling (DOE/EMNV, 2018)

The transport modeling conducted for Rainier Mesa flow and transport was simplified using one-dimensional (1-D) GoldSim models to simulate the potential migration of RNs. Simplifications were made in setting single values for fracture spacing and fracture porosity. A fracture spacing of

Table 5-17
Summary of Fracture Aperture Data (Drellack et al., 1997)

Aperture (m)				
HGU	Amount of Core Examined (m)	Range		Average
		Minimum	Maximum	
VTA	72	9.50E-04	9.50E-04	9.50E-04
WTA	212	4.00E-05	2.19E-03	3.40E-04
LFA	75	8.00E-05	2.09E-03	9.10E-04
TCU	121	3.00E-05	1.51E-03	4.70E-04

Source: Modified from Drellack et al., 1997 (Tables 4-2 and 1-6)

3 m was selected as a representative average value. Table 5-18 shows the effective fracture porosities used for the Rainier Mesa modeling. These values are on the low end of those recommended in the Yucca Flat TDD (SNJV, 2007). Combining the set fracture spacing of 3 m with the fracture porosities leads to the estimated fracture apertures shown in Table 5-19. The values are given by HSU but would be generally applicable to the WTA and LFA HGUs.

Table 5-18
Effective Fracture Porosities for the Rainier Mesa Modeling

HSU	Fracture Porosity Value (Fraction)
BRA, TUBA, and LCA3	3.0E-04
RVA	1.0E-04

Table 5-19
Fracture Apertures for the Rainier Mesa Modeling

HSU	Fracture Aperture (m)
BRA, TUBA, and LCA3	9.0E-04
RVA	3.0E-04

5.6.1.4 Estimated Fractures Apertures (Shaw, 2003)

The parallel plate method was used to estimate fracture apertures in this study based on estimates of hydraulic conductivities and fracture spacing. Specifically, the fracture aperture was estimated from the cubic law:

$$b = [(12\ \mu BK)/g\ \rho]^{1/3} \qquad (5\text{-}8)$$

where

B = mean distance between fractures
μ = viscosity of water: 1.002×10^{-3} Pa-s (20 °C)
g = acceleration due to gravity: 9.80665 meters per square second (m/s^2)
K = hydraulic conductivity of a fracture
ρ = density of water: 998.2 kilogram per cubic meter (kg/m^3) (20 °C)

Values of hydraulic conductivity (K) were obtained from pumping tests, and fracture spacing was estimated from an analysis of fracture location and orientation measurements. The analysis led to the estimates of fracture aperture shown in Table 5-20. The values in the table represent the minimum and maximum values given by HGU.

Table 5-20
Fracture Apertures Estimated in Shaw (2003)

	Aperture (m)			
	WTA	LFA	TCU	VTA
Minimum	2.88E-05	1.81E-04	9.81E-05	1.38E-04
Maximum	1.24E-03	4.19E-03	9.91E-04	1.48E-04

Source: Modified from Shaw, 2003 (Tables 6-6 and 6-13)

5.6.1.5 Fracture Apertures as Estimated by DFN Methods

As discussed above in the fracture spacing section, Makedonska et al. (2020) developed a DFN model to simulate flow and transport at PM. The modeling resulted in the summary statistics for fracture aperture as shown in Table 5-21. The CA was not part of this analysis. Table 5-21 shows that the apertures calculated are dependent on the flow direction. The distinction in the apertures based on flow direction is not incorporated in the comparisons to other methods that follow. A maximum or minimum value selected for the comparisons will be for the maximum or minimum in any flow direction.

Table 5-21
Summary Statistics for Equivalent Continuum Parallel Plate Aperture
(Page 1 of 2)

	Aperture (m)		
	Top-Bottom	**North-South**	**East-West**
Makedonska et al., 2020 (Table 5) TSA			
Minimum	6.51E-04	4.37E-04	5.47E-04
Maximum	6.07E-03	2.84E-03	3.86E-03
Average	1.36E-03	7.36E-04	9.10E-04
Standard Deviation	8.63E-04	3.87E-04	5.84E-04
Makedonska et al., 2020 (Table 5) LFA			
Minimum	5.30E-04	4.19E-04	5.66E-04
Maximum	2.75E-03	3.01E-03	3.32E-03
Average	7.71E-04	8.48E-04	7.80E-04
Standard Deviation	3.79E-04	4.68E-04	3.92E-04
Makedonska et al., 2020 (Table 5) TCA			
Minimum	7.72E-04	6.06E-04	4.23E-04
Maximum	5.30E-03	4.22E-03	5.18E-03
Average	2.13E-03	1.72E-03	1.37E-03
Standard Deviation	8.39E-04	7.60E-04	4.23E-04

Table 5-21
Summary Statistics for Equivalent Continuum Parallel Plate Aperture
(Page 2 of 2)

	Aperture (m)		
	CFA	LNA	LCAP
Parashar et al., 2019 (Table 5) LFA - Drawdown Boundary Condition			
Minimum	4.80E-04	2.84E-04	1.76E-04
Maximum	4.80E-03	6.90E-03	3.06E-04

Source: Modified from Makedonska et al., 2020 (Table 5) and Parashar et al. 2019 (Table 5)

CFA = Constant Fracture Aperture model
LNA = Lognormal distribution apertures model
LCAP = Length-correlated aperture model

Parashar et al. (2019) present DFN models of the BULLION FGE based on stochastically generated fracture networks using available information on fracture statistics for the LFA HGU. They calibrated their models to hydraulic and transport data from the FGE using three different aperture sampling procedures: (1) constant fracture aperture (CFA), (2) lognormal aperture (LNA), and (3) length-correlated aperture (LCAP). Table 5-21 presents their results. It is seen that the Parashar et al. (2019) apertures are consistent with the CDF shown in Figure 5-19; and somewhat lower but on the same order of magnitude as the Makedonska et al. (2020) values.

5.6.2 Comparison of the Results of Analyses

The fracture apertures estimated for this report as well as four other sets of fracture apertures from previous work specific to Pahute Mesa/Rainier Mesa area are presented above. The data have been plotted to give a visual means of comparing the values/ranges of values. The datasets included both physically measured apertures (Drellack et al., 1997) and values estimated by the remaining analyses.

The DOE/EMNV (2018) values for the Rainier Mesa analyses are single estimated values. No estimate was made for the TCU HGU. The remaining analyses all represent the minimum and maximum values derived for a particular HGU. This report estimates fracture aperture based on hydraulic conductivity ranges by HGU and fracture spacing distributions defined in Section 5.5. As mentioned above, the Drellack et al. (1997) work physically measured apertures on a series of cores from PM borings as well as analyzed borehole video logs and scanner records. The Shaw

(2003) report estimated apertures from hydraulic conductivities and fracture spacing.
The Makedonska et al. (2020) values are the result of numerical modeling fits. Unlike the other work, this report estimated values for both HGUs and HSUs. To present the data for comparison, the TSA is plotted as representative of the WTA HGU. No estimate of aperture for the TCU HGU is given.

Figures 5-22 through 5-24 show comparisons of the various values/ranges of values for the WTA, LFA, and TCU HGUs. Figure 5-22 shows that all of the values for the WTA fall in a similar range. The estimates developed in this report present the largest range of values and, in spite of a somewhat greater high-end value estimated by Makedonska et al. (2020), cover the overall range of values. Figure 5-23 shows that the estimated range of values for the LFA in the current report covers a broad range but that some of the other analyses present values that are either somewhat higher or lower. Values of fracture aperture were not estimated for the TCU in either DOE/EMNV (2018) or Makedonska et al. (2020). Figure 5-24 shows the ranges of values given. The values estimated in the current report once again cover a broad range, encompassing those presented in Shaw (2003) but slightly exceeded at the lower end by the values determined by Drellack et al. (1997).

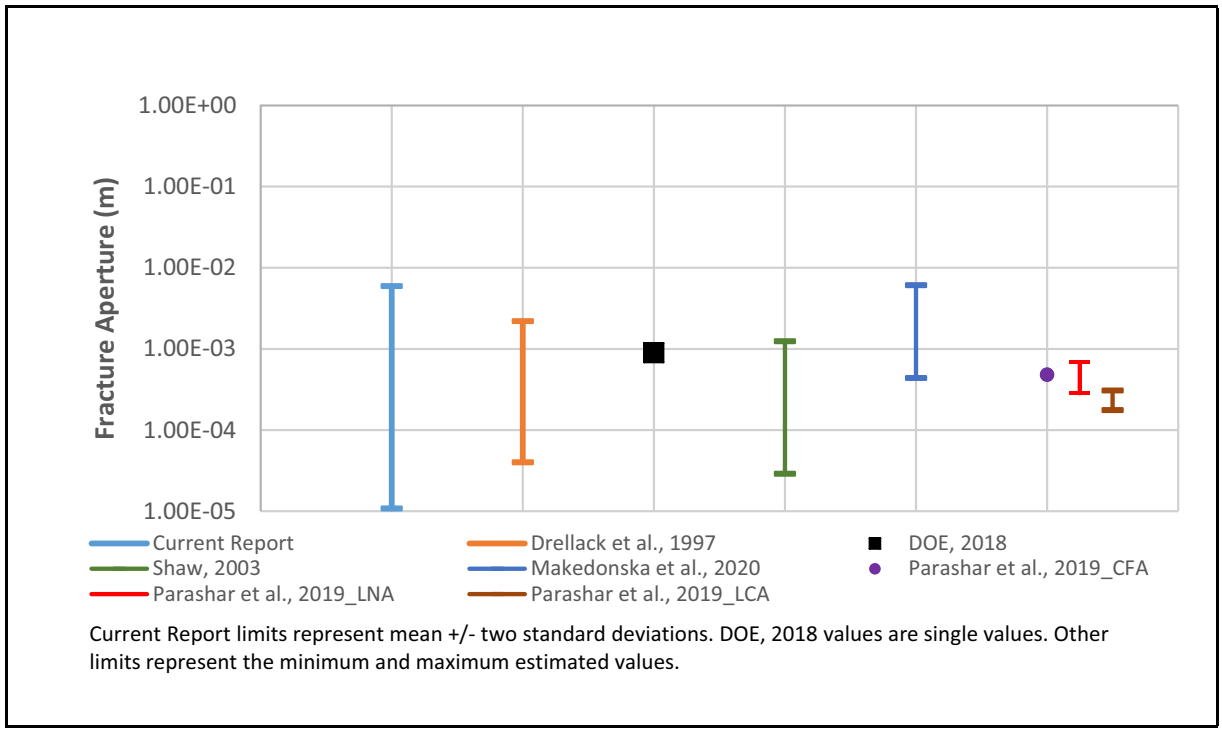

Figure 5-22
Comparisons of Fracture Apertures for the WTA HGU

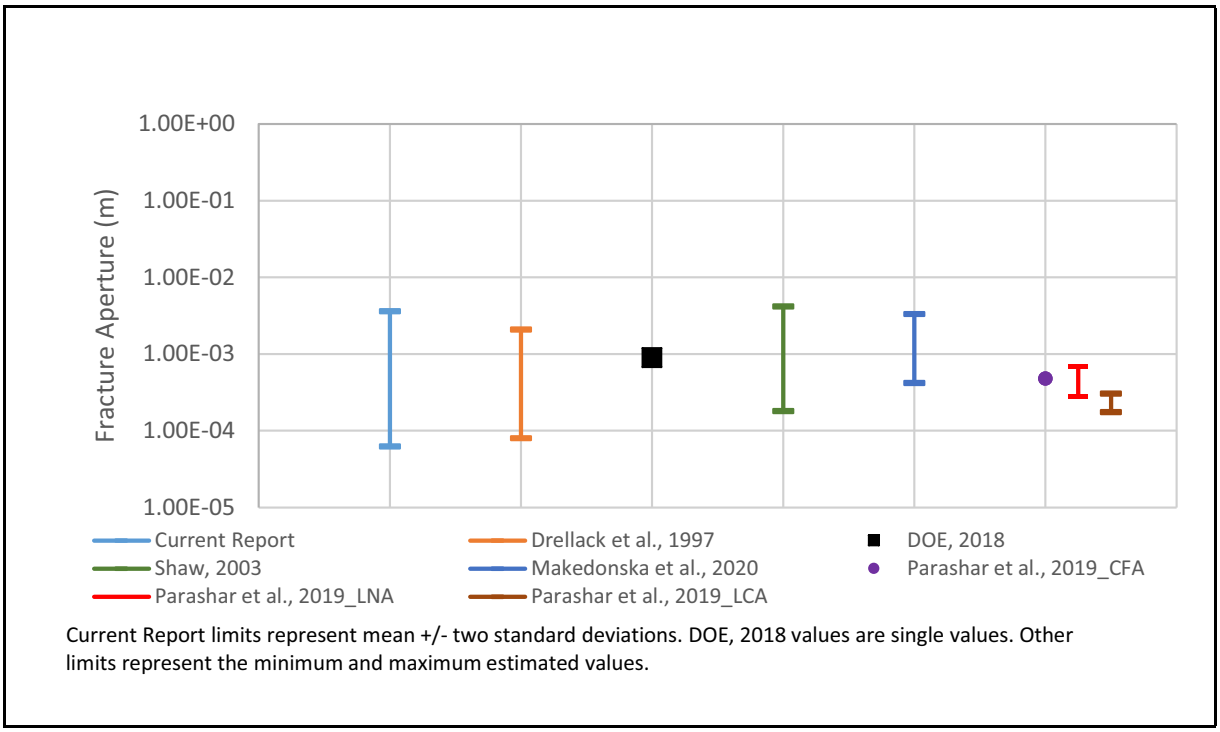

Current Report limits represent mean +/- two standard deviations. DOE, 2018 values are single values. Other limits represent the minimum and maximum estimated values.

Figure 5-23
Comparison of Fracture Apertures for the LFA HGU

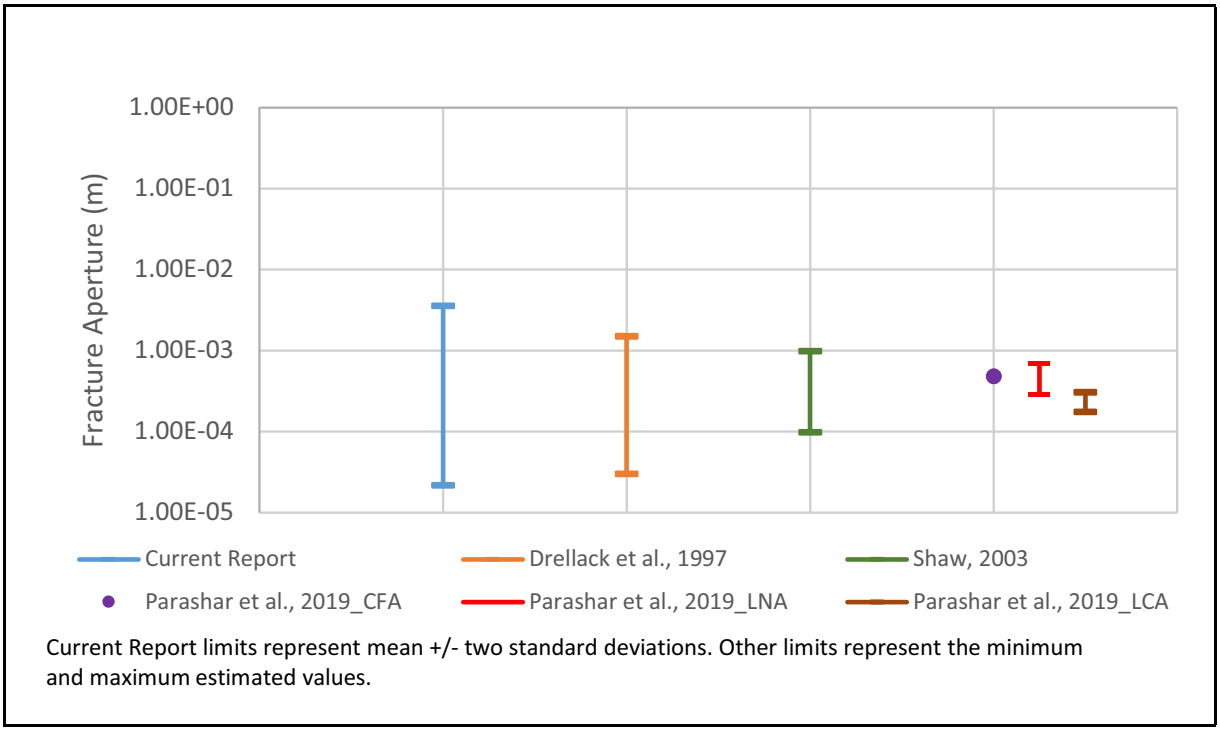

Current Report limits represent mean +/- two standard deviations. Other limits represent the minimum and maximum estimated values.

Figure 5-24
Comparison of Fracture Apertures for the TCU HGU

5.6.3 Data Scaling Considerations

In fractured media, the lateral extent and aperture of fractures is not constant. As a result, open fractures observed at one location may not be found at other locations, and dense fracturing at one location may diminish laterally or become sparse. This difference in scales is important because fracture characteristics determined at the measurement scale should not be expected to be representative to the much larger model scale, in particular if the fracture property is implemented as uniform for the entire HGU or HSU. The presence of a few fractures in a HGU at the local scale, which may indicate a fractured media conceptualization, may in some cases be more appropriately modeled as porous media conceptualized at the CAU scale when one considers the limited number and lateral extent of the fractures (e.g., in a situation where the HGU generally appears to be predominantly unfractured). When a double-porosity conceptualization is appropriate for an HGU, it is necessary to scale the fracture porosities obtained from borehole observations and tracer test interpretations to the CAU scale to appropriately incorporate the fractures in the CAU-scale models, The work of Makedonska et al. (2020) provides such upscaled values at the scale of a model cell (250 m × 250 m × 100 m). These values include those for porosity, fracture spacing and aperture, dispersivity, and dispersion through the DFN model developed.

5.6.4 Limitations

The major limitations associated with the estimates of fracture aperture developed for the PM CAU model are the sparse data environment, the uncertainty in the data inputs and methods used to estimate fracture aperture, and the issue of scaling localized values to values representative at the CAU scale. Estimates of fracture aperture are presented in this section for three fractured HGUs. The scale of these HGUs in the PM CAU model is up to scores of square kilometers. The actual fracture apertures in such a large area will be heterogeneous, varying both in the lateral and vertical directions. Determining values for fracture aperture that capture this heterogeneity would require extensive data collection at time and spatial scales that are impractical. The limitation due to the sparse data environment results in an inability to capture the heterogeneous nature of the effective porosity and its effect on contaminant movement. The use of a distribution and multiple simulations using different values from the distribution is the method implemented to try to bound the effects of heterogeneity in fracture aperture.

As noted above, the work of Makedonska et al. (2020) provides upscaled estimates of parameter values at the model cell scale. Channelization of flow and transport through long transmissive fractures causes much of the available fracture porosity to be bypassed, resulting in lower effective-to-total fracture porosity ratios and larger fracture apertures and spacings. The DFN modeling work of Makedonska et al. (2020) accounts for these effects. The fact that the distributions of transport porosity as well as fracture spacing and aperture are similar between those reported by Makedonska et al. (2020) and other sources reported here suggests that they also account for these effects.

5.7 Dispersivity

This section describes the role of dispersion in contaminant transport in groundwater, the available dispersivity data, analysis of these data, and the associated results. The objective is to use the data from the NNSS and the scientific literature to develop an approach for selecting appropriate dispersivity values for use in the PM CAU groundwater flow and transport model. Conceptually, dispersivity is a modeling parameter to describe plume spreading that accounts for the unmeasured and/or unspecified variability in the hydraulic properties within the flow and transport model domain. Dispersivity is often observed to be scale-dependent (i.e., a function of a representative scale of the problem). Reported dispersivity values (at specific transport scales) are typically derived from data collected during tracer tests, and from model calibration of contaminant plumes and geochemical or environmental isotope distributions in regional flow systems.

5.7.1 Role of Dispersivity

Dispersion is the process of spreading a solute over a volume that is larger than would be predicted based on estimates of the mean groundwater velocity. Dispersion includes molecular dispersion as well as hydrodynamic dispersion. Unlike molecular diffusion, which is an inherent property of a solute in water, mechanical dispersion arises from the complex and heterogeneous movement of water and solute particles through an intricate network of pores and fractures. In practice, the results of mechanical dispersion and molecular diffusion are not easily separable, so hydrodynamic dispersion is defined as a combined effect of both processes. It is common practice in groundwater modeling (Freeze and Cherry, 1979) to represent the effects of dispersion with the use of three independent dispersivities: the longitudinal dispersivity along the direction of the bulk fluid flow, and

two transverse dispersivities orthogonal to the flow direction (Section 3.0). This is the approach planned for use in the PM CAU transport model.

Tracer tests conducted at scales of a few hundred meters may not yield dispersivity values appropriate at the CAU scale because of the apparent trends in dispersivity with scale. With a site as large and as varied as the PM CAU, it is impractical to conduct tracer tests in enough locations to accurately estimate dispersivity, particularly at a physical scale representative of transport for the 1,000-year period of interest. The appropriate dispersivity to use for the PM CAU transport model depends on the size of the plume and expected distance of travel, as well as the scale at which inhomogeneities are explicitly included in the CAU flow model. The treatment of dispersion in the CAU transport model will be documented as part of the model report. This report is intended to document the available data.

5.7.2 Data Compilation

The dispersivity data types, the sources of data, and the data quality evaluation process are described in this section.

5.7.2.1 Data Types

Dispersivity values are derived from interpretation of tracer tests or studies of contaminant plume migration. The types of data used to document dispersivity include the location of the site, primary lithology of the rocks, identity of the tracer or contaminant that migrated, transport scale, data analysis method, dispersivity interpretation results, and data source.

5.7.2.2 Data Sources

Dispersivity data have been determined from one radionuclide migration (RNM) investigation (CAMBRIC) and several tracer tests conducted at or near the NNSS. These studies were conducted at the following sites (Figure 5-25):

- Nye County Early Warning Drilling Program (NC-EWDP) Site 22, Fortymile Wash, NNSS
- ER-6-1 Well Cluster, Yucca Flat, NNSS
- C-holes Complex, YM
- BULLION FGE, PM, NNSS
- Amargosa Tracer Calibration Site, Amargosa Desert, Nevada

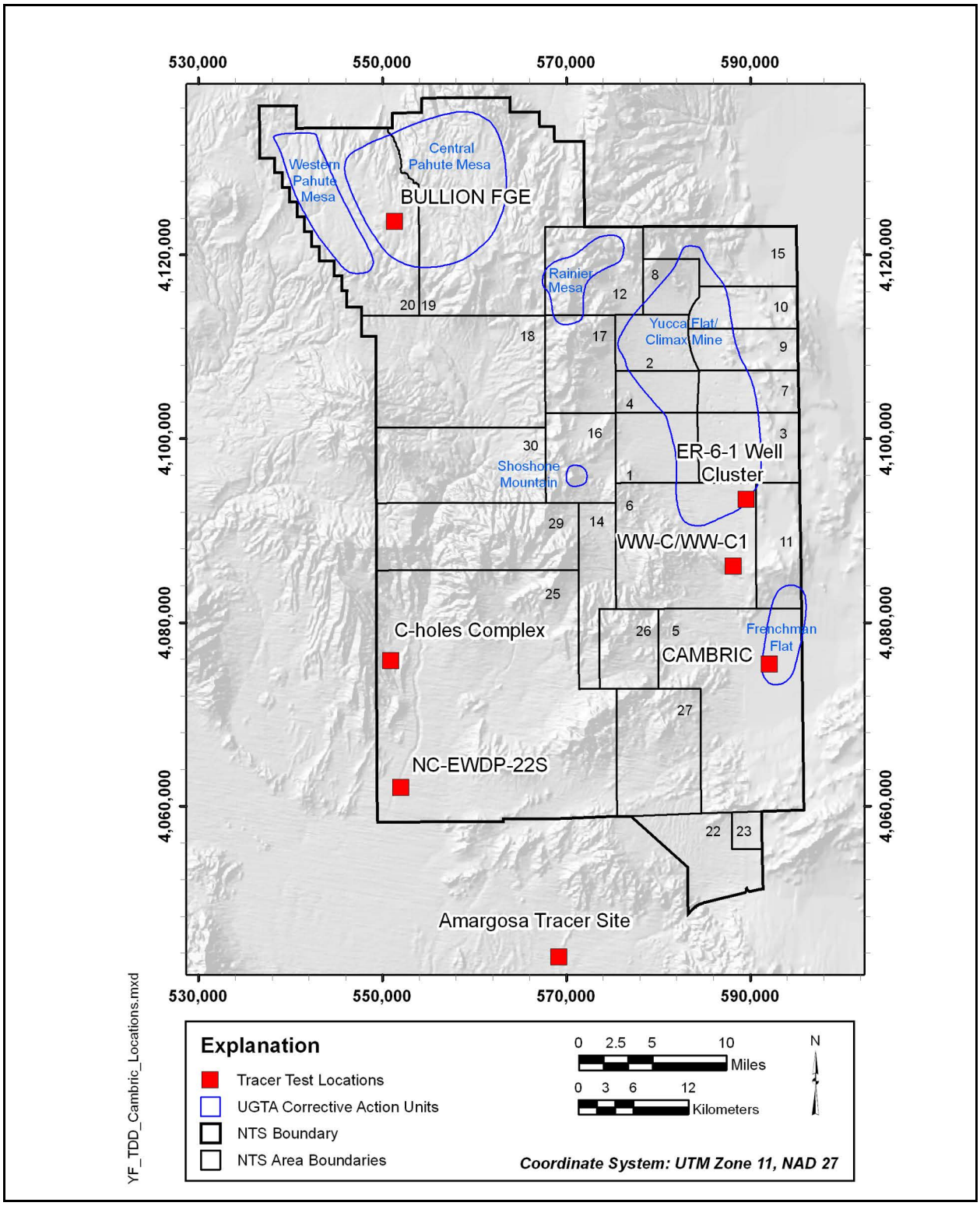

Figure 5-25
Locations of CAMBRIC Radionuclide Migration Experiment (RME) and Tracer Tests at the NNSS and Vicinity
Source: SNJV, 2007

- CAMBRIC site, Frenchman Flat, NNSS
- C-Well Site, Yucca Flat, NNSS

Additional data available from non-NNSS sites were obtained from the scientific literature. Gelhar et al. (1992) published a critical review of data on field-scale dispersion in aquifers reporting data from 59 different field sites. A more recent summary of laboratory and field dispersivity data is presented in Schulze-Makuch (2005); it considered data from 109 authors, including those summarized in Gelhar et al. (1992). These investigations reported in the scientific literature were used to supplement the tracer test data from the NNSS and vicinity to develop a dataset of dispersivity for the work on RM/SM (SNJV, 2008). This dataset, with the inclusion of data from the Yucca Flat C Wells site, described in Appendix G, is used to support the PM CAU transport model.

5.7.2.3 Data Documentation Evaluation

The BULLION FGE is a tracer test conducted under the ERP and is recognized as having adequate documentation available. Documentation of the tracer tests conducted at the CAMBRIC and C-well complex of Yucca Mountain was undertaken outside the ERP, but they are well documented. Documentation on the tracer tests conducted in Yucca Flat and Amargosa Desert is less complete. All other data lacked sufficient documentation on the procedures and their application during field data collection and analysis.

5.7.3 Data Evaluation

The data evaluation approach consisted of summarizing the existing NNSS and vicinity studies, including the range of dispersivity values obtained by different investigators. Data from dispersivity studies available in the scientific literature were also incorporated to determine a range of values appropriate for the scales of interest. These data had been compiled as a part of the effort on the RM/SM CAU (SNJV, 2008). This compilation contains data from tests on PM, YF/CM, Frenchman Flat, and other sites in the vicinity of the NNSS as well as data from non-NNSS sites. This dataset will be used for the PM CAU transport modeling effort. This section provides descriptions of the available data, data quality evaluation, dataset analysis approach, and derived dispersivity-scale relationship results.

The dispersivity data derived from tracer tests and observations of plume migration, geochemical data, or environmental isotope data were compiled into a comprehensive dataset. A subset of the data sources reporting longitudinal dispersivity also provides transverse dispersivity data.

5.7.3.1 NNSS and Vicinity Dispersivity Data

This subsection summarizes dispersivities obtained from the RNM experiment and tracer tests conducted to date at the NNSS and vicinity. Results derived from the migration and tracer test data using different interpretation approaches are included. The data for these experiments are summarized in Table 5-22, with the addition of data from Yucca Flat C Wells site. Summary information and discussion on the test sites, experimental methods, interpretation approaches, and interpreted dispersivity results are presented in this section. The information was taken from work on Frenchman Flat CAU (SNJV, 2005a), YF/CM CAU (SNJV, 2007), and RM/SM CAU (SNJV, 2008).

5.7.3.1.1 Nye County Early Warning Drilling Program (NC-EWDP) Site 22

Single-hole and cross-hole tracer tests have been conducted at Site 22 of the NC-EWDP (Umari et al., 2006), in the southwestern corner of the NNSS, to investigate transport characteristics of the alluvium. The complex consists of four wells arranged in an approximate square with 18-m sides. One of these wells (22S) is screened across multiple intervals and can be pumped at a high rate. The other three wells (22PA, 22PB, and 22PC) are essentially nested piezometers. A cross-hole tracer test was conducted at this site in early 2005, with well 22S as the pumping well and wells 22PA and 22PC as the tracer-injection wells. Tracers trifluorobenzoic acid (TFBA), lithium bromide (LiBr), and lithium chloride (LiCl) were injected into well 22PA and difluorobenzoate (DFBA) into Well 22PC. A second cross-hole tracer test was conducted in the late summer/early fall 2005, with well 22S as the pumping well and well 22PA as the injection well.

The TFBA and DFBA breakthrough curves from the first cross-hole tracer test were interpreted using the Moench (1989 and 1995) analytical solution to the advection-dispersion equation. The observed TFBA breakthrough (22PA to 22S pathway) exhibited three inflection points, suggesting three flow paths. Umari et al. (2006) separated this curve and analyzed each peak individually. They obtained longitudinal dispersivity values of 0.3, 3.0, and 2.4 m for matches to the first, second, and third peaks, respectively. They matched the single peak of the DFBA breakthrough curve (22PC to 22S pathway) using a longitudinal dispersivity of 3.0 m. Using a homogeneous numerical flow and transport model

Table 5-22
Dispersivity Information Summary from Studies at the NNSS and Vicinity
(Page 1 of 2)

Site Location	NNSS Geology	Scale of Test (m)	Test Method	Tracers	Analysis Method	Longitudinal Dispersivity (m)	Reference
CAMBRIC Test, Frenchman Flat, Nevada	Tuffaceous Alluvium	91	Radial converging	Nuclear test RNs: tritium	Sauty, 1980	2.0	Burbey and Wheatcraft, 1986
				Nuclear test RNs: tritium	Sauty, 1980	9.1	Travis et al., 1983
				Nuclear test RNs: tritium	Sauty, 1980	15.1	Thompson, 1988 Ogard et al., 1988
				Nuclear test RNs: Cl-36, tritium	Welty and Gelhar, 1989	3.1 - 9.6	SNJV, 2007
BULLION FGE, Pahute Mesa, Nevada	Fractured Lava-Flow Aquifer, Calico Hills Formation	130.2	Radial converging	PFBA, DFBA, I, CML, polystyrene microspheres	MODFLOWT calibration	10 (horizontal) 3 (horizontal transverse) 2 (vertical transverse)	IT, 1998
		41.5 - 130.2			RELAP (Reimus and Haga, 1999)	8.7 - 25.3	IT, 1998
		88.7 - 130.2			Welty and Gelhar, 1989	3.9 - NA [a]	SNJV, 2007
C-holes Complex, Yucca Mountain, Nevada	Prow Pass Tuff (fractured)	30	Unbalanced dipole	TFBA, I	Moench, 1989	0.27 [b]	Bechtel SAIC, 2004
				PFBA, Br^-, Cl^-, Li	RELAP (Reimus and Haga, 1999)	0.3 - 33.3	Bechtel SAIC, 2004
				TFBA, PFBA, Cl^-	Welty and Gelhar, 1989	1.7 - 8.6	SNJV, 2007
	Bullfrog Tuff (fractured)	30	Unbalanced dipole	PFBA, Br^-, Li	RELAP (Reimus and Haga, 1999)	3.2 - 18.8	Bechtel SAIC, 2004
				PFBA	Welty and Gelhar, 1989	0.8 - 2.6	SNJV, 2007
				DFBA	Moench, 1989	1.9 - 2.4	Bechtel SAIC, 2004
Amargosa Tracer Calibration Site, Amargosa Desert, Nevada	Cambrian Bonanza King Dolomite (fractured)	122.8	Doublet recirculating	tritium, S-25, Br^-	Grove, 1977	15 - 30.5	Leap and Belmonte, 1992

Table 5-22
Dispersivity Information Summary from Studies at the NNSS and Vicinity
(Page 2 of 2)

Site Location	NNSS Geology	Scale of Test (m)	Test Method	Tracers	Analysis Method	Longitudinal Dispersivity (m)	Reference
ER-6-1 Well Cluster	Fractured Limestone	NR	Radial converging	2,4,5-TFBA, I (lower zone)	RELAP (Reimus and Haga, 1999)	34 - 36	SNJV, 2006
		64.1		2,4,5-TFBA, I (lower zone)	Welty and Gelhar, 1989	3.0 - 11.1	SNJV, 2007
		NR		PFBA (upper zone)	RELAP (Reimus and Haga, 1999)	22	SNJV, 2006
		64.1		PFBA (upper zone)	Welty and Gelhar, 1989	3.0 - NA [a]	SNJV, 2007
NC-EWDP Site 22	Alluvium	18	Radial converging	2,4,5-TFBA, DFBA	RELAP (Reimus and Haga, 1999)	2.7 - 5	Reimus, 2006
					Moench, 1989 and 1995	0.3 - 3	Umari et al., 2006
					Welty and Gelhar, 1989	0.8 - 3.6	SNJV, 2007
C-Well Site, Yucca Flat, Nevada	Fractured Limestone	29.3	Radial converging test at WW-C and WW-C1	Fluorescein dye	Welty and Gelhar, 1989	0.6 - 1.4	Winograd and West, 1962 - data; Shaw, 2003 - calculation

Source: SNJV, 2007 and 2008

[a] NA refers to case where falling limb of breakthrough curve was insufficient to allow calculation of dispersivity estimate using the equation from Welty and Gelhar (1989) that requires both rising and falling limbs of the breakthrough curve.
[b] The interpretation accounted for plume spreading by assuming a long, slow release of tracer from the injection well and, therefore, it was not necessary to invoke strong dispersion in the aquifer.

NR = Not reported
2,4,5-TFBA = 2,4,5-trifluorobenzoic acid
CML = Carboxylate-modified latex
DFBA= Difluorobenzoate
I = Iodide
PFBA = Pentafluorobenzoic acid
TFBA = Trifluorobenzoic acid

(MODFLOW), they obtained a horizontal transverse dispersivity of 0.3 m. The breakthrough curves from the cross-hole tracer tests at Site 22 of the NC-EWDP were also analyzed by Reimus (2006) using the semianalytical model RELAP. The fitting parameters for the RELAP analysis were the mean fluid residence time, the Peclet number (equal to the distance between the injection and withdrawal wells divided by the longitudinal dispersivity), the tracer mass fraction participating in the tracer test, and the mass transfer coefficient for matrix diffusion (equal to the square root of the matrix diffusion coefficient times the matrix porosity divided by the fracture half aperture).

Reimus (2006) also analyzed the three inflections observed in the TFBA breakthrough curve from the first test (22PA to 22S pathway) separately. These analyses yielded longitudinal dispersivities of 2.7, 5, and 3.4 m for the first, second, and third peaks, respectively. His analysis of the DFBA breakthrough curve from the first test (22PC to 22S pathway) yielded a longitudinal dispersivity of 3.1 m. Reimus (2006) also analyzed the results from the second cross-hole tracer test conducted at the site. For the second test (22PA to 22S pathway only), the breakthrough curve exhibited two inflection points. Reimus (2006) analyzed those two points separately and obtained dispersivities of 2.7 and 4.6 m for the first and second peaks, respectively.

The TFBA and DFBA breakthrough curves from the first cross-hole tracer test were also analyzed using the method of Welty and Gelhar (1989). Longitudinal dispersivities of 1.8 and 3.6 m were calculated based on the TFBA breakthrough curve, and values of 0.8 and 2.2 m were calculated based on the DFBA breakthrough curve.

5.7.3.1.2 ER-6-1 Well Cluster Tracer Test

A multiple-well aquifer test-tracer test (MWAT-TT) was conducted in the LCA at the ER-6-1 Well Cluster located in Yucca Flat from late April to late July 2004. The test details discussed here were taken from SNJV (2005d and e). Well ER-6-1#2 was the pumping well, and tracers were injected into upper and lower completion intervals in Well ER-6-1, located 64 m from the pumping well, and into Well ER-6-1#1, located 51 m from the pumping well. The direction of tracer migration from the injection wells to the pumping well is approximately aligned with the dominant local fracture orientation. The pumping rate in Well ER-6-1#2 averaged 33.0 liters per second (L/s) over a 434.3-m-thick interval during the MWAT-TT. Tracer injection occurred in four stages. The first stage consisted of the injection of microspheres into the upper zone in Well ER-6-1; the second stage consisted of the injection of 2,5-DFBA into Well ER-6-1#1; the third stage consisted of the injection

of sodium iodide (NaI) and 2,4,5-TFBA into the lower zone in Well ER-6-1; and the fourth stage consisted of the injection of LiBr, LiCl, and PFBA into the upper zone in well Well ER-6-1. For each stage, tracer injection was followed by the injection of chase water to flush the tracer from the borehole. A complete description of tracer breakthrough curves for this test can be found in SNJV (2005e).

The tracer breakthrough curves were analyzed to estimate longitudinal dispersivity using the method of Welty and Gelhar (1989). For the flow path that exhibited the most rapid breakthrough of tracer at the pumping well (Well ER-6-1 lower zone to Well ER-6-1#2), longitudinal dispersivities of about 3.1 and 10.8 m were calculated based on analysis of the iodide and TFBA breakthrough curves. For the flow path that exhibited the slower breakthrough of tracer from Well ER-6-1 to the pumping well (Well ER-6-1 upper zone to Well ER-6-1#2), a longitudinal dispersivity of about 3.0 m was calculated based on analysis of the rising limb of the PFBA breakthrough curve. The falling limb of the breakthrough curve was insufficient to estimate dispersivity using both rising and falling limbs of the breakthrough curve. Dispersivity was not estimated for the flow path from injection Well ER-6-1#1 to the pumping Well ER-6-1#2 because a peak concentration for the breakthrough curve was not attained, and measured concentrations at the pumping well were at or near the detection limit.

Observed tracer breakthrough curves from the tracer tests at the ER-6-1 Well Cluster were analyzed by SNJV (2006b) using the semianalytical model RELAP. The fitting parameters for the RELAP analysis were the mean fluid residence times, the Peclet number (equal to the distance between the injection and withdrawal wells divided by the longitudinal dispersivity), the tracer mass fraction participating in the tracer test, and the mass transfer coefficient (equal to the square root of the matrix diffusion coefficient times the matrix porosity divided by the fracture half aperture).

Analysis of iodide and TFBA injected into the lower zone in Well ER-6-1, using RELAP, was performed using both single- and double-porosity conceptualizations. This analysis yielded longitudinal dispersivities of 27 and 29 m for the single- and double-porosity conceptualizations, respectively. The SNJV (2006b) report states that two inflow zones were identified by flow logging in pumping Well ER-6-1#2 that correspond to the upper injection zone in Well ER-6-1. The report analyzed the PFBA breakthrough in the upper zone, considering these inflow locations as individual pathways. Based on spinner log results, SNJV (2006b) assumed production rates of 40 and 10 percent of the total rate for pathways 1 and 2, respectively. The RELAP analysis of the PFBA breakthrough

curve yielded a longitudinal dispersivity of 19 m for pathway 1 (the upper inflow zone) and a value of 22 m for pathway 2 (the lower inflow zone), assuming a single-porosity conceptualization.

The interpreted dispersivity for the pathway from injection Well ER-6-1#1 to pumping Well ER-6-1#2 using RELAP is very uncertain and has not been included in the dataset because all of the measured tracer concentration data at the pumping well were near the detection limit and a peak concentration for the breakthrough curve was not attained.

5.7.3.1.3 C-Well Complex Site, Yucca Mountain, Nevada

USGS conducted and analyzed four convergent tracer tests and one partially recirculating tracer test in tuffaceous rocks in three boreholes at the C-well complex from 1996 to 1998 (Umari et al., 2007). The C-well complex is at Yucca Mountain, Nevada, less than 16 km south of the PM-OV area. The flow and transport experiments were conducted to determine the properties of the Bullfrog, Tram and Prow Pass volcanic tuffs beneath Yucca Mountain in the SZ. At formation depths, interborehole distances ranged from 28.6 to 86.3 m.

Tracer tests included (1) injection of iodide into the combined Bullfrog-Tram interval; (2) injection of 2,6-DFBA into the lower Bullfrog interval; (3) injection of 3-carbamoyl-2-pyridone into the lower Bullfrog interval; and (4) injection of iodide and 2,4,5-TFBA, followed by 2,3,4,5-TFBA into the Prow Pass Tuff. All tracer tests were analyzed by the Moench single- and dual-porosity analytical solutions to the advection-dispersion equation or by superposition of these solutions.

Longitudinal dispersivity values in the Bullfrog and Tram Tuffs ranged from 1.83 to 2.6 m, flow-porosity values from 0.072 to 0.099, and matrix-porosity values from 0.088 to 0.19. In the Prow Pass Tuff, longitudinal dispersivity was 0.27 m, flow porosity was 4.5×10^{-4}, and matrix porosity was 0.01.

Additional tracer tests were conducted (Winterle and La Femina, 1999), consisting of two pilot tests using PFBA and iodide, and a long-term multiple-tracer test using PFBA and LiBr. Colloidal transport was also performed using 360-nanometer (nm) microspheres. The method used to estimate the aquifer parameters is described in Appendix A of Reimus et al. (1999b). The method applies to 1-D, steady-state, advective-dispersive flow through parallel-plate fractures in a homogeneous, dual-porosity aquifer. The longitudinal dispersivity from the single successful pilot test is reported to

be 1.1 m. The longitudinal dispersivity from the long-term test yielded a range from 3.3 to 59 m. The test provided important information about the relative role of matrix diffusion as a result of normalized peak concentrations between bromide and the PFBA. Although the matrix diffusion was not specifically determined, it was apparent that it played an important role as an effective attenuation mechanism for dissolved species in the volcanic aquifer.

5.7.3.1.4 BULLION Site

The field portion of the BULLION FGE was performed from June to August 1997 at the BULLION underground nuclear test site on PM, Area 20, of the NNSS. Three characterization wells (ER-20-6 #1, #2, and #3) were completed in a fractured LFA, approximately downgradient of the BULLION cavity, aligned with the dominant fracture system. The most downgradient well (#3) was pumped to induce groundwater movement from the BULLION cavity and from Wells #1 and #2 to Well #3. The distance between wells (i.e., straight line length) ranged from 42 to 132 m (IT, 1998). The shortest distance is between Wells #1 and #2 and the largest distance is between Wells #1 and #3. PFBA and yellow polystyrene microsphere tracers were injected into Well #2. NaI, DFBA, and red polystyrene microspheres were injected into Well #1. Tracer concentrations were monitored to determine decline and/or breakthrough curves for each well. Hydraulic data were also collected during the FGE. Groundwater flow and tracer transport were evaluated by analytical (Reimus and Haga, 1999) and numerical modeling (IT, 1998). Based on calibration of the BULLION numerical transport model, the following were determined:

- Dispersivities:
  - Longitudinal: 5, 10, or 25 m (alternative calibrations)
  - Horizontal transverse: 1, 3, or 7.5 m (alternative calibrations)
  - Vertical transverse: 1, 2, or 5 m (alternative calibrations) (IT, 1998).

The semianalytical solutions of Reimus and Haga (1999) yielded the following:

- Dispersivity values:
  - Longitudinal: 9 to 30 m (alternative calibrations)
  - Horizontal transverse: not applicable
  - Vertical transverse: not applicable

The longitudinal and horizontal transverse dispersivities are in the range of measured values summarized by Gelhar et al. (1992) for tests at scales of about 100 m. Both the numerical and semianalytic models simulated matrix diffusion as a separate process. Therefore, the longitudinal dispersivities are representative of mechanical dispersion and are not biased upward by lumping matrix diffusion effects. There is not much confidence in the horizontal transverse dispersivity because the radial flow configuration of the FGE is not sensitive to transverse dispersion due to averaging at the pumped well. The vertical dispersivity is also unreliable because the tracer was vertically mixed within the model layer.

The longitudinal dispersivity estimated with the numerical modeling technique (IT, 1998) for the shorter flow path (42 m from Well #1 to #2) may be too large, based on a sensitivity analysis of dispersivity where it appeared that a relatively large dispersive flux was causing tracer migration upgradient against the direction of groundwater flow. This situation is physically unrealistic (IT, 1998). Another explanation for the large spreading predicted by the model, including upgradient, may be numerical dispersion. If this is a numerical dispersion effect, then part of the dispersive flux is generated by the numerical dispersion and the calibrated longitudinal dispersivity may be too small. The similarity between the numerical and semianalytical (which does not suffer from numerical dispersion) derived longitudinal dispersivity suggests that the impact of numerical dispersion is not too large.

5.7.3.1.5 Amargosa Tracer Calibration Site

Two-well recirculating tracer tests were conducted, beginning in 1971 (Claassen and Cordes, 1975) in the Dolomite aquifer at the Amargosa Tracer Calibration Site in the Amargosa Desert in southern Nevada, approximately 24 km southwest of Mercury, Nevada (Leap and Belmonte, 1992).
The objectives of the tracer tests were as follows:

- Determine the apparent longitudinal dispersivity of a fissured and fractured aquifer within the Cambrian Bonanza King dolomite draining the NNSS.
- Determine the effective porosity of the dolomite aquifer.
- Study the usefulness of ^{3}H, sulfur-35, and bromide as tracers in this aquifer.

The tests were performed under different recirculating rates and pore pressures. Two wells penetrating through the dolomite aquifer, aligned parallel with the direction of regional flow

(northeast to southwest), were used for tracer recirculating tests. The injection well was 122.8 m upgradient of the pumping well, and the wells were connected by a polyvinyl chloride (PVC) pipe. Measurements of the transmissivity of the aquifer ranged from 4,800 to 10,900 square meters per day (m^2/day). The storage coefficient was approximately 5×10^{-4} and the regional hydraulic gradient was between 10^{-4} and 10^{-5}. Two other wells penetrating the dolomite aquifer in the vicinity were used to collect water samples.

Breakthrough curves were constructed from analysis of effluent samples collected from the pumping well. These curves were matched and compared to synthetic curves constructed from various combinations of porosity and longitudinal dispersivity using the Grove method (Grove and Beteem, 1971), which provides a solution to the Fickian dispersion model. Apparent dispersivities of the aquifer were then taken to be those of the best-fit synthetic curves, within an accuracy of plus/minus 3.0 m.

The results of these tests are as follows:

- Test 1 (^{3}H as tracer) yielded a best-fit apparent dispersivity of 15 m and a porosity of 10 percent.
- Test 2 (sulfur-35 in the form of sodium sulfate as tracer) yielded a best-fit dispersivity of 22.9 m and a porosity of 10 percent.
- Test 3 (^{3}H and bromide as tracers), the ^{3}H curve fit yielded an apparent dispersivity of 27.4 m and a porosity of 10 percent; the bromide curve fit yielded an apparent dispersivity of 30.5 m and a porosity of 10 percent.

The tests were run at a recirculation rate of 31 percent less than that of Test 1. The relatively large difference in apparent dispersivity between the sulfur-35 and ^{3}H tests is likely caused by greater adsorption and/or retardation of the more active sulfate ion than that of either the bromide or tritiated water. The 10 percent difference in computed apparent dispersivity between the two tracers (^{3}H and bromide) for the same recirculation rate (Test 3) was attributed to the adsorption or retardation difference between ^{3}H and bromide. The difference between Tests 1 and 3 is more difficult to explain. Leap and Belmonte (1992) postulated that the differences were due to changes in fracture openings caused by the increased pressure for the higher flow test. The variation between Tests 1 and 3 emphasizes the typical range in dispersivity values at a single site. These tests were interpreted using a single-porosity transport conceptualization, ignoring transport in fractures and fracture-matrix

interaction. The impact of this interpretation approach on the dispersivities and porosities determined is unknown. It is noted that the porosities quoted above are on the high side.

5.7.3.1.6 CAMBRIC Site

The CAMBRIC nuclear test was conducted in the subsurface at the NNSS in May 1965. Beginning in 1974, the site was studied under the Hydrology Radionuclide Migration Project (also called the Radionuclide Migration [RNM] Project). The nuclear test took place at a depth of 294 m below land surface and below the water table in the tuffaceous alluvium of Frenchman Flat.

There is very slow ambient groundwater movement at the location, and the RNs resulting from the test remained in the cavity region (Hoffman, 1979). The RNM-1 hole was drilled into the cavity in 1974. An auxiliary well, RNM-2S, was drilled 91 m away to a depth of 350 m. It was pumped continuously at an average rate of about 1.0 m^3/min from October 1975 until October 1977, and then at an average rate of 2.3 m^3/min until August 1991. The concentrations of RNs were monitored. Analyses of water samples showed that the migration velocities of ^{3}H, ^{36}Cl, ^{85}Kr, ^{99}Tc, ^{106}Ru, and ^{129}I were nearly the same, from the explosion site to the pumped well (Bryant, 1992). The concentration of ^{239}Pu at the pumping well was below the detection limit of 106 atoms per milliliter in water collected at the time of peak ^{3}H concentration. As of 1990, in the last samples collected from the cavity, levels of activity of both ^{3}H and ^{85}Kr had fallen almost below the limits of detection capability (Thompson, 1991). Other RNs such as ^{90}Sr and ^{137}Cs decreased considerably in concentration in the cavity region during the period of pumping at Well RNM-2S. Less than 0.5 percent of the total ^{90}Sr and 0.0003 percent of the total ^{137}Cs accompanied the ^{3}H to the pumped well, although both isotopes appear to have migrated away from the source zone to some extent. Additional monitoring results from the CAMBRIC experiment are presented and discussed in SNJV (2005a).

In 1977, two years after initiation of groundwater pumping from Well RNM-2S, ^{3}H began to appear in the water collected from Well RNM-2S. The ^{3}H concentration peaked in late 1980 and has been declining since. Although almost 91 percent of the CAMBRIC ^{3}H source term had been pumped out of Well RNM-2S by September 1990, continued pumping allowed the definition of the tail of the elution curve (Thompson, 1991).

With the above information, the longitudinal dispersivity of the porous aquifer can be estimated by two different approaches. The estimates are presented below.

Welty and Gelhar Method

Welty and Gelhar (1989) developed an equation to estimate the longitudinal dispersivity as follows:

$$\Delta t = t_2 - t_1 = t_m \left[\frac{16\alpha}{3R}\right]^{1/2} \left[\left[1 - \left(1 - \frac{t_2}{t_m}\right)\left|1 - \frac{t_2}{t_m}\right|^{1/2}\right]^{1/2} + \left[1 - \left(1 - \frac{t_1}{t_m}\right)\left|1 - \frac{t_1}{t_m}\right|^{1/2}\right]^{1/2}\right]$$

(5-9)

where

t_1 and t_2 = times corresponding to the breakthrough concentration at the $C_m e^{-1}$ level, respectively, on both sides of the curve.
t_m = time when peak concentration occurs
α = longitudinal dispersivity
R = distance between the injection well and the pumping well

Using the ^3H concentration data:

- Peak concentration $C_m = 7.0 \times 10^6$ picocuries per liter (pCi/L) concentration, $V_m = 5 \times 10^6$ m^3.

where

C_m = peak concentration
V_m = cumulative volume of water pumped corresponding to the time at peak concentration

- The time variables t_1 and t_2 in Equation (5-9) can be calculated from the following information:
- The value for C_m/e is $(7.0 \times 10^6)/2.7183 = 2.6 \times 10^6$ pCi/L.
- The cumulative volume is 2.95×10^6 m^3 (V_1) on the rising limb and 12.5×10^6 m^3 (V_2) on the falling limb.

Assuming continuous pumping at Well RNM-2S with a rate of 2.3 m^3/min (Q), the time at V_1, V_2, and V_m is calculated by $t = V/Q$:

- t_1 = 891 days
- t_2 = 3,774 days
- t_m = 1,510 days

Using Equation (5-9) with R = 91 m, t_1 = 891 days, t_2 = 3,774 days; and t_m = 1,510 days, the longitudinal dispersivity calculated for the CAMBRIC experiment is 9.6 m.

Sauty Model

The transport of tritiated water from the source to the satellite well was compared with Sauty's (1980) two-dimensional (2-D) calculation for instantaneous tracer injection in a radial, converging flow field similar to the RNM well tracer tests (Daniels, 1981; Daniels et al., 1983; Daniels and Thompson, 1984). Sauty provided "type curves" with dimensionless time Tr and dimensionless concentration Cr for different Peclet numbers, where Peclet number (Pe) is defined as the ratio of transport distance to the dispersivity. A dimensionless time Tr = 1 corresponds to the time required to pump the volume of water contained in a cylinder whose radius is the distance from the satellite well to the source, The shape of the elution curve depends on the Pe, which is inversely proportional to the dispersivity. The smaller the Pe, the larger the dispersivity; hence, the broader and more skewed the elution peak.

In the case of CAMBRIC site, the time to pump water from the 91-m radius cylinder from Well RNM-2S was estimated to be 2,100 days. From this point, the initial tracer breakthrough and the time to peak can be related to the dimensional time on Sauty's type curve. Fitting those two points corresponds to a Pe of 45. The corresponding dispersivity is estimated at 2 m.

Burbey and Wheatcraft (1986) used a 3-D, transient, finite difference model to estimate transverse dispersivity from these data. They used a $\alpha_L/\alpha_T = 1.3$, $\alpha_L/\alpha_T = 0.67$, and $\alpha_L/\alpha_T = 10.0$ to produce the ^3H concentration hydrograph. They concluded that the transverse dispersivity, $\alpha_T = 1.5$ m would produce the most accurate peak concentration in relation to the field data.

In the migration study of ^3H and ^{36}Cl, it was found previously that the ^{36}Cl elution at Well RNM-2S preceded the ^3H elution by a significant volume (Thompson, 1988; Ogard et al., 1988). Researchers at LANL attributed this phenomenon to the "anion exclusion" effect, that is, anions such as chloride were eluted before cations or neutral species such as tritiated water. Anions, being of the same charge as the clays and zeolites in the soil, are repelled and effectively prevented from entering the intragranular porosity of the soil particles.

Though a Sauty-type curve with Pe = 10 fits the ^3H data through the maximum, a better fit to the tailing portion of the data up to 12×10^6 m^3 of the water pumped can be made using a type curve with a Pe of 6, which corresponds to a dispersivity of 15.1 m.

The alluvium of Frenchman Flat is heterogeneous with interbedded fine- and coarse-grained material. If the transport processes include diffusive mass exchange with stagnant zones (i.e., dead-end pores, fine-grained layers), the observed dispersivities may be an overestimate of the mechanical dispersion. On the other hand, the excellent fit between observed and theoretical breakthrough curves suggests that using the derived dispersivities will be adequate for simulation of transport in Frenchman Flat alluvium with a single-porosity model.

5.7.3.1.7 C-Well Site, Yucca Flat

This tracer experiment was conducted to understand whether the drilling mud used at Water Well C-1 might be carried by groundwater to production Well C. The wells are at the southern end of Yucca Flat in Area 6 of the NNSS. The objective of the test was to determine the rate of movement of groundwater between two wells (Water Wells C and C-1) 30.5 m apart at the surface (Winograd and West, 1962).

The unconfined aquifer tapped by these wells is fractured limestone of Paleozoic age which, as shown by cores from Water Well C, transmits water primarily through fractures. The total depth of Water Well C is 518.5 m with 32.9 m of screen at the depth of 478.2 to 511.1 m. The submersible pump delivered 1,200 cubic meters per day (m^3/day) creating less than 0.15 m of drawdown. Well C-1 was drilled to a depth of 520.3 m. The opening (uncased hole) begins at the depth of 281.6 m to the bottom of the well. The actual distance between the two wells is 29.3 m at the water table. Fluorescein was used as a tracer and injected in Water Well C-1. The tracer was clearly seen in a sample collected 252 minutes after discharge began. Samples of water were collected periodically for 17 hours after the first appearance of the dye. The concentration of the tracer gradually increased to a maximum in 3 to 4 hours (432 to 492 minutes) after discharge began, and then slowly decreased until, in another 4 to 5 hours (te = 672 to 792 minutes) after discharge began, it was no longer detectable with the naked eye. The velocity of the first arrival was estimated to be 0.12 meters per minute and dispersivity estimated at 1.4 m. The peak concentration was not included in the report, and assumptions had to be made regarding travel times to arrive at this estimate.

5.7.3.2 Non-NNSS Dispersivity Data

Dispersivity data are available for many locations outside the NNSS from the scientific literature with many cases summarized in Gelhar et al. (1992), and Schulze-Makuch (2005). These references

provide detailed tables summarizing dispersivities, scale of transport, and other relevant information describing studies for both tracer tests and contaminant or environmental tracer transport modeling investigations. In addition, dispersivity data interpreted and published in the scientific literature from other tracer tests and modeling studies have been included in the dataset for use in developing a relationship between dispersivity and the scale of transport for the YF/CM CAU. Gelhar et al. (1992) reviewed dispersivity observations from 59 different field sites worldwide. Their review included tabulated information on site location, descriptions of aquifer material, average aquifer saturated thicknesses, hydraulic properties, effective porosities, mean pore velocities, flow configurations, dimensionality of the monitoring networks, tracer types, methods of data interpretation, overall scales of observation, and longitudinal and transverse dispersivities from original sources.

Gelhar et al. (1992) classified the dispersivity data into three reliability classes corresponding to the data reliability. They found that, at a given scale, dispersivity varied over several orders of magnitude, with the higher-reliability data tending to be in the lower part of the dispersivity range. Neuman (1990) noted that part of the large scatter is due to experimental and interpretive errors. An example of an interpretation issue that can lead to apparent scaling of dispersivity is discussed by Domenico and Robbins (1985), where they present calculations showing that interpreted dispersivity will be scaled larger whenever an (n-1)-dimensional model is calibrated to describe transport in an n-dimensional system.

Analyses by various authors indicate a trend of systematic increase in the longitudinal dispersivity with increase in the observation scale. The longitudinal dispersivities reported by Gelhar et al. (1992) ranged from 10^{-2} to 10^{4} m for travel distances ranging from 10^{-1} to 10^{5} m; however, the largest distance with high-reliability data was only 250 m, and the largest high-reliability longitudinal dispersivity was only 4 m. Gelhar et al. (1992) also concluded from the data that, overall, dispersivity values tended to scatter over a similar range for both porous and fractured media.

Schulze-Makuch (2005) presents additional dispersivity values from 39 authors in a similar fashion to that of Gelhar et al. (1992). An evaluation of some of the data summarized by Schulze-Makuch revealed a number of discrepancies as discussed in the YF/CM TDD (SNJV, 2007; Section 9.3.2). As a part of the data evaluation performed for RM/SM TDD, the accuracy of the reported dispersivities and scales of transport tabulated in Gelhar et al. (1992) and Schulze-Makuch (2005) was examined for all those references that could be readily obtained and not already checked for the

dispersivity dataset developed for the YF/CM CAU. The database was then updated. Although included in the database for the YF/CM CAU, data for studies where the interpreted longitudinal dispersivity was greater than the transport scale were removed from the database for the RM/SM CAU. These very large longitudinal dispersivities are considered unrepresentative for modeling studies where some degree of the variability in hydraulic properties is incorporated in the PM CAU flow model with the inclusion of multiple HSUs, variation of properties within HSUs, and large-scale faults and features.

5.7.3.3 Data Quality Evaluation

The dataset developed for the RMSM CAU includes a data quality evaluation flag (DQE_F) that corresponds to the levels of reliability defined by Gelhar et al. (1992) and later adopted by Schulze-Makuch. The reliability levels were defined using the following criteria:

- **Level 1:** Corresponds to "High Reliability," Level I of Gelhar et al. (1992). The tracer study meets the following criteria: (1) tracer test was either ambient flow, radial diverging flow, or two-well instantaneous pulse test without recirculation; (2) tracer input was well-defined; (3) tracer was conservative; (4) spatial dimensionality of the tracer concentration measurements was appropriate; and (5) analysis of the tracer concentration data was appropriate and consistent with the measurements.

- **Level 2:** Corresponds to "Intermediate Reliability," Level II of Gelhar et al. (1992). The study does not meet the criteria for high or low reliability.

- **Level 3:** Corresponds to "Low Reliability," Level III of Gelhar et al. (1992). The tracer study meets the following criteria: (1) two-well recirculating test with step input was used; (2) single-well, injection-withdrawal test where tracer monitoring at the single well was used; (3) tracer input was not clearly defined; (4) tracer breakthrough curve was assumed to be the superposition of breakthrough curves in separate layers; (5) measurement of tracer concentration in space was inadequate; and (6) equation used to obtain dispersivity was not appropriate for the data collected.

The "high-reliability" dispersivity values were considered to be accurate within a factor of two, and the "low-reliability" values were considered to be no more accurate than one to two orders of magnitude.

5.7.4 General Description of the Dispersivity Dataset

5.7.4.1 Longitudinal Dispersivity

A log-log plot of the longitudinal dispersivity versus scale data developed from the NNSS and non-NNSS sources discussed above, including the reliability information (Levels 1, 2, or 3), is shown in Figure 5-26. The longitudinal dispersivity values in the dataset range from 0.005 to 910 m for field transport distances ranging from 1.5 to 50,000 m. Longitudinal dispersivity varies from two to three orders of magnitude for a given scale of transport. The data show a systematic increase in longitudinal dispersivity with increasing transport scale which is consistent with findings by previous authors (e.g., Gelhar et al., 1992). The largest scale with high-reliability data (Level 1) was only 266 m, with a longitudinal dispersivity of 0.55 m. The high-reliability dispersivity values tend to be somewhat smaller in magnitude than other data at any particular scale especially at scales above 70 m. A similar trend was also observed by Gelhar et al. (1992), who stated that dispersivities in the lower half of the range are favored for a given scale. At the larger transport scales (e.g., greater than 300 m), only lower-reliability data are available, which could lead to greater uncertainty in longitudinal dispersivity for large plumes or longer transport distances.

The longitudinal dispersivity values determined from the NNSS region are compared with the worldwide values in Figure 5-27. The longitudinal dispersivities from the NNSS region range from 0.9 to 23.2 m (average values for individual flow paths) with transport scales ranging from 18 to 130 m. It can be seen that the longitudinal dispersivities determined from the contaminant migration experiment and the tracer tests conducted in the NNSS and vicinity are consistent with those obtained from other studies in the literature at similar scales. Further, as discussed in SNJV (2004c) and HGL (2018a), data from NNSS and from other sites do not show a clear difference between longitudinal dispersivities measured in fractured versus porous media.

There are insufficient data across all transport scales for various rock types to allow for a meaningful assessment of whether the dispersivity-scale relationship is a function of rock type. Hence, the analysis to determine a dispersivity-scale relationship used the entire dataset lumped together using all rock types. To illustrate the dataset, cumulative probability distribution function for scale is shown in Figure 5-28. The median scale is about 32 m, 95 percent of the data fall below ~3,200 m scale, and ~75 percent are less than ~800-m scale. These figures show that the majority of the available data are at a scale much less than that for the PM CAU transport model.

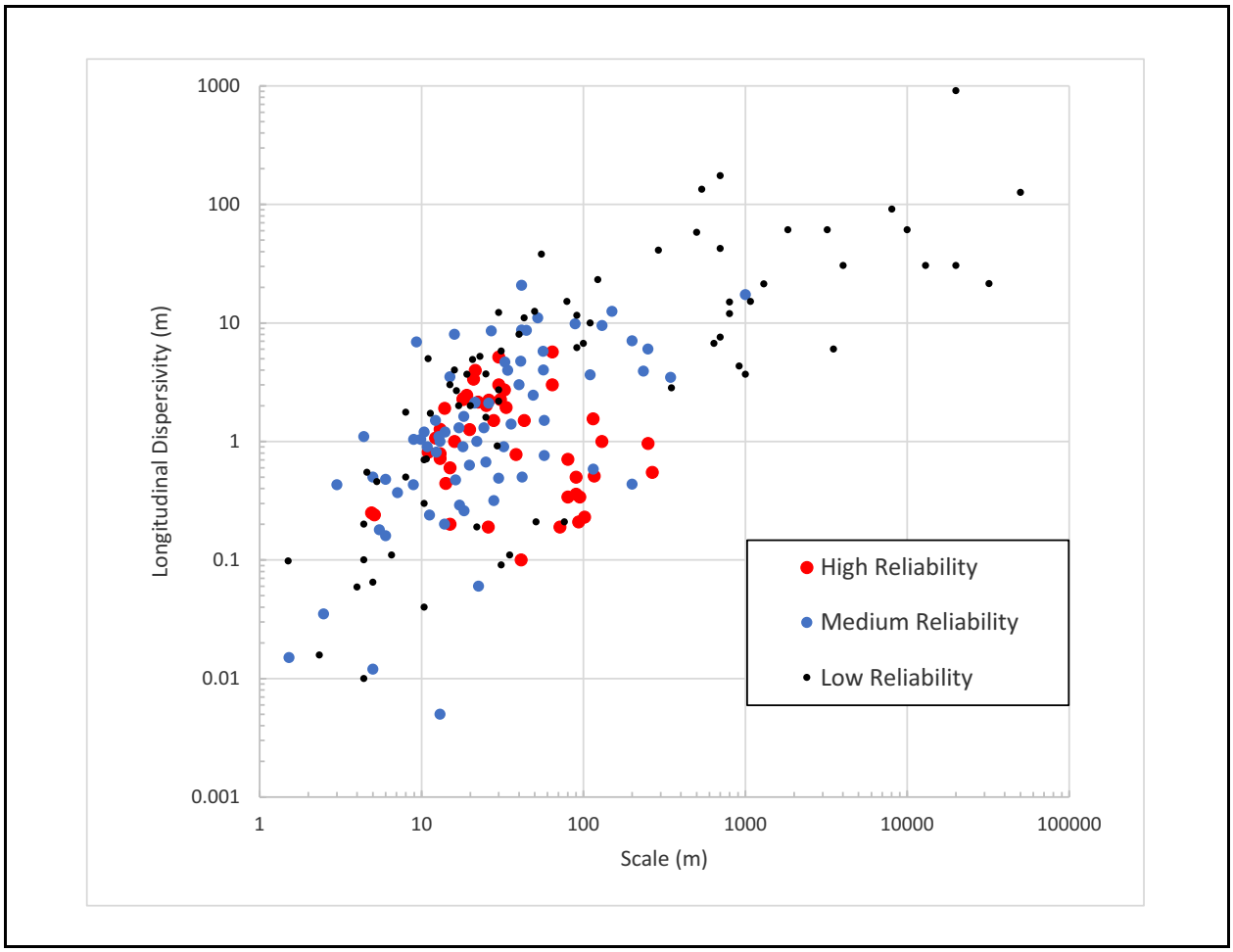

Figure 5-26
Plot of Longitudinal Dispersivity Values with Data Reliability Indicated

The cumulative probability distribution function for longitudinal dispersivity is shown in Figure 5-29. A cumulative lognormal distribution function for the data (calculated with the mean and standard deviation from logarithm to base 10 of the data) is also shown in the figure. The median longitudinal dispersivity is about 1.6 m; 95 percent of the data fall below about 50 m, and 99 percent is less than ~150 m.

5.7.4.2 Transverse Dispersivities

The data available for transverse horizontal dispersivity, or the spreading of solutes at right angles to the direction of horizontal groundwater flow, are shown in Figure 5-30. Transverse horizontal dispersivities up to 1,370 m have been reported. Although the data are much more sparse compared to data available for longitudinal dispersivity, the transverse horizontal dispersivity data exhibit the same pattern of increasing value with transport scale as does the longitudinal dispersivity.

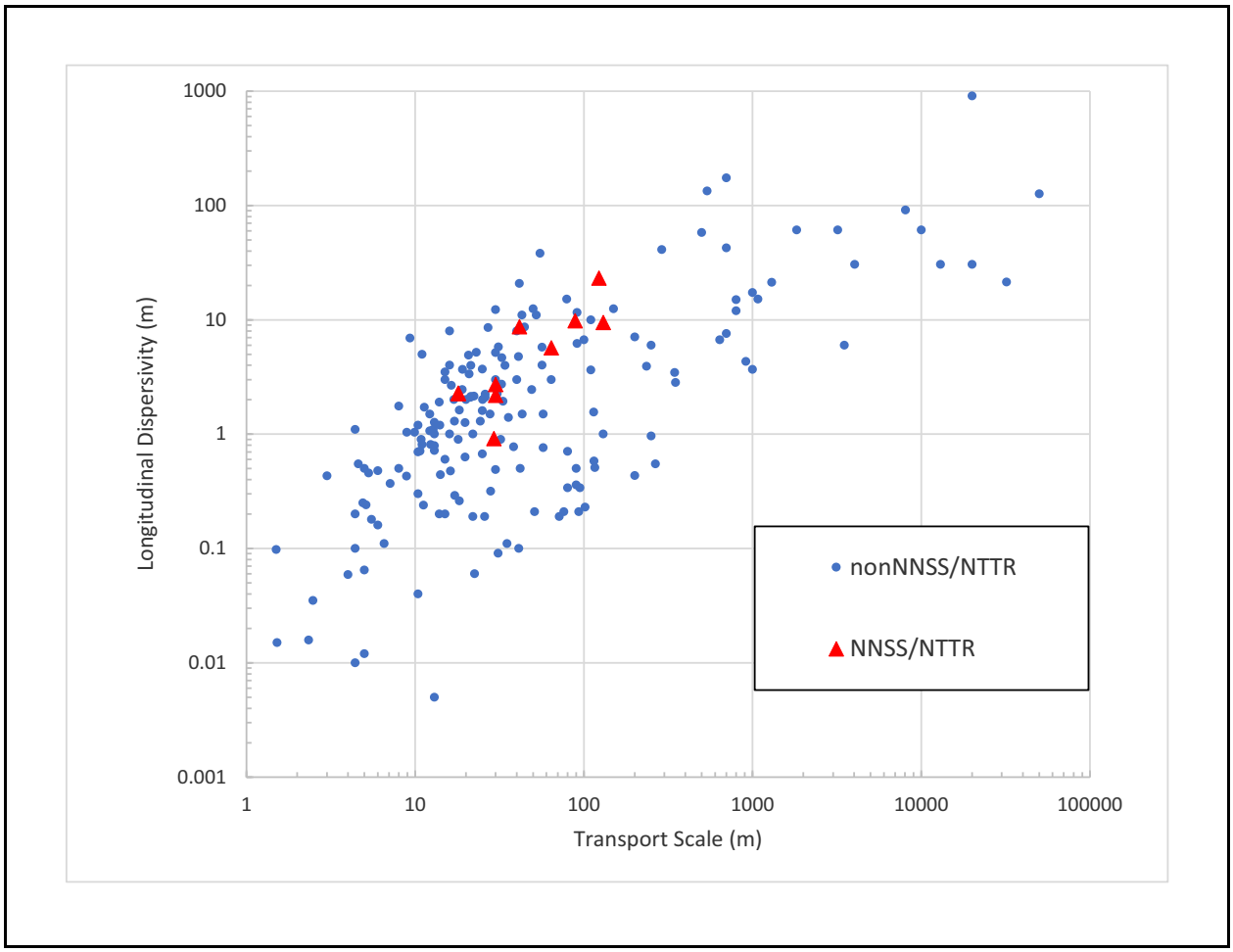

Figure 5-27
Plot of NNSS Longitudinal Dispersivity Values Compared to Worldwide Data

Although the low-reliability data show an increasing trend at larger scales, the trends for intermediate- and high-reliability data are not clear. The ratio of longitudinal to transverse horizontal dispersivity is shown in Figure 5-31. With a few exceptions, the transverse horizontal dispersivity is, in general, a factor of 2 to 100 less than the longitudinal dispersivity. Gelhar et al.(1992) reported that, based on two high-reliability data points, transverse horizontal dispersivity is one order of magnitude less than longitudinal dispersivity. Ratios of longitudinal to transverse horizontal dispersivity of about 10 are typically chosen when developing appropriate values of horizontal transverse dispersivity for use in regional transport models, although somewhat higher ratios (~20 or 30) could be considered on the basis of the limited data presented here. Figure 5-32 depicts the sparse data for transverse vertical dispersivity. Transverse vertical dispersivities up to 3 m have been reported. No trend of transverse vertical dispersivity with transport scale is apparent. The ratio of longitudinal to transverse vertical dispersivity is shown in Figure 5-33. The only significant observation is that the transverse vertical

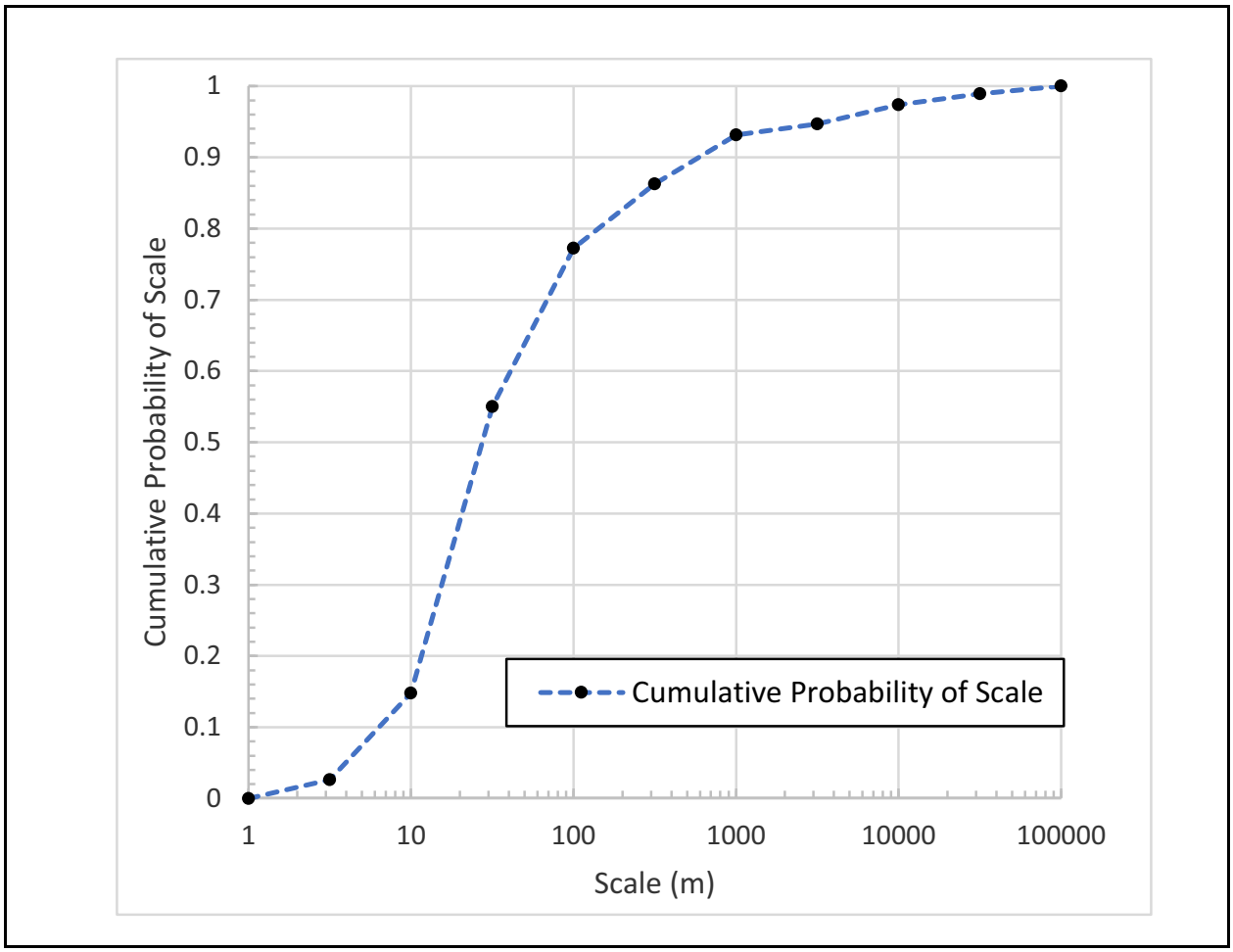

Figure 5-28
Cumulative Probability Distribution of Transport Scale

dispersivity is much less than either the longitudinal or horizontal transverse dispersivity. Gelhar et al. (1992) found that in all cases where both horizontal and vertical transverse dispersivities were measured, the values of vertical transverse dispersivity were one to two orders of magnitude less than those of the horizontal transverse dispersivity. This reduction in spreading may be controlled mainly by the layering of the geologic materials, where less permeable layers will significantly reduce the ability of the tracer to disperse upward or downward.

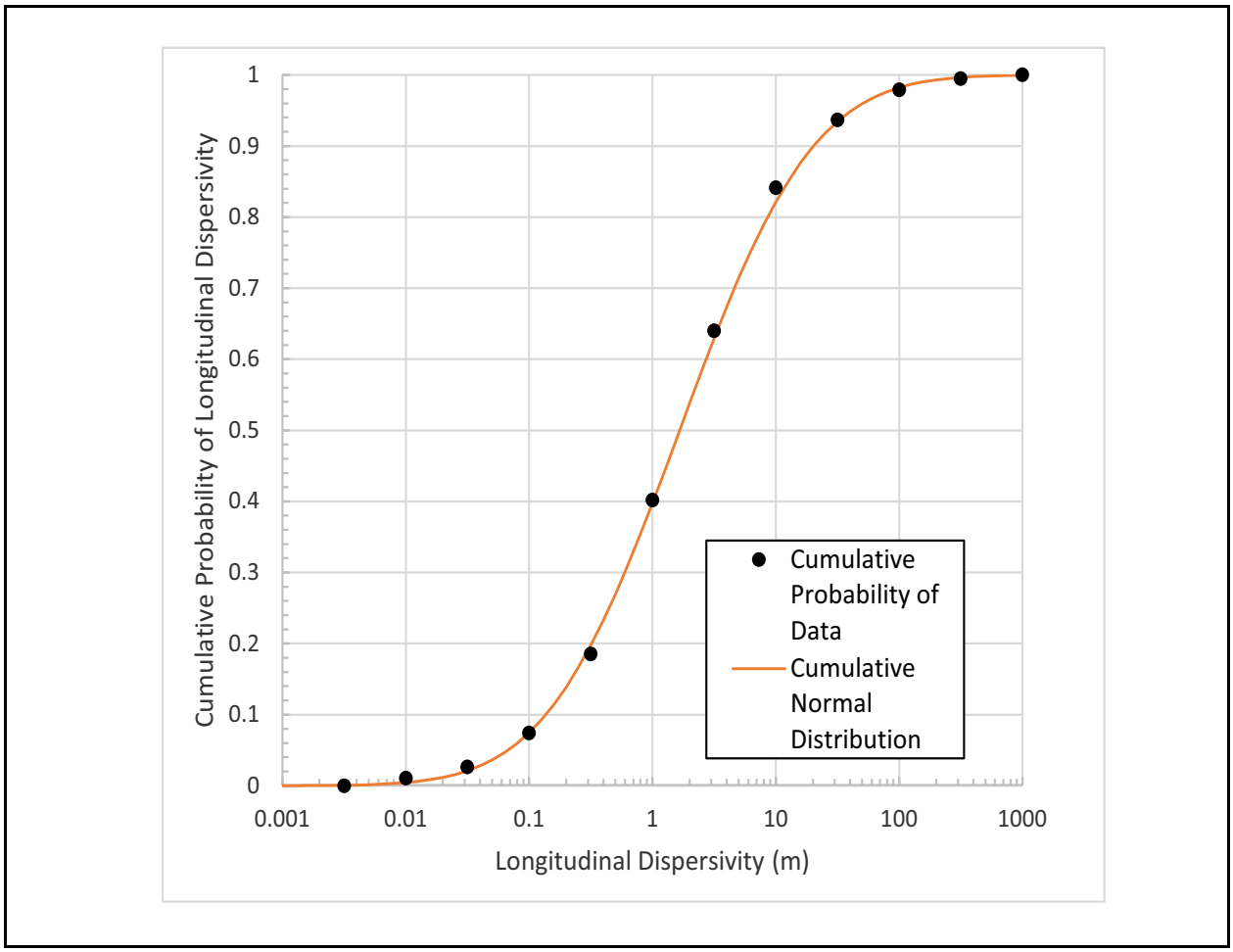

Figure 5-29
Cumulative Probability Distribution of Longitudinal Dispersivity

5.7.4.3 Summary of Observations from Dispersivity Dataset Assessment

Several important observations related to the evaluation of dispersivity data in the literature were summarized in SNJV (2004c, 2005a, and 2007) and SNJV (2008) based on the available information. The major observations are as follows:

- Longitudinal dispersivity apparently increases with scale (distance from the contaminant source or the spacing between tracer-injection and monitoring wells).

- The ratio of longitudinal dispersivity to transverse horizontal dispersivity is generally in the range of 2 to 100, and the ratio of longitudinal dispersivity to transverse vertical dispersivity is generally in the range of 10 to 1,000. The transverse vertical dispersivity is typically one to two orders of magnitude smaller than the transverse horizontal dispersivity.

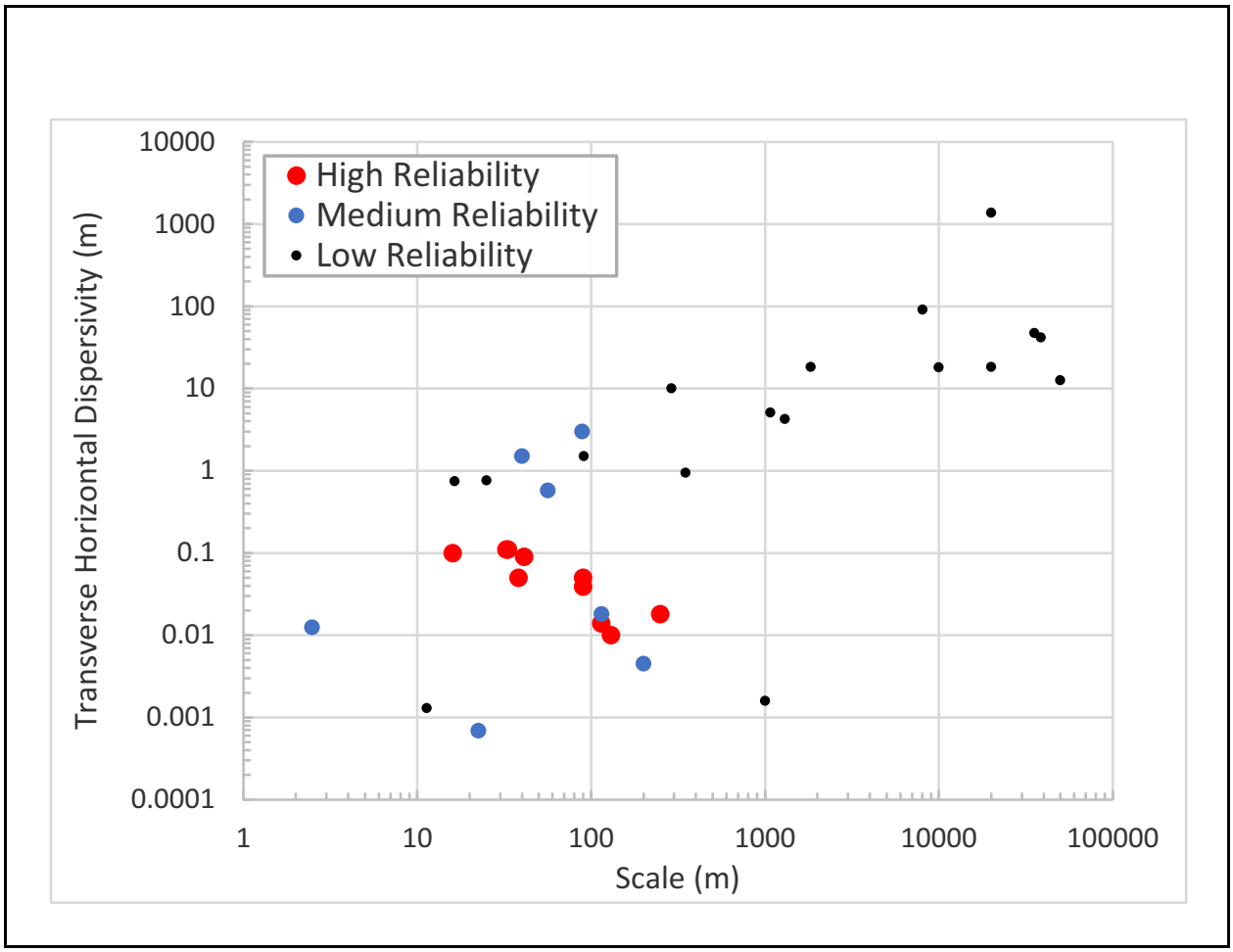

Figure 5-30
Transverse Horizontal Dispersivity as a Function of Transport Scale

- As the density of information on hydraulic conductivity increases, the effect of dispersivity increasing with scale may be reduced. Dispersivity accounts for unmeasured and unspecified variability in the variations in hydraulic properties within the PM CAU flow and transport model. As more of the variability is modeled explicitly, the appropriate dispersivity becomes smaller in magnitude.

- Whether the geologic media is porous or fractured appears to have no significant effect on dispersivity. In other words, dispersivities used for porous media can also be used in fractured media at similar scales.

- The longitudinal dispersivity data from NNSS and vicinity studies fall within the range of values published in the scientific literature for other locations.

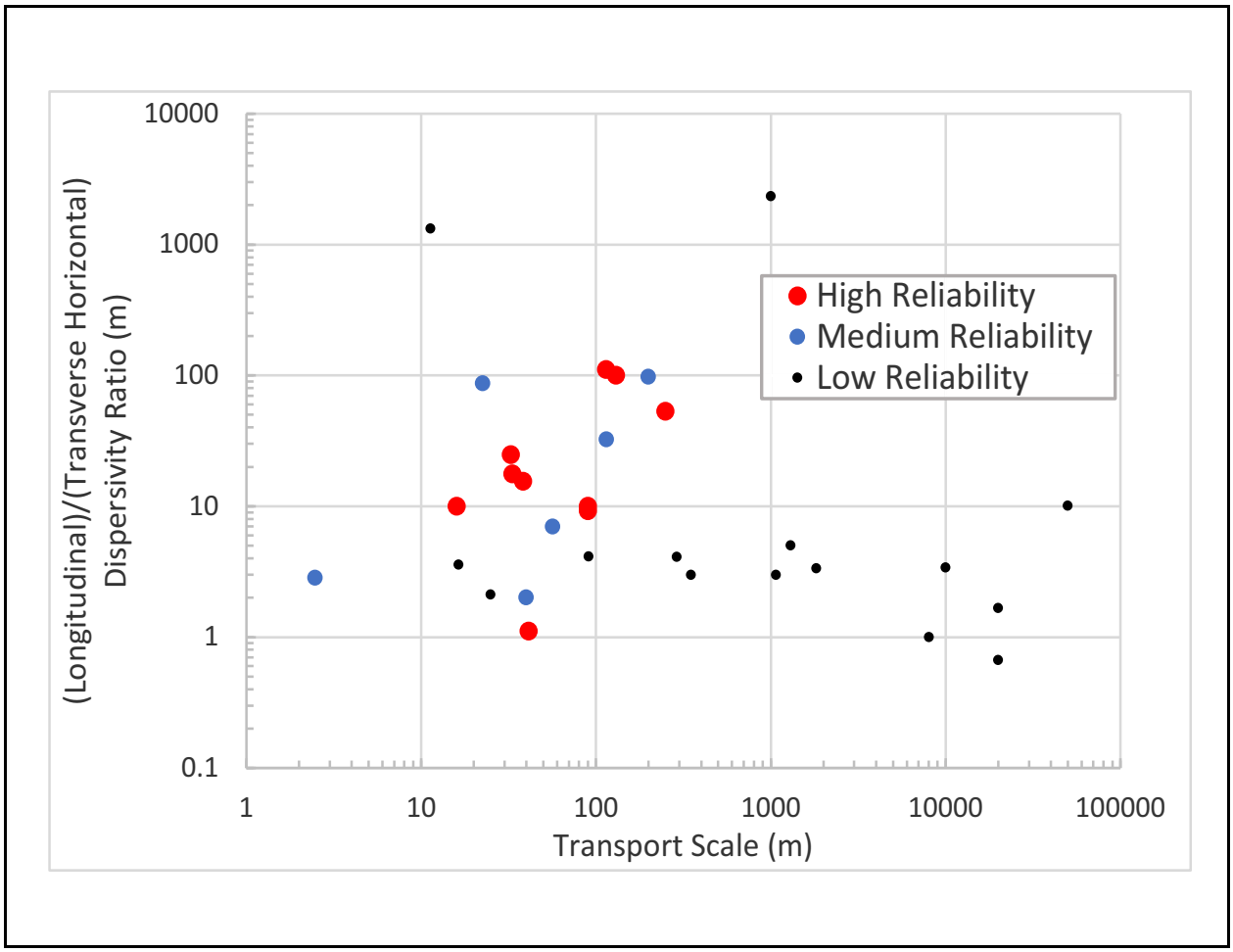

Figure 5-31
Ratio of Longitudinal to Transverse Horizontal Dispersivity as a Function of Transport Scale

5.7.5 Evaluation of Scale Dependency of Dispersivity

The scientific literature documents that longitudinal dispersivity representative of field conditions typically increases with the scale of measurement (Lallemand-Barres and Peaudecerf, 1978; Pickens and Grisak, 1981a and b; Gelhar et al., 1992; Neuman, 1990 and 1995; Neuman and Di Federico, 2003; Schulze-Makuch, 2005; and Xu and Eckstein, 1995). Based on the available data, researchers have developed a number of power-law type relationships between longitudinal dispersivity and log or log-log of the transport scale. SNJV (2008) explores five relationships with respect to the data considered here: log-log linear, log-log piece linear, log-log quadratic, log-log asymptotic, and log-log(log) linear. They conclude that all five of these relationships fit the data reasonably well. HGL (2018a) has suggested the use of an asymptotic relationship that caps the maximum value of the dispersivity for scales exceeding a specified value, although they recognize that existing data are

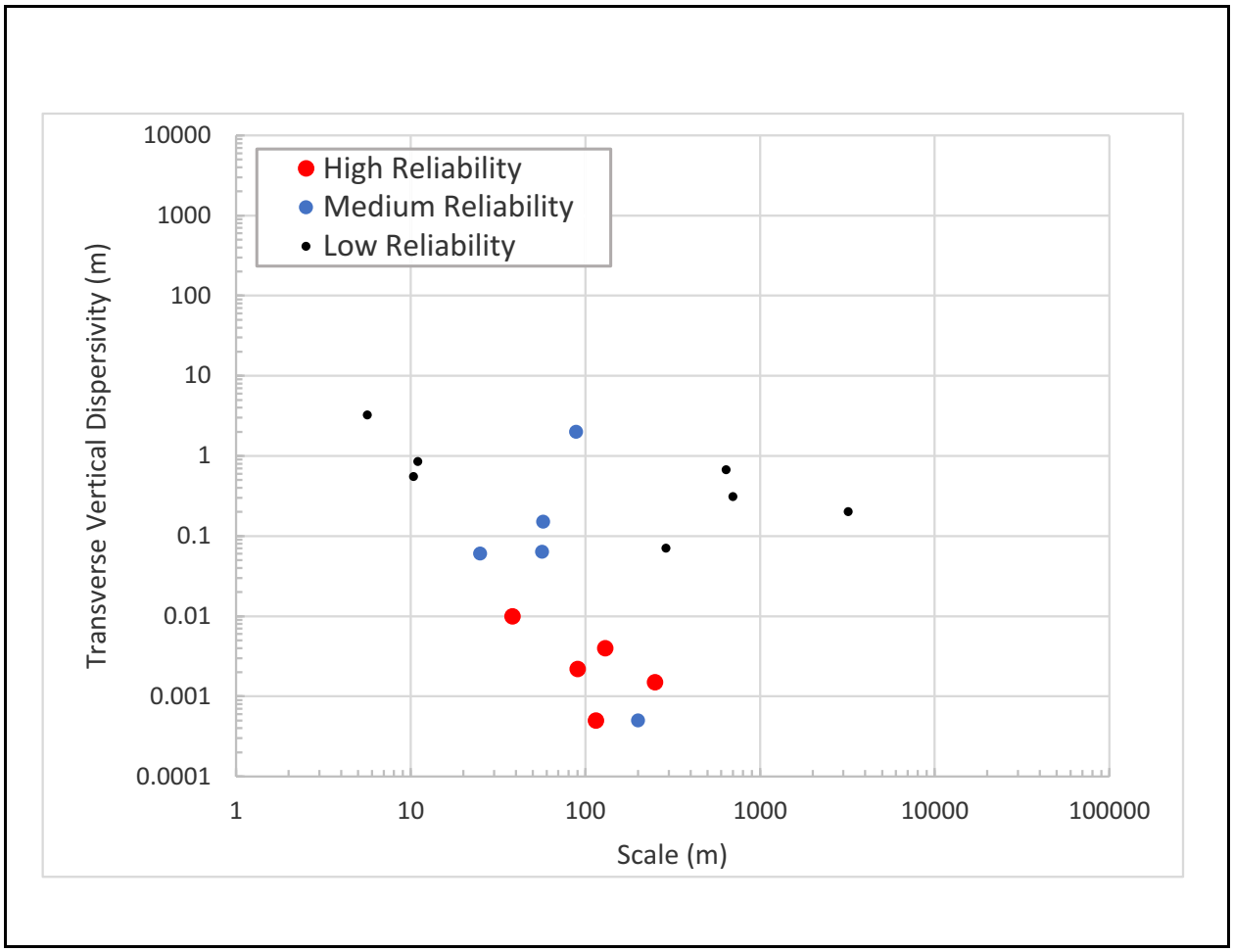

Figure 5-32
Transverse Vertical Dispersivity as a Function of Transport Scale

inconclusive; they recommend an asymptotic value of longitudinal dispersivity of ~110 m for scales greater than 1 to 10 km for the dataset under consideration.

DFN modeling using fracture networks obtained using statistical parameters based on data for the TSA, LFA, and TCA at PM (Makedonska et al., 2020) provide insights regarding dispersivity distributions for scales up to 250 m. They show that the ratio of the longitudinal dispersivity in the horizontal direction to the scale of the model has a mean between 0.09 to 0.24 with a standard deviation between 0.012 to 0.20. This is not inconsistent with the generally used value of 0.1 (e.g., Neuman, 1990; and Gelhar et al., 1992)

Considering the upper range of values for dispersivity, available NNSS data are for scales <130 m with dispersivities less than 31 m; all of the available data with high and intermediate reliability (Gelhar, 1992) have dispersivity values less than 100m (Figure 5-27), although a few low-reliability

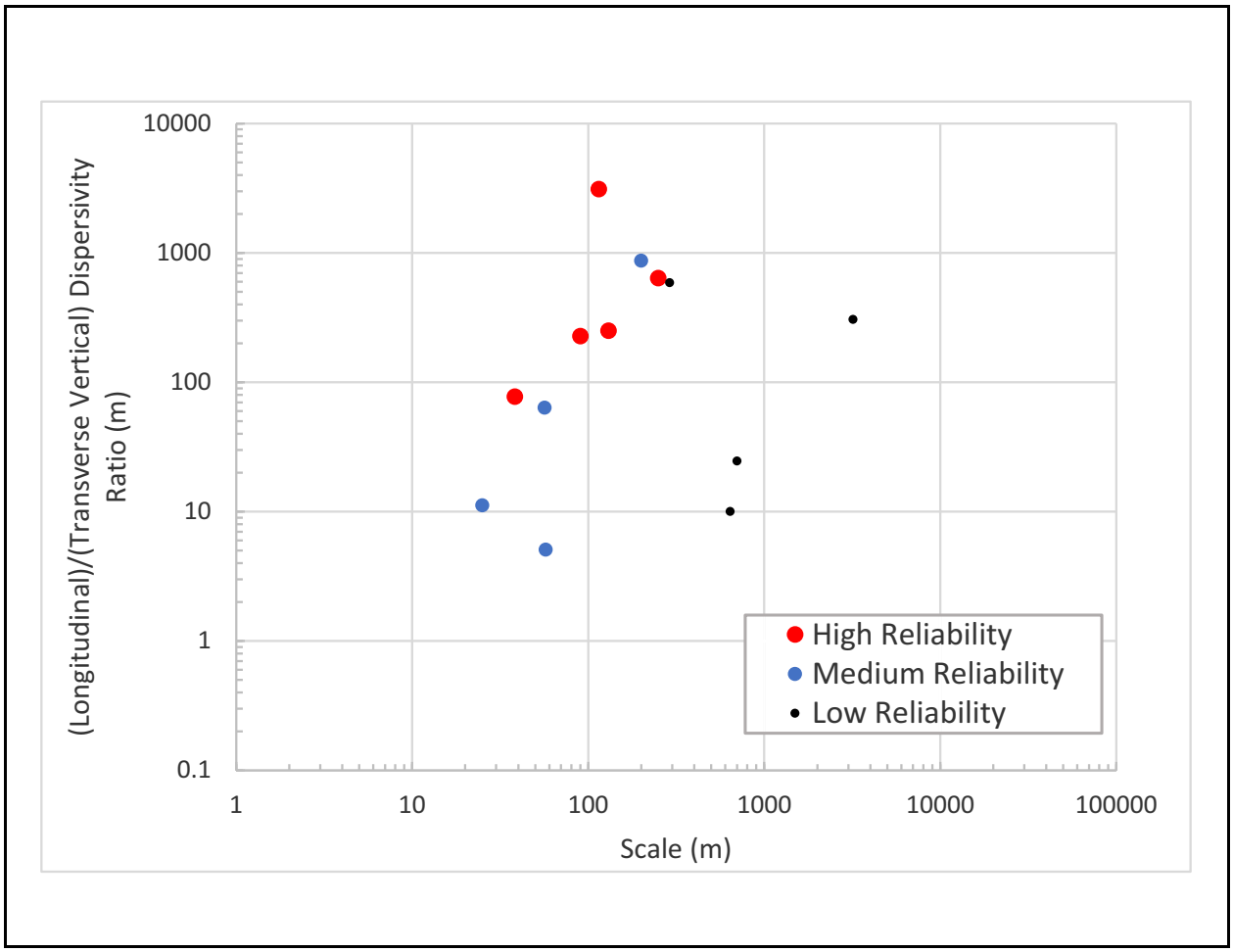

Figure 5-33
Ratio of Longitudinal to Transverse Vertical Dispersivity as a Function of Transport Scale

data do fall between 100 m and 200 m for dispersivity values corresponding to scales ranging from ~500 to ~40,000 m; and only one low-reliability point for a scale of ~20,000 m goes up to a dispersivity value of ~1 km. Hence, 200 m is recommended to be the upper limit of longitudinal dispersivity for the PM CAU transport model. Considering the lower range of values seen in Figure 5-27, the lowest value for scale ~100 m is seen to be around 0.23 m. All dispersivity values are above 1 m for scales above ~300 m. Hence, 1 m is recommended to be the minimum value of longitudinal dispersivity for the PM CAU transport model.

5.7.6 Data Limitations

Dispersivity is not an intrinsic property of the medium in the way that porosity and hydraulic conductivity are thought to be. To have a basis for predicting dispersivity from statistical

distributions, its dependence on the scale of the measurement and on the type of test and method of analysis must be known. The data available from the NNSS area are scarce and mostly consist of quantitative values for longitudinal dispersivity. None of the NNSS tracer tests produced good estimates of transverse dispersivities. The trends in dispersivity with transport distance are compiled from data obtained from locations around the world. As a result, the appropriate longitudinal dispersivity to apply at large scales for the PM CAU transport model has uncertainty associated with the range, statistical distribution, and spatial variability of data.

5.7.7 Summary

As presented in this section, dispersivity values determined from analysis of transport are scale-dependent. The value selected for dispersivity is somewhat dependent on the degree to which the heterogeneity of the groundwater system is defined in the PM CAU transport model. Because of the large areal and vertical extent, the complex hydrostratigraphic and faulted nature, and the relatively sparse well data for heads and hydraulic properties for calibrating the groundwater flow model within the PM CAU, the calibrated PM CAU flow model will likely be only moderately constrained. Dispersivity is a modeling parameter that accounts for unmeasured and unspecified variability in the hydraulic properties within the PM CAU flow and transport model domain. As more of the variability of the groundwater flow regime is modeled explicitly, the appropriate dispersivity to use becomes smaller in magnitude.

For longitudinal dispersivity, following the discussion presented in Section 5.7.5, 200 m is recommended as the upper limit of longitudinal dispersivity for the PM CAU model and 1 m is recommended to be the minimum value of longitudinal dispersivity for the PM CAU model. It is recommended that transverse horizontal and vertical dispersivities be selected based on a ratio of longitudinal to transverse horizontal dispersivity of about 1 to 10 and a ratio of longitudinal to transverse vertical dispersivity of about 1 to 100. The transverse vertical dispersivity is typically one to two orders of magnitude smaller than the transverse horizontal dispersivity.

5.8 Matrix Diffusion

This section describes the role of matrix diffusion in contaminant transport in groundwater, the available data from matrix diffusion experiments, analysis of these data, and the associated results. The objective is to use the data from the NNSS and the scientific literature to develop matrix

diffusion coefficient distributions for use in the PM CAU flow and transport model. Diffusion of solutes occurs in all porous rocks encountered by the groundwater; however, its effect on solute transport becomes more pronounced in regions containing flowing fluids in contact with stagnant or slower-moving fluids. Matrix diffusion coefficients for solutes in a porous medium are smaller in magnitude than free water diffusion coefficients because solutes must diffuse through the tortuous pore space accessible to the pore fluids. Ratio of matrix diffusion to free water diffusion coefficients is defined as the tortuosity.

5.8.1 Role of Matrix Diffusion

Matrix diffusion is typically associated with systems in which flow is predominantly in high-conductivity features such as fractures, while the porous rock matrix surrounding the fractures contains significant quantities of stagnant fluid in diffusive communication with the flowing features. Transport of RNs and other contaminants in saturated fractured rock can be strongly retarded by matrix diffusion. Diffusive mass transfer occurs also in media not dominated by fracture flow, such as alluvium or nonwelded tuffs, by diffusion between the more permeable zones and lower-permeability zones. Diffusion, however, is expected to be less important in such media because the ratio of stagnant to flowing water volume is usually much smaller and the permeability contrast is less severe than in fracture-dominated media.

The importance of the diffusion of solutes from fractures into the adjacent matrix has been studied and reported extensively in the literature and has been established as an important process for retarding the transport of solutes introduced into fractured geologic systems. Numerical models and analytical solutions presenting analyses of the effect of matrix diffusion during transport in fractured geologic media have been reported in the literature, e.g., Neretnieks (1980), Grisak and Pickens (1980 and 1981), Tang et al. (1981), Noorishad and Mehran (1982), and Huyakorn et al. (1983a and b). Laboratory experiments addressing double-porosity transport with matrix diffusion for fractured media have been discussed by Grisak et al. (1980), Grisak and Pickens (1981), Neretnieks et al. (1982), Moreno et al. (1985), Hershey et al. (2003), and Reimus et al. (2006b and c); and for field tracer tests by Jones et al. (1992), Novakowski and Lapcevic (1994), IT (1998), Reimus and Haga (1999), and Reimus et al. (1999 and 2003b).

5.8.1.1 Diffusion Process and Tortuosity

The molecular diffusion conceptualization is based on Fick's second law of diffusion (Crank, 1975) which, for a 1-D system in a porous medium, may be expressed as

$$\frac{\partial C}{\partial t} = D_m \frac{\partial^2 C}{\partial Z^2} \qquad (5\text{-}10)$$

where

C = species concentration (M/L^3)
D_m = effective matrix diffusion coefficient for solutes in the pores (L^2/T)
z = coordinate position (L)
t = time (T)

This form of Fick's second law is seen in many standard hydrogeology texts, including Bear (1972) and Freeze and Cherry (1979). The diffusion in the porous medium is restricted compared to free water because of the presence of the solid phase. The ratio of matrix diffusion coefficient in porous media (D_m) to the free water diffusion coefficient of the solute (D_o). is defined as the tortuosity (τ). Several definitions of tortuosity can be found in literature; this work uses the definition given in Bear (1972):

$$D_m = \tau * D_o \qquad (5\text{-}11)$$

Tortuosity can be defined as a bulk measure of the constrictivity and tortuous nature of the interconnected pore space through which diffusion is occurring. Tortuosity ranges from zero for material with zero porosity (zero pore space) to 1 for material with porosity of 1 (i.e., free water). Smaller tortuosities are indicative of longer diffusional path lengths and greater resistance to diffusion through the medium. Bear (1972) states:

$$\tau = (L/L_e)^2 \qquad (5\text{-}12)$$

where

L = straight-line path length
L_e = actual tortuous path length that a particle would take passing through a sample of length L

Freeze and Cherry (1979) state typical laboratory values for tortuosity range up to 0.5. De Marsily (1986) provides an upper limit of 0.7 for sands. Bear (1972) provides a review and gives an upper bounding value of 0.8 for L/L_e, which would correspond to τ equal to 0.64.

5.8.2 Data Compilation

Free Water Diffusion coefficients: Sources in the literature, including Lerman (1979), Drever (1988), Mills and Lobo (1989), and Newman (1991), provide free water diffusion coefficients for various species. For RNs where free water diffusion coefficients are not readily available in the literature, they can be calculated using the Nernst or Stokes-Einstein equations (Lerman, 1979; Mills and Lobo, 1989). Free water diffusion coefficient is discussed further in Section 5.8.4.1.

Matrix diffusion coefficient: Diffusion data compiled for the RM/SM CAU (SNJV, 2008) augmented by more recent data from Telfeyen et al. (2018). Data from the PM HFM area were supplemented by data from other NNSS CAUs, YMP, and some literature values from other locations for this analysis due to the unavailability of comprehensive data from the PM HFM area for all HGUs. Key data sources are listed in Table 5-23. This topic is discussed further in Section 5.8.4.2.

5.8.3 Data Types and Sources

Matrix diffusion coefficients are determined both in laboratories and in the field. A brief summary is given below.

5.8.3.1 Laboratory Scale

Laboratory estimates of effective matrix diffusion coefficients are traditionally obtained using "diffusion cell" experiments that employ through-diffusion or outward-diffusion using a rock core sample. In the through-diffusion method, a reservoir containing the tracer of interest is separated from a receiving reservoir by a rock sample of known thickness and cross-sectional area and the concentration change of the receiving reservoir is monitored through time. In the outward-diffusion method, diffusion of a tracer out of a rock sample saturated with tracer solution into an initially tracer-free reservoir in which the sample is immersed provides a cheaper, quicker, and simpler alternative because this method does not require the use of a specialized diffusion cell, and it permits diffusion out of both sides of the rock core, expediting the tracer breakthrough times. A study by Telfeyan et al. (2018) compared the merits of these two methods and concluded that they provide similar results. Diffusion cell experiments have been conducted using core collected from boreholes in the PM (Papelis and Um, 2003a; Reimus and Callahan, 2007; Reimus et al., 1999 and 2007, Telfeyan et al. 2018), YF/CM (Reimus et al., 2006c), RM/SM (Walter, 1982), and Frenchman Flat (Papelis and Um, 2003b) CAUs.

Table 5-23
Key Diffusion Data Sources

Author	Year	Field	Laboratory	Description
Callahan et al.	2000			fracture-matrix interaction and dispersion of nonreactive solutes in saturated volcanic rock
Gustavsson and Gunarsson	2005		X	Oskarshamn Lab data on transport properties of rock, Sweden
Hershey et al.	2003		X	diffusion of 14C into NTS CA matrix
Jakob	2004			matrix diffusion for performance assessment, crystalline rock, Switzerland
Maruzek and Jacob	2002		X	Matrix diffusion in non-NTS granitic rock, Sweden
Papelis and Um	2003a		X	cesium, strontium, and lead sorption, desorption, and diffusion in cores from western PM
Papelis and Um	2003b		X	cesium, strontium, and lead sorption, desorption, and diffusion in volcanic tuffs from Frenchman Flat
Reimus and Callahan	2007	X	X	matrix diffusion in fractured volcanic rock at NTS, field and lab
Reimus et al.	2002		X	diffusive and advective transport of ^{3}H, ^{14}C, and ^{99}Tc in saturated, fractured volcanic rocks from PM
Reimus et al.	2006c		X	tracer transport properties in LCA of Yucca Flat
Reimus et al.	2007		X	matrix diffusion coefficients in volcanic rocks at NTS
Reimus et al.	1999a		X	laboratory experiments to support interpretation of the BULLION FGE: update report, draft 4/5/99, 7403 C.2 UGTA
Skagius and Neretnieks	1986		X	porosities and diffusivities of some nonsorbing species in crystalline rocks, Sweden
Telfeyan et al.	2018		X	matrix diffusion coefficients for transport modeling (volcanic tuff from PM)
Triay et al.	1997		X	RN retardation for YMP
Walter	1982		X	matrix diffusion, fractured tuffs from the NTS
Ware et al.	2005		X	radionuclide sorption and transport in fractured rocks of Yucca Flat
Zavarin et al.	2005		X	radionuclide transport in tuff and carbonate fractures form Yucca Flat
Zavarin et al.	2007		X	radionuclide transport experiments in fractured tuff and carbonate rocks from Yucca Flat
Zavarin et al.	2013		X	Colloid-facilitated transport in fractured carbonate rock from Yucca Flat
IT Corporation	1998	X		report and analysis of BULLION FGE
Reimus and Haga	1999	X		tracer response at BULLION FGE, Pahute Mesa, NV.
Reimus et al.	1999	X	X	hydraulic and tracer testing of C-holes, YMP, field and laboratory tests
Reimus et al.	2003b	X		conceptual solute transport model in saturated fractured tuff using tracers in cross-hole tracer tests
Reimus and Callahan	2007	X	X	matrix diffusion in fractured volcanic rock at the NTS, field and lab

Another approach for determining matrix diffusion coefficients consists of fracture core experiments to measure solute transport along a fracture and solute diffusion into the matrix. For these experiments, the transport mechanisms include advective transport of the solute along the fracture and diffusion of the solute from the fracture into the matrix. Fracture core experiments have been conducted on core collected from boreholes in PM (Reimus, 2002; Reimus et al., 1999; Reimus and Callahan, 2007), and Yucca Flat (Reimus et al., 2006c; Zavarin et al., 2005, 2007, and 2013) CAUs. Mass transfer coefficients (from which matrix diffusion coefficients were estimated) have been measured directly in tracer transport experiments in fracture cores in the laboratory (Reimus et al., 2002 and 1999).

Laboratory Data Sources

The matrix diffusion coefficients derived from laboratory experiments were obtained from different references listed in Table 5-23, inclusive of matrix diffusion coefficient databases developed for Yucca Flat (SNJV, 2007), PM (Shaw, 2003), and Frenchman Flat (SNJV, 2005a). A wide range of data and information from these experiments (e.g., sample location, lithology, temperature, depth, mineralogy, tracer species, matrix diffusion coefficient, tortuosity, author comments on experiment quality and results, porosity, permeability) were available. The reported results from the experiments were from NNSS and YMP rock samples, and 10 granite/crystalline measurements from non-NNSS rock. The latter were included for consideration because laboratory diffusion cell experimental measurements are not available for crystalline rock using NNSS source rocks.

Discussion of Laboratory Data

Diffusion Cell Data

The diffusion cell experiments consisted of the diffusion of solute either through, into, or out of a rock sample. In diffusion cell experiments, the only transport mechanism for the solute was matrix diffusion. Several of the experiments consisted of a sample wafer or slab placed between a reservoir containing traced solution and a reservoir containing untraced solution. For these experiments, solute moved from the reservoir containing the traced fluid to the reservoir containing the untraced fluid via diffusion through the sample. Some of the apparatus were oriented horizontally, so matrix diffusion occurred in the horizontal direction, and some were oriented vertically, so matrix diffusion occurred in the vertical direction. For all of these experiments, diffusion was through the sample. For two of the experimental setups, a tracer-saturated sample was placed in a reservoir filled with untraced fluid. For these experiments, diffusion was out of the sample. Diffusion cell experiments have been

conducted using core collected from boreholes in the PM, YF/CM, Frenchman Flat, and RM/SM CAUs. Details of the experimental methods are provided in Reimus et al. (2002), and Reimus et al. (2007).

The tracers used in the diffusion cell experiments varied from researcher to researcher. For many experiments, the researchers used both conservative and nonconservative tracers. For this report, only data based on conservative tracers were considered.

As the matrix diffusion coefficients were determined using different tracers, the matrix diffusion coefficients from different tests are normalized with respective free-water molecular diffusion coefficients. As discussed in Section 5.8.1.1, the ratio of the effective matrix diffusion coefficient to the corresponding free-water is equal to tortuosity. In porous media, tortuosity varies with porosity. Tortuosity data for core samples from the PM and the entire NNSS area are plotted in Figure 5-34 against porosity. A comparison between the PM data and those from all the NNSS areas suggests that the two datasets are very similar. Of note in these figures is that the tortuosity data show considerable scatter, by nearly two orders of magnitude, for any given value of porosity. The data appear to present several vertical columns in these figures, These columns represent samples derived from cores from the same depth interval and the same porosity measured for that depth interval; indicating that the degree of local heterogeneity may be within two orders of magnitude.

To investigate whether the data agreed with a lognormal distribution, the data were divided into four porosity intervals (HGL, 2018a). For each interval the following were determined: log(tortuosity): mean and standard deviation, 95 percent confidence interval for the mean, and 95 percent confidence interval for the data within the interval. Statistical results are shown in Tables 5-24 and 5-25 for PM and for the NNSS area. A lognormality test was performed by HGL (2018a) for each interval using the data available. Using the standard Chi-Square test with the 95 percent confidence criterion, the data for all intervals were determined to be consistent with a lognormal distribution.

Fracture Core Data

The fracture core experiments consisted of solute transport along a fracture and solute diffusion into the matrix. For each experiment, the sample consisted of a length of core containing a single fracture. The fracture was a natural fracture for most of the samples. A fracture was induced in a piece of unfractured core by striking the core with a hammer and chisel for a few samples, and a synthetic

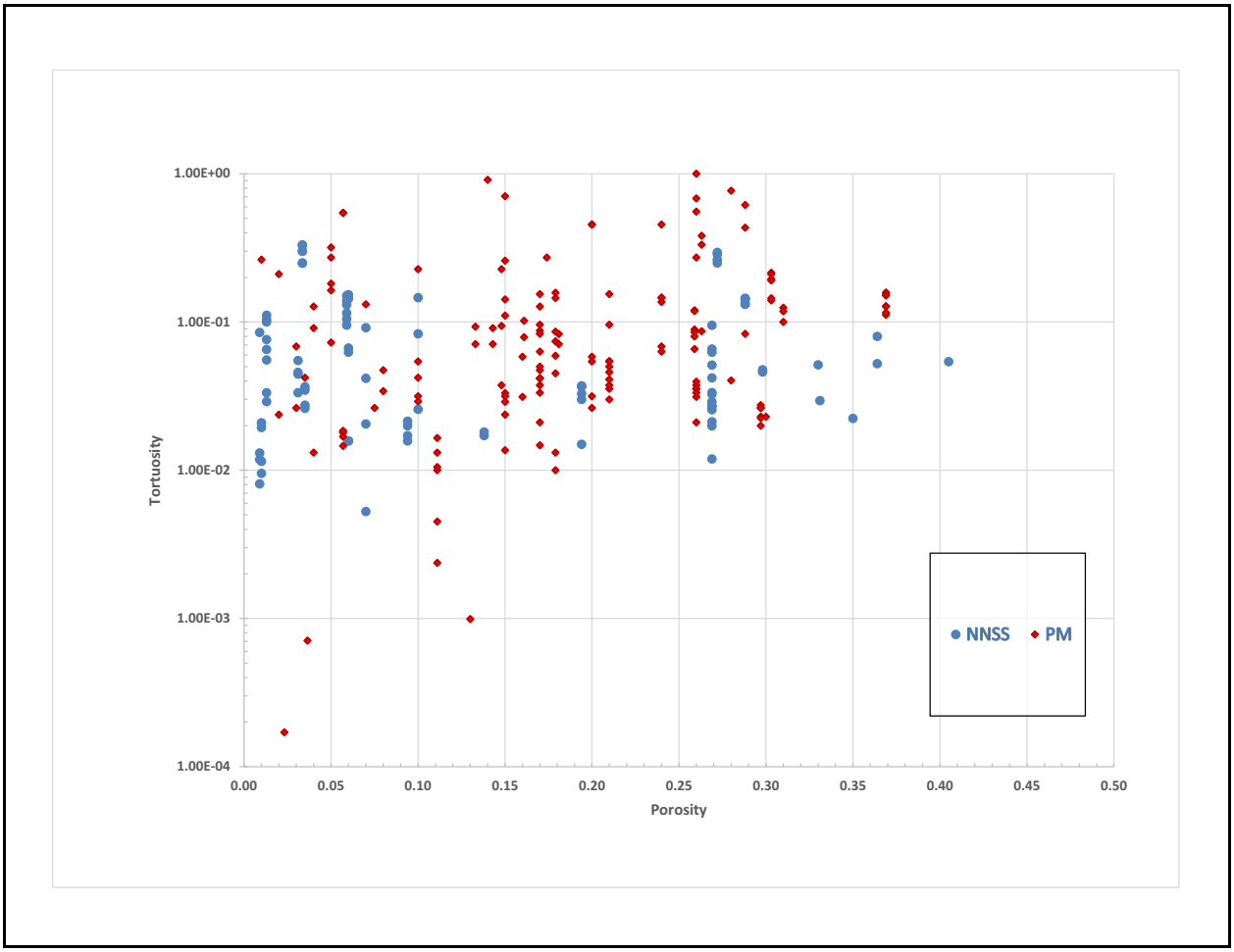

Figure 5-34
Diffusion Cell Tortuosity Data for PM and NNSS

Table 5-24
Pahute Mesa Diffusion Cell Data

Parameter		Parameter Values				
Porosity Range		***0.001 - 0.060***	***0.060 - 0.200***	***0.201-0.300***	***0.301 - 0.405***	***0.001-0.405***
Statistics log_{10} (tortuosity)	Mean	-1.199	-1.318	-1.138	-0.971	-1.196
	Std. Dev	0.485	0.452	0.438	0.259	0.455
Mean Conf. Int. (log_{10})	Low	-1.319	-1.417	-1.239	-1.077	-1.255
	High	-1.080	-1.218	-1.037	-0.865	-1.137
Data Conf. Int. (log_{10})	Low	-2.150	-2.203	-1.996	-1.478	-2.088
	High	-0.249	-0.432	-0.279	-0.464	-0.304
Distribution		Lognormal	Lognormal	Lognormal	Lognormal	Lognormal

Source: HGL, 2018a

Table 5-25
All NNSS Diffusion Cell Data

Parameter		Parameter Values				
Porosity Range		*0.001 - 0.060*	*0.060 - 0.200*	*0.201-0.300*	*0.301 - 0.405*	*0.001-0.405*
Statistics log_{10} (tortuosity)	Mean	-1.246	-1.367	-1.098	-0.971	-1.214
	Std. Dev	0.642	0.513	0.498	0.259	0.549
Mean Conf. Int. (log_{10})	Low	-1.401	-1.478	-1.211	-1.077	-1.284
	High	-1.091	-1.256	-0.984	-0.865	-1.145
Data Conf. Int. (log_{10})	Low	-2.504	-2.371	-2.074	-1.478	-2.290
	High	0.012	-0.362	-0.121	-0.464	-0.139
Distribution		Lognormal	Lognormal	Lognormal	Lognormal	Lognormal

Source: HGL, 2018a

fracture was machine-cut into an originally unfractured piece of core for a few samples. For each experiment, the sample was saturated with an untraced solution, and then a traced solution was introduced into the sample at one end and collected from the sample at the other end. The orientation of the apparatus was horizontal for some of the experiments and vertical for other experiments. The transport mechanisms for the fracture core experiments were advective transport of the solute through the fracture and diffusion of the solute from the fracture to the matrix. Fracture core experiments have been conducted on core collected from boreholes in the PM and Yucca Flat CAUs. A theoretical basis for the analysis is given by Reimus and Haga (1999). The tracers used in the diffusion cell experiments varied from researcher to researcher. For many experiments, the researchers used both conservative and nonconservative tracers. For this work, only data based on conservative tracers were considered.

Comparison between Different Types of Laboratory Data

Diffusion Cell Tests: Through-Diffusion Method versus Outward Diffusion Method

The data for diffusion cell tests are based on two methods: through-diffusion and outward-diffusion methods. With the through-diffusion method, a reservoir containing the tracer of interest is separated from a receiving reservoir by a rock sample of known thickness and cross-sectional area, and the concentration change of the receiving reservoir is monitored through time (Reimus et al., 2007). However, this method can be expensive, time-consuming, and complex, limiting the number of samples that can be analyzed. The outward-diffusion method, involving the diffusion of a tracer out

of a rock sample saturated with tracer solution into an initially tracer-free reservoir in which the sample is immersed may provide a cheaper, quicker, and simpler alternative because this method does not require the use of a specialized diffusion cell, and it permits diffusion from both sides of the rock core, expediting the tracer breakthrough times. A study by Telfeyan et al. (2018) compared the merits of these two methods and concluded that they provide similar results.

Diffusion Cell Tests Versus Fracture Core Tests

Data are analyzed differently using these two methods. With diffusion cell tests, the only transport process is simple diffusion through rock samples. However, with fracture core tests, there are two parameters from which the matrix diffusion coefficient is derived. These are the mass transfer coefficient and mean residence time (Reimus and Haga, 1999). Because tortuosity values are calculated using two interpreted parameters (i.e., the mass transfer coefficient and the mean residence time), some researchers (HGL, 2018a) have considered them to be more prone to error than the tortuosity values calculated from the diffusion cell experiments.

The univariate PDF for tortuosity, developed using the natural logarithm of all the available Diffusion Cell NNSS data, is shown in Figure 5-35. For the sake of clarity, the figure plots tortuosity on a $\log_{10}$ scale. A lognormal distribution is also shown for the sake of comparison. The median value of this distribution corresponds to tortuosity of about 0.06. A similar plot for the PDF from fracture core experiments is shown in Figure 5-36. The median value of this distribution corresponds to tortuosity of about 0.11. It is seen that the median of the tortuosity from diffusion cell data is smaller that the median tortuosity from fracture core data.

5.8.3.2 Field Scale

Two field tracer tests were conducted at the NNSS: the BULLION FGE at the ER-20-6 Wells Complex, southwest corner of the PM area; and at the C-Wells Complex at YM (see Figure 5-25). For the BULLION experiment, Well ER-20-6 #3 was pumped during the experiment to create a strong gradient from Wells ER-20-6 #1 and ER-20-6 #2. Tracers were injected into Wells ER-20-6 #1 and ER-20-6 #2, and the breakthrough curves of these tracers in Wells ER-20-6 #2 and ER-20-6 #3 were characterized with time-series sampling. A complete explanation of the design, and details of the geology, wells and experiment procedure can be found in IT (1998). The C-Wells Complex cross-hole

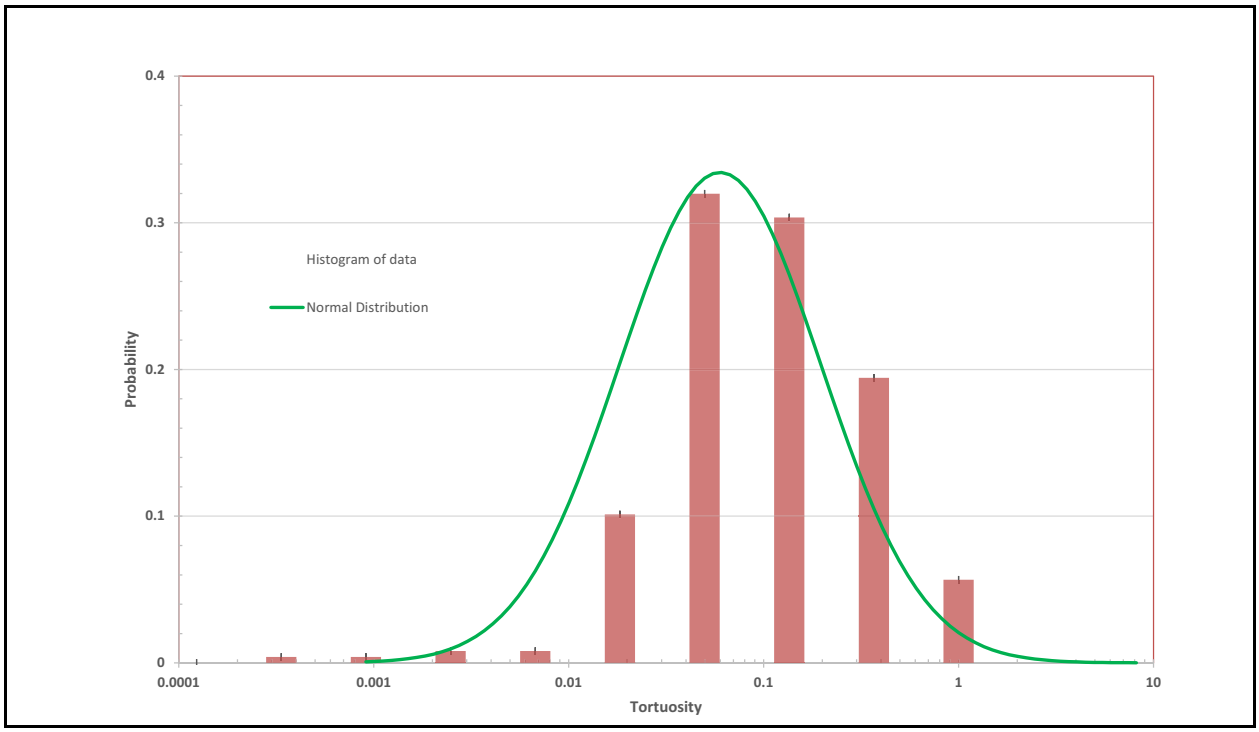

Figure 5-35
Probability Distribution Function of Tortuosity for the NNSS Diffusion Cell Data

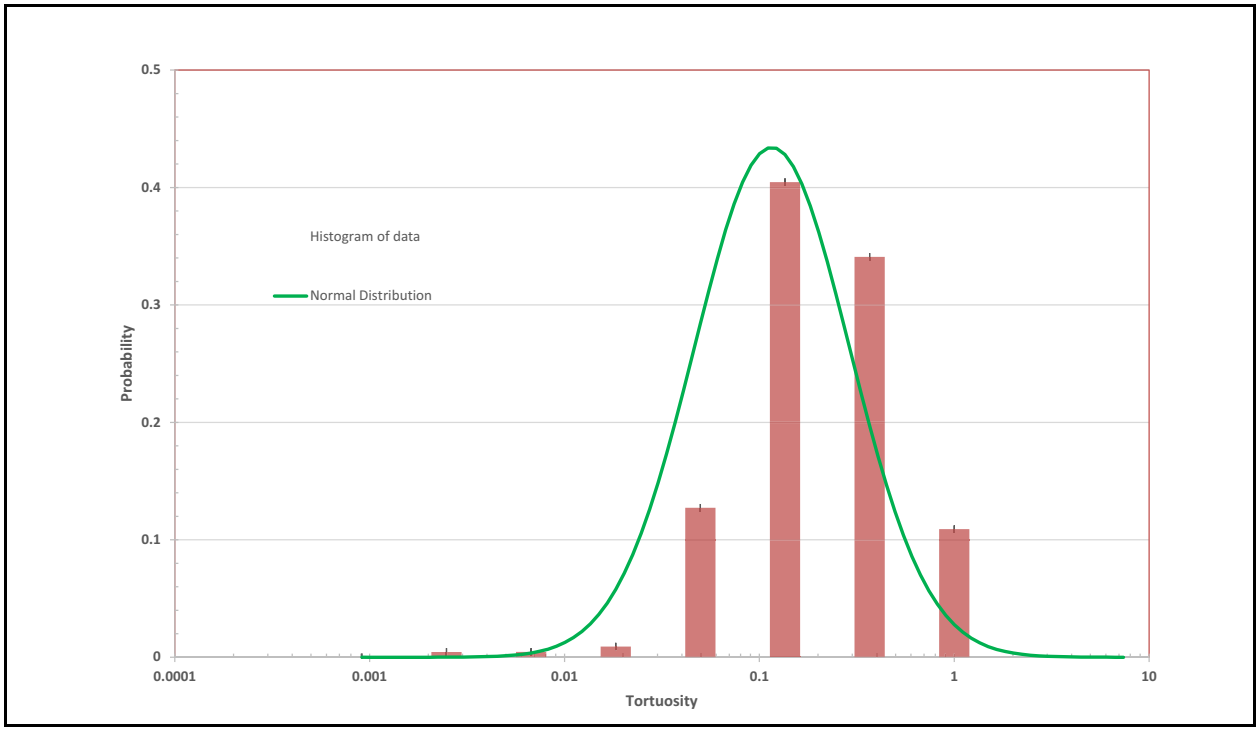

Figure 5-36
Probability Distribution Function of the Fracture Core Tortuosity

tracer tests were conducted at YM between wells C#2 and C#3. Both wells were used alternately as injection and production wells. Details of the tests are given in Reimus et al. (2003b).

Matrix diffusion coefficient estimates were developed based on interpretation of the field tracer tests conducted at the Well ER-20-6 site (IT, 1998; Reimus and Haga, 1999), and at the C-Wells Complex (Reimus et al., 2003b and 2007). Results along with those for laboratory measurements from the same wells are summarized in Table 5-26. An inspection of Table 5-26 indicates that the mass transfer coefficient and matrix diffusion coefficient at the laboratory scale are larger by one to two orders of magnitude than the counterparts at the field scale. Reimus and Callahan (2007) suggested that field-scale aperture could be bigger by one to two orders of magnitude. HGL (2018a) presents another hypothesis that the diffusion coefficient calculated from field tests could be lower due to the reduction of the surface area available for diffusion. They hypothesize that due to flow channelization, the fracture surface area exposed to flow is much smaller than the overall fracture face area, leading to a lower value for the mass transfer coefficient when averaged over the overall fracture surface area.

Table 5-26
Matrix Diffusion Coefficients

Location	Tracer	Mass Transfer Coefficient ($S^{-0.5}$)	Matrix Diffusion Coefficient (cm^2/s)
ER-20-6 Wells			
Laboratory	Iodide	$3\text{-}20 \times 10^{-3}$	$0.09\text{-}4.3 \times 10^{-6}$
	Pentafluorobenzoic acid (PFBA)	N/A	$0.08\text{-}1.45 \times 1\ 0^{-6}$
Field	Iodide	$2.4\text{-}4.9 \times 10^{-4}$	$1.5\text{-}6.0 \times 10^{-8}$
	Pentafluorobenzoic acid (PFBA)	$1.3\text{-}4.2 \times 10^{-4}$	$0.56\text{-}4.4 \times 10^{-8}$
C-Wells Complex			
Laboratory	Bromide	$8.6\text{-}23 \times 10^{-3}$	$0.4\text{-}6.2 \times 10^{-6}$
	Pentafluorobenzoic acid (PFBA)	N/A	$0.35\text{-}2.0 \times 10^{-6}$
Field	Bromide	$2.4\text{-}4.9 \times 10^{-4}$	N/A
	Pentafluorobenzoic acid (PFBA)	$9.5\text{-}15 \times 10^{-4}$	N/A

Sources: HGL, 2018a; Reimus and Haga, 1999; Reimus et al., 2003b and 2007

5.8.4 Data Evaluation

5.8.4.1 Free Water Diffusion Coefficients

The free water diffusion coefficients (D_o) of most species range from 10^{-10} to 10^{-9} m^2/s (Drever, 1988). Free water diffusion coefficients are generally lower for larger molecules or ions with higher charges. A discussion of the various laboratory experimental methods for determining free water diffusion coefficients is presented in Mills and Lobo (1989). Because matrix diffusion coefficients (D_m) are a property of both the rock (through tortuosity) and the tracer species (through D_o), it is important that the best estimates of both are known, particularly when analyzing large sets of measurements from disparate sources. Calculated values of D_m (a property of the rock and the fluid) for any tracer may be determined by multiplying the tortuosity (a property of the rock alone) by the D_o value (a property of the fluid alone). This relationship assumes that the only factor affecting the matrix diffusion coefficient other than porous media properties is the free water diffusion coefficient for the particular tracer species (i.e., no processes other than diffusion are affecting the "apparent" diffusion coefficient [e.g., cation exchange, unaccounted sorption, complexation, anion exclusion, lowering of effective porosity for large molecules excluded from small pores]) and all tracer solutions are dilute (less than 1 molar [M]).

A summary table of the unclassified RN inventory relevant to the PM CAU is provided in Finnegan et al. (2016). Tritium, as hydrogen tritium oxide (HTO), is the RN with the largest free water diffusion coefficient (2.236×10^{-9} m^2/s at 25 °C [Mills, 1973]). The RN with the lowest free water diffusion coefficient is Am (3×10^{-10} m^2/s [DOE/WIPP, 2004]). Thus, these two values bound the range for free water diffusion coefficients for species relevant to the NNSS. It is noted that the approach taken for transport modeling conducted for Frenchman Flat (NNES, 2010), YF/CM (N-I, 2013) and RM/SM (DOE/EMNV, 2018) CAUs was to use a free-water diffusion coefficient of 2.55E-09 m^2/s for RNs with an atomic mass less than or equal to 137, and to use a value of 1.3E-11 m^2/s for plutonium, the only radionuclide of interest with an atomic mass greater than 137.

Several sources, including Lerman (1979), Drever (1988), Mills and Lobo (1989), and Newman (1991) provide free water diffusion coefficients for various species. For RNs where free water diffusion coefficients are not readily available in the literature, they can be calculated using the Nernst or Stokes-Einstein equations (Lerman, 1979; Mills and Lobo, 1989).

The Stokes-Einstein equation predicts that free water diffusion coefficients (D_o) will be directly proportional to absolute temperature and inversely proportional to fluid viscosity, which decreases nonlinearly as temperature increases. Table 5-27 gives the factor by which the D_o increases as a function of temperature in the range or 20 °C to 60 °C.

Table 5-27
Factor by Which Free Water Diffusion Coefficients Change as a Function of Water Temperature

Temperature (°C)	Free Water Diffusion Coefficient Should Be Multiplied by:
20	1
25	1.14
30	1.3
40	1.64
50	2.14
60	2.58

Source: Modified from Shaw, 2003

Within the PM CAU transport model domain, measured temperatures at the water table are generally between 19 °C and 47 °C (SNJV, 2006). As seen from the table, for the PM CAU model, free water diffusion coefficient can be expected to vary by a factor of about 2. This uncertainty will be incorporated in PM CAU transport model when sampling the matrix diffusion coefficients.

Diffusion coefficients are a relatively weak function of ionic strength until ionic strengths become greater than about 1 Molar (M) (Newman, 1991). As ionic strengths greater than 1 M are unlikely to occur at the NNSS (even in cavities), the effect of ionic strength on diffusion coefficients is considered to be relatively minor compared to the effect of rock properties and temperature (SNJV, 2004d). The concentration of the tracer species was not reported in all experiments discussed here; however, when reported, the concentrations were much less than 1 M (SNJV, 2007).

5.8.4.2 Tortuosity and Matrix Diffusion Coefficients

Tortuosity ranges from zero for material with zero porosity (zero pore space) to 1 for material with porosity of 1 (i.e., free water); it is natural to seek a relationship between the matrix porosity and tortuosity. Work on other CAUs at the NNSS has discussed the use of an empirical relationship to

predict tortuosity for a given matrix porosity, since matrix porosity is much more easily measured than the tortuosity. Figure 5-37 shows the available PM diffusion cell data with tortuosity values greater than 0.001 plotted as a function of porosity. As seen in the figure, there is considerable scatter, over a couple of orders of magnitude, in the tortuosity values for a given value of porosity, and the correlation between the two is poor. This finding is consistent with HGL (2018a). Correlation of tortuosity to permeability and porosity together (Reimus et al. 2006b; SNJV, 2007) was found to be somewhat better than that to porosity alone. Including a correlation of tortuosity to permeability is not proposed for PM CAU transport modeling because of the data available for permeability is more limited than the data available for porosity.

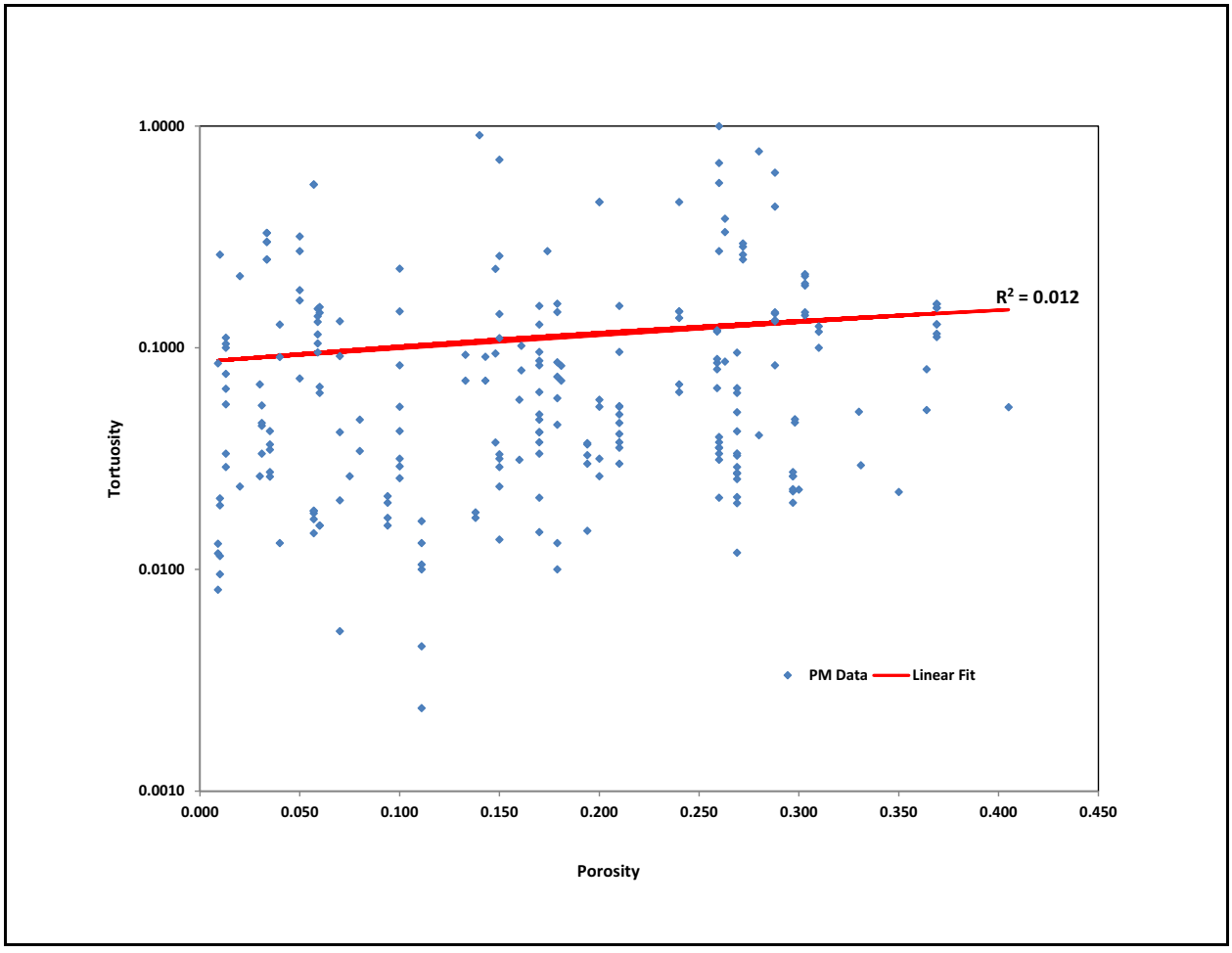

Figure 5-37
PM Diffusion Cell Data versus Porosity

Correlations were examined between tortuosity and a number of hydrogeologic characteristics of the geological formations including HSU designation, degree of welding, degree of alteration, presence

or absence of fractures within the rock samples, and fracture filling/coating (SNJV 2007; HGL, 2018a). It was concluded that definitive correlations could not be ascertained within the available data. However, tortuosity values are computed from porosity and characterized by HGU as reported in SNJV (2008), seen in the box-and-whiskers plot in Figure 5-38, the 5th and 95th percentile values from the data for VTA, TCU and AA lie above 0.1 and those for the WTA lie above 0.02. This observation can help constrain the tortuosity distributions that will be sampled for the CAU transport model.

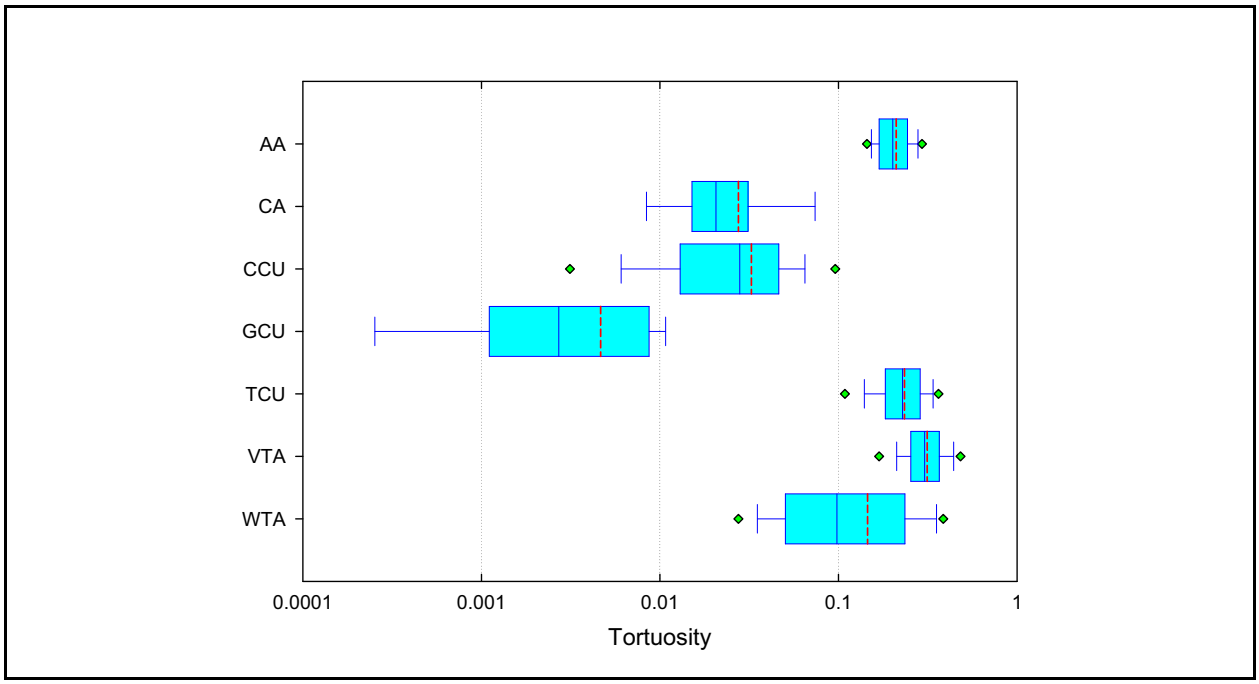

Figure 5-38
Distribution of Tortuosity for NNSS Data
MEAN: Red vertical dashed line; MEDIAN: Blue vertical line in box; 1ST QUARTILE: Left box side; 3RD QUARTILE: Right box side; 10TH PERCENTILE: Left whisker; 90TH PERCENTILE: Right whisker; 5TH PERCENTILE: Left green diamond; 95TH PERCENTILE: Right green diamond
Source: SNJV (2008)

The mean and standard deviation of the natural logarithm of tortuosity data using both the diffusion cell and fractured core techniques, for samples from PM as well as samples from all of NNSS and vicinity, when considered regardless of the hydrogeologic formations, excluding entries with tortuosity greater than 1 or smaller than 0.001, is presented in Table 5-28. The values are seen to be quite similar for the two sets of data. For PM data, this corresponds to a mean value of 0.0860 for tortuosity; and that for all NNSS data corresponds to 0.081 for tortuosity.

Table 5-28
Comparison of Mean and Standard Deviation of ln(T) for PM and All NNSS Samples

	Mean (ln(*T*))	Standard Deviation (ln(*T*))
PM Samples	-2.49	1.18
All NNSS Samples	-2.50	1.12

5.8.5 Scaling Considerations

The CAU transport model is expected to cover distance scales over tens of kilometers, and contain numerical grid blocks with scales ranging from tens of meters to a kilometer; while the available diffusion data is from smaller scales. Hence, scaling considerations are required before relying on the available data for CAU-scale simulations. The available RN observations (Section 3.1.7) will provide constraints on the ranges of values appropriate for field-scale simulations.

Liu et al. (2004) compiled values of effective matrix diffusion coefficients estimated from field tracer tests for a variety of rock types. His analysis demonstrated that the effective matrix diffusion coefficient generally increases with test scale and concluded that simulated travel times may be significantly underestimated when this scale-dependent behavior is not considered. Reimus and Callahan (2007) evaluated scaling considerations in fractured volcanic rocks at the NNSS from matrix diffusion studies from field tracer tests at two locations and laboratory experiments using core samples. The interpreted lumped parameter mass transfer coefficient (includes matrix diffusion coefficient, matrix porosity, and fracture half aperture) appeared to decrease as time and length scales of observation increased. They concluded that this is most likely the result of larger effective apertures as distance increases. HGL (2018a) noted that the values of mass transfer coefficients determined from field data for scales up to a few hundred meters (Reimus and Callahan, 2007) are significantly lower than those determined from laboratory data. They note this could be the result of the scale dependence of the effective surface area accessible to flow and transport. They note that the asymptotic distance at which the mass transfer coefficient would be expected to plateau is currently unknown due to the paucity of data.

Interpretation of field tracer tests to determine matrix diffusion coefficients is inherently uncertain because of factors including non-ideal tracer test operating conditions, heterogeneity of the geologic media being investigated by the tracer test, simplifications in the tracer test interpretation approaches,

and inability to isolate the effect of matrix diffusion alone in the tracer breakthrough response. For these reasons, scale effect for diffusion coefficient is not included in PM CAU transport model.

5.8.6 Data Limitations

This analysis assumes that all nondiffusive processes encountered during matrix diffusion experimental measurements can be neglected or are otherwise explicitly accounted for before matrix diffusion values are reported. Some of the nondiffusive processes that may have affected laboratory diffusion experiments include adsorption, cation exchange, complexation, anion exclusion, lowering of effective porosity for large molecules excluded from small pores, and inadvertent advective transport because of unintentional pressure gradients caused by barometric effects or tracer solution density contrasts. This analysis also assumes that all experimental tracer solutions are dilute (less than 1 M). Multicomponent diffusion effects have not been included in this analysis. The importance of the matrix diffusion coefficient is expected to be greater for transport in fractured media than in alluvial media. Therefore, it will be of more importance in PM CAU transport model realizations where there is significant movement of contaminants in the volcanic aquifers.

5.8.7 Development of Matrix Diffusion Coefficient Distributions

Matrix diffusion coefficient is obtained by multiplying the free water diffusion coefficient by tortuosity. The univariate PDF for natural logarithm of tortuosity developed based on all the available NNSS data excluding entries with tortuosity greater than 1 including both the diffusion cell and fracture core measurements is shown in Figure 5-39, along with a lognormal distribution with the mean ln(Tortuosity) = -2.5043, corresponding to a tortuosity value of ~0.082. The ln(tortuosity) data has a standard deviation of 1.1224, leading to a + or - one standard deviation range of 0.027 to 0.25 in tortuosity.

5.9 Matrix Sorption Parameters

This section includes a description of the matrix sorption process, a review of the available data, and analyses of the data that provide distribution functions. Matrix K_ds are needed to simulate source-term RNs that enter the natural hydrologic systems and react with immobile minerals. The RNs of interest are the sorbing RNs of relevance (Sr, Cs, U and Pu) or potential relevance (Np) to the PM HST as specified in Section 3.1.6.

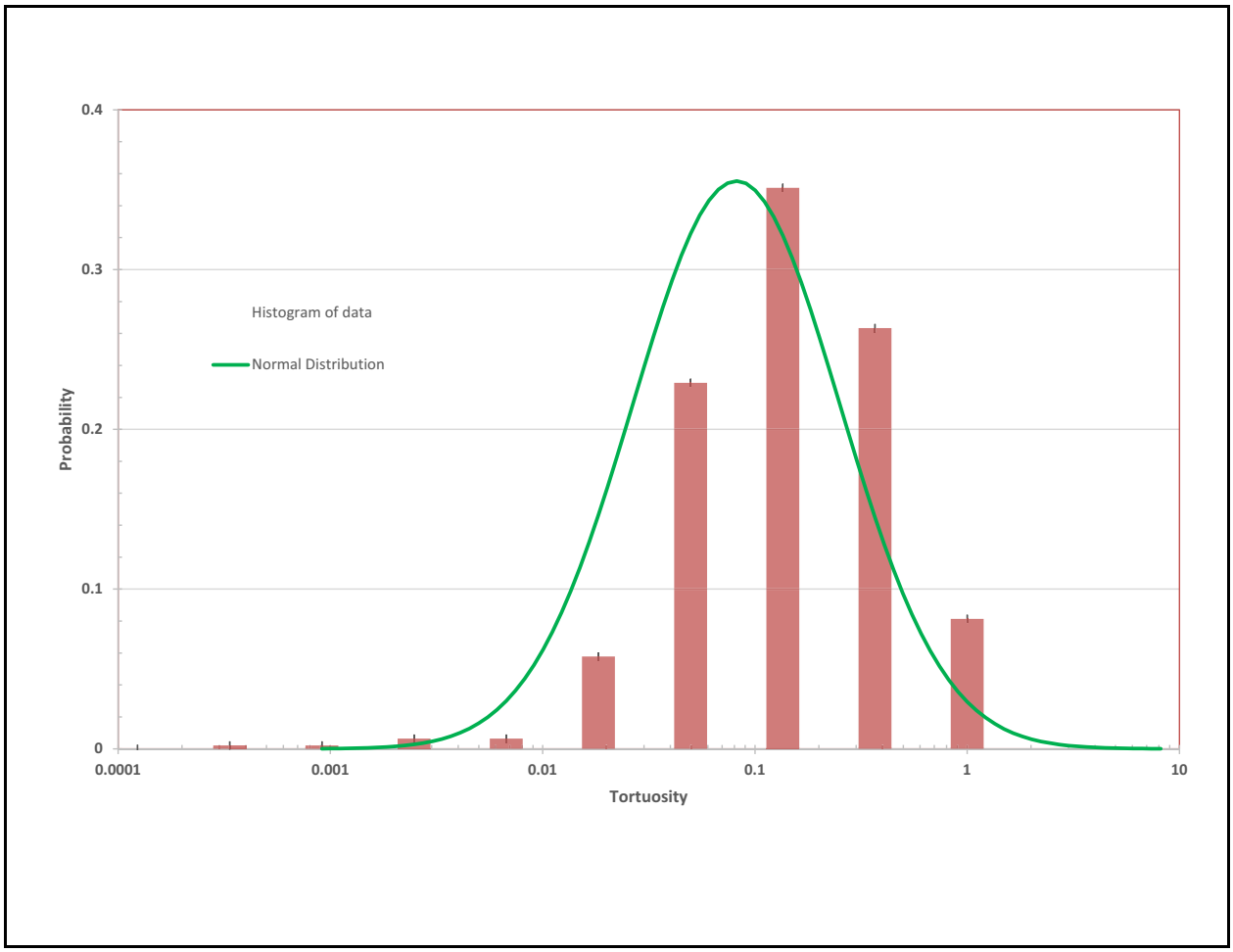

Figure 5-39
Tortuosity Probability Distribution Function for NNSS Data

5.9.1 The Role of Matrix Sorption in Contaminant Transport Models

Matrix sorption is the physiochemical process at mineral-water interfaces that controls solute mobility and, hence, solute retardation within the pore spaces of the immobile rock matrix. Similar physiochemical processes may occur on minerals coating fractures. However, the surface area of the fractures is small compared to that of the matrix. For that reason, sorption to fracture coatings will not be included in the PM CAU transport model.

There are multiple methods for mathematically representing the matrix sorption process in parameterized groundwater transport models. These methods include, but are not limited to (a) mechanistic pore-scale models that represent the sorption process on each immobile mineral grain with thermodynamic relationships for each type of reactive surface, (b) mechanistic complexation and exchange models representing average processes on integrated volumes represented with

discretized continuum models, and (c) isotherms that seek to describe or abstract on a large scale the integrated behavior of the smaller-scale mechanistic processes. An isotherm describes the concentration-dependent partitioning of a chemical species between the solute and liquid phases. For solutes and materials in which this relation is linear, the ratio is a constant known as the linear distribution coefficient, or K_d. Modeling solute transport using K_ds is attractive due to the simplicity with which they are implemented and because the K_ds represent an average behavior over the large volumes likely to be represented in the PM CAU transport model. For the purposes of this document, it is assumed that the matrix sorption parameter for use in the PM CAU transport model is the K_d.

The distribution coefficient K_d provides a relatively simple method for simulating retardation due to equilibrium sorption with immobile minerals. The K_d value is simply defined as

$$K_d = \frac{\textit{Moles of solute per gram of solid phase}}{\textit{Moles of solute per milliliter of solution}} \qquad (5\text{-}13)$$

Assumptions implicit with the use of K_d include (1) only trace amounts of contaminants exist in the aqueous and solid phases, (2) the relationship between the RN activity in the solid and liquid phases is linear, (3) equilibrium conditions exist, (4) equally rapid adsorption and desorption kinetics exist, (5) it describes contaminant partitioning between one RN and one sorbent, and (6) all adsorption sites are accessible and have equal strength (EPA, 1999).

The K_d parameter may be developed by direct measurement on aquifer material samples or it can be computed by upscaling mechanistic processes. Both approaches are discussed in the next sections.

5.9.2 Data Types

Data types include K_d values derived from upscaled mechanistic sorption models and directly measured K_d values.

5.9.3 Data Evaluation

In the PM CAU transport model, RN retardation via sorption is considered for reactions with immobile minerals in matrix material only. For dual-porosity zones, sorption occurs after solutes diffuse out of the fractured material into the immobile matrix continuum. For porous media zones (e.g., confining and vitric units), sorption occurs on the material through which groundwater flows. For the purposes of CAU-scale transport, only equilibrium sorption is considered and is

parameterized by the distribution coefficient, K_d. Although theoretical fracture sorption coefficients are considered in Shaw (2003) and Wolfsberg et al. (2002), there are no compelling datasets that isolate this process and identify parameters. Therefore, the specific process of sorption onto minerals coating fractures, before diffusion, is not considered in this PM CAU transport model. One line of justification for this conservative assumption is that the actual reactive surface area for fracture coatings accessible to aqueous solutes in fracture water is extremely small relative to the surface area accessible to solutes that experience even a small amount of diffusion. Further, if the fracture-coating minerals are not substantially different than those in the matrix, then distinguishing between fracture sorption and matrix sorption becomes less important. Additional discussion of fracture sorption can be found in Shaw (2003), SNJV (2005a), and Wolfsberg et al. (2002).

In support of this work, Shaw (2003) provide detail regarding the sorption process, datasets available at the time of report development, and the development of matrix K_d distributions for use in transport models. This section summarizes K_d data from Shaw (2003) and identifies three alternative sources of sorption K_d distributions. These are UGTA-developed values for K_d based on laboratory measurements (SNJV, 2007); YMP-developed values for K_d based on laboratory measurements but then scaled for field-scale considerations (SNL, 2007a and b); and K_d values as estimated for specific chemistry subareas and DZs (Carle et al., 2020). In addition, values used to represent the LCA for the Yucca Flat flow and transport model (Navarro, 2019a) are presented.

5.9.3.1 Data as Presented in Shaw (2003)

Chapter 9 in Shaw (2003) details the development of K_d distributions from both direct measurements and mechanistic model predictions. Comparing the two for HSUs in the PM-OV groundwater basin domain is difficult because the directly measured data are classified by alteration and the mechanistic model data are classified by stratigraphy. Thus, two summary tables are presented (Tables 5-29 and 5-30). In each case, the data are correlated to HSU characteristics.

Table 5-29 lists the K_d distributions developed from direct measurements (i.e., primarily YMP laboratory measurements reported before 2002). Nearly all of the YMP K_d experiments involve rock samples taken from the field (vitric, devitrified, and zeolitic tuff) with water from, or similar in composition to that from, either Well J-13 or Well UE-25p 1. Well J-13 samples the TSA, and UE-25p 1 samples a carbonate aquifer below the volcanic tuffs at Yucca Mountain. Distributions established using UE-25p 1 are not considered in the summary distributions because such conditions are not

Table 5-29
K_d Distributions Based on Laboratory Experiments Characterized by Material Alteration
(Page 1 of 3)

HSU # [a]	HSU Name	Summary of Contributing K_d Distributions	Sr	Cs	U	Np	Pu
13	PBRCM	Zeolitic tuff, Devitrified tuff Lava	Lognorm(1.3E5, 1.1E5, -1.4E4) Lognorm(31, 5.6) NDA	Lognorm(1.90E4, 2.03E4, 4.36E3) Normal(185, 47.6) NDA	Exp(16.5) Exp(2.28) NDA	Lognorm(4.3, 1.6, -1.9) Exp(0.48) NDA	Logistic(265, 70) Lognormal(72, 215, 5.4) NDA
14	BRA	Lava, Devitrified tuff Zeolitic tuff	NDA Lognorm(31, 5.6) Lognorm(1.3E5, 1.1E5, -1.4E4)	NDA Normal(185, 47.6) Lognorm(1.90E4, 2.03E4, 4.36E3)	NDA Exp(2.28) Exp(16.5)	NDA Exp(0.48) Lognorm(4.3, 1.6, -1.9)	NDA Lognormal(72, 215, 5.4) Logistic(265, 70)
15	BFCU	Zeolitic tuff Lava	Lognorm(1.3E5, 1.1E5, -1.4E4) NDA	Lognorm(1.90E4, 2.03E4, 4.36E3) NDA	Exp(16.5) NDA	Lognorm(4.3, 1.6, -1.9) NDA	Logistic(265, 70) NDA
16	KA	Lava Zeolitic tuff	NDA	NDA	NDA	NDA	NDA
17	CFCU	Zeolitic tuff Lava Vitric tuff	Lognorm(1.3E5, 1.1E5, -1.4E4) NDA Norm(175.1, 18,2)	Lognorm(1.90E4, 2.03E4, 4.36E3) NDA Normal(837, 223)	Exp(16.5) NDA Exp(1.38)	Lognorm(4.3, 1.6, -1.9) NDA Exp(0.66)	Logistic(265, 70) NDA Triang(63.9, 1984, 63.9)
18	CFCM	Lava Zeolitic tuff	NDA	NDA	NDA	NDA Lognorm(4.3, 1.6, -1.9)	NDA Logistic(265, 70)
19	IA	Lava	NDA	NDA	NDA	NDA	NDA
20	CHCU	Zeolitic tuff Lava	Lognorm(1.3E5, 1.1E5, -1.4E4) NDA	Lognorm(1.90E4, 2.03E4, 4.36E3) NDA	Exp(16.5) NDA	Lognorm(4.3, 1.6, -1.9) NDA	Logistic(265, 70) NDA
21	CHZCM	Zeolitic tuff Lava	Lognorm(1.3E5, 1.1E5, -1.4E4) NDA	Lognorm(1.90E4, 2.03E4, 4.36E3) NDA	Exp(16.5) NDA	Lognorm(4.3, 1.6, -1.9) NDA	Logistic(265, 70) NDA
22	CHVCM	Vitric tuff Lava	Normal(175.1, 18,2) NDA	Normal(837, 223) NDA	Exp(1.38) NDA	Exp(0.66) NDA	Triang(63.9, 1984, 63.9) NDA
23	CHVTA	Vitric tuff zeolitic tuff	Normal(175.1, 18,2)	Normal(837, 223)	Exp(1.38)	Exp(0.66)	Triang(63.9, 1984, 63.9)
24	YMCFCM	Zeolitic tuff Lava	Lognorm(1.3E5, 1.1E5, -1.4E4) NDA	Lognorm(1.90E4, 2.03E4, 4.36E3) NDA	Exp(16.5) NDA	Lognorm(4.3, 1.6, -1.9) NDA	Logistic(265, 70) NDA
25	TSA	Devitrified tuff	Lognorm(31, 5.6)	Normal(185, 47.6)	Exp(2.28)	Exp(0.48)	Lognormal(72, 215, 5.4)

Table 5-29
K_d Distributions Based on Laboratory Experiments Characterized by Material Alteration
(Page 2 of 3)

HSU # [a]	HSU Name	Summary of Contributing K_d Distributions	Sr	Cs	U	Np	Pu
26	LPCU	Zeolitic tuff	Lognorm(1.3E5, 1.1E5, -1.4E4)	Lognorm(1.9E4, 2.0E4, 4.4E3)	Exp(16.6)	Lognorm(4.3, 1.6, -1.9)	Logistic(265, 70)
27	PLFA	Lava, Devitrified tuff, Zeolitic tuff, Vitric tuff	NDA Lognorm(31, 5.6)	NDA Normal(185, 47.6)	NDA Exp(2.28)	NDA Exp(0.48)	NDA Lognormal(72, 215, 5.4)
28	TCA	Devitrified tuff	Lognorm(31, 5.6)	Normal(185, 47.6)	Exp(2.28)	Exp(0.48)	Lognormal(72, 215, 5.4)
29	UPCU	Zeolitic tuff Vitric tuff, Basalt, Lava	Lognorm(1.3E5, 1.1E5, -1.4E4)	Lognorm(1.9E4, 2.0E4, 4.4E3)	Exp(16.6)	Lognorm(4.3, 1.6, -1.9)	Logistic(265, 70)
30	BA	Lava Devitrified tuff, Zeolitic tuff	NDA	NDA	NDA	NDA	NDA
31	PVTA	Vitric tuff Devitrified tuff Zeolitic tuff, Lava	Normal(175.1, 18,2) Lognorm(31, 5.6)	Normal(837, 223) Normal(185, 47.6)	Exp(1.38) Exp(2.28)	Exp(0.66) Exp(0.48)	Triang(63.9, 1984, 63.9) Lognormal(72, 215, 5.4)
32	PCM	Devitrified tuff Vitric tuff, Zeolitic tuff, Lava, Alluvium	Lognorm(31, 5.6) NDA Normal(175.1, 18,2)	Normal(185, 47.6) NDA Normal(837, 223)	Exp(2.28) NDA Exp(1.38)	Exp(0.48) NDA Exp(0.66)	Lognormal(72, 215, 5.4) NDA Triang(63.9, 1984, 63.9)
33	WWA	Lava	NDA	NDA	NDA	NDA	NDA
34	FCCU	Zeolitic tuff	Lognorm(1.3E5, 1.1E5, -1.4E4)	Lognorm(1.9E4, 2.0E4, 4.4E3)	Exp(16.6)	Lognorm(4.3, 1.6, -1.9)	Logistic(265, 70)
36	TMA	Devitrified tuff Vitric tuff Zeolitic tuff, Lava, Alluvium	Lognorm(31, 5.6) Normal(175.1, 18,2)	Normal(185, 47.6) Normal(837, 223)	Exp(2.28) Exp(1.38)	Exp(0.48) Exp(0.66)	Lognormal(72, 215, 5.4) Triang(63.9, 1984, 63.9)
37	THCM	Zeolitic tuff Vitric tuff Devitrified tuff	Lognorm(1.3E5, 1.1E5, -1.4E4) Norm(175.1, 18,2)	Lognorm(1.9E4, 2.0E4, 4.4E3) Normal(837, 223)	Exp(16.6) Exp(1.38)	Lognorm(4.3, 1.6, -1.9) Exp(0.66)	Logistic(265, 70) Triang(63.9, 1984, 63.9)
38	THLFA	Lava Alluvium	NDA	NDA	NDA	NDA	NDA
39	TMCM	Zeolitic tuff Devitrified tuff Lava, Vitric tuff, Alluvium	Lognorm(1.3E5, 1.1E5, -1.4E4) Lognorm(31, 5.6) NDA	Lognorm(1.9E4, 2.0E4, 4.4E3) Normal(185, 47.6) NDA	Exp(16.6) Exp(2.28) NDA	Lognorm(4.3, 1.6, -1.9) Exp(0.48) NDA	Logistic(265, 70) Lognormal(72, 215, 5.4) NDA

Table 5-29
K_d Distributions Based on Laboratory Experiments Characterized by Material Alteration
(Page 3 of 3)

HSU # [a]	HSU Name	Summary of Contributing K_d Distributions	Sr	Cs	U	Np	Pu
41	FCCM	Zeolitic tuff Lava Devitrified tuff, Vitric tuff, Basalt, Alluvium	Lognorm(1.3E5, 1.1E5, -1.4E4) NDA	Lognorm(1.9E4, 2.0E4, 4.4E3) NDA	Exp(16.6) NDA	Lognorm(4.3, 1.6, -1.9) NDA	Logistic(265, 70) NDA
43	DVCM	Devitrified tuff	Lognorm(31, 5.6)	Normal(185, 47.6)	Exp(2.28)	Exp(0.48)	Lognormal(72, 215, 5.4)
44	TCVA	Devitrified tuff Vitric tuff Lava, Zeolitic tuff, Alluvium	Lognorm(31, 5.6) Normal(175.1, 18,2)	Normal(185, 47.6) Normal(837, 223)	Exp(2.28) Exp(1.38)	Exp(0.48) Exp(0.66)	Lognormal(72, 215, 5.4) Triang(63.9, 1984, 63.9)
45	YVCM	Devitrified tuff Basalt Alluvium	Lognorm(31, 5.6) NDA	Normal(185, 47.6) NDA	Exp(2.28) NDA	Exp(0.48) NDA	Lognormal(72, 215, 5.4) NDA
46	AA	Alluvium Devitrified tuff Vitric tuff Zeolitic tuff, Basalt	Range(80,22500)	Range(700,3000)	NDA	NDA	NDA

Source: Shaw, 2003 (Figures 9-3 to 9-36 and Table 9-18)

[a] No distributions were available for the following HSUs: HSU #1 (LCCU), 2 (LCA), 3 (UCCU), 4 (LCCU1), 5 (LCA3), 6 (MGCU), and 7-12 (SCICU, CHICU, CCICU, RMICU, ATICU, and BMICU), 35 (SCVCU), 40 (FCA), 42 (DVA).

NDA = No distribution available.

Note: Distributions are defined as follows: Exp(β); Lognormal(μ,σ,shift); Logistic(α,β); Normal(μ,σ); Triang(Minimum,Maximum,Mode). Where α = continuous location parameter; β = continuous scale parameter; μ = mean; σ = standard deviation. Software use for developing these distributions is described in Appendix C of Shaw (2003)

Table 5-30
Summary of K_ds Estimated by Stratigraphy with Mechanistic Model, Correlated to HSUs (Zavarin et al., 2002 and 2004b)
(Page 1 of 4)

HSU # [a]	HSU Name	Stratigraphy	Stratigraphy in Mechanistic Model Dataset	Sr	Cs	U	Np	Pu (10^{-5}) [b]	Pu (10^{-10}) [b]	Pu (10^{-15}) [b]
13	PBRCM[c]	Tr, Tn, Tq, Tu, To, Tk, Te	Tpe (N=2) Tptb (N=2)	Range (668.1,1637.2) (Range (165.3,2086.3)	Range (2236.3,4539.5) Range (1673.6,2814.4)	Range(2.9,19.5) Range(0,0)	Range(1.3,3.1) Range(0,0)	Range(5.9,7.5) Range(0,0)	Range(13,20.4) Range(0,0)	Range (63.8,121.1) Range(0,0)
14	BRA	QTa, Tbd, Tbdb, Tbdc, Tbdk, Tbdl, Tbds, Tbg, Tbgb, Tbgm, Tbgp, Tbgr, Tbgs, Tbq, Tcl, Tn4JK, Trl, Trr, unk	Tcl (N=1)	Range(94.8,94.8)	Range(9233.6,9233.6)	Range(4.2,4.2)	Range(1.8,1.8)	Range(8.5,8.5)	Range(18.6,18.6)	Range(91.2,91.2)
15	BFCU	Tbdl, Tcblp, Tcblr, Tcbp, Tcbr, Tcbs, Tcbx, Tct	Tcbp (N=2) Tct (N=55)	Range (903.3,1553.2) Lognorm (189.8,669.7)	Range (5725.6,12101.7) Exp(9469.2)	Range(0.4,0.4) Exp(5.5)	Range(0.1,0.1) Exp(2.3)	Range(0.8,0.8) Exp(8.7)	Range(1.8,1.8) Exp(19.5)	Range(9.1,9.1) Exp(97.6)
16	KA [d]	Tcg, Tcpk	Tpb (N=7)	Exp(1406.3)	Exp(32993)	Exp(1.3)	Exp(0.6)	Exp(2.7)	Exp(5.9)	Exp(28.7)
17	CFCU [c]	Tcg, Tci, Tcj, Tcpk, Tcps, Tcu, unk	Tpe (N=2) Tptb (N=2)	Range (668.1,1637.2) Range (165.3,2086.3)	Range (2236.3,4539.5) Range (1673.6,2814.4)	Range(2.9,19.5) Range(0,0)	Range(1.3,3.1) Range(0,0)	Range(5.9,7.5) Range(0,0)	Range(13,20.4) Range(0,0)	Range (63.8,121.1) Range(0,0)
18	CFCM [c]	Tcbs, Tcf, Tci, Tcj, Tcpe, Tcpk, Tcps, Tcu, unk	Tpe (N=2) Tptb (N=2)	Range (668.1,1637.2) Range (165.3,2086.3)	Range (2236.3,4539.5) Range (1673.6,2814.4)	Range(2.9,19.5) Range(0,0)	Range(1.3,3.1) Range(0,0)	Range(5.9,7.5) Range(0,0)	Range(13,20.4) Range(0,0)	Range (63.8,121.1) Range(0,0)
19	IA [d]	Tci	Tpb (N=7)	Exp(1406.3)	Exp(32993)	Exp(1.3)	Exp(0.6)	Exp(2.7)	Exp(5.9)	Exp(28.7)
20	CHCU	Tcg, Tci, Thp, Thr, Tpe, Tpr, Tptb	Tpe (N=2) Tptb (N=2)	Range (668.1,1637.2) Range (165.3,2086.3)	Range (2236.3,4539.5) Range (1673.6,2814.4)	Range(2.9,19.5) Range(0,0)	Range(1.3,3.1) Range(0,0)	Range(5.9,7.5) Range(0,0)	Range(13,20.4) Range(0,0)	Range (63.8,121.1) Range(0,0)
21	CHZCM [c]	Tcj, Tcu, Th, Thp, Thr, Tmw, Tpr, Tpt, Tptm, unk	Tpe (N=2) Tptb (N=2)	Range (668.1,1637.2) Range (165.3,2086.3)	Range (2236.3,4539.5) Range (1673.6,2814.4)	Range(2.9,19.5) Range(0,0)	Range(1.3,3.1) Range(0,0)	Range(5.9,7.5) Range(0,0)	Range(13,20.4) Range(0,0)	Range (63.8,121.1) Range(0,0)

Table 5-30
Summary of K_ds Estimated by Stratigraphy with Mechanistic Model, Correlated to HSUs (Zavarin et al., 2002 and 2004b)
(Page 2 of 4)

HSU # [a]	HSU Name	Stratigraphy	Stratigraphy in Mechanistic Model Dataset	Sr	Cs	U	Np	Pu (10^{-5}) [b]	Pu (10^{-10}) [b]	Pu (10^{-15}) [b]
22	CHVCM [c]	Tcj, Tcps, Tcu, Thp, Tpt, unk	Tpe (N=2) Tptb (N=2)	Range (668.1,1637.2) Range (165.3,2086.3)	Range (2236.3,4539.5) Range (1673.6,2814.4)	Range(2.9,19.5) Range(0,0)	Range(1.3,3.1) Range(0,0)	Range(5.9,7.5) Range(0,0)	Range(13,20.4) Range(0,0)	Range (63.8,121.1) Range(0,0)
23	CHVTA	Tcj, Tcpk, Tcps, Tcu, Th, Thp, Tmt, Tpe, Tpr, Tptb, unk	Tpe (N=2) Tptb (N=2)	Range (668.1,1637.2) Range (165.3,2086.3)	Range (2236.3,4539.5) Range (1673.6,2814.4)	Range(2.9,19.5) Range(0,0)	Range(1.3,3.1) Range(0,0)	Range(5.9,7.5) Range(0,0)	Range(13,20.4) Range(0,0)	Range (63.8,121.1) Range(0,0)
24	YMCFCM	Tcby, Tcp, Tct, Thp, Thr	Tcby (N=47) Tcp (N=32) Tct (N=55)	Lognorm (852,14243) Lognorm (1229,17375) Lognorm (189.8,669.7)	Lognorm (7252.8,13979) Exp(2249.3) Exp(9469.2)	Exp(7.7) Exp(2.4) Exp(5.5)	Exp(1.5) Exp(0.9) Exp(2.3)	Exp(4.4) Exp(4) Exp(8.7)	Exp(11) Exp(8.9) Exp(19.5)	Exp(61.1) Exp(44.1) Exp(97.6)
25	TSA [e]	Tptm	Tpcr (N=4)	Range(0,22.6)	Range(0,25415.4)	Range(0,9.1)	Range(0,1.2)	Range(0,2.5)	Range(0,7.4)	Range(0,46.8)
26	LPCU	Thr, Tp, Tpcm, Tpd, Tpe, Tpr, Tptb, Tptm, Tptx	Tp (N=3) Tpd (N=11) Tpe (N=2) Tptb (N=2)	Range (1594,1992.5) Lognorm (2008.6,2747.9) Range (668.1,1637.2) Range (165.3,2086.3)	Range (2150.3,27882) Exp(5843.8) Range (2236.3,4539.5) Range (1673.6,2814.4)	Range(0,0) Exp(0.9) Range(2.9,19.5) Range(0,0)	Range(0,0) Exp(0.4) Range(1.3,3.1) Range(0,0)	Range(0,0) Exp(1.7) Range(5.9,7.5) Range(0,0)	Range(0,0) Exp(3.8) Range(13,20.4) Range(0,0)	Range(0,0) Exp(18.4) Range (63.8,121.1) Range(0,0)
27	PLFA	Tpe, Tpr, Tptb, unk	Tpe (N=2) Tptb (N=2)	Range (668.1,1637.2) Range (165.3,2086.3)	Range (2236.3,4539.5) Range (1673.6,2814.4)	Range(2.9,19.5) Range(0,0)	Range(1.3,3.1) Range(0,0)	Range(5.9,7.5) Range(0,0)	Range(13,20.4) Range(0,0)	Range (63.8,121.1) Range(0,0)
28	TCA	Tpcm, Tpcr	Tpcr (N=4)	Range(0,22.6)	Range(0,25415.4)	Range(0,9.1)	Range(0,1.2)	Range(0,2.5)	Range(0,7.4)	Range(0,46.8)
29	UPCU	Tm, Tmrf, Tmrh, Tmt, Tmw, Tp, Tpb, Tpc, Tpcm, Tpcr, Tpcx, Tpcy, Tpcyp, Tpd, Tpe, unk	Tp (N=3) Tpb (N=7) Tpcr (N=4) Tpd (N=11) Tpe (N=2)	Range (1594,1992.5) Exp(1406.3) Range(0,22.6) Lognorm (2008.6,2747.9) Range (668.1,1637.2)	Range (2150.3,27882) Exp(32993) Range(0,25415.4) Exp(5843.8) Range (2236.3,4539.5)	Range(0,0) Exp(1.3) Range(0,9.1) Exp(0.9) Range(2.9,19.5)	Range(0,0) Exp(0.6) Range(0,1.2) Exp(0.4) Range(1.3,3.1)	Range(0,0) Exp(2.7) Range(0,2.5) Exp(1.7) Range(5.9,7.5)	Range(0,0) Exp(5.9) Range(0,7.4) Exp(3.8) Range(13,20.4)	Range(0,0) Exp(28.7) Range(0,46.8) Exp(18.4) Range (63.8,121.1)

Table 5-30
Summary of K_ds Estimated by Stratigraphy with Mechanistic Model, Correlated to HSUs (Zavarin et al., 2002 and 2004b)
(Page 3 of 4)

HSU # [a]	HSU Name	Stratigraphy	Stratigraphy in Mechanistic Model Dataset	Sr	Cs	U	Np	Pu (10^{-5}) [b]	Pu (10^{-10}) [b]	Pu (10^{-15}) [b]
30	BA	Tpb	Tpb (N=7)	Exp(1406.3)	Exp(32993)	Exp(1.3)	Exp(0.6)	Exp(2.7)	Exp(5.9)	Exp(28.7)
31	PVTA	Tm, Tmra, Tmrd, Tmrf, Tmrh, Tmt, Tp, Tpb, Tpcm, Tpd, Tpe, Tpr, Tptb, unk	Tp (N=3) Tpb (N=7) Tpd (N=11) Tpe (N=2) Tptb (N=2)	Range (1594,1992.5) Exp(1406.3) Lognorm (2008.6,2747.9) Range (668.1,1637.2) Range (165.3,2086.3)	Range (2150.3,27882) Exp(32993) Exp(5843.8) Range (2236.3,4539.5) Range (1673.6,2814.4)	Range(0,0) Exp(1.3) Exp(0.9) Range(2.9,19.5) Range(0,0)	Range(0,0) Exp(0.6) Exp(0.4) Range(1.3,3.1) Range(0,0)	Range(0,0) Exp(2.7) Exp(1.7) Range(5.9,7.5) Range(0,0)	Range(0,0) Exp(5.9) Exp(3.8) Range(13,20.4) Range(0,0)	Range(0,0) Exp(28.7) Exp(18.4) Range (63.8,121.1) Range(0,0)
32	PCM	QTa, Tpcp, Tpg, Tpp, Tptbr, Tptp, Tptr, Tpv, Tpy	Tpcp (N=12) Tpg (N=7) Tptbr (N=6) Tptp (N=82) Tptr (N=12) Tpy (N=4)	Exp(14.3) Log-norm(189,556.9) Exp(637) Exp(286.9) Log-norm(31.3,70.5) Range(0,140.9)	Exp(325.7) Exp(1147.4) Exp(4596.5) Exp(1451) Lognorm (14116,68310) Range(0,388.1)	Exp(1) Exp(3.8) Exp(12.3) Exp(2.8) Exp(3.3) Range(0,21.3)	Exp(0.3) Exp(1.8) Exp(6.4) Exp(1.3) Lognorm (0.7,0.6) Range(0,17)	Exp(1.1) Exp(7.7) Exp(24.8) Exp(3.7) Exp(2) Range(0,42.5)	Exp(2.5) Exp(16.9) Exp(54.5) Exp(8.4) Lognorm (5.3,5.1) Range(0,93.1)	Exp(12.8) Exp(83.1) Exp(269.1) Exp(43.1) Exp(27.6) Range(0,456)
33	WWA [e]	Tmw	Tpcr (N=4)	Range(0,22.6)	Range(0,25415.4)	Range(0,9.1)	Range(0,1.2)	Range(0,2.5)	Range(0,7.4)	Range(0,46.8)
36	TMA [e]	Tmay, Tmaw, Tma, Tmx, Tmat, Tmt, Tmr	Tpcr (N=4)	Range(0,22.6)	Range(0,25415.4)	Range(0,9.1)	Range(0,1.2)	Range(0,2.5)	Range(0,7.4)	Range(0,46.8)
37	THCM [e]	Tmat	Tpcr (N=4)	Range(0,22.6)	Range(0,25415.4)	Range(0,9.1)	Range(0,1.2)	Range(0,2.5)	Range(0,7.4)	Range(0,46.8)
38	THLFA [b]	Tmat	Tpcr (N=4)	Range(0,22.6)	Range(0,25415.4)	Range(0,9.1)	Range(0,1.2)	Range(0,2.5)	Range(0,7.4)	Range(0,46.8)
39	TMCM [e]	Tmay, Tmaw, Tma, Tmx, Tmat, Tmt, Tmr	Tpcr (N=4)	Range(0,22.6)	Range(0,25415.4)	Range(0,9.1)	Range(0,1.2)	Range(0,2.5)	Range(0,7.4)	Range(0,46.8)
41	FCCM [e]	Tfu, Tfs, Tfd, Tfr, Tfb, Tfl, Tff	Tpcr (N=4)	Range(0,22.6)	Range(0,25415.4)	Range(0,9.1)	Range(0,1.2)	Range(0,2.5)	Range(0,7.4)	Range(0,46.8)
43	DVCM [e]	Tf through Tq	Tpcr (N=4)	Range(0,22.6)	Range(0,25415.4)	Range(0,9.1)	Range(0,1.2)	Range(0,2.5)	Range(0,7.4)	Range(0,46.8)
44	TCVA [e]	Ttg, Tth, Tts, Ttt, Ttp, Ttc	Tpcr (N=4)	Range(0,22.6)	Range(0,25415.4)	Range(0,9.1)	Range(0,1.2)	Range(0,2.5)	Range(0,7.4)	Range(0,46.8)

Table 5-30
Summary of K_ds Estimated by Stratigraphy with Mechanistic Model, Correlated to HSUs (Zavarin et al., 2002 and 2004b)
(Page 4 of 4)

HSU # [a]	HSU Name	Stratigraphy	Stratigraphy in Mechanistic Model Dataset	Sr	Cs	U	Np	Pu (10^{-5}) [b]	Pu (10^{-10}) [b]	Pu (10^{-15}) [b]
45	YVCM [e]	Typ	Tpcr (N=4)	Range(0,22.6)	Range(0,25415.4)	Range(0,9.1)	Range(0,1.2)	Range(0,2.5)	Range(0,7.4)	Range(0,46.8)
46	AA [f]	AA	AA	Range (2.18, 2.18)	Triang (2.7,3.7,3.7)	Triang (-0.3,0.8,0.4)	Triang (0.3,1.1,0.7)	Triang (0.4,1.4,0.9)	Triang (0.8,1.8,1.3)	Triang (1.4,2.3,1.9)

Source: Modified from Shaw, 2003

[a] The following HSUs were removed because they were included in Shaw (2003) only for completion purposes; no K_d distributions were reported: HSU #1 (LCCU), 2 (LCA), 3 (UCCU), 4 (LCCU1), 5 (LCA3), 6 (MGCU), and 7-12 (SCICU, CHICU, CCICU, RMICU, ATICU, and BMICU), 34 (FCCU), 35 (SCVCU), 40 (FCA), 42 (DVA).
[b] Oxygen fugacities of 1E-5, 1E-10, and 1E-15 are considered as they affect the speciation and valence of Pu.
[c] K_d ranges assigned based on similarity to CHCU unit.
[d] K_d ranges assigned based on similarity to BA unit.
[e] K_d ranges assigned based on similarity to TCA unit.
[f] K_d ranges for Frenchman Flat alluvium by Zavarin et al., 2002

widely encountered in the PM-OV system. The K_d distributions are correlated to HSUs based on the primary alterations observed within the HSU (Table 5-29). Often, more than one distribution is listed because of the presence of multiple alteration phases found within a given HSU.

Table 5-30 summarizes K_d distributions derived from scaled mechanistic models developed by Zavarin et al. (2004b). This theoretical approach uses component additivity to represent sorption for all minerals present within a series of sample. Zavarin et al. (2004b) estimated K_ds for multiple rock/core samples from multiple NNSS wells. These mechanistic models seek to represent all processes governing retardation of each RN of interest. These include aqueous speciation, surface complexation, ion exchange, and precipitation reactions. These theoretically derived K_ds provide substantial ranges for sensitivity analyses when compared with the directly measured K_ds presented in Table 5-29.

5.9.3.2 Direct Measurement of K_d (SNJV, 2007)

Laboratory sorption experiments measure K_d values directly. The experiments are generally designed with knowledge of the mechanistic processes that affect the K_d but with the goal of simply measuring it given a set of environmental controls. Measurements of K_d values for several RNs on multiple types of minerals and rock material have been collected in support of UGTA and YMP transport studies. Such studies generally provide information on the rock type (rock mineralogy) and the conditions under which the experiment was performed. Such conditions include the following:

- Aqueous ion concentrations
- Temperature
- pH
- Eh (and/or other indicators of oxidation/reduction state such as oxygen fugacity)
- Solute concentration
- Rock characteristics
- Experimental atmospheric conditions (e.g., air, nitrogen gas [N_2], or carbon dioxide [CO_2] to control pH)

Thus, each measured K_d corresponds to a specific set of environmental conditions, albeit generally designed to represent in situ conditions.

Although the experiments used to obtain K_d parameters are relatively fast and simple, there are important limitations associated with the use of such parameters in transport models. Whereas transport processes are dynamic, the K_d measurements are made under static conditions. Likewise, the contact time between the RNs and aquifer materials is considerably different between the laboratory experiments and the PM CAU transport model. The representativeness of K_d batch experiments to in situ rocks may be hard to assess because these experiments are usually performed on freshly created surfaces from crushed or sieved rocks. The K_d simply represents the total mass of the element of interest and thus does not describe the behavior of any particular species. However, if more detailed mechanistic understanding is desired, it is possible to derive the speciation, given the environmental conditions of the experiment. Finally, although the K_d parameter represents an integrated response of a sample brought in contact with the aqueous solute of interest, the sample size is still far smaller than the rock volume in the PM CAU transport model that will be parameterized for flow and transport simulations.

The following sections provide a summary of the laboratory experiments used to measure K_d values for alluvium and volcanic rocks representative of those of the PM CAU. The test results are categorized by the rock types of alluvium, devitrified tuff, vitric tuff, and zeolitic tuff.

5.9.3.2.1 Alluvium

Primary sources of alluvium sorption data included K_d values measured from Yucca Flat-specific experiments reported in Wolfsberg et al. (1983) and Zavarin et al. (2002). Secondary sources are also cited in SNJV (2007). Figure 5-40, taken from SNJV (2007), shows the ranges of K_d measured in alluvium for both the NNSS and YMP. Of note in the figure are the relatively low K_d values for Np, Tc, and U.

5.9.3.2.2 Volcanic Rocks

Zavarin et al. (2007) summarize two studies that investigated RN transport in fractures of the TCU performed in support of the UGTA Project (Zavarin et al., 2005; Ware et al., 2005). The experiments included RN transport through synthetic parallel-plate fractured tuff samples (Zavarin et al., 2007).

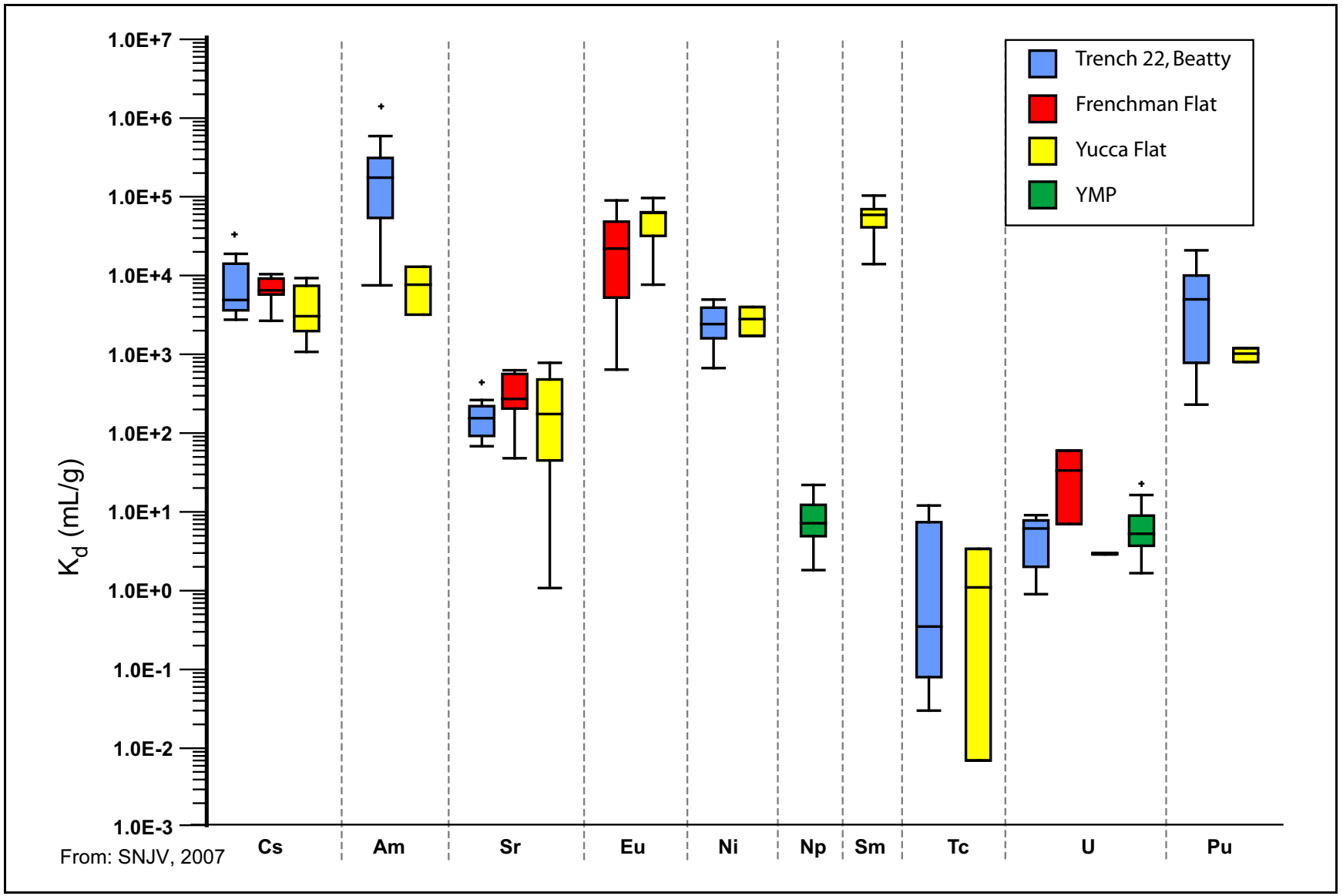

Figure 5-40
Laboratory-measured K_ds for Alluvium Samples

These simplified fracture transport experiments isolated matrix diffusion and sorption effects from all other fracture transport processes (e.g., fracture lining mineral sorption, heterogeneous flow). Additional fracture transport complexity was added by performing iron oxide-coated parallel-plate TCU flow-through experiments (effect of fracture lining minerals.)

A limited number of studies have also been performed at DRI in support of the UGTA Project, primarily involving sorption of lead (Pb), Sr, and Cs on a select number of rocks (tuff and devitrified lava) from PM and Rainier Mesa, and Frenchman Flat boreholes (Papelis and Um, 2003a and b; Decker et al., 2003). Based on sorption data with different solid and metal concentrations, linear sorption isotherms were derived for sorption at pH 8.3, representing a common NNSS groundwater pH. Batch sorption experiments were conducted on crushed rock, and diffusion/sorption experiments were conducted on intact core.

The YMP studied sorption of RNs (Pu, Np, U, Sr, and Cs) on minerals and volcanic rocks for more than two decades. The data and sources are described in SNJV (2007). Reviewing the measured K_d data (SNJV, 2007), the RNs Np, Pu, Sr, and U are noted to exhibit the lowest values of K_d in the rock types tested. Specifically, they represent almost every measurement of K_d with a Log_{10} value of 1 or less. Table 5-31 shows the mean Log_{10} values as well as the Log_{10} standard deviations and standard errors for these RNs for the alluvium and volcanic rock types. Figure 5-41 shows a plot of the mean Log_{10} K_ds for Np, Pu, Sr, and U in devitrified tuff. The devitrified tuff rock type is most relevant to WTA and LFA HGUs. The plot shows a trend that holds for the other rock types as well, i.e., Np and U exhibit the smallest K_d values and Pu and Sr exhibit larger values. The low Np and U K_ds in devitrified tuff are of particular interest because the highly fractured WTAs are typically devitrified.

5.9.3.3 Distribution Coefficients Developed for YMP

Subsequent to Shaw (2003), YMP reanalyzed their data, focusing on the experimental conditions under which the observations were made, the quality of the data, and scaling considerations for site-scale models. This analysis led to new K_d distributions, which were used for YMP transport calculations. The new YMP K_d distributions are documented in SNL (2007a, Appendix A) and SNL (2007b, Appendix C). Those reports show laboratory and data distribution fits, as derived for all RNs considered as well as field-scale K_d distributions used in UZ and SZ models as determined through expert judgment. The YMP K_d values are reported as Table B.1-6 in SNJV (2009).

Table 5-31
Summary of Measured Values of K_d

Rock Type	RN	Count [a]	Log_{10} K_d Average	Log_{10} K_d Standard Deviation	Log_{10} K_d Standard Error
Alluvium	Np	32	0.87	0.27	0.05
	Pu	24	3.37	0.58	0.12
	Sr	75	2.15	0.62	0.07
	U	50	0.69	0.35	0.05
Devitrified Tuff	Np	531	-0.15	0.71	0.03
	Pu	214	1.67	0.54	0.04
	Sr	156	1.84	0.38	0.03
	U	116	0.26	0.36	0.03
Vitric Tuff	Np	461	-0.20	0.53	0.02
	Pu	171	2.34	0.47	0.04
	Sr	32	2.03	0.41	0.07
	U	86	0.07	0.51	0.05
Zeolitic Tuff	Np	686	0.27	0.43	0.02
	Pu	198	2.12	0.57	0.04
	Sr	85	4.19	0.62	0.07
	U	201	0.89	0.60	0.04

Source: Matrix_Sorption_Lab.xls workbook (SNJV, 2007)

[a] The count is of non-negative K_d values before log conversion.

Table 5-32 relates the upscaled YMP K_d distributions for laboratory fits as shown in SNL (2007b). As an introductory note, however, it must be pointed out that the mechanistic K_ds span a range larger than those determined from laboratory measurements. This caution applies not only to the upscaled K_d values developed for YMP and reported here but for mechanistically derived values such as those of Carle et al. (2020), discussed later. Measured K_d represents the ratio of sorbed to aqueous solute in a test tube-scale laboratory experiment under controlled environmental conditions. The mechanistic estimation method allows consideration of chemical conditions (e.g., varying redox potentials and pH) that may occur in the field but are not established in the laboratory.

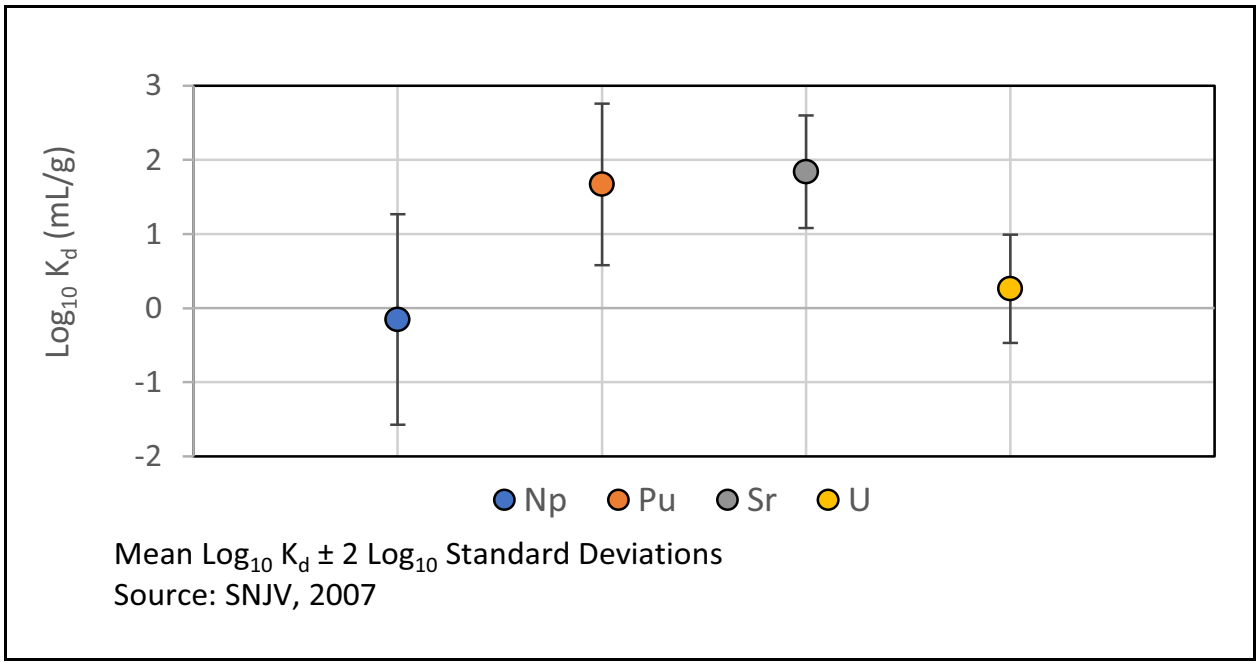

Figure 5-41
Laboratory-measured Distribution Coefficients for Devitrified Tuff Samples

Table 5-32
Recommended Composite Distribution for K_d in Volcanics and Alluvium

Species	Unit/Analysis	Distribution	Coefficients Describing Distribution (mL/g) [a]
U	Composite (Volcanics)	Cumulative	(K_d, prob) (0, 0.) (5.39, 0.05) (8.16, 0.95) (20, 1.0)
	Alluvium	Cumulative	(K_d, prob) (1.7, 0.) (2.9, 0.05) (6.3, 0.95) (8.9, 1.0)
Np	Composite (Volcanics)	Cumulative	(K_d, prob) (0, 0.) (0.99, 0.05) (1.83, 0.90) (6, 1.0)
	Alluvium	Cumulative	(K_d, prob) (1.8, 0.) (4.0, 0.05) (8.7, 0.95) (13, 1.0)
Pu	Composite (Volcanics)	Cumulative	(K_d, prob) (10., 0.) (89.9, 0.25) (129.87, 0.95) (300, 1.0)
	Alluvium (Devitrified)	Beta	μ = 100, range = 50 to 300, σ = 15
Cs	Composite (Volcanics)	Cumulative	(K_d, prob) (100, 0.) (3,000.59, 0.05) (6,782.92, 1.0)
	Alluvium (Devitrified)	Truncated Normal	range = 100 to 1,000; μ = 728, σ = 464
Sr	Volcanics and Alluvium	Uniform	range = 20 to 400

Sources: SNJV, 2009 (Table B.1-6) and SNL, 2007b (Table C-14). Only RNs of relevance or potential relevance are included.

[a] For cumulative distributions, values in parentheses represent probabilities and associated K_d values. For example, for U Composite (Volcanics), the minimum small-scale value was 0 mL/g. Five percent probability was uniformly distributed between 0 mL/g and the lower bound of the scaled distribution at 5.39 mL/g. Ninety-five percent probability was uniformly distributed between 5.39 mL/g and the upper bound of the upscaled distribution at 8.16 mL/g. The remaining 5% probability was uniformly distributed between 8.16 mL/g and the maximum small-scale experimentally observed value of 20 mL/g.

μ = Mean
σ = Standard deviation

5.9.3.4 K_ds Developed by Carle et al. (2020)

Carle et al. (2020) performed a screening analysis requiring the use of K_ds to determine the RNs relevant or potentially relevant to the PM HST (see Section 3.1.6). The K_ds were derived using a component additivity approach described in Zavarin et al. (2004b) that estimates K_d as a function of water chemistry and mass fraction of reactive minerals (i.e., calcite, hematite, mica, smectite, and zeolite). K_ds for the reactive minerals are estimated using mechanistic modeling and laboratory experiments (Zavarin and Bruton, 2004a and b; Zavarin et al., 2005; Zavarin et al. 2007). The water chemistry data are used by the mechanistic model to establish surface complexation, ion exchange, and aqueous complexation reactions that impact RN sorption.

The K_d values developed by Carle et al. (2020) were based on HGU, DZ, and chemistry subarea. The HGUs (AA, VTA, WTA, LFA, TCU, and ICU) were subdivided into DZs and/or alteration description based on their mineralogical content (smectite, zeolite, mica, hematite, and calcite) as shown in Table 5-33. Table 5-33 presents the mean reactive mineral percentage, along with the number of mineralogical samples used in its calculation, for each DZ comprising each HGU (Carle et al., 2020). Five chemistry subareas were identified based on spatial similarities and difference in the groundwater major-ion chemistry (Figure 5-42). The major-ion chemistry of groundwater samples used to represent each subarea are presented in Table 5-34.

Table 5-33
Mean Reactive Mineral Percentage and Number of XRD Data for HGUs within Diagenetic Zones
(Page 1 of 2)

HGU	DZ	% Smectite		% Zeolite		% Mica		% Hematite		% Calcite	
		Mean	N	Mean	N	Mean	N	Mean	N	Mean	N
AA	1	4.0	1	21.5	1	0.6	1	0.5	1	1.5	1
	4	0.0	1	0.0	1	6.5	1	0.6	1	12.7	1
VTA	1	3.9	12	1.9	14	2.4	14	0.8	14	0.1	7
	2	10.0	1	43.8	2	0.5	2	0.0	2	0.0	1
WTA	1	0.9	4	0.6	7	3.8	7	0.8	7	0.2	3
	2	2.2	20	12.8	21	2.9	21	0.5	21	0.0	17
	3	0.9	13	3.7	17	4.3	16	0.6	16	0.1	11
	4	3.1	16	0.0	16	8.0	16	0.6	16	0.7	13

Table 5-33
Mean Reactive Mineral Percentage and Number of XRD Data for HGUs within Diagenetic Zones
(Page 2 of 2)

HGU	DZ	% Smectite		% Zeolite		% Mica		% Hematite		% Calcite	
		Mean	N	Mean	N	Mean	N	Mean	N	Mean	N
LFA	1	2.7	10	0.8	12	2.6	12	0.7	12	0.1	7
	2	3.1	15	21.3	19	3.0	19	0.6	19	0.2	9
	3	1.7	12	10.6	13	2.6	13	0.5	13	0.7	12
	4	0.7	6	0.0	7	5.3	7	0.7	7	0.2	6
TCU	1	6.4	2	51	3	2.1	3	0.0	3	0.0	1
	2	3.7	51	53.1	58	2.7	58	0.1	58	0.2	37
	3	3.6	34	21.3	39	5.0	39	0.3	39	0.5	29
	4	2.3	20	0.1	21	8.2	21	0.3	21	0.4	16
ICU	4	2.0	1	0.0	1	1.0	1	0	1	1	1

Source: Carle et al., 2020

The mean Log_{10} K_d values are shown in Table 5-35, which shows that Np, Sr, and U generally exhibit the lowest distribution coefficients. The standard deviations for the log_{10} K_d values are shown in Table 5-36. Figure 5-43 shows a comparison of the upscaled YMP K_d values (as reported in SNJV, 2009), the measured K_d values (SNJV, 2007), and the ranges of values reported by Carle et al. (2020) for Sr in alluvium. Figures 5-44 and 5-45, in turn, show comparisons for Np in devitrified tuff. The plots show the 5th and 95th percentile values for the SNJV (2009) data. For the SNJV (2007) as well as the Carle et al. (2020) data, the mean values are shown with error bars representing plus/minus one standard error. The Carle et al. (2020) data are represented by many data points to cover the various chemistry subareas and DZs for which values were derived.

5.9.3.5 K_ds for the LCA Reported in Navarro (2019)

The LCA is not a significant aquifer in the PM-OV flow and transport model. As previously mentioned (Section 5.3.7), the LCA is present in less than 1 percent of the flow model cells, almost none of which are downgradient of the testing areas. The LCA rock is dominated by dolomite and calcite minerals with only trace amounts of silicate and iron oxide; therefore, sorption in the matrix is controlled by calcite and dolomite surface chemistry. The K_d distributions recommended for the LCA were developed for use in the YF/CM transport model (Table 5-37). The LCA is the principal aquifer

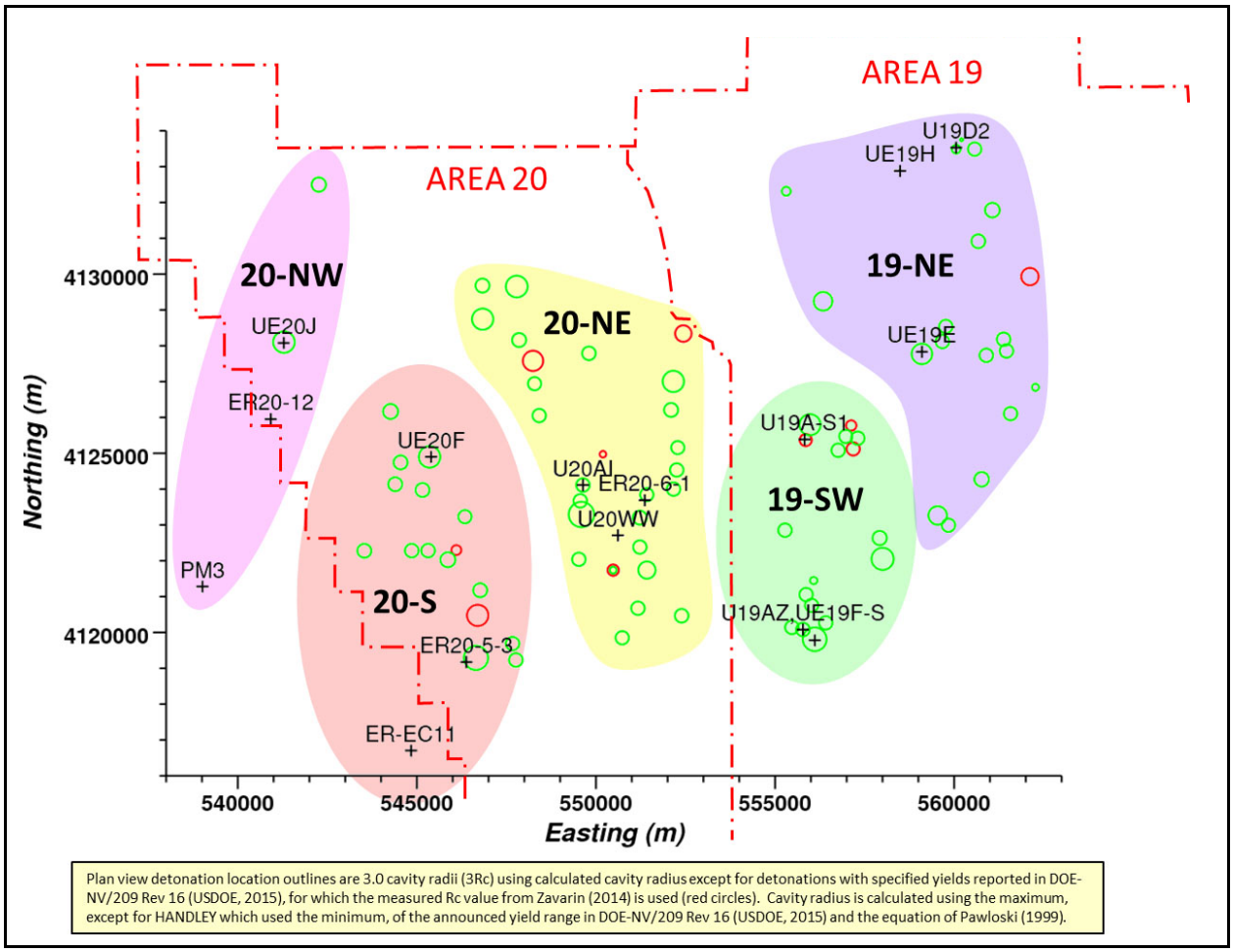

Figure 5-42
Site Map Showing the Chemistry Subareas from Carle et al., 2020

Table 5-34
Water Chemistry Data Used for Mechanistic Modeling of K_d
(Page 1 of 2)

Sub Area	ISPID	Sample Date	pH	Concentration (mg/L)								
				HCO_3	CO_3	SO_4	Cl	NO_3	Na	K	Ca	Mg
20-NW	UE-20j Inst. Hole_o1Z	Average	7.5	150.0	--	135.0	115.0	0.9	138.0	6.4	46.0	1.2
	ER-20-12_m1	04/26/2001	7.9	154.8	--	112.0	82.4	--	147.3	--	17.0	0.3
	PM-3_p2	Average	8.1	135.8	--	117.1	94.2	0.0	125.1	12.9	25.8	2.2
20-S	UE-20f_o1Z	Average	7.2	164.0	--	48.0	40.0	0.1	113.0	2.0	4.8	--
	ER-20-5-3_m1	Average	8.5	100.0	7.3	34.1	17.2	0.0	76.6	4.2	3.8	0.2
	ER-EC-11_m1-2	04/03/2016	7.5	140.2	--	70.0	43.2	--	100.0	0.7	3.9	0.0

Table 5-34
Water Chemistry Data Used for Mechanistic Modeling of K_d
(Page 2 of 2)

Sub Area	ISPID	Sample Date	pH	Concentration (mg/L)								
				HCO_3	CO_3	SO_4	Cl	NO_3	Na	K	Ca	Mg
20-NE	U-20 WW_m1	Average	7.5	105.2	3.6	30.6	11.7	1.8	58.3	1.8	6.1	0.4
	U-20ai_o1Z	03/12/1985	8.4	175.0	2.8	26.0	63.5	1.0	115.0	7.2	4.3	1.1
	ER-20-6-1_m1	Average	8.2	84.5	3.6	34.1	13.5	--	58.7	2.3	5.8	0.4
19-SW	UE-19h_m1	Average	8.2	202.0	--	38.2	9.1	0.1	62.2	3.2	24.1	1.4
	UE-19e/Inst._o1Z	Average	8.0	82.0	--	14.7	5.9	2.6	41.8	0.9	1.3	0.1
	U-19d2_o1Z	Average	7.8	429.7	--	67.2	30.5	10.2	158.7	3.8	43.5	3.6
19-NE	U-19az_o1	Average	8.0	145.0	--	18.7	94.4	0.4	102.0	5.8	19.9	1.8
	UE-19fS_o1Z	08/18/1965	8.1	86.0	--	9.0	6.3	2.2	29.0	3.0	11.0	1.6
	U19aS_o1Z	Average	8.4	213.3	43.0	34.7	11.2	5.2	229.3	6.9	1.4	0.1

Source: Carle et al., 2020

Table 5-35
Mean Log_{10} K_d for RN Analogs by HGU, Diagenetic Zone, and Chemistry Subarea
(Page 1 of 4)

HGU	DZ	Chemistry Subarea	Log_{10} K_d for RN Analogs				
			Cs	Sr	Np	Pu	U
AA	1	20-NW	3.37	2.41	0.15	2.44	0.48
		20-S	3.72	3.17	0.67	2.70	0.61
		20-NE	3.65	3.07	0.54	2.72	0.80
		19-NE	3.66	3.24	0.63	2.65	0.70
		19-SW	3.55	3.06	0.54	2.60	0.68
	4	20-NW	4.25	1.00	0.78	2.20	0.27
		20-S	4.59	1.76	1.50	3.20	0.40
		20-NE	4.53	1.62	1.32	2.91	0.60
		19-NE	4.54	1.80	1.47	3.07	0.52
		19-SW	4.37	1.49	1.33	2.42	0.50

Table 5-35
Mean Log_{10} K_d for RN Analogs by HGU, Diagenetic Zone, and Chemistry Subarea
(Page 2 of 4)

HGU	DZ	Chemistry Subarea	Log_{10} K_d for RN Analogs				
			Cs	Sr	Np	Pu	U
VTA	1	20-NW	3.82	1.49	0.03	2.53	0.60
		20-S	4.16	2.26	0.26	2.64	0.72
		20-NE	4.10	2.14	0.27	2.77	0.92
		19-NE	4.11	2.32	0.16	2.63	0.83
		19-SW	3.94	2.11	0.24	2.69	0.81
	2	20-NW	3.46	1.32	0.15	2.78	0.53
		20-S	3.80	2.08	0.19	2.88	0.70
		20-NE	3.73	1.95	0.26	3.01	0.84
		19-NE	3.75	2.13	0.17	2.86	0.71
		19-SW	3.58	1.88	0.24	2.94	0.68
WTA	1	20-NW	3.80	0.79	-0.19	2.06	0.62
		20-S	4.14	1.55	0.20	2.20	0.71
		20-NE	4.07	1.42	0.18	2.30	0.94
		19-NE	4.09	1.60	0.05	2.19	0.86
		19-SW	3.92	1.33	0.14	2.22	0.84
	2	20-NW	3.90	2.21	-0.36	2.15	0.38
		20-S	4.25	2.98	-0.16	2.24	0.50
		20-NE	4.18	2.87	-0.13	2.38	0.70
		19-NE	4.20	3.05	-0.28	2.23	0.61
		19-SW	4.03	2.86	-0.16	2.30	0.59
	3	20-NW	3.96	1.77	-0.44	1.94	0.39
		20-S	4.30	2.54	-0.13	2.05	0.49
		20-NE	4.23	2.43	-0.13	2.18	0.71
		19-NE	4.25	2.61	-0.28	2.04	0.63
		19-SW	4.08	2.41	-0.17	2.10	0.61
	4	20-NW	4.35	1.22	0.01	2.40	0.51
		20-S	4.68	1.98	0.43	2.59	0.63
		20-NE	4.62	1.84	0.35	2.66	0.82
		19-NE	4.64	2.03	0.37	2.55	0.73
		19-SW	4.46	1.72	0.34	2.56	0.71

Table 5-35
Mean Log_{10} K_d for RN Analogs by HGU, Diagenetic Zone, and Chemistry Subarea
(Page 3 of 4)

HGU	DZ	Chemistry Subarea	Log_{10} K_d for RN Analogs				
			Cs	Sr	Np	Pu	U
LFA	1	20-NW	3.86	1.27	-0.43	1.79	0.56
		20-S	4.20	2.04	-0.02	1.95	0.67
		20-NE	4.14	1.92	-0.06	2.04	0.88
		19-NE	4.15	2.10	-0.15	1.93	0.79
		19-SW	3.98	1.88	-0.09	1.94	0.77
	2	20-NW	3.92	2.38	0.06	2.54	0.54
		20-S	4.26	3.15	0.33	2.66	0.65
		20-NE	4.19	3.04	0.32	2.77	0.85
		19-NE	4.21	3.22	0.24	2.64	0.76
		19-SW	4.05	3.03	0.30	2.69	0.74
	3	20-NW	3.87	1.97	-0.15	2.10	0.38
		20-S	4.21	2.74	0.35	2.36	0.49
		20-NE	4.14	2.63	0.25	2.39	0.70
		19-NE	4.16	2.81	0.30	2.31	0.61
		19-SW	3.99	2.62	0.24	2.26	0.59
	4	20-NW	4.24	1.02	-0.42	1.80	0.39
		20-S	4.58	1.78	0.02	1.99	0.49
		20-NE	4.51	1.64	-0.04	2.06	0.71
		19-NE	4.53	1.83	-0.09	1.96	0.62
		19-SW	4.35	1.52	-0.06	1.96	0.61

Table 5-35
Mean Log_{10} K_d for RN Analogs by HGU, Diagenetic Zone, and Chemistry Subarea
(Page 4 of 4)

HGU	DZ	Chemistry Subarea	Log_{10} K_d for RN Analogs				
			Cs	Sr	Np	Pu	U
TCU	1	20-NW	3.98	2.66	0.04	2.67	0.33
		20-S	4.33	3.43	0.08	2.77	0.50
		20-NE	4.26	3.32	0.15	2.90	0.64
		19-NE	4.28	3.50	0.06	2.75	0.52
		19-SW	4.13	3.31	0.13	2.83	0.49
	2	20-NW	3.91	2.78	-0.10	2.47	0.20
		20-S	4.25	3.55	0.09	2.59	0.36
		20-NE	4.19	3.44	0.08	2.71	0.52
		19-NE	4.20	3.62	0.06	2.57	0.40
		19-SW	4.07	3.44	0.07	2.63	0.38
	3	20-NW	4.12	2.38	-0.10	2.36	0.32
		20-S	4.46	3.15	0.28	2.53	0.47
		20-NE	4.39	3.04	0.20	2.61	0.64
		19-NE	4.41	3.22	0.24	2.50	0.53
		19-SW	4.25	3.03	0.20	2.52	0.51
	4	20-NW	4.35	1.22	-0.20	2.20	0.27
		20-S	4.69	1.98	0.22	2.39	0.40
		20-NE	4.62	1.84	0.14	2.46	0.59
		19-NE	4.64	2.02	0.17	2.35	0.49
		19-SW	4.47	1.73	0.13	2.36	0.47
ICU	4	20-NW	3.45	0.63	-0.13	2.12	-0.17
		20-S	3.78	1.39	0.44	2.44	0.01
		20-NE	3.72	1.25	0.29	2.43	0.14
		19-NE	3.74	1.43	0.41	2.37	0.01
		19-SW	3.56	1.14	0.30	2.28	-0.02

Source: Carle et al., 2020

Note: Subareas 19-W and 19-E reported by Carle et al. (2020) were corrected to 19-NE and 19-SW, respectively.

in Yucca Flat and therefore significant effort was placed on development of K_d distributions (Navarro, 2019a). Site-specific ^{90}Sr and ^{137}Cs K_d distributions were developed as a model evaluation target (Navarro, 2019a) and the K_d distribution for Pu was developed in response to a comment by the

Table 5-36
Standard Deviation of Log_{10} K_d for RN Analogs by HGU, Diagenetic Zone, and Chemistry Subarea
(Page 1 of 3)

HGU	DZ	Chemistry Subarea	Standard Deviation of Log_{10} K_d for RN Analogs				
			Cs	Sr	Np	Pu	U
AA	1	20-NW	0.24	0.26	0.21	0.23	0.23
		20-S	0.22	0.23	0.21	0.23	0.23
		20-NE	0.23	0.23	0.21	0.27	0.30
		19-NE	0.33	0.43	0.38	0.40	0.43
		19-SW	0.24	0.35	0.30	0.32	0.38
	4	20-NW	0.24	0.26	0.25	0.24	0.25
		20-S	0.22	0.23	0.23	0.29	0.25
		20-NE	0.23	0.23	0.23	0.34	0.32
		19-NE	0.32	0.43	0.42	0.45	0.45
		19-SW	0.23	0.31	0.34	0.27	0.39
VTA	1	20-NW	0.53	0.37	0.30	0.38	0.30
		20-S	0.51	0.34	0.35	0.42	0.30
		20-NE	0.52	0.34	0.29	0.41	0.36
		19-NE	0.58	0.52	0.35	0.50	0.48
		19-SW	0.51	0.45	0.29	0.45	0.43
	2	20-NW	0.24	0.26	0.16	0.23	0.20
		20-S	0.22	0.23	0.25	0.29	0.20
		20-NE	0.23	0.22	0.19	0.27	0.28
		19-NE	0.32	0.43	0.18	0.38	0.41
		19-SW	0.23	0.33	0.17	0.32	0.35
WTA	1	20-NW	0.37	0.29	0.23	0.23	0.29
		20-S	0.36	0.26	0.34	0.27	0.29
		20-NE	0.36	0.26	0.27	0.27	0.35
		19-NE	0.43	0.45	0.37	0.38	0.47
		19-SW	0.36	0.36	0.28	0.32	0.42
	2	20-NW	0.42	0.45	0.30	0.36	0.31
		20-S	0.40	0.43	0.40	0.40	0.31
		20-NE	0.41	0.43	0.32	0.39	0.37
		19-NE	0.48	0.60	0.31	0.48	0.49
		19-SW	0.40	0.53	0.29	0.43	0.44

Table 5-36
Standard Deviation of Log_{10} K_d for RN Analogs by HGU, Diagenetic Zone, and Chemistry Subarea
(Page 2 of 3)

HGU	DZ	Chemistry Subarea	Standard Deviation of Log_{10} K_d for RN Analogs				
			Cs	Sr	Np	Pu	U
WTA	3	20-NW	0.36	0.49	0.29	0.34	0.30
		20-S	0.35	0.47	0.39	0.38	0.30
		20-NE	0.35	0.47	0.32	0.37	0.36
		19-NE	0.42	0.63	0.38	0.47	0.48
		19-SW	0.35	0.57	0.32	0.41	0.42
	4	20-NW	0.32	0.34	0.46	0.59	0.38
		20-S	0.30	0.32	0.42	0.58	0.40
		20-NE	0.31	0.32	0.42	0.61	0.43
		19-NE	0.38	0.49	0.53	0.68	0.54
		19-SW	0.31	0.39	0.46	0.66	0.48
LFA	1	20-NW	0.40	0.36	0.46	0.41	0.40
		20-S	0.39	0.34	0.53	0.45	0.40
		20-NE	0.39	0.34	0.48	0.45	0.45
		19-NE	0.46	0.51	0.59	0.57	0.56
		19-SW	0.39	0.43	0.51	0.48	0.51
	2	20-NW	0.37	0.44	0.46	0.44	0.57
		20-S	0.36	0.42	0.55	0.47	0.57
		20-NE	0.36	0.42	0.50	0.47	0.63
		19-NE	0.43	0.58	0.55	0.56	0.74
		19-SW	0.36	0.51	0.51	0.50	0.69
	3	20-NW	0.36	0.49	0.45	0.44	0.43
		20-S	0.34	0.47	0.51	0.46	0.42
		20-NE	0.35	0.47	0.49	0.46	0.48
		19-NE	0.42	0.63	0.65	0.57	0.60
		19-SW	0.34	0.56	0.56	0.50	0.55
	4	20-NW	0.40	0.39	0.33	0.47	0.37
		20-S	0.39	0.36	0.41	0.45	0.38
		20-NE	0.39	0.36	0.34	0.48	0.43
		19-NE	0.46	0.53	0.54	0.54	0.54
		19-SW	0.39	0.42	0.39	0.53	0.49

Table 5-36
Standard Deviation of Log_{10} K_d for RN Analogs by HGU, Diagenetic Zone, and Chemistry Subarea
(Page 3 of 3)

HGU	DZ	Chemistry Subarea	Standard Deviation of Log_{10} K_d for RN Analogs				
			Cs	Sr	Np	Pu	U
TCU	1	20-NW	0.30	0.29	0.16	0.23	0.21
		20-S	0.29	0.26	0.25	0.29	0.21
		20-NE	0.29	0.26	0.19	0.27	0.29
		19-NE	0.37	0.45	0.18	0.38	0.41
		19-SW	0.28	0.37	0.17	0.32	0.36
	2	20-NW	0.40	0.29	0.49	0.56	0.52
		20-S	0.39	0.26	0.50	0.58	0.53
		20-NE	0.39	0.26	0.48	0.58	0.58
		19-NE	0.46	0.44	0.56	0.66	0.68
		19-SW	0.38	0.37	0.49	0.62	0.63
	3	20-NW	0.41	0.33	0.40	0.39	0.35
		20-S	0.39	0.30	0.56	0.42	0.35
		20-NE	0.40	0.30	0.49	0.42	0.41
		19-NE	0.47	0.48	0.71	0.52	0.52
		19-SW	0.39	0.41	0.57	0.46	0.47
	4	20-NW	0.35	0.35	0.42	0.53	0.39
		20-S	0.34	0.33	0.40	0.52	0.40
		20-NE	0.34	0.33	0.39	0.55	0.44
		19-NE	0.41	0.50	0.50	0.62	0.55
		19-SW	0.34	0.41	0.43	0.60	0.50
ICU	4	20-NW	0.24	0.26	0.22	0.23	0.20
		20-S	0.22	0.23	0.22	0.22	0.21
		20-NE	0.23	0.23	0.21	0.27	0.28
		19-NE	0.32	0.43	0.39	0.40	0.41
		19-SW	0.23	0.32	0.31	0.31	0.35

Source: Carle et al., 2020

Note: Subareas 19-W and 19-E reported by Carle et al. (2020) were corrected to 19-NE and 19-SW, respectively.

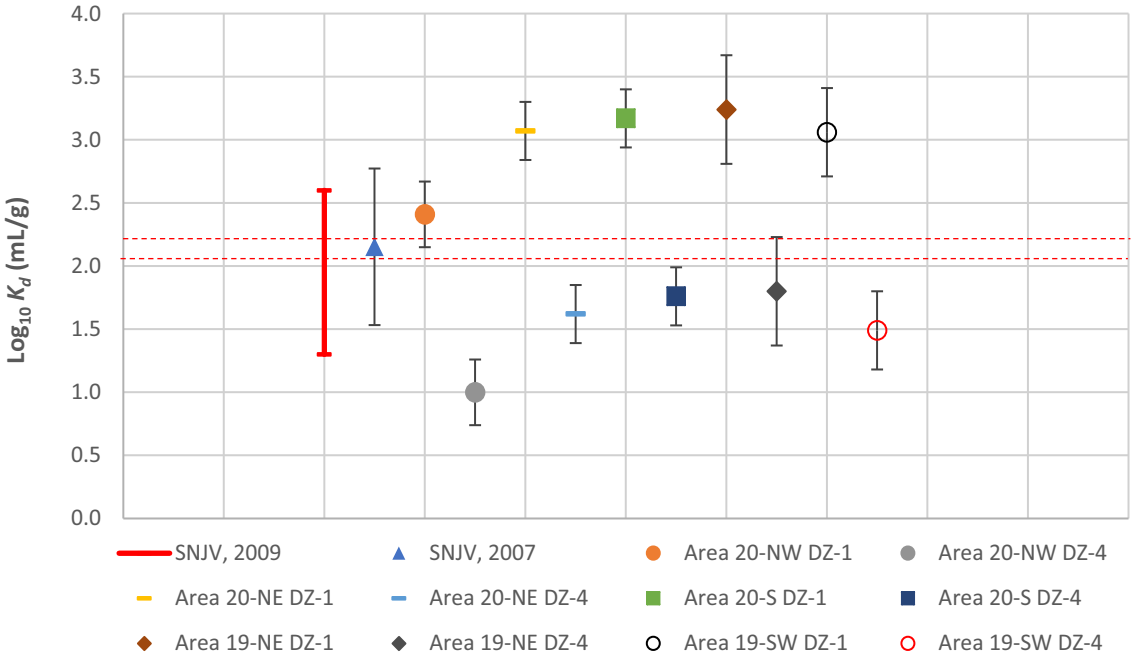

Note:
(1) SNJV, 2009 values represent the 5th and 95th percentiles, all other values are the mean ± standard deviation.
(2) SNJV, 2007 values are measured; red dashed lines represent the range of measured values.
(3) Area specific K_ds from Carle et al., 2020.

Figure 5-43
Comparison of Sr K_d Values in Alluvium

external peer review panel that the values used for Pu retardation may be too high (see Section 2.5.1 and Table 2-10 of Navarro, 2016). The U K_d distribution is from transport studies for WIPP (Rechard and Tierney, 2005).

5.9.4 Scaling Considerations

PM CAU-scale transport simulations for CB assessment will be conducted over various spatial scales. Volumes in the computational model represented with a single set of transport parameters will be much larger than sample volumes used for laboratory measurements. Scaling considerations for K_ds must address how well measurements conducted at the laboratory-scale represent the integrated sorptive behavior of a much larger volume in the PM CAU transport model. Factors include representativeness of the samples used for laboratory measurements relative to variability of the

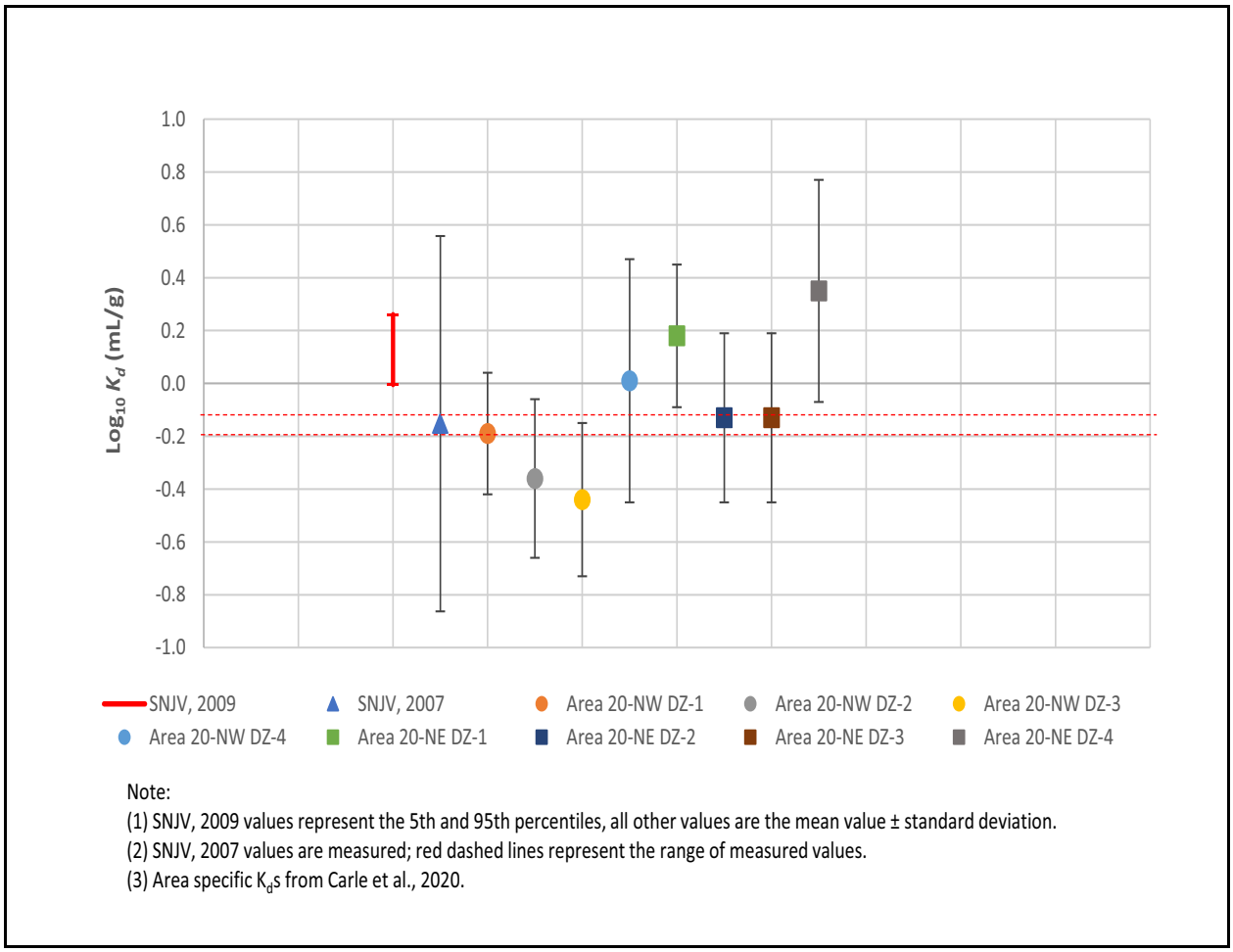

Figure 5-44
Comparison of Np K_d Values in Devitrified Tuff

formation characterized; and larger-scale, longer-term processes that may not be well-characterized in the laboratory.

5.9.5 Data Limitations

The YMP dataset of measured sorption K_ds contains an extensive set of experimentally determined K_d values with which probability distribution functions can be developed. However, the uncertainty in the measured K_d values and the uncertainty in field K_d values may not be governed by the same processes. Multiple rock samples are associated with the K_d distributions, providing some insight into spatial variability within a given HGU. However, all K_d values determined from experimental sorption studies are specific to the small sample of aquifer material and the experimental conditions. Thus, applying the measured K_d values to field simulations involves the assumption that groundwater conditions in the field are similar to those in the experiments and are unchanging, or at least that the

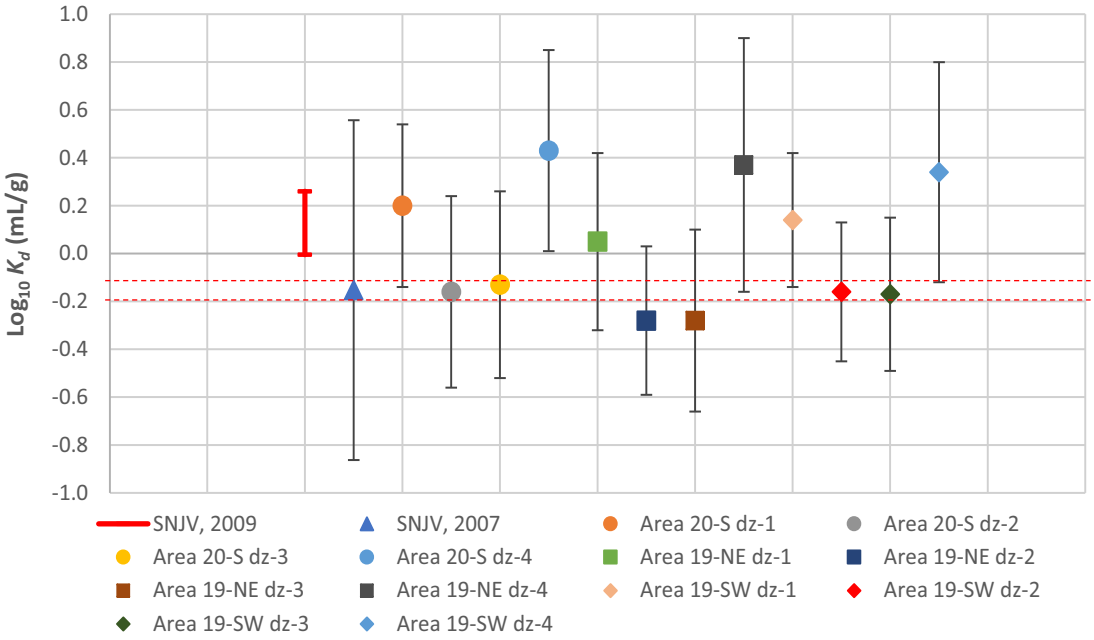

Note:
(1) SNJV, 2009 values represent the 5th and 95th percentiles, all other values are the mean ± standard deviation.
(2) SNJV, 2007 values are measured; red dashed lines represent the range of measured values.
(3) Area specific K_ds from Carle et al., 2020.

Figure 5-45
Additional Comparisons of Np K_d Values in Devitrified Tuff

Table 5-37
LCA Transport Model K_d Distributions

RN	K_d (mL/g)				Source
	Lower Bound	Upper Bound	Mode	Shape	
^{90}Sr	0.05	0.14	0.095	Triangular	Navarro, 2019a
$^{135/137}$Cs	0.02	0.07	0.045	Triangular	Navarro, 2019a
U	0.03	30	15	Triangular	Rechard and Tierney, 2005
$^{239/240/242}$Pu	0.76	1,096	548	Triangular	Navarro, 2016

probability distribution represents variability that may exist in the field. Finally, correlation of the K_ds with mineral composition of the samples is limited (e.g., rock classifications of vitric, devitrified, or

zeolitic). The work of Carle et al. (2020) takes the analysis a step further by using a mechanistic model to upscale the K_d values and dividing the area by DZ and chemistry subarea.

6.0 REFERENCES

Bechtel SAIC, see Bechtel SAIC Company, LLC.

BN, see Bechtel Nevada.

Baecher, B.G., N.A. Lanney, and H.H. Einstein. 1977. "Statistical Descriptions of Rock Properties and Sampling." In *Proceedings of the 18th U.S. Symposium on Rock Mechanics*. American Institute of Mining Engineers.

Bear, J. 1972. *Dynamics of Fluids in Porous Media*. New York, NY: Elsevier Publishing Co.

Bechtel Nevada. 2002. *A Hydrostratigraphic Model and Alternatives for the Groundwater Flow and Contaminant Transport Model of Corrective Action Units 101 and 102: Central and Western Pahute Mesa, Nye County, Nevada*, DOE/NV/11718--706. Prepared for the U.S. Department of Energy, National Nuclear Security Administration Nevada Operations Office. Las Vegas, NV.

Bechtel Nevada. 2006. *A Hydrostratigraphic Model and Alternatives for the Groundwater Flow and Contaminant Transport Model of Corrective Action Unit 97: Yucca Flat-Climax Mine, Lincoln and Nye Counties, Nevada*, DOE/NV/11718--1119. Las Vegas, NV.

Bechtel SAIC Company, LLC. 2004a. *Probability Distribution for Flowing Interval Spacing*, ANL-NBS-MD-000003 REV 01, DOC.20040923.0003. Las Vegas, NV.

Bechtel SAIC Co., LLC, 2004b, *Saturated Zone In-Situ Testing*, ANL-NBS-HS-000039 REV 01.

Bedinger, M.S., K.A. Sargent, W.H. Langer, F.B. Sherman, J.E. Reed, and B.T. Brady. 1989. *Studies of Geology and Hydrology in the Basin and Range Province, Southwestern United States, for Isolation of High-Level Radioactive Waste – Basis of Characterization Evaluation*, Professional Paper 1370-A. Denver, CO: U.S. Geological Survey.

Belcher, W.R., and D.S. Sweetkind eds. 2010. *Death Valley Regional Groundwater Flow System, Nevada and California—Hydrogeologic Framework and Transient Groundwater Flow Model,* Professional Paper 1711. Reston, VA: U.S. Geological Survey.

Berger, D.L. 1992. *Lithologic Properties of Carbonate-Rock Aquifers at Five Test Wells in the Coyote Spring Valley Area, Southern Nevada, as Determined from Geophysical Logs*, Water-Resources Investigations Report 91-4167. Prepared in cooperation with the State of Nevada, the Las Vegas Valley Water District, and the U.S Bureau of Reclamation. Carson City, NV: U.S. Geological Survey.

Berkowitz, B. 2002. "Characterizing Flow and Transport in Fractured Geological Media: A Review." In *Advances in Water Resources* 25, Vol. 25(8–12): pp. 861–884.

Blankennagel, R.K., and J.E. Weir, Jr. 1973. *Geohydrology of the Eastern Part of Pahute Mesa. Nevada Test Site, Nye County, Nevada,* Professional Paper 712-B. Denver, CO: U.S. Geological Survey.

Bradley, H.B., ed. 1992. *Petroleum Engineering Handbook*. Richardson, TX: Society of Petroleum Engineers.

Bryant, E.A. 1992. *The Cambric Migration Experiment, A Summary Report,* LA-12335-MS. Los Alamos, NM: Los Alamos National Laboratory.

Burbey, T.J., and S.W. Wheatcraft. 1986. *Tritium and Chlorine-36 Migration from a Nuclear Explosion Cavity*, DOE/NV/1034-09; Publication No. 45050. Las Vegas, NV: Desert Research Institute.

Burnett, R.D., and E.O. Frind. 1987. "Simulation of Contaminant Transport in Three Dimensions: 2, Dimensionality Effects." In *Water Resources Research* 23, Vol. 23(4): pp 695–705. Washington, DC: American Geophysical Union.

Butkovich, T.R. 1976. *Cavities Produced by Underground Nuclear Explosions*, UCRL-52097. Livermore, CA: Lawrence Livermore National Laboratory.

Butkovich, T.R., and A.E. Lewis. 1973. *Aids for Estimating Effects of Underground Nuclear Explosions*, UCRL-50929. Livermore, CA: Lawrence Livermore National Laboratory.

CFR, see *Code of Federal Regulation*s.

Callahan, T.J., P.W. Reimus, R.S. Bowman, and M.J. Haga. 2000. "Using Multiple Experimental Methods to Determine Fracture/Matrix Interactions and Dispersion of Nonreactive Solutes in Saturated Volcanic Rock." In *Water Resources Research*, Vol. 36(12): pp. 3547–3558. Washington, DC: American Geophysical Union.

Carle, S.F. 2018. *Updated K_d Estimates for Modeling Sorption of Cs, Sr, and Pu Isotopes in Hydrostratigraphic Units of Rainier Mesa and Shoshone Mountain,* LLNL-TR-751397. Livermore, CA: Lawrence Livermore National Laboratory.

Carle, S.F., R.M. Maxwell, and G.A. Pawloski. 2003. *Impact of Test Heat on Groundwater Flow at Pahute Mesa, Nevada Test Site*, UCRL-ID-152599. Livermore, CA: Lawrence Livermore National Laboratory.

Carle, S.F. 2020. *Interpretation of Mineralogical Diagenesis for Assessment of Radionuclide Transport at Pahute Mesa, Nevada National Security Site*, LLNL-TR-810225. Livermore, CA: Lawrence Livermore National Laboratory, CA.

Carle, S.F., A.F.B. Tompson, and M. Zavarin. 2020. *Radionuclide Screening Analysis and Transport Parameters for Pahute Mesa Detonations, Nevada National Security Site*, LLNL-TR-812351, Livermore, CA: Lawrence Livermore National Laboratory.

Carle, S.F., A.F.B. Tompson, and M. Zavarin. 2021. *Review of Cavity Radius and Chimney Height Information for Underground Nuclear Tests at Nevada National Security Site,* LLNL-TR-818725. Livermore, CA: Lawrence Livermore National Laboratory.

Cas, R.A.F., and J.V. Wright. 1987. *Volcanic Successions: Modern and Ancient.* London, UK: Allen and Unwin.

Castany, G. 1967. *Traité Pratique des Eaux Souterraine*s. Paris, France: Dunod.

Claassen, H.C., and E.H. Cordes. 1975. "Two-Well Recirculation Tracer Test in Fractured Carbonate Rock, Nevada." In *Hydrological Sciences Bulletin*, Vol. 20(3): pp. 367–382. Oxford, UK: Blackwell Scientific Publications.

Code of Federal Regulations. 2019. Title 40, CFR Part 141, "National Primary Drinking Water Regulations." Washington, DC: U.S. Government Printing Office.

Code of Federal Regulations. 2020. Title 40, Part 141.66, "Maximum Contaminant Levels for Radionuclides." Washington, DC: U.S. Government Printing Office.

Crank, J. 1975. *The Mathematics of Diffusion*. Oxford, UK: Clarendon Press.

DOE/EMNV, see U.S. Department of Energy, Environmental Management Nevada Program.

DOE/NV, see U.S. Department of Energy, Nevada Operations Office

Daniels, W.R. 1981. *Laboratory and Field Studies Related to the Radionuclide Migration Project, October 1, 1979–September 30, 1980*, LA-8670-PR. Los Alamos, NM: Los Alamos National Laboratory.

Daniels, W.R., B.R. Erdal, and D.T. Vaniman, eds. 1983. *Research and Development Related to the Nevada Nuclear Waste Storage Investigations, July 1–September 30, 1982*, LA-9577-PR. Los Alamos, NM: Los Alamos National Laboratory

Daniels, W.R., and J.L. Thompson, comps. and eds. 1984. *Laboratory and Field Studies Related to the Hydrology/Radionuclide Migration Project, October 1, 1982–September 30, 1983*, LA-10121-PR. Los Alamos, NM: Los Alamos National Laboratory.

Decker, D.L, C. Papelis, R.L. Hershey, R. Harris, and G. Schmett. 2003. *Temperature Dependence of Sorption Behavior of Lead and Cesium Metal Ions on Western Pahute Mesa and Rainier Mesa Aquifer Rocks,* DOE/NV/13609-21; Publication 45193. Reno, NV: Desert Research Institute, Division of Hydrologic Sciences.

de Marsily, G. 1986. *Quantitative Hydrogeology*. Orlando, FL: Academic Press Inc.

Domenico, P.A., and G.A. Robbins. 1985. "The Displacement of Connate Water from Aquifers." In *Geological Society of America Bulletin*, Vol. 96: pp. 328–335.

Domenico, P.A., and F.W. Schwartz. 1990. *Physical and Chemical Hydrogeology,* Second Edition. New York, NY: John Wiley & Sons.

Drellack, S.L., Jr., L.B. Prothro, K.E. Roberson, D.B. Schier, and E.H. Price. 1997. *Analysis of Fractures in Volcanic Cores from Pahute Mesa, Nevada Test Site*, DOE/NV/11718-160. Las Vegas, NV: Bechtel Nevada.

Drever, J.I. 1988. *The Geochemistry of Natural Waters*. Englewood Cliffs, NJ: Prentice Hall, Inc.

Dynamic Graphics, Inc. 2019. *EarthVision 10: Software for 3D Modeling & Visualization*. Alameda, CA.

EPA, see U.S. Environmental Protection Agency.

Ekren, E.B., R.E. Anderson, C.L. Rogers, and D.C. Noble. 1971. *Geology of Northern Nellis Air Force Base Bombing and Gunnery Range, Nye County, Nevada,* Professional Paper 651. Washington, DC: U.S. Geological Survey.

Erickson, J.R., and R.K. Waddell. 1985. *Identification and Characterization of Hydrologic Properties of Fractured Tuff Using Hydraulic and Tracer Tests — Test Well USW H-4, Yucca Mountain, Nye County, Nevada*, Water-Resources Investigations Report 85-4066. Denver, CO: U.S. Geological Survey.

FFACO, see *Federal Facility Agreement and Consent Order.*

Federal Facility Agreement and Consent Order. 1996 (as amended March 2010). Agreed to by the State of Nevada; U.S. Department of Energy, Environmental Management; U.S. Department of Defense; and U.S. Department of Energy, Legacy Management. Appendix VI, which contains the Underground Test Area Strategy, was last modified June 2014, Revision No. 5.

Fenelon, J.M., D.S. Sweetkind, and R.J. Laczniak. 2010. *Groundwater Flow Systems at the Nevada Test Site, Nevada: A Synthesis of Potentiometric Contours, Hydrostratigraphy, and Geologic Structures,* Professional Paper 1771. Reston, VA: U.S. Geological Survey.

Fenelon, J.M., K.J. Halford, and M.T. Moreo. 2016. *Delineation of the Pahute Mesa–Oasis Valley Groundwater Basin, Nevada*, Version 1.1, Scientific Investigations Report 2015-5175. Carson City, NV: U.S. Geological Survey.

Ferguson, J.F., A.H. Cogbill, and R.G. Warren. 1994. "A Geophysical-Geological Transect of the Silent Canyon Caldera Complex, Pahute Mesa, Nevada." In *Journal of Geophysical Research: Solid Earth*, Vol. 99(B3): pp. 4323–4339.

Finnegan, D.L., S.M. Bowen, J.L. Thompson, C.M. Miller, P.L. Baca, L.F. Olivas, C.G. Geoffrion, D.K. Smith, W. Goishi, B.K. Esser, J.W. Meadows, N. Namboodiri, and J.F. Wild. 2016. *Nevada National Security Site Underground Radionuclide Inventory, 1951–1992: Accounting for Radionuclide Decay through September 30, 2012,* LA-UR-16-21749. Los Alamos, NM: Los Alamos National Laboratory.

Freeze, R.A., and J.A. Cherry. 1979. *Groundwater*. Englewood Cliffs, NJ: Prentice Hall.

Freeze, R.A., J. Massmann, L. Smith, T. Sperling, and B. James. 1990. "Hydrogeological Decision Analysis: I. A Framework." In *Ground Water*, Vol. 28 (5): pp. 738–766. Columbus, OH: Groundwater Publishing Company.

Freifeld, B.M. 2001. *Estimation of Fracture Porosity in an Unsaturated Fractured Welded Tuff Using Gas Tracer Testing.* Department of Civil and Environmental Engineering, University of California, Berkeley, Ph.D dissertation.

Fridrich, C.J., S.A. Minor, J.L. Slate, and P.L. Ryder. 2007. *Geologic Map of Oasis Valley Spring-Discharge Area and Vicinity, Nye County, Nevada,* Scientific Investigations Map 2957, 25 p., scale 1:50,000. Denver, CO: U.S. Geological Survey.

Frus, R.J., and K.J. Halford. 2018. *Documentation of Single-Well Aquifer Tests and Integrated Borehole Analyses, Pahute Mesa and Vicinity, Nevada,* Scientific Investigations Report 2018-5096. Reston, VA: U.S. Geological Survey.

Golder, see Golder Associates, Ltd.

Garcia, C.A., J.M. Fenelon, K.J. Halford, S.R. Reiner, and R.J. Laczniak. 2011. *Assessing Hydraulic Connections Across a Complex Sequence of Volcanic Rocks—Analysis of U-20 WW Multiple-Well Aquifer Test, Pahute Mesa, Nevada National Security Site, Nevada*: Scientific Investigations Report 2011–5173, 24 pp. Reston, VA: U.S. Geological Survey

Garcia, C.A., T.R. Jackson, K.J. Halford, D.S. Sweetkind, N.A. Damar, J.M. Fenelon, and S.R. Reiner. 2016. *Hydraulic Characterization of Volcanic Rocks in Pahute Mesa Using an Integrated Analysis of 16 Multiple-Well Aquifer Tests, Nevada National Security Site, 2009–14,* Scientific Investigations Report 2016-5151. Carson City, NV: U.S. Geological Survey.

Geldon, A.L., A.M.A. Umari, M.F. Fahy, J.D. Earle, J.M. Gemmell, and J. Darnell. 2002. *Results of Hydraulic Tests in Miocene Tuffaceous Rocks at the C-Hole Complex, 1995 to 1997, Yucca Mountain, Nye County, Nevada*, Water-Resources Investigations Report 02-4141. Denver, CO: U.S. Geological Survey.

Gelhar, L.W., W. Welty, and K.R. Rehfeldt. 1992. "A Critical Review of Data on Field Scale Dispersion in Aquifers." In *Water Resources Research*, Vol. 28(7): pp. 1955–1974. Washington, DC: American Geophysical Union.

Germain, L.S., and J.S. Kahn. 1968. *Phenomenology and Containment of Underground Nuclear Explosions*, UCRL-50482; TID-4500, UC-2. Livermore, CA: University of California, Lawrence Radiation Laboratory.

Golder Associates, Ltd. 2016. Written communication to K. Rehfeldt (Navarro). Subject: "1.0 Fractures and Groundwater Flow at Pahute Mesa."

Grauch, V.J.S., D.A. Sawyer, C.J. Fridrich, and M.R. Hudson. 1999. *Geophysical Framework of the Southwestern Nevada Volcanic Field and Hydrogeologic Implications,* Professional Paper 1608. Denver, CO: U.S. Geological Survey.

Grisak, G.E., and J.F. Pickens. 1980. "Solute Transport Through Fractured Media: 1. The Effect of Matrix Diffusion." In *Water Resources Research*, Vol. 16(4): pp. 719–730. Washington, DC: American Geophysical Union.

Grisak, G.E., and J.F. Pickens. 1981. "An Analytical Solution for Solute Transport Through Fractured Media with Matrix Diffusion." In *Journal of Hydrology*, Vol. 52(1–2): pp. 47–52. Washington, DC: American Geophysical Union.

Grisak, G.E., J.F. Pickens, and J.A. Cherry. 1980. "Solute Transport Through Fractured Media: 2. Column Study of Fractured Till." In *Water Resources Research*, Vol. 16(4): pp. 731–739. Washington, DC: American Geophysical Union.

Grove, D.B. 1977. *The Use of Galerkin Finite-Element Methods to Solve Mass-Transport Equations*, Water-Resources Investigations Report 77-49. Denver, CO: U.S. Geological Survey.

Grove, D.B., and W.A. Beetem. 1971. "Porosity and Dispersion Constant Calculations for a Fractured Carbonate Aquifer using the Two Well Tracer Method." In *Water Resources Research*, Vol. 7(1): pp. 128–134. Washington, DC: American Geophysical Union.

Gustavsson, E., and M. Gunnarsson. 2005. *Oskarshamm Site Investigation. Laboratory Data from the Site Investigation Programme for the Transport Properties of the Rock. Boreholes KSH01A, KSH02A, and KLX02A, P-05-18*. Stockholm, Sweden: Svensk Karnbranslehantering AB, Swedish Nuclear Fuel and Waste Management Co.

HGL, see HydroGeoLogic, Inc.

Halford, K.J., and T.R. Jackson. 2020. *Groundwater Characterization and Effects of Pumping in the Death Valley Regional Groundwater Flow System, Nevada and California, with Special Reference to Devils Hole*, Professional Paper 1863. Reston, VA: U.S. Geological Survey.

Hershey, R.L., W. Howcroft, and P.W. Reimus. 2003. *Laboratory Experiments to Evaluate Diffusion of ^{14}C into Nevada Test Site Carbonate Aquifer Matrix*, DOE/NV/11508-55; Publication No. 45180. Las Vegas, NV: Desert Research Institute.

Hershey, R.L., R. Parashar, C.A. Cooper, K.M. Heintz, H.V. Pham, and B.F. Lyles. 2020. *Evaluation of Timber Mountain Recharge and Groundwater Flow in Relation to Pahute Mesa-Oasis Valley Flow System*, DOE/NV/0003590-56; Publication No. 45294. Las Vegas, NV: Desert Research Institute.

Hevesi, J.A., A.L. Flint, and L.E. Flint. 2003. *Simulation of Net Infiltration and Potential Recharge Using a Distributed-Parameter Watershed Model of the Death Valley Region, Nevada and California.* Water-Resources Investigations Report 03-4090. Sacramento, CA: U.S. Geological Survey.

Hildenbrand, T.G., V.E. Langenheim, E.A. Mankinen, and E.H. McKee. 1999. *Inversion of Gravity Data To Define the Pre-Tertiary Surface and Regional Structures Possibly Influencing Ground-Water Flow in the Pahute Mesa-Oasis Valley Region, Nye County, Nevada,* Open-File Report 99-49. Menlo Park, CA: U.S. Geological Survey.

Hoaglund, J., 2017. Written communication to K. Rehfeldt (Navarro). Subject: *Effect of Fault Proximity on Large-Scale Hydraulic Conductivity.* Las Vegas, NV.

Hoffman, D.C. 1979. "A Field Study of Radionuclide Migration." In *Radioactive Waste in Geologic Storage*, pp. 149–166. S. Fried ed. Washington, DC: American Chemical Society.

Houser, F.N., R.E. Davis, and W.L. Emerick. 1961. *Geologic Reconnaissance of Granite Intrusive Masses at Gold Meadows, Tem Piute, and Trappman's Camp, Lincoln and Nye Counties, Nevada, and Comparison with Climax Stock of the Nevada Test Site*, TEI-793; Open File Report 61-70. Washington, DC: U.S. Geological Survey.

Hudak, P.F. 1994. "Effective Porosity of Unconsolidated Sand; Estimation and Impact on Capture Zone Geometry." In *Environmental Geology*, Vol. 24(2): pp. 140–143.

Huyakorn, P.S., B.H. Lester, and J.W. Mercer. 1983a. "An Efficient Finite Element Technique for Modeling Transport in Fractured Porous Media: 1. Single Species Transport." In *Water Resources Research*, Vol. 19(3): pp. 841–854. Washington, DC: American Geophysical Union.

Huyakorn, P.S., B.H. Lester, and J.W. Mercer. 1983b. "An Efficient Finite Element Technique for Modeling Transport in Fractured Porous Media: 2. Nuclide Decay Chain Transport." In *Water Resources Research*, Vol. 19(5): pp. 1286–1296. Washington, DC: American Geophysical Union.

HydroGeoLogic, Inc. 2017. Written communication to K. Rehfeldt (Navarro). Subject: "Task Order 3: Fracture Analysis," Technical Data Repository No. UGTA-4-1808, 29 September 29. Reston, VA.

HydroGeoLogic, Inc. 2018a. Written communication to K. Rehfeldt (Navarro). Subject: "Task Order 5: Transport Parameters (Dispersivity, Matrix Diffusion, and Mass Transfer Coefficient)," Technical Data Repository No. UGTA-4-2099, 22 August. Reston, VA.

HydroGeoLogic, Inc. 2018b. Written communication to K. Rehfeldt (Navarro). Subject: "Task Order 6: Porosity (Fracture and Matrix)," Technical Data Repository No. UGTA-4-2100, 30 September. Reston, VA.

IT, see IT Corporation.

Intera. 2014. Written communication. Subject: *Evaluation of Fracture Porosity Data for Pahute Mesa CAU.*

IT Corporation. 1996a. *Hydrologic Parameter Data Documentation Package (Underground Test Area Subproject Phase 1 Data Analysis Documentation, Volume IV),* ITLV/10972-181. Prepared for the U.S. Department of Energy, Nevada Operations Office. Las Vegas, NV.

IT Corporation. 1996b. *Potentiometric Data Documentation Package (Underground Test Area Subproject Phase 1 Data Analysis Documentation, Volume II),* ITLV/10972-181. Prepared for the U.S. Department of Energy, Nevada Operations Office. Las Vegas, NV.

IT Corporation. 1996c. *Regional Geologic Model Data Documentation Package (Underground Test Area Subproject Phase 1 Data Analysis Documentation, Volume I),* ITLV/10972--181. Prepared for the U.S. Department of Energy, Nevada Operations Office. Las Vegas, NV.

IT Corporation. 1996d. *Transport Parameter and Source Term Data Documentation Package (Underground Test Area Subproject Phase 1 Data Analysis Documentation, Volume V)*, ITLV/10972-181. Prepared for the U.S. Department of Energy, Nevada Operations Office. Las Vegas, NV.

IT Corporation. 1998. *Report and Analysis of the BULLION Forced-Gradient Experiment,* DOE/NV/13052-042; ITLV/13052-042, UC-700. Las Vegas, NV.

IT Corporation. 2001. *Underground Test Area Fracture Analysis Report: Analysis of Fractures in Volcanic Rocks of Western Pahute Mesa – Oasis Valley*, ITLV/13052-150. Las Vegas, NV.

IT Corporation. 2002a. *Analysis of Well ER-EC-1 Testing, Western Pahute Mesa-Oasis Valley FY2000 Testing Program*, DOE/NV/13052--846; ITLV/13052--173. Las Vegas, NV.

IT Corporation. 2002b. *Analysis of Well ER-EC-2a Testing, Western Pahute Mesa-Oasis Valley FY 2000 Testing Program*, Rev. 0, DOE/NV/13052--851; ITLV/13052--174. Las Vegas, NV.

IT Corporation. 2002c. *Analysis of Well ER-EC-4 Testing, Western Pahute Mesa-Oasis Valley FY2000 Testing Program*, DOE/NV/13052--850; ITLV/13052--175. Las Vegas, NV.

IT Corporation. 2002d. *Analysis of Well ER-EC-5 Testing, Western Pahute Mesa-Oasis Valley FY 2000 Testing Program,* DOE/NV/13052--848; ITLV/13052--176. Las Vegas, NV.

IT Corporation. 2002e. *Analysis of Well ER-EC-8 Testing, Western Pahute Mesa-Oasis Valley FY 2000 Testing Program*, Rev.0, DOE/NV/13052--847; ITLV/13052--179. Las Vegas, NV.

Jackson, T.R., and J.M. Fenelon. 2018. *Conceptual Framework and Trend Analysis of Water-Level Responses to Hydrologic Stresses, Pahute Mesa–Oasis Valley Groundwater Basin, Nevada, 1966–2016,* Scientific Investigation Report 2018-5064. Reston, VA: U.S. Geological Survey.

Jackson, T.R., J.M. Fenelon, and R.L. Paylor. 2021. *Groundwater Flow Conceptualization of the Pahute Mesa–Oasis Valley Groundwater Basin, Nevada: A Synthesis of Geologic, Hydrologic, Hydraulic-Property, and Tritium Data,* Scientific Investigations Report 2020–5134. Carson City, NV: U.S. Geological Survey.

Jakob, A. 2004. *Matrix Diffusion for Performance Assessment - Experimental Evidence, Modeling Assumptions and Open Issues*, PSI Bericht Nr. 04-08. Villigen, Switzerland: Paul Scherrer Institut, Nuclear Energy and Safety Research Department Laboratory for Waste Management.

Johnston, R.H. 1968. *U.S. Geological Survey Tracer Study, Amargosa Desert, Nye County, Nevada. Part I: Exploratory Drilling, Tracer Well Construction and Testing, and Preliminary Findings*, Open-File Report 68-152. Washington, DC: U.S. Geological Survey.

Jones, T.L., V.A. Kelley, J.F. Pickens, D.T. Upton, R.L. Beauheim, and P.B. Davies. 1992. *Integration of Interpretation Results of Tracer Tests Performed in the Culebra Dolomite at the Waste Isolation Pilot Plant Site*, SAND92-1579-UC-721. Albuquerque, NM: Sandia National Laboratories.

Kane, M.F., M.W. Webring, and B.K. Bhattacharyya. 1981. *A Preliminary Analysis of Gravity and Aeromagnetic Surveys of the Timber Mountain Area, Southern Nevada,* Open-File Report 81-189. Denver, CO: U.S. Geological Survey.

Kersting, A.B., D.W. Efurd, D.L. Finnegan, D.J. Rokop, D.K. Smith, and J.L. Thompson. 1999. "Migration of Plutonium in Ground Water at the Nevada Test Site." In *Nature*, Vol. 397: pp. 56–59.

Kersting, A.B., D.L. Finnegan, A.F.B. Tompson, B.K. Esser, D.K. Smith, M. Zavarin, C.J. Bruton, and G.A. Pawloski. 2003. *Radionuclide Decay and In-growth Technical Basis Document*, UCRL-ID-153798. Livermore, CA: Lawrence Livermore National Laboratory.

Laczniak, R.J., J.C. Cole, D.A. Sawyer, and D.A. Trudeau. 1996. *Summary of Hydrogeologic Controls on Ground-Water Flow at the Nevada Test Site, Nye County, Nevada*, Water-Resources Investigations Report 96-4109. Carson City, NV: U.S. Geological Survey.

Lallemand-Barres, P. and P. Peaudecerf. 1978. *Recherche des Relations entre la Valeur de la Dispersivite Macroscopique d'un Milieu Aquifere, ses Autres Caracteristiques et les Conditions de Mesure,* Etude Bibligraphique: Bulletin, Bureau de Recherches Geologiques et Minieres, Sec. 3/4:227-87

Leap, D.I., and P.M. Belmonte. 1992. "Influence of Pore Pressure on Apparent Dispersivity of a Fissured Dolomitic Aquifer." In *Ground Water,* Vol. 30(1): pp. 87–95. Columbus, OH: Groundwater Publishing Company.

Lee, C.H., and I. Farmer. 1993. *Fluid Flow in Discontinuous Rocks*. London, UK: Chapman and Hall.

Lerman, A. 1979. *Geochemical Processes: Water and Sediment Environments*. New York, NY: John Wiley & Sons.

Lichtner, P.C., S. Kelkar, and B. Robinson. 2002. "New Form of Dispersion Tensor for Axisymmetric Porous Media with Implementation in Particle Tracking." In *Water Resources Research*, Vol. 38(8): pp. 21-1–21-16.

Liu, H.-H., G.S. Bodvarsson, and G. Zhang. 2004. "Scale Dependency of the Effective Matrix Diffusion Coefficient." In *Vadose Zone Journal*, Vol. 3(1): pp. 312–315.

Lu, Z., E. Kwicklis, T. Miller and M. Bourret. 2021. *Development and Calibration of the Pahute Mesa Bench Area Groundwater Flow and Tritium Transport Model, Nevada National Security Site*, LA-UR-21-23595. Los Alamos, NM: Los Alamos National Laboratory.

Makedonska, N., J.D. Hyman, E.M. Kwicklis, and K.H. Birdsell. 2018. "Discrete Fracture Network Modeling and Simulation of Subsurface Transport for the Topopah Spring Aquifer at Pahute Mesa." *Second International Discrete Fracture Network Engineering Conference*, 20–22 June. Seattle, WA.

Makedonska, N., E. Kwicklis, J.D. Hyman, and M. Bourret. 2020. *Discrete Fracture Network Modeling to Estimate Upscaled Parameters for the Topopah Spring, Lava Flow, and Tiva Canyon Aquifers at Pahute Mesa, Nevada National Security Site*, LA-UR-20-22665. Los Alamos, NM: Los Alamos National Laboratory.

Maldonado, F. 1977. *Summary of the Geology and Physical Properties of the Climax Stock, Nevada Test Site*, Open-File Report-77-356. Denver, CO: U.S. Geological Survey.

Maloszewski, P., and A. Zuber. 1985. "On the Theory of Tracer Experiments in Fissured Rocks with a Porous Matrix." In *Journal of Hydrology*, Vol. 79(3–4): p. 333–358.

Mankinen, E.A., T.G. Hildenbrand, G.L. Dixon, E.H. McKee, C.J. Fridrich, and R.J. Laczniak. 1999. *Gravity and Magnetic Study of the Pahute Mesa and Oasis Valley Region, Nye County, Nevada,* Open-File Report 99-303, Version 1.0. Reston, VA; U.S. Geological Survey.

Mankinen, E.A., T.G. Hildenbrand, C.J. Fridrich, E.H. McKee, and C.J. Schenkel. 2003. *Geophysical Setting of the Pahute Mesa-Oasis Valley Region, Southern Nevada,* Report 50. Reno, NV: Nevada Bureau of Mines and Geology.

Mazurek, M., and A. Jakob. 2002. "Evidence for Matrix Diffusion in the TRUE-1 Block at Aspo Based on Fracture Characterization and Modelling of Tracer Tests." In *Radionuclide Retention in Geologic Media*, Workshop Proceedings, Oskarshamn, Sweden, 7–9 May 2001, Nuclear Energy Agency, Paris, France. OECD 2002, 137-154.

Middleton, R.S., E.M. Kwicklis, K.H. Birdsell, D.G. Levitt, and J. Hevesi. 2019. *Net Infiltration Models for the Pahute Mesa Area,* LA-UR-16-27513, Rev 1. Los Alamos, NM: Los Alamos National Laboratory.

Mills, R. 1973. "Self-Diffusion in Normal and Heavy Water in the Range 1-45°." In *The Journal of Physical Chemistry,* Vol. 77(5): pp. 685–688.

Mills, R., and V.M.M. Lobo. 1989. *Self-Diffusion in Electrolyte Solutions, a Critical Examination of Data Compiled from the Literature*. New York, NY: Elsevier Science Publishing Company, Inc.

Moench, A.F. 1989. "Convergent Radial Dispersion: A Laplace Transform Solution for Aquifer Tracer Testing." In *Water Resources Research*, Vol. 25(3): pp. 439–447. Washington, DC: American Geophysical Union.

Moench, A.F. 1995. "Convergent Radial Dispersion in a Double-Porosity Aquifer with Fracture Skin: Analytical Solution and Application to a Field Experiment in Fractured Chalk." In *Water Resources Research*, Vol. 31(8): pp. 1823–1835. Washington, DC: American Geophysical Union.

Moreno, L., I. Neretnieks, and T. Eriksen. 1985. "Analysis of Some Laboratory Tracer Runs in Natural Fissures." In *Water Resources Research*, Vol. 21(7): pp 951–958. Washington, DC: American Geophysical Union.

N-I, see Navarro-Intera, LLC.

NNES, see Navarro Nevada Environmental Services, LLC.

NNSA/NFO, see U.S. Department of Energy, National Nuclear Security Administration Nevada Field Office.

NNSA/NSO, see U.S. Department of Energy, National Nuclear Security Administration Nevada Site Office.

NRC, see National Research Council.

NSTec, see National Security Technologies, LLC.

National Research Council. 1996. *Rock Fractures and Fluid Flow*. Washington, DC: National Academy Press.

National Security Technologies, LLC. 2014. Written communication. Subject: *Phase II Hydrostratigraphic Framework Model for Corrective Action Units 101 and 102 Central and Western Pahute Mesa, Nye County Nevada*. November. Las Vegas, NV.

Navarro. 2016. *Response to External Peer Review Team Report for Corrective Action Unit 97: Yucca Flat/Climax Mine, Nevada National Security Site, Nye County, Nevada,* Rev. 1, N/0002653--031-REV. 1. Las Vegas, NV.

Navarro. 2019a. *Model Evaluation Report for Corrective Action Unit 97: Yucca Flat/Climax Mine, Nevada National Security Site, Nye County, Nevada*, Rev. 1, N/0002653--063. Las Vegas, NV.

Navarro. 2019b. Written communication. Subject: *BENHAM Test Supplemental GoldSim Modeling*, Technical Data Repository No. UGTA-4-2018. Las Vegas, NV.

Navarro. 2019c. Written communication. Subject: *Pahute Mesa Geophysical Log Data Evaluation for Matrix Porosity*, UGTA Technical Data Repository No. UGTA-4-2037. Las Vegas, NV.

Navarro. 2019d. Written communication. Subject: "PM_Extended_HFM_ovpmv28," UGTA Technical Data Repository No. UGTA-4-2028, Las Vegas, NV.

Navarro. 2020a. *Phase II Geochemical and Isotopic Evaluation of Groundwater Flow in the Pahute Mesa–Oasis Valley Flow System, Nevada,* Rev. 1, N/0002653--069. Las Vegas, NV.

Navarro. 2020b. Written communication. Subject: *Hydrologic Data for the Groundwater Flow and Contaminant Transport Model of Corrective Action Units 101 and 102: Central and Western Pahute Mesa, Nye County, Nevada.* Las Vegas, NV.

Navarro. 2020c. Written communication. Subject: "UGTA Chemistry Database (UCDB)," UGTA Technical Data Repository No. UGTA-4-1197. Las Vegas, NV.

Navarro. 2021. *Hydrologic Data for the Groundwater Flow and Contaminant Transport Model of Corrective Action Units 101 and 102: Central and Western Pahute Mesa, Nye County, Nevada,* Rev. 1, N/0002653--073. Las Vegas, NV.

Navarro-Intera, LLC. 2013. *Phase I Flow and Transport Model Document for Corrective Action Unit 97: Yucca Flat/Climax Mine, Nevada National Security Site, Nye County, Nevada*, Rev. 1, N-I/ 28091--080. Las Vegas, NV.

Navarro-Intera, LLC. 2015. Written communication. Subject: "Updated Static Head Contours and Stream Traces Developed for USGS Data (Prof. Paper 1771 and Data Series 533)", UGTA Technical Data Repository No. UGTA-4-964. Las Vegas, NV. As accessed on 6 February.

Navarro Nevada Environmental Services, LLC. 2010. *Phase II Transport Model of Corrective Action Unit 98: Frenchman Flat, Nevada Test Site, Nye County, Nevada,* Rev. 1, N-I/28091--004, S-N/99205--122. Las Vegas, NV.

Neretnieks, I. 1980. "Diffusion in the Rock Matrix: An Important Factor in Radionuclide Retardation?" In *Journal of Geophysical Research*, Vol. 85(B8): pp. 4379–4397. Washington, DC: American Geophysical Union.

Neretnieks, I., T. Eriksen, and P. Tahtinen. 1982. "Tracer Movement in a Single Fissure in Granitic Rock: Some Experimental Results and Their Interpretation." In *Water Resources Research*, Vol. 18(4): pp. 849–858. Washington, DC: American Geophysical Union.

Neuman, S.P. 1990. "Universal Scaling of Hydraulic Conductivities and Dispersivities in Geologic Media." In *Water Resources Research*, Vol. 26 (8): pp. 1749–1758. Washington, DC: American Geophysical Union.

Neuman, S.P. 1995. "On Advective Transport in Fractal Permeability and Velocity Fields." In *Water Resources Research*, Vol. 31(6): pp. 1455–1460. Washington, DC: American Geophysical Union.

Neuman, S.P., and V. Di Federico. 2003. "Multifaceted Nature of Hydrogeologic Scaling and Its Interpretation." In *Reviews of Geophysics*, Vol. 41(3): p. 1014.

Newman, J.S. 1991. *Electrochemical Systems*. Englewood Cliffs, NJ: Prentice Hall.

Nimz, G.J., and J.L. Thompson. 1992. *Underground Radionuclide Migration at the Nevada Test Site*, UCRL-ID-111013. Livermore, CA: Lawrence Livermore National Laboratory.

Noorishad, J., and M. Mehran. 1982. "An Upstream Finite Element Method for Solution of Transient Transport Equation in Fractured Porous Media." In *Water Resources Research*, Vol. 18(3): pp. 588–596. Washington, DC: American Geophysical Union.

Novakowski, K.S., and P.A. Lapcevic. 1994. "Field Measurement of Radial Solute Transport in Fractured Rock." In *Water Resources Research*, Vol. 30(1): pp. 37–44. Washington, DC: American Geophysical Union.

Ogard, A.E., J.L. Thompson, R.S. Rundberg, K. Wolfsberg, P.W. Kubic, D. Eklmore, and H.W. Bentley. 1988. "Migration of Chlorine-36 and Tritium from an Underground Nuclear Test." In *Radiochimica Acta,* Vol. 44/45: pp. 213–217. Munich, Germany: R. Oldenburg.

Ozbek, H., J.A. Fair, and S.L. Phillips. 1977. *Viscosity of Aqueous Sodium Chloride Solutions From 0-150°C*. American Chemical Society Southeast Regional Meeting, 9–11 November. Tampa, FL.

Paces, J.B., K.R. Ludwig, Z.E. Peterman, and L.A. Neymark. 2002 "$^{234}U/^{238}U$ Evidence for Local Recharge and Patterns of Groundwater Flow in the Vicinity of Yucca Mountain, Nevada, USA" In *Applied Geochemistry*, Vol. 17: pp. 751–779.

Papelis, C., and W. Um. 2003a. *Evaluation of Cesium, Strontium, and Lead Sorption, Desorption, and Diffusion in Cores from Western Pahute Mesa, Nevada Test Site, Based on Macroscopic and Spectroscopic Investigations*, DOE/NV/13609-16; Publication No. 45187. Las Vegas, NV: Desert Research Institute.

Papelis, C., and W. Um. 2003b. *Evaluation of Cesium, Strontium, and Lead Sorption, Desorption, and Diffusion in Volcanic Tuffs from Frenchman Flat, Nevada Test Site: Macroscopic and Spectroscopic Investigations*, DOE/NV/13609-18; Publication No. 45189. Las Vegas, NV: Desert Research Institute.

Parashar, R., H.V. Pham, and N.L. Sund. 2019. *Development of Upscaling Techniques and Construction of Calibrated Models for Fractured Rocks Using Discrete Fracture Network Ap*proaches, DOE/NV/0003590-43; Publication No. 45289. Las Vegas, NV: Desert Research Institute.

Pawloski, G.A. 1999. *Development of Phenomenological Models of Underground Nuclear Tests on Pahute Mesa, Nevada Test Site–BENHAM and TYBO*, UCRL-ID-136003. Livermore, CA: Lawrence Livermore National Laboratory.

Pawloski, G.A., A.F.B. Tompson, and S. Carle, eds. 2001. *Evaluation of the Hydrologic Source Term from Underground Nuclear Tests on Pahute Mesa at the Nevada Test Site: The CHESHIRE Test*, UCRL-ID-147023. Livermore, CA: Lawrence Livermore National Laboratory.

Pawloski, G.A., A.F.B. Tompson, S.F. Carle, R.L. Detwiler, Q. Hu, S. Kollet, R.M. Maxwell, W.W. McNab, S.K. Roberts, D.E. Shumaker, Y. Sun, and M. Zavarin. 2008. *Evaluation of Hydrologic Source Term Processes for Underground Nuclear Tests in Yucca Flat, Nevada Test Site: Introduction and Executive Summary*, LLNL-TR-403428. Livermore, CA: Lawrence Livermore National Laboratory.

Pham, H.V., R. Parashar, N.L. Sund, and K.F. Pohlmann. 2020. "Determination of Fracture Apertures Via Calibration of Three-Dimensional Discrete-Fracture-Network Models: Application to Pahute Mesa, Nevada National Security Site, USA." In *Hydrogeology Journal*, Vol. 29(4): pp. 841-857.

Pickens, J.F., and G.E. Grisak. 1981a. "Modeling of Scale-Dependent Dispersion in Hydrogeologic Systems." In *Water Resources Research,* Vol. 17(6): pp. 1701–1711. Washington, DC: American Geophysical Union.

Pickens, J.F., and G.E. Grisak. 1981b. "Scale-Dependent Dispersion in a Stratified Granular Aquifer." In *Water Resources Research,* Vol. 17(4): pp. 1191–1211. Washington, DC: American Geophysical Union.

Poreh. M. 1965. "The Dispersivity Tensor in Isotropic and Axisymmetric Media." In *Journal of Geophvsical Research*. Vol. 70(16): pp. 3909–3914.

Prothro, L.B. 2009. Written communication. Subject: *Analysis and Interpretation of Borehole Image Logs from Well ER-20-7*. October. Las Vegas, NV: National Security Technologies, LLC.

Prothro, L.B. 2010a. Written communication. Subject: *Analysis and Interpretation of Borehole Image Logs from Well ER-20-8*. January. Las Vegas, NV: National Security Technologies, LLC.

Prothro, L.B. 2010b. Written communication. Subject: *Analysis and Interpretation of Borehole Image Logs from Well ER-EC-11*. May. Las Vegas, NV: National Security Technologies, LLC.

Prothro, L.B. 2011a. Written communication. Subject: *Analysis and Interpretation of Borehole Image Logs from Well ER-20-4*. Las Vegas, NV: National Security Technologies, LLC.

Prothro, L.B. 2011b. Written communication. Subject: *Analysis and Interpretation of Borehole Image Logs from Well ER-EC-12*. Las Vegas, NV: National Security Technologies, LLC.

Prothro, L.B. 2012a. Written communication. Subject: *Analysis and Interpretation of Borehole Image Logs from Well ER-EC-13*. Las Vegas, NV: National Security Technologies, LLC.

Prothro, L.B. 2012b. Written communication. Subject: *Analysis and Interpretation of Borehole Image Logs from Well ER-EC-15*. Las Vegas, NV: National Security Technologies, LLC.

Prothro, L.B. 2013a. Written communication. Subject: *Analysis and Interpretation of Borehole Image Logs from Well ER-20-11*. Las Vegas, NV: National Security Technologies, LLC.

Prothro, L.B. 2013b. Written communication. Subject: *Analysis and Interpretation of the Borehole Image Log from Well ER-EC-14*. Las Vegas, NV: National Security Technologies, LLC.

Prothro, L.B., and S.L. Drellack, Jr. 1997. *Nature and Extent of Lava-Flow Aquifers Beneath Pahute Mesa, Nevada Test Site,* DOE/NV-11718-156. Las Vegas, NV: Bechtel Nevada.

Prothro, L.B., M.J. Townsend, S.L Drellack, Jr., and J.L. Gonzales. 1997. *Processing and Geologic Analysis of Conventional Cores from Well ER-20-6#1, Nevada Test Site,* DOE/NV/11718-162, UC-703. Las Vegas, NV: Bechtel Nevada.

Prothro, L.B., S.L. Drellack, D.N. Haugstad, H.E. Huckins-Gang, and M.J. Townsend. 2009. *Observations on Faults and Associated Permeability Structures in Hydrogeologic Units at the Nevada Test Site,* DOE/NV/25946--690. Las Vegas, NV: National Security Technologies, LLC.

Rechard, R.P., and M.S. Tierney. 2005. "Assignment of Probability Distributions for Parameters in the 1996 Performance Assessment for the Waste Isolation Pilot Plant, Part 2: Application of Process." In *Reliability Engineering and System Safety* 88 (1): pp. 33–80.

Reeves, D.M., K.D. Smith, R. Parashar, C. Collins, and K.M. Heintz. 2017. *Investigating the Influence of Regional Stress on Fault and Fracture Permeability at Pahute Mesa, Nevada National Security Site*, DOE/NV/0000939-41; Publication No. 45275. Las Vegas, NV: Desert Research Institute.

Rehfeldt, K., and B. Wilborn. 2020. "Achieving the End State for the Pahute Mesa Corrective Action Units at the Nevada National Security Site – Paper 20355." WM2020 Conference, 8–12 March. Phoenix, AZ.

Reimus, P.W. Los Alamos National Laboratory. 2006. Personal communication to P. Montazer and I. Farnham (SNJV) regarding dispersion data, 6 June. Los Alamos, NM.

Reimus, P.W. 2018. *Evaluation of the Need to Consider Colloid-Facilitated Plutonium Transport in Contaminant Boundary Calculations for Pahute Mesa at the Nevada National Security Site*, LAUR-18-29291. Los Alamos, NM: Los Alamos National Laboratory.

Reimus, P.W., and H. Boukhalfa. 2014. *Chancellor Water Colloids: Characterization and Radionuclide Associated Transport*, LA-UR-14-27538. N. Wasserman, B. Erdmann, A.I. Abdel-Fattah, S.D. Ware, P. He, S. Tarimala, and B. Martinez, contributors. Los Alamos, NM: Los Alamos National Laboratory.

Reimus, P.W., and T.J. Callahan. 2007. "Matrix Diffusion Rates in Fractured Volcanic Rocks at the Nevada Test Site: Evidence for a Dominant Influence of Effective Fracture Apertures." In *Water Resources Research*, Vol. 43, W07421. Washington, DC: American Geophysical Union.

Reimus, P.W., and M.J. Haga. 1999. *Analysis of Tracer Responses in the BULLION Forced-Gradient Experiment at Pahute Mesa, Nevada*, LA-13615-MS. Los Alamos, NM: Los Alamos National Laboratory.

Reimus, P. W., M.J. Haga, A.R. Humphrey, I. Anghel, D. Counce, T.J. Callahan, and S.D. Ware. 1999a. *Laboratory Experiments to Support Interpretation of the BULLION Forced-Gradient Experiment: Update Report, Underground Test Area (UGTA) Project Report* (draft), 7302 c.2. Los Alamos, NM: Los Alamos National Laboratory.

Reimus, P.W., A. Adams, M.J. Haga, A. Humphrey, T. Callahan, I. Anghel, and D. Counce. 1999b. *Results and Interpretation of Hydraulic and Tracer Testing in the Prow Pass Tuff at the C-Holes,* Yucca Mountain Site Characterization Project Milestone Report SP32E7M4. Los Alamos, NM: Los Alamos National Laboratory.

Reimus, P.W., S.D. Ware, F.C. Benedict, R.G. Warren, A. Humphrey, A. Adams, B. Wilson, and D. Gonzales. 2002. *Diffusive and Advective Transport of ^{3}H, ^{14}C, and ^{99}Tc in Saturated, Fractured Volcanic Rocks from Pahute Mesa, Nevada*, LA-13891-MS. Los Alamos, NM: Los Alamos National Laboratory.

Reimus, P., G. Pohll, T. Miheve, J. Chapman, M. Haga, B. Lyles, S. Kosinski, R. Niswonger, and P. Sanders. 2003a. "Testing and Parameterizing a Conceptual Model for Solute Transport in A Fractured Granite Using Multiple Tracers in A Forced-Gradient Test." In *Water Resources Research*, Vol. 39(12): p. 1356. Washington, DC: American Geophysical Union.

Reimus, P.W., Haga, M.J., Adams, A.I., Callahan, T.J., Turin, H.J., Counce, D.A., 2003b. "Testing and Parameterizing a Conceptual Solute Transport Model in Saturated Fractured Tuff Using Sorbing and Nonsorbing Tracers in Cross-hole Tracer Tests." In *Journal of Contaminant Hydrology*: Vols. 62–63: pp. 613–636.

Reimus, P.W., M. Murrell, A. Abdel-Fattah, E. Garcia, D. Norman, S. Goldstein, A. Nunn, R. Gritzo, and B. Martinez. 2006a. *Colloid Characteristics and Radionuclide Associations with Colloids in Near-Field Waters at the Nevada Test Site (FY 2005)*, LA-UR-05-8612. Los Alamos, NM: Los Alamos National Laboratory.

Reimus, P.W., T.J. Callahan, S.D. Ware, M.J. Haga, and D.A. Counce. 2006b. *Matrix Diffusion Coefficients in Volcanic Rocks at the Nevada Test Site: Influence of Matrix Porosity, Matrix Permeability, and Fracture Coating Minerals,* LA-UR-06-7127. Los Alamos, NM: Los Alamos National Laboratory.

Reimus, P.W., R.L. Hershey, D.L. Decker, S.D. Ware, C. Papelis, S. Earman, A. Abdel-Fattah, M. Haga, D. Counce, S. Chipera, and C. Sedlacek. 2006c. *Tracer Transport Properties in the Lower Carbonate Aquifer of Yucca Flat,* LA-UR-06-0486. Los Alamos, NM: Los Alamos National Laboratory.

Reimus, P.W., Callahan, T.J., Ware, S.D., Haga, M.J., Counce, D.A. 2007. "Matrix diffusion coefficients in volcanic rocks at the Nevada test site: influence of matrix porosity, matrix permeability, and fracture coating minerals." In *J. Contam. Hydrol*. 93 (1), pp. 85–95.

Rose T.P., D. K. Smith and D.L. Phinney. 2000. "Chapter 4: Secondary Ion Mass Spectrometry Measurements of Volcanic Tuffs Containing Radionuclides from Underground Nuclear Tests." In *Hydrologic Resources Management Program and Underground Test Area FY 1999 Progress Report*, UCRL-ID-139226. Livermore, CA: Lawrence Livermore National Laboratory.

Russell, C.E., 2019, *Partitioning of Radionuclides Following a Nuclear Cratering Event*: Desert Research Institute, Report DOE/NV/0003590-45.

Shaw, see Shaw Environmental, Inc.

SNJV, see Stoller-Navarro Joint Venture.

SNL, see Sandia National Laboratories.

Sandia National Laboratories. 2007a. *Radionuclide Transport Models Under Ambient Conditions*, MDL-NBS-HS-000008 REV 02 ADD 01. Las Vegas, NV.

Sandia National Laboratories. 2007b. *Site-Scale Saturated Zone Transport*, MDL-NBS-HS-000010 REV 03. Las Vegas, NV.

Sauty, J.-P. 1980. "An Analysis of Hydrodispersive Transfer in Aquifers." In *Water Resources Research,* Vol. 16 (1): pp. 145–158. Washington, DC: American Geophysical Union.

Schulze-Makuch, D. 2005. "Longitudinal Dispersivity Data and Implications for Scaling Behavior." In *Ground Water*, Vol. 43(3): pp. 443–456.

Shaw Environmental, Inc. 2003. *Contaminant Transport Parameters for the Groundwater Flow and Contaminant Transport Model of Corrective Action Units 101 and 102: Central and Western Pahute Mesa, Nye County, Nevada*, Rev. 0, Shaw/13052-201-CD. Las Vegas, NV.

Skagius, K., and I. Neretnieks. 1986. "Porosities and Diffusivities of Some Nonsorbing Species in Crystalline Rocks." In *Water Resources Research*, Vol. 22(3): pp. 389–398. Washington, DC: American Geophysical Union.

Slate, J.L., M.E. Berry, P.D. Rowley, C.J. Fridrich, K.S. Morgan, J.B. Workman, O.D. Young, G.L. Dixon, V.S. Williams, E.H. McKee, D.A. Ponce, T.G. Hildenbrand, W.C. Swadley, S.C. Lundstrom, E.B. Ekren, R.G. Warren, J.C. Cole, R.J. Fleck, M.A. Lanphere, D.A. Sawyer, S.A. Minor, D.J. Grunwald, R.J. Laczniak, C.M. Menges, J.C. Yount, and A.S. Jayko. 1999. *Part A. Digital Geologic Map of the Nevada Test Site and Vicinity, Nye, Lincoln, and Clark Counties, Nevada, and Inyo County, California, Revision 4,* Open-File Report 99-554-A, scale 1:120,000. Denver, CO: U.S. Geological Survey.

Snyder, R.P. 1977. *Geology of the Gold Meadows Stock, Nevada Test Site* (Areas 12-26), Open-File Report 474-179. Denver, CO: U.S. Geological Survey.

Stoller-Navarro Joint Venture. 2004a. *Analysis of Well ER-7-1 Testing, Yucca Flat FY 2003 Testing Program, Nevada Test Site, Nevada,* S-N/99205--021. Las Vegas, NV.

Stoller-Navarro Joint Venture. 2004b. *Hydrologic Data for the Groundwater Flow and Contaminant Transport Model of Corrective Action Units 101 and 102: Central and Western Pahute Mesa, Nye County, Nevada,* Rev. 0, S-N/99205-002; Shaw/13052-204. Las Vegas, NV.

Stoller-Navarro Joint Venture. 2004c. *The Role of Dispersion in Radionuclide Transport - Data and Modeling Requirements,* Rev. 1, S-N/99205-003. Las Vegas, NV.

Stoller-Navarro Joint Venture. 2004d. *Transferability of Data Related to the Underground Test Area Project, Nevada Test Site, Nye County, Nevada,* S-N/99205-020. Las Vegas, NV.

Stoller-Navarro Joint Venture. 2004e. *Unclassified Source Term and Radionuclide Data for the Groundwater Flow and Contaminant Transport Model of Corrective Action Units 101 and 102: Central and Western Pahute Mesa, Nye County, Nevada,* Rev. 0, S-N/99205--022. Las Vegas, NV.

Stoller-Navarro Joint Venture. 2005a. *Phase II Contaminant Transport Parameters for the Groundwater Flow and Contaminant Transport Model of Corrective Action Unit 98: Frenchman Flat, Nye County, Nevada*, S-N/99205--043. Las Vegas, NV.

Stoller-Navarro Joint Venture. 2005b. *Underground Test Area Fracture Analysis Report for Frenchman Flat Well Clusters ER-5-3 and ER-5-4 Nevada Test Site, Nevada,* S-N/99205--060. Las Vegas, NV.

Stoller-Navarro Joint Venture. 2005c. *Underground Test Area Fracture Analysis Report for Yucca Flat Wells ER-2-1, ER-6-1#2, ER-7-1, and ER-12-2 Nevada Test Site, Nevada*, S-N/99205--040. Las Vegas, NV.

Stoller-Navarro Joint Venture. 2005d. Written communication. Subject: "ER-6-1 Well Cluster Multiple Well Aquifer Test – Tracer Test Data Report: Volume I – Overview," Rev. 0. Las Vegas, NV.

Stoller-Navarro Joint Venture. 2005e. Written communication. Subject: "ER-6-1 Well Cluster Multiple Well Aquifer Test – Tracer Test Data Report: Volume III – MWAT-TT," Rev. 0. Las Vegas, NV.

Stoller-Navarro Joint Venture. 2006a. *Groundwater Flow Model of Corrective Action Units 101 and 102: Central and Western Pahute Mesa, Nevada Test Site, Nye County, Nevada*, Rev. 0, S-N/99205--076. Las Vegas, NV.

Stoller-Navarro Joint Venture. 2006b. *Well ER-6-1 Tracer Test Analysis: Yucca Flat, Nevada Test Site, Nye County, Nevada*, S-N/99205-084. Las Vegas, NV.

Stoller Navarro Joint Venture. 2007. *Phase I Contaminant Transport Parameters for the Groundwater Flow and Contaminant Transport Model of Corrective Action Unit 97: Yucca Flat/Climax Mine, Nevada Test Site, Nye County, Nevada*, Revision No. 0, S-N/99205--096. Las Vegas, NV.

Stoller-Navarro Joint Venture. 2008. *Phase I Contaminant Transport Parameters for the Groundwater Flow and Contaminant Transport Model of Corrective Action Unit 99: Rainier Mesa/Shoshone Mountain, Nevada Test Site, Nye County, Nevada,* Rev. 0, S-N/99205--102. Las Vegas, NV.

Stoller-Navarro Joint Venture. 2009. *Phase I Transport Model of Corrective Action Units 101 and 102: Central and Western Pahute Mesa, Nevada Test Site, Nye County, Nevada*, Rev. 1, S-N/99205--111. Las Vegas, NV.

Sudicky, E.A., and E.O. Frind. 1981. "Carbon 14 Dating of Groundwater in Confined Aquifers: Implications of Aquitard Diffusion." In *Water Resources Research*, Vol. 17(4): pp. 1060–1064. Washington, DC: American Geophysical Union.

Tang, D.H., E.O. Frind, and E.A. Sudicky. 1981. "Contaminant Transport in Fractured Porous Media: Analytical Solution for a Single Fracture." In *Water Resources Research*, Vol. 17(3): pp. 555–564. Washington, DC: American Geophysical Union.

Telfeyan, K., S.D. Ware, P.W. Reimus, and K.H. Birdsell. 2018, "Comparison of Experimental Methods for Estimating Matrix Diffusion Coefficients for Contaminant Transport Modeling." In *Journal of Contaminant Hydrology*, Vol. 209: pp. 51–60.

Thompson, J.L., ed. 1988. *Laboratory and Field Studies Related to the Radionuclide Migration Project (October 1, 1986–September 30, 1987)*, LA-11223-PR. Los Alamos, NM: Los Alamos National Laboratory.

Thompson, J.L. 1991. *Laboratory and Field Studies Related to the Hydrology/Radionuclide Migration Project (October 1, 1989–September 30, 1990),* LA-12100-PR. Los Alamos, NM: Los Alamos National Laboratory.

Tompson, A.F.B., M. Zavarin, W.W. McNab, S.F. Carle, D.E. Shumaker, C. Lu, Y. Sun, G.A. Pawloski, Q. Hu, and S.K. Roberts. 2011. *Hydrologic Source Term Processes and Models for Underground Nuclear Tests at Rainier Mesa and Shoshone Mountain, Nevada National Security Site*, LLNL-TR-483852. Livermore, CA: Lawrence Livermore National Laboratory.

Tompson, A., M. Zavarin, D. Shumaker. 2019. *Yield-Weighting Approaches for Calculating Radiologic Inventories for Individual Underground Nuclear Tests at the Nevada National Security Site*, LLNL-TR-773562. Prepared for the U.S. Department of Energy. Livermore, CA: Lawrence Livermore National Laboratory.

Travis, B.J., H.E. Nuttall, S.W. Hodson, and R.S. Rundberg. 1983. "Section B: Transport of Tritium the Cambric Cavity Region to RNM-2S: Modeling." In *Laboratory and Field Studies Related to the Hydrology/Radionuclide Migration Project: October 1, 1981 – September 30, 1982,* LA-9691-PR. Los Alamos, NM: Los Alamos National Laboratory.

Triay, I.R., A. Meijer, J.L. Conca, K.S. Kung, R.S. Rundberg, E.A. Strietelmeier, C.D. Tait, D.L. Clark, M.P. Neu, and D.E. Hobart. 1997. *Summary and Synthesis Report on Radionuclide* Retardation for the Yucca Mountain Site Characterization Project: Yucca Mountain Site *Characterization Program Milestone 3784M,* LA-13262-MS, UC-903 and UC-940. Los Alamos, NM: Los Alamos National Laboratory.

Tsang, Y.W. 1984. "The Effect of Tortuosity on Fluid Flow through a Single Fracture." In *Water Resources Research,* Vol. 20(9): pp. 1209–1215. Washington, DC: American Geophysical Union.

Tsang, Y.W. 1992. "Usage of 'Equivalent Apertures' for Rock Fractures as Derived from Hydraulic and Tracer Tests." In *Water Resources Research*, Vol. 28(5): pp. 1451–14551. Washington, DC: American Geophysical Union.

U.S. Congress/OTA, see U.S. Congress Office of Technology Assessment.

Umari, A., J.D. Earle, and M.F. Fahy. 2006. "Analysis of Single-hole and Cross-hole Tracer Tests Conducted at the Nye County Early Warning Drilling Program Well Complex, Nye County, Nevada." In *International High-Level Waste Management*, 30 April–4 May. Las Vegas, NV.

Umari, A., M.F. Fahy, J.D. Earle, and P. Tucci. 2007. *Analysis of Conservative Tracer Tests in the Bullfrog, Tram, and Prow Pass Tuffs, 1996 to 1998, Yucca Mountain, Nye County, Nevada*, Scientific Investigations Report 2007-5280. Reston, VA: U.S. Geological Survey.

U.S. Congress Office of Technology Assessment. 1989. *The Containment of Underground Nuclear Explosions*, PB90-1561183. Washington, DC.

U.S. Department of Energy Environmental Management Nevada Program. 2018. *Record of Technical Change to Rainier Mesa/Shoshone Mountain Flow and Transport Model Report Nevada National Security Site, Nevada,* Rev. 1, DOE/NV--1588; ROTC No. DOE/NV--1588 Revision 1 ROTC 1, 10 October. Las Vegas, NV.

U.S. Department of Energy Environmental Management Nevada Program. 2019a. *Calendar Year 2018 Underground Test Area Annual Sampling Report, Nevada National Security Site, Nevada*, Rev. 1, DOE/EMNV--0009-REV. 1. Las Vegas, NV.

U.S. Department of Energy Environmental Management Nevada Program. 2019b. *CY2018 Annual Closure Monitoring Report for Corrective Action Unit 98, Frenchman Flat, Underground Test Area, Nevada National Security Site, Nevada (January 2018–December 2018)*, Rev. 1, DOE/EMNV--0006. Las Vegas, NV.

U.S. Department of Energy Environmental Management Nevada Program. 2019c. *Record of Technical Change to Addendum to the Rainier Mesa/Shoshone Mountain Flow and Transport Model Report Nevada National Security Site, Nevada,* Rev. 1, DOE/EMNV--0002; ROTC No. DOE/EMNV--0002-ROTC 1, 28 May. Las Vegas, NV.

U.S. Department of Energy Environmental Management Nevada Program. 2020a. *Pahute Mesa-Oasis Valley Hydrostratigraphic Framework Model for Corrective Action Units 101 and 102: Central and Western Pahute Mesa, Nye County, Nevada*, Rev. 0, DOE/EMNV--0014. Las Vegas, NV.

U.S. Department of Energy Environmental Management Nevada Program. 2020b.*Update to the Phase II Corrective Action Investigation Plan for Corrective Action Units 101 and 102, Central and Western Pahute Mesa, Nevada National Security Site, Nye County, Nevada,* Rev. 1, DOE/EMNV--0018. Las Vegas, NV.

U.S. Department of Energy, National Nuclear Security Administration Nevada Field Office. 2014. *Record of Technical Change to Phase II Corrective Action Investigation Plan for Corrective Action Units 101 and 102: Central and Western Pahute Mesa, Nevada Test Site, Nye County, Nevada*, DOE/NV--1312-Rev. 2; Technical Change No. DOE/NV--1312-Rev. 2 ROTC 2, 25 November. Las Vegas, NV.

U.S. Department of Energy, National Nuclear Security Administration Nevada Field Office. 2015. *United States Nuclear Tests, July 1945 through September 1992,* DOE/NV--209-REV 16. Las Vegas, NV.

U.S. Department of Energy, National Nuclear Security Administration Nevada Field Office. 2016. *Completion Report for Well ER-20-12, Corrective Action Units 101 and 102: Central and Western Pahute Mesa*, DOE/NV--1549. Las Vegas, NV.

U.S. Department of Energy, National Nuclear Security Administration Nevada Site Office. 2011a. *Corrective Action Decision Document/Closure Report for Corrective Action Unit 374: Area 20 Schooner Unit Crater Nevada National Security Site, Nevada,* Rev 0, DOE/NV-1456. Las Vegas, NV.

U.S. Department of Energy, National Nuclear Security Administration Nevada Site Office. 2011b. *Corrective Action Decision Document/Closure Report for Corrective Action Unit 372: Area 20 Cabriolet/Palanquin Unit Craters Nevada National Security Site, Nevada,* Rev 0, DOE/NV-1444. Las Vegas, NV.

U.S. Department of Energy, Nevada Operations Office. 1997. *Regional Groundwater Flow and Tritium Transport Modeling and Risk Assessment of the Underground Test Area, Nevada Test Site, Nevada*, DOE/NV--477. Las Vegas, NV.

U.S. Department of Energy, Nevada Operations Office. 2000a. *Completion Report for Well ER-EC-1*, DOE/NV/11718--381. Las Vegas, NV.

U.S. Department of Energy, Nevada Operations Office. 2000b, *Completion Report for Well ER-EC-4*, DOE/NV/11718--397, U.S. Department of Energy, Nevada Operations Office.

U.S. Department of Energy, Nevada Operations Office. 2004, *Completion Report for Well ER-EC-5*, DOE/NV/11718--424, U.S. Department of Energy, Nevada Operations Office.

U.S. Department of Energy, Waste Isolation Pilot Plant. 2004. Title 40 CFR Part 191 "Compliance Certification Application for the Waste Isolation Pilot Plant," DOE/WIPP 2004-3231. March. Carlsbad, NM: Carlsbad Field Office.

U.S. Environmental Protection Agency. 1988. *Groundwater Modeling: An Overview and Status Report*, EPA/600/2-89/028 Ada, OK: Robert S. Kerr Environmental Research Laboratory.

U.S. Environmental Protection Agency. 1999. *Understanding Variation in Partition Coefficient, K_d, Values Volume II: Review of Geochemistry and Available K_d Values for Cadmium, Cesium, Chromium, Lead, Plutonium, Radon, Strontium, Thorium, Tritium (^3H), and Uranium*, EPA 402-R-99-004B. Washington, DC: Office of Air and Radiation.

U.S. Environmental Protection Agency. 2000. "National Primary Drinking Water Regulations; Radionuclides; Final Rule," 7 December. In *Federal Register,* Vol. 65, No. 236: pp. 76708−76753. Washington, DC.

U.S. Environmental Protection Agency. 2001. *Use of Uranium Drinking Water Standards under 40 CFR 141 and 40 CFR 192 as Remediation Goals for Groundwater at CERCLA sites.* Directive No. 9283.1-14.

U.S. Environmental Protection Agency. 2002. *Radionuclides in Drinking Water: A Small Entity Compliance Guide*. EPA 815-R-02-001. Washington, DC: Office of Ground Water and Drinking Water.

van der Kamp, G., D.R. Van Stempvoort, and L.I. Wassenaar. 1996. "The Radial Diffusion Method 1. Using Intact Cores to Determine Isotopic Composition, Chemistry, and Effective Porosities for Groundwater in Aquitards." In *Water Resources Research*, Vol. 32(6): pp. 1815–1822.

Walker, G.E. 1962. *Ground Water in the Climax Stock, Nevada Test Site, Nye County, Nevada*, USGS-TEI-813. Washington, DC: U.S. Geological Survey.

Walter, G.R. 1982. *Theoretical and Experimental Determination of Matrix Diffusion and Related Solute Transport Properties of Fractured Tuffs from the Nevada Test Site,* LA-9471-MS, UC-70. Los Alamos, NM: Los Alamos National Laboratory.

Ware, S.D., A. Abdel-Fattah, M. Ding, P.W. Reimus, C. Sedlacek, M. Haga, E. Garcia, and S. Chipera. 2005. *Radionuclide Sorption and Transport in Fractured Rocks of Yucca Flat, Nevada Test Site,* LA-UR-05-9279. Los Alamos, NM: Los Alamos National Laboratory.

Warren, R.G., G.L. Cole, and D. Walther. 2000. *A Structural Block Model for the Three-Dimensional Geology of the Southwestern Nevada Volcanic Field,* LA-UR-00-5866. Los Alamos, NM: Los Alamos National Laboratory.

Warren, R.G., D.A. Sawyer, F.M. Byers, Jr., and G.L. Cole. 2000. *A Petrographic/Geochemical Database and Stratigraphic and Structural Framework for the Southwestern Nevada Volcanic Field,* LA-UR-00-3791. Los Alamos, NM: Los Alamos National Laboratory.

Welty, C., and L.W. Gelhar. 1989. *Evaluation of Longitudinal Dispersivity from Tracer Test Data* R89-05, Ralph M. Parsons Laboratory Report. Cambridge, MA: Massachusetts Institute of Technology.

Whitfield, M.S., Jr., W. Thordarson, and E.P. Eshom. 1984. *Geohydrologic and Drill-Hole Data for Test Well USW H-4, Yucca Mountain, Nye County, Nevada*, Open-File Report 84-449. Denver, CO: U.S. Geological Survey.

Winograd, I.J., and W. Thordarson. 1975. *Hydrogeologic and Hydrochemical Framework, South-Central Great Basin, Nevada-California, with Special Reference to the Nevada Test Site,* Professional Paper 712-C. Washington, DC: U.S. Geological Survey.

Winograd, I.J., and L.R. West. 1962. *Preliminary Tracer Experiment to Demonstrate Hydraulic Continuity Between Water Wells C and C-1, Yucca Flat, Nevada Test Site,* USGS Technical Letter NTS-20. Denver, CO: U.S. Geological Survey.

Winterle, J.R., and P.C. La Femina. 1999. *Review and Analysis of Hydraulic andTracer Testing at the C-Holes Complex Near Yucca Mountain, Nevada*. Prepared for Nuclear Regulatory Commission Contract N RC-02-97-009, Center for Nuclear Waste Regulatory Analyses. San Antonio, TX.

Wolfsberg, K., B.P. Bayhurst, S.S. Levy, F.O. Lawrence, S.D. Knight, A.J. Mitchell, A.E. Ogard, and P.L. Wanek. 1983. *Research and Development Related to Sorption of Radionuclides on Soils*, LA-UR-83-800. Los Alamos, NM: Los Alamos National Laboratory.

Wolfsberg, A., L. Glascoe, G. Lu, A. Olson, P. Lichtner, M. McGraw, T. Cherry, and G. Roemer. 2002. *TYBO/BENHAM: Model Analysis of Groundwater Flow and Radionuclide Migration from Underground Nuclear Tests in Southwestern Pahute Mesa, Nevada*, LA-13977. Los Alamos, NM: Los Alamos National Laboratory.

Wood, D.B., 2009. *Digitally Available Interval-Specific Rock-Sample Data Compiled from Historical Records, Nevada Test Site and Vicinity, Nye County, Nevada* (USGS-297).

Wurtz, J., and K. Day. 2018. Written communication. Subject: "Pahute Mesa Phase II HFM: Thirsty Canyon Lineament Alternative." Las Vegas, NV: Navarro Research and Engineering.

Xu, M., and Y. Eckstein. 1995. "Use of Weighted Least-Squares Method in Evaluation of the Relationship between Dispersivity and Field Scale." In *Ground Water,* Vol. 33(6): pp. 905–908.

Zavarin, M., Lawrence Livermore National Laboratory. 2005. Memorandum to B. Wilborn (NNSA/NSO) titled "Isotopic Analyses: Environmental Monitoring Well ER-20-5 #2," 9 November. Livermore, CA.

Zavarin, M., Lawrence Livermore National Laboratory. 2012. Memorandum to B. Wilborn (NNSA/NSO) titled "Isotopic Analyses: Environmental Monitoring Well ER-20-7," 3 October. Livermore, CA.

Zavarin, M. and C.J. Bruton. 2004a, *A Non-Electrostatic Surface Complexation Approach to Modeling Radionuclide Migration at the Nevada Test Site: Aluminosilicates*. UCRL-TR-208672.Livermore, CA: Lawrence Livermore National Laboratory.

Zavarin, M. and C.J. Bruton. 2004b. *A Non-Electrostatic Surface Complexation Approach to Modeling Radionuclide Migration at the Nevada Test Site: Iron Oxides and Calcite.* UCRL-TR-208673. Livermore, CA: Lawrence Livermore National Laboratory.

Zavarin, M., S.K. Roberts, T.P. Rose, and D.L. Phinney. 2002. *Validating Mechanistic Sorption Model Parameters and Processes for Reactive Transport in Alluvium*, UCRL-ID-149728. Livermore, CA: Lawrence Livermore National Laboratory.

Zavarin, M., S.K. Roberts, B.E. Viani, G.A. Pawloski, and T.P. Rose. 2004a. *Nuclear Melt Glass Dissolution and Secondary Mineral Precipitation at 40 to 200 °C*, UCRL-TR-204870. Livermore, CA: Lawrence Livermore National Laboratory.

Zavarin M., S.F. Carle, and R.M. Maxwell. 2004b. *Upscaling Radionuclide Retardation-Linking the Surface Complexation and Ion Exchange Mechanistic Approach to a Linear K_d Approach*. UCRL-TR-204713. Livermore, CA. Lawrence Livermore National Laboratory.

Zavarin, M., M.R. Johnson, S.K. Roberts, R. Pletcher, T.P. Rose, A.B. Kersting, G. Eaton, Q. Hu, E. Ramon, J. Walensky, and P. Zhao. 2005. *Radionuclide Transport in Tuff and Carbonate Fractures from Yucca Flat, Nevada Test Site,* UCRL-TR-219836. Livermore, CA: Lawrence Livermore National Laboratory.

Zavarin, M., S. Roberts, P. Reimus, and M. Johnson. 2007. *Summary of Radionuclide Reactive Transport Experiments in Fractured Tuff and Carbonate Rocks from Yucca Flat, Nevada Test Site,* UCRL-TR-225271. Livermore, CA: Lawrence Livermore National Laboratory.

Zavarin, M., S.K. Roberts, M.R. Johnson, Q. Hu, B.A. Powell, P. Zhao, A.B. Kersting, R.E. Lindvall, and R. Pletcher. 2013. *Colloid-Facilitated Radionuclide Transport in Fractured Carbonate Rock fromYucca Flat, Nevada National Security Site*, LLNL-TR-6119352. Livermore, CA: Lawrence Livermore National Laboratory.

Zavarin, M., P. Zhao, C. Joseph, J. Begg, M. Boggs, Z. Dai, and A.B. Kersting. 2015. *Hydrothermal Alteration of Glass from Underground Nuclear Tests: Formation and Transport of Pu-clay Colloids at the Nevada National Security Site*, LLNL-TR-671402; Lawrence Livermore National Laboratory: Livermore, California, 27 May.

Zavarin, M., P. Zhao, C. Joseph, J.D. Begg, M.A. Boggs, Z. Dai, and A.B. Kersting. 2019. "Hydrothermal Alteration of Nuclear Melt Glass, Colloid Formation, and Plutonium Mobilization at the Nevada National Security Site, U.S.A." In *Environmental Science & Technology*, Vol. 53(13): pp. 7363–7370.

Zhou, Q., H.-H. Liu, F.J. Molz, Y. Zhang, and G.S. Bodvarsson, 2005. "Field-Scale Effective Matrix Diffusion Coefficient for Fractured Rock: Results From Literature Survey." In *Journal of Contaminated Hydrology*, Vol. 93(1–4).

Appendix A

Bibliography of Phase II Investigations

A.1.0 PM PHASE II WELL DRILLING, COMPLETION, DEVELOPMENT, AND ANALYSIS REPORTS

ER-20-4

Navarro-Intera, LLC. 2011. Written communication. Subject: *Pahute Mesa ER-20-4 Well Data Report,* Rev. 0. Las Vegas, NV.

Navarro-Intera, LLC. 2012. Written communication. Subject: *Pahute Mesa Phase II ER-20-4 Well Development, Testing, and Sampling Data Report*, Rev. 0. Las Vegas, NV.

Navarro-Intera, LLC. 2012. *Pahute Mesa Well Development and Testing Analyses for Wells ER-20-8 and ER-20-4, Nevada National Security Site, Nye County, Nevada*, Rev. 0, N-I/28091--061. Las Vegas, NV.

U.S. Department of Energy, National Nuclear Security Administration Nevada Site Office. 2011. *Completion Report for Well ER-20-4, Corrective Action Units 101 and 102: Central and Western Pahute Mesa*, DOE/NV--1447. Prepared by National Security Technologies, LLC. Las Vegas, NV.

ER-20-7

Navarro-Intera, LLC. 2010. Written communication. Subject: *Pahute Mesa ER-20-7 Well Data Report,* Rev. 0. Las Vegas, NV.

Navarro-Intera, LLC. 2011. *Pahute Mesa Well Development and Testing Analyses for Wells ER-20-7, ER-20-8 #2, and ER-EC-11,* Rev. 1, N-I/28091-037. Las Vegas, NV.

Navarro-Intera, LLC. 2011. Written communication. Subject: *Pahute Mesa Phase II ER-20-7 Well Development, Testing, and Sampling Data Report,* Rev. 0. Las Vegas, NV.

U.S. Department of Energy, National Nuclear Security Administration Nevada Site Office. 2010. *Completion Report for Well ER-20-7, Corrective Action Units 101 and 102: Central and Western Pahute Mesa*, DOE/NV--1386. Prepared by National Security Technologies, LLC. Las Vegas, NV.

ER-20-8

Navarro-Intera, LLC. 2010. Written communication. Subject: *Pahute Mesa ER-20-8 Well Data Report,* Rev. 0. Las Vegas, NV.

Navarro-Intera, LLC. 2012. *Pahute Mesa Well Development and Testing Analyses for Wells ER-20-8 and ER-20-4, Nevada National Security Site, Nye County, Nevada,* Rev. 0, N-I/28091--061. Las Vegas, NV.

Navarro-Intera, LLC. 2012. Written communication. Subject: *Pahute Mesa Phase II ER-20-8 Well Development, Testing, and Sampling Data Report,* Rev. 0. Las Vegas, NV.

U.S. Department of Energy, National Nuclear Security Administration Nevada Site Office. 2011. *Completion Report for Wells ER-20-8 and ER-20-8#2, Corrective Action Units 101 and 102: Central and Western Pahute Mesa*, DOE/NV--1440. Prepared by National Security Technologies, LLC. Las Vegas, NV.

ER-20-8#2

Navarro-Intera, LLC. 2010. Written communication. Subject: *Pahute Mesa ER-20-8#2 Well Data Report,* Rev. 0. Las Vegas, NV.

Navarro-Intera, LLC. 2010. Written communication. Subject: *Pahute Mesa Phase II ER-20-8#2 Well Development, Testing, and Sampling Data Report*, Rev. 0. Las Vegas, NV.

Navarro-Intera, LLC. 2011. *Pahute Mesa Well Development and Testing Analyses for Wells ER-20-7, ER-20-8 #2, and ER-EC-11,* Rev. 1, N-I/28091-037. Las Vegas, NV.

U.S. Department of Energy, National Nuclear Security Administration Nevada Site Office. 2011. *Completion Report for Wells ER-20-8 and ER-20-8#2, Corrective Action Units 101 and 102: Central and Western Pahute Mesa*, DOE/NV--1440. Prepared by National Security Technologies, LLC. Las Vegas, NV.

ER-20-11

Navarro. 2016. *Pahute Mesa Well Development and Testing Analyses for Well ER-20-11, Nevada National Security Site, Nye County, Nevada*, Rev. 0, N/0002653--028. Las Vegas, NV.

Navarro-Intera, LLC. 2013. Written communication. Subject: *Pahute Mesa ER-20-11 Well Data Package,* Rev. 0. Las Vegas, NV.

Navarro-Intera, LLC. 2014. Written communication. Subject: *Pahute Mesa Phase II Well ER-20-11 Well Development, Testing, and Sampling Data Report,* Rev. 0. Las Vegas, NV.

U.S. Department of Energy, National Nuclear Security Administration, Nevada Site Office. 2013. *Completion Report for Well ER-20-11 Corrective Action Units 101 and 102: Central and Western Pahute Mesa*, DOE/NV--1498. Las Vegas, NV.

ER-20-12

Navarro. 2016. Written communication. Subject: *Pahute Mesa ER-20-12 Well Data Package,* Rev. 0. Las Vegas, NV.

Navarro. 2018. *Pahute Mesa Phase II Well ER-20-12 Well Development, Testing, and Sampling Data and Analysis Report*. Rev. 0, N/0002653--046. Las Vegas, NV.

U.S. Department of Energy, National Nuclear Security Administration Nevada Field Office. 2016. *Completion Report for Well ER-20-12, Corrective Action Units 101 and 102: Central and Western Pahute Mesa*, DOE/NV--1549. Las Vegas, NV.

ER-EC-11

Navarro-Intera, LLC. 2010. Written communication. Subject: *Pahute Mesa ER-EC-11 Well Data Report*, Rev. 0. Las Vegas, NV.

Navarro-Intera, LLC. 2010. Written communication. Subject: *Pahute Mesa Phase II ER-EC-11 Well Development, Testing, and Sampling Data Report*, Rev. 0. Las Vegas, NV.

Navarro-Intera, LLC. 2011. *Pahute Mesa Well Development and Testing Analyses for Wells ER-20-7, ER-20-8 #2, and ER-EC-11,* Rev. 1, N-I/28091-037. Las Vegas, NV.

U.S. Department of Energy, National Nuclear Security Administration Nevada Field Office. 2013. *Completion Report for Well ER-20-11, Corrective Action Units 101 and 102: Central and Western Pahute Mesa,* DOE/NV--1498. Prepared by National Security Technologies, LLC. Las Vegas, NV.

ER-EC-12

Navarro. 2018. *Pahute Mesa Well Development and Testing Analyses for Wells ER-EC-12 and ER-EC-13, Nevada National Security Site, Nye County, Nevada*. Rev 0. N/0002653--051. Las Vegas, NV.

Navarro-Intera, LLC. 2011. Written communication. Subject: *Pahute Mesa ER-EC-12 Well Data Report,* Rev. 0. Las Vegas, NV.

Navarro-Intera, LLC. 2012. Written communication. Subject: *Pahute Mesa Phase II Well ER-EC-12 Well Development, Testing, and Sampling Data Report,* Rev. 0. Las Vegas, NV.

U.S. Department of Energy, National Nuclear Security Administration Nevada Field Office. 2011. *Completion Report for Well ER-20-12, Corrective Action Units 101 and 102: Central and Western Pahute Mesa,* DOE/NV--1446. Prepared by National Security Technologies, LLC. Las Vegas, NV.

ER-EC-13

Navarro. 2018. *Pahute Mesa Well Development and Testing Analyses for Wells ER-EC-12 and ER-EC-13, Nevada National Security Site, Nye County, Nevada*, Rev 0. N/0002653--051. Las Vegas, NV.

Navarro-Intera, LLC. 2011. Written communication. Subject: *Pahute Mesa ER-EC-13 Well Data Report,* Rev. 0. Las Vegas, NV.

Navarro-Intera, LLC. 2013. Written communication. Subject: *Pahute Mesa Phase II Well ER-EC-13 Well Development, Testing, and Sampling Data Report,* Rev. 0. Las Vegas, NV.

U.S. Department of Energy, National Nuclear Security Administration Nevada Site Office. 2011. *Completion Report for Well ER-EC-13, Corrective Action Units 101 and 102: Central and Western Pahute Mesa*, DOE/NV--1448. Prepared by National Security Technologies, LLC. Las Vegas, NV.

ER-EC-14

Navarro. 2015. *Pahute Mesa Well Development and Testing Analyses for Wells ER-EC-14 and ER-EC-15, Nevada National Security Site, Nye County, Nevada*, Rev. 0, N/0002653--006. Las Vegas, NV.

Navarro-Intera, LLC. 2013. Written communication. Subject: *Pahute Mesa ER-EC-14 Well Data Package,* Rev. 0. Las Vegas, NV.

Navarro-Intera, LLC. 2015. Written communication. Subject: *Pahute Mesa Phase II Well ER-EC-14 Well Development, Testing, and Sampling Data Report,* Rev. 0. Las Vegas, NV.

U.S. Department of Energy, National Nuclear Security Administration Nevada Field Office. 2013. *Completion Report for Well ER-EC-14, Corrective Action Units 101 and 102: Central and Western Pahute Mesa,* DOE/NV--1499. Prepared by National Security Technologies, LLC. Las Vegas, NV.

ER-EC-15

Navarro. 2015. *Pahute Mesa Well Development and Testing Analyses for Wells ER-EC-14 and ER-EC-15, Nevada National Security Site, Nye County, Nevada*, Rev. 0, N/0002653--006. Las Vegas, NV.

Navarro-Intera, LLC. 2011. Written communication. Subject: *Pahute Mesa ER-EC-15 Well Data Report,* Rev. 0. Las Vegas, NV.

Navarro-Intera, LLC. 2014. Written communication. Subject: *Pahute Mesa Phase II Well ER-EC-15 Well Development, Testing, and Sampling Data Report,* Rev. 0. Las Vegas, NV.

U.S. Department of Energy, National Nuclear Security Administration Nevada Site Office. 2011. *Completion Report for the Well ER-EC-15, Corrective Action Units 101 and 102: Central and Western Pahute Mesa*, DOE/NV--1449. Prepared by National Security Technologies, LLC. Las Vegas, NV.

Appendix B

Hydrostratigraphic Model Supporting Information

B.1.0 DESCRIPTION OF THE PM-OV MODEL LAYERS

Brief descriptions of the HSUs used to construct the PM-OV model are provided in Table B-1. They are listed in approximate order from surface to basement, although some are laterally rather than vertically contiguous, and not all units are present in all parts of the model area.

Table B-1
HSUs of the PM-OV HFM
(Page 1 of 14)

Model Layer Number	HSU (Symbol)	Dominant HGU(s) [a]	Stratigraphic Unit Map Symbols [b]	General Description
77	alluvial aquifer (AA) (this term is also used to designate an HGU)	AA	Qay, QTc, Qs, Qam, QTa, QTu, Qb, Tgy, Tgc, Tgm, Tgyx, Tt	Consists mainly of alluvium that fills extensional basins such as Gold Flat, Crater Flat, Kawich Valley, and Sarcobatus Flat. Also includes generally older Tertiary gravels, tuffaceous sediments, and nonwelded tuffs (where thin) that partially fill other basins such as Oasis Valley and the moat of the Timber Mountain caldera complex (TMCC). In the eastern moat area of the TMCC, includes intercalated partially welded ash-flow tuff of the Thirsty Canyon Group.
76	younger volcanic composite unit (YVCM)	LFA, WTA, VTA	Typ	A minor unsaturated HSU that consists of Pliocene to late Miocene basaltic rocks at Thirsty Mountain and Buckboard Mesa.
75	Thirsty Canyon volcanic aquifer (TCVA)	WTA, LFA, lesser VTA	Ttg, Tth, Tts, Ttt, Ttp, Ttc	Consists mainly of welded ash-flow tuff and lava of the Thirsty Canyon Group. Unit is very thick within the Black Mountain caldera. Also is present east and south of the caldera, including the northwestern moat area of the TMCC and the northern portion of the Oasis Valley basin.
74	detached volcanics composite unit (DVCM)	WTA, LFA, TCU	Tf through Tq	Consists of a very complex distribution of lavas and tuffs that form a relatively thin, highly extended interval above the Fluorspar Canyon-Bullfrog Hills (FC-BH) detachment fault in the southwestern portion of the model area. Unit is locally hydrothermally altered.
73	detached volcanics aquifer (DVA)	WTA, LFA	Tgyx, Tf, Tma, Tmr	Consists of welded ash-flow tuff and lava assigned to the Ammonia Tanks Tuff and units of the Volcanics of Fortymile Canyon. Although (like the DVCM) the DVA also overlies the FC-BH detachment fault, it is considered a separate HSU because of the preponderance of WTAs and LFAs that compose the HSU and much smaller degree of hydrothermal alteration present.
72	Shoshone Mountain lava-flow aquifer (SMLFA)	LFA	Tfs	Rhyolitic lava and related dikes, plugs, tuff, and tuff breccias of the rhyolite of Shoshone Mountain. According to Slate et al. (1999): “Forms a volcanic dome straddling the southeastern topographic margin of the Rainier Mesa caldera.” A topographically prominent, but unsaturated HSU.
71	Fortymile Canyon composite unit (FCCM)	TCU	Tfu, Tfs, Tfd, Tfr, Tfb, Tfl, Tff	Consists mainly of zeolitic to quartzofeldspathic nonwelded and bedded tuffs of the Volcanics of Fortymile Canyon that encapsulate intercalated rhyolite lava flows and welded tuffs assigned to different and separate HSUs. The FCCM is generally confined within the moat of the TMCC, where the unit forms a “depositional” ring around the Timber Mountain resurgent dome. Unit is thickest within the northwestern moat of the TMCC where measured thicknesses are 917 m (3,008 ft) at Well ER-EC-2a and greater than 500 m (1,640 ft) at Well ER-EC-13.

Table B-1
HSUs of the PM-OV HFM
(Page 2 of 14)

Model Layer Number	HSU (Symbol)	Dominant HGU(s) [a]	Stratigraphic Unit Map Symbols [b]	General Description
70	Fortymile Canyon upper mafic lava-flow aquifer (FCUMLFA)	LFA	Tfd, Tft, Tfb	Consists of as many as 12 individual flows of dense to scoriaceous trachybasalt, basaltic trachyaneisite, and trachyandesite assigned to the lavas of Dome Mountain. Exposed extensively in the southeastern Timber Mountain moat (Tfd in Slate et al., 1999) where it forms a high volcanic edifice (i.e., Dome Mountain). Encountered in Well ER-30-1 (116.4–217.3-m [382–713-ft] depth interval). Saturated only in its northernmost extent in the eastern Timber Mountain moat. Modeled as a property model within the FCCM.
69	Fortymile Canyon upper lava-flow aquifer 1 (FCULFA1)	LFA, lesser VTA	Tfbw	Consists of a single buried, but shallow, rhyolitic lava flow of the rhyolite of Beatty Wash. Modeled as having limited extent beneath the northwestern Timber Mountain moat. Known only from a single occurrence in Well ER-EC-13 (6.1–147.8-m [20–485-ft] depth interval). Mostly unsaturated, but very basal portions maybe saturated in places. Modeled as a property model within the FCCM.
68	Fortymile Canyon upper lava-flow aquifer 2 (FCULFA2)	LFA	Tfbw	Consists of a single rhyolitic lava flow of the rhyolite of Beatty Wash exposed in the northwestern Timber Mountain moat. Also encountered in Well ER-EC-2a (0–227.4-m [0–746-ft] depth interval). Conceptualized and modeled as an isolated LFA, but could possibly correlate to, and connect with, FCULFA1. Mostly unsaturated, but basal portion is likely saturated in most places. Modeled as a property model within the FCCM.
67	Fortymile Canyon upper lava-flow aquifer 3 (FCULFA3)	LFA	Tfbw	Consists of a single buried rhyolitic lava flow of the rhyolite of Beatty Wash. Known only from a single occurrence in UE-18r (137.2–286.5-m [450–940-ft] depth interval). Conceptualized and modeled as an isolated LFA of limited extent beneath the northern Timber Mountain moat. Unsaturated. Modeled as a property model within the FCCM.
66	Fortymile Canyon upper lava-flow aquifer 4 (FCULFA4)	LFA, lesser TCU	Tfb	Consists of a buried sequence of rhyolitic lava-flow lithologies of the Beatty Wash Formation that likely represent two stacked individual flow units beneath the northwestern Timber Mountain moat. Known only from a single occurrence in Well ER-EC-13 (505.4–771.1-m [1,658–2,530-ft] depth interval). Conceptualized and modeled as having limited extent. Saturated. Modeled as a property model within the FCCM.
65	Fortymile Canyon upper lava-flow aquifer 5 (FCULFA5)	LFA	Tfbw	Consists of a single buried rhyolitic lava flow of the rhyolite of Beatty Wash occurring beneath the southwestern Timber Mountain moat. Known only from a single occurrence in the MYJO Coffer well (387.1–433.4-m [1,270–1,422-ft] depth interval). Conceptualized and modeled as an isolated LFA of limited extent. Saturated. Modeled as a property model within the FCCM.

Table B-1
HSUs of the PM-OV HFM
(Page 3 of 14)

Model Layer Number	HSU (Symbol)	Dominant HGU(s) [a]	Stratigraphic Unit Map Symbols [b]	General Description
64	Fortymile Canyon upper lava-flow aquifer 6 (FCULFA6)	LFA, lesser TCU	Tfb	Consists of a thick and extensive sequence of rhyolitic lava flows of the Beatty Wash Formation, and that outcrop along Beatty Wash in the southern Timber Mountain moat. Encountered in Well ER-EC-7 (12.5–422.5-m [41–1,386-ft] depth interval). Lower portions saturated. Modeled as a property model within the FCCM.
63	Fortymile Canyon upper lava-flow aquifer 7 (FCULFA7)	LFA, lesser TCU	Tf	Consists of a buried sequence of rhyolitic lava flows of the Volcanics of Fortymile Canyon, and that occur beneath the southern Timber Mountain moat. Known only from a single occurrence in the lower portion of Well ER-EC-7 (352.0–422.5-m [1,155–1,386-ft] depth interval). Conceptualized and modeled as an isolated LFA with limited extent. Modeled as a property model within the FCCM.
62	Fortymile Canyon welded-tuff aquifer 1 (FCWTA1)	WTA	Tfb	Consists of a buried interval welded ash-flow tuff of the Beatty Wash Formation that occurs in the northwestern portion of the Timber Mountain moat. Known only from a single occurrence in Well ER-EC-2a (830.9–867.5-m [2,726–2,846-ft] depth interval). Conceptualized and modeled as an isolated WTA of limited extent. Modeled as a property model within the FCCM.
61	Fortymile Canyon welded-tuff aquifer (FCWTA)	WTA, lesser VTA and TCU	Tfb	Consists mostly of partially to moderately welded ash-flow tuff that occurs in the lower portion of the Volcanics of Fortymile Canyon in the southwestern portion of the TMCC. Exposed along the west side of the Transvaal Hills where it is 30 to 60 m (100–200 ft) thick and consists of moderately welded tuff in upper part grading to nonwelded vitric tuff (i.e., VTA) at base (Lipman et al., 1966). West of the Transvaal Hills, the unit is deeply buried and much thicker, and consists of at least two separate welded ash-flow tuff units with the upper unit described as moderately welded and the lower unit as partially welded. The buried portion is known only from a single occurrence in the MYJO Coffer well (529.4–776.3-m [1,737–2,547-ft] depth interval). Zeolitic or quartzofeldspathic bedded tuff of unknown thickness likely occurs between the two buried ash-flow tuff intervals. Mostly saturated except for portions near surface exposures in the Transvaal Hills.

Table B-1
HSUs of the PM-OV HFM
(Page 4 of 14)

Model Layer Number	HSU (Symbol)	Dominant HGU(s) [a]	Stratigraphic Unit Map Symbols [b]	General Description
60	Fortymile Canyon lower lava-flow aquifer (FCLLFA)	LFA, lesser TCU	Tff	Consists of rhyolitic to trachytic lava flows that likely straddle the stratigraphic contact between the Fortymile Canyon and Timber Mountain Groups. The HSU includes two geographically separate occurrences. Between the Transvaal Hills and Timber Mountain, the HSU correlates to the rhyodacite of Fleur-de-Lis Ranch, where it has a maximum exposed thickness of approximately 300 m (1,000 ft) along the west side of Timber Mountain (Slate et al., 1999). Farther west in Oasis Valley basin, the lava flows correlate to the rhyodacite of Fleur-de-Lis Ranch and trachyte of East Cat Canyon. This buried occurrence is known only from a single occurrence in the MYJO Coffer well (776.3–855.0-m [2,547–2,805-ft] depth interval). Zeolitic or quartzofeldspathic bedded tuff of unknown thickness likely occurs between these two units in Oasis Valley basin. Saturated within the Oasis Valley basin, but portions near surface exposures along the west side of Timber Mountain are unsaturated.
59	Fortymile Canyon lower mafic lava-flow aquifer (FCLMLFA)	LFA	Tfbb	Consists of basaltic lava that occurs at the base of the Volcanics of Fortymile Canyon in the eastern Timber Mountain moat. Modeled as having no surface exposure, but may correlate to exposures of older basalt mapped by Byers et al. (1966) in Fortymile Canyon. HSU penetrated in Well ER-30-1 from the depths 289.6–365.2 m (950–1,198 ft) where it directly overlies welded Ammonia Tanks Tuff. Saturated.
58	Ammonia Tanks mafic lava-flow aquifer (ATMLFA)	LFA	Tmay	Consists of trachytic lava flows exposed along the eastern flank of Timber Mountain, and modeled as extending into the subsurface of the southeastern Timber Mountain moat. Maximum exposed thickness is 150 m (490 ft) (Slate et al., 1999). Includes a small isolated rhyolite dome on the northern flank of Timber Mountain. Deeper portions are saturated.

Table B-1
HSUs of the PM-OV HFM
(Page 5 of 14)

Model Layer Number	HSU (Symbol)	Dominant HGU(s) [a]	Stratigraphic Unit Map Symbols [b]	General Description
57	Buttonhook Wash welded-tuff aquifer (BWWTA)	WTA	Tmaw	Consists of welded ash-flow tuff assigned to the tuff of Crooked Canyon and tuff of Buttonhook Wash. Exposed along the base of Timber Mountain (Tmb and Tmc in Byers et al., 1976). Unit is not exposed or encountered outside the margins of the TMCC. Interpreted to be in the subsurface of the southern and northwestern moat area (1,400.3–1,410.0 m [4,594–4,626-ft] depth in Well ER-EC-2a), and between Timber Mountain and the Transvaal Hills. A relatively thin subsurface occurrence is present in Well ER-EC-8 (439.5–448.7-m [1,442–1,472-ft] depth interval), and indicating that a portion of the unit flowed over or around the northern end of the Transvaal Hills. Unit is not present in MYJO Coffer #1, and thus its presence west of the Transvaal Hills is limited to the area around ER-EC-8. Consists of landslide breccia in Well ER-EC-5 (246.9–305.4-m [810–1,002-ft] depth) that is sourced from Timber Mountain during resurgent doming (NNSA/NSO, 2004), and thus may be a poor aquifer in this area. An isolated occurrence is also located in the northeastern Timber Mountain moat (262.7–328.0-m [862–1,076-ft] depth in Well ER-18-2). Becomes saturated at deeper levels away from exposures along Timber Mountain. Maximum exposed thickness is 250 m (820 ft) (Slate et al., 1999). Note: Surface exposures in model are mainly from Byers et al. (1976).
56	Buttonhook Wash confining unit (BWCU)	TCU	Tmaw	Zeolitic nonwelded tuff that occurs between the welded ash-flow tuffs of the Tuff of Buttonhook Wash and Ammonia Tanks Tuff. BWCU has a distribution similar to the BWWTA. Exposures of BWCU are probably present along the western base of Timber Mountain underlying BWWTA (e.g., Tmfu and Tmfl in Lipman et al. [1966]), but are not demarcated/mapped in the model. Maximum cumulative thickness of Tmfu and Tmfl in Lipman et al. (1966) is 83.8 m (275 ft).
55	Ammonia Tanks welded-tuff aquifer (ATWTA)	WTA	Tma	Welded ash-flow tuff assigned to the Ammonia Tanks Tuff. Very thick within the structural margins of the Ammonia Tanks caldera. Thinner, but still thick and extensive within the topographic low formed by the Rainier Mesa caldera. Exposed in the Transvaal Hills and on Timber Mountain. Includes nonwelded zones in the eastern portion of the Ammonia Tanks caldera (Tmb, Tmd, Tmf in Carr and Quinlivan [1966]). This heterogeneity is addressed with the inclusion of ATCCU as a property model within the ATWTA HSU. All units assigned as Tma in Slate et al. (1999) that occur within the margins of the TMCC represent ATWTA surface exposures (with the exception of those units at the base of Timber Mountain that may be assigned to BWWTA after Byers et al. [1976]).

Table B-1
HSUs of the PM-OV HFM
(Page 6 of 14)

Model Layer Number	HSU (Symbol)	Dominant HGU(s) [a]	Stratigraphic Unit Map Symbols [b]	General Description
54	Ammonia Tanks caldera confining unit (ATCCU)	TCU	Tma	Mostly nonwelded tuff exposed on the eastern portion of Timber Mountain (Tmb in Carr and Quinlivan [1966]). Expected to be altered where saturated. Modeled only in the subsurface beneath the northeastern and southeastern portions of the Ammonia Tanks caldera. This unit provides a conceptualization of the known heterogeneity inthe upper and middle portions of the intracaldera Ammonia Tanks Tuff in the eastern portion of the Ammonia Tanks caldera. It is addressed through the use of a property model within the ATWTA HSU. Exposed along the eastern side of Timber Mountain where it is unsaturated and grouped within the ATWTA due to the complex fault-controlled exposures on Timber Mountain. Grouped with Tma and Tml in Slate et al. (1999) and Byers et al. (1976), respectively. Present in UE-18r (897.6–1,027.2 m [2,945–3,370 ft]) as 129.5 m (425 ft) of potassic nonwelded tuff.
53	Timber Mountain upper welded-tuff aquifer (TMUWTA)	WTA, lesser LFA and TCU	Tmap	Unit consists predominately of extracaldera welded ash-flow tuff of the mafic-poor member of the Ammonia Tanks Tuff. Known only from a single occurrence in Well ER-EC-4 where it is 265.8-m (872-ft) thick. The top of the unit at Well ER-EC-4 consists of 3.7 m (12 ft) of mafic lava (i.e., LFA) overlying 15.8 m (52 ft) of zeolitic to quartzofeldspathic bedded and nonwelded tuff (i.e., TCU). The remaining 89% of the HSU consists of welded ash-flow tuff (i.e., WTA). The HSU is conceptualized as occurring within the northern portion of the Oasis Valley basin of Fridrich et al. (2007) south of the Black Mountain caldera, and between the Hogback fault on the west and the TMCC on the east. Although poorly constrained, this conceptualization is based on the thick extracaldera occurrence in Well ER-EC-4, which suggests deposition within a structural basin. Mostly saturated except for westernmost portion.
52	Tannenbaum Hill lava-flow aquifer (THLFA)	LFA, minor VTA and TCU	Tmat	Composed entirely of rhyolitic lava of the rhyolite of Tannenbaum Hill. Main occurrence is on the Bench and just outside the northwestern structural boundary of the TMCC. Mostly unsaturated, but very basal portions become saturated locally.
51	Tannenbaum Hill composite unit (THCM)	Mostly TCU, lesser WTA	Tmat	Zeolitic tuff and lesser welded ash-flow tuff of the rhyolite of Tannenbaum Hill that occurs stratigraphically below Tannenbaum Hill lava and above the rhyolite of Fluorspar Canyon. Distribution is similar to the THLFA. Lower portions to end to be saturated.

Table B-1
HSUs of the PM-OV HFM
(Page 7 of 14)

Model Layer Number	HSU (Symbol)	Dominant HGU(s) [a]	Stratigraphic Unit Map Symbols [b]	General Description
50	Tannenbaum Hill confining unit (THCU)	TCU	Tmat, Tmab, Tmrb	Nonwelded tuff and tuff breccia occurring between the Tannenbaum Hill lava and Rainier Mesa Tuff (1,184.5–1,367.0-m [3,886–4,485-ft] depth in well UE-18r). Also includes nonwelded, bedded tuffs assigned to the bedded Ammonia Tanks Tuff (Tmab) and bedded Rainier Mesa Tuff (Tmrb) of Ferguson et al. (1994). Nonwelded tuffs are assumed to be zeolitic because of the unit's deep intracaldera location below the water table. It is also assumed that thin nonwelded and bedded tuffs are always present between the Ammonia Tanks and Rainier Mesa Tuffs within the TMCC as observed in numerous drill holes on Pahute Mesa. As a result, the unit is present in an intervening position everywhere the Ammonia Tanks Tuff overlies the Rainier Mesa Tuff within the TMCC. Thin unmapped exposures of THCU are assumed to be present in the Transvaal Hills. Mostly saturated, except for elevated occurrences such as Timber Mountain, Transvaal Hills, and portions of the Bench.
49	Timber Mountain welded-tuff aquifer (TMWTA)	WTA, minor VTA	Tmr, Tma	Consists mainly of welded ash-flow tuff of the Rainier Mesa Tuff where it occurs outside the Rainier Mesa caldera (i.e., extracaldera). Includes minor amounts of unsaturated welded ash-flow tuff and vitric bedded tuff of the overlying Ammonia Tanks Tuff outside the limit of the TMUWTA (e.g., in eastern Pahute Mesa). Mostly unsaturated except for deeper portions in the extreme northwest portion of Pahute Mesa, southern portions of the Bench, and in the Oasis Valley basin between the western margins of the TMCC and the Hogback fault.
48	Timber Mountain lower vitric-tuff aquifer (TMLVTA)	VTA	Tmr, Tmrh, Tmrf, Tp	Consists mainly of vitric (i.e., unaltered) nonwelded and bedded tuffs of the lower portion of the Timber Mountain Group. These include the basal nonwelded portion of the Rainier Mesa Tuff, and nonwelded and bedded tuffs of the underlying tuff of Holmes Road and tuff of Fluorspar Canyon. Locally includes minor intervals of vitric lithologies at the top the underlying Paintbrush Group. Mostly unsaturated except for western portions on Pahute Mesa where the lower portion becomes saturated.

Table B-1
HSUs of the PM-OV HFM
(Page 8 of 14)

Model Layer Number	HSU (Symbol)	Dominant HGU(s) [a]	Stratigraphic Unit Map Symbols [b]	General Description
47	Rainier Mesa welded-tuff aquifer (RMWTA)	WTA	Tmr, Tmc	Thick and extensive intracaldera welded ash-flow tuff assigned to the Rainier Mesa Tuff. Exposed only in the Transvaal Hills, where it also includes debris-flow breccia (Tmc in Slate et al. [1999]) for this study. Present everywhere within the structural margins of the Rainier Mesa caldera. Includes both the mafic-rich and mafic-poor members of Ferguson et al. (1994). Modeled thickness is approximately 1,200 m (4,000 ft). Fridrich et al. (2007) shows intra-caldera Rainier Mesa Tuff up to 2,500 m (8,000 ft) thick. Maximum exposed intracaldera thickness is 500 m (1,640 ft) but base is not exposed (Slate et al., 1999). Mostly saturated, except for elevated occurrences such as Timber Mountain, Transvaal Hills, and portions of the Bench where the uppermost portions are unsaturated.
46	Fluorspar Canyon confining unit (FCCU)	TCU	Tmrf	Consists of zeolitic, nonwelded tuff of the rhyolite of Fluorspar Canyon. Locally, includes minor zeolitic lithologies (e.g., pumiceous lava) of the underlying top-most portion of the Paintbrush Group. HSU is confined to the Bench, where it has been structurally down-dropped below the water table, resulting in zeolitic alteration of the unit. On Pahute Mesa to the north, the rhyolite of Fluorspar Canyon is structurally higher, occurring mostly above the water table, and thus is vitric, and assigned to the TMLVTA. Mostly saturated except uppermost portions that are locally unsaturated.
45	Windy Wash aquifer (WWA)	LFA	Tmw	Minor unsaturated HSU consisting of the lava-flow lithofacies of the rhyolite of Windy Wash. Occurs locally along the western (down-thrown) side of the West Greeley fault in Area 20.
44	Paintbrush composite unit (PCM)	WTA, LFA, TCU	Tpc, Tp	Consists mostly of units of the Paintbrush Group that occur in the southern portion of the model area in the vicinity of the Claim Canyon caldera. Unit is dominated by thick, strongly welded Tiva Canyon Tuff within the Claim Canyon caldera. Outside the caldera this unit is more variable, consisting of welded and nonwelded tuff and rhyolitic lava assigned to various formations of the Paintbrush Group. Stratigraphically equivalent units of the Paintbrush Group that occur in the northern portion of the model area beneath Pahute Mesa have been grouped into seven separate HSUs.
43	Comb Peak aquifer (CPA)	LFA	Tpk	Consists of the LFA lithofacies of the rhyolite of Comb Peak at Pahute Mesa. HSU known from only two subsurface occurrences in Wells ER-EC-1 and ER-EC-15, where it is interpreted to consist of a single rhyolite lava flow. TCU-like lithofacies (e.g., zeolitic pumiceous lava) that occur at the top and base of the flow are grouped with the hydrostrigraphically adjacent FCCU and UPCU. Mostly saturated on the Bench. Unsaturated north of the Bench on Pahute Mesa.

Table B-1
HSUs of the PM-OV HFM
(Page 9 of 14)

Model Layer Number	HSU (Symbol)	Dominant HGU(s) [a]	Stratigraphic Unit Map Symbols [b]	General Description
42	Post-Benham Paintbrush confining unit (PBPCU)	TCU	Tp	Zeolitic nonwelded tuff, bedded tuff, and pumiceous lava that locally separates the BA from the CPA. Saturated on the Bench. Unsaturated north of the Bench on Pahute Mesa.
41	Benham aquifer (BA)	LFA	Tpb	Lava-flow lithofacies of the rhyolite of Benham. Occurs north of the TMCC and beneath the southwestern portion of Pahute Mesa.
40	Upper Paintbrush confining unit (UPCU)	TCU	Tp	Zeolitic nonwelded tuff, bedded tuff, and pumiceous lava that separate the SPA and TCA from overlying aquifers (e.g., BA and CPA).
39	Scrugham Peak aquifer (SPA)	LFA	Tps	Consists of the LFA lithofacies of the rhyolite of Scrugham Peak. HSU is exposed along the south face of Pahute Mesa and was encountered in Wells ER-20-8 and ER-20-8-2. Zeolitic pumiceous lava that occurs at the top and of the flow in these wells are grouped with the overlying UPCU.
38	Middle Paintbrush confining unit (MPCU)	TCU	Tp	Zeolitic nonwelded and bedded tuff that separate the TCA and the overlying SPA.
37	Tiva Canyon aquifer (TCA)	WTA	Tpc	The welded ash-flow lithofacies of the Pahute Mesa lobe of the Tiva Canyon Tuff beneath Pahute Mesa. Only saturated west of the Boxcar fault.
36	Paintbrush vitric-tuff aquifer (PVTA)	VTA	Pre-Tmr tuffs, Tp	Typically includes all vitric, nonwelded and bedded tuff units below the Rainier Mesa Tuff to the top of a Paintbrush lava (e.g., Tpb or Tpe) but may extend to base of Paintbrush Tuff in eastern Area 19, where Tpe or Tpr lavas are not present. May also include the vitric pumiceous top of the Tpe lava. Unit occurs in the northern portion of the model area beneath Pahute Mesa.
35	lower Paintbrush confining unit (LPCU)	TCU	Tpe, Tpd, Tpt	Consists of zeolitic bedded and nonwelded tuffs that occur stratigraphically between the Tiva Canyon Tuff and the welded Topopah Spring Tuff. This mainly includes the rhyolite of Delirium Canyon and the bedded and nonwelded Topopah Spring Tuff.
34	Paintbrush lava-flow aquifer (PLFA)	LFA	Tpd, Tpe, Tpr	Lava-flow lithofacies of the rhyolite of Delirium Canyon (Tpd), rhyolite of Echo Peak (Tpe), and rhyolite of Silent Canyon (Tpr). Also includes moderately to densely welded ash-flow tuff of Tpe. Unit occurs in the northern portion of the model area beneath Pahute Mesa.

Table B-1
HSUs of the PM-OV HFM
(Page 10 of 14)

Model Layer Number	HSU (Symbol)	Dominant HGU(s) [a]	Stratigraphic Unit Map Symbols [b]	General Description
33	Topopah Spring aquifer (TSA)	WTA	Tpt	The welded ash-flow lithofacies of the Topopah Spring Tuff in southern Area 20.
32	Yucca Mountain Crater Flat composite unit (YMCFCM)	LFA, WTA, TCU	Tc, Th	Includes all units of the Crater Flat Group and Calico Hills Formation that occur in the southern portion of the model area in the vicinity of Yucca Mountain. Stratigraphically equivalent units that occur in the northern portion of the model area beneath Pahute Mesa have been grouped into nine separate HSUs.
31	Calico Hills vitric-tuff aquifer (CHVTA)	VTA	Th (Tac)	Structurally high, vitric, nonwelded tuffs of the Calico Hills Formation. Present in the northern portion of the model area beneath the eastern portion of Area19. May become partly zeolitic in the lower portions.
30	Calico Hills zeolitic composite unit (CHZCM)	TCU	Th	Formerly in the Phase I HFM, the CHZCM consisted of a complex distribution of rhyolite lava flows (i.e., LFAs) intercalated within thick and extensive mostly zeolitic and quartzofeldspathic nonwelded and bedded tuffs (i.e., TCUs) of the Calico Hills Formation. In the Phase II model, the LFAs have been demarcated and modeled as separate property models within the CHZCM. Although the composite unit designation for the CHZCM is retained in the Phase II HFM, the unit is conceptualized in the Phase II HFM as consisting entirely of TCU. In addition, the Phase I CHCU HSU has been merged with the CHZCM in the Phase II HFM. The CHZCM is present in the northern portion of the model area beneath most of eastern and central Area 20, west of the West Greeley fault. The CHZCM is mostly saturated, particularly west of the Boxcar fault. East of the Boxcar fault, the upper portion of the HSU is above the water table.
29	Calico Hills lava-flow aquifer 1 (CHLFA1)	LFA	Th	The uppermost LFA property model within the CHZCM. Conceptualized as a single rhyolite lava flow of the Calico Hills Formation. Mainly occurs as a north–south-elongated flow between the West Greeley and Boxcar faults. Only the lower portion saturated west of the West Greeley fault.
28	Calico Hills lava-flow aquifer 2 (CHLFA2)	LFA, very minor TCU	Th	An LFA property model within the CHZCM. Although modeled as a single flow, very thin zeolitic bedded tuff observed within the CHLFA2 interval in U-20aj suggests that the property model may consist locally of two separate flows. Occurs in the northern portion of Pahute Mesa, mostly west of the West Greeley fault. Mostly unsaturated. Lower portion saturated in some places.

Table B-1
HSUs of the PM-OV HFM
(Page 11 of 14)

Model Layer Number	HSU (Symbol)	Dominant HGU(s) [a]	Stratigraphic Unit Map Symbols [b]	General Description
27	Calico Hills lava-flow aquifer 3 (CHLFA3)	LFA, minor TCU	Th	An LFA property model within the CHZCM. Although modeled as a single flow, the lithofacies distribution within drill holes penetrating the unit suggests that the property model may consist of more than one flow. Some of the lithofacies are described as zeolitic, which likely imparts TCU-like properties to portions of the flow, although these TCU-like portions appear to thin and thus become minor in occurrence. Similar in size and occurrence to CHLFA2. Fully saturated only west of the Boxcar fault. Lower portion saturated between the West Greeley and Boxcar faults. Mostly unsaturated east of the West Greeley fault.
26	Calico Hills lava-flow aquifer 4 (CHLFA4)	LFA	Th	An LFA property model within the CHZCM. Modeled as a single flow. Occurs as a north–south-elongated flow straddling the West Greeley fault. Mostly fully saturated west of the West Greeley fault. Portions become unsaturated east of the West Greeley fault.
25	Calico Hills lava-flow aquifer 5 (CHLFA5)	LFA	Th	The lowermost and most extensive LFA property model within the CHZCM. Modeled as a single flow. Occurs mainly west of the West Greeley fault. Saturated.
24	Inlet aquifer (IA)	LFA	Tci	Lava-flow lithofacies of the rhyolite of Inlet. Occurs as two thick isolated deposits beneath Pahute Mesa in the northern portion of the model area.
23	Crater Flat composite unit (CFCM)	Mostly LFA, intercalated with TCU	Tc, Tcpj, Tcps, Tcg	Includes welded tuff and lava flow lithofacies of the tuff of Jorum (Tcpj), the rhyolite of Sled (Tcps), and the andesite of Grimy Gulch (Tcg). Occurs in central Area 20 in the northern portion of the model area.
22	Crater Flat confining unit (CFCU)	TCU	Tc	Includes all zeolitic, nonwelded and bedded units below the Calico Hills Formation (Th) to the top of the Bullfrog Tuff (Tcb). Occurs mainly in Area 19 in the northern portion of the model area.
21	Kearsarge aquifer (KA)	LFA	Tcpk	Minor HSU that consists of the lava-flow lithofacies of rhyolite of Kearsarge. Unit is present as a small isolated occurrence in the northeastern portion of the model area.
20	Stockade Wash aquifer (SWA)	WTA	Tcbs	Consists of partially welded ash-flow tuff of the Stockade Wash lobe of the Bullfrog Tuff. Occurs along the eastern margin of the model area where it is extensively exposed. Mostly unsaturated.
19	Lower vitric-tuff aquifer 2 (LVTA2)	VTA	Tc	Two very small, unsaturated occurrences of vitric bedded tuff below the SWA in the extreme eastern portion of the model area.

Table B-1
HSUs of the PM-OV HFM
(Page 12 of 14)

Model Layer Number	HSU (Symbol)	Dominant HGU(s) [a]	Stratigraphic Unit Map Symbols [b]	General Description
18	Bullfrog confining unit (BFCU)	TCU	Tcb	Major confining unit in the northern portion of the model area. Unit consists of thick intracaldera, zeolitic, mostly nonwelded tuff of the Bullfrog Formation.
17	Belted Range aquifer (BRA)	LFA and WTA, with lesser TCU	Tb, Tbg, Tbgs, Tbq	Consists of welded ash-flow tuff and lava of the Belted Range Group (Tb) above the Grouse Canyon Tuff (Tbg) but may also include the lava flow lithofacies of the comendite of Split Ridge (Tbgs) and the comendite of Quartet Dome (Tbq) where present. Occurs in the northern portion of the model area.
16	Pre-Belted Range composite unit (PBRCM)	TCU, WTA, LFA	Tr, Tn, Tq, Tu, To, Tk, Te	Laterally extensive and locally very thick HSU that includes all the volcanic rocks older than the Belted Range Group.
15	subcaldera volcanic confining unit (SCVCU)	TCU	Tm, Tp, Tc, and older, undifferentiated tuffs	A highly conjectural unit that is modeled as consisting of highly altered volcanic rocks that occur stratigraphically between the Rainier Mesa Tuff and basement rocks (ATICU and RMICU) within the deeper portions of the TMCC.
14	lower clastic confining unit - thrust plate (LCCU1)	CCU	Cc, Cz, Czw, Zs	Late Proterozoic to Early Cambrian siliciclastic rocks that occur within the hanging wall of the Belted Range thrust fault.
13	lower carbonate aquifer - thrust plate (LCA3)	CA	Dg through Cc	Cambrian through Devonian, mostly limestone and dolomite, rocks that occur in the hanging wall of the Belted Range thrust fault.
12	upper clastic confining unit (UCCU)	CCU	MDc, MDe	Late Devonian through Mississippian siliciclastic rocks. Present in the eastern third of the model area.
11	lower carbonate aquifer (LCA)	CA	Dg through Cc	Cambrian through Devonian mostly limestone and dolomite. Widespread throughout the model area.
10	lower clastic confining unit (LCCU)	CCU	Cc, Cz, Czw, Zs, Zj	Late Proterozoic through Early Cambrian siliciclastic rocks. Widespread throughout the model area.

Table B-1
HSUs of the PM-OV HFM
(Page 13 of 14)

Model Layer Number	HSU (Symbol)	Dominant HGU(s) [a]	Stratigraphic Unit Map Symbols [b]	General Description
9	Silent Canyon intrusive confining unit (SCICU)	IICU	Tc, Tb	Although modeled as single intrusive masses beneath the Silent Canyon and Redrock Valley calderas, the actual nature of these units is unknown. They may consist exclusively of igneous intrusive rocks, or older volcanic and pre-Tertiary sedimentary rocks that are intruded to varying degrees by igneous rocks ranging in composition from granite to basalt.
8	Redrock Valley intrusive confining unit (RVICU)	IICU	Tori	
7	Mesozoic granite confining unit (MGCU)	GCU	Kg	Consists of granitic rocks that make up the Gold Meadows stock along the northeastern margin of the model area.
6	Black Mountain intrusive confining unit (BMICU)	IICU	Not Defined	Although modeled as single intrusive masses beneath each of the Black Mountain, Ammonia Tanks, Rainier Mesa, and Claim Canyon calderas, and the Calico Hills area, the actual nature of these units is unknown. They may consist exclusively of igneous intrusive rocks, or older volcanic and pre-Tertiary sedimentary rocks that are intruded to varying degrees by igneous rocks ranging in composition from granite to basalt.
5	Calico Hills intrusive confining unit (CHICU)	IICU	Not Defined	
4	Claim Canyon intrusive confining unit (CCICU)	IICU	Not Defined	
3	Rainier Mesa intrusive confining unit (RMICU)	IICU	Not Defined	

Table B-1
HSUs of the PM-OV HFM
(Page 14 of 14)

Model Layer Number	HSU (Symbol)	Dominant HGU(s) [a]	Stratigraphic Unit Map Symbols [b]	General Description
2	Ammonia Tanks intrusive confining unit (ATICU)	IICU	Not Defined	Although modeled as single intrusive masses beneath each of the Black Mountain, Ammonia Tanks, Rainier Mesa, and Claim Canyon calderas, and the Calico Hills area, the actual nature of these units is unknown. They may consist exclusively of igneous intrusive rocks, or older volcanic and pre-Tertiary sedimentary rocks that are intruded to varying degrees by igneous rocks ranging in composition from granite to basalt.
1	Pahute Mesa Northern Extension intrusive confining unit (PMNICU)	IICU	Not Defined	Modeled as individual intrusive confining units for the Mount Helen caldera and Cathedral Ridge calderas.

[a] See Table 2-2 for definitions of HGUs.
[b] See Tables 4-1 and 4-2 of the PM-OV HFM (DOE/EMNV, 2020a) for definitions of stratigraphic unit map symbols.

B.2.0 REFERENCES

Byers, F.M., Jr., C.L. Rogers, W.J. Carr, and S.J. Luft. 1966. *Geologic Map of the Buckboard Mesa Quadrangle, Nye County, Nevada*, Map GQ-552, scale 1:24,000. Washington, DC: U.S. Geological Survey

Byers, F.M., Jr., W.J. Carr, R.L. Christiansen, P.W. Lipman, P.P. Orkild, and W.D. Quinlivan. 1976. *Geologic Map of the Timber Mountain Caldera Area, Nye County, Nevada,* Map, I-891, scale 1:48,000. Reston, VA: U.S. Geological Survey

Carr, W.J., and W.D. Quinlivan. 1966. *Geologic Map of the Timber Mountain Quadrangle, Nye County, Nevada*, Map GQ-503, scale 1:24,000. Washington, DC: U.S. Geological Survey.

DOE/EMNV, see U.S. Department of Energy Environmental Management Nevada Program.

Ferguson, J.F., A.H. Cogbill, and R.G. Warren. 1994. "A Geophysical-Geological Transect of the Silent Canyon Caldera Complex, Pahute Mesa, Nevada." In J*ournal of Geophysical Research: Solid Earth*, Vol. 99(B3): pp. 4323–4339.

Fridrich, C.J., S.A. Minor, J.L. Slate, and P.L. Ryder. 2007. *Geologic Map of Oasis Valley Spring-Discharge Area and Vicinity, Nye County, Nevada*, Scientific Investigations Map 2957, 25 p., scale 1:50,000. Denver, CO: U.S. Geological Survey.

Lipman, P. W., W. D. Quinlivan, W. J. Carr, and R. E. Anderson, 1966. *Geologic Map of the Thirsty Canyon SE Quadrangle, Nye County, Nevada*. U.S. Geological Survey Geologic Quadrangle Map GQ-489, scale, 1:24,000

NNSA/NSO, see U.S. Department of Energy National Nuclear Security Administration Nevada Site Office.

Slate, J.L., M.E. Berry, P.D. Rowley, C.J. Fridrich, K.S. Morgan, J.B. Workman, O.D. Young, G.L. Dixon, V.S. Williams, E.H. McKee, D.A. Ponce, T.G. Hildenbrand, W.C. Swadley, S.C. Lundstrom, E.B. Ekren, R.G. Warren, J.C. Cole, R.J. Fleck, M.A. Lanphere, D.A. Sawyer, S.A. Minor, D.J. Grunwald, R.J. Laczniak, C.M. Menges, J.C. Yount, and A.S. Jayko. 1999. *Part A. Digital Geologic Map of the Nevada Test Site and Vicinity, Nye, Lincoln, and Clark Counties, Nevada, and Inyo County, California, Revision 4*, Open-File Report 99-554-A, scale 1:120,000. Denver, CO: U.S. Geological Survey.

U.S. Department of Energy Environmental Management Nevada Program. 2020. *Pahute Mesa-Oasis Valley Hydrostratigraphic Framework Model for Corrective Action Units 101 and 102: Central and Western Pahute Mesa, Nye County, Nevada*, Rev. 0, DOE/EMNV--014; Las Vegas, NV.

U.S. Department of Energy, National Nuclear Security Administration Nevada Site Office. 2004. *Completion Report for Well ER-EC-8*, DOE/NV/11718--435, UC-700. Prepared by Bechtel Nevada. Las Vegas, NV.

Appendix C

Use of Non-Direct Data

C.1.0 INTRODUCTION

The UGTA Activity is modeling flow and transport in aquifers of the NNSS and surrounding areas that have been contaminated from underground testing of nuclear devices. Modeling is used as a method of forecasting how the hydrogeologic system, including the underground test cavities, will behave over time with the goal of assessing the migration of RNs away from these cavities. To this end, flow and transport models are being developed over a range of scales for the UGTA CAUs. For the Central and Western Pahute Mesa CAUs, the predominant hydrologic flow pathways from the test cavities are through locally hydrologically conductive Cenozoic volcanic rocks that were erupted and deposited during multiple eruptive cycles of the Timber Mountain caldera complex (TMCC) and Silent Canyon caldera complex (SCCC) (Christiansen et al., 1977; Byers et al., 1976 and 1989; Broxton et al., 1989; Sawyer et al., 1994). Probability distributions for flow and transport parameters for these rocks are required input for the models.

A major effort of the UGTA Activity is to compile and assess the suitability of the existing data for these models. Modeling of the UGTA CAUs is not a common groundwater contaminant modeling problem. Most groundwater contamination problems consist of migration of contaminants from relatively well-characterized sources over short flow paths through shallow aquifers. There is often some information about contaminant distribution as a result of monitoring and site characterization. In contrast, the PM CAU model will require prediction of contaminant movement through deep aquifers in a large system (tens of kms on a side). Information about sources and RN distribution in the aquifer is sparse. Test cavities on PM are as deep as 1,450 m, making extensive characterization of the source and contaminant migration difficult and expensive.

Using experience from other sites to reduce parameter uncertainty is an appropriate approach when developing models in a sparse data environment (Freeze et al., 1990). This approach incorporates flow and transport parameter data from investigations of similar environments when developing prior distributions for parameters to be used in modeling the study area. Utilization of such existing data can be both cost-effective and necessary for a modeling effort in a sparse data environment.

The UGTA Quality Assurance Plan (QAP), Rev. 2 (NNSA/NFO, 2015) requires the justification of non-direct datasets and data sources used in support of UGTA models. All data used in the modeling will be reviewed in relation to the QAP requirements; however, the following general acceptance criteria were developed to guide use of the non-direct data most commonly used:

1. **UGTA data documents** present flow and transport model data, including data quality assessments, data analyses to derive expected values or probability distributions, and parameter uncertainty estimates. The documents are developed under the QAP requirements in place at the time of their preparation and were reviewed by the preemptive review (PER) committees, DOE, and NDEP. The data in these documents are considered to be valid for use.

2. **Peer-reviewed literature,** including handbooks of physical or chemical constants, is considered acceptable and does not require additional source acceptance justification. These documents have received sufficient technical reviews.

3. **UGTA-sponsored technical reports** completed before the current QAP (NNSA/NFO, 2015) have adequately justified their data sources and datasets, and the technical reviews have been sufficient to justify the results and conclusions. The documents were generally reviewed by the PER committees (or predecessor), DOE, and NDEP.

4. **Historical NNSS (or NTS) data** produced by LANL, LLNL, USGS, and contractors have applied sufficient QA and/or technical review to justify the use of the data. Data contained in the USGS Rock-Property Database (USGS, 2020; and previous versions) and the Database of NNSS Groundwater Levels and Hydrograph Descriptions (Elliott and Fenelon, 2010; and previous versions) have been formally accepted by UGTA.

5. **Other DOE programs** such as the Yucca Mountain Project, and the Low-Level Radioactive Waste Management programs in Areas 3 and 5 of the NNSS in Nevada and the Waste Isolation Project Plant (WIPP) in New Mexico were developed under QA programs equivalent to UGTA's and thereby satisfy current UGTA requirements.

6. **USGS data**, reports, and analyses are used in the development of UGTA documents. USGS is an UGTA Activity participant, and the information used was developed for the project. USGS works under a QA program that meets the UGTA Activity QAP requirements, and no further justification is necessary for use of this organization's information.

7. **Other federal or international entities—**such as the National Oceanic and Atmospheric Administration, International Atomic Energy Agency, and European Space Agency—have sufficient internal review and QA procedures, and no further justification is necessary.

8. **UGTA databases** developed and updated in compliance with QA procedures existing at the time of compilation are sufficient to justify the data, even if the data were originally generated from a non-UGTA entity, such as the weapons program and the Routine Radiological Environmental Monitoring Plan.

9. **Non-direct data from other non-UGTA reports** that are cited to provide the overall scientific context for the UGTA generated work but are not used directly in the models do not require any further justification.

C.2.0 REFERENCES

Broxton, D.E., R.G. Warren, F.M. Byers, and R.B. Scott. 1989. "Chemical and Mineralogic Trends within the Timber Mountain–Oasis Valley Caldera Complex, Nevada: Evidence for Multiple Cycles of Chemical Evolution in a Long-Lived Silicic Magma System." In *Journal of Geophysical Research: Solid Earth*, Vol. 94(B5): pp. 5961–5985.

Byers, F.M., Jr., W.J. Carr, R.L. Christiansen, P.W. Lipman, P.P. Orkild, and W.D. Quinlivan. 1976. *Geologic Map of the Timber Mountain Caldera Area, Nye County, Nevada,* Map, I-891, scale 1:48,000. Reston, VA: U.S. Geological Survey

Byers, F.M., Jr., W.J. Carr, and P.P. Orkild. 1989. "Volcanic Centers of Southwestern Nevada: Evolution and Understanding, 1960–1988." In *Journal of Geophysical Research: Solid Earth,* Vol. 94(B5): pp. 5908–5924.

Christiansen, R.L., P.W. Lipman, W.J. Carr, F.M. Byers, Jr., P.P. Orkild, and K.A. Sargent. 1977. "Timber Mountain-Oasis Valley Caldera Complex of Southern Nevada." In *Geological Society of America Bulletin*, Vol. 88(7): pp. 943–959.

Elliott, P.E., and J.M. Fenelon. 2010. *Database of Groundwater Levels and Hydrograph Descriptions for the Nevada Test Site Area, Nye County, Nevada*, *1941–2010,* Data Series 533. Reston, VA: U.S. Geological Survey. (Version 9.0 released in February 2019).

Freeze, R.A., J. Massmann, L. Smith, T. Sperling, and B. James. 1990. "Hydrogeological Decision Analysis: 1. A Framework." In *Ground Water*, Vol. 28(5): 738–766.

NNSA/NFO, see U.S. Department of Energy, National Nuclear Security Administration Nevada Field Office.

Sawyer, D.A., R.J. Fleck, M.A. Lanphere, R.G. Warren, D.E. Broxton, and M.R. Hudson. 1994. "Episodic Caldera Volcanism in the Miocene Southwestern Nevada Volcanic Field: Revised Stratigraphic Caldera Framework, $^{40}Ar/^{39}Ar$ Geochronology, and Implications for Magmatism and Extension." In *Geological Society of America Bulletin*, Vol. 106(10): pp. 1304–1318.

USGS, see U.S. Geological Survey.

U.S. Department of Energy, National Nuclear Security Administration Nevada Field Office. 2015. *Underground Test Area Activity Quality Assurance Plan, Nevada National Security Site, Nevada*, Rev. 2, DOE/NV--1450-REV.2. Las Vegas, NV.

U.S. Geological Survey. 2020. "Mercury Core Library and Data Center, Rock-Property Database." As accessed at http://nevada.usgs.gov/mercury/ on 1 May. Mercury, NV.

Appendix D

Matrix Porosity

D.1.0 MATRIX POROSITY

D.1.1 Introduction

The Phase I PM TDD (Shaw, 2003) provides estimates of porosity for many of the HSUs in the PM CAU transport model. These initial estimates are based on core and cuttings analysis in the laboratory and interpretations of geophysical logs. Where possible, and this applies to the large majority of the HSUs in the model, these initial estimates have been supplemented with porosity estimates derived from recent (Navarro, 2019) interpretations of geophysical logs, specifically density logs. The purpose of this section is to describe the process followed to utilize density log data from borings in the PM area to arrive at estimates of porosity.

D.1.2 Data Sources

The porosity dataset from the Phase I PM TDD (Shaw, 2003) was supplemented by the analysis of the density logs of a select group of Phase I and II PM wells as documented in Navarro (2019). The analysis of the density log data provides estimates of porosity for many HSUs for which an estimate is not provided in Shaw (2003).

Table D-1 lists the HSUs found in the PM CAU transport model and the sources for the estimates of average HSU matrix porosity given in this report. The first column lists the HSUs in the model. Multiple appearances of the same HSU in the model are not included (e.g., CHLFA1, CHLFA2). Of the HSUs listed, 44 are found in the boring logs of wells within the PM-OV HFM area. The HSUs found in the borings of the PM-OV HFM area are shown in the second column. The third and fourth columns show the sources for the estimates of average matrix porosity given in this report. Forty of the HSUs in the PM CAU transport model have estimates of average matrix porosity derived from the analysis of density log data (Navarro, 2019). Thirty-one of the HSUs have estimated average matrix porosity values in the Phase I PM TDD (Shaw, 2003).

The HSU assignments in the PM CAU transport model reflect the PM-OV HFM (DOE/EMNV, 2020a). Although some of the HSUs in the transport model are not found in borings in the PM-OV HFM area, these HSUs are in the PM-OV HFM. The depths of the borings affect the HSUs they are able to intercept. Although an HSU is thought to be present, based on lines of evidence other than the physical borings, the borings themselves may not be deep enough to show them.

Table D-1
HSUs in PM CAU Transport Model and Sources of Estimates of Average Matrix Porosities
(Page 1 of 3)

HSUs in the PM-OV Basin Flow Model	HSUs Reflected in the PM-OV HFM Area Borings	Average HSU Porosity Estimated from Lithologies	Average HSU Porosity Sourced from Phase I Pahute Mesa TDD
AA	YES	NO	YES
ATCCU	NO	NO	YES
ATICU	NO	NO	YES
ATWTA	YES	YES	NO
BA	YES	YES	YES
BFCU	YES	YES	NO
BRA	YES	YES	YES
BWCU	YES	YES	NO
BWWTA	YES	NO	NO
CFCM	YES	YES	YES
CFCU	YES	YES	NO
CHLFA	YES	YES	NO
CHVTA	YES	YES	YES
CHZCM	YES	YES	YES
CPA	YES	YES	NO
DVA	YES	YES	YES
DVCM	NO	NO	YES
FCCM	YES	YES	YES
FCCU	YES	YES	NO
FCLLFA	YES	YES	NO
FCULFA	YES	YES	NO
FCWTA	YES	YES	NO
IA	YES	YES	YES
KA	YES	YES	YES
LCA	NO	NO	YES
LCCU	YES	NO	YES
LPCU	YES	YES	NO
MGCU	NO	NO	YES
MPCU	YES	YES	NO
PBPCU	YES	YES	NO
PBRCM	YES	YES	YES

Table D-1
HSUs in PM CAU Transport Model and Sources of Estimates of Average Matrix Porosities
(Page 2 of 3)

HSUs in the PM-OV Basin Flow Model	HSUs Reflected in the PM-OV HFM Area Borings	Average HSU Porosity Estimated from Lithologies	Average HSU Porosity Sourced from Phase I Pahute Mesa TDD
PCM	YES	YES	YES
PLFA	YES	YES	YES
PMNICU	NO	NO	YES
PVTA	YES	YES	YES
RMICU	NO	NO	YES
RMWTA	YES	YES	NO
SCVCU	NO	NO	YES
SPA	YES	YES	NO
TCA	YES	YES	NO
TCVA	YES	YES	YES
THCM	YES	YES	YES
THCU	YES	YES	NO
THLFA	YES	YES	YES
TMLVTA	YES	YES	NO
TMUWTA	YES	YES	NO
TMWTA	YES	YES	NO
TSA	YES	YES	YES
UCCU	NO	NO	YES
UPCU	YES	YES	NO
WWA	YES	YES	YES

Table D-1
HSUs in PM CAU Transport Model and Sources of Estimates of Average Matrix Porosities
(Page 3 of 3)

HSUs in the PM-OV Basin Flow Model	HSUs Reflected in the PM-OV HFM Area Borings	Average HSU Porosity Estimated from Lithologies	Average HSU Porosity Sourced from Phase I Pahute Mesa TDD
YMCFCM	YES	YES	YES
YVCM	YES	NO	YES

AA = Alluvial aquifer
ATCCU = Ammonia Tanks caldera confining unit
ATICU = Ammonia Tanks intrusive confining unit
ATWTA = Ammonia Tanks welded-tuff aquifer
BA = Benham aquifer
BFCU = Bullfrog confining unit
BRA = Belted Range aquifer
BWCU = Buttonhook Wash confining unit
BWWTA = Buttonhook Wash welded-tuff aquifer
CFCM = Crater Flat composite unit
CFCU = Crater Flat confining unit
CHLFA = Calico Hills lava-flow aquifer
CHVTA = Calico Hills vitric-tuff aquifer
CHZCM = Calico Hills zeolitic composite unit
CPA = Comb Peak aquifer
DVA = Detached volcanic aquifer
DVCM = Detached volcanic composite unit
FCCM = Fortymile Canyon composite unit
FCCU = Fluorspar Canyon confining unit
FCLLFA = Fortymile Canyon lower lava-flow aquifer
FCULFA = Fortymile Canyon upper lava-flow aquifer
FCWTA = Fortymile Canyon welded-tuff aquifer
IA = Inlet aquifer
KA = Kearsarge aquifer
LCA = Lower carbonate aquifer
LCCU = Lower clastic confining unit
LPCU = Lower Paintbrush confining unit
MGCU = Mesozoic granite confining unit
MPCU = Middle Paintbrush confining unit
PBPCU = Post-Benham Paintbrush confining unit
PBRCM = Pre-Belted Range composite unit
PCM = Paintbrush composite unit
PLFA = Paintbrush lava-flow aquifer
PMNICU = Pahute Mesa Northern Extension intrusive confining unit
PVTA = Paintbrush vitric-tuff aquifer
RMICU = Rainier Mesa intrusive confining unit
RMWTA = Rainier Mesa welded-tuff aquifer
SCVCU = Subcaldera volcanic confining unit
SPA = Scrugham Peak aquifer
TCA = Tiva Canyon aquifer
TCVA = Thirsty Canyon volcanic aquifer
THCM = Tannenbaum Hill composite unit
THCU = Tannenbaum Hill confining unit
THLFA = Tannenbaum Hill lava-flow aquifer
TMLVTA = Timber Mountain lower vitric-tuff aquifer
TMUWTA = Timber Mountain upper welded-tuff aquifer
TMWTA = Timber Mountain welded-tuff aquifer
TSA = Topopah Spring aquifer
UCCU = Upper clastic confining unit
UPCU = Upper Paintbrush confining unit
WWA = Windy Wash aquifer
YMCFCM = Yucca Mountain Crater Flat composite unit
YVCM = Younger volcanic composite unit

In addition, the borings are generally not closely spaced and the model area is large, leaving geologic interpretation to define the areas between borings.

D.1.3 Data Quality

The data used in this analysis conforms to the project QAP. Most of the data were generated under the UGTA QAP. The data not specifically from work done under the project QAP are from programs with equivalent QAP standards, as described in Appendix C.

D.1.4 Estimates of Matrix Porosity Derived from Density Log Data

During the drilling of a new well, a suite of geophysical logs for subsurface investigation is acquired from the open borehole. These logs provide a set of depth-specific physical measurements of rock properties and provide information on borehole conditions. Each type of log provides several datasets.

Estimates of matrix porosity were developed from the geophysical logs of a set of Phase I and II PM wells. This evaluation is documented in the Pahute Mesa Geophysical Log Data Evaluation for Matrix Porosity data document (Navarro, 2019). The estimates of porosity derived from the density logs are used to supplement the values found in the PM Phase I Transport Data Document presented in this report.

The downhole logs used for the porosity evaluation of PM wells were acquired by two well logging service companies, Schlumberger and Baker Hughes. The geophysical logs acquired by these companies provide basically the same types of log data. While all the logs in the logging suite were reviewed, the focus of the evaluation conducted was to estimate formation porosity. Only the log data below the water table were considered. The source of the water levels used for this purpose is the USGS Professional Paper No. 1771 (Fenelon et al., 2010). The logs evaluated include compensated density, neutron porosity, acoustic porosity, resistivity, caliper, and gamma ray. The evaluation included the geophysical log data for 13 wells: ER-18-2, ER-20-4, ER-20-7, ER-20-8, ER-20-11, ER-20-12, ER-EC-1, ER-EC-6, ER-EC-11, ER-EC-12, ER-EC-13, ER-EC-14, and ER-EC-15. The geophysical logs used for this evaluation were found in the UGTA Geophysics Library (Navarro, 2018). Figure D-1 provides the location on PM for the wells used in this evaluation.

The method of analysis used to develop estimates of matrix porosity from the density log data required grain densities. Core/cuttings data from the RPd were used to estimate grain densities to be used to calculate formation porosities from logs. Data from the following wells in Areas 20 and Area 18 on PM were used for this evaluation: PM-1, PM-2, U-20a, U-20a 2 WW, U-20ac, U-20af, U-20ag, U-20ah, U-20ai, U-20aj, U-20ak, U-20aL, U-20am, U-20an, U-20ao, U-20ap, U-20aq, U-20ar, U-20as, U-20at, U-20av, U-20aw, U-20ax, U-20ay, U-20az, U-20bb, U-20bb 1, U-20bc, U-20bd, U-20bd 1, U-20bd 2, U-20be, U-20bf, U-20c, U-20g, U-20i, U-20m, U-20n, UE-18r, UE-18t, UE-20ab, UE-20ad, UE-20ae, UE-20av, UE-20c, UE-20d, UE-20e, UE-20e 1, UE-20f, UE-20h, UE-20j, and UE-20p. These wells with available grain density measurements were selected from the

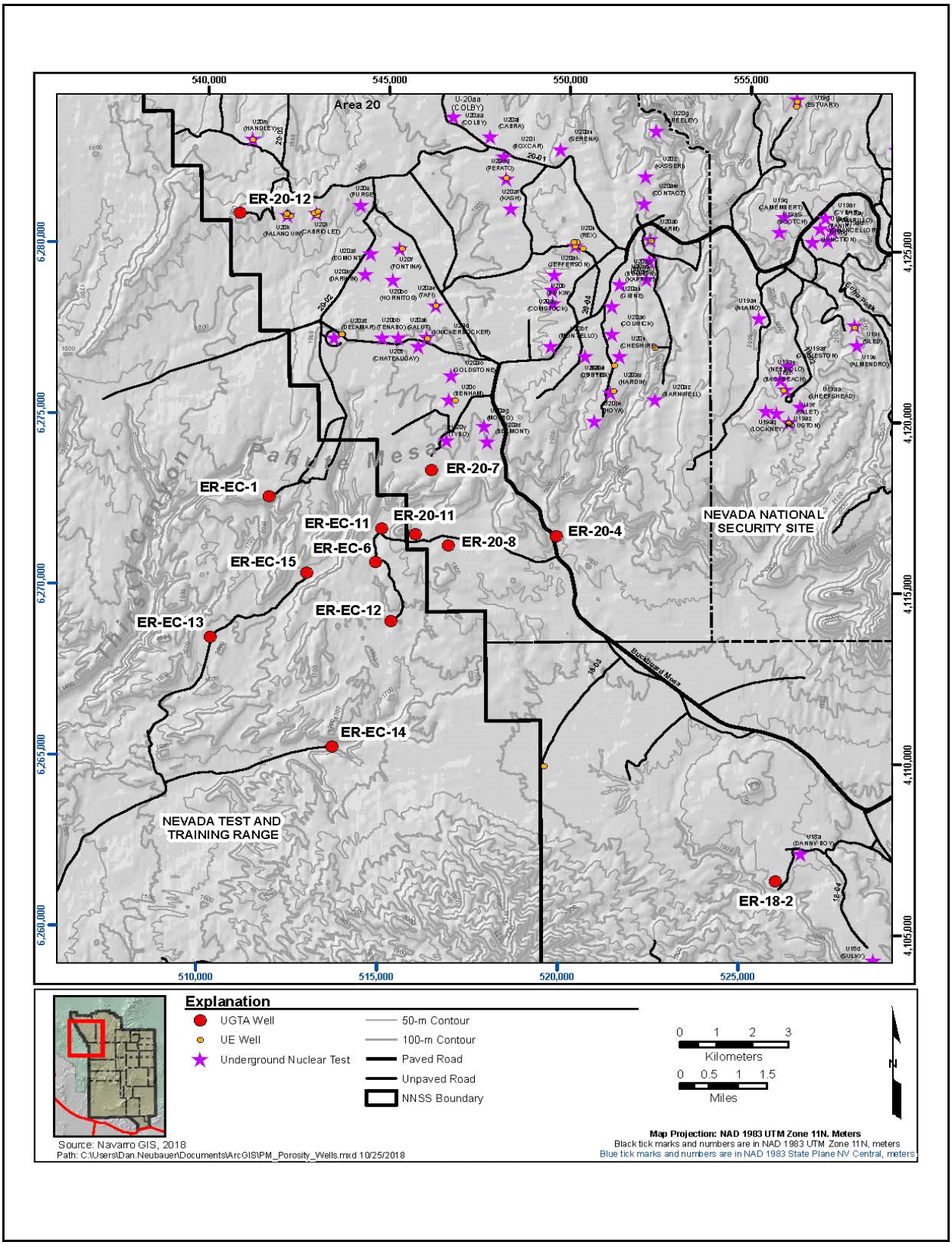

Figure D-1
Map Showing Locations of Wells for which Geophysical Log Data Were Analyzed

RPd and are not the same wells for which the density log analyses were performed. However, the data are for the same lithologies as analyzed in the density log interpretations and come from wells in the same general area. It is acknowledged that grain density measurements in the RPd may be prone to overestimation in the zeolitized zones (Carle, 2020).

D.1.4.1 Density Log Analysis

Density porosity is calculated from the density log using the following equation (Schlumberger, 1989):

$$Ø = (\sigma_{ma} - \sigma_b) / (\sigma_{ma} - \sigma_f) \quad (D\text{-}1)$$

where

- $Ø$ = calculated density porosity
- σ_b = density (g/cm^3) measured from geophysical log (bulk density)
- σ_{ma} = formation matrix density (g/cm^3)
- σ_f = formation fluid density (g/cm^3)

The formation matrix density is the grain density. For any given sample, it is a constant and is a commonly measured property in the analysis of rock core/cuttings. Grain densities from the (RPd, (Wood, 2009) based on lithology, are listed in Table D-2. Because only the logs below the water table were used in this evaluation, the formation fluid is assumed to be water with a fluid density of 1 g/cm^3. The statistics from the core/cuttings, as tabulated in Table D-2, along with the neutron, acoustic, and resistivity log porosities were used to select an appropriate grain density for calculating density porosity.

The RPd contains data from a variety of locations in and around the NNSS. The data include the analysis of rock core and cuttings reporting the well name, depth of sample bgs, and calculated porosities amongst other fields. The wells from which grain density measurements were selected from the RPd are not the same wells for which the density log analyses were performed. However, the data are for the same lithologies as analyzed in the density log interpretations, and the data come from wells in the same general area. Specifically, data from the following wells in Areas 20 and 18 on PM were used for this evaluation: PM-1, PM-2, U-20a, U-20a 2 WW, U-20ac, U-20af, U-20ag, U-20ah, U-20ai, U-20aj, U-20ak, U-20aL, U-20am, U-20an, U-20ao, U-20ap, U-20aq, U-20ar, U-20as, U-20at, U-20av, U-20aw, U-20ax, U-20ay, U-20az, U-20bb, U-20bb 1, U-20bc, U-20bd, U-20bd 1, U-20bd 2, U-20be, U-20bf, U-20c, U-20g, U-20i, U-20m, U-20n, UE-18r, UE-18t, UE-20ab,

Table D-2
Descriptive Statistics for Grain Densities per Lithology

Units of g/cm³	BED	DWT	FB	IN	LA	MWT	NWT
Mean	2.49E+00	2.56E+00	2.47E+00	2.65E+00	2.47E+00	2.56E+00	2.51E+00
Standard Error	3.27E-03	6.96E-03	9.19E-03	1.50E-02	5.82E-03	4.42E-03	6.18E-03
Median	2.50E+00	2.54E+00	2.47E+00	2.62E+00	2.47E+00	2.57E+00	2.52E+00
Mode	2.37E+00	2.53E+00	2.39E+00	2.62E+00	2.60E+00	2.54E+00	2.43E+00
Standard Deviation	1.02E-01	5.82E-02	1.06E-01	4.50E-02	1.28E-01	5.93E-02	9.91E-02
Sample Variance	1.04E-02	3.39E-03	1.12E-02	2.03E-03	1.63E-02	3.52E-03	9.83E-03
Kurtosis	3.09E-01	1.63E-01	1.27E+00	-1.84E+00	7.40E-01	1.33E+00	7.83E-01
Skewness	-3.15E-01	7.80E-01	6.43E-01	2.65E-01	-1.65E-01	-8.91E-01	-6.50E-01
Range	6.70E-01	2.60E-01	7.10E-01	1.20E-01	8.00E-01	3.20E-01	5.80E-01
Minimum	2.13E+00	2.44E+00	2.19E+00	2.59E+00	2.08E+00	2.36E+00	2.15E+00
Maximum	2.80E+00	2.70E+00	2.90E+00	2.71E+00	2.88E+00	2.68E+00	2.73E+00
Count	9.77E+02	7.00E+01	1.33E+02	9.00E+00	4.81E+02	1.80E+02	2.57E+02
Units of g/cm³	**NWT/PWT**	**PL**	**PL/FB**	**PWT**	**RWT**	**TB**	**VT**
Mean	2.52E+00	2.45E+00	2.15E+00	2.56E+00	2.43E+00	2.55E+00	2.45E+00
Standard Error	2.68E-02	1.84E-02	2.39E-02	6.95E-03	5.97E-02	3.69E-02	1.76E-02
Median	2.51E+00	2.45E+00	2.13E+00	2.58E+00	2.45E+00	2.58E+00	2.43E+00
Mode	#N/A	2.45E+00	2.11E+00	2.60E+00	2.59E+00	2.61E+00	2.37E+00
Standard Deviation	7.58E-02	1.04E-01	5.85E-02	8.59E-02	1.69E-01	9.04E-02	8.44E-02
Sample Variance	5.74E-03	1.08E-02	3.43E-03	7.38E-03	2.85E-02	8.18E-03	7.12E-03
Kurtosis	-1.18E+00	8.63E-01	1.39E+00	3.44E+00	-2.46E+00	4.66E+00	1.47E+00
Skewness	2.36E-01	-7.42E-01	1.25E+00	-1.46E+00	-1.08E-01	-2.09E+00	1.33E+00
Range	2.10E-01	4.40E-01	1.60E-01	5.50E-01	3.80E-01	2.40E-01	3.20E-01
Minimum	2.42E+00	2.17E+00	2.09E+00	2.18E+00	2.23E+00	2.37E+00	2.36E+00
Maximum	2.63E+00	2.61E+00	2.25E+00	2.73E+00	2.61E+00	2.61E+00	2.68E+00
Count	8.00E+00	3.20E+01	6.00E+00	1.53E+02	8.00E+00	6.00E+00	2.30E+01

#N/A = No duplicate values found.

BED = Bedded tuff
DWT = Densely welded ash-flow tuff
FB = Flow breccia
IN = Intrusive
LA = Lava
MWT = Moderately welded ash-flow tuff
NWT = Nonwelded ash-flow tuff
PL = Pumiceous lava
PWT = Partially welded ash-flow tuff
RWT = Reworked tuff
TB = Tuff breccia
VT = Vitrophyre

UE-20ad, UE-20ae, UE-20av, UE-20c, UE-20d, UE-20e, UE-20e 1, UE-20f, UE-20h, UE-20j, and UE-20p.

The analysis described above is documented in Navarro (2019). It resulted in estimates of matrix porosity for each of the well logs analyzed, typically at increments of 0.25 ft. The HGU and lithology were identified for each measurement. These data were further sorted using the stratigraphy identified for each of the wells in the project Stratigraphy-Lithology database to identify the HSU associated with each measurement.

Tables D-3 through D-5 show the statistics derived for the estimates of matrix porosity derived from the density log data. Table D-3 shows the porosity by lithology; Table D-4 shows it by HSU; and Table D-5 shows the estimates by HGU. In addition to standard parameters of minimum and maximum values, median, etc., the matrix porosity estimates for each HSU were analyzed via box and whisker plots. The quartile information shown in the table refers to the box and whisker plot values. In many cases, the box and whisker plot analysis classifies some of the values as outliers.

Table D-3
Estimates of Matrix Porosity by Lithology Developed from Density Logs
(Page 1 of 2)

	BED	DWT	FB	LA	LD	MWT	NWT
minimum	8.48	3.54	5.06	2.79	13.80	4.38	6.47
maximum	54.50	32.33	54.76	54.90	50.51	49.81	52.91
average	29.97	12.18	23.41	19.79	29.90	15.62	29.32
median	29.24	11.67	18.98	18.29	30.13	14.94	27.63
standard deviation	8.19	3.96	10.95	7.03	5.58	5.33	11.05
standard error	0.06	0.07	0.21	0.06	0.13	0.04	0.10
count	20,117	2,845	2,720	14,532	1,945	14,826	11,741
first quartile value	23.86	9.74	15.51	15.00	25.89	11.60	19.36
third quartile value	36.14	14.42	29.23	22.85	33.80	18.78	38.86
min quartile value	8.48	3.54	5.06	3.27	14.05	5.06	6.47
max quartile value	54.50	21.37	49.68	34.62	45.25	29.49	52.91
	PL	**PWT**	**TB**	**VT**	**BED-NWT**	**BED-RWT**	**LA-FB**
minimum	10.71	5.19	21.55	5.03	8.91	31.28	7.78
maximum	55.00	55.26	51.00	48.90	51.48	45.70	42.61
average	28.98	22.40	38.91	19.27	28.42	39.21	19.16
median	26.48	19.81	38.74	18.41	23.33	38.99	18.64

Table D-3
Estimates of Matrix Porosity by Lithology Developed from Density Logs
(Page 2 of 2)

	PL	PWT	TB	VT	BED-NWT	BED-RWT	LA-FB
standard deviation	10.80	9.35	6.58	6.70	11.12	3.33	5.51
standard error	0.14	0.15	0.15	0.10	0.21	0.29	0.13
count	5,804	3,729	1,904	4,176	2,889	132	1,669
first quartile value	19.49	14.74	33.69	14.22	20.00	37.60	15.13
third quartile value	39.35	28.75	44.77	24.18	42.48	41.91	22.03
min quartile value	10.71	5.19	21.55	5.03	8.91	31.28	7.78
max quartile value	55.00	49.74	50.58	39.05	51.48	45.70	32.16
	MWT-DWT	**PWT-MWT**	**PWT-NWT**	**PL-NWT**	**VT-PL**	--	--
minimum	2.18	18.40	13.91	11.59	5.72	--	--
maximum	40.54	48.26	39.41	35.36	39.17	--	--
average	10.65	32.09	28.48	21.98	16.20	--	--
median	10.31	29.08	28.01	21.52	15.31	--	--
standard deviation	4.18	6.87	5.03	5.77	5.23	--	--
standard error	0.06	0.29	0.14	0.32	0.14	--	--
count	5,262	578	1,356	320	1,374	--	--
first quartile value	7.82	27.00	25.26	16.67	12.76	--	--
third quartile value	12.56	39.64	31.91	26.61	18.62	--	--
min quartile value	2.18	18.40	15.64	11.59	5.72	--	--
max quartile value	19.63	48.26	39.41	35.36	27.38	--	--

-- = No data available

Table D-4
Estimates of Matrix Porosity by HSU Developed from Density Logs
(Page 1 of 3)

	BA	BRA	CFCM	CFCU	CHLFA	CHZCM	CPA
minimum	6.67	3.54	5.03	14.05	3.83	6.47	4.22
maximum	54.56	47.19	49.81	36.46	54.90	55.00	54.75
average	20.91	21.84	17.19	21.92	18.94	28.10	22.72
median	19.68	23.01	16.28	22.05	16.01	26.90	20.63
standard deviation	6.26	10.62	5.42	3.17	8.15	10.99	8.57
standard error	0.08	0.38	0.07	0.06	0.14	0.11	0.15
count	5,911	782	6,867	2,683	3,287	10,646	3,107
first quartile value	16.67	10.23	13.86	17.47	13.92	18.80	16.65

Table D-4
Estimates of Matrix Porosity by HSU Developed from Density Logs
(Page 2 of 3)

	BA	BRA	CFCM	CFCU	CHLFA	CHZCM	CPA
third quartile value	23.86	30.98	18.92	23.46	21.71	36.76	26.60
min quartile value	6.67	3.54	6.28	11.08	3.83	6.47	4.22
max quartile value	34.62	47.19	26.48	32.31	33.33	55.00	41.52
	FCCM	**FCCU**	**FCULFA**	**LPCU**	**MPCU**	**PBPCU**	**PBRCM**
minimum	7.93	18.80	5.72	7.56	19.19	12.66	10.18
maximum	52.53	54.37	40.00	54.50	51.88	43.35	42.61
average	31.28	37.60	19.31	27.30	37.28	32.19	21.57
median	30.84	39.01	19.05	25.95	37.52	32.21	20.64
standard deviation	9.80	7.30	5.36	7.09	5.36	5.93	4.71
standard error	0.15	0.08	0.09	0.08	0.17	0.34	0.15
count	4,098	7,904	3,404	8,259	1,009	304	1,033
first quartile value	23.23	31.08	15.79	22.45	32.85	29.72	18.38
third quartile value	39.37	43.98	22.21	32.53	41.21	36.01	23.94
min quartile value	7.93	18.80	6.34	7.56	20.34	20.70	10.18
max quartile value	52.53	54.37	31.77	47.65	51.88	43.35	32.16
	RMWTA	**SPA**	**TCA**	**THCM**	**THCU**	**TMLVTA**	**TMWTA**
minimum	2.18	2.79	5.19	13.80	25.17	5.26	6.52
maximum	44.38	36.39	49.81	55.26	50.07	48.26	23.13
average	12.68	16.27	18.56	31.54	35.65	36.28	13.53
median	11.19	15.51	17.95	31.33	34.97	39.85	13.35
standard deviation	6.25	5.29	5.54	7.04	4.58	9.51	2.36
standard error	0.07	0.13	0.06	0.14	0.16	0.28	0.12
count	9,121	1,577	8,965	2,437	800	1,116	385
first quartile value	8.56	12.41	14.18	26.46	32.60	36.63	12.13
third quartile value	14.68	19.18	20.51	35.25	37.42	41.91	15.06
min quartile value	2.18	2.79	5.19	13.80	25.50	28.86	7.96
max quartile value	23.85	29.32	30.00	48.29	44.64	48.26	19.44
	TSA	**UPCU**	--	--	--	--	--
minimum	5.06	8.01	--	--	--	--	--
maximum	42.05	53.91	--	--	--	--	--
average	16.76	31.48	--	--	--	--	--
median	14.23	31.77	--	--	--	--	--
standard deviation	7.67	8.58	--	--	--	--	--

Table D-4
Estimates of Matrix Porosity by HSU Developed from Density Logs
(Page 3 of 3)

	TSA	UPCU	--	--	--	--	--
standard error	0.08	0.14	--	--	--	--	--
count	10,290	3,937	--	--	--	--	--
first quartile value	11.35	24.56	--	--	--	--	--
third quartile value	20.06	38.26	--	--	--	--	--
min quartile value	5.06	8.01	--	--	--	--	--
max quartile value	33.14	53.91	--	--	--	--	--

-- = No data available

Table D-5
Estimates of Matrix Porosity by HGU Developed from Density Logs

	LFA	TCU	VTA	WTA
minimum	2.79	6.47	5.26	2.18
maximum	54.90	55.00	48.26	55.26
average	19.42	29.69	36.17	16.29
median	17.72	28.54	38.83	14.71
standard deviation	7.34	9.65	8.42	7.25
standard error	0.05	0.05	0.22	0.04
count	21,169	44,856	1,429	30,468
first quartile value	14.62	22.05	35.32	11.15
third quartile value	22.38	37.15	41.39	20.13
min quartile value	3.06	6.47	26.22	2.18
max quartile value	34.01	55.00	48.28	33.57

LFA = Lava-flow aquifer
TCU = Tuff confining unit
VTA = Vitric-tuff aquifer
WTA = Welded-tuff aquifer

D.1.4.2 Estimates of HSU Matrix Porosity Based on Lithology

Although the density log data analysis provides estimates of matrix porosity (Table D-4), only 23 of the HSUs present in the PM-OV HFM model are directly represented in the analysis. All of the HSUs present in the model require estimates of porosity. One approach to use values derived from the analysis of density logs is to estimate HSU matrix porosities using weighted averages of the matrix porosities of the lithologies that make up the HSUs. As shown in Table D-1, this approach yields values of estimated average matrix porosity for 40 of the HSUs in the model. The discussion that

follows describes how the average porosities of the lithologies that make up the HSUs were used to calculate estimates of average matrix porosities.

The project Stratigraphy-Lithology database (SLd) contains the stratigraphy for the wells at the NNSS and vicinity in terms of HSUs and the lithologies that compose them. The SLd was queried for all wells in the PM-OV HFM area (Navarro, 2020) and sorted by HSU and lithologies. This query resulted in a list of HSUs found in the PM CAU transport model. For each HSU, the lithologies that are included in it are given in terms of length (m).

In the PM-OV HFM area, there is a record of HSU stratigraphy found in the PM CAU transport model for a total length of 175,656 m. Of this length, 162,146 m (92 percent) is defined by lithologies for which the density log analysis provides estimates of matrix porosity. When broken down by specific HSUs, the majority (58 percent) are fully defined by lithologies with estimates of matrix porosity. Only one of the HSUs is entirely made up of lithologies for which an estimate of matrix porosity is not available. This is the LCCU. An additional three—the AA, BWWTA, and YVCM—are less than 80 percent defined by lithologies for which an estimate of matrix porosity from the density log analysis is available.

Tables D-6 and D-7 show the breakdown of the HSUs present in the PM-OV HFM area by lithology. The HSUs are listed in the leftmost column with the lithologies that compose them shown along the top. Table D-6 shows the HSUs and lithologies for which there are no estimates of matrix porosity derived from the analysis of density logs (Navarro, 2019). Table D-7 shows the HSUs and lithologies for which there are such estimates of matrix porosity. Referring to either table, there is an entry in the table for each HSU and lithology. Referring to the BA HSU in Table D-7, there is an entry of 409.92 m for the FB lithology. In addition, in the fourth column from the right side of the table, there is an entry of 3,136.28 m in the "Total Both With and Without Lithology Porosity (m)" column. The 3,136.28 m value represents the total combined length of the BA HSU found in all the borings in the PM area. The 409.92 m value shows that of the total combined length of 3,136.28 m of BA, 409.92 m consists of the FB lithology. Both tables show the total length of a lithology for which there is an estimate of matrix porosity and the total length of the HSU (with and without estimates of matrix porosity based on lithology). Referring to the totals shown at the lower right-hand corner of the table, 162,146 m of HSUs have estimates of matrix porosity from the density log study out of a total of 175,656 m of HSU record. The last columns in Table D-7 show the fraction of the HSU for which no

estimates of matrix porosity (based on lithology) are available in the Navarro (2019) analysis as well as the estimated average matrix porosity and associated standard deviation calculated for the HSU based on the lithologies.

Table D-6
Lithologies for Which There Are No Estimates of Matrix Porosity Derived from Density Log Data
(Page 1 of 2)

	LITHOLOGY																										
HSU	**AL**	**BD**	**BED/TS**	**BS**	**CL**	**DM**	**DWT/VT**	**IN**	**ITL**	**LB**	**MWT/VT**	**NULL**	**NWT/MWT**	**NWT/RWT**	**PCL**	**PL/FB**	**RWT**	**RWT/TSS**	**SLT**	**SLT/QTZ/SS**	**TG**	**TS**	**TS/RWT**	**TSLT/WT**	**unk**	**VL**	**WT**	**Total (m)**
AA	827.45	--	--	9.20	--	--	--	--	--	--	--	--	--	--	--	--	47.20	--	--	--	--	--	--	--	--	--	--	883.85
ATCU	--	--	--	--	--	--	--	--	--	--	--	--	--	--	--	--	--	--	--	--	--	--	--	--	--	--	--	0.00
ATWTA	--	--	--	--	--	--	13.10	--	--	--	--	--	--	--	--	--	--	--	--	--	--	--	--	--	--	--	--	13.10
BA	--	--	--	--	--	--	--	--	--	--	--	--	--	--	--	--	--	--	--	--	--	--	--	--	--	--	--	0.00
BFCU	--	--	--	--	--	--	--	--	--	--	--	--	--	--	--	--	--	--	--	--	--	--	--	--	--	--	--	0.00
BRA	--	--	--	--	--	--	--	--	187.40	--	--	--	7.60	--	--	--	--	--	--	--	--	--	--	--	--	--	39.60	234.60
BWCU	--	--	--	--	--	--	--	--	--	--	--	--	--	42.10	--	--	16.50	--	--	--	--	--	--	--	--	--	--	58.60
BWWTA	--	--	--	--	--	--	--	--	--	39.60	--	--	--	--	--	--	--	--	--	--	9.70	--	--	--	--	--	--	49.30
CFCM	--	--	--	5.20	--	--	--	--	--	--	--	--	--	--	--	--	--	--	--	--	--	--	--	--	--	--	--	5.20
CFCU	--	9.80	--	--	--	--	--	--	53.10	--	--	--	--	--	--	--	11.30	--	--	--	--	--	--	--	--	--	--	74.20
CHLFA	--	--	--	--	--	--	--	102.10	--	--	--	--	--	--	--	--	--	--	--	--	--	--	--	--	--	--	--	102.10
CHVTA	--	--	--	--	--	--	--	--	--	--	--	--	--	--	--	--	--	--	--	--	--	--	--	--	--	--	--	0.00
CHZCM	--	--	--	--	--	--	--	45.70	--	--	--	--	--	--	--	125.80	26.80	--	--	--	--	--	--	--	--	--	--	198.30
CPA	--	--	--	--	--	--	--	--	--	--	--	--	--	--	--	--	--	--	--	--	--	--	--	--	--	--	--	0.00
DVA	--	--	--	--	--	--	--	--	--	--	--	--	--	--	--	--	--	--	--	--	--	--	--	--	--	--	--	0.00
FCCM	--	--	16.80	--	--	--	--	--	--	--	--	--	--	7.30	--	--	112.70	--	--	--	--	--	--	--	--	--	--	136.80
FCCU	--	--	--	--	--	--	--	--	--	--	--	--	--	--	--	--	--	--	--	--	--	--	--	--	--	--	--	0.00
FCLLFA	--	--	--	--	--	--	--	--	--	--	--	--	--	--	--	--	--	--	--	--	--	--	--	--	--	--	--	0.00
FCLMLFA	--	--	--	75.60	--	--	--	--	--	--	--	--	--	--	--	--	--	--	--	--	--	--	--	--	--	--	--	75.60
FCULFA	--	--	--	--	--	--	--	--	--	--	--	--	--	--	--	--	--	--	--	--	--	--	--	--	18.30	16.80	--	35.10
FCUMLFA	--	--	--	100.90	--	--	--	--	--	--	--	--	--	--	--	--	--	--	--	--	--	--	--	--	--	--	--	100.90
FCWTA	--	--	--	--	--	--	--	--	--	--	--	--	--	--	--	--	18.30	8.20	--	--	--	--	--	15.50	--	--	--	42.00
IA	--	--	--	--	--	--	--	--	--	--	--	--	--	--	--	--	--	--	--	--	--	--	--	--	--	--	--	0.00
KA	--	--	--	--	--	--	--	--	1.90	--	--	--	--	--	--	--	--	--	--	--	--	--	--	--	--	--	--	1.90
LCA3	--	--	--	--	--	144.79	--	--	--	--	--	--	--	--	--	--	--	--	--	--	--	--	--	--	--	--	--	144.79
LCCU	--	--	--	--	--	--	--	--	--	--	--	--	--	--	--	--	--	--	--	70.40	--	--	--	--	--	--	--	223.46
LPCU	--	--	--	--	--	--	--	--	--	--	--	--	--	--	--	--	--	--	--	--	--	--	--	--	--	--	--	0.00
MPCU	--	--	--	--	--	--	--	--	--	--	--	--	--	--	--	--	--	--	--	--	--	--	--	--	--	--	--	0.00
PBPCU	--	--	--	--	--	--	--	--	--	--	--	--	--	--	--	--	--	--	--	--	--	--	--	--	--	--	--	0.00
PBRCM	--	--	--	--	--	--	--	156.10	--	--	--	--	--	--	9.40	--	--	--	--	--	--	--	--	--	--	--	--	165.50
PCM	--	--	--	--	--	--	--	--	--	--	--	--	--	--	--	--	--	--	--	--	--	--	--	--	--	--	--	0.00
PLFA	--	--	--	--	--	--	--	--	--	--	--	--	--	--		--	--	--	--	--	--	--	--	--	--	--	--	0.00
PVTA	--	--	--	--	--	--	--	--	--	--	--	--	--	--	--	--	--	--	--	--	--	--	--	--	--	--	--	0.00
RMWTA	--	--	--	--	--	--	--	--	--	--	--	--	--	--	--	--	--	--	--	--	--	--	--	--	--	--	--	0.00
SPA	--	--	--	--	--	--	--	--	--	--	--	--	--	--	--	--	--	--	--	--	--	--	--	--	--	--	--	0.00
TCA	--	--	--	--	--	--	--	--	--	--	--	--	--	--	--	--	--	--	--	--	--	--	--	--	--	--	414.10	414.10
TCVA	--	--	--	6.69	6.70	--	17.68	--	287.07	--	--	--	--	--	--	--	76.50	--	--	--	--	--	--	--	3.00	--	1,291.80	1,689.44
THCM	--	--	--	--	--	--	--	--	--	--	31.09	--	--	--	--	--	13.68	--	--	--	--	--	--	--	--	--	--	44.77

Table D-6
Lithologies for Which There Are No Estimates of Matrix Porosity Derived from Density Log Data
(Page 2 of 2)

	LITHOLOGY																										
HSU	**AL**	**BD**	**BED/TS**	**BS**	**CL**	**DM**	**DWT/VT**	**IN**	**ITL**	**LB**	**MWT/VT**	**NULL**	**NWT/MWT**	**NWT/RWT**	**PCL**	**PL/FB**	**RWT**	**RWT/TSS**	**SLT**	**SLT/QTZ/SS**	**TG**	**TS**	**TS/RWT**	**TSLT/WT**	**unk**	**VL**	**WT**	**Total (m)**
THCU	--	--	--	--	--	--	--	--	--	--	--	--	--	--	--	--	--	--	--	--	--	--	--	--	--	--	--	0.00
THLFA	--	--	--	--	--	--	--	--	--	--	--	--	--	--	--	--	--	--	--	--	--	--	--	--	--	--	--	0.00
TMLVTA	103.60	--	--	186.50	--	--	--	--	--	--	--	--	--	--	--	--	415.20	--	--	--	--	--	--	--	--	--	--	705.30
TMUWTA	--	--	--	--	--	--	21.00	--	--	--	--	--	--	--	--	--	--	--	--	--	--	--	--	--	--	--	--	21.00
TMWTA	71.60	4.20	--	--	--	--	--	--	--	--	--	--	28.96	24.69	--	--	1.90	--	--	--	--	--	--	--	--	--	7,362.90	7,494.25
TSA	--	--	--	--	--	--	--	--	--	--	--	--	--	--	--	--	--	--	--	--	--	--	--	--	--	--	--	0.00
UPCU	--	--	--	18.30	--	--	--	--	--	--	--	--	--	--	--	--	158.80	--	--	--	--	--	--	--	--	--	9.10	186.20
WWA	--	--	--	--	--	--	--	--	--	--	--	--	--	--	--	--	--	--	--	--	--	--	--	--	--	--	13.70	13.70
YMCFCM	--	--	--	--	--	--	--	--	--	--	--	--	--	--	--	--	--	--	--	--	--	--	--	--	--	--	--	0.00
YVCM	227.80	--	--	51.20	--	--	--	--	--	--	--	--	--	--	--	--	--	--	--	--	45.70	71.00	--	--	--	--	--	395.70
Grand Total	**1,230.45**	**14.00**	**16.80**	**453.59**	**6.70**	**144.79**	**51.78**	**303.90**	**529.47**	**39.60**	**31.09**	**0.00**	**36.56**	**74.09**	**9.40**	**125.80**	**898.88**	**8.20**	**153.06**	**70.40**	**9.70**	**45.70**	**71.00**	**15.50**	**21.30**	**16.80**	**9,131.20**	**13,509.75**

NOTE: Values in table represent the total length of a lithology within the combined length of all instances of an HSU in the Pahute Mesa HFM area.

-- = Lithology not found in the Pahute Mesa cores examined

Table D-7
Lithologies for Which There Are Estimates of Matrix Porosity Derived from Density Log Data
(Page 1 of 2)

	LITHOLOGY																									
HSU	**BED**	**BED/ NWT**	**BED/ RWT**	**DWT**	**FB**	**LA**	**LA/FB**	**LD**	**MWT**	**MWT/ DWT**	**NWT**	**NWT**	**NWT/ BED**	**PWT/ NWT**	**PL**	**PL/ NWT**	**PWT**	**PWT/ MWT**	**PWT/ NWT**	**TB**	**VT**	**VT/PL**	**Total with Porosity Estimate (m)**	**Total Both With and Without Lithology Porosity (m)**	**Fraction of HSU without Estimated Porosity**	**Estimate of HSU Average Porosity**	**Estimate of the Standard Deviation**
AA	48.80	--	--	--	--	--	--	--	--	--	55.40	--	--	--	--	--	--	--	--	--	--	--	104.20	988.05	0.89	29.52	--
ATCU	--	--	--	--	--	--	--	--	--	--	129.60	--	--	--	--	--	--	--	--	--	--	--	129.60	129.60	0.00	28.97	--
ATWTA	42.80	--	--	142.90	--	--	--	--	1,153.82	127.40	--	--	--	202.04	--	--	301.30	--	--	--	7.60	--	1,977.86	1,990.96	0.01	17.73	6.03
BA	--	--	--	--	409.92	2,518.56	--	--	--	--	--	--	--	--	64.91	--	--	--	--	--	142.89	--	3,136.28	3,136.28	0.00	20.43	7.73
BFCU	863.56	--	--	--	187.19	651.66	--	--	87.00	--	5,880.14	--	--	--	6.70	--	303.73	--	--	317.85	--	--	8,297.83	8,297.83	0.00	28.25	10.26
BRA	880.58	--	--	2,108.10	929.70	8,470.73	--	--	1,207.10	21.64	622.10	--	--	--	85.00	--	470.60	--	--	--	--	--	14,795.55	15,030.15	0.02	19.72	7.27
BWCU	--	--	--	--	--	--	--	--	9.70	--	70.10	--	188.40	--	--	--	--	--	--	--	--	--	268.20	326.80	0.18	28.30	11.08
BWWTA	9.20	--	--	--	--	--	--	--	--	--	30.80	--	--	--	--	--	20.10	9.20	--	--	2.40	--	71.70	121.00	0.41	27.36	--
CFCM	451.99	--	--	--	178.08	490.80	72.20	--	--	--	148.40	--	--	--	161.10	--	--	--	--	36.50	14.70	--	1,553.77	1,558.97	0.00	25.46	8.66
CFCU	1,284.89	--	--	--	27.27	345.00	--	--	--	--	1,324.20	--	96.32	--	201.60	--	--	--	--	3.00	--	--	3,282.28	3,356.48	0.02	28.42	9.59
CHLFA	765.56	--	--	--	592.96	8,552.38	--	--	--	--	--	--	--	--	68.14	--	11.90	--	--	--	131.91	--	10,122.85	10,224.95	0.01	20.84	7.43
CHVTA	1,904.18	--	--	--	478.90	542.40	--	--	--	--	3,560.18	--	--	--	840.42	--	--	--	--	--	--	--	7,326.08	7,326.08	0.00	28.23	10.06
CHZCM	6,659.22	8.53	--	--	413.95	455.19	--	--	--	--	2,619.91	--	49.38	158.50	1,384.17	--	35.30	--	--	34.80	0.74	--	11,819.69	12,017.99	0.02	29.09	9.22
CPA	--	--	--	--	18.90	163.68	--	--	--	--	--	--	--	--	--	--	--	--	--	--	70.07	--	252.65	252.65	0.00	19.92	7.31
DVA	--	--	--	--	--	--	--	--	73.50	--	177.04	--	--	--	--	--	--	61.00	--	--	--	--	311.54	311.54	0.00	26.43	9.24
FCCM	1,120.02	108.85	--	--	38.10	--	--	--	--	--	937.13	--	7.33	--	181.12	24.38	----	--	--	145.08	7.32	14.02	2,583.36	2,720.16	0.05	29.78	9.56
FCCU	462.39	--	10.06	--	--	--	--	--	0.01	--	428.23	--	105.15	--	161.32	--	33.53	--	--	--	--	--	1,200.70	1,200.70	0.00	29.31	9.91
FCLLFA	--	--	--	--	46.70	32.00	--	--	--	--	--	--	--	--	--	--	--	--	--	--	--	--	78.70	78.70	0.00	21.94	9.55
FCLMLFA	--	--	--	--	--	--	--	--	--	--	--	--	--	--	--	--	--	--	--	--	--	--	0.00	75.60	1.00	0.00	--
FCULFA	--	--	--	--	32.60	894.78	--	--	--	--	--	--	--	--	121.31	--	--	--	--	--	11.28	107.59	1,167.56	1,202.66	0.03	20.51	7.50
FCUMLFA	--	--	--	--	--	--	--	--	--	--	--	--	--	--	--	--	--	--	--	--	--	--	0.00	100.90	1.00	0.00	--
FCWTA	--	--	15.00	--	--	--	--	--	174.40	--	256.60	--	--	--	--	--	109.10	--	--	--	--	--	555.10	597.10	0.07	23.76	9.10
IA	--	--	--	--	48.60	628.27	--	--	134.20	--	--	--	--	--	--	--	--	--	--	--	--	--	811.07	811.07	0.00	19.32	7.08
KA	27.40	--	--	--	180.63	1,999.00	--	--	--	--	--	--	--	--	90.70	--	--	--	--	--	--	--	2,297.73	2,299.63	0.00	20.56	7.60
LCA3	--	--	--	--	--	--	--	--	--	--	--	--	--	--	--	--	--	--	--	--	--	--	0.00	144.79	1.00	0.00	--
LCCU	--	--	--	--	--	--	--	--	--	--	--	--	--	--	--	--	--	--	--	--	--	--	0.00	223.46	1.00	0.00	--
LPCU	1,447.21	--	--	--	4.50	--	--	--	--	--	509.15	--	--	--	--	--	--	--	--	4.60	--	--	1,965.47	1,965.47	0.00	29.85	8.95
MPCU	94.16	--	--	--	--	--	--	--	--	--	7.92	--	--	--	--	--	--	--	--	--	--	--	102.08	102.08	0.00	30.06	8.36
PBPCU	505.99	--	--	--	20.11	--	--	--	--	--	58.60	--	--	--	11.28	--	--	--	--	--	--	--	595.97	595.97	0.00	29.78	8.59
PBRCM	3,033.35	--	--	332.70	676.90	2,620.77	79.25		1,007.97	135.40	2,451.01	--	--	--	--	--	668.73	74.40	--	206.20	--	--	11,286.68	11,452.18	0.01	24.66	8.51
PCM	19.50	--	--	324.00	--	45.30	--	--	28.60	--	95.20	--	--	--	--	--	47.00	--	--	--	11.90	--	571.50	571.50	0.00	17.35	6.70
PLFA	64.10	--	--	245.24	454.08	5,211.49	--	--	303.30	--	259.20	--	--	--	570.36	--	138.20	--	--	--	253.86	--	7,499.84	7,499.84	0.00	20.73	7.75
PVTA	759.30	--	--	--	--	--	--	--	--	--	419.60	--	--	--	550.40	--	--	--	--	--	--	--	1,729.30	1,729.30	0.00	29.49	9.77
RMWTA	--	--	--	19.50	--	--	--	--	627.29	364.83	--	--	--	--	--	--	28.34	21.95	--	83.52	39.10		1,184.53	1,184.53	0.00	16.26	5.31
SPA	--	--	--	--	--	58.52	64.61	--	--	--	--	--	--	--	--	--	--	--	--	--	118.26	--	241.40	241.40	0.00	19.37	6.49
TCA	0.01	--	--	304.16	--	--	--	--	1,178.44	--	3.10	--	--	9.70	--	--	411.02	--	28.34	--	316.40	--	2,251.18	2,665.28	0.16	17.14	6.31
TCVA	1,876.32	22.00	--	428.10	--	709.00	10.36	--	1,469.08	--	830.19	--	15.24	225.56	--	--	2,152.76	36.31	--	61.56	--	--	7,836.48	9,525.92	0.18	23.26	8.07

Table D-7
Lithologies for Which There Are Estimates of Matrix Porosity Derived from Density Log Data
(Page 2 of 2)

	LITHOLOGY																									
HSU	**BED**	**BED/ NWT**	**BED/ RWT**	**DWT**	**FB**	**LA**	**LA/FB**	**LD**	**MWT**	**MWT/ DWT**	**NWT**	**NWT**	**NWT/ BED**	**PWT/ NWT**	**PL**	**PL/ NWT**	**PWT**	**PWT/ MWT**	**PWT/ NWT**	**TB**	**VT**	**VT/PL**	**Total with Porosity Estimate (m)**	**Total Both With and Without Lithology Porosity (m)**	**Fraction of HSU without Estimated Porosity**	**Estimate of HSU Average Porosity**	**Estimate of the Standard Deviation**
THCM	464.15	--	--	--	12.80	--	--	150.57	25.00	--	136.52	--	--	--	--	--	126.78	--	--	--	--	--	915.83	960.60	0.05	28.37	8.43
THCU	79.80	--	--	--	--	--	--	--	--	--	406.50	--	--	--	--	--	--	--	--	--	--	--	486.30	486.30	0.00	29.16	10.62
THLFA	64.02	--	--	--	122.13	1,593.32	18.29	--	--	--	--	--	--	--	129.55	--	0.01	--	--	--	178.94	--	2,106.27	2,106.27	0.00	20.83	7.59
TMLVTA	3,702.49	--	--	--	54.80	132.90	--	--	--	--	3,319.14	--	--	24.40	368.30	--	--	37.80	--	--	10.97	--	7,650.81	8,356.11	0.08	29.34	9.61
TMUWTA	3.60	--	--	--	--	3.70	--	--	209.20	--	46.70	--	--	--	--	--	16.10	--	--	--	--	--	279.30	300.30	0.07	18.49	6.95
TMWTA	2,384.24	--	--	5,228.22	177.00	498.70	--	--	18,443.80	188.97	1,202.45	14.33	--	368.10	134.90	--	5,976.39	52.10	--	--	920.60	--	35,589.79	43,084.04	0.17	18.06	6.60
TSA	0.01	--	--	205.44	--	--	--	--	910.01	--	0.01	--	--	75.62	--	--	316.07	5.20	--	--	25.60	--	1,537.96	1,537.96	0.00	17.30	6.25
UPCU	3,251.97	--	--	--	10.40	--	--	--	--	--	706.62	--	--	--	78.61	--	--	--	--	7.60	--	--	4,055.22	4,241.42	0.04	29.92	8.74
WWA	--	--	--	--	109.10	910.40	--	--	--	--	--	--	--	--	--	--	--	--	--	--	--	--	1,019.50	1,033.20	0.01	20.18	7.55
YMCFCM	85.86	--	--	--	--	356.50	--	--	70.40	--	415.34	--	--	--	--	--	123.60	--	--	--	--	--	1,051.70	1,051.70	0.00	24.29	9.08
YVCM	--	--	--	--	--	--	--	--	4.60	--	3.60	--	--	--	--	--	36.80	--	--	--	--	--	45.00	440.70	0.90	22.23	--
Grand Total	**32,356.68**	**139.38**	**25.06**	**9,338.36**	**5,225.34**	**37,885.07**	**244.72**	**150.57**	**27,117.43**	**838.25**	**27,110.67**	**14.33**	**461.82**	**1,063.91**	**5,209.90**	**24.38**	**11,327.39**	**297.96**	**28.35**	**900.71**	**2,264.53**	**121.62**	**162,146.42**	**175,656.17**			

NOTE: Values in table represent the total length of a lithology within the combined length of all instances of an HSU in the Pahute Mesa HFM area.
-- = Lithology not found in the Pahute Mesa cores examined

D.1.5 Methodology

The matrix porosities for the lithologies in Table D-3 were combined with the fractions of each HSU they represent (see Table D-7) to develop estimated average porosities for the HSUs. Table D-8 lists the lithologies for which average matrix porosities were estimated using the density log data (Navarro, 2019) as well as the porosities and associated values of standard deviation determined. Table D-8 shows that the estimated matrix porosities range from a low of 10.65 for the MWT/DWT lithology to a high of 39.21 for the BED/RWT.

Table D-8
Lithologies and Estimates of Average Matrix Porosities

Lithology	Average Estimated Matrix Porosity Based on Density Log Analysis (%)	Standard Deviation	Variance
BED	30.15	8.09	65.41
BED/NWT	28.71	11.30	127.74
BED/RWT	39.21	3.33	11.11
DWT	12.18	3.96	15.66
FB	23.41	10.95	119.94
LA	19.79	7.03	49.43
LA/FB	19.16	5.51	30.36
LD	29.90	5.58	31.17
MWT	15.62	5.33	28.43
MWT/DWT	10.65	4.18	17.50
NWT	28.97	11.05	122.17
PL	28.98	10.80	116.68
PL/NWT	21.98	5.77	33.24
PWT	22.40	9.35	87.40
PWT/MWT	32.09	6.87	47.17
PWT/NWT	28.48	5.03	25.27
TB	38.91	6.58	43.30
VT	19.27	6.70	44.83
VT/PL	16.20	5.23	27.31

To estimate an average HSU matrix porosity based on a weighted sum of the average matrix porosities of the lithologies which compose it, the following equation was used:

$$\varphi h = \Sigma\,(\varphi l1 * w1) + (\phi l2 * w2) + (\phi l3 * w3) + \cdots \qquad \textit{(D-2)}$$

where

ϕh = estimated average matrix porosity for the HSU

$\phi l1$ = estimated average matrix porosity for the first lithology

$w1$ = weight applied to the first lithology estimated average matrix porosity

The weights applied to the estimated average matrix porosities are equal to length of the lithology in question divided by the total length of the lithologies for that HSU with estimated average matrix porosities.

By way of example, Table D-7 shows there is a combined total record of the CPA HSU of 252.7 m. The CPA HSU in the PM-OV HFM area is composed of the following lithologies: 18.90 m FB, 163.68 m LA, and 70.07 m VT. The estimated matrix porosities for each of these lithologies are 23.41, 19.79, and 19.27 percent, respectively. Taking a weighted average of these porosities based on their representative lengths leads to an estimated average matrix porosity for the CPA HSU of 19.92 percent.

To arrive at an average standard deviation to associate with the estimated HSU matrix porosities, the following equation was used:

(D-3)

$$\bar{\sigma} = \left(\sqrt{\sum_{i=1}^{i=n} (var l1 \times w1) + (var l2 \times w2) + (var l3 \times w3) + \ldots} \right)$$

where

σ = standard deviation of the estimated average matrix porosity for the HSU

$var l1$ = variance for the estimated average matrix porosity for the first lithology

n = total number of lithologies making up an HSU that have average matrix porosity values estimated from the density log data analyzed (Navarro, 2019)

For some of the HSUs for which estimates of matrix porosity can be derived from the query of lithologies, greater than 20 percent of the lithologies making them up do not have estimates of matrix porosity derived from the density log analysis (Navarro, 2019). For these HSUs (i.e., AA, BWWTA, LCCU, and YVCM), the estimates of average matrix porosity are taken from the Phase I PM TDD (Shaw, 2003).

As noted earlier, some of the HSUs represented in the PM-OV Basin groundwater model were not found in the query of the SLd. These HSUs are the ATCCU, ATICU, DVCM, LCA, MGCU, PMNICU, RMICU, SCVCU, and UCCU. The estimates of average matrix porosity for these HSUs are also taken from the Phase I Pahute Mesa TDD (Shaw, 2003).

Table D-9 is a summary table showing the estimated average matrix porosities and associated standard deviations assigned to each of the HSUs in the PM CAU transport model. For those HSUs where it was not possible to derive an estimated average porosity based on the values for the lithologies that compose them, values were either from the Phase I PM TDD or based on the similarity of the HSU to another for which an estimated value was determined. The table is broken down by the source used to assign the values of matrix porosity. The first values shown are those derived using weighted averages of the matrix porosities for the lithologies of which they are composed, as described above. The next category is those values for which an average matrix porosity could not be calculated in this way. The porosity values in this group are taken from Tables 5-7 and 6-15 of the Phase I PM TDD (Shaw, 2003). The last category of matrix porosities are those for which it was not possible to derive an average value based on the lithologies and which are not listed in the Phase I PM TDD. The values here are assigned based on the similarity of the HSU in question to an HSU with an available porosity estimate based on lithologies, or are reported in Table 5-7 of the Phase I PM TDD.

Table D-9
Summary of Estimated Average Matrix Porosities
(Page 1 of 2)

HSUs in the PM-OV Basin Flow Model	Estimated Average Matrix Porosity (%)	Estimated Weighted Standard Deviation	Fraction of HSU Represented by Lithologies for Which There Are No Estimated Porosities
Porosity Estimates Based on Lithologies			
ATWTA	17.7	6.0	0.01
BA	20.4	7.7	0.00
BFCU	28.2	10.3	0.00
BRA	19.7	7.3	0.02
BWCU	28.3	11.1	0.18
CFCM	25.5	8.7	0.00
CFCU	28.4	9.6	0.02
CHLFA	20.8	7.4	0.01
CHVTA	28.2	10.1	0.00
CHZCM	29.1	9.2	0.02
CPA	19.9	7.3	0.00
DVA	26.4	9.2	0.00
FCCM	29.8	9.6	0.05
FCCU	29.3	9.9	0.00
FCLLFA	21.9	9.6	0.00
FCULFA	20.5	7.5	0.03
FCWTA	23.8	9.1	0.07
IA	19.3	7.1	0.00
KA	20.6	7.6	0.00
LPCU	29.8	9.0	0.00
MPCU	30.1	8.4	0.00
PBPCU	29.8	8.6	0.00
PBRCM	24.7	8.5	0.01
PCM	17.4	6.7	0.00
PLFA	20.7	7.7	0.00
PVTA	29.5	9.8	0.00
RMWTA	16.3	5.3	0.00
SPA	19.4	6.5	0.00
TCA	17.1	6.3	0.16
TCVA	23.3	8.1	0.18

Table D-9
Summary of Estimated Average Matrix Porosities
(Page 2 of 2)

HSUs in the PM-OV Basin Flow Model	Estimated Average Matrix Porosity (%)	Estimated Weighted Standard Deviation	Fraction of HSU Represented by Lithologies for Which There Are No Estimated Porosities
THCM	28.4	8.4	0.05
THCU	29.2	10.6	0.00
THLFA	20.8	7.6	0.00
TMLVTA	29.3	9.6	0.08
TMUWTA	18.5	6.9	0.07
TMWTA	18.1	6.6	0.17
TSA	17.3	6.2	0.00
UPCU	29.9	8.7	0.04
WWA	20.2	7.5	0.01
YMCFCM	24.3	9.1	0.00
Porosity Estimates Directly from the Pahute Mesa Phase I TDD (Table 5-7)			
HSU	**Lower Bound**	**Mean**	**Upper Bound**
AA[1]	23.8	32.0	40.2
ATICU[1]	5E-06	5E-05	9E-03
DVCM	6.0	34.1	75.0
LCA	1.0	5.0	9.7
LCA3	1.0	5.0	9.7
LCCU	0.2	3.3	10.0
MGCU	0.2	1.8	10.3
RMICU	0.2	1.8	10.3
SCVCU[1]	0.1	0.4	0.6
UCCU[1]	5E-06	3E-05	5E-04
YVCM	6.0	34.1	75.0
Porosity Estimates Taken From the Pahute Mesa Phase I TDD Based on Similarity of the HSUs[2]			
HSU	**Lower Bound**	**Mean**	**Upper Bound**
ATCCU	4.0	41.0	70.0
BWWTA	4.4	28.6	68.4
PMNICU	0.2	1.8	10.3

[1] Value for effective porosity (Shaw, 2003) (Table 6-15)
[2] Assignment based on written communication (email) from Christopher Lewis (Navarro) June 2, 2020

D.2.0 REFERENCES

Carle, S.F. 2020. *Interpretation of Mineralogical Diagenesis for Assessment of Radionuclide Transport at Pahute Mesa, Nevada National Security Site*, LLNL-TR-810225. Lawrence Livermore National Laboratory, CA.

DOE/EMNV, see U.S. Department of Energy Environmental Management Nevada Program.

Fenelon, J.M., D.S. Sweetkind, and R.J. Laczniak. 2010. *Groundwater Flow Systems at the Nevada Test Site, Nevada: A Synthesis of Potentiometric Contours, Hydrostratigraphy, and Geologic Structures,* Professional Paper 1771. Reston, VA: U.S. Geological Survey.

Navarro. 2018. Written communication. Subject: "SharePoint Geophysics Library," Las Vegas, NV. As accessed on October 1 at https://ugta.nv.doe.gov/sites/Geophysics%20Database/default.aspx and the "UGTA Field Operations Site" at https://ugta.nv.doe.gov/sites/Field%20Operations/default.aspx.

Navarro. 2019. Written communication. Subject: *Pahute Mesa Geophysical Log Data Evaluation for Matrix Porosity*, UGTA Technical Data Repository Database Identification Number UGTA-4-2037. Las Vegas, NV. As accessed on February 06, 2015.

Shaw, see Shaw Environmental, Inc.

Shaw Environmental, Inc. 2003. *Contaminant Transport Parameters for the Groundwater Flow and Contaminant Transport Model of Corrective Actions Units 101 and 102: Central and Western Pahute Mesa, Nye County, Nevada,* Rev. 0, Shaw/13052--201. Las Vegas, NV.

U.S. Department of Energy Environmental Management Nevada Program. 2020. *Pahute Mesa-Oasis Valley Hydrostratigraphic Framework Model for Corrective Action Units 101 and 102: Central and Western Pahute Mesa, Nye County, Nevada,* Rev. 0, DOE/EMNV--0014. Las Vegas, NV.

Wood, D.B. 2009. *Digitally Available Interval-Specific Rock-Sample Data Compiled from Historical Records, Nevada Test Site and Vicinity, Nye County, Nevada* (USGS-297).

Appendix E

Effective Porosity

E.1.0 EFFECTIVE POROSITY

The available literature was reviewed in an effort to collect information related to the stratigraphy, rock characteristics, and structural features associated with the different sites from which data were obtained and used to calculate/estimate fracture porosity values. This review focused on the volcanic rocks found in the PM-OV groundwater basin.

In addition, a number of data sources were reviewed to provide a range of fracture porosity to be used with the CA HGU. The following discussion treats the literature review for the volcanics first, followed by descriptions of the sources reviewed for the carbonates.

E.1.1 Literature Review Focusing on the Volcanics

The following is a brief summary of each location with a fracture porosity estimate, as discussed in Section 5.3.

E.1.1.1 C-Holes Complex

Tracer Test Interpretations (Bechtel SAIC Co., 2004)

Used fracture porosity from multiple-tracer tests

Injections into Prow Pass Tuff and lower Bullfrog Tuff

Injection into #2 and recovery in #3 for lower Bullfrog (against natural gradient)

Injection into #3 and recovery in #2 for Prow Pass (with natural gradient)

Week dipole flow field

Lower Bullfrog Tuff

- High transmissivity interval.
- Double peak response.

- Attributed to tracer migration through two flow paths.
  - Faster upper flow path – approximately 25 percent of tracer mass on this pathway.
  - Slower lower flow path – approximately 75 percent of tracer mass on this pathway.
- Response consistent with double-porosity conceptualization.

Prow Pass Tuff

- Low transmissivity interval.
- Single peak response.
- Response consistent with double-porosity conceptualization.

Interpretations

- Fracture porosity calculated using

$$\eta = \frac{Q\tau}{\pi r_L^{\,2} T} \qquad \textit{(E-1)}$$

where

η = effective flow porosity
Q = production flow rate
τ = mean residence or transport time from RELAP
r_L = distance between wells
T = formation thickness (assumed to be the interval length)

- Range in results based on mean residence time from assumed linear and radial flow
- Prow Pass – fracture porosity 0.003 to 0.006
- Lower Bullfrog – fracture porosity 0.003
- Assumptions
  - Homogeneous and isotropic medium
  - Either radial or linear flow regime
  - 2-D flow only
  - Steady-state flow

Hydrogeologic Setting

- Miocene tuffaceous rocks (Bechtel SAIC Co., 2004)
  - Consists of nonwelded to densely welded ash-flow tuff with intervals of ash-fall tuff and volcaniclastic rocks.

- Have pervasive tectonic and cooling fractures that strike predominantly north-northeast to north-northwest and dip west at angles of 50 to 87 degrees.
- Northerly and northwesterly trending high-angle faults in vicinity of complex.
- Behave as a single fissure-block aquifer.
- Flow comes primarily from discrete intervals.
- Fractures have no preferred orientation.
- Fracture density appears unrelated to the extent of welding and permeability.
- Flow is not confined to stratigraphic or lithologic boundaries.
  - Suggests fracture networks conducting flow extend beyond stratigraphic and lithologic contacts.

- Geldon et al. (2002)
  - Indicates offsetting faults at the bottom of the Bullfrog and top of the Tram at the C-Holes Complex (Tram underlies Bullfrog).
  - States that because these hydrogeologic intervals are defined by spatially related faults and fracture zones, their existence and hydraulic properties cannot be extended beyond the immediate vicinity of the C-Holes Complex.
  - Hydraulic testing indicates hydraulic connection across geologic and lithostratigraphic contacts believed to be the results of interconnected faults, fractures, and intervals with large matrix permeability.
    - Drawdown occurred in all monitored intervals and other observation wells regardless of the geologic interval being pumped.
    - The Miocene tuffaceous rocks appear to respond to pumping as a single aquifer in the YM area.
    - The designation of separate aquifers and confining units within the Miocene tuffaceous rocks may not be appropriate in the area of the C-Holes.
  - Prow Pass
    - Zones of moderately to very fractured rock separated by thin to thick unfractured or sparsely fractured intervals
    - Some large matrix permeability in unfractured or sparsely fractured intervals
    - Open parting between Prow Pass and Bullfrog
    - Very little flow
    - T = 30-60 m^2/day (T decreases as distance from faults increases) (Bechtel SAIC Co., 2004)
  - Bullfrog
    - Mostly moderately to very fractured rock
    - Thin intervals of sparsely fractured or nonfractured rock
    - Large matrix permeability in upper part

- Majority of flow
- T = 1,300-1,900 m^2/day (Bechtel SAIC Co., 2004)

Conceptual Model

- Decreasing T and fracture density as distance from faults increases.
- Rock characteristics impacted by faulting that intersects the lower Bullfrog and upper Tram at the C-Holes Complex.
- Discrete flow zones.
- Hydraulic connection between discrete flow zones, likely due to faulting and fracturing.

References

Bechtel SAIC Co., LLC. 2004. *Saturated Zone In-Situ Testing*, ANL-NBS-HS-000039 REV 01.

Geldon, A.L., A.M.A. Umari, M.F. Fahy, J.D. Earle, J.M, Gemmell, and J. Darnell. 2002. *Results of Hydraulic Test in Miocene Tuffaceous Rocks at the C-Hole Complex, 1995 to 1997, Yucca Mountain, Nye County, Nevada*, USGS, Water-Resources Investigations Report 02-4141.

E.1.1.2 Gas Tracer Testing (Freifeld, 2001)

- Testing conducted in Topopah Spring tuff at Yucca Mountain.
  - Tested unsaturated portion of tuff.
  - Tested the middle nonlithophysal zone.
    - Densely fractured
    - Few lithophysal inclusions
    - Includes numerous areas containing small brecciated zones
- Used two methods to estimate fracture porosity
  - Constant mass flux air-injection test transient analysis
    - Results show large uncertainties in fracture porosity.
  - Gas tracer transport tests
    - Results reveal high confidence in parameter estimates.
- Testing conducted at the Exploratory Studies Facility.
- Data interpreted using a random-walk particle method incorporating Fickian transport.
- Transport distance about 8 to 9 m.

References

Freifeld, B.M. 2001. *Estimation of Fracture Porosity in an Unsaturated Fractured Welded Tuff Using Gas Tracer Testing*, Ph.D. Thesis, Department of Civil and Environmental Engineering and Earth Sciences Division, Ernest Orlando Lawrence Berkeley National Laboratory, University of California, Berkeley.

E.1.1.3 USW H-4 (Erickson and Waddell, 1985)

- Borehole is on western boundary of NNSS Area 25.
- Penetrates volcanic tuffs.
  - Units investigated are as follows:
    - Prow Pass, Bullfrog, and Tram members of Crater Flat Tuff Formation.
- Many faults in the vicinity of the borehole.
- Located near the C-Holes Complex.
- 33 flow zones identified with temperature survey.
  - Flow zones generally in
    - Lower Prow Pass and upper Bullfrog
    - Lower Bullfrog and upper Tram
  - Large area of upper Prow Pass and lower Tram with no flow based on temperature log
- 10 flow zones indicated by in-borehole tracer data.
  - Flow zones generally in
    - Middle and lower Prow Pass
    - Upper and lower Bullfrog
    - Upper Tram
- Large interval (700 ft with no flow to very little flow).
- Look at report with detailed lithology (Whitfield et al., 1984).
  - Don’t see anything drastically different between zones with and without flow.
  - Prow Pass interval
    - 495.9 to 689.8 m (193.9-m thick)
    - Enlarged borehole assumed to be associated with fractures over 103 m of Prow Pass (53 percent).
  - Bullfrog interval
    - 693.4 to 805.9 m (112.5-m thick)
    - Enlarged borehole assumed to be associated with fractures over 55 m of Bullfrog (49 percent).
  - Tram interval
    - 812.0 to 1154.6 m (342.6-m thick)
    - No areas of enlarged borehole in the Tram.
- With exception of zone in middle Prow Pass, the temperature log and in-borehole tracer data give consistent results.
- Fracture porosity

- Estimated using fracture orientation and fracture frequency from television and acoustic-televiewer surveys.
- Number of producing zones based on temperature log (33 flow zones).
- Calculated fracture aperture assuming the following:
  - Each point of production was due to a single fracture (i.e., 33 flowing intervals so assumed 33 fractures).
  - All fractures had the same aperture.
  - All fractures have equal permeability.
- Calculated fracture frequency error cause by high-dip angle fractures relative to the borehole.
- Calculated as
  - Fracture apertures times corrected number of fractures divided by the length of the borehole along which production was determined.
- Assumed transmissivities of 2,152 and 8,500 ft^2/d
- Assumed roughness coefficients of 1.0, 0.1, and 0.01

References

Erickson, J.R., and R.K. Waddell. 1985. *Identification and Characterization of Hydrologic Properties of Fractured Tuff Using Hydraulic and tracer Tests – Test Well USW H-4, Yucca Mountain, Nye County, Nevada*, USGS Water-Resources Investigations Report 85-4066.

Whitfield, M.S., Jr., W. Thordarson, and E.P. Eshom. 1984. *Geohydrologic and Drill-Hole Data for Test Well USW H-4, Yucca Mountain, Nye County, Nevada*, USGS, Open-File Report 84-449.

E.1.1.4 ER-EC-5

Completion Report (NNSA/NSO, 2004)

- Location
  - Within Nellis Air Force Range complex.
  - Approximately 6.5 miles west of the NNSS.
  - In the Timber Mountain caldera complex.
    - In the moat of the Timber Mountain caldera complex.
  - Stratigraphic information strongly suggests located within the Ammonia Tanks caldera.
  - Near the western structural margin of the Ammonia Tanks caldera.
- Total depth = 2,500 ft
- Water production
  - First noted at depth about 1,007 ft.

  - Reached maximum near bottom of hole.
- Collected composite drill cuttings every 100 ft from 70 ft to total depth (TD).
- Collected 18 sidewall core samples at various depths below 1,147 ft.
- Geophysical logs run
- Main water-producing unit
  - Welded ash-flow tuff of the Ammonia Tanks Tuff
- Three completion intervals (all three alternating slotted and blank casing).
  - 1,196.6 to 1,398.5 ft
    - Total of 4 slotted sections
  - 1,892.4 to 2,094.0 ft
    - Total of 4 slotted sections
  - 2,245.7 to 2,417.2 ft
    - Total of 3 slotted sections
- Three gravel packed intervals
  - 1,187 to 1,444 ft
  - 1,855 to 2,146 ft
  - 2,223 to 2,480 ft
- Geology and hydrogeology
  - Thirsty Canyon Group (213 ft thick)
    - Pahute Mesa Tuff (123 ft thick)
    - Rocket Wash Tuff (90 ft thick)
  - Caldera moat-filling sedimentary deposits (185 ft thick)
  - Rhyolite of Beatty Wash (412 ft thick)
  - Timber Mountain landslide breccia (246 ft thick)
  - Mafic-rich Ammonia Tanks Tuff (1,169 ft thick)
    - MW to vitrophyric, mafic-rich ash-flow tuff
    - Abundant felsic phenocrysts, clinophyroxene present
    - Increase in biotite relative to Beatty Wash
    - Interval of vitrophyric ash-flow near top (1,056 to 1,099 ft)
      - Devitrified
    - Quartzofeldspathic
  - Mafic-poor Ammonia Tanks Tuff (penetrated 275 ft)
    - Densely welded (DW) at base of hole
    - Abundant felsic phenocrysts, clinophyroxene present

- Less biotite than mafic-rich Ammonia Tanks Tuff
- Interval of vitrophyric ash-flow near top (2,233 to 2,240 ft)
  - Vitric
- Quartzofeldspathic

Analysis of Testing Report (IT, 2002)

- Calculated K for
  - Screen 1 (1,196.60-1,257.60 ft)
  - Screen 2 (1,297-97-1,328.10 ft)
  - Screen 4 (1,892.41-1,952.71 ft)
  - Screen 5 (1,993.26-2,023.42 ft)
  - Screen 6 (2,063.84-2,093.99 ft)
  - Screen 7 (2,245.74-2,275.89 ft)
  - Screen 8 (2,316.40-2,346.55 ft)
  - Screen 9 (2,387.06-2,417.21 ft)
- Screens 1, 2, 4, 5, 6,
  - In mafic-rich Ammonia Tanks Tuff
    - Moderately welded (MW)
- Screens 7, 8, 9
  - In mafic-poor Ammonia Tanks Tuff
    - MW-DW

Fracture Data (IT, 2001)

- Located
  - West of Timber Mountain and northeast of Oasis Valley
  - Inside and near the western margin of the Timber Mountain caldera complex
  - Within the structural moat margin of both the Timber Mountain and Ammonia Tanks calderas (within the Timber Mountain moat)
- Borehole image logs used to identify fractures.
- Fracture density
  - No fractures identified in the upper completion interval (top 4 screens) due to poor image log.
  - 3 to 11 fractures/100 ft in middle completion interval (middle 4 screens).
  - 8 fractures/100 ft in upper portion of the gravel pack in the lower completion interval (bottom 3 screens) (fractures located above the uppermost screen in this interval).

  - 7 fractures/100 ft in lower portion of the gravel pack in the lower completion interval (bottom 3 screens) (fractures located below the lowermost screen in this interval).
- A good correlation between fractures and increases in water production is apparent at about 1,980 ft (no screen at this location).
- Most fractures are concentrated in comparatively high-density fracture zones.
- Difficult to determine the effect of fractures during well development and hydraulic testing due to limited stress on the aquifers.
- Comparison of mean fracture orientation with local structural geology suggests that structure at depth is more similar to the Timber Mountain Dome structural block to the east than expected for a well in the Timber Mountain Moat structural block.
- Structure in upper portion of well is unknown due to poor or missing image log.

Calculation of Fracture Porosity (YF TDD)

- Since no fracture data for screens 1, 2, and 4 in the upper completion interval, did not calculate fracture porosity for these there screened intervals.
- Used an average spacing for calculating fracture porosity for screens in the middle and lower completion intervals.
- Calculated range of fracture porosity 1.3E-4 to 3.7E-4.

References

IT Corporation. 2001. *Underground Test Area Fracture Analysis Report: Analysis of Fractures in Volcanic Rocks of Western Pahute Mesa – Oasis Valley*, ITLV/13052-150.

IT Corporation. 2002. *Analysis of Well ER-EC-5 Testing, Western Pahute Mesa-Oasis Valley FY 2000 Testing Program*, DOE/NV/13052--848, ITLV/13052--176.

U.S. Department of Energy, National Nuclear Security Administration Nevada Site Office. 2004. *Completion Report for Well ER-EC-5*, DOE/NV/11718--424.

E.1.1.5 BULLION FGE

Well Information (Prothro et al., 1997)

- Wells located 544 to 971 feet from BULLION nuclear test.
- Wells located in the Silent Canyon caldera complex.
- Only ER-20-6#1 core discussed.
  - Total of 129.5 ft of core recovered (out of 3,200-ft-deep drill hole).
  - 6 core segments were recovered.
- Cores examined megascopically.
- Binocular microscope used for more detailed examination.
- Fracture analysis performed on core samples.

- Only described natural fractures.
- No test-induced fractures definitively identified, but there were some indications that nuclear testing may have resulted in fractures.

- ER-20-6#1
  - Completed into LFA believed to communicate with the BULLION cavity.
    - Target aquifer was the rhyolite lava flow within the Calico Hills Formation.
    - Two completion zones.
      - Predominantly in the mafic-poor, rhyolite lava flow Calico Hills Formation (WTA and LFA).
      - Top of uppermost completion interval and bottom of lowermost completion interval in the bedded tuff, zeolitized zones of the mafic-poor Calico Hills Formation (TCU).
  - At closest, it is estimated to be 1.5 R_c from the edge of the BULLION collapse chimney (based on the maximum announced yield [NNSA/NFO, 2015] and the equation in Pawloski [1999]).
  - Fractures
    - Most fractures were observed within the denser and more brittle rhyolite lava and flow breccia.
    - Very little aperture observed for fractures in the bedded and nonwelded tuffs.
      - Most completely closed or healed by zeolitic material.
    - In lava and flow breccia
      - Average 2.6 fractures per vertical foot.
      - Fracture apertures generally less than 0.5 millimeters (mm) in width.
      - Wide range of apertures observed including up to 2 centimeters (cm).
      - Many fractures observed are irregular and discontinuous with little aperture and openness.
      - Rocks contain vesicles and appear to have some interstitial porosity and permeability.

Report and Analysis of BULLION FGE (IT, 1998)

- ER-20-6 wells located in an area with lots of fault traces at surface (Fig 1-2).
- Calculated effective (fracture) porosities using tracer peak arrival times assuming plug flow.
  - Used only data for tracers recovered in the pumping well.
  - NOTE: Injection wells were pumped at low rate 3 days after tracer injection.
  - Estimated fracture porosity: 4.9E-3 to 6.8E-3.
- Also estimated fracture porosity from double-porosity numerical analysis using fracture porosity as one of the fitting parameters.
  - In additional to fracture porosity, other calibration parameters were matrix porosity, longitudinal dispersivity, effective matrix diffusion and, if needed, also adjusted fracture spacing, hydraulic anisotropy rations, and volume of injected and withdrawn water.

- Sensitivity analysis indicated calibration was non-unique.
- Factor of two was estimated for the uncertainty in fracture porosity because any change greater than that made calibration to the observed data extremely difficult.
- Estimated fracture porosity: 1.8E-2 to 2.3E-2.

Analysis by Reimus and Haga (1999)

- Wells completed over approximately a 120-m interval of mostly devitrified lava within the Calico Hills Formation.
- Tracer data analyzed using RELAP.
- Estimated fracture porosity using the mean residence time obtained from RELAP and the plug flow equation

$$\varphi_f = \frac{Q_\tau}{\pi\left(R_o^2 - R_i^2 \right) b} \qquad \text{(E-2)}$$

where

Q = production rate

τ = mean residence time from RELAP

R_o = distance from injection well to production well

R_i = distance from measurement well to production well (= 0 if measurement well is production well)

- Estimated mean residence time assuming both radian and linear flow.
- Their range in fracture porosity: 3.6E-4 to 2.1E-2.

References

IT Corporation. 1998. R*eport and Analysis of the BULLION Forced-Gradient Experiment*, DOE/NV/13052-042, ITLV/13052-042, UC-700.

Prothro, L.B., M.J. Townsend, S.L. Drellack, Jr., and J.L. Gonzales. 1997. *Processing and Geologic Analysis of Conventional Cores from Well ER-2-6#1, Nevada Test Site*, DOE/NV/11718-162, UC-703, Bechtel Nevada.

Reimus, P.W., and M.J. Haga. 1999. *Analysis of Tracer Responses in the BULLION Forced-Gradient Experiment at Pahute Mesa, Nevada*, LA-13615-MS.

E.1.1.6 ER-EC-1

Completion Report (DOE/NV, 2000)

- Located on the southern edge of PM.
- Water production during drilling.

- First noted at 2,003 ft.
- Significant production began at 2,270 ft.
- Reached maximum at depths below 4,710 ft.

- Three completion intervals (all three alternating slotted and blank casing).
  - 2,297.9 to 2,821.4 ft
    - Total of 8 slotted sections
  - 3,347.6 to 3,760.4 ft
    - Total of 6 slotted sections
  - 4,448.5 to 4,749.5 ft
    - Total of 4 slotted sections
- Three gravel-packed intervals
  - 2,284 to 2,863 ft
    - LFA
      - Rhyolite of Benham in Paintbrush Group
      - Rhyolitic lava, devitrified and silicic
    - TCU
      - Rhyolite of Benham in Paintbrush Group
      - Bedded tuff, zeolitic
    - WTA
      - PM lobe of Tiva Canton Tuff in Paintbrush Group
      - PW to MW ash-flow tuff, devitrified
  - 3,318 to 3,776 ft
    - TCU
      - Mafic-rich Calico Hills Formation
      - Thin zone at top, bedded and NW tuff, zeolitic
    - Predominantly WTA
      - Prow Pass Tuff of Crater Flat Group
      - NW to vitrophyric ash-flow tuff, devitrified, lesser vitric
    - TCU
      - Stockade Wash lobe of Bullfrog Tuff of Crater Flat Group
      - Thin zone at base, bedded tuff, quartzofeldspathic
  - 4,433 to 4,895 ft
    - LFA
      - Tuff of Schooner in Volcanics of Quartz Mountain
      - Rhyolitic lava and flow breccia, minor bedded tuff, quartzofeldspathic

    - TCU
        - Tuff of Schooner in Volcanics of Quartz Mountain
        - Rhyolitic lava and flow breccia, minor bedded tuff, quartzofeldspathic
    - LFA
        - Lower biotite-bearing rhyolite of Quartz Mountain
        - Thin zone at base, rhyolitic lava and flow breccia, minor bedded tuff, quartzofeldspathic
- Gravel packed across slotted intervals.
- Composite drill cuttings collected continuously at 10-ft intervals from 70 ft to TD (5,000 ft).
- Collected 31 sidewall core samples.
- Geophysical logs run.
- Geology and hydrogeology.
    - Thirsty Canyon Group, undivided
    - Timber Mountain Group
        - Mafic-poor Ammonia Tanks Tuff
        - Rhyolite of Tannenbaum Hill
        - Mafic-rich Rainier Mesa Tuff
        - Rhyolite of Fluorspar Canyon
    - Paintbrush Group
        - Rhyolite of Benham
        - PM lobe of Tiva Canyon Tuff
    - Mafic-rich Calico Hills Formation
    - Crater Flat Group
        - Prow Pass Tuff
        - Stockade Wash lobe of Bullfrog Tuff
    - Volcanics of Quartz Mountain
        - Tuff of Schooner
        - Lower biotite-bearing rhyolite of Quartz Mountain
- Report does not give depth intervals for HGUs.

Analysis of Testing Report (IT, 2002)

- Flow logging indicated flow in the upper 4 slotted sections in the upper completion interval and no flow in the remaining slotted sections in the upper completion interval and all slotted sections in the middle and lower completion intervals.
- K was calculated for the upper four screens in upper completion interval (only ones with observed flow.
- Lithology of upper 4 slotted sections.

- Screen 1 – lava rhyolite
- Screen 2 – lava rhyolite
- Screen 3 – lava rhyolite
- Screen 4 – mostly lava vitric

- Authors indicate that lack of flow in all screens but the top 4 may be somewhat the result of the multiple-completion well design extending over great vertical depth.

Fracture Data (IT, 2001)

- Located on south edge of PM and north-northwest of Timber Mountain.
- Located within Timber Mountain caldera complex.
- Well considered to be within the Silent Canyon caldera complex.
- Borehole image logs used to identify fractures.
- Fracture density.
  - Lots of fractures in upper completion interval (where the flow logging indicated flow).
    - Density varies from 1 to 19 fractures/100 ft.
    - Density highest in the TCU (~11-15 fractures/100 ft).
    - Density intermediate in the LFA(~4-8 fractures/100 ft).
    - Density lowest in the WTA(~1-15 fractures/100 ft).
  - Just a few fractures in the middle completion interval.
  - Just a few fractures in the lower completion interval.
- Fracture apertures were not determined.
- One fault was identified. Fault was located between middle and lower completion intervals.
- Good correlation with fractures and increased drilling water production, but difficult to determine the effect of fractures during well development and testing due to limited stress on the aquifer.
- Comparison of mean fracture orientation with local structural geology suggests that structures within the well are similar to the nearby Boxcar and Purse faults.

Calculation of Fracture Porosity (YF TDD)

- Used K data from top 4 screened intervals.
- Used fracture spacing associated with the location of the top 4 screened intervals.
- Calculated range of fracture porosity 1E-4 to 3.7E-4.

References

IT Corporation. 2001. *Underground Test Area Fracture analysis Report: Analysis of Fractures in Volcanic Rocks of Western Pahute Mesa – Oasis Valley*, ITLV/13052-150.

IT Corporation. 2002. *Analysis of Well ER-EC-1 Testing, Western Pahute Mesa-Oasis Valley FY2000 Testing Program*, DOE/NV/13052--846, ITLV/13052--173.

U.S. Department of Energy, Nevada Operations Office. 2000. *Completion Report for Well ER-EC-1*, DOE/NV/11718--381.

E.1.1.7 ER-EC-4

Completion Report (DOE/NV, 2000)

- Located
  - 9 miles southwest of Area 20.
  - On east flank of Thirsty Mountain.
    - Thirsty Mountain is a shield volcano.
  - Just west of geophysically inferred north-northeast-striking structure (Thirsty Canyon Lineament).
  - Outside of the Rainier Mesa caldera (caldera boundary must be to east of the well).
- TD = 3,487 ft
- Water production
  - First noted at about 700 ft.
  - Maximum production at 3,400 ft.
  - Welded and vitrophyric ash-flow tuffs of Ammonia Tanks Tuff and Rainier Mesa Tuff were primary water-producing units.
- Composite drill cuttings collected every 10 ft from 30 ft to TD.
- Collected 35 sidewall core samples at various depths below 940 ft.
- Geophysical logs run.
- Three completion intervals (all three alternating slotted and blank casing).
  - 989.1 to 1,220.9 ft
    - Total of 5 slotted sections
  - 1,910.0 to 2,253.0 ft
    - Total of 6 slotted sections
  - 3,103.3 to 3,404.8 ft
    - Total of 6 slotted sections
- Three gravel-packed intervals
  - 965 to 1,240 ft
    - LFA
      - Trachyte of Ribbon Cliff in Thirsty Canyon Group

- Lava, devitrified, minor vitric, zeolitic, quartzofeldspathic

- 1,874 to 2,296 ft
  - TCU
    - Rhyolite of Beatty Wash in Beatty Wash Formation and trachyte of East Cat Canyon in Timber Mountain Group
    - Bedded and reworked tuff, very thin upper part zeolitic, rest quartzofeldspathic
  - WTA
    - Mafic-poor Ammonia Tanks Tuff of Timber Mountain Group
    - PW to vitrophyric ash-flow tuff, quartzofeldspathic
- 3,074 to 3,468 ft
  - TCU
    - Mafic-poor Rainier Mesa Tuff of Timber Mountain Group
    - Thin zone at top, bedded and NW tuff, quartzofeldspathic
  - WTA
    - Mafic-poor Ammonia Tanks Tuff of Timber Mountain Group
    - PW to vitrophyric ash-flow tuff, quartzofeldspathic
  - TCU
    - Pre-Rainier Mesa Tuff
    - Thin zone at base, of bedded tuff at its base, quartzofeldspathic

- Geology and hydrogeology
  - Pliocene basalts (~50-ft thick)
  - Thirsty Canton Group (~895-ft thick)
    - Gold Flat Tuff
    - Trail Ridge Tuff
    - Pahute Mesa Tuff
    - Rocket Was Tuff
    - Trachyte of Ribbon Cliff
  - Beatty Wash Formation (~282-ft thick)
    - Rhyolite of Chukar Canyon
    - Rhyolite of Beatty Wash
  - Timber Mountain Group
    - Trachyte of East Cat Canyon (~24 ft thick)
    - Mafic-poor Ammonia Tanks Tuff (~961 ft thick)
    - Bedded Ammonia Tanks Tuff (~84 ft thick)
    - Bedded Rainier Mesa Tuff (~67 ft thick)
    - Mafic-poor Rainer Mesa Tuff (~362 ft thick)

  - Pre-Rainier Mesa Tuff
- Report does not give depth intervals for HGUs.

Analysis of Testing Report (IT, 2004)

- Flow logging indicated flow in the upper 4 slotted sections in the upper completion interval and no flow in the remaining slotted sections in the upper completion interval and all slotted sections in the middle and lower completion intervals.
- K was calculated for the upper 3 screens in upper completion interval (only ones with observed flow).
- Lithology of upper 3 slotted sections.
  - Screen 1 – Lava flow, trachyte of Ribbon Cliff of Thirsty Canyon Group
  - Screen 2 – Lava flow, trachyte of Ribbon Cliff of Thirsty Canyon Group
  - Screen 3 – Lava flow, trachyte of Ribbon Cliff of Thirsty Canyon Group
- Authors indicate that lack of flow in all screens but the top 4 may be somewhat the result of the multiple-completion well design extending over great vertical depth.
- Authors also indicate lots of noise in the drawdown data and the low drawdown resulted in difficulty observing the response above the noise level.

Fracture Data (IT, 2001)

- Located on southwest edge of PM and north-northwest of Timber Mountain.
- Located along the linear, geophysically inferred, north-northeast-striking feature informally referred to as the Thirsty Canyon Lineament.
- Geophysical surveys indicate that a buried north-northeast-striking structure occurs about 3,500 ft east of the well.
  - The nature of the structure is unknown.
  - Some interpretations suggest that structure includes major faults and that the faults could define the western boundary of the Timber Mountain caldera complex.
- Borehole image logs used to identify fractures.
- Fractures
  - Distributed throughout the logged interval (which spans the three completion intervals).
  - Fracture density
    - Max is 9 fractures/100 ft (found in the middle completion interval).
    - No fractures in approximately the upper third of upper completion interval.
    - Density is 2 fractures/100 ft in approximately the middle third of upper completion interval.
    - Density is 6 fractures/100 ft in approximately the lower third of upper completion interval.

  - Fracture density in middle and lower completion intervals is similar to that in the upper completion interval.
- Fracture apertures were not determined.
- Comparison of mean fracture orientation with local structural geology suggests that structures within the well are controlled by similar stresses to those that generated faults within the surrounding northern Thirsty Canyon structural block.
- Fair correlation between the fractures and highly variable water production during drilling is inconclusive, but difficult to determine the effect of fractures during well development and hydraulic testing due to limited stress on the aquifers.

Calculation of Fracture Porosity (YF TDD)

- Used K data from top 3 screened intervals.
- Used fracture spacing associated with the location of the top 3 screened intervals.
- Calculated range of fracture porosity 1.8E-4 to 4.8E-4.

References

IT Corporation. 2001. *Underground Test Area Fracture analysis Report: Analysis of Fractures in Volcanic Rocks of Western Pahute Mesa – Oasis Valley,* ITLV/13052-150.

IT Corporation. 2002. *Analysis of Well ER-EC-4 Testing, Western Pahute Mesa-Oasis Valley FY2000 Testing Program*, DOE/NV/13052--850, ITLV/13052--175.

U.S. Department of Energy, Nevada Operations Office. 2000. *Completion Report for Well ER-EC-4*, DOE/NV/11718--397.

E.1.1.8 Fracture Porosities from TYBO/BENHAM

Wolfsberg et al., 2002 (Numerical Model)

- Plutonium from BENHAM was found in ER-20-5 observation wells sampling the TSA (WTA HGU) and a lava formation (LFA HGU) embedded with the CHZCM (predominantly TCU HGU with embedded LFA HGU).
- TSA (Ammonia Tanks Tuff) characteristics
  - Shows a typical ash-flow tuff welding profile; NW to PW top and base with MW to DW interior; partially opened fracture observed in MW PW portion; mineral coating and partial filling of fractures with quartz, smectite, feldspar, and mica, extensive fracturing.
- CHZCM characteristics
  - Zeolitized composite unit with an embedded lava flow.
- Used fracture spacing and fracture aperture data from Drellack et al., 1997.
- Calculated fracture porosity from Drellack spacing and aperture data assuming the following:
  - 1 set of parallel fractures to obtain low-porosity estimate.

  - 3 orthogonal sets of fractures to obtain high-porosity estimate.
- Calculated base case porosity as log mean of low- and high-porosity estimates.
- Made correction in fracture spacing based on groupings of fracture spacing (high-, medium-, low-angle fractures).
- Used data from Drellack et al., 1997 for WTA and LFA to estimate fracture porosities for WTA and LFA, respectively.

Drellack et al., 1997

- Obtained fracture data from
  - Cores collected at 8 drill holes in the Pahute Mesa/Timber Mountain area.
    - Continuous core from UE-18t and UE-19x.
    - Core segments from UE-18r, U-20c,UE-20c, UE-20e#1, UE-20f, and UE-20bh#1.
  - Borehole televiewer data and Formation MicroScanner data.
    - UE-18r, UE-20bh#1, ER-20-2#1, ER-20-5#1
- Characteristics determined from core
  - Surface texture
  - Type of secondary mineral coating(s) present
  - Estimate of percent of fracture surfaces coated with secondary minerals
  - Measured dip of the fracture
  - Estimate of the representative aperture
  - Estimate of the percent of the fracture open
  - Any additional information such as shape
- Characteristics determined from televiewer and MicroScanner data
  - In situ orientation
- HSUs with fracture data from cores
  - Timber Mountain Aquifer (TMA)
  - Tuff Cone (TC)
  - Bullfrog Confining Unit (BFCU)
  - Belted Range Aquifer (BRA)
  - Basal Confining Unit (BCU)
  - Basal Aquifer (BAQ)
- Fracture characteristics by HGU and well
  - WTA (core length in parentheses)
    - UE-18r (10 ft)

  - UE-18t (1,287 ft)
  - UE-19x (871 ft)
  - U-20c/UE-20c (91 ft)
  - UE-20f (26 ft)
- LFA
  - UE-18r (22 ft)
  - UE-19x (681 ft)
  - UE-20bh#1 (4 ft)
  - UE-20c/UE-20c (15 ft)
  - UE-20e#1 (31.5 ft)
  - UE-20f (54 ft)

- Fracture density
  - The number of observed natural fractures per vertical foot of core
- Observed fracture densities
  - WTA
    - All holes
      - Open fractures – 0.63 fractures/vertical foot
      - Closed fractures – 0.49 fractures/vertical foot
    - PM holes only
      - Open fractures – 0.85 fractures/vertical foot
      - Closed fractures – 0.31 fractures/vertical foot
    - Area 18 holes only
      - Open fractures – 0.3 fractures/vertical foot
      - Closed fractures – 0.76 fractures/vertical foot
  - LFA
    - All holes
      - Open fractures – 0.14 fractures/vertical foot
      - Closed fractures – 0.52 fractures/vertical foot
    - PM holes only
      - Open fractures – 0.12 fractures/vertical foot
      - Closed fractures – 0.55 fractures/vertical foot
    - Area 18 holes only
      - Open fractures – 0.23 fractures/vertical foot
      - Closed fractures – 0.41 fractures/vertical foot
- Fracture aperture
  - Defined as the average width of the void space between fracture surfaces.

        - The average was a visual estimate of the representative width that falls between the minimum and maximum widths.
    - Average measured with a feeler gauge.
- Average apertures
    - WTA
        - UE-18r (0.04 mm)
        - UE-18t (2.19 mm)
        - UE-19x (0.21 mm)
        - U-20c/UE-20c (0.42 mm)
        - UE-20f (0.17 mm)
        - Average from all drill holes – 0.34 mm
    - LFA
        - UE-18r (2.09 mm)
        - UE-19x (0.98 mm)
        - UE-20bh#1 (na – no open fracture recognized)
        - UE-20c/UE-20c (na – no open fracture recognized)
        - UE-20e#1 (0.08 mm)
        - UE-20f (0.53 mm)
        - Average from all drill holes – 0.53 mm

References

Drellack, S.L., Jr., L.B. Prothro, K.E. Roberson, D.B. Schier, and E.H. Price. 1997. *Analysis of Fractures in Volcanic Cores from Pahute Mesa, Nevada Test Site,* DOE/NV/11718-160.

Wolfsberg, A., L. Glascoe, G. Lu, A. Olson, P. Lichtner, M. McGraw, T. Cherry, and G. Roemer. 2002. *TYBO/BENHAM: Model Analysis of Groundwater Flow and Radionuclide Migration from Underground Nuclear Tests in Southwestern Pahute Mesa, Nevada*, LA-13977.

E.1.2 Literature Review Focusing on the Carbonates

The following is a brief summary of each of the data sources reviewed regarding assigning a range of representative fracture porosities to the carbonates, as discussed in Section 5.3.

E.1.2.1 Data Sources

The data presented to provide recommended values for the effective porosity of the CA HGU are drawn from a number of sources. These include the following:

- Tracer test analyses
- Hydraulic conductivity and fracture aperture analyses
- Fracture spacing and aperture analyses
- Analysis of geophysical logging data
- A literature review
- Previous values used in numerical models for the NNSS

Each of these data sources with references is discussed below.

E.1.2.2 Tracer Tests

Convergent Flow Tracer Test Between Water Wells C and C-1 in Yucca Flat

Winograd and West (1962) report on a convergent-flow tracer test conducted in the LCA between WW-C and C-1 in Yucca Flat. These two wells are about 29.3 m (96 ft) apart at the water table. The slotted interval is 32.9 m (108 ft) thick in WW-C. Water Well C-1 is completed open hole across 239 m (784 ft) of the LCA. Initial tracer breakthrough occurred after about 4.2 hours, and peak tracer concentration was observed between 3 and 4 hours later. The discharge rate at the withdrawal well was 13.9 L/s (220 gpm). For a radial flow field, the time for plug flow between the pumping and injection wells can be estimated. Using the parameter values from Winograd and West (1962) given above and peak-concentration arrival of about 3.5 hours after first tracer breakthrough, (7.7 hours after tracer injection), a porosity-thickness product of 0.14 m (0.46 ft) was calculated (SNJV, 2007). A maximum effective porosity of 4.3×10^{-3} was calculated, assuming a thickness equivalent to the slotted interval length of 32.9 m (108 ft) in WW-C. A minimum effective porosity of 5.9×10^{-4} was calculated assuming a thickness equivalent to the open interval length of 239 m (784 ft) in WW-C-1.

Convergent Flow Tracer Test at the ER-6-1 Well Cluster in Yucca Flat

A multiple-well aquifer test-tracer test (MWAT-TT) was conducted in the LCA at the ER-6-1 Well Cluster located in Yucca Flat from late April to late July 2004. The test details discussed here were taken from SNJV (2005a). Well ER-6-1#2 was the pumping well and tracers were injected into upper and lower completion intervals in Well ER-6-1, located 64 m (201 ft) from the pumping well, and

Well ER-6-1#1, located 50.8 m (167 ft) from the pumping well. The direction of tracer migration from the injection wells to the pumping well is approximately aligned with the dominant local fracture orientation. The pumping rate in well Well ER-6-1#2 averaged 33.0 L/s (523 gpm) over a 434.3-m-thick (1,425 ft) interval during the MWAT-TT. Tracer injection occurred in four stages. The first stage consisted of the injection of microspheres into the upper zone in Well ER-6-1; the second stage consisted of the injection of 2,5-DFBA into Well ER-6-1#1; the third stage consisted of the injection of NaI and 2,4,5-TFBA into the lower zone in Well ER-6-1; and the fourth stage consisted of the injection of LiBr, LiCl, and PFBA into the upper zone in Well ER-6-1. For each stage, tracer injection was followed by the injection of chase water to flush the tracer from the borehole. A complete description of tracer breakthrough for this test can be found in SNJV (2005a).

Fracture porosities for the LCA were estimated using the breakthrough curves for the tracers injected into Well ER-6-1 during the Well ER-6-1 MWAT-TT based on peak-concentration arrival time and the theoretical plug flow method (SNJV, 2007). Both of the breakthrough curves for tracers injected into the lower zone of Well ER-6-1 show peak arrival at about nine days. Although the total pumping rate during the test averaged 33.0 L/s (523 gpm), the relative amounts of flow through the upper and lower zones of the LCA at the Well ER-6-1 complex were determined based on the flow logging results. Flow logging indicates that flow in the lower portion of Well ER-6-1 is about 31 percent of the total flow and flow in the lower portion of Well ER-6-1#2 is about 39 percent of the total flow. Using the average of these two percentages (35 percent) and multiplying by the total flow rate yields an adjusted flow rate of 11.6 L/s (184 gpm) for the lower zone. An interval thickness of 148.1 m (486 ft) for the lower zone was used in the calculation. This thickness corresponds to the length between the top of the lower zone in Well ER-6-1 at a depth of 792.5 m (2,600 ft) and the top of the Eureka Quartzite at a depth of 940.6 m (3,086 ft). Flow into and out of the borehole was assumed to be negligible in the Eureka Quartzite. Using these values yields a fracture porosity of 4.7×10^{-3} based on the breakthrough of tracers injected into the lower zone in Well ER-6-1 (Table E-1).

This same method was used to estimate a fracture porosity based on the breakthrough curves for tracers injected into the upper zone in Well ER-6-1 (SNJV, 2007). Peak arrival for these tracers occurred at about 29 days. Flow into the upper zone in Well ER-6-1 is about 69 percent of the total flow, and flow into the upper portion of Well ER-6-1#2 is about 61 percent based on flow logging results. Using the average of these two values (65 percent) and multiplying it by the total flow rate yields an adjusted flow rate of 21.5 L/s (340 gpm). An interval thickness of 252.7 m (829 ft) was

Table E-1
Summary of Effective Porosities Determined Using the Breakthrough Curves from the ER-6-1 Well Cluster Tracer Test

Injection Well/Zone	ER-6-1 Lower			ER-6-1 Upper			ER-6-1#1	
	Current Report	SNJV, 2006d		Current Report	SNJV, 2006d		Current Report	SNJV, 2006d
		Single Porosity	Double Porosity		Pathway 1 Single Porosity	Pathway 2 Single Porosity		
Time	9 days [a]	34.4 days [b]	32.5 days [b]	29 days [a]	66.7 days [b]	145.8 days [b]	N/A [c]	137.5 days [b]
Flow rate	11.6 L/s [d]	$Q_T \times 0.4$ [e]	$Q_T \times 0.4$ [e]	21.5 L/s [f]	$Q_T \times 0.4$ [e]	$Q_T \times 0.1$ [g]	N/A	$Q_T \times 0.4$ [e]
Thickness	148.1 m	125 m	125 m	252.7 m	300 m	300 m	N/A	300 m
Distance	64 m	NR	NR	64 m	NR	NR	N/A	64 m
Effective Porosity	4.7×10^{-3}	1×10^{-2}	9×10^{-3}	1.7×10^{-2}	9×10^{-3}	6×10^{-3}	N/A	2.0×10^{-2}

Source: SNJV, 2007; Table 8-15

Note: Shaded values were not used in developing the effective porosity distribution for the CA HGU (see discussion in text).

[a] Time to peak arrival.
[b] Mean residence time as determined by RELAP analysis.
[c] No peak concentration identifiable in tracer breakthrough curve.
[d] 35 percent of total production rate of 33.0 L/s.
[e] Total production rate times 40 percent; actual value used not reported.
[f] 65 percent of total production rate of 33.0 L/s.
[g] Total production rate times 10 percent; actual value used not reported.

N/A = Not applicable
NR = Not reported

used. This thickness corresponds to the length between the top of the LCA at a depth of 539.5 m (1,770 ft) and the bottom of the upper zone at a depth of 792.2 m (2,599 ft). Using these values yields a fracture porosity of 1.7×10^{-2}.

Observed tracer breakthrough curves from the tracer tests at the Well ER-6-1 cluster were analyzed by SNJV (2006) using the semi-analytical model RELAP. Based on interpretations of hydraulic data at the cluster, analysis of the tracer test results assumed a linear flow regime. This analysis assumed diffusion into a matrix with a 3 percent porosity. The breakthrough curves for I and 2,4,5-TFBA, injected into the lower zone in Well ER-6-1 and recovered in pumping Well ER-6-1#2, were analyzed using both single- and double-porosity conceptualizations. The RELAP analyses yield a mean residence time for the tracers. The analysis (SNJV, 2006) then used this mean residence time and the assumption of plug flow to calculate the flow (or effective) porosity. The interpreted mean residence times were 825 hours (34.4 days) for the single-porosity conceptualization and 780 hours (32.5 days) for the double-porosity conceptualization (SNJV, 2006). Note that these mean residence times are significantly larger than the peak-concentration arrival time of nine days discussed above. In their calculation of the flow porosity, they used a production rate equal to 40 percent of the total rate and an interval thickness of 125 m (410 m). Both of these values are slightly different from those used in the calculations discussed in the previous paragraph. For the RELAP interpretation of transport of tracers injected into the Well ER-6-1 lower zone, the flow porosities reported by SNJV (2006) are 1×10^{-2} for the single-porosity conceptualization and 9×10^{-3} for the double-porosity conceptualization.
The two interpreted values are similar, indicating a minimal effect of matrix diffusion; however, the effective porosity from the double-porosity interpretation is considered more representative for comparison purposes.

The SNJV (2006) report states that two inflow zones were identified by flow logging in pumping Well ER-6-1#2 that correspond to the upper injection zone in Well ER-6-1. The analysis of the PFBA breakthrough in the upper zone considered these inflow locations as individual pathways. Spinner log results indicate that flow in the lower of these two inflow zones is less than 10 percent of the total flow rate. The RELAP analysis of the PFBA breakthrough curve yielded a mean residence time of 1,600 hours (66.7 days) for pathway 1 (the upper inflow zone in the upper injection zone) and 3,500 hours (145.8 days) for pathway 2 (the lower inflow zone in the upper injection zone) for a single-porosity conceptualization. The estimated mean residence times are much larger than the tracer peak-concentration arrival time of 29 days. They calculated the flow porosity using mean residence

times determined with RELAP. For the upper injections into Well ER-6-1, they assumed an interval thickness of 300 m (984 ft) and production rates of 40 and 10 percent of the total rate for pathways 1 and 2, respectively. Their calculated flow (effective) porosities are 9×10^{-3} for pathway 1 and 6×10^{-3} for pathway 2 (Table E-1).

A single-porosity interpretation of the breakthrough of 2,5-DFBA, which was injected into Well ER-6-1#1, using RELAP yielded a mean residence time of 3,300 hours (137.5 days). Using this time, an interval thickness of 300 m (984 ft), a production rate 40 percent of the total rate, and a distance of 92 m (302 ft), SNJV (2006) calculated a flow porosity of 2.0×10^{-2} (Table E-1). The breakthrough curve for 2,5-DFBA for the Well ER-6-1#1 to ER-6-1#2 flow path exhibited a large amount of noise because measured concentrations were near the detection limit; thus any interpretation of the breakthrough curve is uncertain. The effective porosity from the RELAP single-porosity interpretation for this flow path is not recommended for inclusion in determining a representative range from the Well ER-6-1 tracer test.

Two-Well Recirculating Tracer Tests at the Amargosa Tracer Site

Johnston (1968) discusses the tracer well construction program for a two-well recirculating tracer test performed in the carbonate aquifer at the Amargosa tracer site. This site is about 31.5 km (19.6 miles) southwest of Mercury, Nevada. The injection well is completed in the lower 20.7 m (68 ft) of the 22.9-m (75 ft)-thick Bonanza King Formation and in 41.8 m (137 ft) of the underlying Carrara Formations. The pumping well is completed in the lower 45.4 m (149 ft) of the 48.5-m (159 ft)-thick Bonanza King Formation and in the upper 6.4 m (21 ft) of the underlying Carrara Formation. The Bonanza King Formation consists primarily of brecciated dolomite while the Carrara Formation consists primarily of coarsely crystalline limestone. The Bonanza King Formation is highly permeable compared to the low permeability of the Carrara Formation. The injection and withdrawal wells are located 122.7 m (402.6 ft) apart at ground surface and were considered to be aligned approximately parallel to the direction of regional groundwater flow. Both wells were completed open hole in the carbonate portion except for a section of perforated casing across a fault zone in both wells that caused extensive caving of the holes. The fault zone was between the dolomite of the Bonanza King Formation and the limestone of the Carrara Formation in the injection well, and in the Bonanza King Formation in the withdrawal well. A tracejector survey in the injection well identified two zones of greatest permeability: an upper zone approximately 1.5 m (5 ft) thick at the top of the carbonate section below the casing shoe, and a lower zone in the 14.9-m (48.9 ft)-thick fault zone.

The rate of inflow in the upper zone was a factor of 11 greater than the rate of inflow in the lower zone. For the pumping well, the 9.8-m (32 ft)-thick fault zone was shown by a tracejector survey to be the most permeable interval in the well. The tracer for the recirculating tracer test consisted of tritiated water injected into the injection well.

Claassen and Cordes (1975) analyzed the breakthrough of the tritiated water at the pumping well for the two-well recirculating tracer test conducted at the Amargosa tracer site as described by Johnston (1968) above. They used the dispersion model method of analysis described in Grove and Beetem (1971) and Grove (1971) to analyze the test. This method involves developing theoretical breakthrough curves for various assumed longitudinal dispersion-porosity combinations, and then comparing those curves to the observed data. The theoretical curve that best matches the observed data gives the longitudinal dispersion and porosity for the tracer test. The analysis by Claassen and Cordes (1975) yielded a dispersivity of 15 m (49.2 ft) and a porosity-thickness product of 0.88 m (2.9 ft). The active thickness for the tracer test at the Amargosa tracer site is unknown. Tracejector survey data (Johnston, 1968) suggest a range of 16.5 m (54 ft) (thickness of upper and lower permeable zones in the injection well) to 1.5 m (5 ft) (thickness of upper permeable zone only in the injection well). Using this range for thickness (16.5 to 1.5 m) and the porosity-thickness product from Claassen and Cordes (1975) yields a porosity range of 5.3×10^{-2} to 0.59, respectively. Claassen and Cordes (1975) found that the analysis results were more sensitive to changes in the porosity-thickness product than to changes in the dispersivity.

Leap and Belmonte (1992) discuss three two-well recirculating tracer tests conducted at the Amargosa tracer site. The first test is the same as that reported in Claassen and Cordes (1975). Leap and Belmonte (1992) do not present a reanalysis of this first test, but rather report the results from Claassen and Cordes (1975). The second and third tests used the same injection and withdrawal wells as did the first test. Sulfur-35 was the tracer for the second test, and ^{3}H and Br were the tracers for the third test. Leap and Belmonte (1992) also analyzed these tests using the method of Grove (1971) and obtained a porosity-thickness product of 0.84 m (2.8 ft) for all three breakthrough curves. They report a thickness for the Bonanza King Formation of 3.0 m (9.8 ft) at the injection well and 14.6 m (47.9 ft) at the withdrawal well. Using the average of these two thicknesses (8.8 m) (28.9 ft), Leap and Belmonte (1992) interpreted a porosity of 10 percent based on the analysis of the ^{35}S, ^{3}H, and Br breakthrough curves. Their analyses also yielded apparent dispersivities of 22.9, 27.4, and 30.5 m (75.1, 89.9, and 100.1 ft) based on analysis of the ^{35}S, ^{3}H, and Br breakthrough curves, respectively.

Note that the focus of the analyses by Leap and Belmonte (1992) was determination of dispersivity, not determination of porosity.

For 100 percent recirculation the plug flow time for tracer to travel from the injection well to the withdrawal well in a two-well recirculating tracer test is given by Equation (E-3).

$$t = \frac{\phi \pi b R^2}{3Q} \quad \Rightarrow \quad \phi = \frac{3Qt}{\pi b R^2} \qquad \textit{(E-3)}$$

where

t = plug flow travel time
φ = porosity
b = fracture aperture
R = distance between tracer-injection and withdrawal wells
Q = production rate

Table E-2 summarizes the approximate time to reach peak concentration, the pumping rate, the porosity-thickness product calculated using Equation (E-3), and the calculated porosity for several assumed effective thicknesses for each of the three two-well recirculating tracer tests conducted at the Amargosa tracer site. Assuming an average thickness of 9.0 m (29.5 ft), the calculated effective porosity ranges from about 5.7×10^{-2} to 8.4×10^{-2}.

Johnston (1968) describes the carbonate aquifer at the Amargosa tracer site as having a few zones of very high permeability separated by rock of comparatively lower permeability. He states that "the zones of high permeability occur in faulted, highly brecciated intervals in the dolomite (Bonanza King Formation)." The estimated porosities of 3 to 10 percent determined from the tracer tests at the Amargosa tracer site appear large if the tracer transport was controlled by a direct pathway in the fractures between the injection and pumping wells. Tracer tests conducted in fractured dolomite at the WIPP near Carlsbad, New Mexico, indicate that the direction of the tracer transport path relative to the primary fracture direction has a significant impact on the fracture porosities calculated using the peak-concentration arrival time (see discussion below). For three tracer test locations at the WIPP site, the fracture porosity calculated for the path aligned with the fractures (the fast path) were about 10^{-3}, while the apparent effective porosities calculated for paths not aligned with the fractures (the slow paths) were an order of magnitude or more higher (Jones et al., 1992).

Table E-2
Calculated Porosities for the Two-Well Recirculating Tracer Tests Conducted at the Amargosa Tracer Site Assuming Plug Flow

Tracer Test	Approx. Time to Peak Arrival (days) [a]	Pumping Rate (L/s)	Porosity-Thickness Product (m) [b]	Porosity (fraction)		
				1.5-m Thickness [c]	9.0-m Thickness [d]	16.5-m Thickness [e]
Test 1	6.2	22.5 [f]	0.764	0.51	8.4×10^{-2}	4.6×10^{-2}
Test 2	6.9	13.7 [g]	0.517	0.34	5.7×10^{-2}	3.1×10^{-2}
Test 3		15.5 [g]				
^{3}H	7.4		0.628	0.42	6.9×10^{-2}	3.8×10^{-2}
Br	7.8		0.662	0.44	7.3×10^{-2}	4.0×10^{-2}

Source: SNJV, 2007; Table 8-16

Note: Shaded values were not used in developing the effective porosity distribution for the CA HGU (see discussion in text).

[a] Estimated from breakthrough curves given in Leap and Belmonte, 1992
[b] Calculated using Equation (E-3)
[c] Minimum estimated effective thickness
[d] Average estimated effective thickness
[e] Maximum estimated effective thickness
[f] Claassen and Cordes, 1975
[g] Leap and Belmonte, 1992

Travel along pathways not aligned with the predominate fracture direction will be more tortuous and undergo more molecular diffusion than pathways aligned with the fractures. Both of these factors may result in slower transport times, which result in the calculated fracture porosity being an overestimate.

The large porosities calculated for the tracer tests at the Amargosa tracer site suggest the possibility that the tracer flow path for the tests was not aligned with the predominate fracture direction. Therefore, the porosities determined from the tests may not be representative of the fracture porosity. In addition, fracture flow only in a geologic medium with a 10 percent fracture porosity would yield extremely large transmissivities (not consistent with those interpreted for the site). Because of these uncertainties, the porosities determined from these tests were not used in developing the effective porosity distribution for the CA HGU.

Tracer Test in the Culebra Dolomite at the Gnome Site, New Mexico

Grove and Beetem (1971) analyzed a two-well recirculating tracer test conducted in the Culebra Dolomite at the Gnome site in Eddy County, New Mexico. The Culebra Dolomite is similar to the LCA at the NNSS in that it is a fractured dolomite aquifer. The two wells were originally designed to

be parallel to the direction of regional flow in the aquifer. However, due to drilling problems, one of the wells deviated from vertical, and the flow direction between the two wells is estimated to be about 35 degrees from the regional flow direction. The distance between the wells at the depth of the Culebra is 54.9 m (180 ft), the Culebra thickness is 10.4 m (34 ft), the withdrawal-injection rate was 2.8 L/s (44 gpm), and the time to peak concentration was about 12.8 days. Using their analysis method, Grove and Beetem (1971) obtained an estimated porosity of 0.12. Assuming plug flow and, a porosity of 9.4×10^{-2} is calculated for this tracer test. For comparison, tracer tests conducted in the Culebra Dolomite at the WIPP site near Carlsbad, New Mexico, yielded estimated fracture porosities of about 10^{-3} (Jones et al., 1992). The high porosities determined for the test at the Gnome site are considered to be the result of the tracer travel path not being aligned with the predominate fracture direction. If that is the case, these porosities do not reflect the fracture porosity of the Culebra Dolomite at this site. Therefore, these porosities were not used in developing the effective porosity distribution for the CA HGU.

Tracer Tests in the Culebra Dolomite at the WIPP, New Mexico

Fracture porosities have been determined by analysis of three convergent-flow tracer tests conducted in the Culebra Dolomite at three different hydropad locations (H-3, H-6, and H-11) at the WIPP site near Carlsbad, New Mexico (Jones et al., 1992). At the H-3 and H-6 hydropads, tracer was injected into two wells and recovered in a third well. At the H-11 hydropad, tracer was injected into three wells and recovered in a fourth well. At all three locations, tracer transport during the test was rapid along one path and much slower along the other path(s). The rapid transport path was considered to be aligned approximately parallel to the dominant direction of fracture orientation. As a result, transport along the rapid path was assumed to be dominated by fracture flow. Numerical analysis of the tracer breakthrough curves for the rapid transport path for these three convergent-flow tracer tests yielded fracture porosities for the Culebra Dolomite ranging from 5.0×10^{-4} to 1.5×10^{-3} (Jones et al., 1992) (Table E-3).

The porosities determined by Jones et al. (1992) are much lower than the value of 0.12 interpreted by Grove and Beetem (1971) for the Culebra at the Gnome site. This is likely the result of the transport direction for the recirculating tracer test at the Gnome site not being aligned parallel to the dominant fracture direction. Fracture porosities for the convergent-flow tracer tests discussed in Jones et al. (1992) were initially calculated using the peak-concentration arrival time and assuming plug flow. Those calculated porosities are also given in Table E-3. Notice that the calculated fracture porosities

Table E-3
Summary of Fracture Porosities Determined for the Culebra Dolomite at the WIPP Site

Test Location	Path [a]/Tracer	Injection Well to Pumping Well Distance (m)	Fracture Porosity Determined from Model Calibration [b] (fraction)	Porosity Calculated Assuming Plug Flow [c] (fraction)
H-3 Hydropad	fast (m-TFMB)	30.7	1.2×10^{-3}	1.9×10^{-3}
	slow (PFBA)	26.8		2.3×10^{-2}
H-6 Hydropad	fast (PFBA)	29.9	1.5×10^{-3}	3.1×10^{-3}
	slow (m-TFMB)	29.9		5.6×10^{-2}
H-11 Hydropad	fast (m-TFMB)	20.9	5.0×10^{-4}	1.0×10^{-3}
	slow (PFBA)	21.4		1.8×10^{-2}
	slow (o-TFMB)	43.1		1.8×10^{-2}

Source: SNJV, 2007; Table 8-17

Note: Shaded values were not used in developing the effective porosity distribution for the CA HGU (see discussion in text).

[a] Fast path means travel path with the most rapid tracer breakthrough; slow path means travel path with slower tracer breakthrough.
[b] Model calibration only to breakthrough curve from fast travel path (Jones et al.,1992).
[c] Calculated for this report assuming plug flow using Equation (E-3).

are higher than those determined through model calibration. As expected, fracture porosities calculated using Equation (E-3) are an overestimate even when determined from pathways with fracture-dominated transport because the delayed response resulting from matrix diffusion and dispersion is ignored. Also notice that the fracture porosities calculated for the fast transport paths, the paths assumed to be aligned approximately parallel with the fracture orientation, are more than one order of magnitude lower than those for the slow transport paths, which are not aligned with the fractures. This indicates that if the tracer transport path is not aligned with the major fracture direction, the calculated fracture porosity will likely be greatly overestimated.

E.1.2.3 Hydraulic Conductivity and Fracture Spacing Calculations

The Phase I Yucca Flat/Climax Mine TDD (SNJV, 2007; Section 8.5.2.6) discusses a methodology for calculation of fracture porosity using hydraulic conductivity data from hydraulic tests and fracture spacings from borehole fracture data. This method was used to calculate fracture porosities for wells ER-6-1#2 and ER-7-1 located in Yucca Flat and completed to the LCA. Well ER-5-3#2, located in Frenchman Flat, is also completed to the LCA. Analysis of the formation microimager log conducted

in well ER-5-3#2 is provided in SNJV (2005b). The quality of this log is poor due to numerous washouts and breakouts in the well (SNJV, 2005b). These features cause intermittent contact between the logging tool pad and the borehole well. Because of the poor quality of the log, the fracture density in well ER-5-3#2 was considered to be uncertain, and no fracture porosity was calculated using hydraulic conductivity and fracture spacing.

ER-6-1#2

Hydraulic conductivity data for well ER-6-1#2 are reported in SNJV (2005a). A hydraulic conductivity value of 1.3×10^{-4} m/s (36.9 ft/day) was determined for the entire completion interval through analysis of a 90-day pumping test with ER-6-1#2 as the pumping well. Hydraulic conductivities determined through analysis of data from the spinner flow meter log conducted in the well were also reported. Fracture data from analysis of an electric microimager log conducted in well ER-6-1#2 is provided in SNJV (2005c). This report provides general information regarding fractures in the borehole. Specific locations and dip angles for the individual fractures were obtained from SNJV (2005c). Using these data, a fracture spacing was calculated for the entire completion interval and for each of the intervals associated with the reported hydraulic conductivities from analysis of the spinner flow log data. Table E-4 summarizes the fracture porosities calculated for well ER-6-1#2 using hydraulic conductivity and fracture spacing. These porosities range from 2.0×10^{-4} to 8.3×10^{-4}.

Table E-4
Fracture Porosities Calculated for Wells ER-6-1#2 and ER-7-1 Using Hydraulic Conductivity and Fracture Spacing
(Page 1 of 2)

Well	Interval (m bgs)		Hydraulic Conductivity (m/s)		Fracture Spacing (m)	Calculated Fracture Porosity (fraction)	
	Top	Bottom	Minimum	Maximum		Minimum	Maximum
ER-6-1#2	541.0	941.8	1.3×10^{-4} [a]		2.5	2.9×10^{-4}	
	563.9	593.1	ND [b]		1.4	N/A	
	593.1	619.0	2.8×10^{-4} [c]		1.0	7.0×10^{-4}	
	619.0	629.7	1.01×10^{-3} [c]		4.6	3.9×10^{-4}	
	629.7	645.0	ND [b]		4.4	N/A	
	645.0	649.5	3.93×10^{-3} [c]		0.8	2.0×10^{-3}	
	649.5	655.6	ND [b]		No fractures	N/A	
	655.6	678.5	5.66×10^{-3} [c]		16.5	2.9×10^{-4}	
	678.5	710.5	ND [b]		3.4	N/A	

Table E-4
Fracture Porosities Calculated for Wells ER-6-1#2 and ER-7-1 Using Hydraulic Conductivity and Fracture Spacing
(Page 2 of 2)

Well	Interval (m bgs)		Hydraulic Conductivity (m/s)		Fracture Spacing (m)	Calculated Fracture Porosity (fraction)	
	Top	Bottom	Minimum	Maximum		Minimum	Maximum
ER-6-1#2	710.5	733.3	1.10×10^{-3} [c]		1.9	7.2×10^{-4}	
	733.3	750.1	ND [b]		1.4	N/A	
	750.1	776.0	1.11×10^{-3} [c]		2.4	6.2×10^{-4}	
	776.0	858.3	1.5×10^{-4} [c]		4.9	2.0×10^{-4}	
	858.3	869.0	3.54×10^{-3} [c]		7.6	4.2×10^{-4}	
	869.0	899.5	2.95×10^{-3} [c]		2.5	8.3×10^{-4}	
ER-7-1	664.9	722.4	8.1×10^{-4} [d]	4.9×10^{-3} [e]	1.0	1.0×10^{-3}	1.8×10^{-3}

Source: SNJV, 2007; Table 8-18

[a] Value determined from analysis of pumping test.
[b] ND - No value determined because normalized flow rate was zero.
[c] Value determined from analysis of spinner flow log.
[d] 5th empirical percentile of K distribution determined through analysis of constant-rate test.
[e] 95th empirical percentile of K distribution determined through analysis of constant-rate test.

K - Hydraulic conductivity
N/A - Not applicable

ER-7-1

Hydraulic conductivity data for well ER-7-1 are reported in SNJV (2004). The nSIGHTS (n-Dimensional Statistical Inverse Graphical Hydraulic Test Simulator) code and a 50-simulation perturbation analysis were used to simulate 50 hydraulic conductivity solutions. They defined the range in hydraulic conductivity values as the central 90 percent of the solution distribution. This yielded hydraulic conductivities of 8.1×10^{-4} (230 ft/day) and 4.9×10^{-3} m/s (1,389 ft/day). Fracture data from analysis of an electric microimager log conducted in Well ER-6-1#2 are provided in SNJV (2005c). This report provides general information regarding fractures in the borehole. Using these data, a fracture spacing of 1.0 m (3.3 ft) was calculated for the effective interval as determined with an impeller flowmeter. Table E-4 summarizes the minimum and maximum fracture porosities calculated for Well ER-7-1 using the minimum and maximum hydraulic conductivities and the fracture spacing. These porosities are 1.0×10^{-3} to 1.8×10^{-3}.

E.1.2.4 Fracture Spacing and Aperture Calculations

The SNJV (2005c) report provides a fracture analysis for four boreholes in Yucca Flat based predominately on the results from borehole electric microimager logs. These four boreholes are ER-2-1 in north-central Yucca Flat, ER-6-1#2 in the southeastern corner of Yucca Flat, ER-7-1 in eastern Yucca Flat, and ER-12-2 in northwestern Yucca Flat. Two of these boreholes, ER-6-1#2 and ER-7-1, are completed in the LCA. The results from the borehole image logs were processed (enhanced) and then manually interpreted and statistically analyzed for fractures, bedding, and borehole washouts/breakouts. The analysis provided fracture aperture, fracture dip, fracture orientation, and fraction of fracture infilling. Mineral infilling was considered to be 0 to 50 percent for fractures identified as open, 50 to 80 percent for fractures identified as mineral filled, and 80 to 100 percent for fractures identified as closed (SNJV, 2005c).

Estimates of the fracture porosity for the lower carbonate interval in boreholes ER-6-1#2 and ER-7-1 based on fracture data from the borehole image logs were determined using the following relationship given in Bryant (2005):

$$\phi_f = \frac{\left[b_1 \cdot o_1 \Big/ \cos(\theta_1) + b_2 \cdot o_2 \Big/ \cos(\theta_2) + \ldots + b_n \cdot o_n \Big/ \cos(\theta_n) \right]}{t_T} \qquad \text{(E-4)}$$

where:

ϕ_f = fracture porosity (unitless),
b = fracture aperture (L),
o = fraction of the fracture that is open (unitless),
θ = fracture dip angle,
t_T = total interval thickness (L), and
n = number of fractures.

The data for fracture aperture, fracture dip, and fraction of fracture infilling were obtained from SNJV (2005c). Two fracture porosities were calculated for each borehole. The first corresponds to the LCA interval, and the second corresponds to the interval within the LCA that is most productive.
The depths for LCA intervals in each borehole were taken from BN (2006). The depths for the most productive interval or the water-producing zone based on fluid logging were taken from SNJV (2005c) for borehole ER-6-1#2 and from SNJV (2004) for borehole ER-7-1. The fracture porosity for the perforated interval in ER-7-1, taken from SNJV (2004), was also calculated. In some instances, the top or bottom of the interval used in the calculation was defined by the depth range of the

borehole image logging. Table E-5 summarizes the fracture porosities for boreholes ER-6-1#2 and ER-7-1 calculated using Equation (E-4). For each interval, a minimum and maximum fracture porosity was calculated using the minimum and maximum from the range of infilling for the fracture. The calculated fracture porosities range from 1.9×10^{-3} to 9.4×10^{-3}. Some of the limitations involved with these calculations include the following:

- The manual interpretation used to estimate fracture data from the image logs is subject to human bias/error.
- Undersampling of vertical fractures is possible because the boreholes are vertical.
- The three ranges of mineral infilling used in the calculations most likely do not adequately characterize the nature of infilling in the fractures; also, the infilling may be removed locally by the drilling action, and therefore the degree of openness is likely overestimated.
- Each fracture aperture is assumed to be constant in thickness, although this is highly unlikely.
- The fractures are assumed to be continuous in lateral extent, although this is highly unlikely.

Table E-5
Calculated Fracture Porosities for Boreholes ER-6-1#2 and ER-7-1 Using Fracture Spacing and Aperture Calculations

Interval	Depth to Interval Top (m)	Depth to Interval Bottom (m)	Minimum Fracture Porosity (fraction)	Maximum Fracture Porosity (fraction)
ER-6-1#2				
LCA	545.59 [a]	975.4 [b]	2.5×10^{-3}	5.6×10^{-3}
Producing Zone	883.92 [c]	975.4 [b]	1.9×10^{-3}	4.3×10^{-3}
ER-7-1				
LCA	539.50 [a]	758.65 [d]	3.8×10^{-3}	9.4×10^{-3}
Most Conductive Interval	665.07 [c]	722.38 [e]	2.4×10^{-3}	5.9×10^{-3}
Slotted Casing Interval	655.07 [f]	755.9 [g]	2.7×10^{-3}	6.8×10^{-3}

Source: SNJV, 2007; Table 8-19

[a] Depth to the top of the borehole image log (SNJV, 2005c)
[b] Total depth of the borehole (BN, 2006)
[c] Depth to the top of producing zone (SNJV, 2005c)
[d] Depth to the bottom of the borehole image log (SNJV, 2005c)
[e] Depth to the bottom of the producing zone (SNJV, 2004)
[f] Depth to the top of the slotted interval in the borehole (SNJV, 2004)
[g] Depth to the bottom of the slotted interval in the borehole (SNJV, 2004)

E.1.2.5 Geophysical Logging

Berger (1992) reports porosities for carbonate-rock aquifers in the Coyote Spring Valley Area determined from geophysical logging. These aquifers were investigated as part of the Nevada Carbonate Aquifers Program as potential sources for water supply and correlate to the CA HGU at the NNSS. Coyote Spring Valley is about 100 km (60 miles) due east of Frenchman Flat. Berger (1992) "describes the application and results of borehole geophysical log analyses from five test wells that penetrated the carbonate-rock aquifers." He used litho-porosity plots (*M*-*N* plots) to detect secondary (fracture) porosity in the test wells. The porosity-independent parameters *M* and *N* are calculated from responses of neutron, gamma-gamma, and acoustic logs by (Berger, 1992):

$$M = \frac{\Delta t_f - \Delta t}{\rho_b - \rho_f} \qquad \text{(E-5)}$$

and

$$N = \frac{\phi_f - \phi_{LS}}{\rho_b - \rho_f} \qquad \text{(E-6)}$$

where:

Δt_f = transit time of the fluid (200 microseconds per foot [μsec/ft]),
Δt = transit time recorded by the acoustic log (μsec/ft),
ρ_b = bulk density recorded by the gamma-gamma log (grams per cubic centimeter [g/cm^3]),
ρ_f = fluid density (1 g/cm^3),
ϕ_f = neutron porosity of fluid (100 percent as decimal), and
ϕ_{LS} = neutron porosity recorded by the neutron log (percent as decimal).

Values for *M* and *N* are calculated for pure lithologies of silica, calcite, and dolomite and for the lithologies in the test wells. Values of *M* are plotted versus *N* values. Well test zones with values that plot above the lithology triangle created by the pure mineral endpoints (which represents a shale-free carbonate zone) are considered to have secondary porosity. The magnitude of the secondary porosity is determined by the distance from the lithology triangle to the plotted point. Using this method, Berger (1992) identified secondary porosity in only one of the test wells (CE-DT-4). He determined secondary (fracture) porosity values for this well ranging from 6.0×10^{-3} to 9.6×10^{-2}. Due to the fact that only one of the five wells showed secondary porosity using this method and the method calculates secondary porosity indirectly, these values were not used in developing the effective porosity distribution for the CA HGU.

E.1.2.6 Literature Review of Basin and Range Province Rocks

Bedinger et al. (1989) developed distributions for hydraulic properties of rocks in the Basin and Range Province in the southwestern United States. They conducted a literature review of hydraulic conductivity and effective porosity for rocks in the Basin and Range Province and for rocks of similar types in other areas. The collected data were then synthesized, and the mean and 16.5 and 93.5 percentiles were determined for each rock type. Table E-6 summarizes their findings of effective porosity for carbonate rocks, including limestone, dolomite, and marble. Because the degree to which the characteristics of the carbonate rocks found in the review by Bedinger et al. (1989) match the characteristics of the CA HGU is unknown and the methods used to determine the porosities are unknown, these effective porosities were not used in developing the effective porosity distribution for the CA HGU.

Table E-6
Effective Porosity Estimates for Carbonate Rocks in the Basin and Range Province (after Bedinger et al., 1989)

Rock Type	Description	Effective Porosity (fraction)		
		16.5 Percentile	Mean	83.5 Percentile
Carbonate Rocks, including limestone, dolomite, and marble	Fractured, karstic, cavernous	0.09	0.12	0.16
	Dense to moderately dense	0.005	0.01	0.02

Source: SNJV, 2007; Table 8-20

Note: Shaded values were not used in developing the effective porosity distribution for the CA HGU (see discussion in text).

E.1.2.7 Values Used in Previous NNSS Modeling Studies

The DOE/NV (1997) report presents regional groundwater flow and ^{3}H transport models to evaluate migration from the underground testing areas of the NNSS. They compiled hydrogeologic data for a large portion of southern Nevada and California, including the NNSS. They looked at porosities for the LCA based on the tracer tests at the Amargosa tracer site (Leap and Belmonte, 1992) and the tracer test between wells C and C-1 in Yucca Flat (Winograd and West, 1962) analyzed using the method of Welty and Gelhar (1989). They also looked at the fracture analysis of core from Well ER-6-2 (IT, 1996). For Well ER-6-2, they calculated a true fracture spacing of 0.22 m (0.72 ft) from the mean of the reported fracture dip angle (81 degrees) and fracture aperture (0.9 mm) (3×10^{-3} ft). They then divided the mean fracture aperture by the calculated true fracture spacing to determine a

fracture porosity of 4×10^{-3}. They conducted a literature review and found fracture porosities ranging from 2×10^{-4} to 2×10^{-2} reported as representative for the Culebra Dolomite at the WIPP site (Tomasko et al., 1989). For their modeling of ^{3}H transport, DOE/NV (1997) assumed a lognormal distribution having a $\log_{10}$ mean value of -2.46 and a $\log_{10}$ SD of 0.25 for the effective porosity of the LCA. This translates to a mean effective porosity of 3.47×10^{-3}. The effective porosity range, defined by two SDs, is 1.1×10^{-3} to 1.1×10^{-2}.

Recommended Ranges in Previous NNSS Data Document Reports

Distributions and ranges of effective porosity for the CA HGU for use in PM CAU transport model have been estimated and reported for PM CAU (Shaw, 2003) and Frenchman Flat CAU (SNJV, 2005b). The distribution selected by Shaw (2003) for PM is the distribution used by DOE/NV (1997) for their regional ^{3}H model (see previous section). The SNJV (2005a) report selected a log-uniform distribution for the effective porosity of the CA HGU with a range of 6.4×10^{-4} to 1.6×10^{-2} for Frenchman Flat.

E.2.0 REFERENCES

BN, see Bechtel Nevada.

Bedinger, M.S., K.A. Sargent, W.H. Langer, F.B. Sherman, J.E. Reed, and B.T. Brady. 1989. *Studies of Geology and Hydrology in the Basin and Range Province, Southwestern United States, for Isolation of High-Level Radioactive Waste – Basis of Characterization Evaluation*, Professional Paper 1370-A. U.S. Geological Survey.

Bechtel Nevada. 2006. *A Hydrostratigraphic Model and Alternatives for the Groundwater Flow and Contaminant Transport Model of Corrective Action Unit 97: Yucca Flat-Climax Mine, Lincoln and Nye Counties, Nevada*, DOE/NV/11718--1119. Las Vegas, NV.

Berger, D.L. 1992. *Lithologic Properties of Carbonate-Rock Aquifers at Five Test Wells in the Coyote Spring Valley Area, Southern Nevada, as Determined from Geophysical Logs,* Water-Resources Investigations Report 91-4167. Carson City, NV: U.S. Geological Survey.

Bryant, N.A. 2005. *Letter Report: Analysis of Hydraulic Conductivity and Fracture Porosity in ER-5-3 #2 and ER-5-4 #2 Based on Fracture Data from Borehole Image Logs with Implications for the Tuff Confining Unit Flow Framework, Nevada Test Site, Nevada*. Las Vegas, NV: Stoller-Navarro Joint Venture.

Claassen, H.C., and E.H. Cordes. 1975. "Two-Well Recirculation Tracer Test in Fractured Carbonate Rock, Nevada." In *Hydrological Sciences Bulletin*, Vol. 20 (3): 367 - 382. Oxford: Blackwell Scientific Publications.

DOE/NV, see U.S. Department of Energy, Nevada Operations Office.

Grove, D.B., and W.A. Beetem. 1971. "Porosity and Dispersion Constant Calculations for a Fractured Carbonate Aquifer using the Two Well Tracer Method." In *Water Resources Research*, Vol. 7(1): 128-134. Washington, DC: American Geophysical Union.

Grove, D.B. 1971. *U.S. Geological Survey Tracer Study, Amargosa Desert, Nye County, Nevada Part II: An Analysis of the Flow Field of a Discharging Recharging Pair of Wells*, USGS-474-99 U.S. Geological Survey.

IT, see IT Corporation.

IT Corporation. 1996. *Wells ER-6-1 and ER-6-2 Core Fracture Analyses and Geophysical Log Comparisons,* ITLV/10972-171. Las Vegas, NV.

Johnston, R.H. 1968. *U.S. Geological Survey Tracer Study, Amargosa Desert, Nye County, Nevada. Part I: Exploratory Drilling, Tracer Well Construction and Testing, and Preliminary Findings*, Open-File Report 68-152. Washington, DC: U.S. Geological Survey.

Jones, T.L., V.A. Kelley, J.F. Pickens, D.T. Upton, R.L. Beauheim, and P.B. Davies. 1992. *Integration of Interpretation Results of Tracer Tests Performed in the Culebra Dolomite at the Waste Isolation Pilot Plant Site*, SAND92-1579-UC-721. Albuquerque, NM: Sandia National Laboratories.

Leap, D.I., and P.M. Belmonte. 1992. "Influence of Pore Pressure on Apparent Dispersivity of a Fissured Mitic Dolomitic Aquifer." In *Groundwater*, Vol. 30(1): 87-95. Columbus, OH: Groundwater Publishing Company.

NNSA/NFO, see U.S. Department of Energy, National Nuclear Security Administration Nevada Field Office.

Pawloski, G.A. 1999. *Development of Phenomenological Models of Underground Nuclear Tests on Pahute Mesa, Nevada Test Site–BENHAM and TYBO,* UCRL-ID-136003. Livermore, CA: Lawrence Livermore National Laboratory.

Shaw, see Shaw Environmental, Inc.

Shaw Environmental, Inc. 2003. *Contaminant Transport Parameters for the Groundwater Flow and Contaminant Transport Model of Correction Action Units 101 and 102: Central and Western Pahute Mesa, Nye County, Nevada*, Shaw/13052-201. Las Vegas, NV: Shaw Environmental, Inc.

SNJV, see Stoller-Navarro Joint Venture.

Stoller-Navarro Joint Venture. 2004. *Analysis of Well ER-7-1 Testing, Yucca Flat FY 2003 Testing Program, Nevada Test Site, Nevada*, S-N/99205--021. Las Vegas, NV.

Stoller-Navarro Joint Venture. 2005a. *ER-6-1 Well Cluster Multiple Well Aquifer Test – Tracer Test Data Report: Volume I, II, and III*, Rev. 0. Las Vegas, NV.

Stoller-Navarro Joint Venture. 2005b. *Underground Test Area Fracture Analysis Report for Frenchman Flat Well Clusters ER-5-3 and ER-5-4 Nevada Test Site, Nevada*, S-N/99205--060. Las Vegas, NV.

Stoller-Navarro Joint Venture. 2005c. *Underground Test Area Fracture Analysis Report for Yucca Flat Wells ER-2-1, ER-6-1#2, ER-7-1, and ER-12-2 Nevada Test Site, Nevada*, S-N/99205--040. Las Vegas, NV.

Stoller-Navarro Joint Venture. 2006. *Well ER-6-1 Tracer Test Analysis: Yucca Flat, Nevada Test Site, Nye County, Nevada*, S-N/99205-084. Las Vegas, NV.

Stoller-Navarro Joint Venture, 2007, *Phase I Contaminant Transport Parameters for the Groundwater Flow and Contaminant Transport Model of Corrective Action Unit 97: Yucca Flat/Climax Mine, Nevada Test Site, Nye County, Nevada*, S-N/99205--096.

Tomasko, D., M. Reeves, V.A. Kelley, and J.F. Pickens. 1989. "Parameter Sensitivity and Importance for Radionuclide Transport in Double-Porosity Systems." In *Proceedings of the Conference on Geostatistical Sensitivity, and Uncertainty Methods for Ground-Water Flow and Radionuclide Transport Modeling*, p. 279-321, September 15-17, 1987, B.E. Bufton, ed. Battell Press. San Francisco, CA.

U.S. Department of Energy, National Nuclear Security Administration Nevada Field Office. 2015. *United States Nuclear Tests, July 1945 through September 1992*, DOE/NV--209-REV 16. Las Vegas, NV.

U.S. Department of Energy, Nevada Operations Office. 1997. *Regional Groundwater Flow and Tritium Transport Modeling and Risk Assessment of the Underground Test Area, Nevada Test Site, Nevada*, DOE/NV--477. Las Vegas, NV.

U.S. Department of Energy, National Nuclear Security Administration Nevada Site Office. 2004. *Completion Report for Well ER-EC-5,* DOE/NV/11718--424. Prepared by Bechtel Nevada. Las Vegas, NV.

Welty, C., and L.W. Gelhar. 1989. *Evaluating of Longitudinal Dispersivity from Tracer Test Data,* R89-05, Ralph M. Parsons Laboratory Report. Cambridge, MA: Massachusetts Institute of Technology.

Winograd, I.J., and L.R. West. 1962. *Preliminary Tracer Experiment to Demonstrate Hydraulic Continuity Between Water Wells C and C-1, Yucca Flat, Nevada Test Site*, Technical Letter NTS-20. Denver, CO: U.S. Geological Survey.

Appendix F

Dispersion

F.1.0 INTRODUCTION

Dispersivity data compiled from literature covering sites from NNSS and NTTR as well as around the world for the work on RM/SM CAU (SNJV, 2008) are organized and tabulated as described in Table F-1. These data were augmented with an entry for the C-Wells (WW-C and WW C-1) site in the Yucca Flat at the NNSS (SNJV, 2007) presented in Table F-2.

F.2.0 DATASET SUMMARY

Each record of the dispersivity dataset contains information about a given tracer test and the results of the data analysis following a specific method of analysis. The dataset is, therefore, organized primarily by the tracer test location and secondarily by the data analysis method. The dispersivity dataset contains data from sites throughout the world. The dataset contains information about the data source, the method of analysis, the various dispersivity types, and an indication of the quality of the data by author reliability.

Data from SNJV (2008) are organized and tabulated as described in Table F-1. The additional data taken from SNJV (2007) are presented in Table F-2. Note that this table presents only those data fields for which information is available.

Table F-1
Description of the Dispersivity Data Spreadsheet
(Source: SNJV, 2008)

Sheet	Sheet Description	Column Name	Column Description
Dispersivity Data	Dispersivity data compiled from literature, used for general analysis	Site_Name	Name of site where the test was conducted
		Rock_Types	Rock-type category per NTS HGUs
		Aquifer_Material	Description of the type of rock/material in which the test was conducted
		Minimum_Scale_of_Test (m)	Minimum scale of the test
		Maximum_Scale_of_Test (m)	Maximum scale of the test
		Average_Scale_of_Test (m)	Average scale of the test
		Dispersivity_Longitudinal_Min (m)	Minimum longitudinal dispersivity
		Dispersivity_ Longitudinal_ Intermediate (m)	Intermediate longitudinal dispersivity
		Dispersivity_Longitudinal_Max (m)	Maximum longitudinal dispersivity
		Dispersivity_Longitudinal_Geomean (m)	Geometric mean of longitudinal dispersivity
		Percent of Scale	Dispersivity/scale of test
		Dispersivity_Transverse (m)	Transverse dispersivity
		Dispersivity_Vertical (m)	Vertical dispersivity
		DDE_F	Assigned DDE_F level
		Author_ Reliability	Author_ Reliability
		Author_ Reliability_Unified	Author_ Reliability_Unified
		Data Value ID	Description of data value derivation (if applicable)
		Data_Source	Data_Source
DDE_F levels	Explanation of Data Documentation levels	Data Documentation Evaluation	Explanation and descriptions of DDE_F levels
Reference Citations	Citations for all data sources (literature references)	Reference ID	ID for reference used in the 'Dispersivity Data' worksheet
		Reference Citation	Citation for reference

Table F-2
Dispersivity Values from C-Wells Data, Yucca Flat, NNSS
(Source: SNJV, 2007)

Site Name	Rock Types	Aquifer Material	Average Scale of Test (m)	Dispersivity Longitudinal Min (m)	Dispersivity Longitudinal Max (m)	Dispersivity Longitudinal Geomean (m)	Author Reliability	Author Reliability Unified	data_source
C-Well Site, Yucca Flat, Nevada	Carbonate Rocks	fractured limestone	29.3	0.6	1.4	0.92	3	III	Welty and Gelhar (1989) Eq using tracer data reported in Winograd and West [1962]

F.3.0 REFERENCES

SNJV, see Stoller-Navarro Joint Venture

Stoller Navarro Joint Venture. 2007. *Phase I Contaminant Transport Parameters for the Groundwater Flow and Contaminant Transport Model of Corrective Action Unit 97: Yucca Flat/Climax Mine, Nevada Test Site, Nye County, Nevada,* Revision No. 0, S-N/99205--096. Las Vegas, NV.

Stoller-Navarro Joint Venture. 2008. *Phase I Contaminant Transport Parameters for the Groundwater Flow and Contaminant Transport Model of Corrective Action Unit 99: Rainier Mesa/Shoshone Mountain, Nevada Test Site, Nye County, Nevada,* Rev. 0, S-N/99205--102. Las Vegas, NV.

Welty, C., and L.W. Gelhar. 1989. *Evaluation of Longitudinal Dispersivity from Tracer Test Data* R89-05, Ralph M. Parsons Laboratory Report. Cambridge, MA: Massachusetts Institute of Technology.

Winograd, I.J., and L.R. West. 1962. *Preliminary Tracer Experiment to Demonstrate Hydraulic Continuity Between Water Wells C and C-1, Yucca Flat*, Nevada Test Site, USGS Technical Letter NTS-20. Denver, CO: U.S. Geological Survey.

Appendix G

Matrix Diffusion

G.1.0 INTRODUCTION

Matrix diffusion and tortuosity data compiled from literature for NNSS as well as other sites (Jones, 2014) were augmented with the more recent data for samples from PM (Telfeyan et al., 2018).

G.2.0 DATASET SUMMARY

Data from SNJV (2007 and 2008) and Jones (2014) are organized and tabulated as described in Table G-1. Telfeyan et al. (2018) present additional data for samples from PM. The tortuosities calculated from the matrix diffusion and free water diffusion coefficients given in Telfeyan et al. (2018) are presented in Table G-2.

Table G-1
Description of the Matrix Diffusion Data Spreadsheet (SNJV, 2008)
(Page 1 of 3)

Sheet	Sheet Description	Column Name	Column Description
Matrix_Diffusion_Dataset	NTS Matrix Diffusion Data	SampleID	The number of data entry
		Sample number	The name of the well, unique sample numbers, and typically the depth in feet
		Location	Yucca Flat (YF), Yucca Mountain (YM), Rainier Mesa (RM), or Pahute Mesa (PM)
		Porosity	The fraction of void space within the rock, the void volume divided by the bulk volume
		Effective Porosity	The fraction of void space within the rock that is interconnected and available for fluid flow (only two references reported effective porosity [2, 3])
		HSU	Hydrostratigraphic unit for this sample
		Lithology	The type of rock: quartz, carbonate, tuff, zeolitic tuff, or granite/crystalline
		Depth (m)	The depth below ground surface of the well core from which the rock sample was obtained
		Entry Date	The date that the matrix diffusion data were added to this dataset (or substantially modified or updated)
		Diffusion coef (m2/s)	Experimentally derived diffusion coefficient, in m^2/s
		Derived diffusion	Matrix diffusion coefficient that is not reported directly in the reference source, but rather calculated or derived from the reported tortuosity and the free water diffusion coefficient

Table G-1
Description of the Matrix Diffusion Data Spreadsheet (SNJV, 2008)
(Page 2 of 3)

Sheet	Sheet Description	Column Name	Column Description
Matrix_Diffusion_Dataset	NTS Matrix Diffusion Data	Chemical species	Tracer chemical used in the diffusion cell experiment
		Species adj diffusion coeff (to tritiated water) m2/s	Experimentally derived diffusion coefficient, in m^2/s, adjusted from the actual tracer species used in the measurement to a tritiated water basis, to achieve a consistent tracer basis for the entire dataset of measurements
		Original source	Reference source reporting the diffusion coefficient measurement
		Source page #, Table #	Page and table number, where available, from original source reporting diffusion coefficient measurement and other raw data
		Tortuosity	The bulk measure of the constrictivity and tortuous nature of the interconnected pore space through which diffusion is occurring; tortuosity should always have a magnitude greater than zero and less than one
		Derived tortuosity	Tortuosity that is not reported directly in the reference source, but rather calculated or derived from the reported matrix diffusion coefficient and the free water diffusion coefficient
		Permeability(m2)	A measure of the ability of a porous material to transmit fluids; related to the constrictivity or tortuosity of the rock
		Temp(^{o}C)	Temperature at which matrix diffusion was measured (rarely reported)
		Diffus measur method	Lab diffusion cell experiment (DCE); diffusion wafer experiment (DWE); method other than DCE, such as X-ray or neutron imaging, electrical conductivity, batch experiments, using pulverized particles, etc. (non-DCE); unknown (UnK)
		Frac in sample?	Fractures present in sample ?
		Sample thickness, cm	Thickness of sample in centimeters
		M1a meas method factor	Multiplier Factor for measurement method
		M1b frac meas factor	Multiplier Factor for presence of coated fracture surfaces
		M1c sample thick factor	Multiplier Factor for representative sample thickness

Table G-1
Description of the Matrix Diffusion Data Spreadsheet (SNJV, 2008)
(Page 3 of 3)

Sheet	Sheet Description	Column Name	Column Description
Matrix_Diffusion_Dataset	NTS Matrix Diffusion Data	M1 meas meth	Measurement Method Factor: = M1a x M1b x M1c
		M2a test series meth	Multiplier Factor for the quality of the test series experimental method and calibration
		M2b1 indiv meas meth	Multiplier Factor for authors' evaluation of the quality of the test series experimental method and calibration
		M2b2 indiv meas meth	Multiplier Factor for authors' evaluation of the quality of the test series experimental method and calibration. Also, if calculated matrix diffusivity is greater than free water diffusivity, experimental problems are indicated and M2b2 = 0
		M2b test series meth	Test Series Method Factor: = M2b1 x M2b2
		M2 data anal meth	Data Reduction and Analysis Method Factor: = M2a x M2b
		M3 doc qual	Quality of the Documentation Factor
		M Total Multiplier	Total Multiplier: = M1 x M2 x M3
		Total Score	Total Score: = W x M
		Multiplier comments	Notes concerning multiplier factors
		Comments	General notes on the sample

Table G-2
Tortuosities for Core Samples from PM Reported in Telfeyan et al. (2018)

Sample	Well	CAU	Porosity	Tortuosity
Telfeyan 2022 UE-20c-2131.1-2131.5A	UE-20c	PM	0.181	0.083
Telfeyan 2021 UE-20c-2131.1-2131.5B	UE-20c	PM	0.179	0.086
Telfeyan 2018 UE-20c-1925.1-1925.3	UE-20c	PM	0.143	0.091
Telfeyan 2019 UE-20c-1353-1353.28	UE-20c	PM	0.161	0.079
Telfeyan 2020 UE-20c-1189-1189.25	UE-20c	PM	0.133	0.071
Telfeyan 2022 UE-20c-2131.1-2131.5A	UE-20c	PM	0.181	0.071
Telfeyan 2021 UE-20c-2131.1-2131.5B	UE-20c	PM	0.179	0.074
Telfeyan 2018 UE-20c-1925.1-1925.3	UE-20c	PM	0.143	0.071
Telfeyan 2019 UE-20c-1353-1353.28	UE-20c	PM	0.161	0.102
Telfeyan 2020 UE-20c-1189-1189.25	UE-20c	PM	0.133	0.093

G.3.0 REFERENCES

Jones, T. 2014. Written communication. Subject: *Development of a Conceptual Model of Matrix Diffusion for the Pahute Mesa CAU.* UGTA-4-995. Las Vegas, NV.

SNJV, see Stoller-Navarro Joint Venture

Stoller Navarro Joint Venture. 2007. *Phase I Contaminant Transport Parameters for the Groundwater Flow and Contaminant Transport Model of Corrective Action Unit 97: Yucca Flat/Climax Mine, Nevada Test Site, Nye County, Nevada,* Revision No. 0, S-N/99205--096. Las Vegas, NV.

Stoller-Navarro Joint Venture. 2008. *Phase I Contaminant Transport Parameters for the Groundwater Flow and Contaminant Transport Model of Corrective Action Unit 99: Rainier Mesa/Shoshone Mountain, Nevada Test Site, Nye County, Nevada,* Rev. 0, S-N/99205--102. Las Vegas, NV.

Telfeyan, K., S.D. Ware, P.W. Reimus, and K.H. Birdsell. 2018, "Comparison of experimental methods for estimating matrix diffusion coefficients for contaminant transport modeling," In *Journal of Contaminant Hydrology*, Vol. 209: pp 51–60.

Appendix H

Nevada Division of Environmental Protection Comments

(6 Pages)

NEVADA ENVIRONMENTAL MANAGEMENT OPERATIONS ACTIVITY
DOCUMENT REVIEW SHEET

1. Document Title/Number: Contaminant Transport Parameters for the Groundwater Flow and Contaminant Transport Model of Corrective Action Units 101 and 102: Central and Western Pahute Mesa, Nye County, Nevada	2. Document Date: April 2021
3. Revision Number: Revision 0	4. Originator/Organization: Navarro
5. Responsible EM Nevada Program Activity Lead: John Myers	6. Date Comments Due: 25 June 2021
7. Review Criteria:	
8. Reviewer/Organization Phone No.: NDEP	9. Reviewer's Signature:

10. Comment Number/Location		11. Type[a]	12. Comment	13. Comment Response
1.	Page 1-7, Section 1.1.2, First Paragraph, Fifth Sentence		Please clarify the approval date given in this sentence because based on the wording and 2009 date, the Phase II document was approved before it was developed.	Changed to read as follows: "A Phase II CAIP (NNSA/NFO, 2014) was developed, submitted, and signed in 2014."
2.	Page 2-1, Section 2.0, First Paragraph, First Sentence		Please include a reference for the PM-OV HFM.	Reference added: "(DOE/EMNV, 2020a)."
3.	Page 3-1, Section 3.1, First Paragraph, Sixth Sentence		Please reference a Figure that shows the location of Well PM-2 to aid the reader.	Added the following text: "(see Figure 2-5, lower right inset, for the location of Well PM-2)."

[a]Comment Types: M = Mandatory, S = Suggested.
Return Document Review Sheets to Environmental Management Nevada Program Operations Activity, Attn: QAC, M/S NSF 505

NEVADA ENVIRONMENTAL MANAGEMENT OPERATIONS ACTIVITY
DOCUMENT REVIEW SHEET

1. Document Title/Number: Contaminant Transport Parameters for the Groundwater Flow and Contaminant Transport Model of Corrective Action Units 101 and 102: Central and Western Pahute Mesa, Nye County, Nevada	2. Document Date: April 2021
3. Revision Number: Revision 0	4. Originator/Organization: Navarro
5. Responsible EM Nevada Program Activity Lead: John Myers	6. Date Comments Due: 25 June 2021
7. Review Criteria:	
8. Reviewer/Organization Phone No.: NDEP	9. Reviewer's Signature:

10. Comment Number/Location		11. Type[a]	12. Comment	13. Comment Response
4.	Page 3-19, Section 3.1.7.3, Third Paragraph, Second Sentence:		Please explain in detail in the text how a RN measurement at a well (a point measurement) can reflect transport parameters over large spatial and temporal scales. Please provide reference material and studies that demonstrate this concept	Added the following: "This is because RNs enter the groundwater in the source regions and are transported over time via groundwater to distal locations. Concentrations expected to occur at distal locations represent the integrated effects of transport processes along the entire length of the transport pathway. It is assumed in this work that the RN concentrations measured in the groundwaters sampled from wells represent the local values of concentrations. Hence, the RN data from wells located several kilometers from the point of release incorporate processes active over that distance for the past three to five decades. For modeling purposes, the sample results are interpreted to represent the integrated effect of processes over timescales of decades and spatial scales of kilometers. Parameter values obtained by calibration to the well data represent integrated values over timescales of decades and spatial scales of kilometers that are pertinent to RN transport behavior relevant to the CB forecasts."

[a]Comment Types: M = Mandatory, S = Suggested.
Return Document Review Sheets to Environmental Management Nevada Program Operations Activity, Attn: QAC, M/S NSF 505

NEVADA ENVIRONMENTAL MANAGEMENT OPERATIONS ACTIVITY
DOCUMENT REVIEW SHEET

1. Document Title/Number: Contaminant Transport Parameters for the Groundwater Flow and Contaminant Transport Model of Corrective Action Units 101 and 102: Central and Western Pahute Mesa, Nye County, Nevada	2. Document Date: April 2021
3. Revision Number: Revision 0	4. Originator/Organization: Navarro
5. Responsible EM Nevada Program Activity Lead: John Myers	6. Date Comments Due: 25 June 2021
7. Review Criteria:	
8. Reviewer/Organization Phone No.: NDEP	9. Reviewer's Signature:

10. Comment Number/Location		11. Type[a]	12. Comment	13. Comment Response
5.	Page 3-21, Section 3.2.2, First Paragraph, Second and Third Sentences:		Please explain in the text the basis for the assumptions made in these two sentences, namely, "that pore sizes and fracture apertures are much greater than the sizes of the aqueous RNs."; the concept that "solutes occur at concentrations small enough to neglect their effects on the motion of the pore fluid."; and "that the RNs dissolved in the pore fluid have negligible effect on fluid density and are carried along by the pore fluid moving at its local velocity."	Typical pore sizes of the volcanic rocks at PM are expected to be on the order of fractions of microns, while U atom is less than a nanometer in size. Solute concentrations: Take uranium, for example. From the results presented by Carle et al. (2020, Figure 13), a typical concentration at the source is at or below 100 MCL. Using an MCL=15 pCI/L, that translates to 1,500 pCI/L, which converts to ~2,000 µm/L, or 2 x E-3 gm/L. A liter of pure water at standard conditions has a mass of 1 x E+03 gm. Hence, the U causes negligible change to the density of water. Change in viscosity of water for NaCl solution of 0.1M concentration at 20ºC is ~0.01 cp (pp 37 of Ozbek, Fair, and Phillips,1977. *Viscosity of Aqueous Sodium Chloride Solutions From 0-150ºC*. American Chemical Society Southeast Regional Meeting, Nov. 9-11, 1977, Tampa, FL.). 2 x E-3 gm/L U-238 converts to ~E-05 M. Hence, a change in viscosity would be approximately E-06 cp, which is negligible. Text changed as follows: "Typical pore sizes (fractions of microns) and fracture apertures (micron or larger) are much greater than the sizes of the aqueous RNs (nanometers), and solutes are expected to occur at low concentrations (e.g., 1,500 pCi/L, or ~2E-03 gm/L based on natural relative abundance for U [Carle et al. 2020]). Their effect on the fluid density and fluid viscosity (Ozbek et al., 1997) is expected to be small. Hence, it is assumed that their effect on the motion of the pore fluid is negligible."

[a]Comment Types: M = Mandatory, S = Suggested.
Return Document Review Sheets to Environmental Management Nevada Program Operations Activity, Attn: QAC, M/S NSF 505

NEVADA ENVIRONMENTAL MANAGEMENT OPERATIONS ACTIVITY
DOCUMENT REVIEW SHEET

1. Document Title/Number: Contaminant Transport Parameters for the Groundwater Flow and Contaminant Transport Model of Corrective Action Units 101 and 102: Central and Western Pahute Mesa, Nye County, Nevada	2. Document Date: April 2021
3. Revision Number: Revision 0	4. Originator/Organization: Navarro
5. Responsible EM Nevada Program Activity Lead: John Myers	6. Date Comments Due: 25 June 2021
7. Review Criteria:	
8. Reviewer/Organization Phone No.: NDEP	9. Reviewer's Signature:

10. Comment Number/Location		11. Type[a]	12. Comment	13. Comment Response
6.	Page 5-11, Section 5.2.6.2, First partial Paragraph, Last Sentence:		"Figure 5-1 shows agreement among all methods used ... " Please add to the sentence, "within SD presented for data" if this is indeed a correct statement.	Added to the sentence as suggested
7.	Page 5-19, Section 5.3.4, First paragraph:		Both effective porosity and fracture porosity are used in this paragraph. Are they the same value? If so, please state this in the text.	In Section 5.3, Paragraph 1, deleted the words "…and are discussed in detail" in the third sentence. Added the following: "The fracture porosity of fractured rock units is discussed in this section." Added the following in Section 5.3.1, Paragraph 2: "In fractured media, fracture porosity is considered the effective porosity for modeling purposes."
8.	Pages 5-19 through 5-36, Section 5.3.4:		Several methods are presented to estimate fracture porosity. The methods rely on estimates of other fracture structural features, such as fracture spacing and apertures. In addition, the methods vary by spatial scale. Please indicate in the text that this leads to uncertainty in the facture porosity values to be used in the modeling. This information will need to be evaluated thoroughly in interpreting the model forecasts.	Added the following to the end of Section 5.3.4.5: "Large uncertainty is associated with fracture porosity and thus the corresponding effective porosity. The available data will be used for setting bounds on the range of permissible values for this parameter. Matching model forecasts to the measured RN observations at sampling wells will help constrain the range of values for the purpose of forecasting CBs." .
9.	Page 5-25, Section 5.3.4.2, Third Paragraph, Third Sentence:		The three colors shown on Figures 5-4 and 5-5 are not labeled as to the three different types of data. Please provide a key on the Figures for this information.	Inserted explanation of colors into the figure captions in Figures 5-4 and 5-5.

[a]Comment Types: M = Mandatory, S = Suggested.
Return Document Review Sheets to Environmental Management Nevada Program Operations Activity, Attn: QAC, M/S NSF 505

NEVADA ENVIRONMENTAL MANAGEMENT OPERATIONS ACTIVITY
DOCUMENT REVIEW SHEET

1. Document Title/Number: Contaminant Transport Parameters for the Groundwater Flow and Contaminant Transport Model of Corrective Action Units 101 and 102: Central and Western Pahute Mesa, Nye County, Nevada				2. Document Date: April 2021
3. Revision Number: Revision 0				4. Originator/Organization: Navarro
5. Responsible EM Nevada Program Activity Lead: John Myers				6. Date Comments Due: 25 June 2021
7. Review Criteria:				
8. Reviewer/Organization Phone No.: NDEP				9. Reviewer's Signature:
10. Comment Number/Location		11. Type[a]	12. Comment	13. Comment Response
10.	Page 5-32, Section 5.3.4.4.1, First Paragraph, Last Sentence:		The conclusion presented in this sentence needs to be explained in more detail in the text as to what comparisons are being used to come to this conclusion and how the comparisons demonstrate this concept.	Changed the last sentence to read as follows: "The comparison of the hydraulic and tracer test-derived fracture porosities supports the conclusion that fracture porosities calculated from hydraulic data are smaller than those obtained from tracer test data."

[a]Comment Types: M = Mandatory, S = Suggested.
Return Document Review Sheets to Environmental Management Nevada Program Operations Activity, Attn: QAC, M/S NSF 505

11.	Page 5-58, Table 5-16 and Page 5-59, Table 5-17:		Please add a column in each Table indicating the number of data available in the calculation of the standard deviation.	In Table 5-16, values are calculated from hydraulic conductivity and fracture spacing data. Added a column showing the number of samples for each data type for each HGU. Deleted the column showing standard deviation. Changed the text to read as follows: "Table 5-16 lists the estimated mean, minimum, and maximum fracture apertures for each of the HGUs calculated from fracture spacing and hydraulic conductivity. The number of values available for hydraulic conductivity and fracture spacing are also shown in Table 5-16. Because the numbers of values available for hydraulic conductivity were different from that for fracture spacing, the mean, minimum, and maximum fracture aperture values were estimated using the respective mean, minimum, and maximum values of fracture spacing and hydraulic conductivity yielding the three estimates of fracture aperture shown for each HGU." In Table 5-17, values reported by Drellack et al. (1997) are obtained from core inspection, so a column was added showing the length of the core examined in that study (Table 1-6 of the reference). Replaced the paragraph with the following: "Table 5-17 summarizes the findings regarding aperture reported by Drellack et al. (1997) obtained from core inspection. The table also shows the length of the core examined by HGU in that study. The minimum and maximum in Table 5-17 are formed from the data taken from Table 4-2 of Drellack et al. (1997), and the averages are taken from the same table. Section 1.3.1 of Drellack et al. (1997) states that "A total of 1,578 meters (m) (5,177 feet) of core was examined from December 1995 to February 1996…A total of 2,851 natural fractures was examined during the analysis. Because only natural fractures were described, it was necessary to differentiate between natural fractures and breaks induced during coring or handling." The estimated "percent open" of the fractures examined is included in the same table and ranges from 1 to 99 percent, depending on the boring and HGU examined."
12.	Page 5-109, Section 5.8.4.2, Figure 5-37:		Please add an R2 value for the linear fit to the Figure.	Value added.

[a]Comment Types: M = Mandatory, S = Suggested.
Return Document Review Sheets to Environmental Management Nevada Program Operations Activity, Attn: QAC, M/S NSF 505

Plate 1

Correlation of Stratigraphic and Hydrostratigraphic Units of the Pahute Mesa-Oasis Valley Hydrostratigraphic Framework Model

Plate 1
Correlation of Stratigraphic and Hydrostratigraphic Units of the Pahute Mesa-Oasis Valley Hydrostratigraphic Framework Model

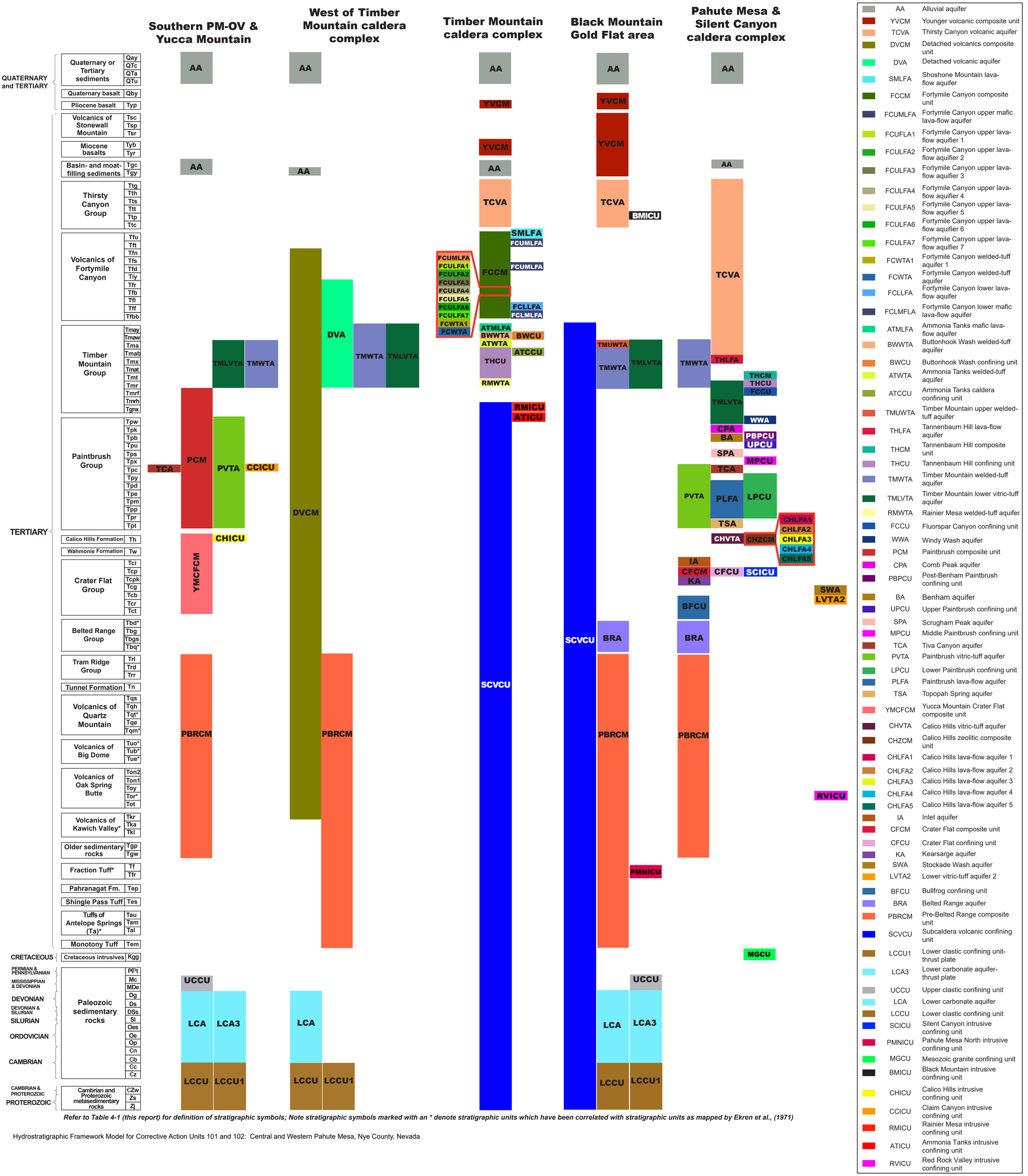

*Refer to Table 4-1 (this report) for definition of stratigraphic symbols; Note stratigraphic symbols marked with an * denote stratigraphic units which have been correlated with stratigraphic units as mapped by Ekren et al., (1971)*

DISTRIBUTION

	Copies
W.R. Wilborn Environmental Management Nevada Program 100 N. City Parkway, Suite 1750 Las Vegas, NV 89106	1 electronic media
John Myers Environmental Management Nevada Program 100 N. City Parkway, Suite 1750 Las Vegas, NV 89106	1 electronic media
Chris Andres State of Nevada Nevada Division of Environmental Protection 375 E. Warm Springs Road, Suite 200 Las Vegas, NV 89119	1 electronic media
Michelle Bourret Los Alamos National Laboratory Bikini Atoll Road, SM-30, MS T003 Los Alamos, NM 87545	1 electronic media
Steve Carle Lawrence Livermore National Laboratory 7000 East Avenue, L-231 Livermore, CA 94551-9900	1 electronic media
Andrew Tompson Lawrence Livermore National Laboratory 7000 East Avenue, L-103 Livermore, CA 94550-9909	1 electronic media
Mavrik Zavarin Lawrence Livermore National Laboratory 7000 East Avenue, L-103 Livermore, CA 94550-9909	1 electronic media
Jeff V. Sanders U.S. Geological Survey 160 N. Stephanie Street Henderson, NV 89074	1 electronic media

	Copies
Tracie Jackson U.S. Geological Survey 160 N. Stephanie Street Henderson, NV 89074	1 electronic media
Ken Ortego Mission Support and Test Services, LLC P.O. Box 98521, M/S NLV 082 Las Vegas, NV 89193-8521	1 electronic media
Chuck E. Russell Desert Research Institute 755 E. Flamingo Las Vegas, NV 89119	1 electronic media
Mark Hausner Desert Research Institute 2215 Raggio Parkway Reno, NV 89512	1 electronic media
Ken Rehfeldt Navarro 100 N. City Parkway, Suite 1750 Las Vegas, NV 89106	1 electronic media
Sharad Kelkar Navarro/HGL 100 N. City Parkway, Suite 1750 Las Vegas, NV 89106	1 electronic media
Irene Farnham Navarro 100 N. City Parkway, Suite 1750 Las Vegas, NV 89106	1 electronic media
Brian Haight Navarro 100 N. City Parkway, Suite 1750 Las Vegas, NV 89106	1 electronic media

	Copies
John Londergan Navarro 100 N. City Parkway, Suite 1750 Las Vegas, NV 89106	1 electronic media
Jeff Wurtz Navarro 100 N. City Parkway, Suite 1750 Las Vegas, NV 89106	1 electronic media
Tim deBues Navarro 100 N. City Parkway, Suite 1750 Las Vegas, NV 89106	1 electronic media
Environmental Management Records Environmental Management Nevada Program 100 N. City Parkway, Suite 1750 Las Vegas, NV 89106	1 electronic media
Navarro Central Files 100 N. City Parkway, Suite 1750 Las Vegas, NV 89106	1 electronic media